ELECTROMAGNETIC SCATTERING FROM VEGETATION CANOPIES

by

Kamal Sarabandi

A dissertation submitted in partial fulfillment
of the requirements for the degree of
Doctor of Philosophy
(Electrical Engineering)
in The University of Michigan
1989

Doctoral Committee:

Professor F.T. Ulaby, Co-chairman
Professor T.B.A. Senior, Co-chairman
Professor C.M. Chu
Professor P.G. Federbush
Associate Professor P.B. Katehi

ABSTRACT

ELECTROMAGNETIC SCATTERING FROM VEGETATION CANOPIES

by

Kamal Sarabandi

Chairpersons: F.T. Ulaby, T.B.A. Senior

Satellite-borne imaging radar has been proposed by the remote sensing community as a potential sensor for the acquisition of quantitative information about forested area on a global scale. To achieve this goal, it is necessary to develop retrieved algorithms that can provide reasonable estimate of vegetation biomass, leaf moisture content, and other physical parameters of tree canopies from multi-frequency/multipolarization observations of their radar backscattering coefficients. Ritrieval algorithms often are called "inverse problem" because their input/output parameters are the inverse of those associated with the direct problem, which in the present case refers to the development of a radar scattering model that relates the radar response to the canopy architecture and associated parameters.

This thesis provides electromagnetic solutions to several problems associated with scattering from tree canopies. The forest canopy is modelled in the form of layers comprised of randomly distributed particles with known statistical properties. In

Chapters 2-8 effective scattering models for different constituent particles of vegetation canopies are developed by employing appropriate asymptotic solutions and approximations. The effects of various physical features of the particles, such as curvature and variation in thickness for planar leaves and roughness for tree trunks, on their scattering behavior are examined. In Chapter 9 the scattering problem of inhomogeneous layered media is formulated *via* the vector radiative transfer equations and a first-order solution for the radar scattering coefficients is obtained. The radiative transfer solution is formulated in terms of two sets of input functions: the scattering matrices of the constituent particles, which are given in Chapters 2-8, and the size and orientation distribution functions of the particles.

The radar scattering model and associated input functions can be used to conduct sensitivity analyses to determine the response to individual canopy parameters or combination of parameters. The results of such sensitivity studies often are the key ingredients needed for the development of effective retrieval algorithms.

To my mother Fatemeh-Jale, my father Abas-Ali, and my wife Shiva for their love, support and encouragement.

ACKNOWLEDGEMENTS

The author wishes to express his gratitude to the members of his committee and to the Radiation Laboratory for supporting this research. Special thanks are due to Professors Thomas B. A. Senior and Fawwaz T. Ulaby, the committee chairmen, for their guidance and invaluable support throughout the course of this work.

He would also like to thank the following friends and colleagues for their friendship and enlightening conversations during his graduate studies: Kasra Barkeshli, Jianming Jin, Leland Pierce, Kyle McDonald, Mark Ricoy, Mohammad-Ali Tassoudji, Ahad Tavakoli, Saeid Tehrani, and Mike Whitt.

TABLE OF CONTENTS

LIST OF FIGURES

Figure

LIST OF TABLES

LIST OF APPENDICES

Appendix

CHAPTER I

INTRODUCTION

1.1 Motivations and Objectives

The ability of microwaves to penetrate through the atmosphere, clouds and to some extent rain, has made the microwave spectrum particularly useful for remote sensing applications. In addition to these advantages, microwave sensors can operate independently of the sun as a source of illumination and microwaves can penetrate more deeply into vegetation and ground than, for example, optical waves.

Understanding the interaction of electromagnetic waves with geophysical media is necessary for the interpretation of remote sensing observations. To this end, radar remote sensing investigations have been conducted for snowpacks, ice-covered land [Waite and McDonald 1969; Hofer and Shanda 1978] and water surfaces, vegetation media [Bush and Ulaby 1976; Engheta and Elachi 1982], and soil moisture applications. Geophysical media often are mixtures of different types of particles. Their behavior at microwave frequencies can be characterized by the physical parameters of the particles, such as size, concentrations or fractional volumes, shapes, orientations, and dielectric properties. These physical parameters usually are determined by ground-truth measurements.

One of the research areas of interest in remote sensing is the development of theo-

retical models for vegetation-covered terrain. At centimeter and shorter wavelengths, a vegetation canopy may be considered as an inhomogeneous medium comprised of discrete scatterers, such as leaves and stalks, distributed randomly in a free-space background. The angular, spectral, and polarization behavior of canopy scattering is determined by the sizes, shapes, and dielectric properties of the individual scatterers.

Several theoretical models have been constructed for interpreting remote sensing measurements. Because of the complex nature of the scattering problem, it is very difficult to find an exact solution. Therefore, various kinds of simplifications to the physical parameters and approximations to the equations must be applied in order to find a solution. The available models for vegetation-covered land may be categorized into two groups, semi-empirical models, and approximate theoretical models.

Semi-empirical models consist of simple formulae that can be calculated readily [Attema and Ulaby 1978]. They are often derived heuristically and contain matching parameters that sometimes do not correspond to the physical parameters of the target.

Existing theoretical models for electromagnetic backscattering from a collection of discrete scatterers may in turn be categorized into two modeling techniques, continuous and discrete random medium techniques. In the continuous case, the random medium is modeled by assuming that its permittivity $\epsilon(x, y, z)$ is a random process whose statistical behavior is known. The analysis of this problem can then proceed in a number of ways. One method involves calculating the mean field using the Foldy approximation [Lang 1981], from which an equivalent medium for the scattering region can be defined. The backscattered energy is found by viewing the scatterer as being embedded in the equivalent medium, and then single scattering theory is used to find the scattered field. This technique is referred to in the literature [Rosenbaum

and Bowles 1974] as the distorted-Born approximation. To simplify the mathematics involved in this technique, the particles usually are assumed to have simple shapes such as dipoles or spheres. Another method used to obtain the scattered fields from a continuous random medium is the radiative transport approach [Ishimaru 1978]. Here, it is assumed that there is no correlation between fields in different directions of propagation and, therefore, the addition of powers rather than the addition of fields holds. The transport equations are obtained in terms of the statistic of $\epsilon(x, y, z)$ [Tsang and Kong 1978]. Study of radiative transfer equations has focused on single and multiple scattering, and to keep the formulation tractable, the particles usually are assumed to be spherical. This leads to the absence of depolarization, whereas for natural particles the shape is conducive to the generation of significant depolarization in the backscattering direction.

In the discrete case, it is assumed that the particles are sparse in the random medium and single scattering theory is applied to evaluate the backscattered energy [Engheta and Elachi 1982: Karam et al 1987].

To model a vegetation-covered medium accurately, complete knowledge of single scattering behavior of the constituent particles is necessary. This allows us to investigate the significance of the associated physical parameters, and to determine the range of validity of different approximations and simplifications.

In all of the above mentioned models for vegetation-covered ground the leaves are assumed to be small dipoles, spheres, or planar dielectric discs, and the branches and trunks are taken to be circular homogeneous dielectric cylinders. In nature, leaves are not planar and tree trunks are not necessarily circular and homogeneous. Furthermore, trunks usually have a rough surface. The objective of this thesis is to develop more realistic single scattering models for the constituent particles of a

vegetation canopy and a more realistic model for forest covered land. The thesis is composed of three major parts:

(1) The development of an effective model for vegetation leaves and examination of the effects of surface curvature and the spatial variations in thickness and moisture content across the planar leaves. Also the developement of a scattering model for vegetation needles with different cross section geometries.

(2) The development of a scattering model for tree trunks and branches with arbitrary cross section, taking into account the effects of surface roughness of the bark layer and the radial variations of moisture content.

(3) The development a scattering model for forest canopies using the radiative transfer theory.

1.2 Dielectric Behavior of Vegetation Materials

The dielectric constant and shape of an object are the two major factors that affect its electromagnetic scattering properties. Here, we shall briefly discuss the primary parameters that control the dielectric constant of leaves and branches, and then we shall follow up with a preliminary examination of their structures.

Characterization of the dielectric constant of vegetation materials has received extensive attention because of its important role in scattering of electromagnetic waves. Vegetation material is a heterogeneous mixture of water, minerals, bulk vegetation material and air. An "effective", or equivalent, dielectric constant for a heterogeneous medium may easily be obtained if the size of the inclusions is much smaller than the wavelength.

Expressions for the equivalent dielectric constant of a heterogeneous vegetation

material usually are functions of the microwave frequency, the gravimetric water content, the salinity of the fluid contained in the vegetation, and the vegetation density [El-Rayes and Ulaby 1987].

Because a large part of the vegetation material is water, its dielectric constant is strongly governed by the dielectric constant of water and the water content . The dielectric constant of pure water is relatively high at microwave frequencies because the water molecule is polarized and behaves like a small free electric dipole whose direction follows the applied electric field. A model for the dielectric constant of water based on the interaction of charge displacement in nuclei and the dipole moment of molecules was first derived by Debye. The complex dielectric constant $\epsilon = \epsilon' + i\epsilon''$ is given as a function of frequency by

$$\epsilon = \epsilon_\infty + \frac{\epsilon_s - \epsilon_\infty}{1 - i\omega T}$$

where ϵ_∞ and ϵ_s are the dielectric constant of water at very high and very low frequencies, respectively, T is the relaxation time-constant due to inertia of the dipole moments. The quantities ϵ_s and T are functions of temperature. Consequently, the complex dielectric constant of water also depends on temperature [Stogryn 1971].

Dissolved impurities in water can change the dielectric constant of pure water by introducing an ionic conductivity term:

$$\epsilon = \epsilon_\infty + \frac{\epsilon_s - \epsilon_\infty}{1 - i\omega T} + i\frac{\sigma_i}{\omega\epsilon_0}$$

where σ_i is the ionic conductivity. The salinity of a solution is defined as the total mass of dissolved solid salt in grams in one kilogram of solution. Salinity exercises a minor influence on the permittivity ϵ' of a saline solution, but has a direct effect on the loss factor ϵ'' (through σ_i), particularly at frequencies below 5 GHz.

Density of bulk vegetation material also affects its dielectric constant. This effect is recognizable at low moisture levels or at high frequencies where the dielectric constant of water is not the dominant factor. A general semi-empirical expression for dielectric constant of vegetation material was developed by El-Rayes and Ulaby [1987] which shows the influence of each physical parameter on the dielectric constant. Accuracy of these models are within $\pm 20\%$ and in order to obtained accurate values of dielectric constant a measurement technique is proposed as explained in Appendix A.

1.3 The Structure of a Tree

In order to characterize the electromagnetic scattering behavior of trees, we first need to understand their biophysical structure. From an electromagnetic scattering point of view, plants are comprised of two major constituents: leaves, and trunks and stems. Here, we briefly discuss the pertinent biophysical structure and function of leaves, trunks and stems in trees.

1.3.1 Leaf Structure

Leaves come in various shapes and sizes and in general are categorized into needle-shaped and planar. Vegetation needles uaually have a very small cross section compared to their length and come with semi-circular, triangular, or circular sector cross section. Planar leaves range from broad fronds to tiny scales with a wide variety of shapes. A leaf mainly consists of photosynthetic cells known as *parenchyma*. These cells are many-sided with thin, flexible cell walls. Leaves contain two types of photosynthetic parenchyma cells: *palisade parenchyma*, consisting of column-shaped cells in which most photosynthesis takes place, and *spongy parenchyma*, which consists of

irregularly shaped cells with large spaces between them Fig. 1.1. These spaces are filled with gases, including water vapor, oxygen, and carbon dioxide.

Palisade and spongy parenchyma make up the *mesophyll* which is completely enclosed in an almost airtight wrapping made up of epidermal cells. These cells secrete a waxy substance that forms a coating, the cuticle, over the outer surface of the epidermis. The epidermal cells and the cuticle are transparent, permitting light to penetrate to the photosynthetic cells.

Substances move into and out of the leaf by two different ways. Water and minerals are supplied to the leaf cells by the veins. The veins pass through the leaf stalk and are connected to the vascular tissues of the stem and the root. The veins branch and divide into finer and finer bundles, reaching within a short distance of every photosynthetic cell.

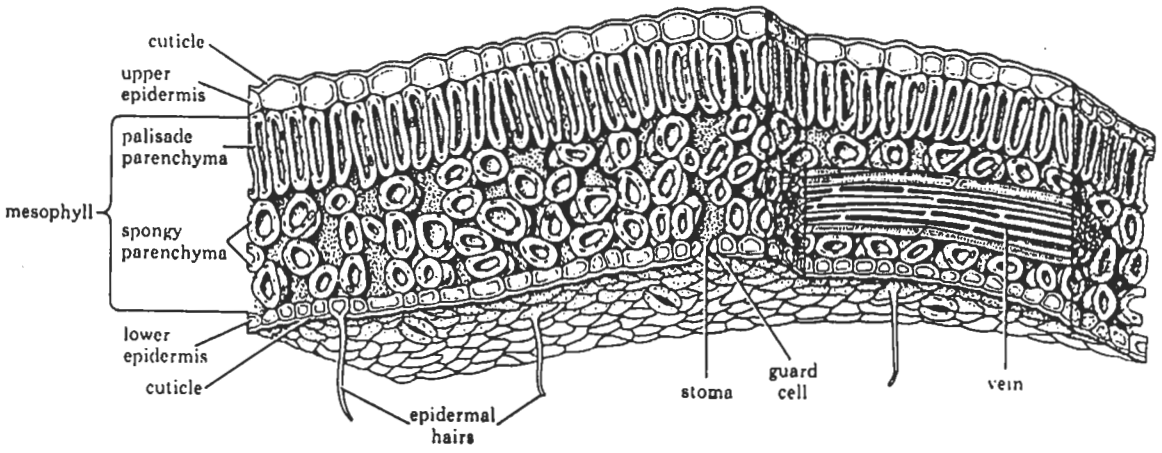

Figure 1.1: The structure of a leaf

Carbon dioxide, water vapor, and oxygen move into and out of the leaf by diffusion through *stomata*. A stoma consists of a small opening, or pore; it is surrounded by two specialized cells in the leaf epidermis, called guard cells, that open and close the

pore. Stomata are commonly most abundant on the undersurface of the leaves.

The water content and the density, and in turn the dielectric constant, are higher in the upper surface (palisade region) of a leaf than in its undersurface (spongy region). Because the leaf thickness is much smaller than the wavelength of the incident wave at centimeter wavelengths, a leaf can be considered a homogeneous dielectric slab. At higher frequencies, a stack of dielectric slabs with different dielectric constants is a more accurate representation. Most leaves are thin, curved sheets whose thickness ranges from 0.1 mm to 0.5 mm. Both thickness and water content of a leaf are slightly higher at its center than at the edges.

1.3.2 Trunk and Branch Structure

Trunks and branches are mainly composed of vascular tissues known as *phloem* and *xylem* Fig. 1.2, which, in turn, consist of specialized conducting cells, supporting fibers, and *parenchyma* cells (companion cells). Conducting cells of phloem transport the product of photosynthesis , chiefly sucrose, from leaves to the nonphotosynthetic cells of the plant. Specialized cells in the xylem conduct water and other minerals from the roots to the other parts of the plant's body. The conducting cells of the xylem are *tracheids* and *vessel members*. These cells are dead at functional maturity. Water passes from one tracheid to another through the pits. Vessel members form a continuous vessel which is a more effective conduit than a series of tracheids.

The production of new cells by *lateral meristem*, which are known as *vascular cambium* and *cork cambium*, increases the diameter of trunks and stems. This is known as secondary growth. The vascular cambium is a thin cylindrical sheath of tissue that exists in-between the xylem and phloem. During the growing season, the cambium cells divide continually and add new xylem cells toward the inside of

the cambium and new phloem cells toward the outside. As the tree grows older, the living cells of the xylem in the center of the trunk die and form a dense central supporting column of the tree.

When the circumference of the stem increases by secondary growth, the outer skin (*epidermis*)becomes stretched and torn. Cork , the rough outer layer, which is a dead tissue at maturity, is produced from the cork cambium and functions as a protective layer for inner tissues by keeping them from drying out and by safeguarding them from mechanical injuries.

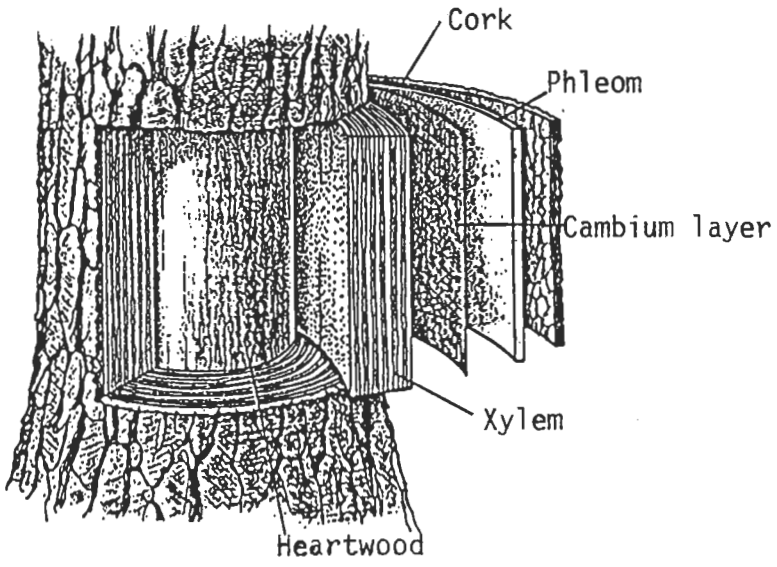

Figure 1.2: A tree trunk showing the relationships of the successive layers.

From a scattering point of view, the tree trunk is an inhomogeneous dielectric body. For waves with wavelengths much longer than the width of the annual rings, the trunk structure may be simplified into a three-layer stratified cylinder. The outer layer is rough and consists of dead cells; hence, its dielectric constant is low and only slightly lossy. The central layer, sapwood, contains tracheids and vessel members that carry high-dielectric fluids. Consequently, its dielectric constant is high and very lossy. The inner layer, heartwood, is denser, relatively drier, and its dielectric

constant is slightly smaller than that of the central layer. This characterization of the dielectric-constant profile of a tree trunk is consistent with the dielectric measurements of walnut trees at L-band [Dobson,1987].

The dielectric constant of each trunk layer for a given tree depends on the temperature, the time of day, the season, and several environmental factors. The peak-to-peak variation of the dielectric constant over a diurnal cycle is much larger for the central layer than for the inner and outer layers. This is due to the variation of water content in the xylem tissues which is directly proportional to the photosynthetic activities of the plant.

Shape is another important factor governing the scattering behavior of an object. At microwave frequencies and higher, the height of almost any tree is much greater than the wavelength of the incident wave. Hence, a tree trunk may be viewed as an infinitely long cylinder. The cross-section of the trunk is approximately circular. At frequencies in the lower part of the microwave spectrum the trunk cross-section may be considered exactly circular, but the effects of surface roughness and deviations from perfect circular geometry become significant as the electromagnetic wavelength approaches the spatial wavelength of the roughness spectrum. The thickness of each layer depends on the diameter of the trunk and on the specific tree type and age, but usually the bark thickness is very small compared with the diameter of the trunk cross-section. The thickness variation of the bark layer may be azimuthally periodic, random, or both.

1.4 Basic Equations and Definitions

The fundamental equations relating the four electromagnetic vector quantities, electric field ($\mathbf{E}$), magnetic field ($\mathbf{H}$), electric flux density ($\mathbf{D}$), and magnetic flux

density ($\mathbf{B}$) are known as Maxwell's equations. Physically, the sources of an electromagnetic field is a distribution of electric charge (ρ_e) and current ($\mathbf{J}_e$), but it is mathematically convenient to use magnetic charge (ρ_m) and current ($\mathbf{J}_m$) as well. If an explicit time dependence of the form $e^{-i\omega t}$ is assumed for all of the field quantities, the postulated Maxwell's equations become

$$\begin{aligned} \nabla \times \mathbf{E} &= i\omega\mathbf{B} - \mathbf{J}_m \\ \nabla \times \mathbf{H} &= -i\omega\mathbf{D} + \mathbf{J}_e \\ \nabla \cdot \mathbf{D} &= \rho_e \\ \nabla \cdot \mathbf{B} &= \rho_m \end{aligned} \tag{1.1}$$

with the following constitutive relations

$$\mathbf{D} = \epsilon\mathbf{E}$$

$$\mathbf{B} = \mu\mathbf{H}$$

For an impressed electric or magnetic source, a primary (or incident) field $\mathbf{E}^i$, $\mathbf{H}^i$ is established in the medium. If an object (scatterer) is placed in the medium, the original field will be perturbed and the perturbation is known as the scattered field $\mathbf{E}^s$, $\mathbf{H}^s$. Therefore through all space

$$\mathbf{E}^s = \mathbf{E} - \mathbf{E}^i \qquad \mathbf{H}^s = \mathbf{H} - \mathbf{H}^i$$

where $\mathbf{E}$, $\mathbf{H}$ is the total field in the presence of the body. When the body is finite in extent and the observation point is far from the body, the scattered field appears to originate at a point and the scatterer is described as a point target, as opposed to a distributed target like terrain. The scattering is attributable to electric currents that are induced inside and on the surface of the scatterer. The scattered field at any point $\mathbf{r}$ in space can then be determined from the electric and magnetic Hertz

vectors

$$\begin{aligned}\mathbf{\Pi}_e(\mathbf{r}) &= \tfrac{iZ_0}{4\pi k_0}\int_V \mathbf{J}_e(\mathbf{r}')\tfrac{e^{ik_0|\mathbf{r}-\mathbf{r}'|}}{|\mathbf{r}-\mathbf{r}'|}\mathrm{d}V' \\ \mathbf{\Pi}_m(\mathbf{r}) &= \tfrac{iY_0}{4\pi k_0}\int_V \mathbf{J}_m(\mathbf{r}')\tfrac{e^{ik_0|\mathbf{r}-\mathbf{r}'|}}{|\mathbf{r}-\mathbf{r}'|}\mathrm{d}V'\end{aligned} \tag{1.2}$$

where $\mathbf{J}_e$, $\mathbf{J}_m$ are the volume electric and magnetic current densities respectively, and the integration is carried out over the volume V occupied by the body. In (1.2) k_0 and $Z_0(=1/Y_0)$ are the propagation constant and intrinsic impedance, respectively, of free space. In terms of the Hertz vectors $\mathbf{\Pi}_e$, $\mathbf{\Pi}_m$, the scattered field is expressed as

$$\begin{aligned}\mathbf{E}^s(\mathbf{r}) &= \nabla\times\nabla\times\mathbf{\Pi}_e(\mathbf{r}) + ik_0Z_0\nabla\times\mathbf{\Pi}_m(\mathbf{r}) \\ \mathbf{H}^s(\mathbf{r}) &= \nabla\times\nabla\times\mathbf{\Pi}_m(\mathbf{r}) - ik_0Y_0\nabla\times\mathbf{\Pi}_e(\mathbf{r})\ .\end{aligned} \tag{1.3}$$

At large distances from the body, $\nabla\times() \approx ik_0\hat{r}\times()$ and hence

$$\begin{aligned}\mathbf{E}^s(\mathbf{r}) &= -k_0^2\{\hat{r}\times\hat{r}\times\mathbf{\Pi}_e + \hat{r}\times Z_0\mathbf{\Pi}_m\} \\ \mathbf{H}^s(\mathbf{r}) &= -k_0^2\{\hat{r}\times\hat{r}\times\mathbf{\Pi}_m + \hat{r}\times Y_0\mathbf{\Pi}_e\}\end{aligned} \tag{1.4}$$

which implies the fact that $\mathbf{E}^s$, $\mathbf{H}^S$ are perpendicular to $\hat{r}$. Moreover,

$$|\,\mathbf{r}-\mathbf{r}'\,| \approx r - \hat{r}\cdot\mathbf{r}' + \frac{1}{2}\frac{r'^2}{r}\{1-(\hat{r}\cdot\hat{r}')^2\}\ , \tag{1.5}$$

and if r is so large that over the entire volume occupied by the body the third term on the right hand side of (1.5) is negligible even when in the phase factor,

$$\int_V \mathbf{J}_{e,m}(\mathbf{r}')\frac{e^{ik_0|\mathbf{r}-\mathbf{r}'|}}{|\,\mathbf{r}-\mathbf{r}'\,|}\mathrm{d}v' = \frac{e^{ik_0r}}{r}\int_V \mathbf{J}_{e,m}(\mathbf{r}')e^{-ik_0\hat{r}\cdot\mathbf{r}'}\mathrm{d}v'\ . \tag{1.6}$$

The accepted requirement for the validity of (1.6) is

$$r > \frac{2D^2}{\lambda_0} \tag{1.7}$$

where D is the maximum dimension (diameter) of the body, and this implies that phase differences of up to 22.5 degrees between the contributions from individual parts of the body are deemed negligible. Equation (1.7) defines the far zone of the

body, and (1.4) and (1.6) then show that in the far zone the scattered field looks like a spherically outgoing wave attributable to electric and magnetic sources located at the origin.

To model a medium consisting of discrete randomly oriented particles, it is often required to express the incident and scattered fields of a single particle with respect to a fixed coordinate frame. Suppose the particle is located at the origin of a general Cartesian coordinate system (X, Y, Z) and the incident field is a plane wave. If the plane wave is travelling in direction $\hat{k}_i$, its electric field vector may be written in terms of vertical and horizontal polarization components, E_v^i and E_h^i , using the right-handed coordinate system $(\hat{v}_i, \hat{h}_i, \hat{k}_i)$ shown in Fig. 1.3,

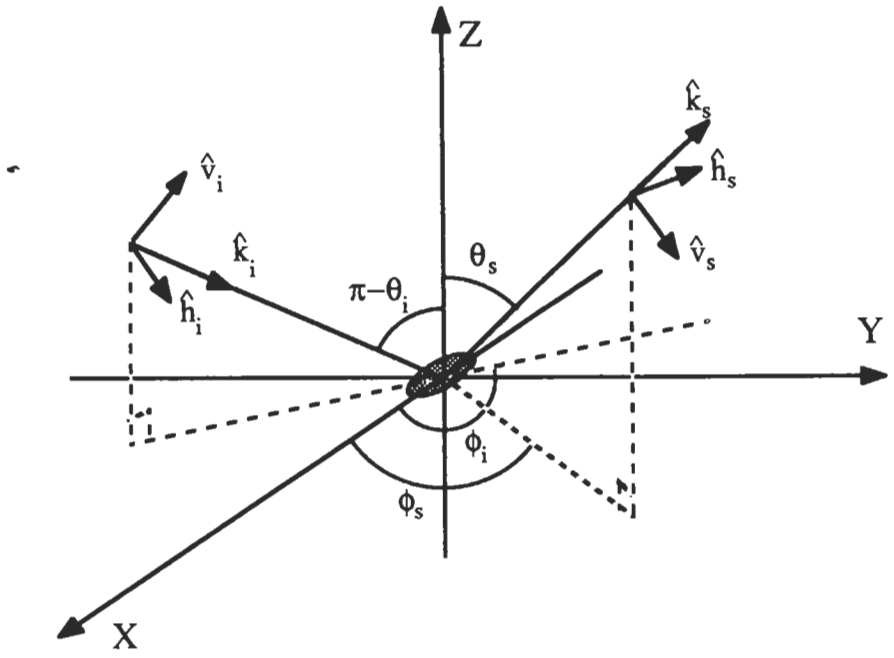

Figure 1.3: Geometry of scattering of a plane wave from a particle.

$$\mathbf{E}^i = (E_v^i \hat{\mathbf{v}}_i + E_h^i \hat{\mathbf{h}}_i) e^{ik_0 \hat{k}_i \cdot \mathbf{r}}, \tag{1.8}$$

where

$$\begin{aligned} \hat{v}_i &= \cos\theta_i \cos\phi_i \hat{x} + \cos\theta_i \sin\phi_i \hat{y} - \sin\theta_i \hat{z} \\ \hat{h}_i &= -\sin\phi_i \hat{x} + \cos\phi_i \hat{y} \\ \hat{k}_i &= \sin\theta_i \cos\phi_i \hat{x} + \sin\theta_i \sin\phi_i \hat{y} + \cos\theta_i \hat{z}. \end{aligned} \tag{1.9}$$

The scattered field in the far zone of the point target, in the direction $\hat{k}_s$, is a spherical wave that can be expressed in terms of the scattered coordinate system $(\hat{v}_s, \hat{h}_s, \hat{k}_s)$ as

$$\mathbf{E}^s = E_v^s \hat{\mathbf{v}}_s + E_h^s \hat{\mathbf{h}}_s,$$

where

$$\begin{aligned} \hat{v}_s &= \cos\theta_s \cos\phi_s \hat{x} + \cos\theta_s \sin\phi_s \hat{y} - \sin\theta_s \hat{z} \\ \hat{h}_s &= -\sin\phi_s \hat{x} + \cos\phi_s \hat{y} \\ \hat{k}_s &= \sin\theta_s \cos\phi_s \hat{x} + \sin\theta_s \sin\phi_s \hat{y} + \cos\theta_s \hat{z}. \end{aligned} \tag{1.10}$$

For the backscattering case, $\theta_i + \theta_s = \pi$, $\phi_i + \phi_s = \pi$, $\hat{k}_s = -\hat{k}_i$, $\hat{v}_s = \hat{v}_i$, and $\hat{h}_s = -\hat{h}_i$.

Apart from the spherical phase and amplitude factors, the scattered field is related to the incident field by the scattering matrix $\mathbf{S}$, i.e.

$$\mathbf{E}^s = \frac{e^{ik_0 r}}{r} \mathbf{S} \mathbf{E}^i, \tag{1.11}$$

where

$$\mathbf{S} = \begin{bmatrix} S_{vv} & S_{vh} \\ S_{hv} & S_{hh} \end{bmatrix}$$

is defined in terms of the scattering amplitudes S_{mn} with m and n denoting the polarizations (v or h) of the scattered and incident fields, respectively. The scattering amplitude S_{mn} is, in general, a complex quantity in terms of which the radar cross section (RCS) of the target, σ_{mn}, is given by

$$\sigma_{mn} = 4\pi \mid S_{mn} \mid^2 \tag{1.12}$$

Interest in measuring **S** stems from the fact that if the elements of **S** are known, we can compute the RCS of the target that would be observed by a radar with any specified combination of transmit and receive antenna configurations, including elliptical and circular polarizations [Zebker et al, 1987].

CHAPTER II

SCATTERING MODEL FOR A FLAT LEAF

2.1 Introduction

Leaves are a significant feature of any vegetation canopy, and for remote sensing purposes it is important to develop an effective model for predicting the scattering from a leaf. Although most leaves are irregular in shape and are not flat, they are often modeled as flat circular discs with known radius, thickness, and dielectric constant [Levine et al, 1983, 1985]. This brings up the following set of fundamental questions:

(1) What formulation might one use to characterize the backscattering and extinction cross sections of a regularly-shaped (elliptical or rectangular) flat leaf?

(2) How does one relate the radar cross section σ to the leaf moisture content Mg?

(3) Is it possible to approximate the scattering and extinction cross sections of a flat irregularly-shaped leaf using the formulations for a rectangular leaf of equal physical area?

(4) What is the effect of leaf curvature on its scattering behavior?

In this chapter we shall address the first two questions by proposing a resistive sheet model in conjunction with physical optics and verifying the model with experimental

measurements conducted for sections of leaves (all cut in the shape of a rectangle) at various levels of moisture content. The scattering is determined by the (complex) resistivity which is, in turn, entirely specified by the gravimetric moisture content of the leaf. The result based on the physical optics approximation is compared with the exact solution obtained using the method of moments for a resistive strip, and with a uniform second order GTD solution for perfectly conducting strip. The third question is partially examined by comparing the scattering pattern calculated for a rectangular plate with measurements obtained for an irregularly-shaped leaf. Exploration of the effects of leaf curvature will be the subject of Chapter 3.

2.2 Experimental Procedure

The radar cross section (RCS) measurements reported in this chapter were made at 10 GHz using a small rectangular horn antenna connected to a HP 8510A network analyzer, as illustrated by the sketch in Fig. 2.1. The network analyzer has a time domain capability which enables us to separate the target return from other spurious system environment responses. The horn antenna, whose aperture measured $6cm \times 6cm$, was located at the throat of a small anechoic chamber, and the leaf was supported by a set of parallel strings stretched between two synchronously rotating stepper motors at the top and bottom of the chamber to facilitate the target positioning. The computer controlled stepper motors permit measurements in specified increments in angle θ between the backscattered direction and the normal to the plane of the leaf. Also a tilt angle β between the horizontal plane and normal to the plane of the leaf can be achieved by inserting a piece of styrofoam between the strings.

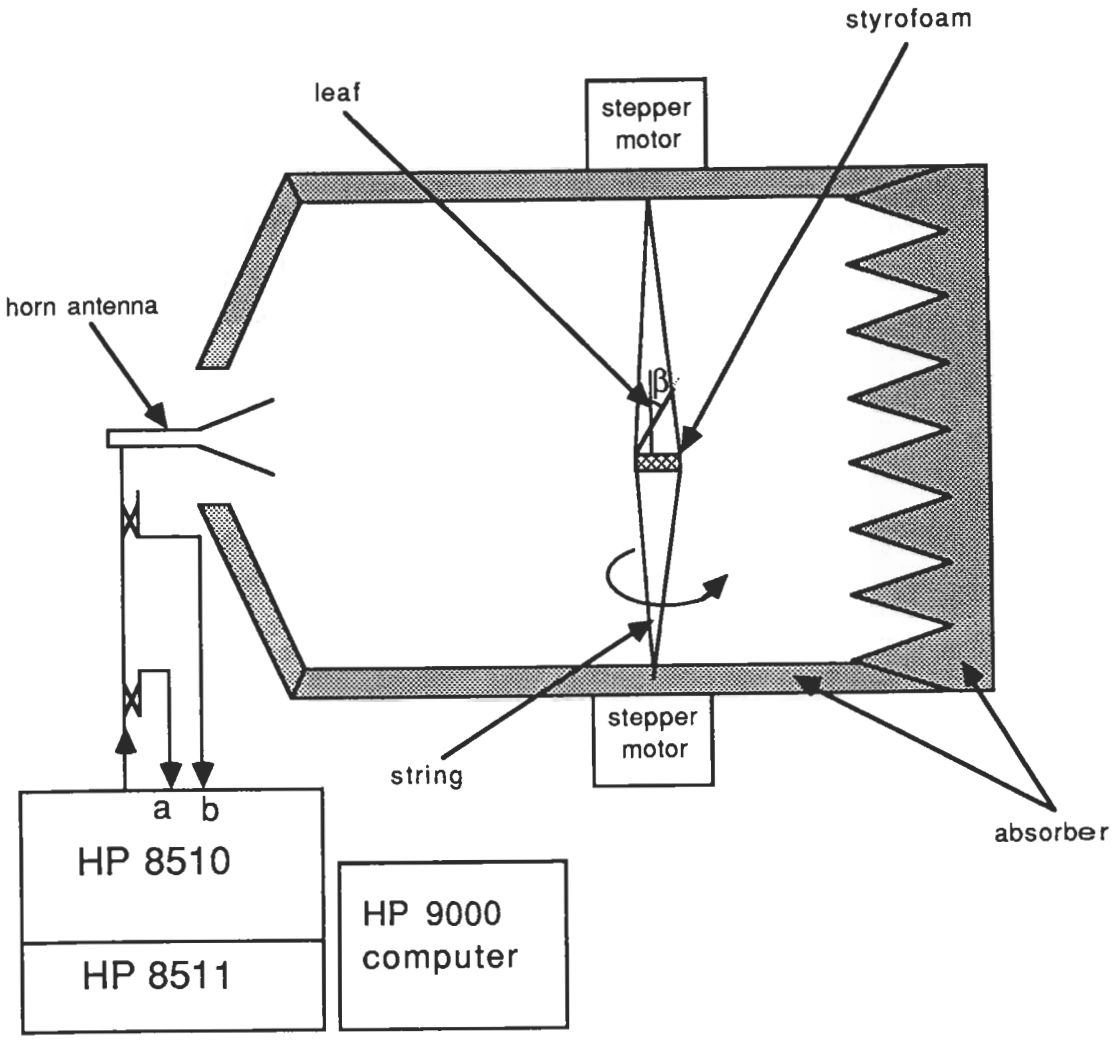

Figure 2.1: Schematic of the RCS measurement system.

2.2.1 System Sensitivity and Calibration

The HP 8510A is a vector network analyzer capable of measuring both the amplitude and phase of the reflected signal (channel b in Fig. 2.1) relative to a sample of the transmitted signal (channel a in Fig. 2.1). To enhance the measurement sensitivity of the system, two measurements are made: one for the background alone, which includes the strings, and another with the target present. By subtracting the complex signal recorded for the background alone from that measured in the presence of the target, significant improvement is obtained in the target-to-background ratio.

Absolute calibration of the system was achieved by measuring the cross section σ of a metal sphere at the target range from the antenna. According to these measurements, the noise-equivalent σ of the system is about -80 dBsm. Consequently, in most cases only data above -60 dBsm was recorded, which corresponds to a target-to-background ratio of 20 dB or greater.

To test the linearity of the system and establish the extent of its dynamic range, RCS measurements were performed for seven metal spheres with diameters from 0.79 cm to $3.81cm$. The largest sphere was used to calibrate the system and the other six were used to evaluate the system accuracy by comparing the measured RCS with theoretical values computed from the Mie series. The continuous curve in Fig. 2.2 is a plot of σ/λ_0^2 as a function of D/λ_0 for a perfectly conducting sphere of diameter D, and the "o" represent the measured data. The rms error, computed for the six test spheres, is 0.33 dB.

2.2.2 Leaf Moisture and Thickness

The leaf moisture content was determined by measuring its weight immediately after measuring its RCS, and once again at the conclusion of the experiment. The

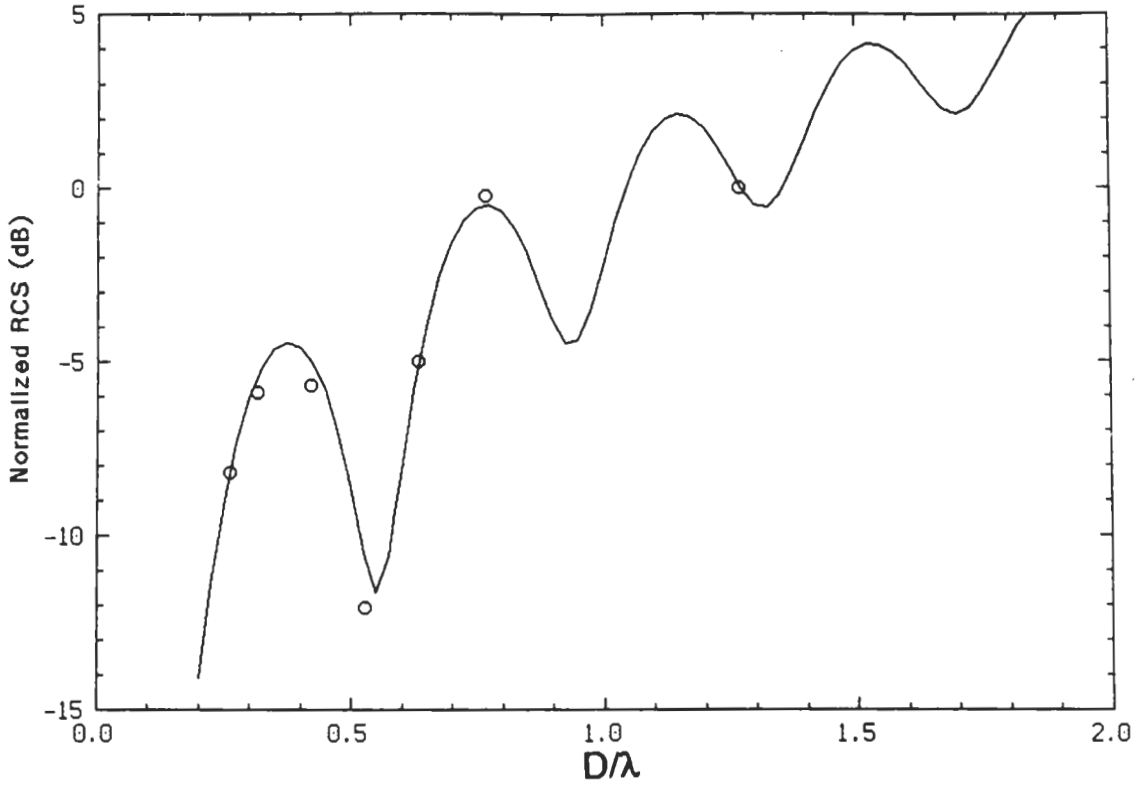

Figure 2.2: The calibration accuracy and dynamic range of the measurement system were evaluated by comparing the measured RCS of metal spheres (o) with theory.

latter measurement was made after drying the leaf in an oven at $70°C$ until equilibrium was reached. The difference in weight represents the weight of liquid water that was present in the leaf when its RCS was measured. The gravimetric moisture content Mg is the weight fraction of water in the leaf to the total weight.

Using the data measured and the models developed by Ulaby and El-Rayes [1987] for the dielectric constant of vegetation, the following simple expressions were generated to characterize the relative dielectric constant ϵ at 10 GHz and room temperature ($T = 22°C$):

$$\begin{aligned} \epsilon' &= 3.95e^{(2.79Mg)} - 2.25 \\ \epsilon'' &= 2.69e^{(2.15Mg)} - 2.68 \end{aligned} \tag{2.1}$$

It should also be mentioned that a more accurate estimate for the dielectric constant can be obtained if the volumetric moisture content M_v instead of M_g is known.

Leaf thickness, which was measured using a micrometer, was found to decrease slowly with time after cutting as a result of shrinking due to loss of water. The variation of leaf thickness τ (mm) with Mg is given by the empirical expression

$$\tau = 0.032Mg^2 + 0.091Mg + 0.075 \tag{2.2}$$

In addition, it was observed that the drying took place from the outer edges of the leaf inwards, so that the moisture content was no longer uniform across the leaf. In reality, however, the thickness generally decreases from base to tip and from center to sides and may vary by as much as 50% over the surface. Expression (2.2) provides an average value for thickness.

2.2.3 Types of RCS Measurements

Two sets of RCS measurements were conducted. The first data set involved a leaf that had been cut in the form of a rectangular plate $4cm \times 6cm$ in area. With

the long dimension oriented vertically, the cross section of the leaf was measured as a function of the angle of rotation θ about a vertical axis, with $\theta = 0$ corresponding to normal incidence. Each measurement scan consisted of σ versus θ in 5° steps from $-90°$ to $+90°$. Usually two scans were made, one with the antenna polarized with the electric vector vertical (E polarization) and the other with the magnetic vector vertical (H polarization). The first data set consisted of four pairs of scans corresponding to the rectangular leaf at $Mg = 85\%$ (freshly cut), 62% (a day later), and 0% (dry). The data comprising the second set are similar to those in the first except that the leaf was measured in its natural state without altering its shape. A profile is shown in the inset of Fig. 2.9.

Maintaining the leaf flat to within a fraction of a wavelength was a consistent problem in this phase of the investigation, particularly for the "naturally" shaped leaf after it had been allowed to dry for a few days.

2.3 Theoretical Model

2.3.1 A Resistive Sheet

A leaf can be viewed as a thin layer (of thickness τ) of a non-magnetic dielectric material whose complex relative permittivity is ϵ, and a widely-used model for such a layer is an infinitesimally thin resistive sheet whose resistivity is

$$R = \frac{iZ_0}{k_0\tau(\epsilon - 1)} \tag{2.3}$$

ohms per square. When $R = 0$ the sheet appears perfectly conducting and when $R = \infty$ it ceases to exist. The sheet is simply an electric current sheet whose strength is proportional to the local tangential electric field [Harrington and Mautz, 1975] *via* the single measurable quantity R. If $\hat{n}$ is the unit vector normal drawn

outwards to the upper (positive) side of the sheet and $[\ ]_-^+$ denotes the discontinuity across the sheet, the boundary conditions are

$$[\hat{n} \times \mathbf{E}]_-^+ = 0 \tag{2.4}$$

implying continuity of the tangential electric field (a consequence of the absence of any magnetic current), and

$$\hat{n} \times (\hat{n} \times \mathbf{E}) = -R\mathbf{J} \tag{2.5}$$

where

$$\mathbf{J} = [\hat{n} \times \mathbf{H}]_-^+ \tag{2.6}$$

is the total electric current supported. In recent years resistive sheets have been successfully employed in simulating a variety of dielectric structures. Diffraction effects have been studied analytically (see, for example, Senior [1979]) and, in addition, computer programs have been written to determine the field scattered by resistive strips and plates of arbitrary shape.

2.3.2 Scattering by an Infinite Planar Sheet

The scattering properties of a resistive sheet are most easily understood by considering the simple problem of a plane wave incident on an infinite sheet lying in the plane $y = 0$ of a Cartesian coordinate system (x, y, z).

For the case of E polarization in which the incident electric vector is perpendicular to the $x - y$ plane of incidence, we assume

$$\mathbf{E}^i = \hat{z} e^{ik_0(x \sin\theta_i - y \cos\theta_i)} \qquad (|\ \theta_i\ | \leq \pi/2) \tag{2.7}$$

implying

$$\mathbf{H}^i = -Y_0(\hat{x} \cos\theta_i + \hat{y} \sin\theta_i) e^{ik_0(x \sin\theta_i - y \cos\theta_i)}$$

The reflected and transmitted electric vectors can be written as

$$\mathbf{E}^r = -\hat{z}\Gamma_E e^{ik_0(x\sin\theta_i + y\cos\theta_i)}$$

and

$$\mathbf{E}^t = \hat{z}T_E e^{ik_0(x\sin\theta_i - y\cos\theta_i)}$$

respectively, where Γ_E and T_E are constants still to be determined, and by applying the boundary conditions (2.4)-(2.6) we obtain

$$\Gamma_E = \left(1 + \frac{2R}{Z_0}\cos\theta_i\right)^{-1}, \tag{2.8}$$

$$T_E = \frac{2R}{Z_0}\cos\theta_i\Gamma_E \tag{2.9}$$

The current density $\mathbf{J}$ supported by the sheet is $\mathbf{J} = \hat{z}J_z$ with

$$J_z = 2Y_0\cos\theta_i\Gamma_E e^{ik_0 x\sin\theta_i}, \tag{2.10}$$

and recognizing that for a perfectly conducting sheet the resistivity is zero which implies $\Gamma_E = 1$ and it follows that

$$J_z = \Gamma_E J_z^{pc} \tag{2.11}$$

where the superscript *pc* refers to the perfectly conducting case.

The analysis for H polarization in which the incident magnetic vector is perpendicular to the plane of incidence is very similar. The reflection and transmission coefficients are

$$\Gamma_H = \left(1 + \frac{2R}{Z_0}\sec\theta_i\right)^{-1} \tag{2.12}$$

and

$$T_H = \frac{2R}{Z_0}\sec\theta_i\Gamma_H \tag{2.13}$$

respectively, and the current density $\mathbf{J}$ supported by the sheet has only an x component ($\mathbf{J} = \hat{x}J_x$) with

$$J_x = 2\Gamma_H e^{ik_0 x \sin\theta_i} \ . \tag{2.14}$$

Thus

$$J_x = \Gamma_H J_x^{pc} \tag{2.15}$$

If $R \neq 0$, Γ_H decreases with increasing θ_i and vanishes at grazing incidence ($\theta_i = \pm\pi/2$).

2.3.3 Scattering by a Rectangular Resistive Plate

As a simple model of a leaf we consider a rectangular resistive plate occupying the region $|x| \leq a/2$, $|z| \leq b/2$ of the plane $y = 0$, and seek the physical optics approximation to the bistatic scattered field. From the expressions (2.11) and (2.15) for the currents on an infinite sheet it is evident that the analysis is very similar to that for a perfectly conducting plate, and it is sufficient to summarize the derivation.

For E polarization in which the incident electric vector is (2.7), the physical optics approximation to the current induced in the plate is given in (2.10). Since only an electric current is supported, the scattered field can be attributed to the electric Hertz vector

$$\mathbf{\Pi}_e(\mathbf{r}) = \hat{z}\frac{iZ_0}{4\pi k_0}\int_{-a/2}^{a/2}\int_{-b/2}^{b/2} J_z(x',z')\frac{e^{ik_0|\mathbf{r}-\mathbf{r}'|}}{|\mathbf{r}-\mathbf{r}'|}\mathrm{d}x'\mathrm{d}z'$$

where

$$\mathbf{r} = r(-\hat{x}\sin\theta_s + \hat{y}\cos\theta_s)$$

$$\mathbf{r}' = \hat{x}x' + \hat{z}z'$$

and in the far field

$$\mathbf{\Pi}_e(\mathbf{r}) = \hat{z}\frac{e^{ik_0 r}}{r}\frac{i}{2\pi k_0}ab\cos\theta_i\Gamma_E\frac{\sin X}{X}$$

with

$$X = \frac{k_0 a}{2}(\sin\theta_s + \sin\theta_i)$$

The scattered electric field is then

$$\mathbf{E}^s = \frac{e^{ik_0 r}}{r}\mathbf{S}_E(\theta_s, \theta_i)$$

where the far field amplitude is

$$\mathbf{S}_E(\theta_s, \theta_i) = \hat{z}\frac{i}{2\pi}k_0 ab\cos\theta_i \Gamma_E \frac{\sin X}{X} \tag{2.16}$$

In terms of the far field amplitude the bistatic scattering cross section is

$$\sigma = 4\pi|\mathbf{S}|^2 \tag{2.17}$$

implying

$$\sigma_E(\theta_s, \theta_i) = 4\pi \mid \frac{ab}{\lambda_0}\cos\theta_i \Gamma_E \frac{\sin X}{X} \mid^2 \tag{2.18}$$

For H polarization in which the incident magnetic vector is in the z direction, the analysis is similar. The physical optics approximation to the current is (2.14), and in the far field the resulting electric Hertz vector is

$$\mathbf{\Pi}_e(\mathbf{r}) = \hat{x}\frac{e^{ik_0 r}}{r}\frac{iZ_0}{2\pi k_0}ab\Gamma_H \frac{\sin X}{X}$$

The scattered magnetic field is then

$$\mathbf{H}^s = \frac{e^{ik_0 r}}{r}\mathbf{S}_H(\theta_s, \theta_i)$$

with

$$\mathbf{S}_H(\theta_s, \theta_i) = \hat{z}\frac{-i}{2\pi}k_0 ab\cos\theta_s \Gamma_H \frac{\sin X}{X} \tag{2.19}$$

and the bistatic scattering cross section is

$$\sigma_H(\theta_s, \theta_i) = 4\pi \mid \frac{ab}{\lambda_0}\cos\theta_s \Gamma_H \frac{\sin X}{X} \mid^2 \tag{2.20}$$

In the backscattering direction ($\theta_i = \theta_s$) the only polarization dependence is provided by the parameter Γ and

$$\sigma_{E,H}(\theta_i, \theta_i) = \mid \Gamma_{E,H} \mid^2 \sigma_{pc} \tag{2.21}$$

where σ_{pc} is the backscattering cross section of the perfectly conducting plate:

$$\sigma_{pc} = 4\pi \left\{ \frac{A}{\lambda_0} \cos\theta_i \frac{\sin(k_0 a \sin\theta_i)}{k_0 a \sin\theta_i} \right\}^2 \tag{2.22}$$

in which $A = ab$ is the plate area. In terms of the far field amplitude $\mathbf{S}(\theta_s, \theta_i)$ the extinction cross section is

$$\sigma^{ext} = \frac{4\pi}{k_0} \mathrm{Im}[\mathbf{S}(\theta_i + \pi, \theta_i)] \tag{2.23}$$

and thus

$$\sigma^{ext}_{E,H} = 2A \cos\theta_s \mathrm{Re}[\Gamma_{E,H}] \tag{2.24}$$

We recognize $2A\cos\theta_i$ as the extinction cross section of a perfectly conducting plate of area A, and at normal incidence

$$\sigma^{ext}_E = \sigma^{ext}_H$$

2.4 Comparison with Measured Data

In addition to the RCS of an actual leaf and a rectangular cutout, measurements were also made using a rectangular plate to gain confidence in the accuracy of the experimental procedures and the theoretical approximations. It is convenient to discuss them in the reverse order.

2.4.1 Rectangular Metal Plate

When a rectangular plate is illuminated with the direction of incidence in a principal plane, an approximate expression for the backscattered field can be obtained

by treating the plate as a length b of an infinite strip or ribbon of width a. For a perfectly conducting strip, a uniform second order GTD expression for the bistatic scattered field has been developed by Senior [1979]. If the incident field is H polarized, the formula is equivalent to an asymptotic expansion of the uniform results of Khaskind and Vainshteyn [1964], and when specialized to the case of backscattering, the far field amplitude of the plate is

$$\begin{aligned}\mathbf{S}_H(\theta_s,\theta_s) = \; & -\tfrac{b}{4\pi\sin\theta_s}\{(1+\sin\theta_s)[1-\tfrac{2}{\sqrt{\pi}}e^{-i\pi/4}\cos(\tfrac{\pi}{4}-\tfrac{\theta_s}{2}) \\ & \mathcal{F}(\sqrt{2k_0a}\sin(\tfrac{\pi}{4}-\tfrac{\theta_s}{2}))]^2 e^{ik_0a\sin\theta_s} - (1-\sin\theta_s) \\ & \cdot[1-\tfrac{2}{\sqrt{\pi}}e^{-i\pi/4}\sin(\tfrac{\pi}{4}-\tfrac{\theta_s}{2})\mathcal{F}(\sqrt{2k_0a}\cos(\tfrac{\pi}{4}-\tfrac{\theta_s}{2}))]^2 e^{-ik_0a\sin\theta_s}\}\end{aligned} \tag{2.25}$$

for $|\theta_s| \leq \pi/2$, where the phase origin has been chosen at the center of the plate and $\mathcal{F}(x)$ is the Fresnel integral

$$\mathcal{F}(x) = \int_x^\infty e^{i\mu^2}\,\mathrm{d}\mu \tag{2.26}$$

We remark that S_H is finite and continuous for all θ_s including $\theta_s = 0$ corresponding to normal incidence, and in terms of S_H the backscattering cross section is given in (2.17).

In the case of E polarization, a similar approach applied to the uniform results of Fialkovskiy [1966] gives

$$\begin{aligned}\mathbf{S}_E(\theta_s,\theta_s) = \; & \tfrac{b}{4\pi\sin\theta_s}\{(1-\sin\theta_s)[1-\tfrac{2}{\sqrt{\pi}}e^{-i\pi/4}\cos^3(\tfrac{\pi}{4}-\tfrac{\theta_s}{2}) \\ & \mathcal{G}(\sqrt{2k_0a}\sin(\tfrac{\pi}{4}-\tfrac{\theta_s}{2}))]^2 e^{ik_0a\sin\theta_s} - (1+\sin\theta_s) \\ & \cdot[1-\tfrac{2}{\sqrt{\pi}}e^{-i\pi/4}\sin^3(\tfrac{\pi}{4}-\tfrac{\theta_s}{2})\mathcal{G}(\sqrt{2k_0a}\cos(\tfrac{\pi}{4}-\tfrac{\theta_s}{2}))]^2 e^{-ik_0a\sin\theta_s}\}\end{aligned} \tag{2.27}$$

[Senior, 1979] where

$$\mathcal{G}(x) = \mathcal{F}(x) - \frac{i}{2x} e^{ix^2} \tag{2.28}$$

In Figs. 2.3 and 2.4 the theoretical expressions are compared with measured data for a plate having $b = 2\lambda_0$ and $a = 1.33\lambda_0$. Overall the agreement is excellent. With (2.25) used to compute σ_H, the strip model accurately reproduces the main features of the scattering pattern of a plate for H polarization, including the traveling wave lobes whose maxima occur at $\theta_i = \pm 54$ degrees and which override the outer side lobes of the specular flash. A similar agreement is found for E polarization, and the failure of (2.27) to reproduce the observed oscillation at angles close to grazing can be attributed to the effect of the currents borne by the side edges of the plate that are not accounted for by the strip model. The physical optics approximation (2.22) is included in Fig. 2.3, and the improved accuracy provided by (2.25) and (2.27) is most evident at angles within (about) 45 degrees from grazing.

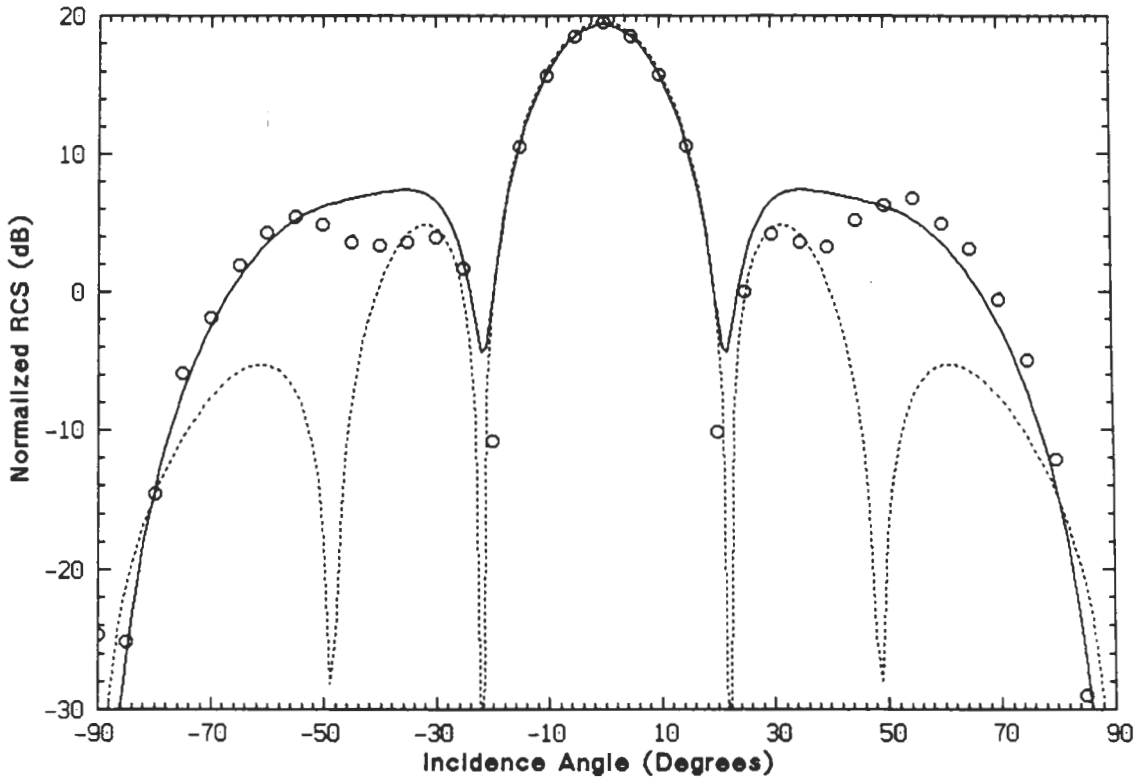

Figure 2.3: Normalized RCS (σ/λ_0^2) of a thin metal plate with $a = 4cm$ and $b = 6cm$ for H polarization: (——) theoretical expressions (2.25), (- - -) physical optics, and (o o o) measurements.

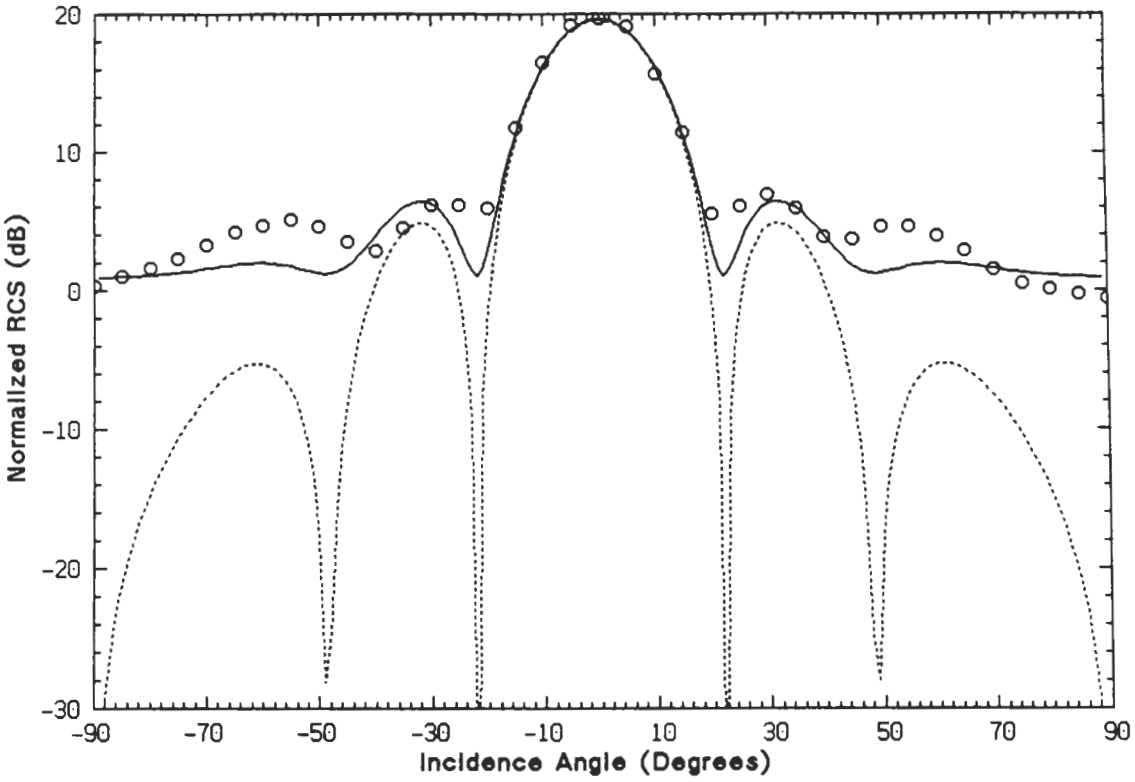

Figure 2.4: Normalized RCS (σ/λ_0^2) of a thin metal plate with $a = 4cm$ and $b = 6cm$ for E polarization: (——) theoretical expressions (2.27) , (- - -) physical optics, and (o o o) measurements.

2.4.2 Rectangular Resistive Plate

For a rectangular plate of uniform resistivity R, the scattering mechanism is similar to the perfectly conducting plate and formulas analogous to (2.25) and (2.27) can be derived from the GTD expression for the bistatic scattered field of a resistive strip [Senior 1979; Herman and Volakis, 1987]. As the resistivity increases, the improvement over the physical optics formula for a resistive plate diminishes. Even a resistivity as low as 20 ohms per square effectively eliminates the traveling wave lobe for H polarization [Senior, 1985] and exposes the underlying side lobes of the specular flash. Similarly, for E polarization, the resistivity reduces the strong edge effects, including the influence of the side edges of the plate.

The net result is to improve the accuracy of the physical optics approximation (2.21), and this is illustrated in Figs. 2.5 and 2.6 where the measured data for a rectangular leaf are compared with the results of the physical optics and a moment method code. The moment method code is for two-dimensional resistive strip which is extended to the three-dimensional case (see Appendix B). The rectangle was cut from a fresh coleus leaf having $Mg = 0.85$, and the resistivity was computed from (2.3) using (2.1) and (2.2). The only significant differences between the strip and physical optics formulas occur for incidence angles within a few degrees of grazing, and the physical optics approximation is in good agreement with the measured data over most of the angular range. Similar agreement was found for other moisture contents, and Fig. 2.7 shows the results for a dried leaf having $Mg = 0$. The measured data shown in this figure all correspond to RCS> -60 dBsm. Even at this low level of reflectivity the physical optics approximation (2.21) retains its accuracy. In Fig. 2.8 the measured and computed normalized RCS (σ/λ_0^2) at normal incidence for various moisture contents are compared.

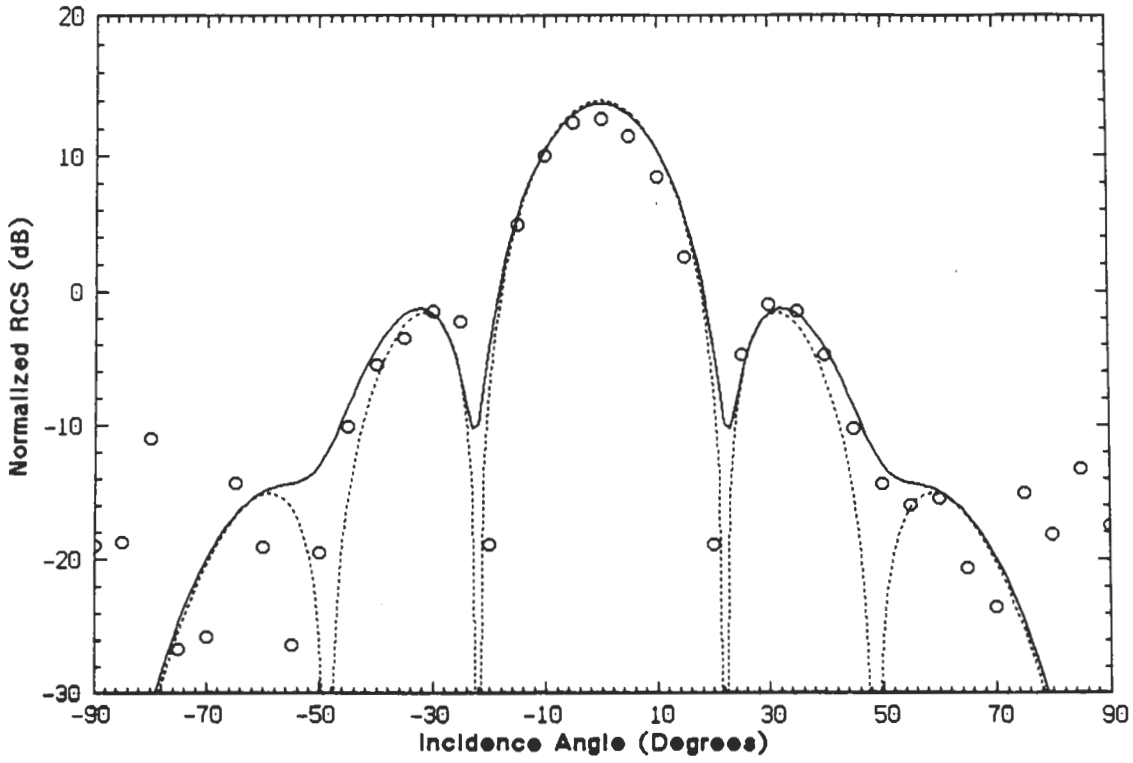

Figure 2.5: Normalized RCS (σ/λ_0^2) of a rectangular section ($a = 4cm$, $b = 6cm$) of a freshly cut coleus leaf ($Mg = 0.85$) for H polarization: (——) moment method solution, (- - -) physical optics approximation (2.21), and (o o o) measurements.

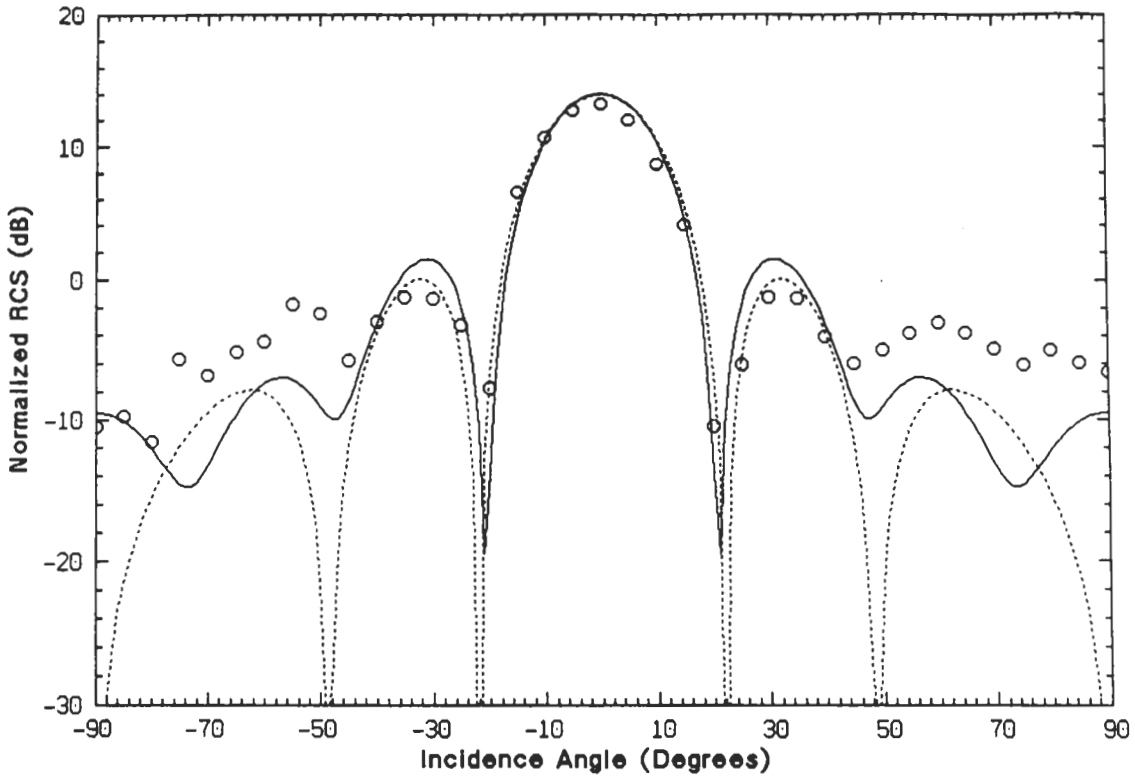

Figure 2.6: Normalized RCS (σ/λ_0^2) of a rectangular section ($a = 4cm$, $b = 6cm$) of a freshly cut coleus leaf ($Mg = 0.85$) for E polarization: (——) moment method solution, (- - -) physical optics approximation (2.21), and (o o o) measurements.

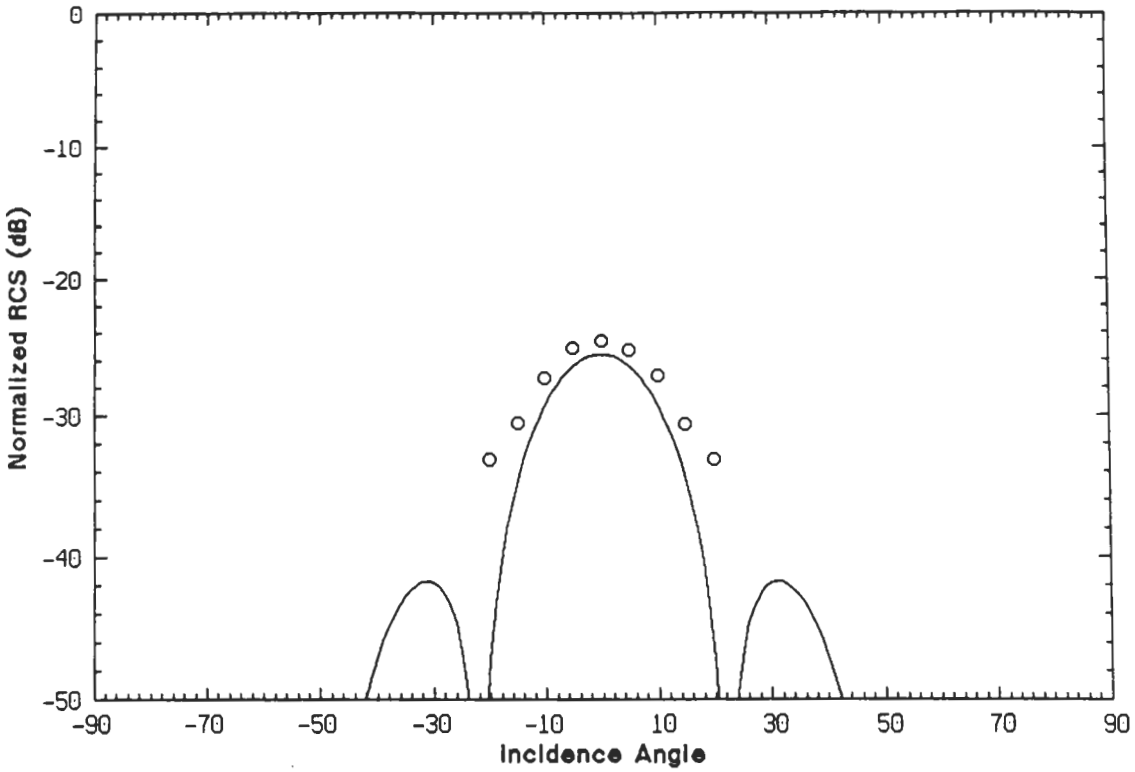

Figure 2.7: Normalized RCS (σ/λ_0^2) of a rectangular section ($a = 4cm$, $b = 6cm$) of a dried leaf ($Mg = 0$) for H polarization: (——) physical optics approximation (2 21) and (o o o) measurements.

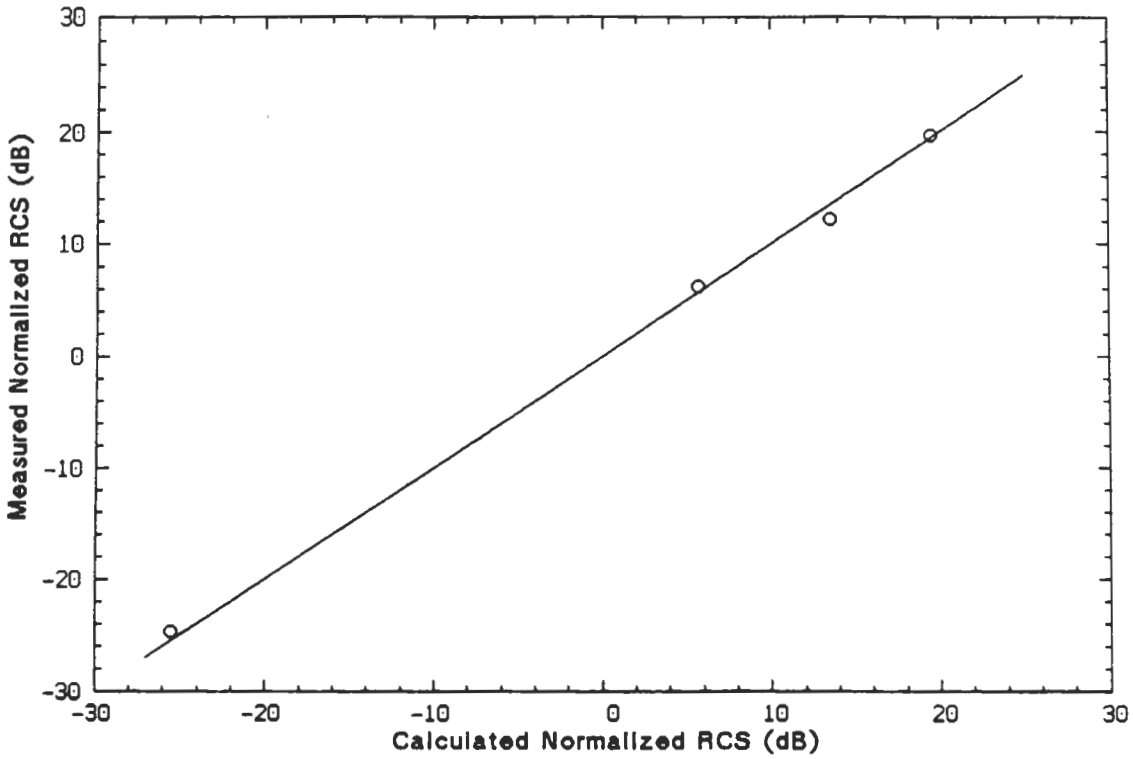

Figure 2.8: The measured normalized RCS (o o o) of the leaf section for various moisture contents at normal incidence are in excellent agreement with the physical optics values. The 1:1 line is shown.

2.4.3 Natural Leaf

In light of the above results it was anticipated that the physical optics approximation applied to the resistive sheet model would provide a good approximation to the RCS of an actual leaf at most angles of incidence. To test this, measurements were made using a coleus leaf whose area was $A = 39.5cm^2$. The width of the equivalent rectangle was chosen as $5.6cm$, implying $b = 7.1cm$, and the measured normalized RCS of the freshly cut leaf ($Mg = 0.77$) is compared with the physical optics approximation (2.21) in Figs. 2.9 and 2.10. In view of the obvious uncertainty in the specification of a (or b), the agreement is good down to at least 20 dB below the broadside peak. Similar agreement was found for the same leaf with $Mg = 0.85$ and 0.04.

The theoretical extinction and backscattering cross sections (2.24) and (2.21) respectively, normalized to their perfectly conducting values, are plotted as functions of the moisture content Mg for normal incidence ($\theta = 0$) in Fig. 2.11. The measured values of σ/σ^{pc} for the rectangular and natural leaves are included, and the agreement is excellent.

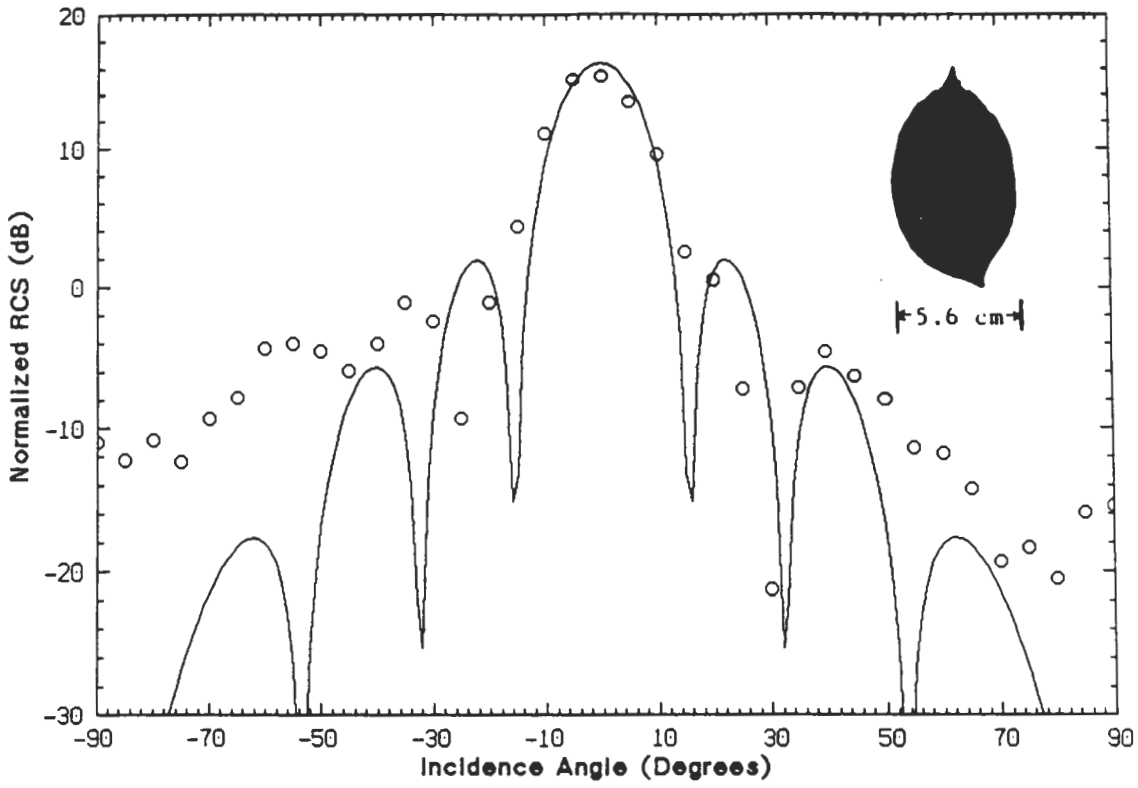

Figure 2.9: Normalized RCS (σ/λ_0^2) of a natural coleus leaf having $A = 39.5cm^2$ and $Mg = 0.77$ for H polarization assuming $a = 5.6cm$: (——) physical optics and (o o o) measurements.

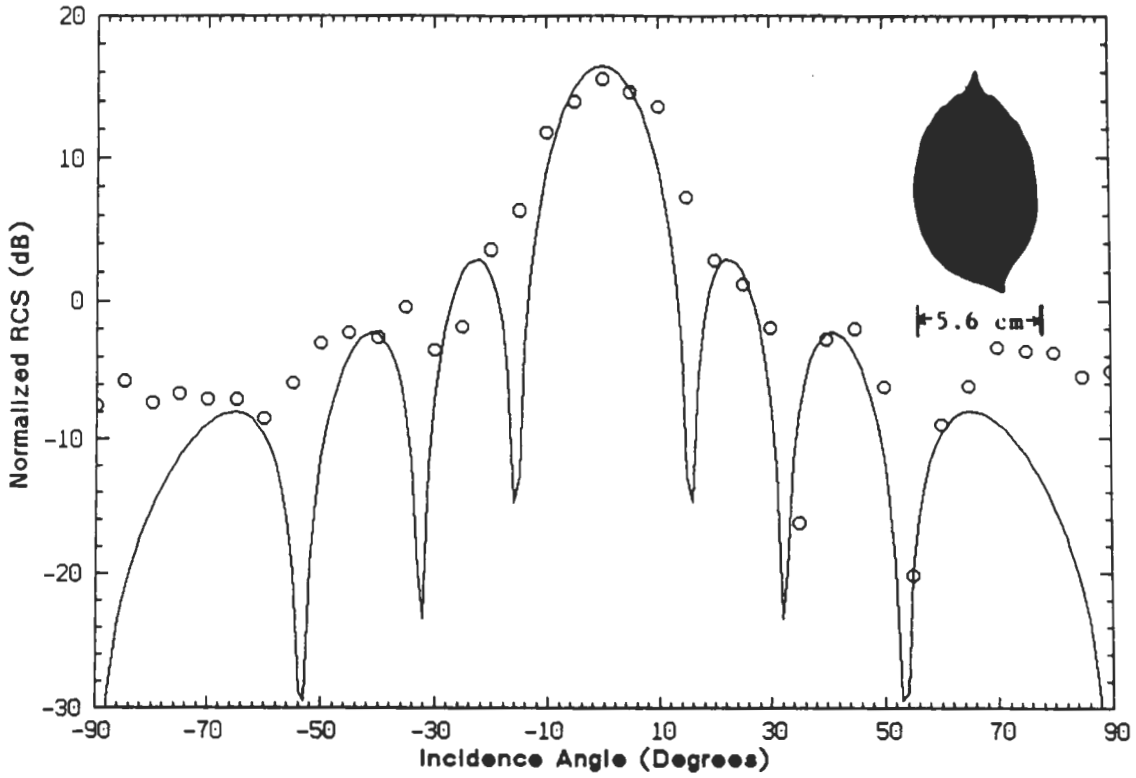

Figure 2.10: Normalized RCS (σ/λ_0^2) of a natural coleus leaf having $A = 39.5cm^2$ and $Mg = 0.77$ for E polarization assuming $a = 5.6cm$: (——) physical optics and (o o o) measurements.

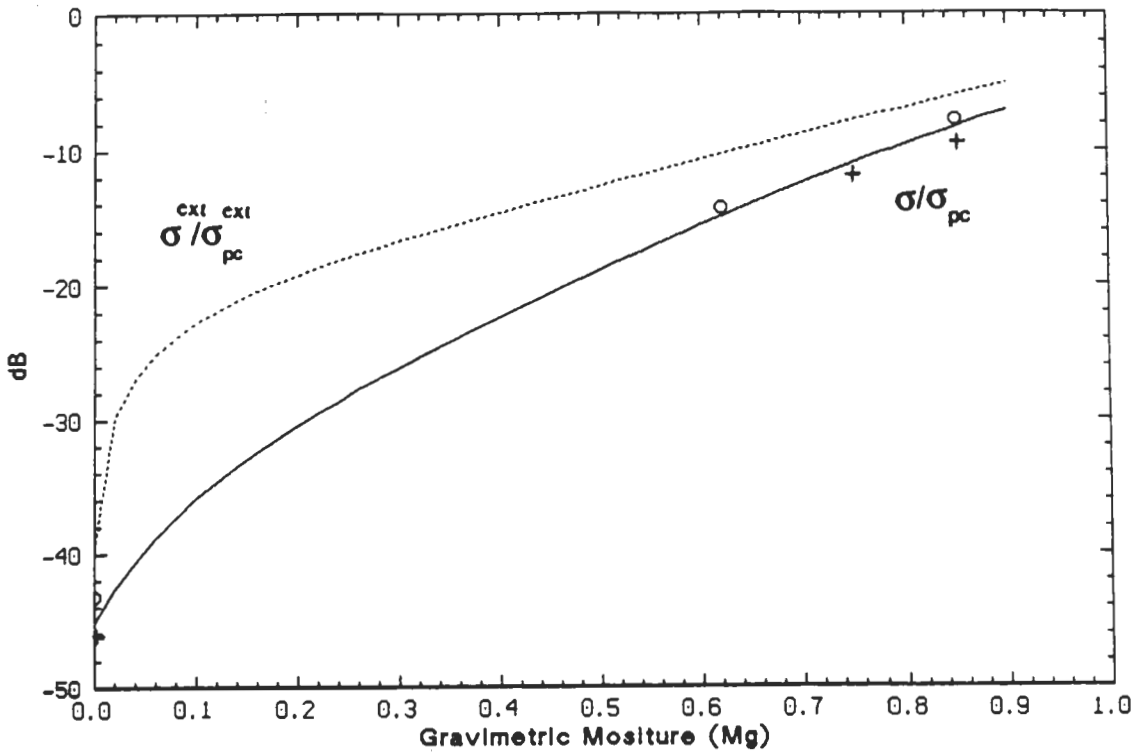

Figure 2.11: The normalized RCS (σ/σ_{pc}) and extinction cross section ($\sigma^{ext}/\sigma_{pc}^{ext}$) of rectangular leaves as functions of Mg at normal incidence: (——) physical optics, (o o o) measurements for rectangular leaf, and (+ + +) measurements for natural leaf.

2.5 Leaf in a General Coordinate System

As explained in Chapter 1 for purposes of modeling the scattering from a medium containing sparsely distributed randomly distributed leaves, the bistatic scattering formula for a single leaf with arbitrary orientation in a (X, Y, Z) coordinate system is required. For a circular leaf the orientation is completely specified by the normal to the plane of the leaf $(\hat{n}')$ which in turn can be specified by two spherical coordinate angles θ_j and ϕ_j, i.e.

$$\hat{n}' = \sin\theta_j \cos\phi_j \hat{x} + \sin\theta_j \sin\phi_j \hat{y} + \cos\theta_j \hat{z} \tag{2.29}$$

For leaves with other geometries, such as rectangular leaves, another angle is needed to specify the orientation.

Suppose a thin flat plate is illuminated by a plane wave whose amplitude and polarization is denoted by $\mathbf{E}_0$ $(\mathbf{H}_0)$. If the plate is perfectly conducting, the physical optics approximation in the far zone gives

$$\mathbf{\Pi}_e(\mathbf{r}) = \frac{e^{ik_0 r}}{r} \hat{n}' \times \mathbf{H_0} \frac{iZ_0}{2\pi k_0} \int_s e^{ik_0(\hat{k}_i - \hat{k}_s)\cdot \mathbf{r}'} ds' \tag{2.30}$$

where $\hat{n}'$ is the normal to the illuminated face and the phase origin is at the center of the plate. Hence

$$\mathbf{S} = \left[(\hat{n}' \cdot \mathbf{E}_0)\left\{(\hat{k}_i \cdot \hat{k}_s)\hat{k}_s - \hat{k}_i\right\} - (\hat{n}' \cdot \hat{k}_i)\left\{(\hat{k}_s \cdot \mathbf{E}_0)\hat{k}_s - \mathbf{E}_0\right\}\right] K \tag{2.31}$$

where

$$K = -\frac{i}{\lambda_0} \int_s e^{ik_0(\hat{k}_i - \hat{k}_s)\cdot \mathbf{r}'} ds' \,. \tag{2.32}$$

In the case of a circular disk of radius a,

$$K = -i \frac{a}{|(\hat{k}_i - \hat{k}_s)\cdot \hat{\rho}'|} J_1(|(\hat{k}_i - \hat{k}_s)\cdot \hat{\rho}'| k_0 a)$$

where $\hat{\rho}'$ is an arbitrary unit vector in the plane of the disk and J_1 is the Bessel function of the first order. For a rectangular plate with $-\frac{a}{2} < x' < \frac{a}{2}$ and $-\frac{b}{2} < y' < \frac{b}{2}$ where x' and y' are Cartesian coordinates in its plane,

$$K = -\frac{iab}{\lambda_0}\frac{\sin U}{U}\frac{\sin V}{V}$$

with

$$U = \frac{1}{2}k_0 a(\hat{k}_i - \hat{k}_s)\cdot\hat{x}' \ , \qquad V = \frac{1}{2}k_0 b(\hat{k}_i - \hat{k}_s)\cdot\hat{y}' \ , \tag{2.33}$$

and for other geometries the integral expression (2.32) can be evaluated numerically.

As evident from (2.32) if $(\hat{k}_i - \hat{k}_s)\cdot\mathbf{r}' = 0$

$$K = -\frac{iA}{\lambda_0} \ ,$$

independent of geometry, where A is the plate area.

If the plate is not perfectly conducting, the resistive sheet simulation is employed, and it is then necessary to resolve $\mathbf{H}_0$ into components perpendicular and parallel to the plane of incidence. Let

$$\hat{t}_1 = \frac{\hat{n}'\times\hat{k}_i}{|\hat{n}'\times\hat{k}_i|} \ , \quad \hat{t}_2 = \frac{\hat{k}_i\times(\hat{n}'\times\hat{k}_i)}{|\hat{n}'\times\hat{k}_i|} \tag{2.34}$$

in terms of which

$$\hat{n}'\times\mathbf{H}_0 = c_1\hat{t}_1 + c_2\hat{t}_2 \tag{2.35}$$

where

$$c_1 = -\frac{(\hat{n}'\cdot\mathbf{H}_0)(\hat{n}'\cdot\hat{k}_i)}{|\hat{n}'\times\hat{k}_i|} \ , \quad c_2 = -\frac{Y_0(\hat{n}'\cdot\mathbf{E}_0)(\hat{n}'\cdot\hat{k}_i)}{|\hat{n}'\times\hat{k}_i|} \ .$$

The physical optics approximation for current is

$$\mathbf{J} = 2(c_1\Gamma_H\hat{t}_1 + c_2\Gamma_E\hat{t}_2)e^{ik_0\hat{k}_i\cdot\mathbf{r}'} \ .$$

Here Γ_E and Γ_H are the reflection coefficients as given in (2.8) and (2.12) respectively in which θ_i is replaced with

$$\phi_1 = -\arccos(\hat{k}_i\cdot\hat{n}') \ .$$

In the far zone

$$\mathbf{\Pi}_e(\mathbf{r}) = \frac{e^{ik_0 r}}{r}\left\{(\hat{n}'\cdot\mathbf{E}_0)\Gamma_E\hat{k}_i\times(\hat{n}'\times\hat{k}_i)+(\hat{n}'\cdot\mathbf{H}_0)\Gamma_H(\hat{n}'\times\hat{k}_i)\right\}\frac{K(\hat{n}'\cdot\hat{k}_i)}{k_0^2|\hat{n}'\times\hat{k}_i|^2}\ . \tag{2.36}$$

The scattering amplitude is therefore

$$\begin{aligned}\mathbf{S} = \ & \Big\{(\hat{n}'\cdot\mathbf{E}_0)\Gamma_E\hat{k}_s\times\hat{k}_s\times\left[(\hat{n}'\cdot\hat{k}_i)\hat{k}_i-\hat{n}'\right]+(\hat{n}'\cdot\mathbf{H}_0)Z_0\Gamma_H \\ & \left[(\hat{k}_s\cdot\hat{k}_i)(\hat{n}'\times\hat{k}_s)+(\hat{n}\cdot\hat{k}_s)(\hat{k}_s\times\hat{k}_i)\right]\Big\}\tfrac{\hat{n}'\cdot\hat{k}_i}{|\hat{n}'\times\hat{k}_i|^2}K\end{aligned} \tag{2.37}$$

where K is given in (2.32), and the elements of the scattering matrix are

$$\begin{aligned}S_{VV} = \ & \{(\hat{n}'\cdot\hat{v}_i)\left[(\hat{n}'\cdot\hat{v}_s)-(\hat{n}'\cdot\hat{k}_i)(\hat{k}_i\cdot\hat{v}_s)\right]\Gamma_E \\ & +(\hat{n}'\cdot\hat{h}_i)\left[(\hat{k}_i\cdot\hat{k}_s)(\hat{n}'\cdot\hat{h}_s)-(\hat{k}_i\cdot\hat{h}_s)(\hat{n}'\cdot\hat{k}_s)\right]\Gamma_H\}\tfrac{(\hat{n}'\cdot\hat{k}_i)}{|\hat{n}'\times\hat{k}_i|^2}K\end{aligned} \tag{2.38}$$

$$\begin{aligned}S_{VH} = \ & \{(\hat{n}'\cdot\hat{h}_i)\left[(\hat{n}'\cdot\hat{v}_s)-(\hat{n}'\cdot\hat{k}_i)(\hat{k}_i\cdot\hat{v}_s)\right]\Gamma_E \\ & -(\hat{n}'\cdot\hat{v}_i)\left[(\hat{k}_i\cdot\hat{k}_s)(\hat{n}'\cdot\hat{h}_s)-(\hat{k}_i\cdot\hat{h}_s)(\hat{n}'\cdot\hat{k}_s)\right]\Gamma_H\}\tfrac{(\hat{n}'\cdot\hat{k}_i)}{|\hat{n}'\times\hat{k}_i|^2}K\end{aligned} \tag{2.39}$$

$$\begin{aligned}S_{HV} = \ & \{(\hat{n}'\cdot\hat{v}_i)\left[(\hat{n}'\cdot\hat{h}_s)-(\hat{n}'\cdot\hat{k}_i)(\hat{k}_i\cdot\hat{h}_s)\right]\Gamma_E \\ & -(\hat{n}'\cdot\hat{h}_i)\left[(\hat{k}_i\cdot\hat{k}_s)(\hat{n}'\cdot\hat{v}_s)-(\hat{k}_i\cdot\hat{v}_s)(\hat{n}'\cdot\hat{k}_s)\right]\Gamma_H\}\tfrac{(\hat{n}'\cdot\hat{k}_i)}{|\hat{n}'\times\hat{k}_i|^2}K\end{aligned} \tag{2.40}$$

$$\begin{aligned}S_{HH} = \ & \{(\hat{n}'\cdot\hat{h}_i)\left[(\hat{n}'\cdot\hat{h}_s)-(\hat{n}'\cdot\hat{k}_i)(\hat{k}_i\cdot\hat{h}_s)\right]\Gamma_E \\ & +(\hat{n}'\cdot\hat{v}_i)\left[(\hat{k}_i\cdot\hat{k}_s)(\hat{n}'\cdot\hat{v}_s)-(\hat{k}_i\cdot\hat{v}_s)(\hat{n}'\cdot\hat{k}_s)\right]\Gamma_H\}\tfrac{(\hat{n}'\cdot\hat{k}_i)}{|\hat{n}'\times\hat{k}_i|^2}K\ .\end{aligned} \tag{2.41}$$

To check the above expressions a comparison with measured data is shown in Fig. 2.12 for a rectangular plate having $a = 1.33\lambda_0$ and $b = 2\lambda_0$ with its larger principle (y') axis tilted back 8 degrees. The angle with the plane of incidence is therefore 82 degrees, and once again there is good agreement over the main lobe where most of the energy is concentrated. The discrepancies at wider angles are attributable to travelling wave and edge effects which are not accurately simulated

by physical optics. When the tilted plate is lossy having $R = 0.163 + i0.442$ [1] , a similar comparison with measured data for E polarization is given in Fig. 2.13, and for completeness we have included here the cross-polarized cross section computed using physical optics. The agreement now extends to wider angles. It should be noted that since physical optics is a high frequency technique, its accuracy generally improves as the frequency and/or plate dimensions increase.

2.6 Conclusions

Using measurements of the backscattered field of coleus leaves in varying stages of dryness, it has been shown that a resistive sheet constitutes an effective model of a leaf. The resistivity is entirely specified by the moisture content, and for a rectangular section of a leaf, the predicted backscattering cross sections are in excellent agreement with the measured data for both principal polarizations, including the special case of a rectangular metal plate whose resistivity is zero. As the resistivity increases, the effect of the currents borne by the edges of the plate diminishes, and the accuracy of the physical optics approximation improves. Indeed, for a natural leaf, the physical optics approximation in conjunction with the resistive sheet model faithfully reproduces the dominant features of the scattering patterns for all of the moisture conditions investigated, representing a dynamic range of more than 50 dB. The simplicity of the formulation is such that the bistatic and extinction cross sections can also be computed, and the aspect angle averaging that may be necessary in a practical situation is easily performed.

[1] Lossy plate is a rectangular cut of a leaf whose resistivity is measured in a waveguide (see Appendix A.)

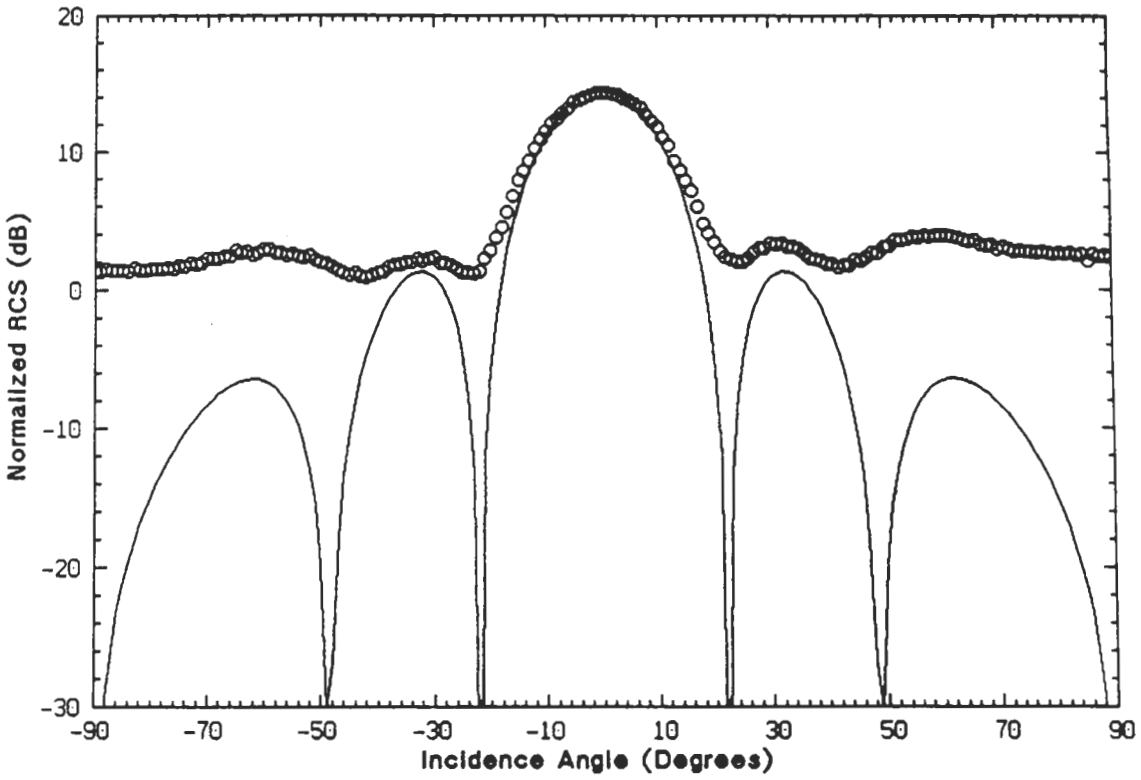

Figure 2.12: Normalized RCS (σ/λ_0^2) of a rectangular perfectly conducting plate for E polarization with $a = 1.33\lambda_0$, $b = 2\lambda_0$, and tilt angle $\beta = 8°$: (——) physical optics, (o o o) measurements.

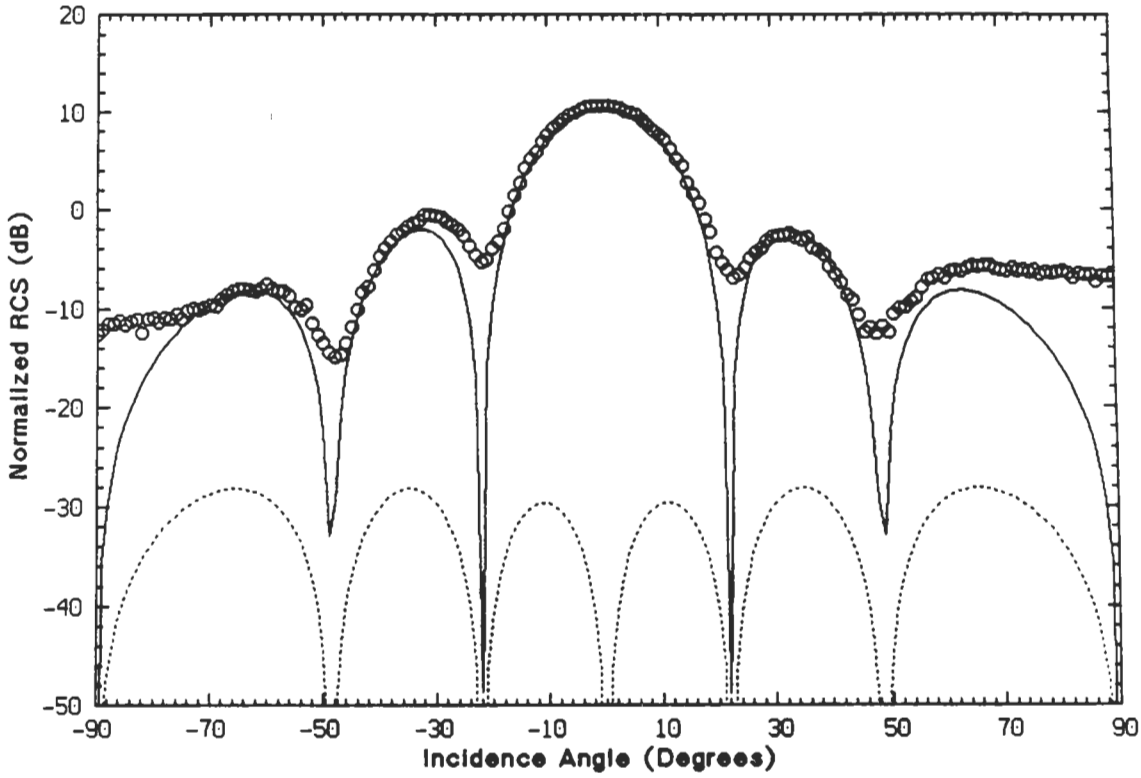

Figure 2.13: Normalized RCS (σ/λ_0^2) of a rectangular resistive sheet for E polarization with $R = 0.163, +i0.442$, $a = 1.33\lambda_0$, $b = 2\lambda_0$, and tilt angle $\beta = 8°$: (——) physical optics, (o o o) measurements.

CHAPTER III

EFFECT OF CURVATURE ON THE BACKSCATTERING FROM A LEAF

3.1 Introduction

In the previous chapter it was shown that for a typical planar leaf at X-band frequencies and above [1], a resistive sheet model in conjunction with the physical optics approximation accurately predicts the backscattering cross section at almost all angles of incidence. The (complex) resistivity of the sheet is a function of the gravimetric moisture content Mg of the leaf, and for all moisture contents, the accuracy of the resulting prediction is adequate for most practical purposes.

In their natural state leaves are not generally flat, and any curvature may reduce their backscattering cross sections. For remote sensing purposes we seek a simple expression that accounts for the effect of curvature. Using the resistive sheet model and the physical optics approximation, for a rectangular section of a leaf curved in one and two dimensions, an integral expression for the backscattered field is obtained. The integral is evaluated numerically and by a stationary phase approximation, leading to a simple analytical expression for the cross section reduction produced by the curvature. To explore the range of validity of these expressions, measurements have

[1] Lateral dimensions of the leaf must be larger than the wavelength and the thickness of the leaf must be much smaller than the wavelength.

been carried out using a rectangular portion of a coleus leaf attached to the surfaces of styrofoam cylinders and spheres of different radii. For a wide range of curvatures, the reduction in the normal incidence backscattering cross section at X-band is accurately predicted by the physical optics approximation, and the results of a numerical evaluation of the physical optics integral are almost identical to a Fresnel integral expression derived from a stationary phase evaluation.

3.2 Leaf Model

Here again it is convenient to regard a leaf as part of a thin, non-magnetic lossy dielectric layer, and an effective model for such a layer is an infinitesimally thin resistive sheet. The complex resistivity of the sheet given by (2.3) is a function of leaf thickness and dielectric constant which in turn is primarily determined by the gravimetric moisture content (Mg) of the leaf.

For the geometries of curved leaves that we will consider in this chapter it is required to obtain the far field amplitude expression for a flat leaf in a special coordinate system. Consider a sheet lying in the plane $\zeta = 0$ of a Cartesian coordinate system (ξ, η, ζ) and illuminated by a plane electromagnetic wave having

$$\mathbf{E}^i = (\hat{\xi} \sin\alpha \sin\phi + \hat{\eta} \sin\alpha \cos\phi + \hat{\zeta} \cos\alpha) e^{-ik_0(\zeta \cos\phi - \eta \sin\phi)} \tag{3.1}$$

(see Figure 1), the induced electric current is

$$\mathbf{J} = 2Y_0\{\hat{\eta} \sin\alpha \Gamma_H(\phi) + \hat{\zeta} \cos\alpha \cos\phi \Gamma_E(\phi)\} e^{ik_0\eta \sin\phi} \tag{3.2}$$

where $\Gamma_E(\phi)$ and $\Gamma_H(\phi)$ respectively are the plane wave reflection coefficients for E polarization ($\alpha = 0$) and for H polarization ($\alpha = \pi/2$) given by (2.8) and (2.12). Since $R = 0$ corresponds to perfect conductivity, Γ_H and Γ_E show how the current

differs from the current $\mathbf{J}_{pc}$ supported by a perfectly conducting surface. Indeed,

$$\mathbf{J} = \mathbf{J}_{pc} \cdot \hat{\eta}\Gamma_H(\phi) + \mathbf{J}_{pc} \cdot \hat{\zeta}\Gamma_E(\phi) \tag{3.3}$$

where $\hat{\eta}$ and $\hat{\zeta}$ are unit tangent vectors in and perpendicular to the plane of incidence respectively.

Consider a rectangular section of resistive sheet occupying the region $-\frac{a}{2} < \eta < \frac{a}{2}$, $-\frac{b}{2} < \zeta < \frac{b}{2}$ of the plane $\xi = 0$ as shown in Fig. 3.1. Since there is only an electric current induced in the plate, the scattered field can be attributed to an electric Hertz vector $\mathbf{\Pi}_e$. In the backscattering direction the far field expression for $\mathbf{\Pi}_e$ is

$$\begin{aligned} \mathbf{\Pi}_e &= \tfrac{e^{ik_0 r}}{k_0 r} \tfrac{i}{2\pi} \int_{\frac{-a}{2}}^{\frac{a}{2}} \int_{\frac{-b}{2}}^{\frac{b}{2}} \{\hat{\eta} \sin\alpha\Gamma_H(\phi) + \hat{\zeta} \cos\alpha \cos\phi\Gamma_E(\phi)\} e^{i2k_0\eta \sin\phi} \mathrm{d}\eta \mathrm{d}\zeta \\ &= \tfrac{e^{ik_0 r}}{k_0 r} \tfrac{iab}{2\pi} \{\hat{\eta} \sin\alpha\Gamma_H(\phi) + \hat{\zeta} \cos\alpha \cos\phi\Gamma_E(\phi)\} \tfrac{\sin U}{U} \end{aligned} \tag{3.4}$$

where

$$U = k_0 a \sin\phi\,, \tag{3.5}$$

and the backscattered far field amplitude is

$$\mathbf{S} = \frac{ik_0 ab}{2\pi} \left\{ (\hat{\xi} \sin\phi + \hat{\eta} \cos\phi) \sin\alpha\Gamma_H(\phi) + \hat{\zeta} \cos\alpha\Gamma_E(\phi) \right\} \cos\phi \frac{\sin U}{U} \tag{3.6}$$

The above example corresponds to the rotation of the direction of incidence in the $\xi - \eta$ plane and is equivalent to the rotation of the plate through an angle ϕ about the ζ axis with the illumination fixed in space. A more general situation is that in which the plate is first tilted back through an angle β (see Fig. 3.2) prior to rotation. In terms of a rotated coordinate system (ξ', η', ζ') where $\hat{\xi}' = \hat{\xi} \cos\beta + \hat{\zeta} \sin\beta$, $\hat{\eta}' = \hat{\eta}$, $\hat{\zeta}' = -\hat{\xi} \sin\beta + \hat{\zeta} \cos\beta$, the plate now occupies $-\frac{a}{2} < \eta' < \frac{a}{2}$, $-\frac{b}{2} < \zeta' < \frac{b}{2}$, and the electric field is

$$\mathbf{E}^i = (\hat{\xi} \sin\alpha \sin\phi + \hat{\eta} \sin\alpha \cos\phi + \hat{\zeta} \cos\alpha) e^{-ik_0(\xi' \cos\beta \cos\phi - \eta' \sin\phi - \zeta' \sin\beta \cos\phi)}$$

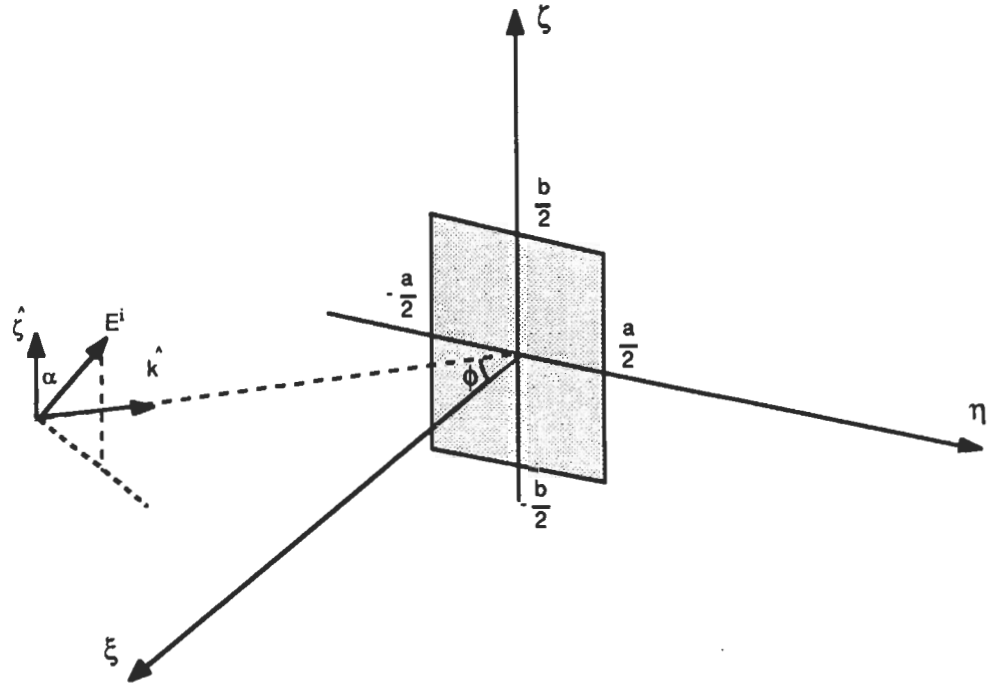

Figure 3.1: Geometry for the scattering of a plane wave from a resistive sheet lying in the plane $\zeta = 0$.

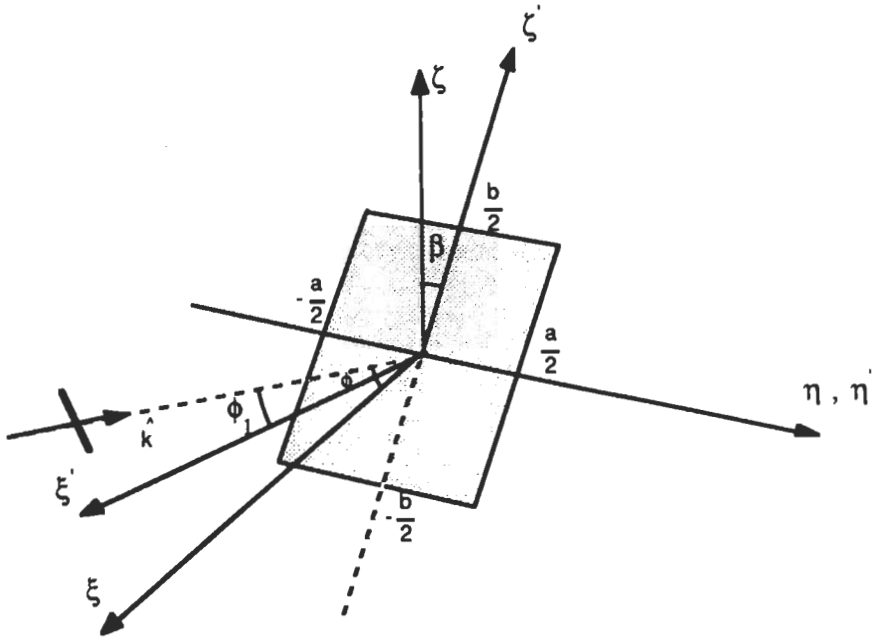

Figure 3.2: Geometry for the scattering of a plane wave by a tilted resistive sheet.

Since the unit vector normal to the plate is $\hat{\xi}'$, the physical optics expression for the current that would be induced if the plate were perfectly conducting is

$$\begin{aligned}\mathbf{J}_{pc} = \; & 2Y_0 \left\{ -\hat{\xi} \cos\alpha \sin\beta \cos\phi + \hat{\eta}(\sin\alpha \cos\beta + \cos\alpha \sin\beta \sin\phi) \right. \\ & \left. + \hat{\zeta} \cos\alpha \cos\beta \cos\phi \right\} e^{ik_0(\eta' \sin\phi + \zeta' \sin\beta \cos\phi)}\end{aligned}$$

which can be written as

$$\begin{aligned}\mathbf{J}_{pc} = \; & 2Y_0 \{ (\sin\alpha \cos\beta \sin\phi + \cos\alpha \sin\beta)\hat{\eta}_1 - (\sin\alpha \sin\beta - \cos\alpha \cos\beta \sin\phi) \\ & \cdot \cos\beta \cos\phi \hat{\zeta}_1 \} P e^{ik_0(\eta' \sin\phi + \zeta' \sin\beta \cos\phi)}\end{aligned}$$

where

$$P = (1 - \cos^2\beta \cos^2\phi)^{-\frac{1}{2}}$$

and

$$\hat{\eta}_1 = P(-\hat{\xi} \sin^2\beta \cos\phi + \hat{\eta} \sin\phi + \hat{\zeta} \sin\beta \cos\beta \cos\phi)$$

$$\hat{\xi}_1 = P(-\hat{\xi} \sin\beta \sin\phi - \hat{\eta} \sin\beta \cos\phi + \hat{\zeta} \cos\beta \sin\phi)$$

are, respectively, unit vectors in and perpendicular to the plane of incidence, lying in the plane of the plate. The current induced in the resistive plate is therefore

$$\begin{aligned}\mathbf{J} = \; & 2Y_0 \{ (\sin\alpha \cos\beta \sin\phi + \cos\alpha \sin\beta)\Gamma_H(\phi_1)\hat{\eta}_1 - (\sin\alpha \sin\beta - \cos\alpha \cos\beta \sin\phi) \\ & \cdot \cos\beta \cos\phi \Gamma_E(\phi_1)\hat{\zeta}_1 \Big\} P e^{ik_0(\eta' \sin\phi + \zeta' \sin\beta \cos\phi)}\end{aligned} \tag{3.7}$$

where ϕ_1 is the angle between the negative of the incident field direction and the normal to the plate, i.e. $\arccos(\cos\beta \cos\phi)$. Now it is a trivial task to obtain the far field amplitude which has the following form

$$\begin{aligned}\mathbf{S} = \; & \tfrac{ik_0ab}{2\pi} \{ (\hat{\xi} \sin\phi + \hat{\eta} \cos\phi)[\sin\alpha \left(\cos^2\beta \sin^2\phi \Gamma_H(\phi_1) + \sin^2\beta \Gamma_E(\phi_1) \right) \\ & + \cos\alpha \sin\beta \cos\beta \sin\phi \, (\Gamma_H(\phi_1) - \Gamma_E(\phi_1))] \\ & + \hat{\zeta}[\cos\alpha \left(\sin^2\beta \Gamma_H(\phi_1) + \cos^2\beta \sin^2\phi \Gamma_E(\phi_1) \right) \\ & + \sin\alpha \sin\beta \cos\beta \sin\phi \, (\Gamma_H(\phi_1) - \Gamma_E(\phi_1))] \} P^2 \cos\beta \cos\phi \tfrac{\sin U}{U} \; \tfrac{\sin V}{V}\end{aligned} \tag{3.8}$$

where U is given by (3.5) and

$$V = k_0 b \sin\beta \cos\phi \, .$$

3.3 One Dimensional Curvature

We now concentrate on the case of the curved leaves and first examine the effect on the backscattering cross section when the plate is given a constant radius of curvature ρ in a principal plane. As a result of the bending, the plate conforms to a portion of the surface of a right circular cylinder of radius ρ as shown in Fig. 3.3.

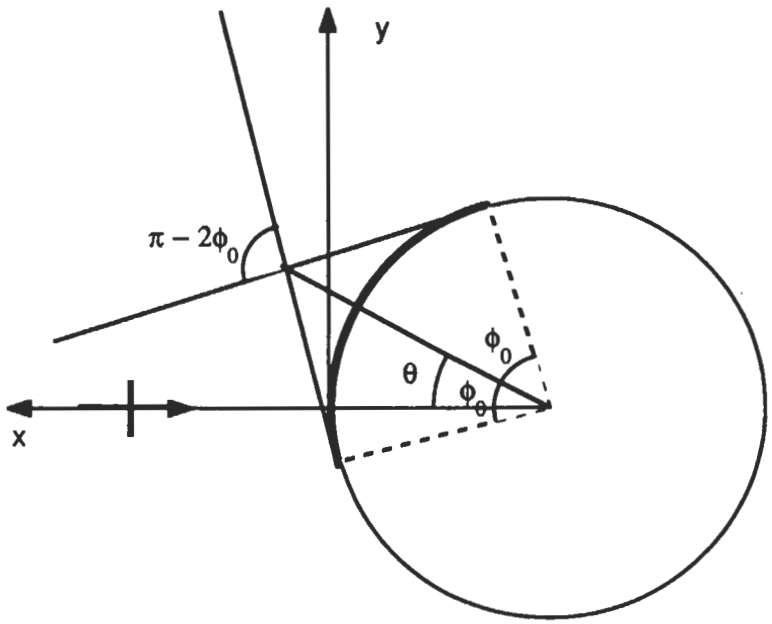

Figure 3.3: Geometry for the scattering of a plane wave from a resistive sheet which conforms to a portion of the surface of a right circular cylinder of radius ρ.

If the flat plate has length a in the z' direction and width b in the y' direction, then $b = 2\rho\phi_0$. The illuminating field is a plane wave propagating in the negative x' direction with

$$\mathbf{E}^i = (\hat{y}' \sin\alpha + \hat{z}' \cos\alpha) e^{-ik_0(x'-\rho)} \tag{3.9}$$

and in the backscattering direction the far field expression for the Hertz vector $\mathbf{\Pi}_e$ is

$$\mathbf{\Pi}_e(\mathbf{x}') = \frac{e^{ik_0 x'}}{x'} \frac{iZ_0}{4\pi k_0} a\rho \int_{\theta-\phi_0}^{\theta+\phi_0} \mathbf{J}(\phi') e^{ik_0\rho(1-\cos\phi')} \mathrm{d}\phi'$$

where the phase origin has been chosen at the front of the cylinder. Since resistive sheets are penetrable, obtaining the physical optics current becomes very complicated if a portion of the leaf surface is shadowed. To ensure that no portion of the outer surface of the plate is shadowed, it is necessary that $|\theta| \leq \frac{\pi}{2} - \phi_0$. If the radius of curvature is much larger than the width of the plate ($\rho \gg b$), shadowing happens only at near grazing angles. The resistive sheet current $\mathbf{J}$ is given by (3.2) with the identification

$$\begin{aligned} \phi &= \phi' , \\ \hat{\zeta} &= \hat{z}' , \\ \hat{\eta} &= -\hat{x}' \sin\phi' + \hat{y}' \cos\phi' . \end{aligned}$$

Recognizing that the exponent in (3.4) is simply the incident field phase at the surface,

$$\mathbf{J}(\phi') = 2Y_0\{(-\hat{x}' \sin\phi' + \hat{y}' \cos\phi') \sin\alpha\Gamma_H(\phi') + \hat{z}' \cos\alpha \cos\phi'\Gamma_E(\phi')\} e^{ik_0\rho(1-\cos\phi')} ,$$

and therefore the Hertz vector potential becomes

$$\begin{aligned} \mathbf{\Pi}_e(\mathbf{x}') = \tfrac{e^{ik_0 x'}}{x'} \tfrac{ia\rho}{2\pi k_0} \textstyle\int_{\theta-\phi_0}^{\theta+\phi_0} & \{(-\hat{x}' \sin\phi' + \hat{y}' \cos\phi') \sin\alpha\Gamma_H(\phi') \\ & + \hat{z}' \cos\alpha \cos\phi'\Gamma_E(\phi')\} \, e^{ik_0(1-\cos\phi')} \, e^{2ik_0\rho(1-\cos\phi')} \mathrm{d}\phi' \end{aligned}$$

The scattered electric field and the far field amplitude in terms of the hertz vector can be evaluated from (1.4) and (1.11) respectively. The resulting expression for the far field amplitude is

$$\mathbf{S} = \frac{ik_0 a\rho}{2\pi} \int_{\theta-\phi_0}^{\theta+\phi_0} \{\hat{y}' \sin\alpha\Gamma_H(\phi') + \hat{z}' \cos\alpha\Gamma_E(\phi')\} \cos\phi' e^{2ik_0\rho(1-\cos\phi')} \mathrm{d}\phi' \qquad (3.10)$$

in terms of which the like- and cross-polarized backscattering cross sections are

$$\sigma = 4\pi \mid (\hat{y}' \sin\alpha + \hat{z}' \cos\alpha) \cdot \mathbf{S} \mid^2 , \qquad (3.11)$$

$$\sigma_{cross} = 4\pi \mid (\hat{y}' \cos\alpha - \hat{z}' \sin\alpha) \cdot \mathbf{S} \mid^2 . \qquad (3.12)$$

Two methods were employed to evaluate the integral expression (3.10) for $\mathbf{S}$. In the first, the arc $\theta - \phi_0 < \phi' < \theta + \phi_0$ was subdivided into $2M$ segments and each replaced by a planar strip of width $\Delta = \rho\phi_0/M$ centered at $\phi' = \phi'_m$, $m = 1, 2, \cdots, M$, and tangential to the cylinder. From the formula (3.6) for the backscattered far field amplitude of an inclined plate, we then have

$$\mathbf{S} = \frac{ik_0 a\Delta}{2\pi} \sum_{m=1}^{2M} \{\hat{y}' \sin\alpha\Gamma_H(\phi'_m) + \hat{z}' \cos\alpha\Gamma_E(\phi'_m)\} \cos\phi'_m e^{2ik_0\rho(1-\cos\phi'_m)} \frac{\sin U'}{U'} \quad (3.13)$$

with $U' = k_0\Delta \sin\phi'_m$. The summation was carried out numerically, and a comparison with data obtained from a moment method solution of the integral equation for a curved resistive strip is given in Section 3.5.

The second method is entirely analytical and is based on the stationary phase (SP) approximation. The SP point of the integral in (3.10) is $\phi' = 0$ and on the assumption that $k_0\rho \gg 1$, with $\theta < \phi_0$ so that the SP point lies within the range of integration,

$$\begin{aligned} \mathbf{S} = \; & \tfrac{ia}{2\pi}\sqrt{k_0\rho}\,\{\hat{y}' \sin\alpha\Gamma_H(0) + \hat{z}' \cos\alpha\Gamma_E(0)\} \\ & \left\{\mathcal{F}[\sqrt{k_0\rho}(\phi_0 + \theta)] + \mathcal{F}[\sqrt{k_0\rho}(\phi_0 - \theta)]\right\} \end{aligned}$$

where

$$\mathcal{F}(\tau) = \int_0^\tau e^{iu^2}\,\mathrm{d}u \quad (3.14)$$

is the finite range Fresnel integral. We remark that for $|\tau| \ll 1$

$$\mathcal{F}(\tau) = \tau + O(\tau^3)\,, \quad (3.15)$$

whereas for $|\tau| \gg 1$

$$\mathcal{F}(\tau) \approx \frac{1}{2}\sqrt{\pi}e^{i\pi/4} \quad (3.16)$$

Since $\Gamma_E(0) = \Gamma_H(0)$ it now follows that

$$\mathbf{S} = \frac{ia}{2\pi}\sqrt{k_0\rho}\{\hat{y}' \sin\alpha + \hat{z}' \cos\alpha\}\Gamma_H(0)\{\mathcal{F}[\sqrt{k_0\rho}(\phi_0 + \theta)] + \mathcal{F}[\sqrt{k_0\rho}(\phi_0 - \theta)]\} \quad (3.17)$$

showing that to this approximation there is no depolarization in the backscattering direction.

It is instructive to examine separately the special case of symmetric (normal) incidence when $\theta = 0$. The argument of the Fresnel integrals in (3.17) is then $b/2\sqrt{k_0/\rho}$, and if $\rho \gg k_0 b^2/4$, the approximation (3.15) implies

$$\mathbf{S} = \frac{ik_0 ab}{2\pi}(\hat{y}\sin\alpha + \hat{z}\cos\alpha)\Gamma_H(0) \tag{3.18}$$

in agreement with the known expression for the backscattered far field amplitude of a planar resistive plate at normal incidence. On the other hand, if $\rho \ll k_0 b^2/4$, (3.16) gives

$$\mathbf{S} = -\frac{a}{2}\sqrt{\frac{k_0\rho}{\pi}}\,(\hat{y}\sin\alpha + \hat{z}\cos\alpha)\,\Gamma_H(0)e^{-i\frac{\pi}{4}}$$

which is the result for a resistive circular cylinder of radius ρ and length a. For intermediate values of ρ the Fresnel integral must be retained, and when the far field amplitude is normalized to the flat plate expression (3.18), denoted by the affix fp,

$$\frac{\mathbf{S}}{\mathbf{S}^{fp}} = \frac{1}{\gamma}\mathcal{F}(\gamma) \tag{3.19}$$

independent of the resistivity, where

$$\gamma = \frac{b}{2}\sqrt{\frac{k_0}{\rho}} \tag{3.20}$$

The above results are also valid for a concave surface if $\mathcal{F}(\gamma)$ is replaced by its complex conjugate. Calculations based on the formulas (3.13), (3.17) and (3.19) are compared with numerical results obtained using the moment method and with measured data in Section 3.5.

A similar result for the bistatic far field amplitude of a cylindrically curved leaf in the general coordinate system (X, Y, Z) can be obtained (see Fig. 3.4). If the curved

plate is perfectly conducting, the associated Hertz potential can be found from (2.30) with

$$\mathbf{r}' = \rho\{(\cos\phi' - 1)\hat{x}' + \sin\phi'\hat{y}'\} + z'\hat{z}' \tag{3.21}$$

and we have

$$\mathbf{\Pi}_e(\mathbf{r}) = \frac{e^{ik_0 r}}{r} e^{ik_0\rho(\hat{k}_s - \hat{k}_i)\cdot\hat{x}'} \frac{iZ_0\rho}{2\pi k_0} \int_{-\frac{a}{2}}^{\frac{a}{2}} \int_{-\phi_0}^{\phi_0} \hat{n}'(\phi') \times \mathbf{H}_0 e^{-ik_0 B\rho\cos(\phi' - \tilde{\phi})} e^{-ik_0(\hat{k}_s - \hat{k}_i)\cdot\hat{z}'z'} \mathrm{d}\phi' \mathrm{d}z' \tag{3.22}$$

where

$$\cos\tilde{\phi} = \frac{1}{B}(\hat{k}_s - \hat{k}_i)\cdot\hat{x}' \,, \qquad \sin\tilde{\phi} = \frac{1}{B}(\hat{k}_s - \hat{k}_i)\cdot\hat{y}'$$

and

$$B = \left[\left\{(\hat{k}_s - \hat{k}_i)\cdot\hat{x}'\right\}^2 + \left\{(\hat{k}_s - \hat{k}_i)\cdot\hat{y}'\right\}^2\right]^{\frac{1}{2}}$$

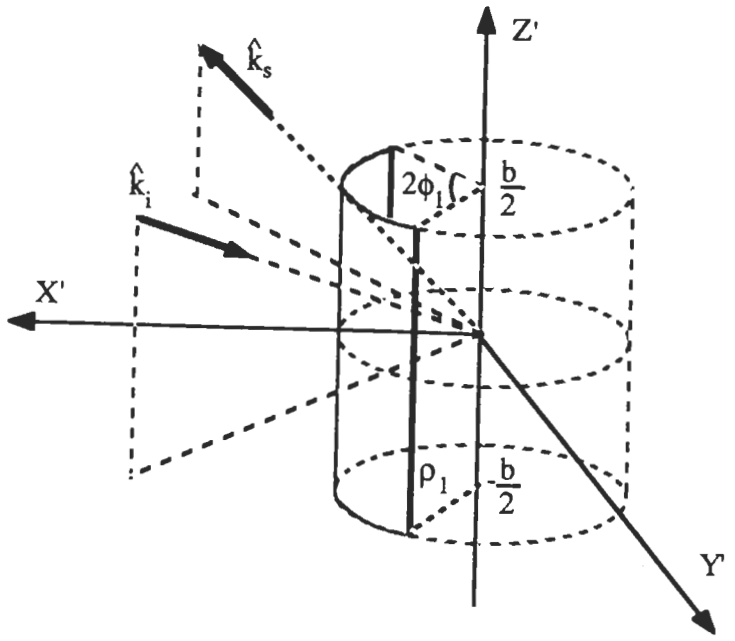

Figure 3.4: Geometry of a curved plate and coordinate system.

To ensure that the outer surface of the plate is completely illuminated, it is

necessary that

$$\hat{k}_i \cdot \hat{x}' < -\sin\phi_0 \ .$$

The z' integration can be carried out immediately and yields $a\frac{\sin V}{V}$ where

$$V = \frac{1}{2}k_0 a(\hat{k}_i - \hat{k}_s)\cdot\hat{z}' \ .$$

The ϕ' integral can be evaluated using the stationary phase approximation as before. The SP point is $\phi' = \tilde{\phi}$, and on the assumption that $k_0 B\rho \gg 1$ with $-\phi_0 < \tilde{\phi} < \phi_0$ (so that the SP point lies within the range of integration), the non-exponential portion of the integrand can be evaluated at its value at the SP point. In view of (2.31) the expression for the scattering amplitude is then

$$\mathbf{S} = e^{ik_0\rho\{(\hat{k}_s-\hat{k}_i)\cdot\hat{x}'-B\}}\left\{(\hat{n}'\cdot\mathbf{E}_0)\left[(\hat{k}_i\cdot\hat{k}_s)\hat{k}_s - \hat{k}_i\right] - (\hat{n}'\cdot\hat{k}_i)\left[(\hat{k}_s\cdot\mathbf{E}_0)\hat{k}_s - \mathbf{E}_0\right]\right\}K \tag{3.23}$$

with

$$K = -ia\sqrt{\frac{\rho}{\pi\lambda_0 B}}\left\{\mathcal{F}\left[\sqrt{\frac{k_0 B\rho}{2}}(\phi_0+\tilde{\phi})\right] + \mathcal{F}\left[\sqrt{\frac{k_0 B\rho}{2}}(\phi_0-\tilde{\phi})\right]\right\}\frac{\sin V}{V} \tag{3.24}$$

The bracketed terms in (3.23) are evaluated at the SP point $\phi' = \tilde{\phi}$ which is located at the point where the bisector of the angle between $\hat{k}_s$ and $-\hat{k}_i$ intersects the surface. This is the "specular" point of geometrical (ray) optics, and shows up at visible wavelengths as a bright streak parallel to the z' axis on the surface. Close to the forward scattering direction $\hat{k}_s = \hat{k}_i$, $k_0 B\rho$ is no longer large, and a method of evaluation appropriate to this range is discussed in Chapter 7.

For a curved resistive plate the analysis is similar, and the result is (see (2.37))

$$\begin{aligned}\mathbf{S} = \ & e^{ik_0\rho\{(\hat{k}_s-\hat{k}_i)\cdot\hat{x}'-B\}}\left\{(\hat{n}'\cdot\mathbf{E}_0)\Gamma_E\hat{k}_s\times\hat{k}_s\times\left[(\hat{n}'\cdot\hat{k}_i)\hat{k}_i - \hat{n}'\right]\right. \\ & \left.+(\hat{n}'\cdot\mathbf{H}_0)Z_0\Gamma_H\left[(\hat{k}_s\cdot\hat{k}_i)(\hat{n}'\times\hat{k}_s) + (\hat{n}'\cdot\hat{k}_s)(\hat{k}_s\times\hat{k}_i)\right]\right\}\frac{\hat{n}'\cdot\hat{k}_i}{|\hat{n}'\times\hat{k}_i|^2}K\end{aligned} \tag{3.25}$$

where the terms in brackets are evaluated at the SP point and K is as shown in (3.24).

3.4 Two Dimensional Curvature

We now examine the effect of giving the plate the same curvature in both principal planes, so that the plate conforms to a portion of a spherical surface of radius r. The geometry is shown in Fig. 3.5.

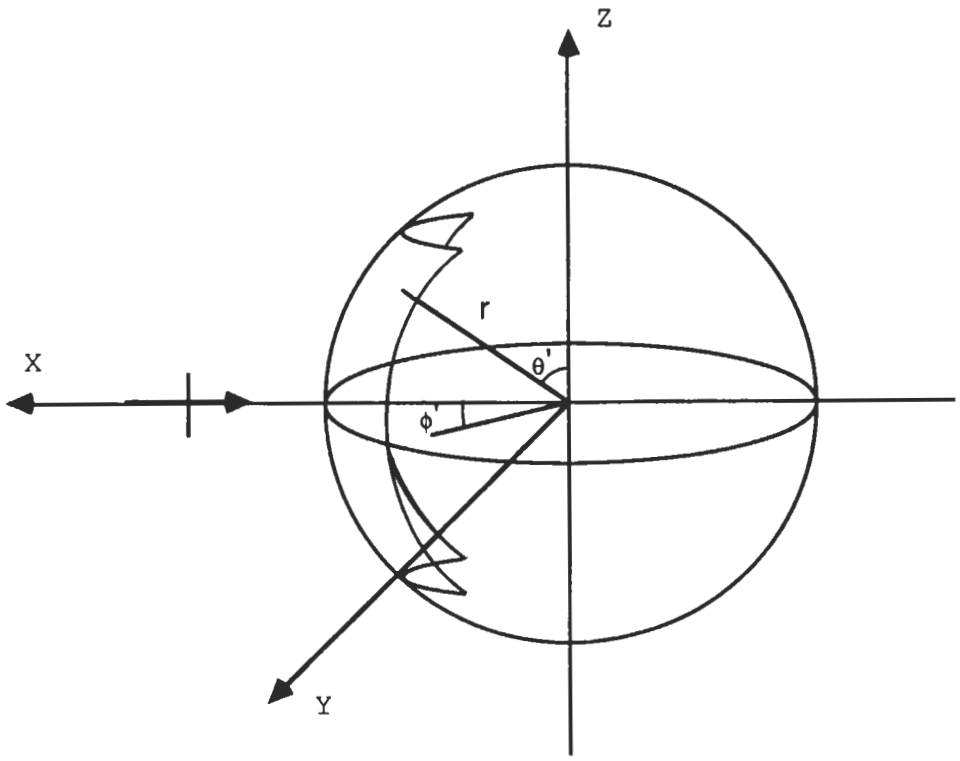

Figure 3.5: Geometry for the scattering of a plane wave from a resistive sheet which occupies a portion of the surface of a sphere of radius r at normal incidence.

In terms of the spherical polar coordinates (r, θ', ϕ') such that $x' = r\sin\theta'\cos\phi'$, $y' = r\sin\theta'\sin\phi'$ and $z' = r\cos\theta'$, the plate occupies the surface region $\frac{\pi}{2} - \theta_0 < \theta' < \frac{\pi}{2} + \theta_0$, $-f(\theta') < \phi' < f(\theta')$ where $\theta_0 = b/(2r)$ and $f(\theta') = a/(2r\sin\theta')$. The incident electric field is the same as that in Section 3.3, and for a perfectly conducting plate the physical optics expression for the induced electric current at a point θ', ϕ' on the

surface is

$$\begin{aligned}\mathbf{J}_{pc} = \; & 2Y_0 \{\sin\alpha \sin\theta'(-\hat{x}\sin\phi' + \hat{y}\cos\phi') \\ & + \cos\alpha(-\hat{x}\cos\theta' + \hat{z}\sin\theta'\cos\phi')\} \, e^{ik_0 r(1-\sin\theta'\cos\phi')}\end{aligned}$$

Unit vectors tangential to the surface and parallel and perpendicular respectively to the plane of incidence are

$$\hat{\eta}_1 = Q\{-\hat{x}(1-\sin^2\theta'\cos^2\phi') + (\hat{y}\sin\theta'\sin\phi' + \hat{z}\cos\theta')\sin\theta'\cos\phi'\}$$

$$\hat{\zeta}_1 = Q(-\hat{y}\cos\theta' + \hat{z}\sin\theta'\sin\phi')$$

where

$$Q = (1-\sin^2\theta'\cos^2\phi')^{-\frac{1}{2}}$$

and in terms of $\hat{\eta}_1$ and $\hat{\zeta}_1$ the perfectly conducting plate current is

$$\begin{aligned}\mathbf{J}_{pc} = \; & 2Y_0\{(\sin\alpha\sin\theta'\sin\phi' + \cos\alpha\cos\theta')\hat{\eta}_1 - \sin\theta'\cos\phi' \\ & \cdot(\sin\alpha\cos\theta' - \cos\alpha\sin\theta'\sin\phi')\hat{\zeta}_1\} Q e^{ik_0 r(1-\sin\theta'\cos\phi')}\end{aligned}$$

From (3.3) it now follows that for a resistive plate the current is

$$\begin{aligned}\mathbf{J} = \; & 2Y_0\{(\sin\alpha\sin\theta'\sin\phi' + \cos\alpha\cos\theta')\Gamma_H(\phi)\hat{\eta}_1 - \sin\theta'\cos\phi' \\ & \cdot(\sin\alpha\cos\theta' - \cos\alpha\sin\theta'\sin\phi')\Gamma_E(\phi)\hat{\zeta}_1\} Q e^{ik_0 r(1-\sin\theta'\cos\phi')}\end{aligned} \tag{3.26}$$

where the angle ϕ is such that

$$\cos\phi = \sin\theta'\cos\phi' \; .$$

In the backscattering direction the far field expression for the Hertz vector $\mathbf{\Pi}_e$ is

$$\mathbf{\Pi}_e(x) = \frac{e^{ik_0 x}}{x}\frac{iZ_0 r^2}{4\pi k_0}\int_{\frac{\pi}{2}-\theta_0}^{\frac{\pi}{2}+\theta_0}\int_{-f(\theta')}^{f(\theta')} \mathbf{J}(\theta',\phi') e^{ik_0 r(1-\sin\theta'\cos\phi')}\sin\theta' \mathrm{d}\theta' \mathrm{d}\phi'$$

and when the formula (3.26) for physical optics current is inserted, the backscattering far field amplitude for the curved resistive plate is found to be

$$\begin{aligned}\mathbf{S} = \; & \tfrac{ik_0r^2}{2\pi}\int_{\frac{\pi}{2}-\theta_0}^{\frac{\pi}{2}+\theta_0}\int_{-f(\theta')}^{f(\theta')}\{\sin\alpha[\sin^2\theta'\sin^2\phi'\Gamma_H(\phi)+\cos^2\theta'\Gamma_E(\phi)]\hat{y} \\ & +\cos\alpha[\sin^2\theta'\sin^2\phi'\Gamma_E(\phi)+\cos^2\theta'\Gamma_H(\phi)]\hat{z} \\ & +(\cos\alpha\hat{y}-\sin\alpha\hat{z})\sin\theta'\cos\theta'\sin\phi'[\Gamma_E(\phi)-\Gamma_H(\phi)]\} \\ & \cdot Q^2\sin^2\theta'\cos\phi' e^{2ik_0r(1-\sin\theta'\cos\phi')}\sin\theta'\mathrm{d}\theta'\mathrm{d}\phi'\end{aligned} \tag{3.27}$$

The like- and cross-polarized backscattering cross sections can be computed by substituting (3.27) in (3.11) and (3.12), and depolarization occurs to the extent that Γ_H and Γ_E differ over those portions of the plate that contribute to the integral.

The expression for $\mathbf{S}$ was evaluated using methods similar to those employed for one dimensional curvature. The first method is numerical. By subdividing the θ' and ϕ' ranges into $2L$ and $2M$ increments respectively and treating each elementary patch as a rectangular flat plate centered at $\theta'=\theta'_\ell$, $\phi'=\phi'_m$ ($\ell=1,2,\cdots,L; m=1,2,\cdots,M$) with dimensions $\Delta_1=r\Delta\theta'$, $\Delta_2=r\sin\theta'_2\Delta\phi'$ where $\Delta\theta'=\theta_0/L$ and $\Delta\phi'=f(\theta')/M$ and using (3.8) the result is

$$\mathbf{S}=\frac{ik_0}{2\pi}\sum_{\ell}^{2L}\sum_{m=1}^{2M}\{\quad\}\Delta_1\Delta_2Q^2\sin\theta'_\ell\cos\phi'_m e^{2ik_0r(1-\cos\theta'_\ell\cos\phi'_m)}\frac{\sin U_1}{U_1}\frac{\sin V_1}{V_1} \tag{3.28}$$

Here

$$\begin{aligned}U_1 &= k_0\Delta_1\cos\theta_\ell\cos\phi'_m \\ V_1 &= k_0\Delta_2\sin\phi'_m\end{aligned}$$

and $\{\quad\}$ denotes the terms in curly brackets in (3.27).

The second method is based on the stationary phase approximation. The (double) SP point of the integrand in (3.27) is $\theta'=\pi/2$, $\phi'=0$, and when all the non-exponential terms are removed from the integrand at this point, we have

$$\mathbf{S}=\frac{ik_0r^2}{2\pi}(\hat{y}\sin\alpha+\hat{z}\cos\alpha)\Gamma_H(0)\int_{\frac{\pi}{2}-\theta_0}^{\frac{\pi}{2}+\theta_0}\int_{-f(\theta')}^{f(\theta')}e^{2ik_0r(1-\sin\theta'\cos\phi')}\mathrm{d}\theta'\mathrm{d}\phi'$$

where we have used the fact that $\Gamma_E(0) = \Gamma_H(0)$. By expanding the exponent about the SP point and retaining only the quadratic terms, we then obtain

$$\mathbf{S} = \frac{2ir}{\pi}(\hat{y}\sin\alpha + \hat{z}\cos\alpha)\Gamma_H(0)\mathcal{F}\left(\frac{a}{2}\sqrt{\frac{k_0}{r}}\right)\mathcal{F}\left(\frac{b}{2}\sqrt{\frac{k_0}{r}}\right) \tag{3.29}$$

showing that to this approximation there is no depolarization. The amplitude normalized to its flat plate value (3.18) is

$$\frac{\mathbf{S}}{\mathbf{S}^{fp}} = \frac{1}{\gamma_1}\mathcal{F}(\gamma_1)\cdot\frac{1}{\gamma_2}\mathcal{F}(\gamma_2) \tag{3.30}$$

independent of the resistivity where

$$\begin{aligned}\gamma_1 &= \tfrac{a}{2}\sqrt{\tfrac{k_0}{r}} \\ \gamma_2 &= \tfrac{b}{2}\sqrt{\tfrac{k_0}{r}}\end{aligned} \tag{3.31}$$

and the reduction in $\mathbf{S}^{fp}$ is simply the product of the factors appropriate to a one-dimensional curvature in each of the principal planes of the plate.

The extension to the case of a plane wave which is not incident symmetrically is trivial. If the plate is rotated through an angle θ about the y axis (see Fig. 3.3) with $|\theta| \leq \frac{\pi}{2} - \theta_0$ so that no part of the plate is shadowed, the far field amplitude corresponding to (3.29) is

$$\begin{aligned}\mathbf{S} = \; & \tfrac{ir}{\pi}(\hat{y}\sin\alpha + \hat{z}\cos\alpha)\Gamma_H(0)\mathcal{F}\left(\tfrac{a}{2}\sqrt{\tfrac{k_0}{r}}\right) \\ & \cdot\left\{\mathcal{F}\left[\tfrac{b}{2}\sqrt{\tfrac{k_0}{r}}(1+\tfrac{\theta}{\theta_0})\right] + \mathcal{F}\left[\tfrac{b}{2}\sqrt{\tfrac{k_0}{r}}(1-\tfrac{\theta}{\theta_0})\right]\right\}\end{aligned} \tag{3.32}$$

Here also the expression is a natural extension of the formula for a one-dimensional curvature.

3.5 Comparison with Experimental Data

To test the validity of the physical optics model and to explore the effect of leaf curvature, a series of measurements was carried out using rectangular leaf sections.

Here again coleus leaves were chosen because they retain their moisture after being cut: at room temperature ($23°C$) the change in moisture content after 20 minutes was less than one percent. The scattering measurements were made at X-band in a small tapered anechoic chamber using an HP 8510A network analyzer. A schematic of the equipment is shown in Fig. 2.1, and the general procedures employed are described in Section 2.2. Since a single linearly-polarized horn antenna was used to radiate and receive the signals, only the like-polarized backscattering cross section could be measured. A small metal sphere was employed for calibration.

With the confidence that physical optics in conjunction with the resistive sheet model is adequate for planar leaves, we now compare the predictions for curved leaves with moment method data and with experimental results. To check the accuracy of (3.8), the backscattering was computed using a two-dimensional moment method code [Liepa et al, 1974] for resistive strip extended to the three dimensional case by assuming that the current on the curved plate is independent of z'. In Figs. 3.6 and 3.7 the normalized backscattering cross section (σ/λ_0^2) computed using 3.13 is compared with the moment method data for a flat leaf ($\rho = \infty$) and for a curved leaf having radius of curvature $\rho = 2\lambda_0$ respectively. Other pertinent parameters of the leaf are $a = 1.33\lambda_0$, $b = 2\lambda_0$, $\tau = 0.0107\lambda_0$, and $\epsilon = 20 + i7$. The overall agreement is good out to 70 and 50 degrees respectively, where the lower limit for the curved leaf corresponds to the onset of shadowing. As it is evident from Figs. 3.6 and 3.7 curvature causes a significant drop in backscattering around normal incidence and broadens the backscattering pattern. In Figs. 3.8 and 3.9 the Fresnel integral approximation (3.17) is compared with (3.13) for curved leaves having $\rho = 2\lambda_0$ and $\rho = 3\lambda_0$ respectively. The agreement is excellent as long as the stationary point is on the leaf, i.e., for $|\theta| < 28$ and 19 degrees respectively, but remains good for incidence

angles out to about 45 degrees.

Experimental measurement were also performed. In the first experiment a rectangular leaf section of the same size as before was attached to the surface of a right circular cylinder of styrofoam and the normal incidence backscattering cross section was measured. Cylinders of six different radii were used and the cross sections were normalized to that of the planar leaf. The measured cross section reductions for E polarization are plotted as a function of ρ in Fig. 3.9 and compared with the curves computed using the numerical summation (3.13) and the stationary phase approximation (3.19). The agreement is excellent. As ρ decreases from 33 to 3, γ increases from 0.76 to 3.14. Over the entire range, (3.13) and (3.19) yield virtually identical results, and (3.19) provides a simple and accurate expression for the cross section reduction.

For the case of a two dimensional curvature a similar experiment was performed in which a leaf section was mounted on the surface of a styrofoam sphere. Spheres of six different radii were used. To facilitate the mounting a naturally-curved leaf was chosen and cut to conform to the spherical region $\frac{\pi}{2}-\theta_0 < \theta' < \frac{\pi}{2}+\theta_0$, $-\phi_0 < \phi' < \phi_0$ where $\theta_0 = b/(2r)$, $\phi_0 = a(2r\sin\theta_0)$, with $a = 1.33\lambda_0$ and $b = 2\lambda_0$. The region is slightly different from that specified in Section 3.4, and the leaf sections are no longer rectangular when flattened out, but calculations based on the summation (3.28) showed that the cross section reduction is the same for both. The measured data are compared with the numerical and analytical results (3.28) and (3.30) in Fig. 3.11. The agreement is again excellent and confirms the validity of the simple formula (3.30) for curvature in two dimensions.

As evident from the preceding figures, curvature can have a significant effect on the backscattering cross section, and in a practical situation, it is important to know

the frequency range where any curvature of a leaf must be taken into account. To this end, Fig. 3.12 shows the cross section reductions versus frequency for three leaf sections $6cm$ on a side, curved in one dimension with radii 3, 6 and $12cm$. In all three cases $Mg = 0.7$, $\tau = 0.5mm$ and the frequency dependence implied by the resistivity R and the Debye-Cole dielectric model [Ulaby and El-Rayes, 1987] was included. Once again (3.13) and (3.19) yield virtually identical results and if, for example, $\rho = 12cm$, the curvature produces a significant effect only at C-band frequencies and above.

3.6 Conclusions

The resistive sheet model in conjunction with the physical optics approximation which was previously shown to accurately predict the backscattering cross section of a planar leaf has been extended to the case of a curved leaf. For a rectangular section of a leaf curved in one and two dimensions, the physical optics expression for the backscattered field was evaluated numerically and by a stationary phase approximation. The latter leads to simple analytical expressions for the cross section reduction produced by the curvature. Numerical results based on the two methods are virtually identical and in excellent agreement with measured X-band data for rectangular sections of coleus leaves applied to surfaces of styrofoam cylinders and spheres of different radii. As a result of these comparisons, it is concluded that the curvature effect is accurately simulated by a multiplicative factor involving a Fresnel integral whose argument is a function of the relevant leaf dimension, the radius of curvature and the frequency, but independent of the material properties of the leaf.

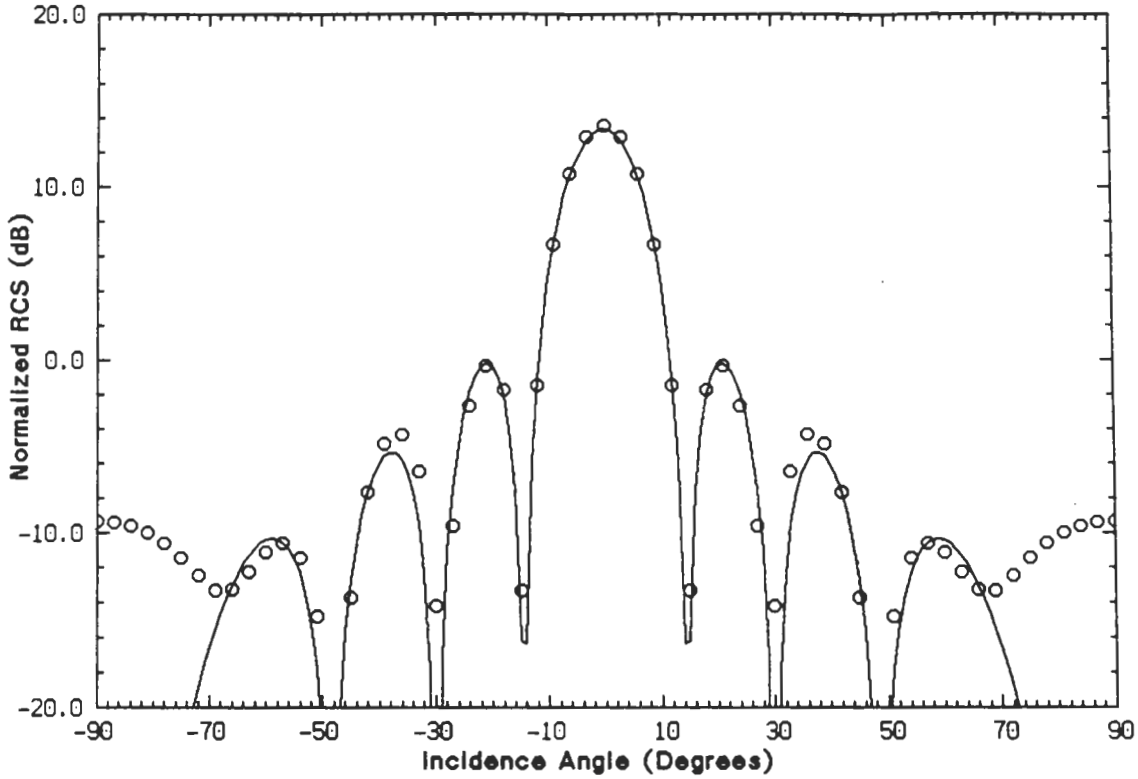

Figure 3.6: Normalized RCS (σ/λ_0^2) for a flat ($\rho = \infty$) rectangular section of a leaf with $a = 1.33\lambda_0$, $d = 2\lambda_0$, $\tau = 0.0107\lambda_0$, and $\epsilon = 20 + i7$ for E polarization: (——) numerical summation (3.13), (o o o) moment method.

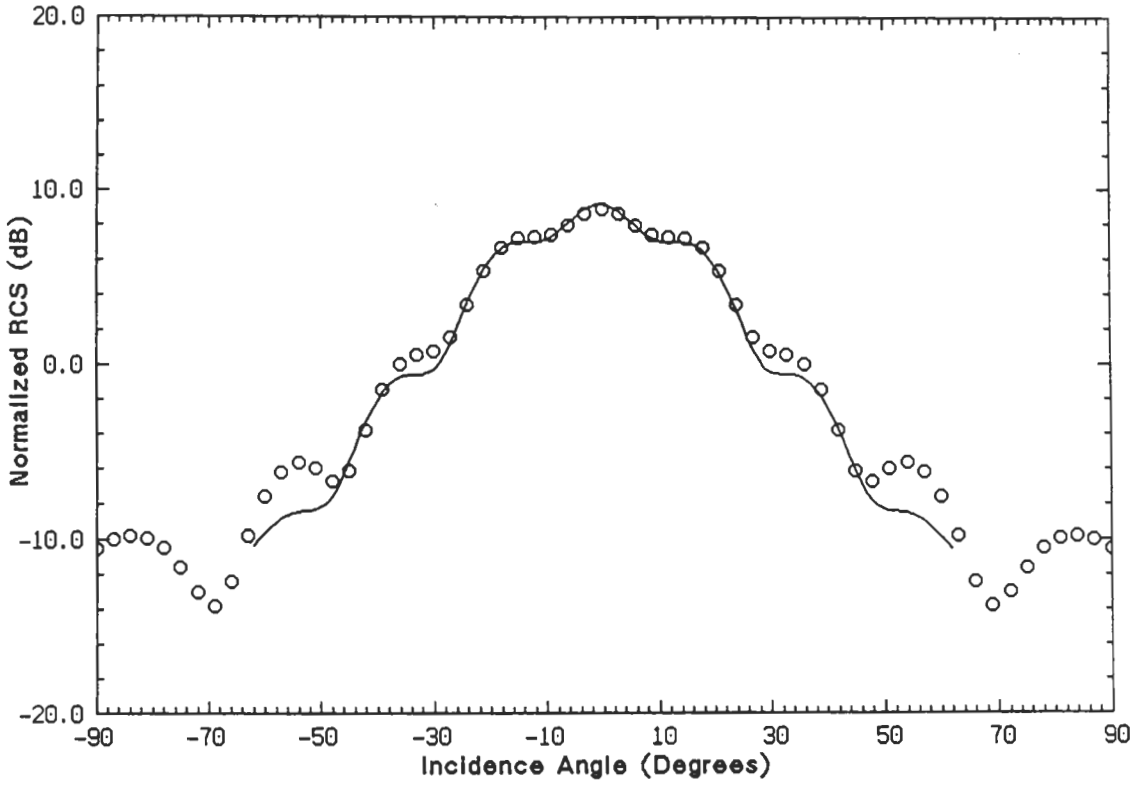

Figure 3.7: Normalized RCS (σ/λ_0^2) for a one dimensionally curved rectangular section of a leaf with $a = 1.33\lambda_0$, $d = 2\lambda_0$, $\tau = 0.0107\lambda_0$, $\epsilon = 20 + i7$, and $\rho = 2\lambda_0$ for E polarization: (——) numerical summation (3.13), (o o o) moment method.

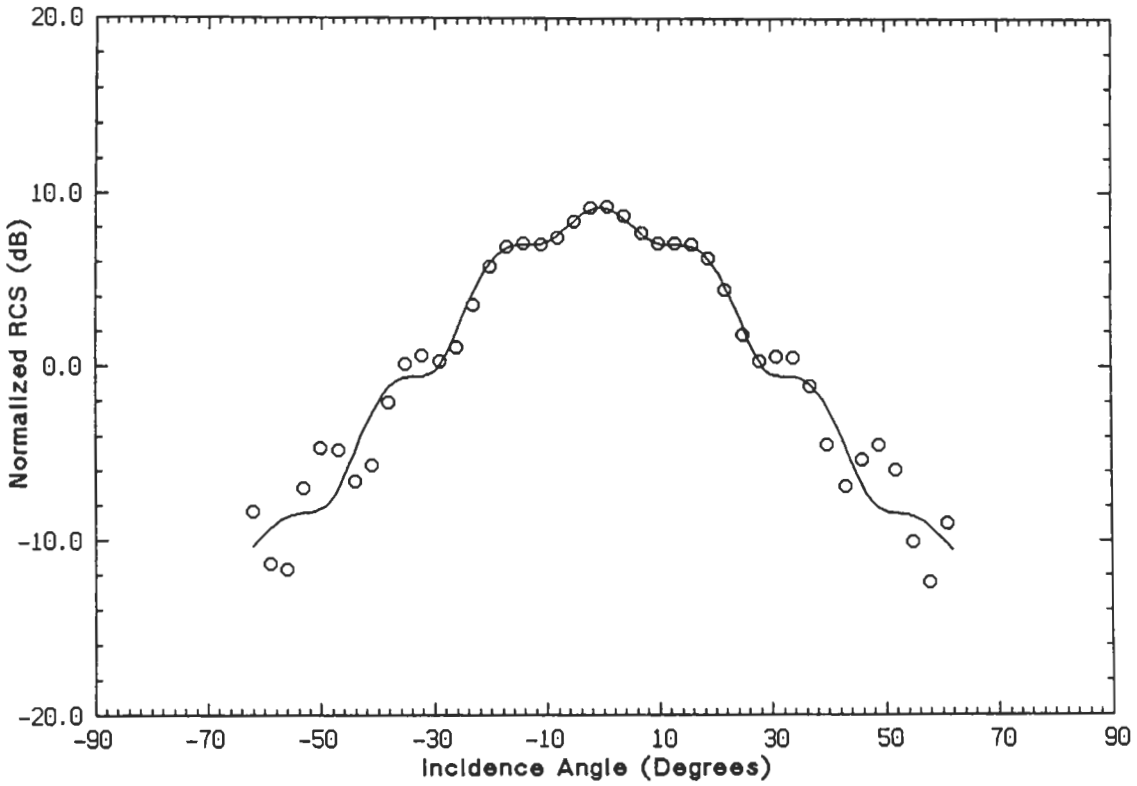

Figure 3.8: Normalized RCS (σ/λ_0^2) for a one dimensionally curved rectangular section of a leaf with $a = 1.33\lambda_0$, $d = 2\lambda_0$, $\tau = 0.0107\lambda_0$, $\epsilon = 20 + i7$, and $\rho = 2\lambda_0$ for E polarization: (——) numerical summation (3.13), (o o o) Fresnel integral approximation (3.17).

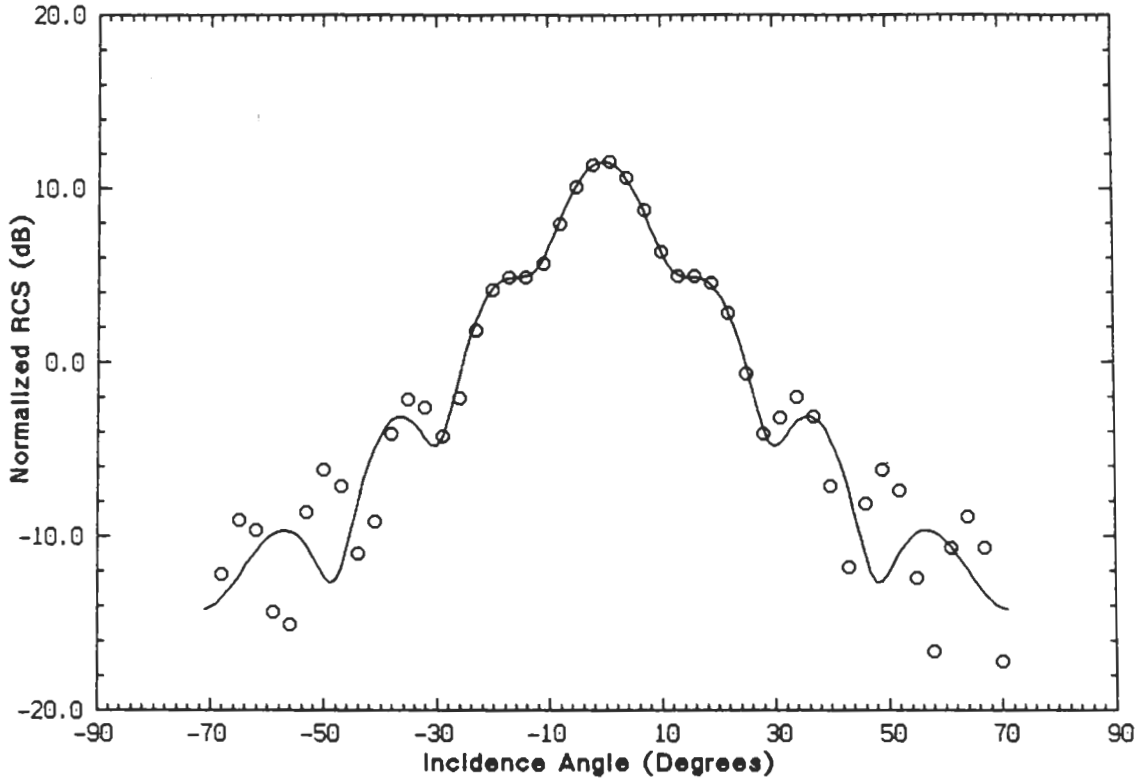

Figure 3.9: Normalized RCS (σ/λ_0^2) for a one dimensionally curved rectangular section of a leaf with $a = 1.33\lambda_0$, $d = 2\lambda_0$, $\tau = 0.0107\lambda_0$, $\epsilon = 20 + i7$, and $\rho = 3\lambda_0$ for E polarization: (——) numerical summation (3.13), (o o o) Fresnel integral approximation (3.17).

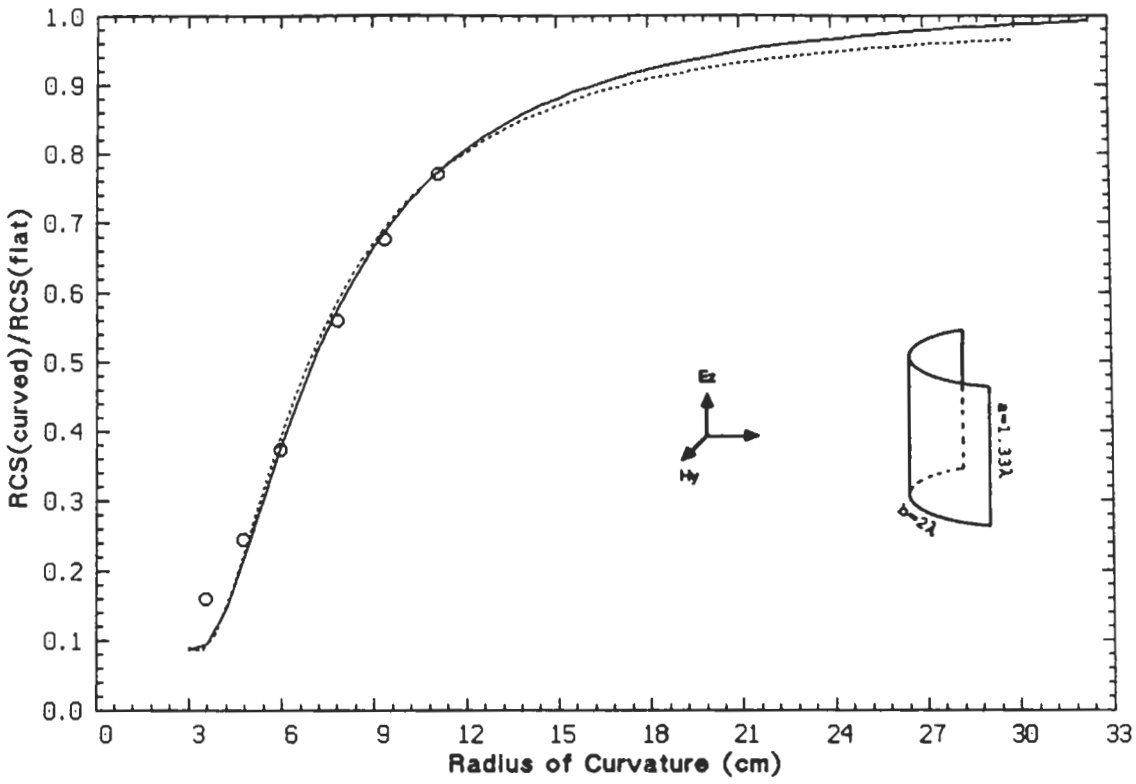

Figure 3.10: Comparison of the measured RCS (o o o) reduction at normal incidence with the numerical summation (3.13) (——) and Fresnel integral approximation (3.19) (- - -) for a one dimensionally curved rectangular section of a coleus leaf versus radius of curvature ($\tau = 0.32mm$, $\lambda_0 = 3cm$).

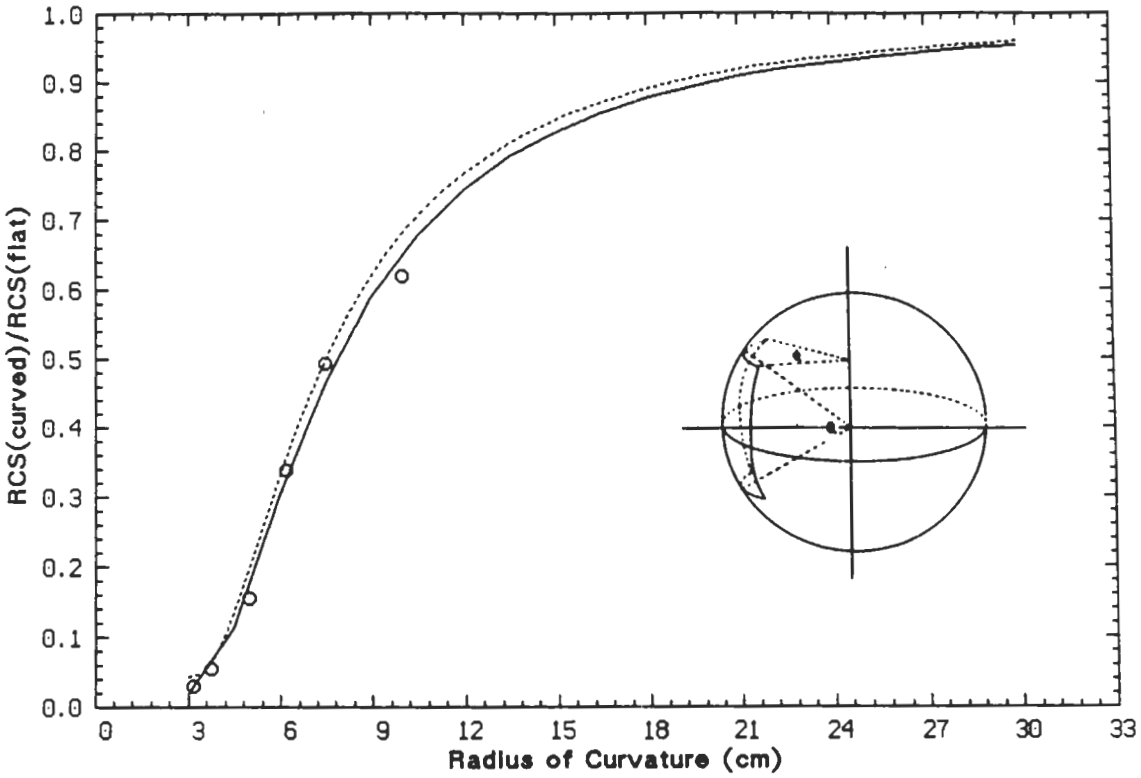

Figure 3.11: Comparison of the measured RCS (o o o) reduction at normal incidence with the numerical summation (3.28) (——) and Fresnel integral approximation (3.30) (- - -) for a spherically curved section of a coleus leaf versus radius of curvature ($\tau = 0.32mm$, $\lambda_0 = 3cm$).

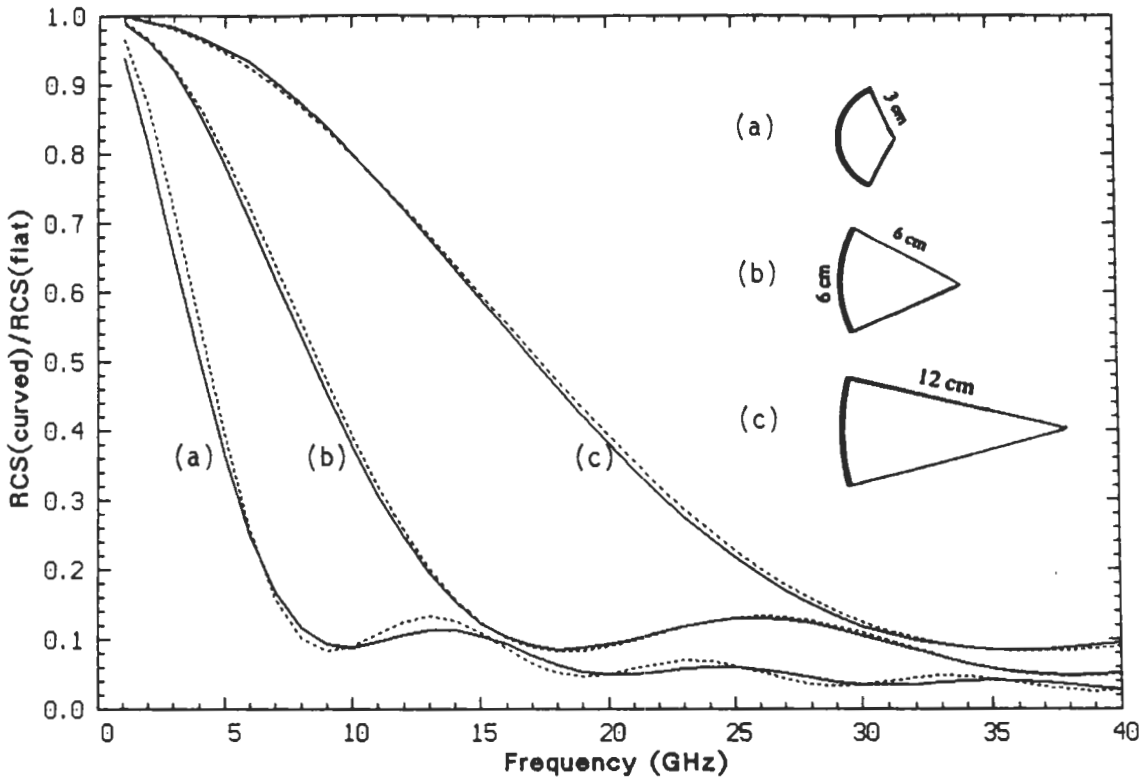

Figure 3.12: Normalized incidence RCS reduction versus frequency due to the one dimensional curvature of a rectangular section of a leaf with $Mg = 0.7$ and $\tau = 0.5mm$ for three different radii of curvature using the numerical (3.13) (——) and analytical (3.19) (- - -) expressions.

CHAPTER IV

SCATTERING MODEL FOR A LEAF AT MILLIMETER WAVELENGTHS

4.1 Introduction

At millimeter wave frequencies a typical leaf is a significant fraction of a wavelength in thickness, and its nonuniform dielectric profile now affects the scattering. At microwave frequencies where a typical leaf is electrically thin with lateral dimensions at least comparable to the free space wavelength λ_0, several methods have been proposed [e.g. Le Vine et al 1985, Willis et al, 1988] all based on the physical optics approximation applied to a uniform dielectric slab. In particular, if the leaf thickness is no more than about $\lambda_0/50$, physical optics in conjunction with a resistive sheet model predicts the scattering at most angles of incidence (see Chapter 2) and can also handle curved leaves (see Chapter 3).

On the other hand, at millimeter wavelengths the thickness can be a significant fraction of a wavelength, and it is also necessary to take into account the internal structure of a leaf. At least two different types of cell can be distinguished, and their differing water content affects the dielectric constant, leading to a nonuniform dielectric profile. To compute the scattering at these higher frequencies, two different physical optics approximations are examined. The first of these employs the

polarization current which would exist in an infinite slab consisting of one, two or more layers simulating the dielectric profile of the leaf, and this is referred to as the volume integral physical optics (VIPO) approximation. When there are many layers, a convenient method of implementation is described in Section 4.4. The second (and simpler) approach postulates a surface current which, for an infinite slab, produces a plane wave identical to the reflected field, and this is the surface current physical optics (SCPO) approximation.

For an electrically thin leaf or plate, the two approximations are indistinguishable, but as the thickness (or frequency) increases, the predicted scattering differs in most directions, and by comparison with the results of a moment method solution of the volume integral equation, it is shown that VIPO is superior. In addition, for a two layer material, it is no longer adequate to treat the plate as homogeneous one having an average dielectric constant. Provided the actual dielectric profile of a leaf is simulated, it appears that VIPO can predict the scattering behavior of a leaf to an accuracy that is sufficient for most practical purposes at millimeter wavelengths.

4.2 Structure of a Leaf

The simplified structure of a typical vegetation leaf is shown in Fig. 4.1. The type and number density of cells may vary as a function of depth into the leaf which, in turn, results in a nonuniform dielectric profile. The effect of this nonuniformity becomes observable at higher frequencies where the thickness of the leaf is comparable to the wavelength.

As was explained in Section 1.3.1 leaves mainly consist of two types of photosynthetic cells: palisade parenchyma, consisting of column-shaped cells in which most photosynthesis takes place, and spongy parenchyma, which consist of irregularly

shaped cells with large spaces between them. Because a large part of the vegetation material is water, its dielectric constant is strongly influenced by the dielectric constant of water and the water content. For most leaves, the water content is higher in its upper layer (palisade region) than in the under surface (spongy region).

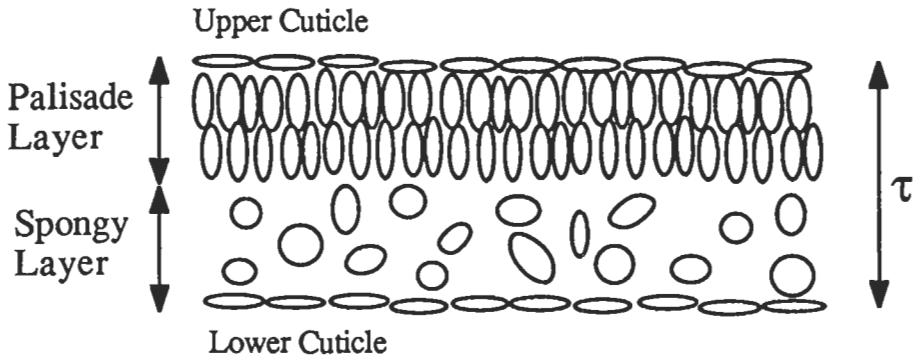

Figure 4.1: The structure of a typical vegetation leaf.

The sensitivity of the dielectric constant to water content is much greater in the lower part of the millimeter wave spectrum than in the upper, but this is more than counterbalanced by the thickness to wavelength ratio. The net result is that the sensitivity to dielectric variations is greater at the higher frequencies.

To examine the effect of the nonuniform dielectric profile on the scattering properties of the leaf at millimeter wavelengths, we computed the normal incidence reflection coefficient Γ_0 of a two-layer dielectric slab and compared it with the reflection coefficient of a uniform dielectric slab whose dielectric constant is the average. The computation was performed for a leaf thickness of $0.5mm$, and the water content ratio of the two layer was chosen to be 4 to 1, representing a marked variation between

the upper and lower surfaces of the leaf. From the data in Table 4.1, it is seen that when the two-layer slab is approximated by a uniform slab the error in the reflection

f (GHz)	ϵ_1	ϵ_2	$\epsilon_{(avg)} = \frac{\epsilon_1+\epsilon_2}{2}$	Γ_0	$\Gamma_{0(avg)}$
35	20+i21	6+i3	13+i12	$0.74\angle 6$	$0.78\angle -0.16$
94	6+i5	2+i1	4+i3	$0.59\angle 12$	$0.48\angle 27$
140	5+i4	2+i1	3.5+i2.5	$0.50\angle 20$	$0.34\angle 26.1$

Table 4.1: Voltage reflection coefficient for a two-layer and average dielectric slab

coefficient increases with increasing frequency, and is as large as 4 dB at 140 GHz.

4.3 Physical Optics Approximations

At microwave frequencies where a typical leaf is no more than about $\lambda_0/50$ in thickness with lateral dimensions comparable to or larger than the wavelength, the scattering properties can be accurately predicted using the physical optics approximation applied to a resistive sheet model of a leaf. In effect, the leaf is modeled as an infinitesimally thin layer, but as the frequency increases the sheet model fails and it is necessary to take the leaf thickness in to account. There are now two types of physical optics approximation that can be employed. The standard one is the surface current (SCPO) approach in which an infinite dielectric slab is replaced by an equivalent sheet current that produces a plane wave identical to the reflected wave of the slab. This current is then used as an approximation to the equivalent surface current over the upper surface of a finite dielectric plate. Alternatively, the induced (volume) polarization current in the plate can be approximated by the current in the infinite dielectric slab, and we shall refer to this as the volume integral physical

optics (VIPO) method. It is more accurate than the SCPO method, although the latter is more convenient to use for evaluating the scattered field.

To illustrate the two procedures, consider a dielectric plate consisting of a homogeneous dielectric of thickness d_1 and relative permittivity ϵ_1 atop a second material of thickness $d_2 - d_1$ and relative permittivity ϵ_2. The plate occupies the region $-\frac{a}{2} \leq x \leq \frac{a}{2}$, $-\frac{b}{2} \leq y \leq \frac{b}{2}$, and $-d_2 \leq z \leq 0$ as shown in Fig. 4.2, and is illuminated by an E-polarized plane wave whose electric vector is

$$\mathbf{E}^i = \hat{y} e^{ik_0(x \sin\theta_i - z\cos\theta_i)} \tag{4.1}$$

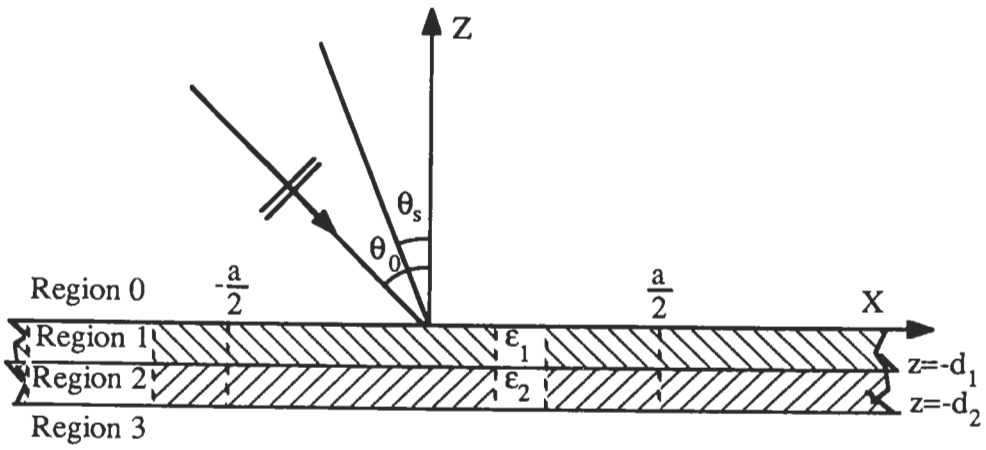

Figure 4.2: The geometry of the scattering of a plane wave from a two-layer dielectric slab.

When the plate is treated as an infinitely extended slab, the electric field can be

written as

$$\begin{aligned} E_y &= (e^{-ik_{0z}z} + \Gamma e^{ik_{0z}z})e^{ik_0 \sin\theta_i x} && (0 \le z) \\ E_y &= (B_1 e^{-ik_{1z}z} + A_1 e^{ik_{1z}z})e^{ik_0 \sin\theta_i x} && (-d_1 \le z \le 0) \\ E_y &= (B_2 e^{-ik_{2z}z} + A_2 e^{ik_{2z}z})e^{ik_0 \sin\theta_i x} && (-d_2 \le z \le -d_1) \\ E_y &= B_3 e^{-ik_{0z}z} e^{ik_0 \sin\theta_i x} && (z \le -d_2) \end{aligned} \tag{4.2}$$

where

$$k_{0z} = k_0 \cos\theta_i, \qquad k_{jz} = k_0\sqrt{\epsilon_j - \sin^2\theta_i}$$

for $j = 1, 2$. If R_1 and R_2 are the reflection coefficients at the upper and lower surfaces where

$$R_1 = \frac{k_{0z} - k_{1z}}{k_{0z} + k_{1z}}, \qquad R_2 = \frac{k_{0z} - k_{2z}}{k_{0z} + k_{2z}}$$

and

$$C_\pm = 1 \pm \frac{k_{2z}}{k_{1z}} \left\{1 + R_2 e^{2ik_{2z}(d_2 - d_1)}\right\} \left\{1 - R_2 e^{2ik_{2z}(d_2 - d_1)}\right\}^{-1},$$

application of the boundary condition at the three interfaces gives

$$\begin{aligned} B_1 &= \tfrac{C_+(1+R_1)}{C_+ + C_- R_1 e^{2ik_{1z}d_1}}, && A_1 = \frac{C_-}{C_+} e^{2ik_{1z}d_1} B_1 \\ B_2 &= \tfrac{e^{i(k_{1z} - k_{2z})d_1}}{1 - R_2 e^{2ik_{2z}(d_2 - d_1)}} \cdot \frac{2}{C_+} B_1, && A_2 = -R_2 e^{2ik_{2z}d_2} B_2 \\ B_3 &= e^{i(k_{2z} - k_{0z})d_2}(1 - R_2) B_2 \end{aligned}$$

and

$$\Gamma = \frac{C_+ R_1 + C_- e^{2ik_{1z}d_1}}{C_+ + C_- R_1 e^{2ik_{1z}d_1}}.$$

The corresponding results for a single layer of thickness d_1 and relative dielectric constant ϵ_1 can be obtained by putting $d_2 = d_1$ and $k_{2z} = k_{1z}$, implying $B_2 = B_1$ and $A_2 = A_1$.

Given a volume distribution of electric ($\mathbf{J}_e$) and magnetic ($\mathbf{J}_m$) current in free space, the corresponding Hertz vector and scattered field can be obtained from (1.2) and (1.4) respectively. In the dielectric slab the volume current $\mathbf{J}_e$ is the polarization current

$$\mathbf{J}_e = -ik_0 Y_0(\epsilon_j - 1)E_y\hat{y} \ . \tag{4.3}$$

where E_y has the value appropriate to each layer ($j = 1, 2$), and when this is inserted into (1.2) and the integration carried out over the volume occupied by the plate, we obtain the VIPO approximation. For scattering in the direction θ_s indicated in Fig. 4.2 the expression for the Hertz vector is

$$\mathbf{\Pi}_e^{VIPO} = \hat{y}\frac{e^{ik_0 r}}{r}\frac{ab}{4\pi}\frac{\sin X}{X}F \tag{4.4}$$

where

$$\begin{aligned} F = \ & (\epsilon_1 - 1)\left\{\frac{1-e^{-i(k_{1z}-k_0\cos\theta_s)d_1}}{i(k_{1z}-k_0\cos\theta_s)}A_1 - \frac{1-e^{-i(k_{1z}+k_0\cos\theta_s)d_1}}{i(k_{1z}+k_0\cos\theta_s)}B_1\right\} \\ & +(\epsilon_2 - 1)\left\{\frac{e^{-i(k_{2z}-k_0\cos\theta_s)d_1} - e^{-i(k_{1z}-k_0\cos\theta_s)d_2}}{i(k_{2z}-k_0\cos\theta_s)}A_2\right. \\ & \left. -\frac{e^{i(k_{2z}+k_0\cos\theta_s)d_1} - e^{-i(k_{2z}+k_0\cos\theta_s)d_2}}{i(k_{2z}+k_0\cos\theta_s)}B_2\right\} \end{aligned} \tag{4.5}$$

and

$$X = \frac{k_0 a}{2}(\sin\theta_s + \sin\theta_i) \ .$$

The far zone scattered field can then be obtained from (1.4) and written as

$$\mathbf{E}^s = \frac{e^{ik_0 r}}{r}\mathbf{S}_E(\theta_s, \theta_i)$$

where $\mathbf{S}_E(\theta_s, \theta_i)$ is the far field amplitude, and for the VIPO approximation the result is

$$\mathbf{S}_E^{VIPO}(\theta_s, \theta_i) = \hat{y}\frac{k_0^2 ab}{4\pi}\frac{\sin X}{X}F. \tag{4.6}$$

The more conventional SCPO approximation can be obtained by noting that the electric current sheet[1]

$$\mathbf{J}_e = -2Y_0 \cos\theta_i \Gamma e^{ik_0 \sin\theta_i x}\delta(z)\hat{y} \tag{4.7}$$

produces a plane wave identical to the field reflected from the dielectric slab. As evident from the impulse function $\delta(z)$ in (4.7), the current is located at the upper surface of the slab, and when (4.7) is inserted into (1.2) we find

$$\mathbf{\Pi}_e^{SCPO} \approx \hat{y}\frac{e^{ik_0 r}}{r} \cdot \frac{-i}{2\pi k_0} \cos\theta_i \Gamma ab \frac{\sin X}{X},$$

and the far field amplitude is then

$$\mathbf{S}_E^{SCPO}(\theta_s, \theta_i) = \hat{y}\frac{-ik_0}{2\pi} \cos\theta_i \Gamma ab \frac{\sin X}{X}. \tag{4.8}$$

In the specular ($\theta_s = -\theta_i$) and backscattering ($\theta_s = \theta_i$) directions it can be verified that (4.6) and (4.8) are identical, but in the other directions the two approximations differ.

In the case of H polarization for which

$$\begin{aligned} \mathbf{E}^i = &\quad -Z_0(\cos\theta_i \hat{x} + \sin\theta_i \hat{z}) e^{ik_0(x\sin\theta_i - z\cos\theta_i)}, \\ \mathbf{H}^i = &\quad \hat{y} e^{ik_0(x\sin\theta_i - z\cos\theta_i)}. \end{aligned} \tag{4.9}$$

the analysis is similar. With H_y represented as shown in (4.2), the various coefficients (now indicated by primes) differ from those for E polarization in having k_{1z} replaced by k_{1z}/ϵ_1 and k_{2z} replaced by k_{2z}/ϵ_2 everywhere except in the exponents. The induced polarization current then has two components and is given by

$$\mathbf{J}_e = -ik_0 Y_0 (\epsilon_j - 1)(E_x \hat{x} + E_z \hat{z}) \; . \tag{4.10}$$

[1]This new equivalent physical optics surface current is different from the traditional physical optics surface current (see Chapter 8.)

where $E_x = (ik_0\epsilon_j)^{-1}Z_0\partial H_y/\partial z$ and $E_z = -(ik_0\epsilon_j)^{-1}Z_0\partial H_y/\partial x$ have the values appropriate to each layer ($j = 1, 2$). The Hertz vector can be computed using (1.2), and for the scattered field $\mathbf{H}^s$, the far field amplitude is found to be

$$\mathbf{S}_H^{VIPO}(\theta_s, \theta_i) = \hat{y}\frac{k_0^2 ab}{4\pi}\frac{\sin X}{X}(\cos\theta_s F_1' - \sin\theta_s F_2'). \tag{4.11}$$

where

$$\begin{aligned} F_1' = \; & \{\tfrac{k_{1z}(\epsilon_1-1)}{k_0\epsilon_1}\left[\tfrac{1-e^{-i(k_{1z}-k_0\cos\theta_s)d_1}}{i(k_{1z}-k_0\cos\theta_s)}A_1' + \tfrac{1-e^{i(k_{1z}+k_0\cos\theta_s)d_1}}{i(k_{1z}+k_0\cos\theta_s)}B_1'\right] \\ & + \tfrac{k_{2z}(\epsilon_2-1)}{k_0\epsilon_2}\left[\tfrac{e^{-i(k_{2z}-k_0\cos\theta_s)d_1} - e^{-i(k_{1z}-k_0\cos\theta_s)d_2}}{i(k_{2z}-k_0\cos\theta_s)}A_2'\right. \\ & \left. + \tfrac{e^{i(k_{2z}+k_0\cos\theta_s)d_1} - e^{-i(k_{2z}+k_0\cos\theta_s)d_2}}{i(k_{2z}+k_0\cos\theta_s)}B_2'\right]\}\ , \end{aligned} \tag{4.12}$$

and

$$\begin{aligned} F_2' = \; & \sin\theta_i\{\tfrac{(\epsilon_1-1)}{\epsilon_1}\left[\tfrac{1-e^{-i(k_{1z}-k_0\cos\theta_s)d_1}}{i(k_{1z}-k_0\cos\theta_s)}A_1' - \tfrac{1-e^{i(k_{1z}+k_0\cos\theta_s)d_1}}{i(k_{1z}+k_0\cos\theta_s)}B_1'\right] \\ & + \tfrac{(\epsilon_2-1)}{\epsilon_2}\left[\tfrac{e^{-i(k_{2z}-k_0\cos\theta_s)d_1} - e^{-i(k_{1z}-k_0\cos\theta_s)d_2}}{i(k_{2z}-k_0\cos\theta_s)}A_2'\right. \\ & \left. - \tfrac{e^{i(k_{2z}+k_0\cos\theta_s)d_1} - e^{-i(k_{2z}+k_0\cos\theta_s)d_2}}{i(k_{2z}+k_0\cos\theta_s)}B_2'\right]\}\ . \end{aligned} \tag{4.13}$$

The SCPO approximation can also be obtained by noting that a magnetic current sheet of the form

$$\mathbf{J}_m = -2Z_0\cos\theta_i\Gamma' e^{ik_0\sin\theta_i x}\delta(z)\hat{y} \tag{4.14}$$

generates a plane wave identical to the reflected wave. Using this as the equivalent surface current on the dielectric plate, the magnetic far field amplitude becomes

$$\mathbf{S}_H^{SCPO}(\theta_s, \theta_i) = \hat{y}\frac{-ik_0}{2\pi}\cos\theta_i\Gamma' ab\frac{\sin X}{X}\ . \tag{4.15}$$

As in the case of E polarization, the two approximations are identical in the specular direction, but (4.11) and (4.15) differ in all other directions, including backscattering ($\theta_s = \theta_i$) unless $\theta_i = 0$.

4.4 Combined Sheets Model

When using the VIPO approximation, an efficient way to take into account the effect of any non-uniformity in the dielectric profile is to model the leaf as a stack of N combined current sheets. Each sheet simulates a very thin dielectric layer whose thickness is less than $\lambda/15$ where λ is the wavelength in the material. A combined sheet consists of coincident resistive and modified conductive sheets that support electric and magnetic currents respectively, with the conductive sheet accounting for the electric currents flowing perpendicular to the dielectric layer. The n^{th} layer sheets are characterized by a complex resistivity and conductivity R_n and R_n^*, respectively, where

$$\begin{aligned} R_n &= \frac{iZ_0}{k_0\Delta_n(\epsilon_n-1)} \\ R_n^* &= \frac{iY_0\epsilon_n}{k_0\Delta_n(\epsilon_n-1)} \end{aligned} \quad . \tag{4.16}$$

Here ϵ_n and Δ_m are the relative dielectric constant and thickness of the n^{th} layer, and $\tau = \sum_{n=1}^{N} \Delta_n$ is the total thickness of the dielectric slab.

The boundary conditions at the n^{th} combined sheet are as follows [Senior and Volakis, 1987]:

$$\hat{n}' \times \left\{\hat{n}' \times [\mathbf{E}^+ + \mathbf{E}^-]\right\} = -2R_n\mathbf{J}_{en} \tag{4.17}$$

$$\mathbf{J}_{en} = \hat{n}' \times [\mathbf{H}^+ - \mathbf{H}^-] \tag{4.18}$$

where $\mathbf{J}_{en}$ is the total electric current supported by the resistive sheet, and

$$\hat{n}' \times \left\{\hat{n}' \times [\mathbf{H}^+ + \mathbf{H}^-]\right\} - \frac{iY_0}{k_0}\hat{n}' \times \frac{\partial}{\partial n'}[\mathbf{E}^+ + \mathbf{E}^-] = -2R_n^*\mathbf{J}_{mn} \tag{4.19}$$

$$\mathbf{J}_{en} = -\hat{n}' \times [\mathbf{E}^+ - \mathbf{E}^-] \tag{4.20}$$

where $\mathbf{J}_{mn}$ is the total magnetic current supported by the conductive sheet. The superscripts $^{+,-}$ refer to the upper $(+)$ and lower $(-)$ sides of the sheet, and $\hat{n}'$ is the unit vector outward normal to the upper side.

4.5 Scattering by a Stack of N Planar Sheets

Consider a stack of N infinite planar combined sheets that are all parallel to the $x-y$ plane of a Cartesian coordinate system (x, y, z) as depicted in Fig. 4.3.

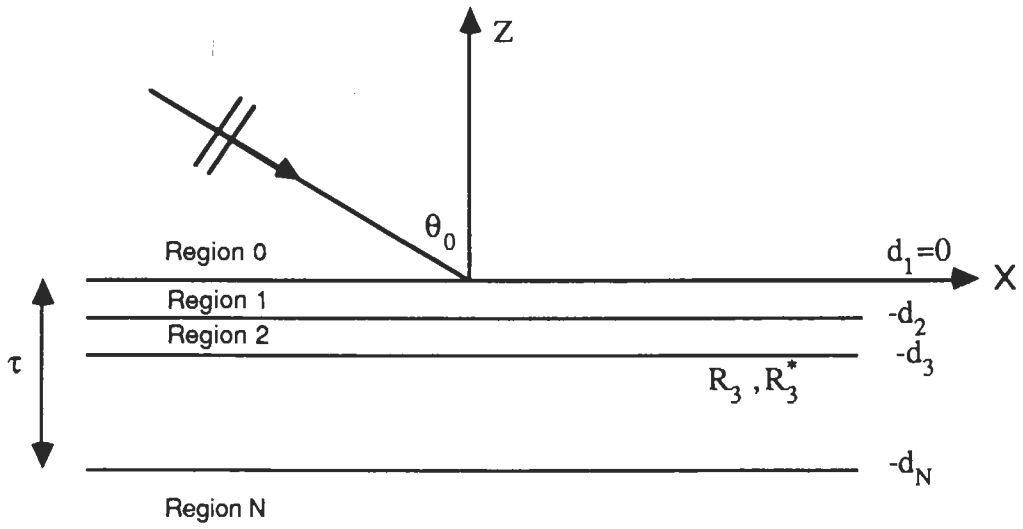

Figure 4.3: N layer of combined-sheets simulating infinite dielectric slab.

The top sheet is in the $z = 0$ plane and the n^{th} sheet is located at $z = -d_n$, where $d_1 = 0$. The space between the n^{th} and $(n+1)^{th}$ sheets is denoted by region n, and we note that region 0 $(z > 0)$ and region N $(z < -d_N)$ are semi-infinite free space. A plane wave whose plane of incidence is parallel to the $x-z$ plane impinges on the stack of sheets from above. From the symmetry of the problem, all the field vectors are independent of y (i.e., $\frac{\partial}{\partial y} = 0$), as a result of which the field components in each region can be separated into $E-$ and $H-$polarized waves which are the dual of each other. From Maxwell's equation the field components in region n for an E-polarized wave must satisfy

$$H_{nx} = -\frac{1}{i\omega\mu_0}\frac{\partial}{\partial z}E_{ny} \ , \tag{4.21}$$

$$H_{nz} = \frac{1}{i\omega\mu_0}\frac{\partial}{\partial x}E_{ny} \ , \tag{4.22}$$

$$(\frac{\partial^2}{\partial x^2} + \frac{\partial^2}{\partial z^2} + k_0^2)E_{ny} = 0 \ , \tag{4.23}$$

and for a H-polarized wave

$$E_{nx} = \frac{1}{i\omega\epsilon_0}\frac{\partial}{\partial z}H_{ny} \ , \tag{4.24}$$

$$E_{nz} = -\frac{1}{i\omega\epsilon_0}\frac{\partial}{\partial x}H_{ny} \ , \tag{4.25}$$

$$(\frac{\partial^2}{\partial x^2} + \frac{\partial^2}{\partial z^2} + k_0^2)H_{ny} = 0 \ . \tag{4.26}$$

Equations (4.24)-(4.26) are the dual of (4.21)-(4.23) and each can be obtained from the other on replacing E_n by H_n, H_n by $-E_n$, and $\epsilon_0(\mu_0)$ by $\mu_0(\epsilon_0)$.

4.5.1 E Polarization

For the case of E polarization in which the electric field vector of the incident wave is perpendicular to the plane of incidence, the incident field is given by (4.1). From (4.23), (4.21) and (4.22) the field vector in region n can be expressed as

$$E_{ny} = [C_n^i e^{-ik_0\cos\theta_i z} + C_n^r e^{ik_0\cos\theta_i z}]e^{ik_0\sin\theta_i x} \tag{4.27}$$

$$H_{nx} = Y_0\cos\theta_i[C_n^i e^{-ik_0\cos\theta_i Z} - C_n^r e^{ik_0\cos\theta_i z}]e^{ik_0\sin\theta_i x} \tag{4.28}$$

$$H_{nz} = Y_0\sin\theta_i[C_n^i e^{-ik_0\cos\theta_i z} + C_n^r e^{ik_0\cos\theta_i z}]e^{ik_0\sin\theta_i x} \tag{4.29}$$

The coefficients C_n^i and C_n^r are the amplitudes of the waves travelling in the $-z$ and $+z$ directions, respectively, in region n. In region 0, $C_0^i = 1$ and $C_0^r = \Gamma_E$ (the

total reflection coefficient) and in region N, $C_N^r = 0$, $C_N^i = T_E$ (the total transmission coefficient). Hence, using the boundary conditions (4.17)-(4.20), there are $2N$ unknowns and $2N$ equations that can be solved simultaneously. The quantities of primary interest are the total reflection and transmission coefficients which can be obtained directly as follows. From boundary condition (4.19) we have

$$\hat{z} \times \left\{ \hat{z} \times \hat{x}[H_{(n-1)x} + H_{nx}] \right\} - \frac{iY_0}{k_0} \hat{z} \times \frac{\partial}{\partial z}[E_{(n-1)y} + E_{ny}] = -2R_n^* \mathbf{J}_{mn} \qquad (4.30)$$

Upon substitution of (4.27) and (4.28) into (4.30) the left hand side of (4.30) vanishes resulting in $\mathbf{J}_{mn} = 0$. Thus, the conductive sheet is not excited in this polarization, as expected since there is no current in the z direction in the dielectric slab. In the absence of a magnetic source the tangential component of the electric field must be continuous as given by (4.20)

$$\left(E_{(m-1)y} - E_{my} \right) |_{z=-d_m} = 0 \qquad (4.31)$$

Upon inserting the expressions (4.27) and (4.28) into (4.31), (4.17), and (4.18) the following set of equations is obtained

$$C_{(n-1)}^i e^{ik_0 \cos\theta_i d_n} + C_{(n-1)}^r e^{-ik_0 \cos\theta_i d_n} = C_n^i e^{ik_0 \cos\theta_i d_n} + C_n^r e^{-ik_0 \cos\theta_i d_n} \qquad (4.32)$$

$$\begin{aligned} C_n^i e^{ik_0 \cos\theta_i d_n} + C_n^r e^{-ik_0 \cos\theta_i d_n} = \; & Y_0 \cos\theta_i R_n [C_{(n-1)}^i e^{ik_0 \cos\theta_i d} - C_{(n-1)}^r e^{-ik_0 \cos\theta_i d_n} \\ & - C_n^i e^{ik_0 \cos\theta_i d_n} + C_n^r e^{-ik_0 \cos\theta_i d_n}] \end{aligned}$$

By defining the reflection coefficient in region n as

$$\Gamma_n^E \triangleq \frac{C_n^r}{C_n^i} e^{-2ik_0 \cos\theta_i d_{n+1}} ,$$

the following relations can be obtained:

$$\Gamma_{n-1}^E = \frac{-1 + (2Y_0 \cos\theta_i R_{n-1})\, e^{2ik_0 \cos\theta_i (d_{n+1} - d_n)} \Gamma_n^E}{(1 + 2Y_0 \cos\theta_i R_n) + e^{2ik_0 \cos\theta_i (d_{n+1} - d_n)} \Gamma_n^E} \qquad (4.33)$$

$$C_n^i = \frac{1+\Gamma_{n-1}^E}{1+e^{2ik_0\cos\theta_i(d_{n+1}-d_n)}\Gamma_n^E} C_{n-1}^i \tag{4.34}$$

The induced electric current in the n^{th} sheet can also be obtained from (4.18) and by application of (4.32) it can be expressed as (excluding the phase factor $e^{ik_0\sin\theta_i x}$)

$$\mathbf{J}_{en}^E = \hat{y}2Y_0\cos\theta_i\left[C_n^r - C_{n-1}^r\right]e^{-ik_0\cos\theta_i d_n} \tag{4.35}$$

This induced current may be expressed in terms of the reflection coefficients of different layers:

$$\begin{aligned}\mathbf{J}_{en}^E &= \hat{y}2Y_0\cos\theta_i[C_{n-1}^i - C_n^i]e^{ik_0\cos\theta_i d_n} \\ &= \hat{y}2Y_0\cos\theta_i e^{ik_0\cos\theta_i d_n}[1-\tfrac{1+\Gamma_n^E}{1+e^{2ik_0\cos\theta_i(d_{n+1}-d_n)}\Gamma_n^E}] \\ &\quad\cdot\textstyle\prod_{\ell=1}^{n-1}(\tfrac{1+\Gamma_{\ell-1}^E}{1+e^{2ik_0\cos\theta_i(d_{\ell+1}-d_\ell)}\Gamma_\ell^E})\end{aligned} \tag{4.36}$$

Now, the total reflection coefficient in region 0 ($\Gamma_E(\theta_i) = \Gamma_0^E$) can be evaluated from the recursive relation (4.33) by noting that $\Gamma_N^E = 0$ (the region N is semi-infinite). The total transmission coefficient can also be obtained from (4.34) and (4.33) as follows:

$$T_E(\theta_i) \triangleq \frac{C_N^i}{C_0^i} = \prod_{n=1}^{N}\left[\frac{1+\Gamma_{n-1}^E}{1+e^{2ik_0\cos\theta_i(d_{n+1}-d_n)}\Gamma_n^E}\right] \tag{4.37}$$

4.5.2 H Polarization

Unlike the E-polarized case where the magnetic current is zero, an H-polarized incident wave excites a magnetic current in the y direction and neither of the tangential electric or magnetic field is continuous across the combined sheets. The tangential field vectors in region n can be obtained by applying the duality relationships to equation (4.27) and (4.28). Therefore,

$$H_{ny} = \left[B_n^i e^{-ik_0\cos\theta_i z} + B_n^r e^{ik_0\cos\theta_i z}\right]e^{ik_0\sin\theta_i x} \tag{4.38}$$

and

$$E_{nx} = -Z_0 \cos\theta_i \left[B_n^i e^{-ik_0 \cos\theta_i z} - B_n^r e^{ik_0 \cos\theta_i z}\right] e^{ik_0 \sin\theta_i x} \tag{4.39}$$

where as before B_n^i and B_n^r are the amplitudes of the waves travelling in the $-z$ and $+z$ directions respectively. By applying the boundary conditions (4.17)-(4.20) at the n^{th} sheet and resorting to equations (4.38) and (4.39) the following relations between the field amplitudes in region $(n-1)$ and region n are obtained:

$$B_{n-1}^i e^{ik_0 \cos\theta_i d_n} + B_{n-1}^r e^{-ik_0 \cos\theta_i d_n} + B_n^i e^{ik_0 \cos\theta_i d_n} + B_n^r e^{-ik_0 \cos\theta_i d_n} =$$
$$\frac{2R_n^* Z_0 \cos\theta_0}{\sin^2\theta_i} \cdot [B_{n-1}^i e^{ik_0 cos\theta_i d_n} - B_{n-1}^r e^{-ik_0 \cos\theta_i d_n} - B_n^i e^{ik_0 \cos\theta_i d_n} + B_n^r e^{-ik_0 \cos\theta_i d_n}] \tag{4.40}$$

$$B_{n-1}^i e^{ik_0 \cos\theta_i d_n} - B_{n-1}^r e^{-ik_0 \cos\theta_i d_n} + B_n^i e^{ik_0 \cos\theta_i d_n} - B_n^r e^{-ik_0 \cos\theta_i d_n} =$$
$$\frac{2Rn \sec\theta_i}{z_0} [B_{n-1}^i e^{ik_0 \cos\theta_i d_n} + B_{n-1}^r e^{-ik_0 \cos\theta_i d_n} - B_n^i e^{ik_0 \cos\theta_i d_n} - B_n^r e^{-ik_0 \cos\theta_i d_n}] \tag{4.41}$$

By denoting the reflection coefficient in region n by

$$\Gamma_n^H \triangleq \frac{B_n^r}{B_n^i} e^{-2ik_0 \cos\theta_i d_{n+1}}$$

after some algebraic manipulation of (4.40) and (4.41) we obtain

$$\Gamma_{n-1}^H = \frac{(Q_n P_n - 1) - (1 - P_n)(Q_n - 1)\Gamma_n^H e^{2ik_0 \cos\theta_i (d_{n+1} - d_n)}}{-(1 + P_n)(1 + Q_n) + (1 - Q_n P_n)\Gamma_n^H e^{2ik_0 \cos\theta_i (d_{n+1} - d_n)}} \tag{4.42}$$

$$B_n^i = \frac{(Q_n - 1) + (1 + Q_n)\Gamma_{n-1}^H}{-(1 + Q_n) + (1 - Q_n)\Gamma_n^H e^{2ik_0 \cos\theta_i (d_{n+1} - d_n)}} B_{n-1}^i \tag{4.43}$$

where the parameters Q_n and P_n are

$$Q_n = \frac{sin^2\theta_i}{2R_n^* Z_0 \cos\theta_i}$$

$$P_n = \frac{2R_n \sec\theta_i}{Z_0}.$$

Recursive relation (4.42) gives the total reflection coefficient in region 0 ($\Gamma_H(\theta_i) = \Gamma_0^H$) noting that $\Gamma_N^H = 0$ and the total transmission coefficient using (4.43) is given

by

$$T_H(\theta_i) = \prod_{n=1}^{N} \left[\frac{(Q_n - 1) + (1 + Q_n)\Gamma_{n-1}^H}{-(1 + Q_n) + (1 - Q_n)\Gamma_n^H e^{2ik_0 \cos\theta_i (d_{n+1} - d_n)}} \right] \tag{4.44}$$

The induced electric and magnetic currents in the n^{th} sheet can be obtained by inserting equations (4.38) and (4.39) into equations (4.18) and (4.20). Excluding the phase factor $e^{ik_0 \sin\theta_i x}$, they are given by

$$\mathbf{J}_{en}^H = -(B_{n-1}^i e^{ik_0 \cos\theta_i d_n} + B_{n-1}^r e^{-ik_0 \cos\theta_i d_n} - B_n^i e^{ik_0 \cos\theta_i d_n} - B_n^r e^{-ik_0 \cos\theta_i d_n})\hat{x} \tag{4.45}$$

$$\mathbf{J}_{mn}^H = Z_0 \cos\theta_i (B_{n-1}^i e^{ik_0 \cos\theta_i d_n} - B_{n-1}^r e^{-ik_0 \cos\theta_i d_n} - B^i e^{ik_0 \cos\theta_i d_n} + B_n^r e^{-ik_0 \cos\theta_i d_n})\hat{y} \tag{4.46}$$

after using (4.43) the induced currents may be expressed in terms of the reflection coefficients as follows

$$\begin{aligned} \mathbf{J}_{en}^H = \; & -\hat{x} e^{ik_0 \cos\theta_i d_{n-1}} [(1 + \Gamma_{n-1}^H) + (1 + \Gamma_n^H e^{2ik_0 \cos\theta_i (d_{n+1} - d_n)}) \\ & \cdot \frac{(Q_n - 1) + (1 + Q_n)\Gamma_{n-1}^H}{(1 + Q_n) + (1 - Q_n)\Gamma_n^H e^{ik \cos\theta_i (d_{n+1} - d_n)}}] \cdot \prod_{\ell=1}^{n-1} [\frac{(Q_\ell - 1) + (1 + Q_\ell)\Gamma_{\ell-1}^H}{(1 + Q_\ell) + (1 - Q_\ell)\Gamma_\ell^H e^{ik_0 \cos\theta_i (d_{\ell+1} - d_\ell)}}] \end{aligned} \tag{4.47}$$

and

$$\begin{aligned} \mathbf{J}_{mn}^H = \; & \hat{y} Z_0 cos\theta_i \cdot e^{ik_0 \cos\theta_i d_{n-1}} [(1 - \Gamma_{n-1}^H) + (1 - \Gamma_n^H e^{2ik_0 \cos\theta_i (d_{n+1} - d_n)}) \\ & \cdot \frac{(Q_n - 1) + (1 + Q_n)\Gamma_{n-1}^H}{(1 + Q_n) + (1 - Q_n)\Gamma_n^H e^{ik \cos\theta_i (d_{n+1} - d_n)}}] \cdot \prod_{\ell=1}^{n-1} [\frac{(Q_\ell - 1) + (1 + Q_\ell)\Gamma_{\ell-1}^H}{(1 + Q_\ell) + (1 - Q_\ell)\Gamma_\ell^H e^{ik_0 \cos\theta_i (d_{\ell+1} - d_\ell)}}] \end{aligned} \tag{4.48}$$

Note that here $\mathbf{J}_{en}^H(x) = \mathbf{J}_{en}^H e^{ik_0 \sin\theta_i x}$ and $\mathbf{J}_{mn}^H(x) = \mathbf{J}_{mn}^H e^{ik_0 \sin\theta_i x}$.

4.6 Scattering by a Rectangular Stack

Consider a portion of an N-layered stack of combined sheets in the form of a rectangle occupying the region $-\frac{a}{2} \leq x \leq \frac{a}{2}$, $-\frac{b}{2} \leq y \leq \frac{b}{2}$ as depicted in Fig. 4.4. The illumination and observation directions are such that the planes of incidence and observation are parallel to the x axis.

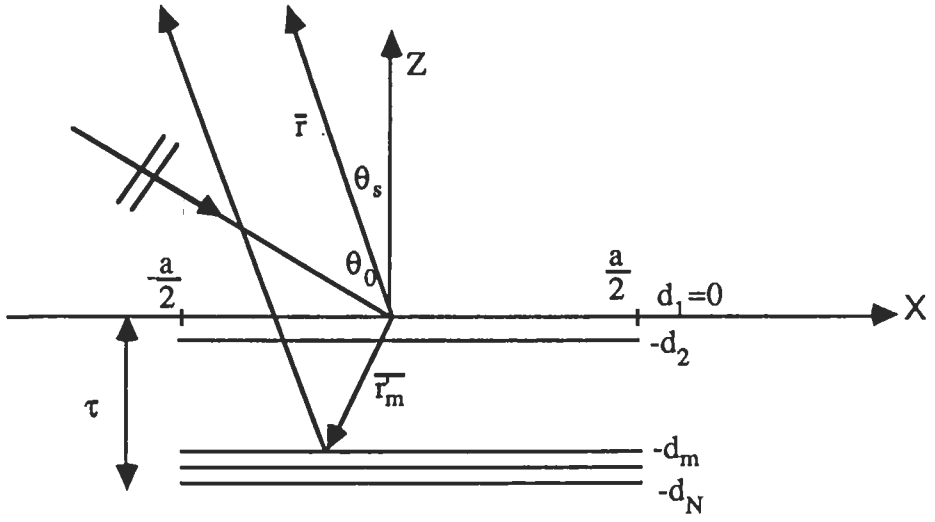

Figure 4.4: The geometry of scattering of a plane wave from a finite N-layer combined-sheet.

If the induced electric and magnetic currents in the n^{th} sheet are denoted by $\mathbf{J}_{en}$ and $\mathbf{J}_{mn}$ then the scattered field can be attributed to the electric and magnetic Hertz vector potentials and have the following form:

$$\mathbf{\Pi}_e(\mathrm{r}) = \frac{iZ_0}{4\pi k_0} \sum_{n=1}^{N} \int \mathbf{J}_{en}(\mathrm{r}') \frac{e^{ik_0|\mathrm{r}-\mathrm{r}'_n|}}{|\,\mathrm{r}-\mathrm{r}'_n\,|} \mathrm{d}s'_n$$

$$\mathbf{\Pi}_m(\mathrm{r}) = \frac{iY_0}{4\pi k_0} \sum_{n=1}^{N} \int \mathbf{J}_{mn}(\mathrm{r}') \frac{e^{ik_0|\mathrm{r}-\mathrm{r}'_n|}}{|\,\mathrm{r}-\mathrm{r}'_n\,|} \mathrm{d}s'_n$$

where

$$\mathrm{r} = r(-\sin\theta_s \hat{x} + \cos\theta_s \hat{z}) \ ,$$

$$\mathrm{r}'_n = x'\hat{x} + y'\hat{y} - d_n\hat{z} \ .$$

In the far zone the approximation

$$|\,\mathrm{r}-\mathrm{r}'_n\,| \approx r + \sin\theta_s x' + \cos\theta_s d_n$$

leads to

$$\mathbf{\Pi}_e(\mathbf{r}) \approx \frac{e^{ik_0 r}}{r}\frac{iZ_0}{4\pi k_0}\int_{-a/2}^{a/2}\int_{-b/2}^{b/2}(\sum_{n=1}^{N}\mathbf{J}_{en}(\mathbf{r}')e^{ik_0\cos\theta_s d_n})e^{ik_0\sin\theta_s x'}\mathrm{d}x'\mathrm{d}y' \ , \tag{4.49}$$

$$\mathbf{\Pi}_m(\mathbf{r}) \approx \frac{e^{ik_0 r}}{r}\frac{iY_0}{4\pi k_0}\int_{-a/2}^{a/2}\int_{-b/2}^{b/2}(\sum_{n=1}^{N}\mathbf{J}_{mn}(\mathbf{r}')e^{ik_0\cos\theta_s d_n})e^{ik_0\sin\theta_s x'}\mathrm{d}x'\mathrm{d}y' \ . \tag{4.50}$$

Using the physical optics approximation, the currents obtained for the infinite layered sheets will be substituted in expressions (4.49) and (4.50) in order to find the scattered fields.

4.6.1 E polarization

For E polarization the induced magnetic current $\mathbf{J}_{mn}^{E}$ is zero which renders $\mathbf{\Pi}_m = 0$, and upon inserting expression (4.36) for $\mathbf{J}_{en}(x)$ in (4.49) we have

$$\mathbf{\Pi}_e(\mathbf{r}) = \hat{\mathbf{y}}\frac{e^{ik_0 r}}{k_0 r}\frac{iZ_0}{4\pi}(\sum_{n=1}^{N}\mathbf{J}_{en}^{E}e^{ik_0\cos\theta_s d_n})ab\frac{\sin X}{X} \tag{4.51}$$

where, as before, $X = \frac{k_0 a}{2}(\sin\theta_s + \sin\theta_i)$. In this case the far-field amplitude has the following form:

$$\mathbf{S}_E(\theta_s,\theta_i) = \hat{y}\frac{i}{4\pi}k_0 abZ_0(\sum_{n=1}^{N}\mathbf{J}_{en}^{E}e^{ik_0\cos\theta_s d_n})\frac{\sin X}{X} \ , \tag{4.52}$$

from which the bistatic scattering cross section can be obtained. For backscattering ($\theta_s = \theta_i$) and in the specular direction ($\theta_s = -\theta_i$) the summation term in (4.52) reduces to a telescopic series using equation (4.35) for $\mathbf{J}_{en}^{E}$, resulting in

$$\sum_{n=1}^{N}\mathbf{J}_{en}^{E}e^{ik_0\cos\theta_i d_n} = 2Y_0\cos\theta_i C_0^r = 2Y_0\cos\theta_i\Gamma_E(\theta_i),$$

and

$$\sigma_E(\theta_i,\theta_i) = 4\pi\frac{(ab)^2}{\lambda_0^2}\cos^2\theta_i \mid \Gamma_E(\theta_i)\mid^2 \frac{\sin^2(k_0 a\sin\theta_i)}{(k_0 a\sin\theta_i)^2} \ .$$

The extinction cross section can also be simplified using (4.36) as follows:

$$\sum_{n=1}^{N} \mathbf{J}_{en}^{E} e^{-ik_0 \cos\theta_i d_n} = 2Y_0 \cos\theta_i (1 - T_E(\theta_i)),$$

and

$$\sigma_E^{ext} = 2ab \cos\theta_i Re[1 - T_E(\theta_i)].$$

4.6.2 H polarization

For H polarization the Hertz vector potentials are of the form

$$\mathbf{\Pi}_e(\mathbf{r}) = \hat{x} \frac{e^{ik_0 r}}{r} \frac{iZ_0}{4\pi k_0} \left(\sum_{n=1}^{N} \mathbf{J}_{en}^{H} e^{ik_0 \cos\theta_s d_n}\right) ab \frac{sinX}{X},$$

$$\mathbf{\Pi}_m(\mathbf{r}) = \hat{y} \frac{e^{ik_0 r}}{r} \frac{iY_0}{4\pi k_0} \left(\sum_{n=1}^{N} \mathbf{J}_{mn}^{H} e^{ik_0 \cos\theta_s d_n}\right) ab \frac{sinX}{X},$$

and the scattered magnetic field is given by

$$\mathbf{H}^s = \frac{e^{ik_0 r}}{r} \mathbf{S}_H(\theta_s, \theta_i),$$

where

$$\mathbf{S}_H(\theta_s, \theta_i) = \hat{y} \frac{i}{4\pi} k_0 ab \left[\sum_{n=1}^{N} (\cos\theta_s \mathbf{J}_{en}^{H} + Y_0 \mathbf{J}_{mn}^{H}) e^{ik_0 \cos\theta_s d_n}\right] \frac{\sin X}{X}. \tag{4.53}$$

The bistatic cross section can be obtained from (1.12) and the backscattering cross section can be simplified using expressions (4.45) and (4.46) for J_{en}^{H} and J_{mn}^{H}:

$$\begin{aligned} &\textstyle\sum_{n=1}^{N} (cos\theta_i J_{en}^{H} + Y_0 J_{mn}^{H}) e^{ik_0 \cos\theta_i d_n} = \\ &-2\cos\theta_i \textstyle\sum_{n=1}^{N} (B_{n-1}^{r} - B_n^{r}) = -2\cos\theta_i B_0^{r} = -2\cos\theta_i \Gamma_H(\theta_i), \end{aligned} \tag{4.54}$$

which leads to

$$\sigma_H(\theta_i, \theta_i) = 4\pi \frac{(ab)^2}{\lambda_0^2} \cos^2\theta_i \mid \Gamma_H(\theta_i) \mid^2 \frac{\sin^2(k_0 a \sin\theta_i)}{(k_0 a \sin\theta_i)^2}.$$

The extinction cross section also can be simplified by noting that

$$\sum_{n=1}^{N} (-\cos\theta_i J_{en}^{H} + Y_0 J_{mn}^{H}) e^{-ik_0 \cos\theta_i d_n} = 2\cos\theta_i (1 - T_H(\theta_i))$$

from which we obtain

$$\sigma_H^{ext} = 2ab\cos\theta_i Re[1 - T_H(\theta_i)].$$

It is worth noting that the expressions obtained in Chapter 2 and Chapter 3 for the far field amplitude of leaves in the general coordinate system can be easily extended for a thick leaf upon replacing Γ_E and Γ_H by

$$\Gamma_E = \frac{Z_0}{2\cos\theta_i}\sum_{n=1}^{N}\mathbf{J}_{en}^{E}e^{ik_0\cos\theta_s d_n}$$

$$\Gamma_H = -\frac{1}{2\cos\theta_s}\sum_{n=1}^{N}(\cos\theta_s\mathbf{J}_{en}^{H} + Y_0\mathbf{J}_{mn}^{H})e^{ik_0\cos\theta_s d_n}$$

4.7 Numerical Results

To illustrate the difference between the VIPO and SCPO approximations we consider a homogeneous (single layer) plate of thickness $d_2 = \lambda_0/4$ with $\epsilon_2 = \epsilon_1 = 3+i0.1$. For an E-polarized plane wave incident at 30 degrees, the amplitude and phase of $\mathbf{S}^{VIPO}/\mathbf{S}^{SCPO}$ are given in Figs. 4.5 and 4.6, and these show that the difference increases away from the specular and backscattering directions. At a fixed scattering angle, the difference increases with the electrical thickness of the plate up to the first resonance and then decreases. To test their accuracy the two approximations have been compared with the results of a moment method solution of the volume integral equation as given in Appendix B. The numerical code is a two-dimensional one which was extended to three dimensions by assuming that the induced currents are independent of the y coordinate. Since the dielectric constant of most vegetation materials is high, it is necessary to have the cell sizes very small, and one consequence of this is the need to compute the matrix elements extremely accurately, especially for H polarization. For a $2\lambda_0$ square plate formed from the above-mentioned layer and illuminated by an E-polarized plane wave at normal incidence, the two approximations

are compared with the moment method solution in Fig. 4.7, and the superiority of VIPO is clear.

In the case of a thin plate the two approximations are indistinguishable. This is illustrated in Fig. 4.8 showing the VIPO expression (4.6) and the moment method solution for a $2\lambda_0$ square plate of thickness $d_2 = \lambda_0/50$ for E polarization. The plate is a homogeneous one having $\epsilon = 13 + i12$ corresponding to the average permittivity at 35 GHz in Table 4.1. The SCPO expression (4.8) yields the same results, as does a two-layer model having the permittivities listed in Table 4.1. The analogous data for H polarization are given in Fig. 4.9, and over a wide range of scattering angles, the approximate and moment method solutions are in excellent agreement.

As the frequency and, hence, the electrical thickness of the plate increase, the superiority of the VIPO approximation becomes apparent and, in addition, it becomes necessary to take the layering of the plate into account. In Figs. 4.10 and 4.11 the simulated frequency is 140 GHz, but to keep the moment method calculations tractable, the plate has been reduced in size to $1.4\lambda_0$ by $2\lambda_0$. The curves shown are for a two-layer plate having $d_2 = 2d_1 = 0.5mm$ with $\epsilon_1 = 5 + i4$ and $\epsilon_2 = 2 + i1$, and for a single layer having the average permittivity $\epsilon_{avg} = 3.5 + i2.5$ (see Table 4.1). Since the accuracy of the physical optics approximation increases with the plate size, the agreement between the two-layer VIPO approximation and the moment method solution is remarkably good, and significantly better than if a single layer had been used.

To test the validity of the combined-sheet multilayer model, the reflection coefficient Γ was computed using (4.33) for a dielectric slab with a uniform dielectric profile and then compared with the exact solution for the reflection coefficient of a uniform dielectric slab. Figure 4.12, which depicts the amplitude of the reflection

coefficient as a function of slab thickness, contains three plots: (a)| Γ | for the uniform slab (exact solution), (b)| Γ | for a multilayer slab (combined sheet model) composed of identical layers each $\lambda_0/100$-thick, and (c) | Γ | of a single-sheet slab, included here for comparison. Figure 4.13 shows similar plots for the phase of the reflection coefficient. The results indicate that the overall agreement between (a) and (b) is excellent, and that the single sheet model can successfully predict the reflection coefficient if the layer thickness is less than $\lambda_0/50(\sim \frac{\lambda_0}{15\sqrt{|\epsilon|}})$.

Now the combined-sheet multilayer model when used in conjunction with physical optics will be checked against the method of moments. Figure 4.14 shows a plot of the bistatic scattering cross section of a $2\lambda_0 \times 2\lambda_0$ dielectric slab with thickness $\lambda_0/100$ computed using the physical optics expression (4.52) and a second plot computed according to the moment method, both for E polarization at 35 GHz. Similar plots are shown in Fig. 4.15 using expression (4.53) for H polarization. The result of combined-sheet model are in very good agreement with the numerical data (moment method) over a wide range of the scattering angle θ_s.

To examine the formulation for thick dielectric slabs while keeping the numerical code tractable, our next example is a $1\lambda_0 \times 2\lambda_0$ dielectric slab whose thickness is $\lambda_0/10$. Figures 4.16 and 4.17 compare the bistatic radar cross section of the thick slab at 35 GHz computed using a 5-layer and a 1-layer combined-sheet model with the physical optics approximation with the numerical data for E and H polarizations, respectively. Keeping in mind that the accuracy of the physical optics approximation improves as the width of the slab increases, the good agreement of the 5-layer sheet with the numerical data around the specular region ($| \theta_s | \leq \pi/4$ in this case) provides good support for the model proposed in this paper.

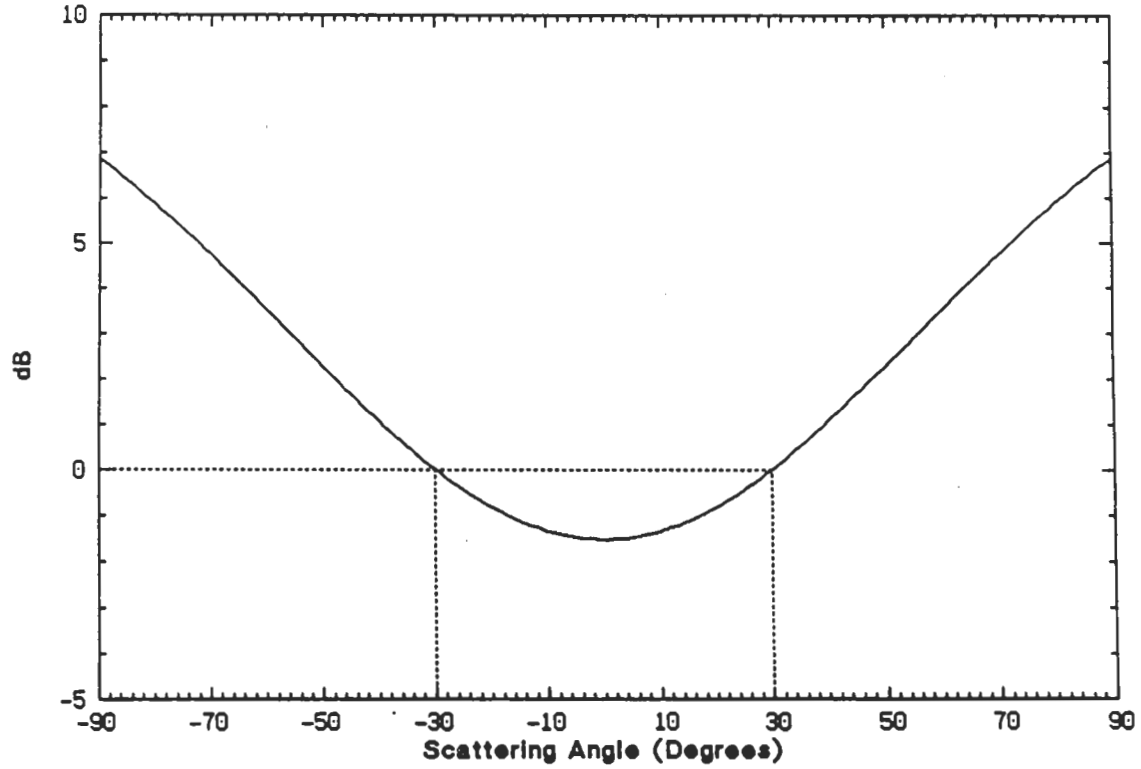

Figure 4.5: Amplitude of the ratio of the bistatic far field amplitude of VIPO to SCPO for E polarization of a dielectric plate with $d_2 = \lambda_0/4$ and $\epsilon_1 = \epsilon_2 = 3 + i0.1$ at $\theta_i = 30$ degrees.

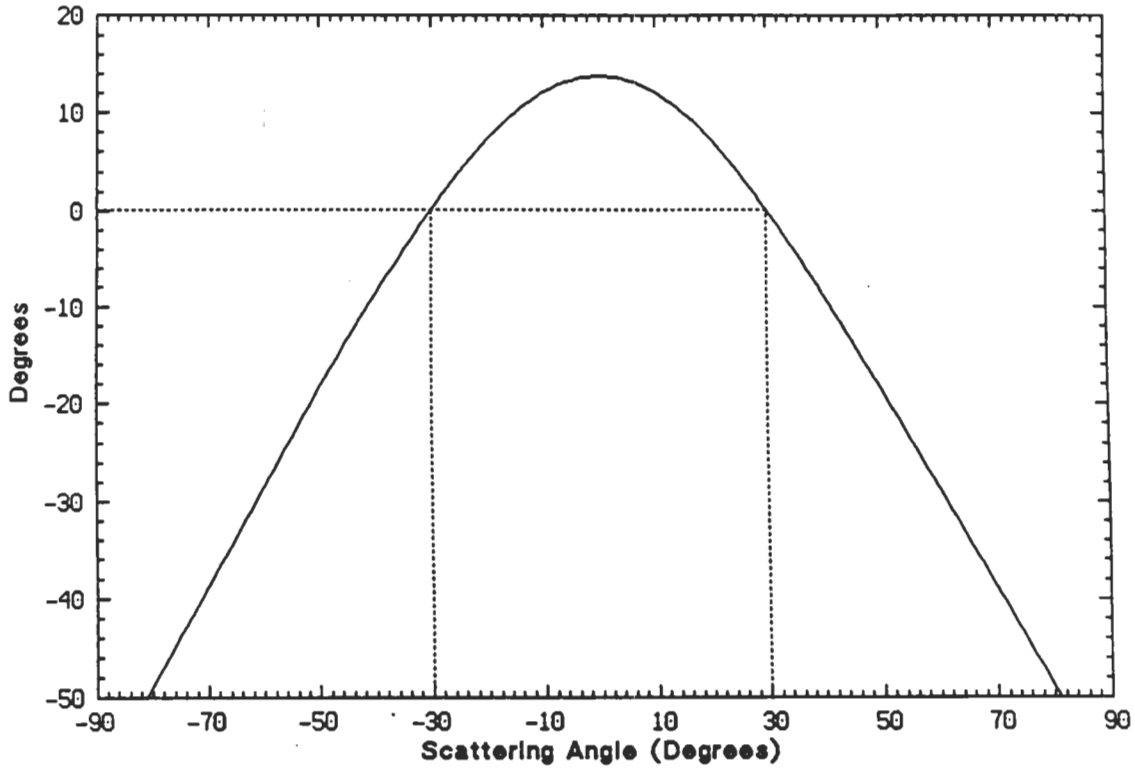

Figure 4.6: Phase of the ratio of the bistatic far field amplitude of VIPO to SCPO for E polarization of a dielectric plate with $d_2 = \lambda_0/4$ and $\epsilon_1 = \epsilon_2 = 3 + i0.1$ at $\theta_i = 30$ degrees.

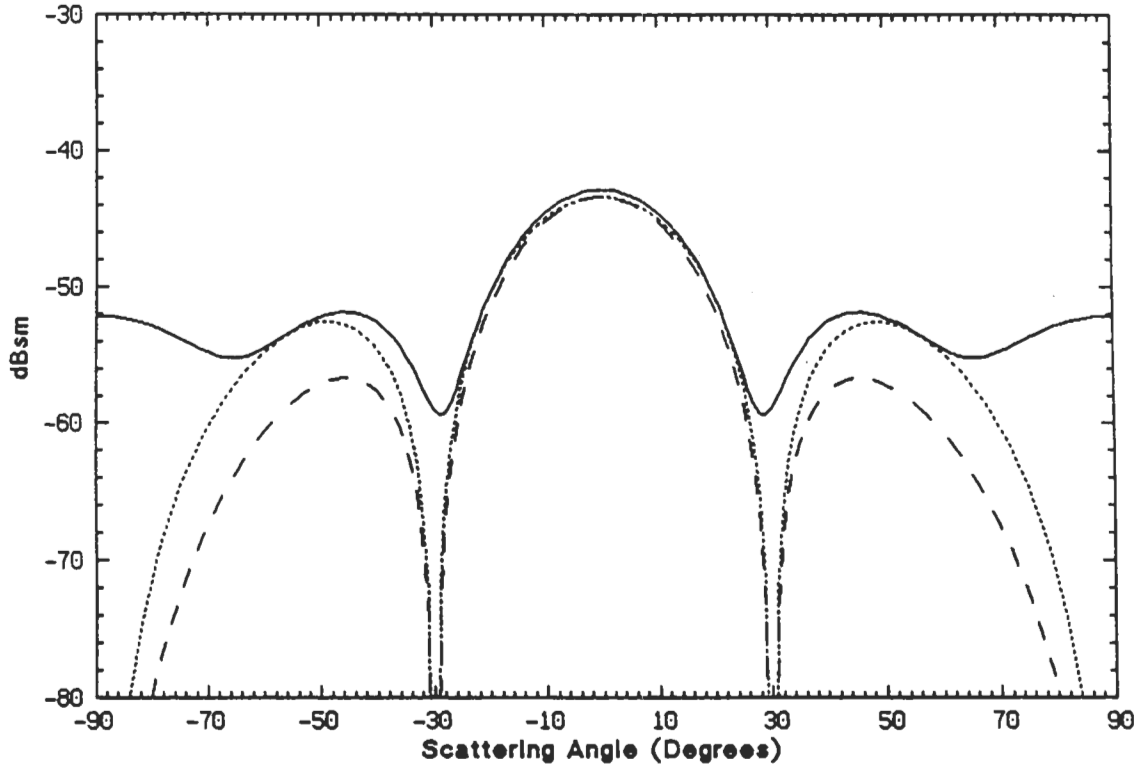

Figure 4.7: The bistatic cross section of a $2\lambda_0 \times 2\lambda_0$ plate for E polarization with $d_2 = \lambda_0/4$ and $\epsilon_1 = \epsilon_2 = 3 + i0.1$ at normal incidence: (——) moment method solution, (- - -) VIPO, (– –) SCPO.

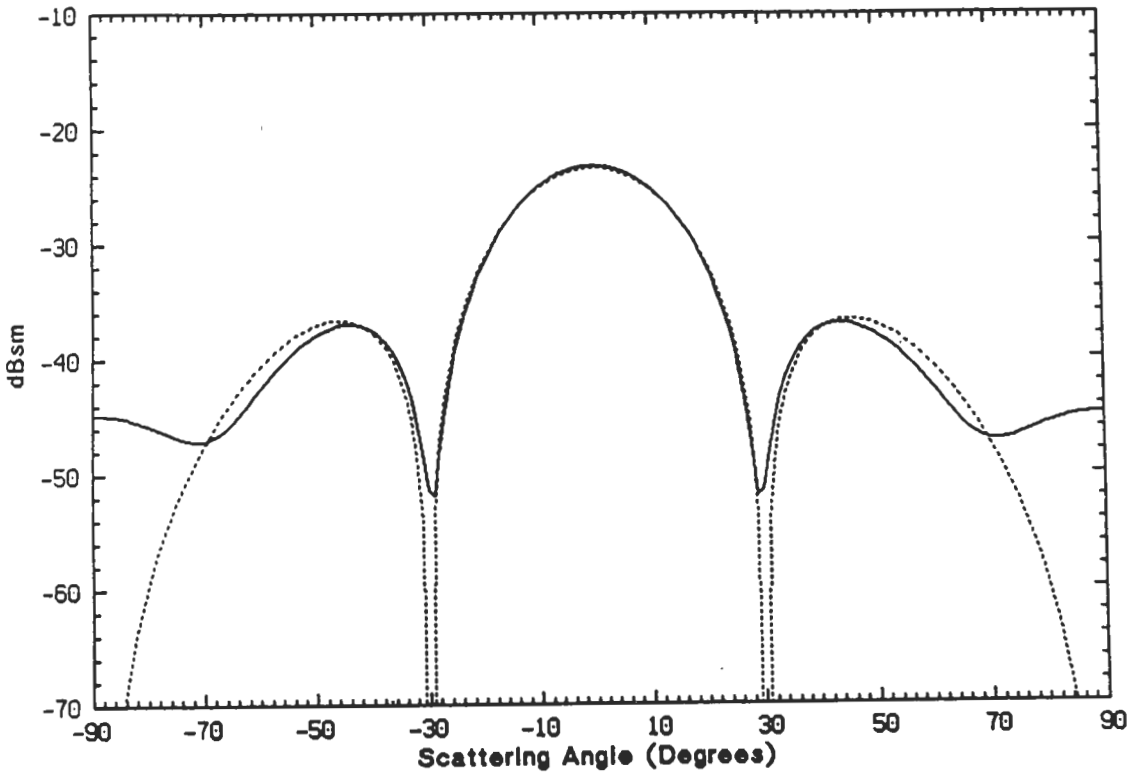

Figure 4.8: The bistatic cross section area of a $2\lambda_0 \times 2\lambda_0$ plate for E polarization with $d_2 = \lambda_0/50$ and $\epsilon_{avg} = 13 + i12$ at normal incidence: (——) moment method solution, (- - -) VIPO or SCPO.

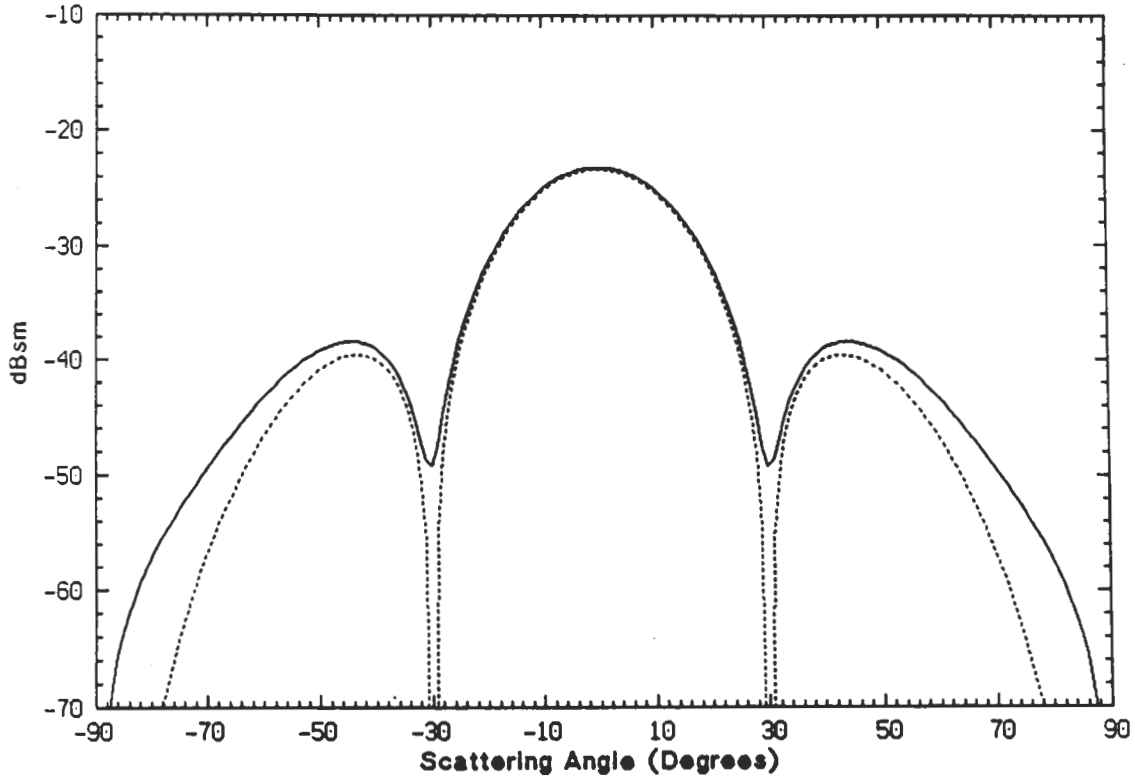

Figure 4.9: The bistatic cross section of a $2\lambda_0 \times 2\lambda_0$ plate for H polarization with $d_2 = \lambda_0/50$ and $\epsilon_{avg} = 13 + i12$ at normal incidence: (——) moment method solution, (- - -) VIPO or SCPO.

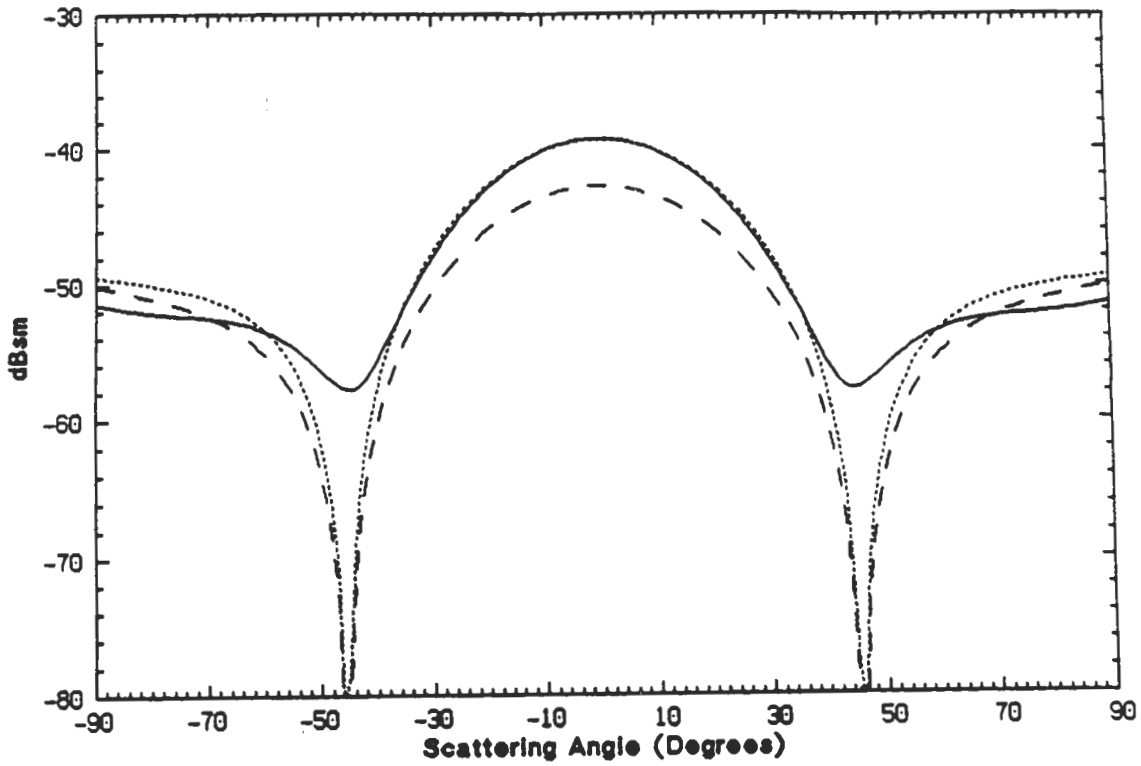

Figure 4.10: The bistatic cross section of a $1.4\lambda_0 \times 2\lambda_0$ plate for E polarization with $d_2 = 2d_1 = 0.5mm$ and f =140 GHz at normal incidence: (——) moment method solution with $\epsilon_1 = 5+i4$, $\epsilon_2 = 2+i1$, (- - -) VIPO with $\epsilon_1 = 5+i4$, $\epsilon_2 = 2 + i1$, (– –) VIPO with $\epsilon_2 = \epsilon_1 = 3.5 + i2.5$.

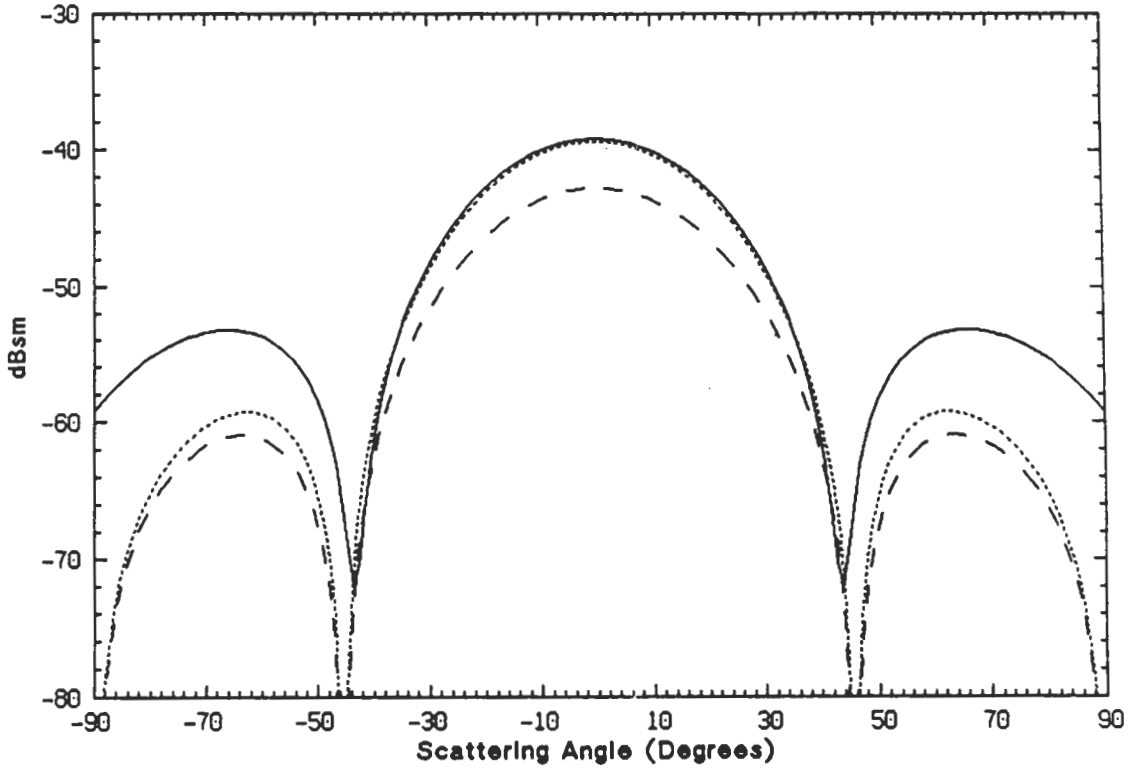

Figure 4.11: The bistatic cross section area of a $1.4\lambda_0 \times 2\lambda_0$ plate for H polarization with $d_2 = 2d_1 = 0.5mm$ and f =140 GHz at normal incidence: (——) moment method solution with $\epsilon_1 = 5 + i4$, $\epsilon_2 = 2 + i1$, (- - -) VIPO with $\epsilon_1 = 5 + i4$ $\epsilon_2 = 2 + i1$, (– –) VIPO with $\epsilon_2 = \epsilon_1 = 3.5 + i2.5$.

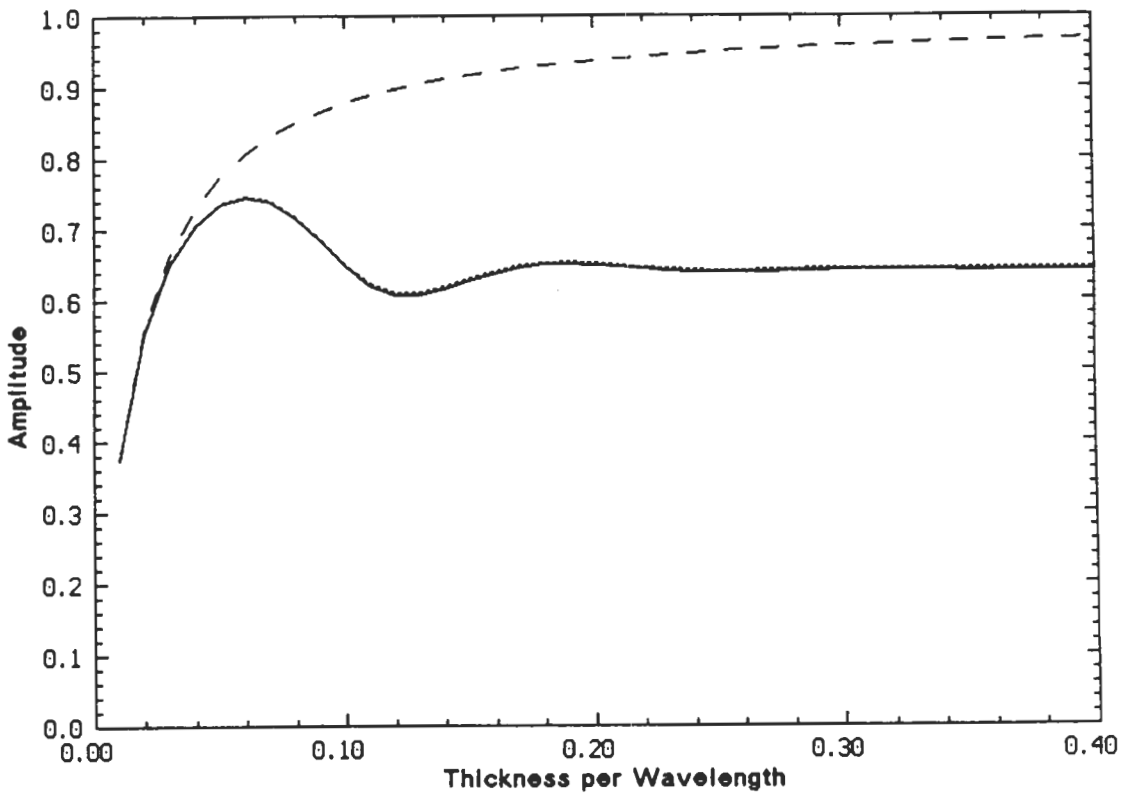

Figure 4.12: Amplitude of the reflection coefficient at f=35GHz, $\theta_i = 0$,and $\epsilon = 13 + i12$ as a function of thickness: (——) exact solution, (- - -) N-layered combined-sheet model $\Delta = \lambda_0/100$, (– –) single-sheet $\Delta = \tau$.

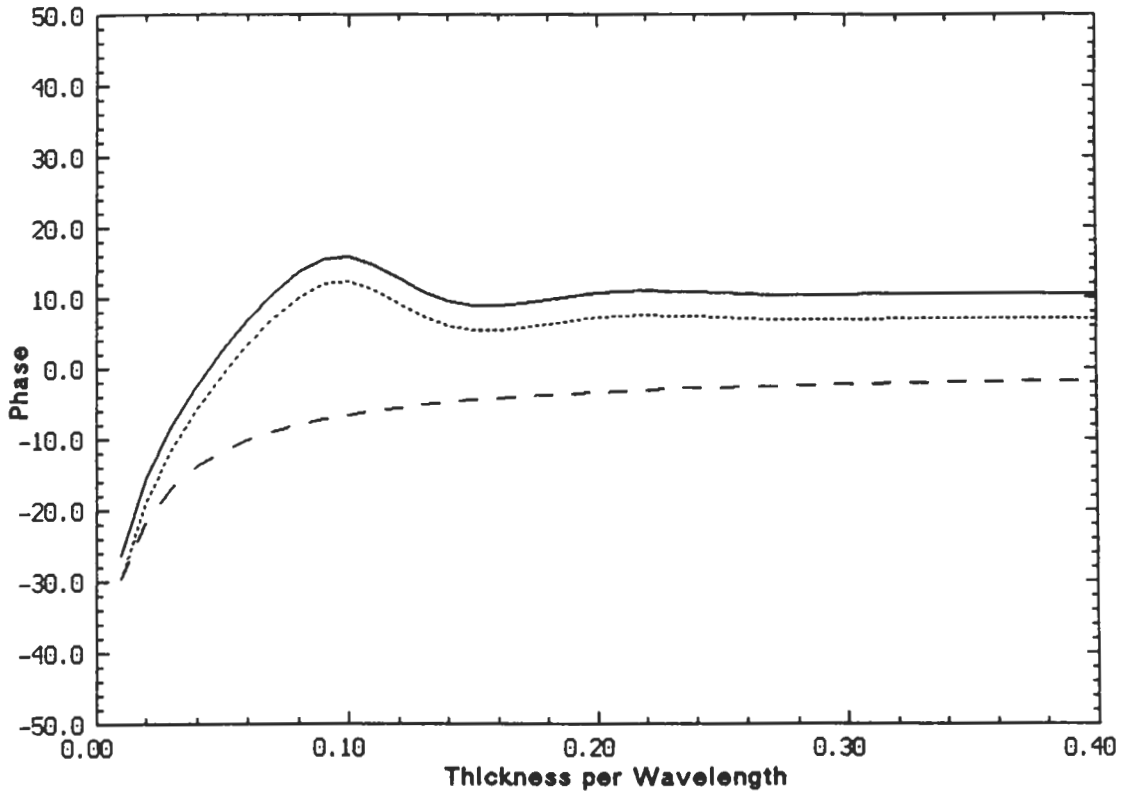

Figure 4.13: Phase of the reflection coefficient at f=35GHz, $\theta_i = 0$,and $\epsilon = 13 + i12$ as a function of thickness: (——) exact solution, (- - -) N-layered combined-sheet model $\Delta = \lambda_0/100$, (– –) single-sheet $\Delta = \tau$.

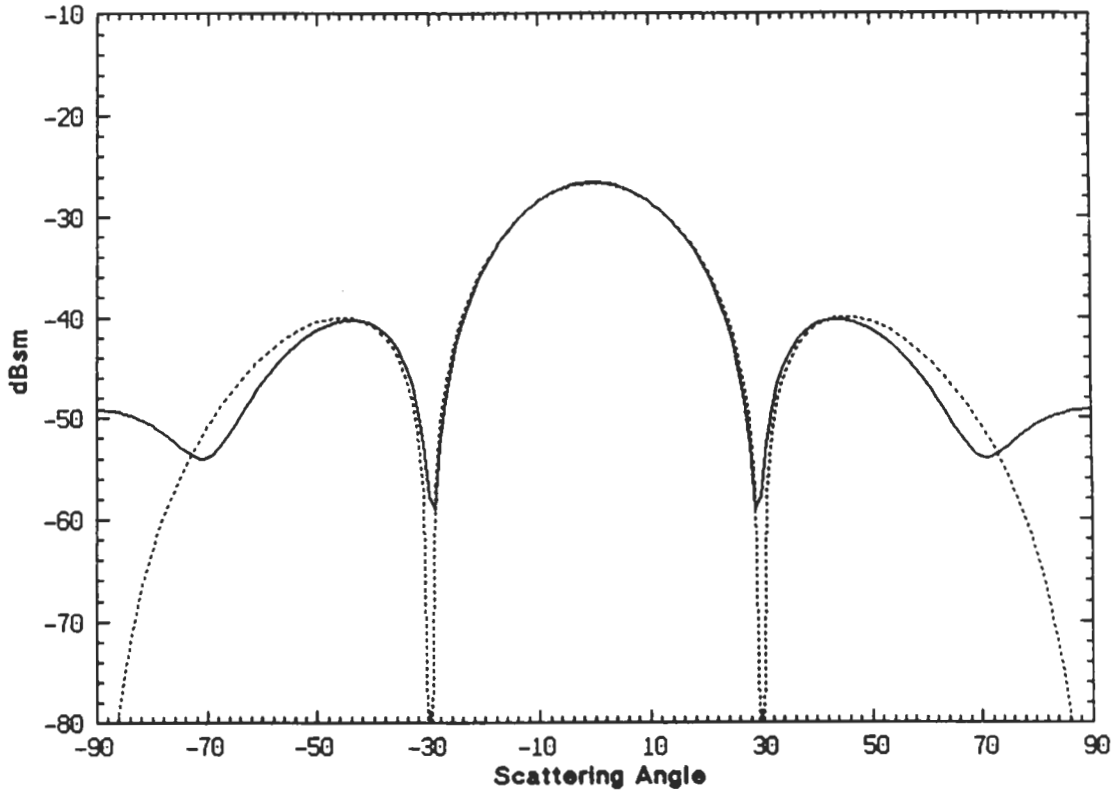

Figure 4.14: Bistatic scattering cross section of a $2\lambda_0 \times 2\lambda_0$ dielectric plate with $\tau = \lambda_0/100$ for E polarization at f=35GHz, $\theta_i = 0$, and $\epsilon = 13 + i12$ as function of scattering angle: (——) moment method, (- - -) single-layered combined-sheet model.

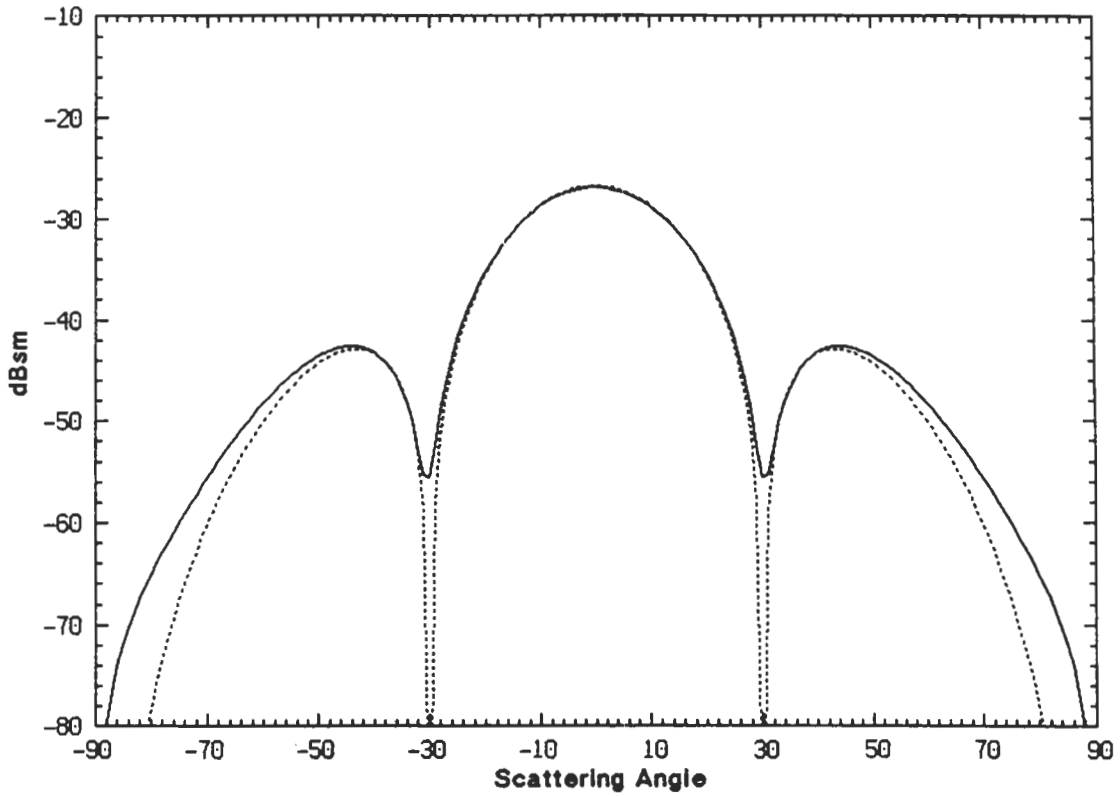

Figure 4.15: Bistatic scattering cross section of a $2\lambda_0 \times 2\lambda_0$ dielectric plate with $\tau = \lambda_0/100$ for H polarization at f=35GHz, $\theta_i = 0$, and $\epsilon = 13 + i12$ as function of scattering angle: (——) moment method, (- - -) single-layered combined-sheet model.

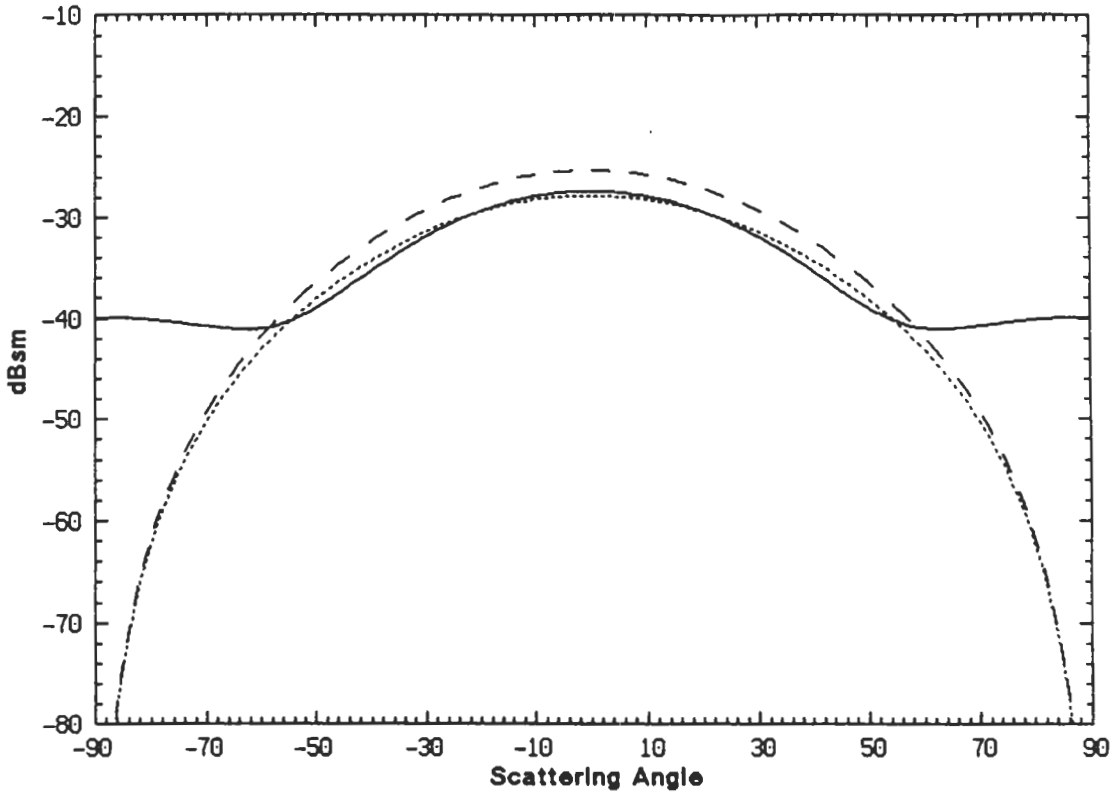

Figure 4.16: Bistatic scattering cross section of a $1\lambda_0 \times 2\lambda_0$ dielectric plate with $\tau = \lambda_0/10$ for E polarization at f=35GHz, $\theta_i = 0$, and $\epsilon = 13 + i12$ as function of scattering angle: (——) moment method, (- - -) 5-layered combined-sheet model, (– –) single-sheet.

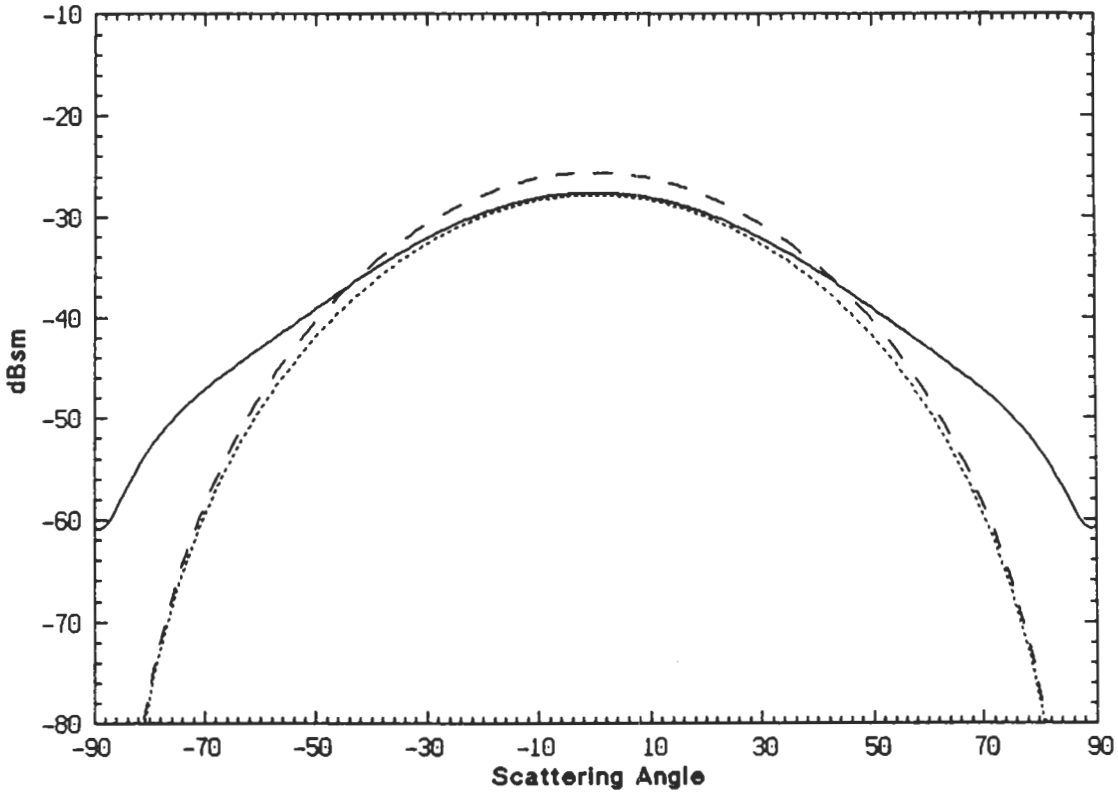

Figure 4.17: Bistatic scattering cross section of a $1\lambda_0 \times 2\lambda_0$ dielectric plate with $\tau = \lambda_0/10$ for H polarization at f=35GHz, $\theta_i = 0$, and $\epsilon = 13 + i12$ as function of scattering angle: (——) moment method, (- - -) 5-layered combined-sheet model, (– –) single-sheet.

4.8 Conclusions

A typical leaf has at least two dielectric layers whose cells have differing water content, and this produces a nonuniform dielectric profile which can now affect the scattering. At microwave frequencies where the leaf is no more than (about) $\lambda_0/50$ in thickness, the nonuniformity is not important, and the leaf can be modelled as a resistive sheet using an average value for the permittivity. If the physical optics approximation is then applied, the resulting scattering is attributed to a surface current, and this method is equivalent to the SCPO approximation. At higher frequencies, however, the thickness and structure of a leaf are more significant. At 100 GHz and above a leaf is a considerable fraction of a wavelength in thickness, and in spite of the reduced sensitivity to water content, the nonuniformity affects the scattering.

For a two-layer model of a leaf, the SCPO approximation has been compared with the volume integral (VIPO) approximation. When the leaf is thin the two approximations are identical and in good agreement with data obtained from a moment method solution of the integral equation, but as the electrical thickness increases, the two approximations diverge in all directions except the specular and (for E polarization) backscattering ones. Although the VIPO approximation is more complicated, its accuracy is greater, and the agreement with the moment method data is better using a two-layer model than when a single layer of average permittivity is employed.

For most practical purposes it would appear that VIPO in conjunction with an accurate dielectric profile of a leaf provides an adequate approximation to the scattering at millimeter wavelengths. As our knowledge of the profile increases, it may be desirable to use a multi-layer model which could even simulate a continuous,

nonuniform profile. We also note that at frequencies for which the leaf thickness is comparable to $\lambda_m/2$ where λ_m is the (average) wavelength in the leaf, the scattering is greatly reduced at some angle of incidence, and because the permittivity is complex, there is actually a range of angles for which this is true. Since the reduction is accompanied by an increase in the field transmitted through the leaf, this could provide a means for penetration through a vegetation canopy.

CHAPTER V

SCATTERING FROM VARIABLE RESISTIVE AND IMPEDANCE SHEETS

5.1 Introduction

Another feature of planar leaves that needs to be investigated is the effect of variation (across their surface) in thickness and dielectric constant on scattering. The thickness and moisture content of a leaf, generally, decrease from center to sides and can be modelled by a variable resistive sheet. The variable resistivity $R(x)$ is an explicit function of the thickness and material properties of the leaf (see (2.3)). Since the mathematics involved in obtaining the solution for a resistive sheet is closely related to that of the impedance sheet, we generalize the solution to include the impedance sheet problem also.

In view of the difficulties associated with obtaining exact solutions of Maxwell's equations under given initial and boundary conditions, approximate solutions are often sought instead. A common approximation technique is perturbation theory which is useful primarily when the problem under consideration closely resembles one whose exact solution is known. Perturbational methods have been successfully used for many problems such as cavity and waveguide problems [e.g. Stephen et al 1967, Eftimiu and Huddleston 1983], scattering from stratified media [Bates and

Wall 1976], and scattering from rough metallic surfaces [Rice 1951].

In this chapter we will employ a perturbation method to solve the scattering problem of variable resistive and impedance sheets. A solution to this problem has number of important applications other than modelling a variable thickness dielectric slab. For example, a periodic resistive sheet has application to spatial filters and polarizers. Characterization of the scattering behavior of a variable impedance sheet is also a matter of increasing concern since dielectric coated perfect conductors can be modelled by a surface impedance, and a variation of the material property of a terrain surface can be represented by a variable impedance surface.

An approximate solution is obtained using a perturbation technique in the Fourier domain. The solution for the induced current on the sheet in terms of the resistivity function is given in a recursive form. The closed form nature of the solution enables us to study the statistical behavior of the scattered field when the resistivity function is a random process. The solution for the current on an impedance sheet with impedance $\eta(x)$ is identical with that of the resistive sheet and can be obtained by replacing $R(x)$ with $\eta(x)/2$.

The solution to any desired order for a periodic perturbation is obtained analytically and the results are compared with an exact solution obtained using a moment method. To demonstrate the ability of this perturbation technique to handle sharp variations in the spatial domain, the problem of scattering from an impedance insert is considered and compared with a uniform GTD solution [Herman and Volakis 1988]. The technique is also used to characterize the scattering behavior of a thin dielectric slab with a hump and the solution is compared to that obtained using the moment method in conjunction with the exact image theory for resistive sheets.

5.2 Derivation of Integral Equation

5.2.1 Resistive Sheet

The resistive sheet is simply an electric current sheet modelling a thin dielectric layer capable of supporting electric currents. The electric current on the sheet is proportional to the tangential electric field and the proportionality constant is denoted by a complex resistivity R given by (2.3). The electromagnetic boundary conditions that govern the fields on the resistive sheet are also given by (2.4)-(2.6)

Consider a planar resistive sheet occupying the $x-y$ plane and having a resistivity which is only a function of x. Suppose a plane wave is incident on the sheet at an angle ϕ_0 measured from the normal. The geometry of the problem is depicted in Fig. 5.1. For the E polarization case we assume

$$\mathbf{E}^i = \hat{y} e^{ik_0(\sin\phi_0 x - \cos\phi_0 z)} \tag{5.1}$$

$$\mathbf{H}^i = Y_0(\cos\phi_0 \hat{x} + \sin\phi_0 \hat{z}) e^{ik_0(\sin\phi_0 x - \cos\phi_0 z)}. \tag{5.2}$$

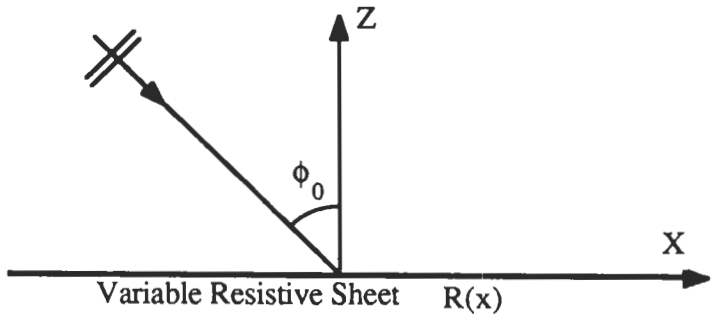

Figure 5.1: Geometry of the scattering problem for a variable resistive sheet.

The scattered field due to the induced current is

$$\mathbf{E}^s(\bar{\rho}) = -i\omega\mu_0 \int_s \mathbf{J}(bar\rho') \cdot \overline{\overline{\Gamma}}(\bar{\rho}, \bar{\rho}')\mathrm{d}s' \tag{5.3}$$

where $\overline{\overline{\Gamma}}(\bar{\rho},\bar{\rho}')$ is the two-dimensional dyadic Green's function and is given by

$$\overline{\overline{\Gamma}}(\bar{\rho},\bar{\rho}') = -\frac{i}{4}[\overline{\overline{I}} + \frac{\nabla\nabla}{k_0^2}]H_0^{(1)}(k_0 \mid \bar{\rho} - \bar{\rho}' \mid) \tag{5.4}$$

Here, $H_0^{(1)}$ is the Hankel function of first kind and zeroth-order. The induced current in this case has only a y component, and from (5.3) the scattered field is found to be

$$\mathbf{E}^s(\bar{\rho}) = -\hat{y}\frac{k_0 Z_0}{4}\int_{-\infty}^{+\infty} J_y(x')H_0^{(1)}(k_0 \mid \bar{\rho} - \bar{\rho}' \mid)\mathrm{d}x' \tag{5.5}$$

The induced current and the total electric field given by

$$\mathbf{E}^t = \mathbf{E}^i + \mathbf{E}^s \tag{5.6}$$

must satisfy the boundary condition given by (2.5). Noting that $\hat{n} = \hat{z}$ and substituting for $\mathbf{E}^i$ and $\mathbf{E}^s$ from (5.1) and (5.5) the following integral equation for the induced current can be obtained:

$$R(x)J_y(x) = e^{ik_0 \sin\phi_0 x} - \frac{k_0 Z_0}{4}\int_{-\infty}^{+\infty} J_y(x')H_0^{(1)}(k_0 \mid x - x' \mid)\mathrm{d}x' \tag{5.7}$$

For the H polarization case in which the magnetic field vector is perpendicular to the plane of incidence, we have

$$\mathbf{E}^i = -(\cos\phi_0\hat{x} + \sin\phi_0\hat{z})e^{ik_0(\sin\phi_0 x - \cos\phi_0 z)} \tag{5.8}$$

$$\mathbf{H}^i = \hat{y}Y_0 e^{ik_0(\sin\phi_0 x - \cos\phi_0 z)}. \tag{5.9}$$

In this case the induced current has only a x component and from (5.3) the scattered electric field components are

$$E_x^s(x,z) = -\frac{k_0 Z_0}{4}\int_{-\infty}^{+\infty} J_x(x')(1 + \frac{1}{k_0^2}\frac{\partial^2}{\partial x^2})H_0^{(1)}(k_0\sqrt{(x-x')^2 + z^2})\mathrm{d}x' \tag{5.10}$$

$$E_z^s(x,z) = -\frac{Z_0}{4k_0}\int_{-\infty}^{+\infty} J_x(x')\frac{\partial^2}{\partial x\partial z}H_0^{(1)}(k_0\sqrt{(x-x')^2 + z^2})\mathrm{d}x' \tag{5.11}$$

The scattered magnetic field is in the y direction and can be obtained from

$$H_y^s(x,z) = -\frac{1}{4i}\int_{-\infty}^{+\infty} J_x(x')\frac{\partial}{\partial z}H_0^{(1)}(k_0\sqrt{(x-x')^2+z^2})\mathrm{d}x' \tag{5.12}$$

By obtaining the total field at the surface of the sheet and applying the boundary condition (2.5) the following integral equation for the induced current in the H polarization case can be derived:

$$R(x)J_x(x) = -\cos\phi_0 e^{ik_0\sin\phi_0 x} - \frac{k_0 Z_0}{4}\int_{-\infty}^{+\infty} J_x(x')(1+\frac{1}{k_0^2}\frac{\partial^2}{\partial x^2})H_0^{(1)}(k_0 \mid x-x' \mid)\mathrm{d}x' \,. \tag{5.13}$$

5.2.2 Impedance Sheet

Consider an impedance surface occupying the $x-y$ plane. Suppose the impedance is a function only of the variable x and is denoted by $\eta(x)$. Further assume that this surface is illuminated by a plane wave at an angle ϕ_0 as depicted in Fig. 5.1. The boundary condition on the surface is

$$\hat{n}\times(\hat{n}\times\mathbf{E}) = -\eta(x)\hat{n}\times\mathbf{H} \tag{5.14}$$

The field scattered from this surface can be obtained by replacing the total tangential magnetic field on the surface by an electric current over a perfect magnetic conductor using the field equivalence principle [Harrington, 1961]. The equivalent electric current is

$$\mathbf{J} = \hat{n}\times\mathbf{H}\,. \tag{5.15}$$

and by invoking image theory, the magnetic wall can be removed by doubling the electric current.

The incident electric and magnetic field in the E polarization case are given by (5.1) and (5.2) respectively. In this case the total tangential magnetic field on the

surface is in the x direction which implies that the electric current is in the y direction. The scattered electric field can be obtained from expression (5.5) and is

$$E_y^s(x,z) = -\frac{k_0 Z_0}{2}\int_{-\infty}^{+\infty} J_y(x')H_0^{(1)}(k_0\sqrt{(x-x')^2+z^2})\mathrm{d}x'. \tag{5.16}$$

The total electric field on the surface is composed of the incident field, the field reflected from the magnetic wall, and the scattered field. From (5.14) and (5.15) we have

$$[E_y^i + E_y^r + E_y^s]_{z=0} = \eta(x)J_y(x) \tag{5.17}$$

which leads to the following integral equation for the electric current:

$$\frac{\eta(x)}{2}J_y(x) = e^{ik_0\sin\phi_0 x} - \frac{k_0 Z_0}{4}\int_{-\infty}^{+\infty} J_y(x')H_0^{(1)}(k_0 \mid x-x' \mid)\mathrm{d}x'. \tag{5.18}$$

When the incident field is H-polarized the total tangential magnetic field is in the y direction which implies that the equivalent electric current flows in the x direction. The scattered electric field can be obtained from (5.10) and (5.11) by doubling the electric current. Also, from the boundary condition (5.13), we have

$$[E_x^i + E_x^r + E_x^s]_{z=0} = \eta(x)J_x(x). \tag{5.19}$$

Upon substituting the appropriate quantities from equations (5.8) and (5.10) into the above equation the following integral equation for the electric current can be obtained:

$$\frac{\eta(x)}{2}J_x(x) = -\cos\phi_0 e^{ik_0\sin\phi_0 x} - \frac{k_0 Z_0}{4}\int_{-\infty}^{+\infty} J_x(x')(1+\frac{1}{k_0^2}\frac{\partial^2}{\partial x^2})H_0^{(1)}(k_0 \mid x-x' \mid)\mathrm{d}x'. \tag{5.20}$$

The scattered magnetic field in this case is

$$H_y^s(x,z) = -\frac{1}{2i}\int_{-\infty}^{+\infty} J_x(x')\frac{\partial}{\partial z}H_0^{(1)}(k_0\sqrt{(x-x')^2+z^2})\mathrm{d}x' . \tag{5.21}$$

Note that the integral equations obtained for the impedance sheet are identical to those obtained for the resistive sheet if $R(x)$ is replaced by $\eta(x)/2$. Therefore all the analysis that will be carried out for the resistive sheet can be applied to the corresponding impedance sheet.

5.3 Perturbation Solution

The integral equations for the induced current on the resistive sheet are Fredholm integral equations of the second type, and for an arbitrary resistivity function $R(x)$ there is no known technique for finding their exact solution. Here we obtain an approximate iterative solution to these integral equations using a perturbation technique and Fourier transform. For the sake of simplicity let us represent the integral equations (5.7) and (5.13) by the following equation:

$$R(x)J(x) = ae^{ik_0 \sin\phi_0 x} - \frac{k_0 Z_0}{4}(J * g)(x) \tag{5.22}$$

where $g(x)$ is the kernel of the integral equation and $(J*g)(x)$ denotes the convolution integral. The kernel function $g(x)$ and constant a are

$$g(x) = \begin{cases} H_0^{(1)}(k_0 \mid x \mid) & \text{E-polarization} \\ (1 + \frac{1}{k_0^2}\frac{\partial^2}{\partial x^2})H_0^{(1)}(k_0 \mid x \mid) & \text{H-polarization} \end{cases} \tag{5.23}$$

$$a = \begin{cases} 1 & \text{E-polarization} \\ -\cos\phi_0 & \text{H-polarization} \end{cases} \tag{5.24}$$

By taking the Fourier transform of (5.22), the integral equation in the Fourier domain becomes

$$\frac{1}{2\pi}(\tilde{R} * \tilde{J})(\alpha) = 2\pi a\delta(\alpha - k_0 \sin\phi_0) - \frac{k_0 Z_0}{4}\tilde{J}(\alpha)\tilde{g}(\alpha) \tag{5.25}$$

where the Fourier transform of functions are denoted by a tilda and δ is the Dirac delta function. The Fourier transform of the kernel function for E and H polarization

cases respectively are given by

$$\tilde{g}(\alpha) = \frac{2}{\sqrt{k_0^2 - \alpha^2}} \tag{5.26}$$

$$\tilde{g}(\alpha) = \frac{2}{k_0^2}\sqrt{k_0^2 - \alpha^2} \tag{5.27}$$

where the branch of square root is defined such that $\sqrt{-1} = i$. When the resistivity of the sheet is constant, an exact solution to the integral equation (5.24) can be obtained, and if $R(x) = R_0$, then

$$\tilde{R}(\alpha) = 2\pi R_0 \delta(\alpha). \tag{5.28}$$

The transform of the current can be obtained from (5.25) and is given by

$$\tilde{J}_0(\alpha) = \frac{a[2\pi\delta(\alpha - k_0 \sin\phi_0)]}{R_0 + \frac{k_0 Z_0}{4}\tilde{g}(\alpha)}, \tag{5.29}$$

and the induced current in the spatial domain for E and H polarization respectively are

$$\mathbf{J}_0^e(x) = \hat{y}\frac{2Y_0 \cos\phi_0}{1 + 2R_0 Y_0 \cos\phi_0} e^{ik_0 \sin\phi_0 x}\ , \tag{5.30}$$

$$\mathbf{J}_0^h(x) = \hat{x}\frac{-2Y_0 \cos\phi_0}{2R_0 Y_0 + \cos\phi_0} e^{ik_0 \sin\phi_0 x}\ . \tag{5.31}$$

which are identical to the result obtained from a plane wave reflection coefficient calculation (see (2.11)).

If the resistivity has a small variation as a function of position, let

$$R(x) = R_0(1 + \Delta r(x)) \tag{5.32}$$

where $r(x)$ is the perturbation function assuming $\mid r(x) \mid \leq 1$ and Δ is a complex constant ($\mid \Delta \mid < 1$). The induced current on the sheet is assumed to be

$$J(x) = \sum_{n=0}^{+\infty} J_n(x)\Delta^n\ , \tag{5.33}$$

where $J_n(x)$ denotes the n^{th} component of the induced current. Obviously, if $\Delta = 0$ then $J(x) = J_0(x)$. From (5.32) and (5.33)

$$\tilde{R}(\alpha) = 2\pi R_0 \delta(\alpha) + R_0 \tilde{r}(\alpha)\Delta \tag{5.34}$$

$$\tilde{J}(\alpha) = \sum_{n=0}^{+\infty} \tilde{J}_n(\alpha)\Delta^n, \tag{5.35}$$

and when substituted into (5.25), the terms given by (5.29) can be cancelled, and the remaining terms can be written as

$$\sum_{n=1}^{+\infty} \{R_0[\tilde{J}_n(\alpha) + \frac{1}{2\pi}\tilde{r}(\alpha) * \tilde{J}_{n-1}(\alpha)] + \frac{k_0 Z_0}{4}\tilde{g}(\alpha)\tilde{J}_n(\alpha)\}\Delta^n = 0 \tag{5.36}$$

Since this must hold for any value of Δ, all of the coefficients must be zero. Thus for E polarization

$$\tilde{J}_n^e(\alpha) = -2Y_0 R_0 \cdot \frac{\sqrt{1 - \frac{\alpha^2}{k_0^2}}}{1 + 2Y_0 R_0 \sqrt{1 - \frac{\alpha^2}{k_0^2}}} \cdot \frac{1}{2\pi}(\tilde{r} * \tilde{J}_{n-1}^e)(\alpha), \tag{5.37}$$

and for H polarization we have

$$\tilde{J}_n^h(\alpha) = -2Y_0 R_0 \cdot \frac{1}{2Y_0 R_0 + \sqrt{1 - \frac{\alpha^2}{k_0^2}}} \cdot \frac{1}{2\pi}(\tilde{r} * \tilde{J}_{n-1}^h)(\alpha). \tag{5.38}$$

The above recursive relations along with the expressions for $\tilde{J}_0(\alpha)$ given in (5.29) can be used to derive the induced currents to any desired order of approximation. The first-order solution can be obtained very easily and the transforms of the first component of the induced current for E and H polarizations are

$$\tilde{J}_1^e(\alpha) = \frac{-4Y_0^2 R_0 \cos\phi_0}{1 + 2Y_0 R_0 \cos\phi_0} \cdot \frac{\sqrt{1 - \frac{\alpha^2}{k_0^2}}}{1 + 2Y_0 R_0 \sqrt{1 - \frac{\alpha^2}{k_0^2}}} \tilde{r}(\alpha - k_0 \sin\phi_0) \tag{5.39}$$

$$\tilde{J}_1^h(\alpha) = \frac{4Y_0^2 R_0 \cos\phi_0}{\cos\phi_0 + 2Y_0 R_0} \cdot \frac{1}{2Y_0 R_0 + \sqrt{1 - \frac{\alpha^2}{k_0^2}}} \tilde{r}(\alpha - k_0 \sin\phi_0) \tag{5.40}$$

The complexity of obtaining high-order solutions depends on the perturbation function $r(x)$.

5.4 Periodic Resistivity

5.4.1 Perturbation solution

A simple case where it is possible to determine the nth components of the induced currents is a periodic resistivity with period L. In this case we can write

$$r(x) = \sum_{m=-\infty}^{+\infty} c_m e^{i\frac{2\pi m}{L}x}, \tag{5.41}$$

and the Fourier transform of the perturbation function is

$$\tilde{r}(\alpha) = 2\pi \sum_{m=-\infty}^{+\infty} c_m \delta(\alpha - \frac{2\pi m}{L}). \tag{5.42}$$

For the E polarization case the transform of the nth component of the induced current can be obtained from (5.37) and (5.42) and is

$$\tilde{J}_n^e(\alpha) = -2Y_0R_0 \cdot \frac{1}{2Y_0R_0 + \sqrt{1-\frac{\alpha^2}{k_0^2}}} \cdot \sum_{m=-\infty}^{+\infty} c_m \tilde{J}_{n-1}^e(\alpha - \frac{2\pi m}{L}) \tag{5.43}$$

By employing the expression (5.29) for $\tilde{J}_0(\alpha)$ and after some algebraic manipulation, a closed form for $\tilde{J}_n(\alpha)$ can be obtained:

$$\begin{aligned}\tilde{J}_n^e(\alpha) = \; & \frac{-2Y_0R_0\cos\phi_0(-2Y_0R_0)^n}{1+2Y_0R_0\cos\phi_0} \\ & \cdot \sum_{m_n=-\infty}^{+\infty} \cdots \sum_{m_1=-\infty}^{+\infty} [\prod_{i=1}^{n} \frac{\sqrt{1-(\sin\phi_0+\frac{\lambda_0}{L}\sum_{j=1}^{i} m_j)^2}}{(1+2Y_0R_0\sqrt{1-(\sin\phi_0+\frac{\lambda_0}{L}\sum_{j=1}^{i} m_j)^2}}] \\ & \cdot c_{m_n}\cdots c_{m_1} 2\pi\delta[\alpha - k_0\sin\phi_0 - \tfrac{2\pi}{L}(\textstyle\sum_{\ell=1}^{n} m_\ell)]\end{aligned} \tag{5.44}$$

and in the spatial domain

$$\begin{aligned}J_n^e(x) = \; & \frac{2Y_0R_0\cos\phi_0(-2Y_0R_0)^n}{1+2Y_0R_0\cos\phi_0} \\ & \cdot \sum_{m_n=-\infty}^{+\infty} \cdots \sum_{m_1=-\infty}^{+\infty} [\prod_{i=1}^{n} \frac{\sqrt{1-(\sin\phi_0+\frac{\lambda_0}{L}\sum_{j=1}^{i} m_j)^2}}{(1+2Y_0R_0\sqrt{1-(\sin\phi_0+\frac{\lambda_0}{L}\sum_{j=1}^{i} m_j)^2}}] \\ & \cdot c_{m_n}\cdots c_{m_1} e^{i(k_0\sin\phi_0+\frac{2\pi}{L}\sum_{\ell=1}^{n} m_\ell)x}\end{aligned} \tag{5.45}$$

For H polarization the analysis is similar and the expression for the nth component of the induced current in the Fourier and spatial domains respectively are given by:

$$\begin{aligned}\tilde{J}_n^h(\alpha) = & \frac{-2Y_0R_0\cos\phi_0(-2Y_0R_0)^n}{2Y_0R_0+\cos\phi_0} \\ & \cdot\sum_{m_n=-\infty}^{+\infty}\cdots\sum_{m_1=-\infty}^{+\infty}\prod_{i=1}^{n}\frac{1}{(2Y_0R_0+\sqrt{1-(\sin\phi_0+\frac{\lambda_0}{L}\sum_{j=1}^{i}m_j)^2}} \\ & c_{m_n}\cdots c_{m_1}2\pi\delta[\alpha-k_0\sin\phi_0-\tfrac{2\pi}{L}(\textstyle\sum_{\ell=1}^{n}m_\ell)]\end{aligned} \tag{5.46}$$

$$\begin{aligned}J_n^h(x) = & \frac{-2Y_0R_0\cos\phi_0(-2Y_0R_0)^n}{2Y_0R_0+\cos\phi_0} \\ & \cdot\sum_{m_n=-\infty}^{+\infty}\cdots\sum_{m_1=-\infty}^{+\infty}\prod_{i=1}^{n}\frac{1}{(2Y_0R_0+\sqrt{1-(\sin\phi_0+\frac{\lambda_0}{L}\sum_{j=1}^{i}m_j)^2}} \\ & \cdot c_{m_n}\cdots c_{m_1}e^{i(k_0\sin\phi_0+\frac{2\pi}{L}\sum_{\ell=1}^{n}m_\ell)x}.\end{aligned} \tag{5.47}$$

The closed form expression for the induced current enables us to study the case when the perturbation is a periodic random process. In this case the perturbation function may still be represented as a Fourier series but with the Fourier coefficients ($c_m's$) as random variables. It can be shown from (5.59) that the average value of the diffracted field is directly proportional to the average value of the induced current. To obtain the average value of the current, assume that the periodic process has zero mean, which implies that the Fourier coefficients have zero mean ($\langle c_m\rangle = 0$), and further assume that the Fourier coefficients are mutually independent. These assumptions imply that the process is wide sense stationary, and from (5.45) and (5.47) the following expressions for the mean value of the components of the induced current can be obtained:

$$\begin{aligned}\langle J_n^e(x)\rangle = & \frac{2Y_0R_0\cos\phi_0(-2Y_0R_0)^n}{1+2Y_0R_0\cos\phi_0} \\ & \cdot\sum_{m=-\infty}^{+\infty}\prod_{i=1}^{n}\Big[\frac{\sqrt{1-(\sin\phi_0+\frac{i\lambda_0 m}{L})^2}}{(1+2Y_0R_0\sqrt{1-(\sin\phi_0+\frac{i\lambda_0 m}{L})^2}}\Big]\langle c_m^n\rangle e^{i(k_0\sin\phi_0+\frac{2\pi nm}{L})x}\end{aligned} \tag{5.48}$$

$$\begin{aligned}\langle J_n^h(x)\rangle = & \frac{-2Y_0R_0\cos\phi_0(-2Y_0R_0)^n}{2Y_0R_0+\cos\phi_0} \\ & \cdot\sum_{m=-\infty}^{+\infty}\prod_{i=1}^{n}\Big[\frac{1}{(2Y_0R_0+\sqrt{1-(\sin\phi_0+\frac{i\lambda_0 m}{L})^2}}\Big]\langle c_m^n\rangle e^{i(k_0\sin\phi_0+\frac{2\pi nm}{L})x}.\end{aligned} \tag{5.49}$$

A problem associated with the perturbation techniques is that when there is a sharp variation in the perturbation function there could be a sharp variation in the solution which is not to the order of perturbation. Therefore in an n^{th} – order solution it is not guaranteed that the solution is of $O(\Delta^{n+1})$ for all values of the variable in the domain of the integral equation. To check the validity of our assumption we consider two limiting cases: 1) when the perturbation function has sharp variations in the spatial domain and 2) when the perturbation function has sharp variations in the Fourier domain. The first case will be studied in Section 5.5 and to study the latter case we consider a constant function ($r(x) = 1$) for the perturbation function. Note that the perturbation technique was applied to the integral equation (5.25), and in this case the perturbation function $\tilde{r}(\alpha) = 2\pi\delta(\alpha)$ has the sharpest variation possible. When $r(x) = 1$ the resistivity is constant and from equation (5.30) it follows directly that

$$J_0^e(x) = \frac{2Y_0 \cos\phi_0}{1 + 2Y_0R_0(1+\Delta)\cos\phi_0} e^{ik_0 \sin\phi_0 x}. \tag{5.50}$$

The solution based on the perturbation technique can be obtained from equation (5.45) with $L = \infty$ and

$$c_m = \begin{cases} 1 & m = 0 \\ 0 & \text{otherwise} \end{cases};$$

thus

$$J_n^e(x) = \frac{2Y_0 \cos\phi_0(-2Y_0R_0)^n}{(1 + 2Y_0R_0\cos\phi_0)^{n+1}} e^{ik_0 \sin\phi_0 x},$$

and

$$J^e(x) = \sum_{n=0}^{+\infty} \frac{2Y_0 \cos\phi_0(-2Y_0R_0)^n}{(1 + 2Y_0R_0\cos\phi_0)^{n+1}} e^{ik_0 \sin\phi_0 x}\Delta^n.$$

This series is absolutely convergent and represents the Taylor series expansion of equation (5.50), implying that the perturbation solution can be made as close as we wish to the exact solution.

5.4.2 Moment Method Solution for Periodic Resistive Sheet

For a resistive sheet which is periodic in one dimension with period L, we have

$$R(x+L) = R(x)$$

If the resistive sheet is illuminated by the plane wave (5.1) or (5.8) , the induced current on the sheet must satisfy the periodicity requirements imposed by Floquet's theorem, i.e.

$$J(x+nL) = J(x)e^{ik_0 \sin\phi_0 nL} \tag{5.51}$$

Let us first consider E polarization case . The scattered electric field can derived from (5.5). By subdividing the integral into multiples of a period, the equation can be written as

$$E_y^s = -\frac{k_0 Z_0}{4} \sum_{n=-\infty}^{+\infty} \int_{x_0+nL}^{x_0+(n+1)L} J_y(x') H_0^{(1)}(k_0\sqrt{(x-x')^2+z^2})\mathrm{d}x'$$

If the variable x' is now changed to $x'+nL$ and the property (5.51) is employed, we get

$$E_y^s = -\frac{k_0 Z_0}{4} \int_{x_0}^{x_0+L} J_y(x') G_e(x,x',z)\mathrm{d}x',$$

where

$$G_e(x,x',z) \equiv \sum_{n=-\infty}^{+\infty} H_0^{(1)}(k_0\sqrt{(x-x'-nL)^2+z^2})e^{ik_0 \sin\phi_0 nL} \tag{5.52}$$

is the Green's function of the problem. The series is very slowly converging, specially when L is small compared to the wavelength. To make the problem computationally tractable a better form for the Green's function is needed. If the Fourier integral representation of the Hankel function is inserted into (5.52) and the order of summation, integration reversed, we have

$$G_e(x,x',z) = \frac{1}{\pi} \int_{-\infty}^{+\infty} \frac{e^{i[\sqrt{k_0^2-\alpha^2}|z|+\alpha(x-x')]}}{\sqrt{k_0^2-\alpha^2}} \sum_{n=-\infty}^{+\infty} e^{-in(\alpha-k_0\sin\phi_0)L}\mathrm{d}\alpha \ . \tag{5.53}$$

But

$$\sum_{n=-\infty}^{+\infty} e^{-in(\alpha-k_0\sin\phi_0)L} = 2\pi \sum_{n=-\infty}^{+\infty} \delta[(\alpha - k_0\sin\phi_0)L - 2\pi n].$$

Applying the above identity to (5.53) and changing the order of summation and integration one more time provides the following expression for the Green's function:

$$G_e(x,x',z) = \frac{2}{L}\sum_{n=-\infty}^{+\infty} \frac{e^{i\sqrt{k_0^2-(\frac{2\pi n}{L}+k_0\sin\phi_0)^2}|z|}}{\sqrt{k_0^2-(\frac{2\pi n}{L}+k_0\sin\phi_0)^2}} e^{i(\frac{2\pi n}{L}+k_0\sin\phi_0)(x-x')}. \tag{5.54}$$

This series converges very fast specially when z is relatively large, and with the aid of this Green's function, the integral equation for the induced current given in (5.7) becomes

$$R(x)J_y(x) = e^{ik_0\sin\phi_0 x} - \frac{k_0 Z_0}{4}\int_{x_0}^{x_0+L} J_y(x')G_e(x,x',0^+)\mathrm{d}x' \tag{5.55}$$

By a similar technique the Green's function for a periodic resistive sheet in the H polarization case can be derived and is given by

$$G_h(x,x',z) = \frac{2}{L}(1+\frac{1}{k_0^2}\frac{\partial^2}{\partial x^2})\sum_{n=-\infty}^{+\infty} \frac{e^{i\sqrt{k_0^2-(\frac{2\pi n}{L}+k_0\sin\phi_0)^2}|z|}}{\sqrt{k_0^2-(\frac{2\pi n}{L}+k_0\sin\phi_0)^2}} e^{i(\frac{2\pi n}{L}+k_0\sin\phi_0)(x-x')}, \tag{5.56}$$

and the resulting integral equation for the induced current is

$$R(x)J_x(x) = -\cos\phi_0 e^{ik_0\sin\phi_0 x} - \frac{k_0 Z_0}{4}\int_{x_0}^{x_0+L} J_x(x')G_h(x,x',0^+)\mathrm{d}x'. \tag{5.57}$$

The form of the Green's functions shows that the scattered field is composed of two types of waves: 1) propagating waves and 2) surface waves. The latter decay exponentially away from the surface and there are an infinite number of them. In contrast, the number of propagating waves is finite, depending upon the period L and the angle of incidence. The n^{th} mode is a propagating mode if n belongs to set $\mathcal{N}$ defined by

$$\mathcal{N} = \{n; -\frac{L}{\lambda_0}(1+\sin\phi_0) < n < \frac{L}{\lambda_0}(1-\sin\phi_0)\} \tag{5.58}$$

Note that even for $L < \lambda_0$ we get two propagating modes corresponding to $n = 0$ and $n = -1$. In the far zone only the propagating modes are observable and the electric field of the n$^{\text{th}}$ mode for E polarization is, for example, given by ($n \in \mathcal{N}$)

$$E_y^n = -[\frac{k_0 Z_0}{2L} \frac{\int_{x_0}^{x_0+L} J_y(x') e^{-i(\frac{2\pi n}{L} + k_0 \sin\phi_0)x'} dx'}{\sqrt{k_0^2 - (\frac{2\pi n}{L} + k_0 \sin\phi_0)^2}}] e^{i\sqrt{k_0^2 - (\frac{2\pi n}{L} + k_0 \sin\phi_0)^2}|z|} e^{i(\frac{2\pi n}{L} + k_0 \sin\phi_0)x}. \tag{5.59}$$

For H polarization the scattered magnetic field corresponding to the n$^{\text{th}}$ propagating mode can be obtained from

$$H_y^n = \mp[\frac{1}{2L} \int_{x_0}^{x_0+L} J_x(x') e^{-i(\frac{2\pi n}{L} + k_0 \sin\phi_0)x'} dx'] e^{i\sqrt{k_0^2 - (\frac{2\pi n}{L} + k_0 \sin\phi_0)^2}|z|} e^{i(\frac{2\pi n}{L} + k_0 \sin\phi_0)x}, \tag{5.60}$$

where the upper and lower signs apply for an observation point in the upper or lower half-spaces respectively.

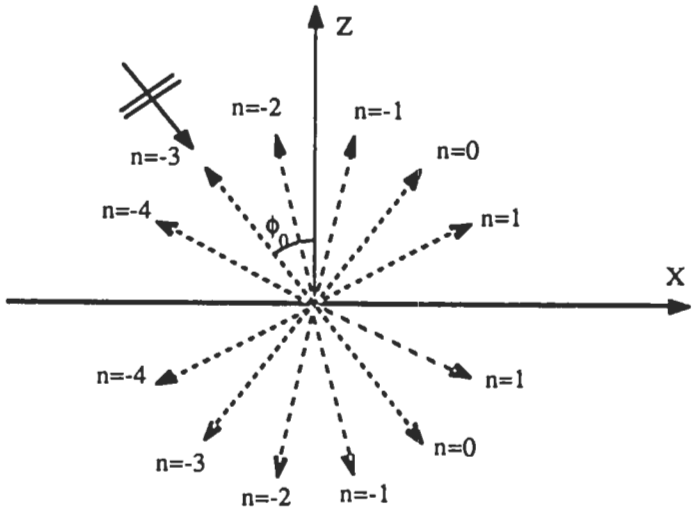

Figure 5.2: Scattering directions of propagating waves for a periodic resistive sheet with $L = 3\lambda_0$ and $\phi_0 = \frac{\pi}{6}$.

The direction of propagation of each mode is defined by the angle ϕ_n^s measured from the normal to the surface and can be obtained from

$$\sin\phi_n^s = \frac{\lambda_0}{L} n + \sin\phi_0 \tag{5.61}$$

Figure 5.2 depicts the scattering directions of the propagating waves as indicated by (5.61).

Numerical solutions of the integral equations (5.55) and (5.57) can be obtained by the method of moments. The unknown current is represented approximately by an expansion of pulse basis functions as

$$J(x) = \sum_{m=1}^{M} J_m P(x - x_m) \tag{5.62}$$

where J_m are the unknown coefficients to be found, M is the total number of segments, and $P(x)$ is the pulse function defined by

$$P(x) = \begin{cases} 1 & |\, x \,| < \frac{\Delta x}{2} \\ 0 & \text{otherwise} \end{cases}$$

In the case of E polarization, by substituting (5.62) into integral equation (5.55) and setting $x_0 = -\frac{L}{2}$ we get

$$R(x)J(x) = e^{ik_0 \sin\phi_0 x} - \frac{k_0 Z_0}{4} \sum_{m=1}^{M} J_m \int_{x_m - \frac{\Delta x}{2}}^{x_m + \frac{\Delta x}{2}} G_e(x, x', 0^+) \mathrm{d}x'$$

After evaluating the integral and setting the observation point at $x = x_k$, the following expression results:

$$R(x_k)J(x_k) = e^{ik_0 \sin\phi_0 x_k} \quad -\frac{k_0 Z_0}{L} \sum_{m=1}^{M} J_m \cdot \left[\sum_{n=-\infty}^{+\infty} \frac{e^{i(\frac{2\pi n}{L} + k_0 \sin\phi_0)(x_k - x_m)} \sin((\frac{2\pi n}{L} + k_0 \sin\phi_0)\frac{\Delta x}{2})}{(\frac{2\pi n}{L} + k_0 \sin\phi_0)\sqrt{k_0^2 - (\frac{2\pi n}{L} + k_0 \sin\phi_0)^2}} \right]$$

This can be cast in matrix form as

$$[\mathcal{Z}][\mathcal{J}] = [\mathcal{V}] \tag{5.63}$$

where $[\mathcal{Z}]$ is the impedance matrix and its entries are

$$z_{km} = \frac{k_0 Z_0}{L} \sum_{n=-\infty}^{+\infty} \frac{e^{i(\frac{2\pi n}{L} + k_0 \sin\phi_0)(x_k - x_m)} \sin((\frac{2\pi n}{L} + k_0 \sin\phi_0)\frac{\Delta x}{2})}{(\frac{2\pi n}{L} + k_0 \sin\phi_0)\sqrt{k_0^2 - (\frac{2\pi n}{L} + k_0 \sin\phi_0)^2}} \qquad k \neq m$$

$$z_{kk} = \frac{k_0 Z_0}{L} \sum_{n=-\infty}^{+\infty} \frac{\sin((\frac{2\pi n}{L} + k_0 \sin\phi_0)\frac{\Delta x}{2})}{(\frac{2\pi n}{L} + k_0 \sin\phi_0)\sqrt{k_0^2 - (\frac{2\pi n}{L} + k_0 \sin\phi_0)^2}} + R(x_k) \qquad k = m$$

$[\mathcal{J}]$ is a column vector whose components are the unknown J_m's and $[\mathcal{V}]$ is the excitation vector whose components are given by

$$v_k = e^{ik_0 \sin\phi_0 x_k}.$$

Derivation of the impedance matrix for H polarization is rather difficult because of the higher order singularity of the Green's function. Using the same expansion of the induced current as before and inserting it into the integral equation (5.57) we obtain

$$R(x)J(x) = -\cos\phi_0 e^{ik_0 \sin\phi_0 x} - \frac{k_0 Z_0}{4} \sum_{m=1}^{M} J_m \int_{x_m - \frac{\Delta x}{2}}^{x_m + \frac{\Delta x}{2}} (1 + \frac{\partial^2}{\partial x^2}) G_h(x, x', 0^+) \mathrm{d}x' \tag{5.64}$$

To find the impedance matrix consider the following integral:

$$\int \frac{\partial^2}{\partial x^2} G_h(x, x', z) \mathrm{d}x' = -G_h'(x, x', z)$$

where $G_h'(x, x', z)$ is the derivative of $G_h(x, x', z)$ with respect to x and is given by

$$G_h'(x, x', z) = \frac{2}{L} \sum_{n=-\infty}^{+\infty} \frac{e^{i\sqrt{k_0^2 - (\frac{2\pi n}{L} + k_0 \sin\phi_0)^2}|z|}}{\sqrt{k_0^2 - (\frac{2\pi n}{L} + k_0 \sin\phi_0)^2}} \cdot i(\frac{2\pi n}{L} + k_0 \sin\phi_0) e^{i(\frac{2\pi n}{L} + k_0 \sin\phi_0)(x - x')}. \tag{5.65}$$

The convergence of the series is very poor when $z \to 0$, but the limit does exist. To achieve a better convergence rate, consider the following geometric series based on the asymptotic behavior of the individual terms in (5.65) for large n, positive and negative:

$$S_1 = \frac{2}{L} \sum_{n=1}^{+\infty} e^{-\frac{2\pi n}{L}|z|} e^{i(\frac{2\pi n}{L} + k_0 \sin\phi_0)(x - x')} = \frac{2}{L} e^{-ik_0 \sin\phi_0 (x - x')} \frac{e^{-\frac{2\pi}{L}(|z| + i(x' - x))}}{1 - e^{-\frac{2\pi}{L}(|z| + i(x' - x))}}$$

$$S_2 = \frac{2}{L} \sum_{n=-\infty}^{-1} e^{\frac{2\pi n}{L}|z|} e^{i(\frac{2\pi n}{L} + k_0 \sin\phi_0)(x - x')} = \frac{2}{L} e^{-ik_0 \sin\phi_0 (x - x')} \frac{e^{-\frac{2\pi}{L}(|z| - i(x' - x))}}{1 - e^{-\frac{2\pi}{L}(|z| - i(x' - x))}}$$

By adding and subtracting the above series from $G_h'(x,x',z)$ and then letting $z \to 0$ it follows that

$$\begin{aligned} G_h'(x,x',0^+) &= \lim_{z\to 0}[G_h'(x,x',z) - S_1 - S_2] \\ &\quad + \frac{2}{L}e^{ik_0 \sin\phi_0(x-x')}\left[\frac{e^{-i\frac{2\pi}{L}(x'-x)}}{1-e^{-i\frac{2\pi}{L}(x'-x)}} - \frac{e^{i\frac{2\pi}{L}(x'-x)}}{1-e^{i\frac{2\pi}{L}(x'-x)}}\right], \end{aligned}$$

which can be rearranged to give

$$\begin{aligned} G_h'(x,x',0^+) &= \frac{2}{L}e^{-ik_0\sin\phi_0(x-x')}\{\sum_{n=1}^{+\infty}[(\frac{i(\frac{2\pi n}{L}+k_0\sin\phi_0)}{\sqrt{k_0^2-(\frac{2\pi n}{L}+k_0\sin\phi_0)^2}} - 1)e^{-i\frac{2\pi n}{L}(x'-x)} \\ &\quad + (\frac{i(-\frac{2\pi n}{L}+k_0\sin\phi_0)}{\sqrt{k_0^2-(-\frac{2\pi n}{L}+k_0\sin\phi_0)^2}} + 1)e^{i\frac{2\pi n}{L}(x'-x)}] \\ &\quad + [i\tan\phi_0 + \frac{e^{-i\frac{2\pi}{L}(x'-x)}}{1-e^{-i\frac{2\pi}{L}(x'-x)}} - \frac{e^{i\frac{2\pi}{L}(x'-x)}}{1-e^{i\frac{2\pi}{L}(x'-x)}}]\} \end{aligned} \tag{5.66}$$

The above series is absolutely convergent and its rate of convergence is relatively fast (like $\frac{1}{n^2}$). By defining the following parameters:

$$\begin{aligned} A(x,x_m) = \; & \frac{1}{k_0^2}\int_{x_m-\frac{\Delta x}{2}}^{x_m+\frac{\Delta x}{2}} \frac{\partial^2}{\partial x^2}G_h(x,x',0^+)\mathrm{d}x' = \frac{4i}{Lk_0^2}e^{ik_0\sin\phi_0(x-x_m)} \\ & \cdot\{\sum_{n=1}^{+\infty}[(\frac{i(\frac{2\pi n}{L}+k_0\sin\phi_0)}{\sqrt{k_0^2-(\frac{2\pi n}{L}+k_0\sin\phi_0)^2}} - 1)e^{i\frac{2\pi n}{L}(x-x_m)}\sin((\frac{2\pi n}{L}+k_0\sin\phi_0)\frac{\Delta x}{2}) \\ & + (\frac{i(-\frac{2\pi n}{L}+k_0\sin\phi_0)}{\sqrt{k_0^2-(-\frac{2\pi n}{L}+k_0\sin\phi_0)^2}} + 1)e^{-i\frac{2\pi n}{L}(x-x_m)}\sin((-\frac{2\pi n}{L}+k_0\sin\phi_0)\frac{\Delta x}{2})] \\ & + i\tan\phi_0\sin(k_0\sin\phi_0\frac{\Delta x}{2}) + \frac{1}{2}\cot(\frac{\pi}{L}(x-x_m+\frac{\Delta x}{2}))e^{i(k_0\sin\phi_0\frac{\Delta x}{2})} \\ & - \frac{1}{2}\cot(\frac{\pi}{L}(x-x_m-\frac{\Delta x}{2}))e^{-i(k_0\sin\phi_0\frac{\Delta x}{2})}\}, \end{aligned}$$

$$\begin{aligned} B(x,x_m) &= \int_{x_m-\frac{\Delta x}{2}}^{x_m+\frac{\Delta x}{2}} G_h(x,x',0^+)\mathrm{d}x' \\ &= \frac{4}{L}e^{ik_0\sin\phi_0(x-x_m)}\sum_{n=-\infty}^{+\infty}\frac{e^{i\frac{2\pi n}{L}(x-x_m)}\sin((\frac{2\pi n}{L}+k_0\sin\phi_0)\frac{\Delta x}{2})}{(\frac{2\pi n}{L}+k_0\sin\phi_0)\sqrt{k_0^2-(\frac{2\pi n}{L}+k_0\sin\phi_0)^2}} \end{aligned}$$

and setting the observation point $x = x_k$, (5.64) can be written as

$$R(x_k)J(x_k) = -\cos\phi_0 e^{ik_0\sin\phi_0 x} - \frac{k_0 Z_0}{4}\sum_{m=1}^{M} J_m[A(x_k,x_m) + B(x_k,x_m)]$$

This can be cast as a matrix equation similar to (5.63) with the impedance matrix and excitation vector having entries

$$z_{km} = \frac{k_0 Z_0}{4}[A(x_k,x_m) + B(x_k,x_m)] \quad k \neq m$$

$$z_{kk} = \frac{k_0 Z_0}{4}[A(x_k,x_k) + B(x_k,x_k)] \quad k = m$$

$$v_k = -\cos\phi_0 e^{ik_0 \sin\phi_0 x_k}.$$

5.4.3 Numerical Comparison

We are now in a position to compare the solution based on the perturbation technique with the solution based on the moment method for periodic resistive sheets. Figures 5.3 and 5.4 show the amplitude and phase of the induced current on a resistive sheet with sinusoidal variation of period $L = 2\lambda_0$ and $\Delta = 0.7$ for E polarization. In these plots the first through fourth order solutions are presented using the expression (5.45), and compared with the data obtained by the moment method (solution to (5.63)). It is seen that by increasing the order of solution we can get as close as we wish to the exact solution, and that the fourth order solution provides excellent agreement with the moment method data. We note here that the required order is directly proportional to Δ and L/λ_0. Similar results are shown in Figs. 5.5 and 5.6 for H polarization. The normalized field amplitudes of the propagating modes (Bragg modes) defined in (5.59) and (5.60) are given in Table 5.1 for a sinusoidal resistivity with $L = 3\lambda_0$, $\Delta = 0.7$, and $R_0 = 0 + i100$ at angle $\phi_0 = 30$ degrees. Since the resistivity is pure imaginary, there is no power loss and the total power carried by all of the modes is equal to the incident power. Table 5.2 gives the normalized field amplitude for a lossy resistive sheet $R_0 = 180 + i270$. In this case 31% and 29% of the incident power is dissipated in the resistive sheet for E and H polarization respectively. Note that apart from the case $n = 0$, $E_n^- = E_n^+$ and $H_n^- = -H_n+$, where $E_n^\pm$ and $H_n^\pm$ are the field amplitudes of n^{th} mode in the upper (+) and lower (-) half-spaces for E and H polarizations respectively. When $n = 0$ the incident field should be added to the zeroth mode in the lower half-space, i.e. $E_0^- = E_0^+ + E^i$ and $H_0^- = -H_0^+ + H^i$.

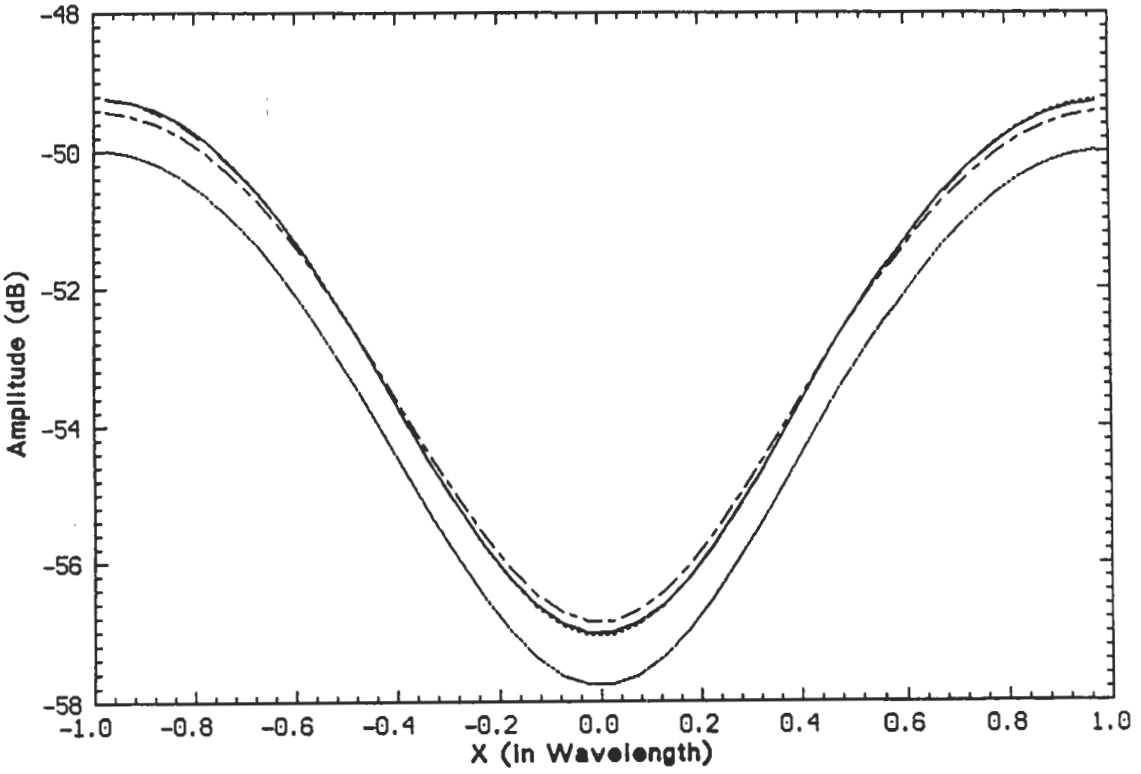

Figure 5.3: The amplitude of the induced current on a periodic resistive sheet with resistivity $R(x) = (180 + i270)(1 + 0.7\cos\frac{2\pi x}{L})$, $L = 2\lambda_0$ at normal incidence for E polarization: (——) moment method, (- - - - -) fourth order solution, (— —) third order solution, (— - —) second order solution, (— - - - —) first order solution.

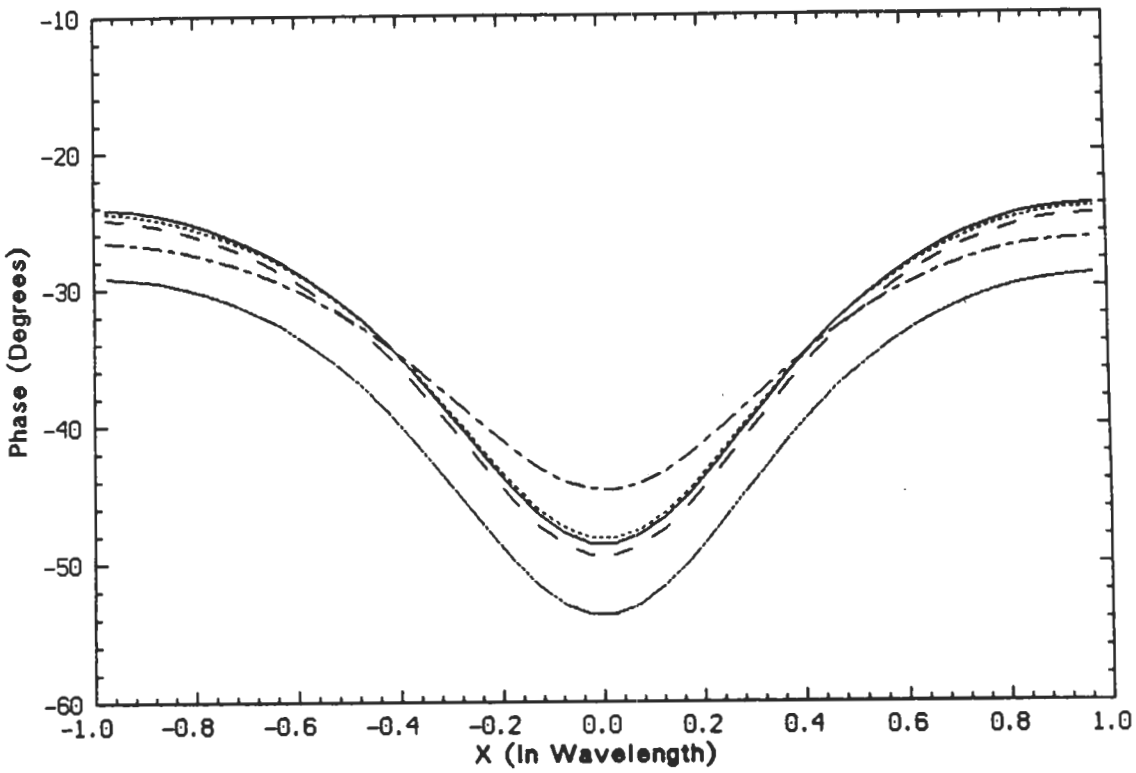

Figure 5.4: The phase of the induced current on a periodic resistive sheet with resistivity $R(x) = (180 + i270)(1 + 0.7\cos\frac{2\pi x}{L})$, $L = 2\lambda_0$ at normal incidence for E polarization: (——) moment method, (- - - - -) fourth order solution, (— —) third order solution, (— - —) second order solution, (— - - - - —) first order solution.

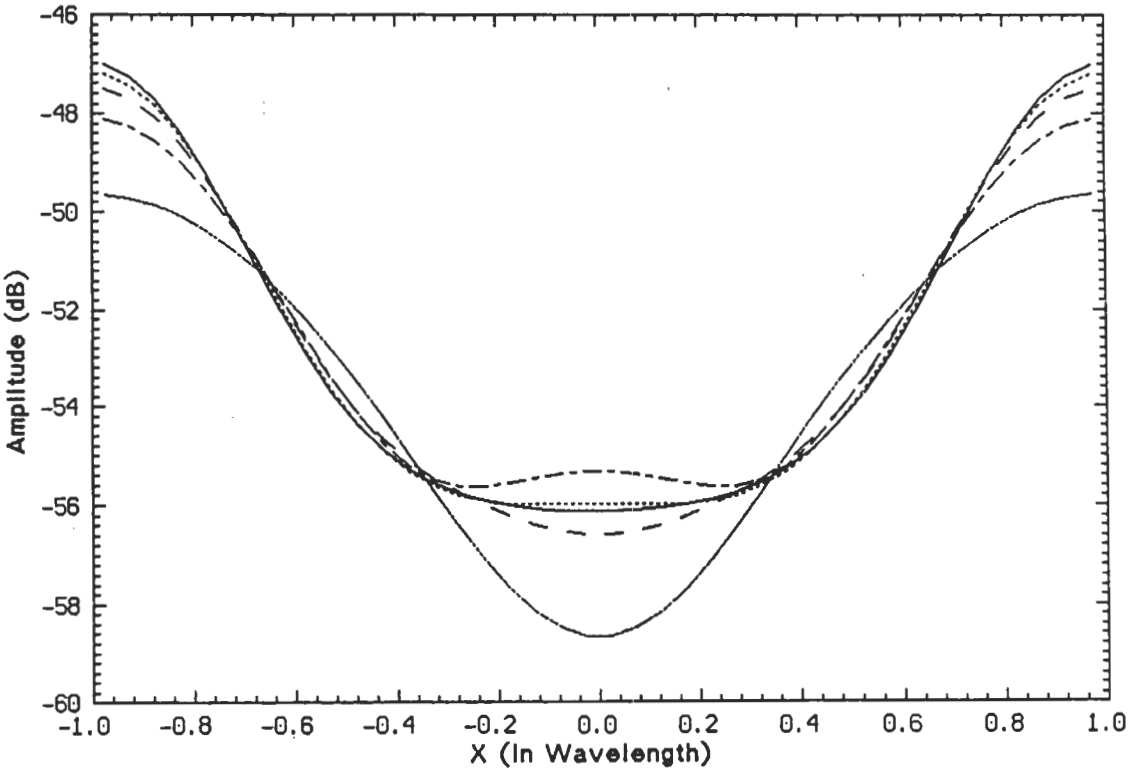

Figure 5.5: The amplitude of the induced current on a periodic resistive sheet with resistivity $R(x) = (180 + i270)(1 + 0.7\cos\frac{2\pi x}{L})$, $L = 2\lambda_0$ at normal incidence for H polarization: (——) moment method, (- - - - -) fourth order solution, (-- —) third order solution, (— - —) second order solution, (— - - - —) first order solution.

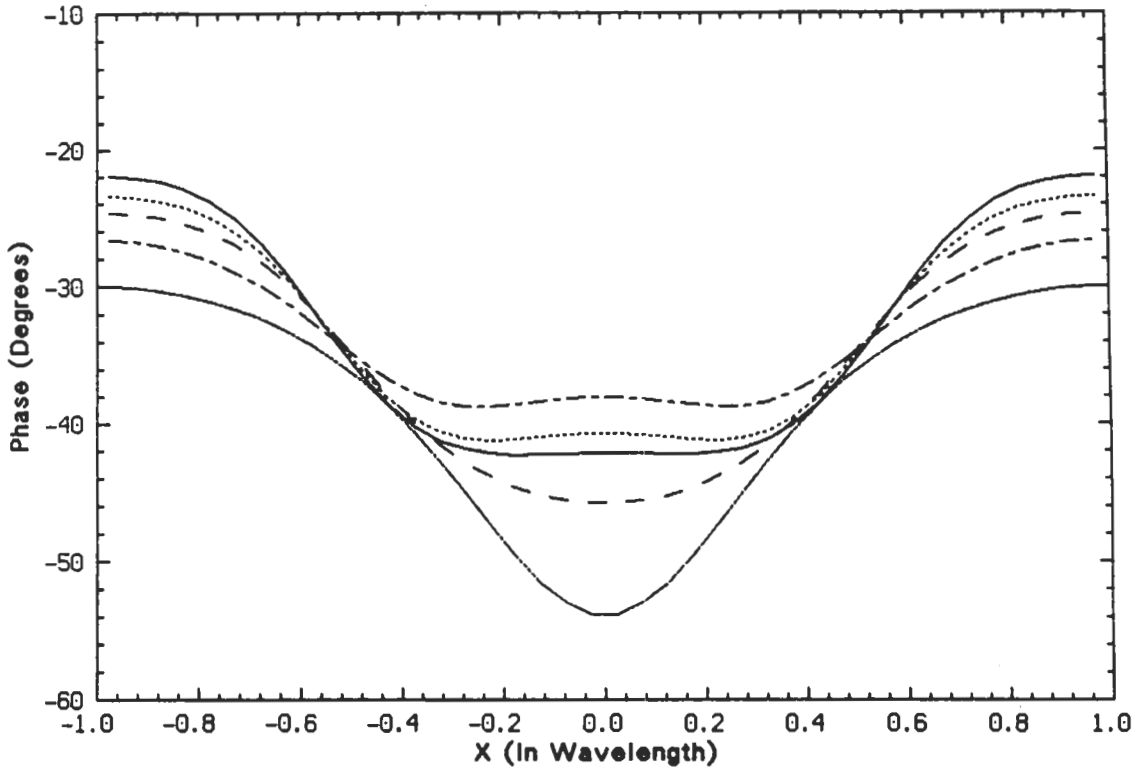

Figure 5.6: The phase of the induced current on a periodic resistive sheet with resistivity $R(x) = (180 + i270)(1 + 0.7\cos\frac{2\pi x}{L})$, $L = 2\lambda_0$ at normal incidence for H polarization: (——) moment method, (- - - - -) fourth order solution, (— —) third order solution, (— - —) second order solution, (— - - - —) first order solution.

	E-polarization		H-polarization	
n	E_n^+/E^i	E_n^-/E^i	H_n^+/H^i	H_n^-/H^i
-4	0.001∠62.37	0.001∠62.37	0.001∠-150.10	0.001∠29.90
-3	0.003∠169.70	0.003∠169.70	0.004∠-18.57	0.004∠161.43
-2	0.020∠-76.15	0.020∠-76.15	0.022∠99.93	0.022∠-80.07
-1	0.124∠40.43	0.124∠40.43	0.136∠-143.68	0.136∠36.32
0	0.887∠156.86	0.394∠62.13	0.831∠-27.13	0.460∠55.50
1	0.136∠49.53	0.136∠49.53	0.210∠-158.67	0.210∠21.33

Table 5.1: Normalized field amplitude of the propagating modes in the upper (+) and lower (-) half-spaces for a periodic resistive sheet $R(x) = R_0(1 + 0.7\cos\frac{2\pi x}{L})$ with $R_0 = 0 + i100$ and $L = 3\lambda_0$ at $\phi_0 = 30$ degree.

	E-polarization		H-polarization	
n	E_n^+/E^i	E_n^-/E^i	H_n^+/H^i	H_n^-/H^i
-4	0.002∠-105.65	0.002∠-105.65	0.003∠47.66	0.003∠-132.34
-3	0.008∠40.63	0.008∠40.63	0.008∠-145.58	0.008∠34.42
-2	0.028∠-163.62	0.026∠-163.62	0.030∠13.43	0.030∠-166.57
-1	0.110∠-6.41	0.110∠-6.41	0.112∠170.56	0.112∠-9.44
0	0.484∠150.69	0.625∠22.29	0.425∠-32.24	0.679∠19.49
1	0.141∠4.41	0.141∠4.41	0.135∠161.00	0.135∠-19.00

Table 5.2: Normalized field amplitude of the propagating modes in the upper (+) and lower (-) half-spaces for a periodic resistive sheet $R(x) = R_0(1 + 0.7\cos\frac{2\pi x}{L})$ with $R_0 = 180 + i270$ and $L = 3\lambda_0$ at $\phi_0 = 30$ degree.

5.5 Scattering from Impedance Insert

Another example that illustrates the ability of the perturbation technique in handling sharp variations in spatial domain is the scattering of a plane wave from an impedance insert whose geometry is shown in Fig. 5.7.

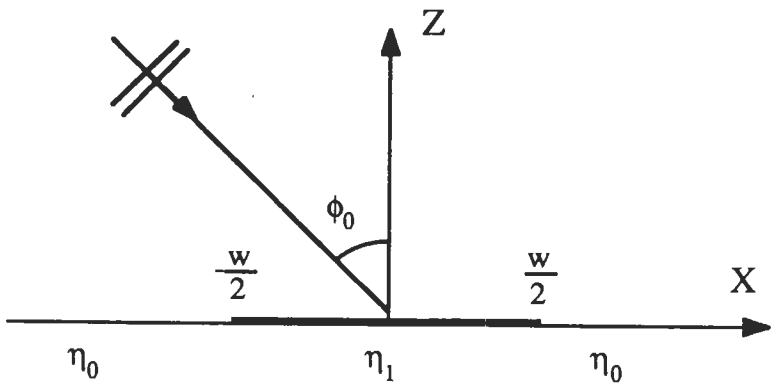

Figure 5.7: Geometry of an impedance insert.

The impedance of this surface can be represented as

$$\eta(x) = \eta_0(1 + \Delta \prod(\frac{x}{w}))$$

where $\prod(x)$ is the gate function defined by

$$\prod(x) = \begin{cases} 1 & \mid x \mid \leq \frac{1}{2} \\ 0 & \text{otherwise} \end{cases},$$

w is the width of the insert, and as before, Δ is a constant with $\mid \Delta \mid < 1$. The transform of the first components of the induced current for E and H polarization respectively can be obtained from (5.39) and (5.40) by replacing R_0 by $\eta_0/2$ as follows:

$$\tilde{J}_1^e(\alpha) = \frac{-2Y_0^2\eta_0 \cos\phi_0}{1 + Y_0\eta_0 \cos\phi_0} \cdot \frac{\sqrt{1 - \frac{\alpha^2}{k_0^2}}}{1 + Y_0\eta_0\sqrt{1 - \frac{\alpha^2}{k_0^2}}} w \frac{\sin(w(\alpha - k_0 \sin\phi_0)/2)}{w(\alpha - k_0 \sin\phi_0)/2} \qquad (5.67)$$

$$\tilde{J}_1^h(\alpha) = \frac{2Y_0^2\eta_0\cos\phi_0}{\cos\phi_0 + Y_0\eta_0} \cdot \frac{1}{Y_0\eta_0 + \sqrt{1-\frac{\alpha^2}{k_0^2}}} w \frac{\sin(w(\alpha - k_0\sin\phi_0)/2)}{w(\alpha - k_0\sin\phi_0)/2} \tag{5.68}$$

Unfortunately, analytical expressions for the higher order components of the induced current cannot be obtained for this case but they can be found numerically. To observe the behavior of the current in the spatial domain, expressions (5.67) and (5.68) were transformed numerically and the results are shown in Figs. 5.8 and 5.9. They show the expected behavior of the currents at the edges.

The scattered field due to the zeroth-order induced current consists of reflected and transmitted plane waves in the specular and forward directions, while the first component of the induced current gives rise to a cylindrical wave which will be denoted by the superscript s. In the far zone

$$\sqrt{(x-x')^2+z^2} \simeq \rho - x'\sin\phi_s$$

where ρ and ϕ_s denote the distance and direction of observation point, and

$$H_0^{(1)}(k_0\sqrt{(x-x')^2+z^2}) \simeq \sqrt{\frac{2}{\pi k_0\rho}} e^{i(k_0\rho-\frac{\pi}{4})} e^{-ik_0\sin\phi_s x'}, \tag{5.69}$$

$$\frac{1}{k_0^2}\frac{\partial^2}{\partial x^2} H_0^{(1)}(k_0\sqrt{(x-x')^2+z^2}) \simeq \sqrt{\frac{2}{\pi k_0\rho}} e^{i(k_0\rho-\frac{\pi}{4})} \cos^2\phi_s e^{-ik_0\sin\phi_s x'}, \tag{5.70}$$

$$\frac{1}{k_0^2}\frac{\partial^2}{\partial x\partial z} H_0^{(1)}(k_0\sqrt{(x-x')^2+z^2}) \simeq -\sqrt{\frac{2}{\pi k_0\rho}} e^{i(k_0\rho-\frac{\pi}{4})} \cos\phi_s \sin\phi_s e^{-ik_0\sin\phi_s x'}. \tag{5.71}$$

It is now easy to obtain the far field amplitude $\mathbf{P}(\phi_0, \phi_s)$ defined by

$$\mathbf{E}^s \simeq \sqrt{\frac{2}{\pi k_0\rho}} e^{i(k_0\rho-\frac{\pi}{4})} \mathbf{P}(\phi_0, \phi_s). \tag{5.72}$$

in terms of which the bistatic echo width is

$$\sigma(\phi_0, \phi_s) = \frac{2\lambda_0}{\pi} \mid \mathbf{P}(\phi_0, \phi_s) \mid^2 . \tag{5.73}$$

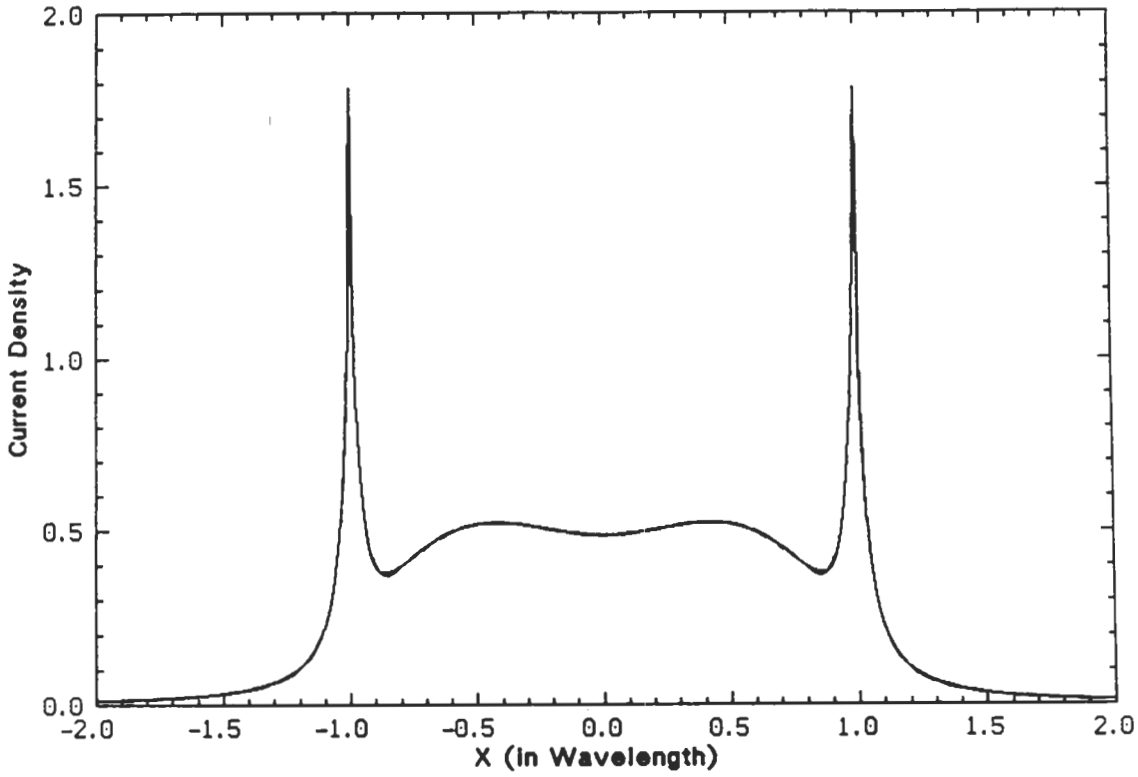

Figure 5.8: Distribution of the first component of induced current on an impedance insert for E polarization.

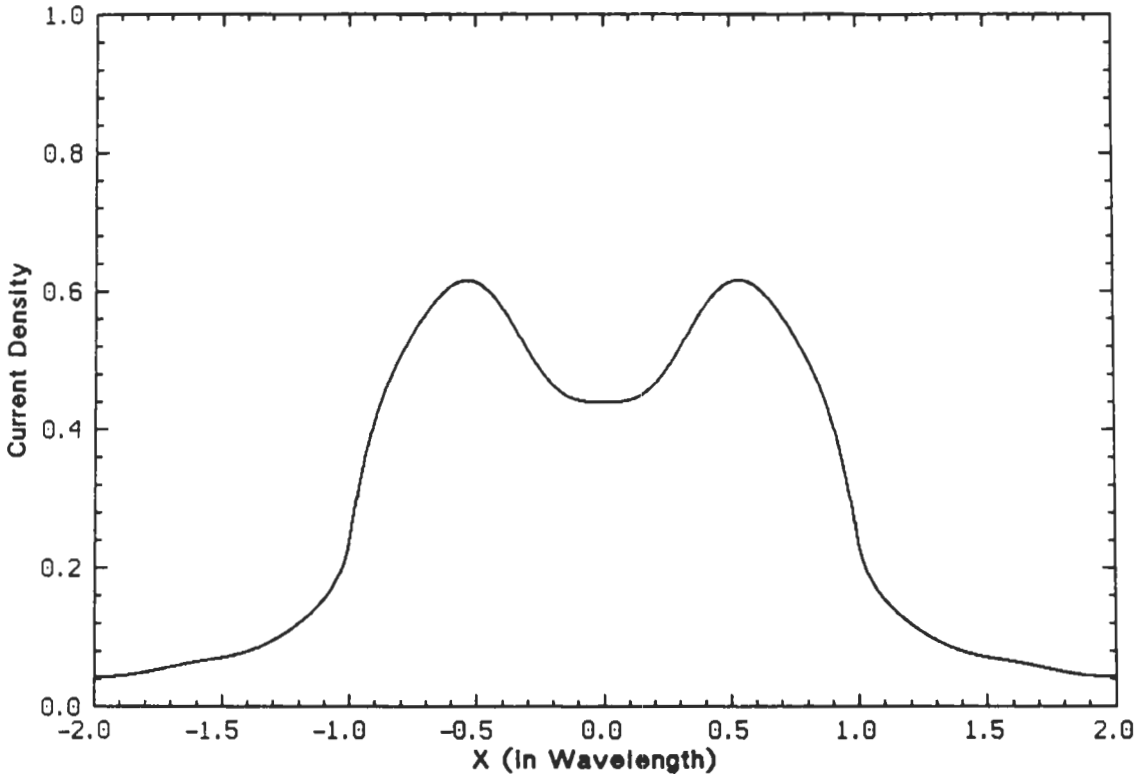

Figure 5.9: Distribution of the first component of induced current on an impedance insert for H polarization.

In the E polarization case the scattered field is in the y direction and

$$\mathbf{P}_e(\phi_0,\phi_s)=\hat{y}\frac{-k_0Z_0}{2}\int_{-\infty}^{+\infty}J_1^e(x')e^{-ik_0\sin\phi_s x'}\,\mathrm{d}x'=\hat{y}\frac{-k_0Z_0}{4}\tilde{J}_1^e(k_0\sin\phi_s). \tag{5.74}$$

For H polarization substitution of (5.70) and (5.71) into (5.10) and (5.11) shows that the scattered field has only a $\hat{\phi}$ component, and the far field amplitude is

$$\mathbf{P}_h(\phi_0,\phi_s)=\hat{\phi}\cos\phi_s\frac{k_0Z_0}{2}\int_{-\infty}^{+\infty}J_1^h(x')e^{-ik_0\sin\phi_s x'}\,\mathrm{d}x'=\hat{\phi}\frac{k_0Z_0}{4}\cos\phi_s\tilde{J}_1^h(k_0\sin\phi_s). \tag{5.75}$$

Thus

$$\mathbf{P}_e(\phi_0,\phi_s)=\hat{y}\frac{-k_0Y_0\eta_0\cos\phi_0}{1+Y_0\eta_0\cos\phi_0}\cdot\frac{\cos\phi_s}{1+Y_0\eta_0\cos\phi_s}\cdot w\Delta\frac{\sin(wk_0(\sin\phi_s-\sin\phi_0)/2)}{wk_0(\sin\phi_s-\sin\phi_0)/2},$$

$$\mathbf{P}_h(\phi_0,\phi_s)=\hat{\phi}\frac{-k_0Y_0\eta_0\cos\phi_0}{\cos\phi_0+Y_0\eta_0}\cdot\frac{\cos\phi_s}{Y_0\eta_0+\cos\phi_s}\cdot w\Delta\frac{\sin(wk_0(\sin\phi_s-\sin\phi_0)/2)}{wk_0(\sin\phi_s-\sin\phi_0)/2}.$$

The results of this technique are now compared with a uniform GTD solution [Herman and Volakis, 1988] that accounts for up to third order diffracted fields. Figures 5.10-5.15 compare the results of the perturbation method and the GTD technique for the impedance insert problem where there are sharp variations in perturbation function in the spatial domain. The figures show the normalized bistatic echo width (σ/λ_0) of an impedance insert having $w=2\lambda_0$ and $\eta_0=40-i40$ using the two methods. The agreement is excellent (for $\Delta=0.5$ the error is only 0.3 dB) in spite of the sharp changes in the perturbation function in the spatial domain.

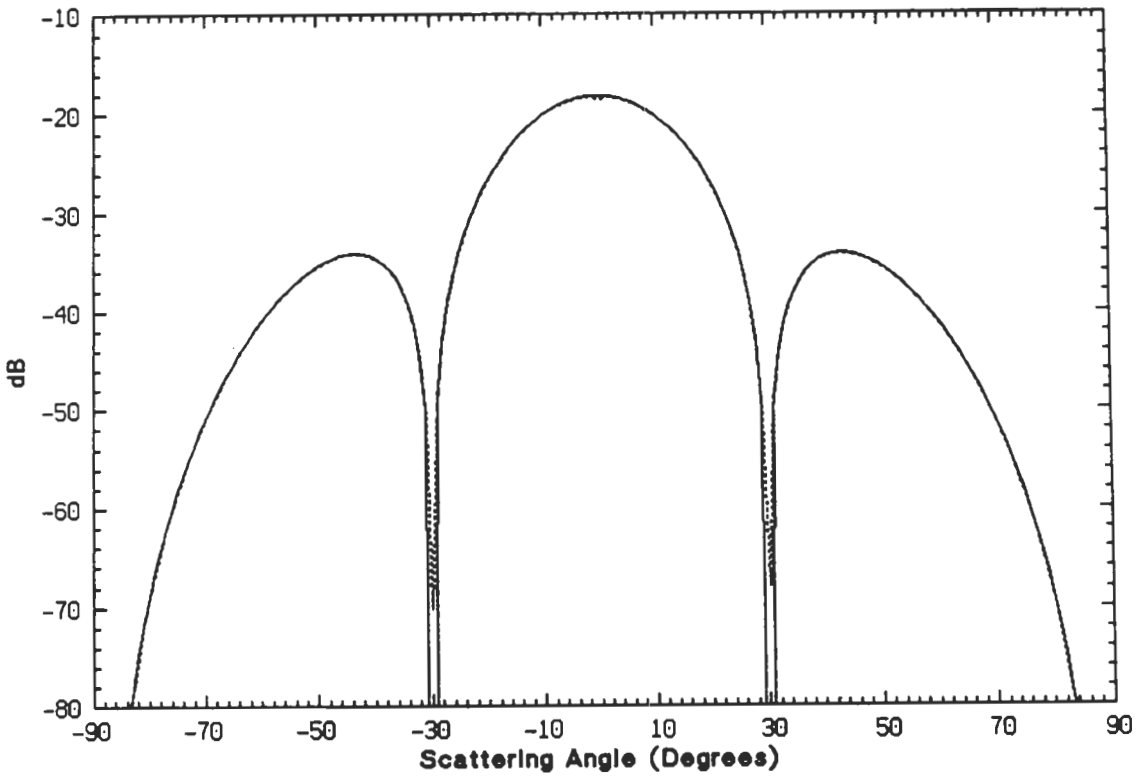

Figure 5.10: Normalized bistatic echo width (σ/λ_0) of an impedance insert with $w = 2\lambda_0$, $\eta_1 = 44 - i44$, $\eta_0 = 40 - i40$ ($\Delta = 0.1$) at $\phi_0 = 0$ degrees for E polarization: (——) perturbation technique, (- - - - -) GTD technique.

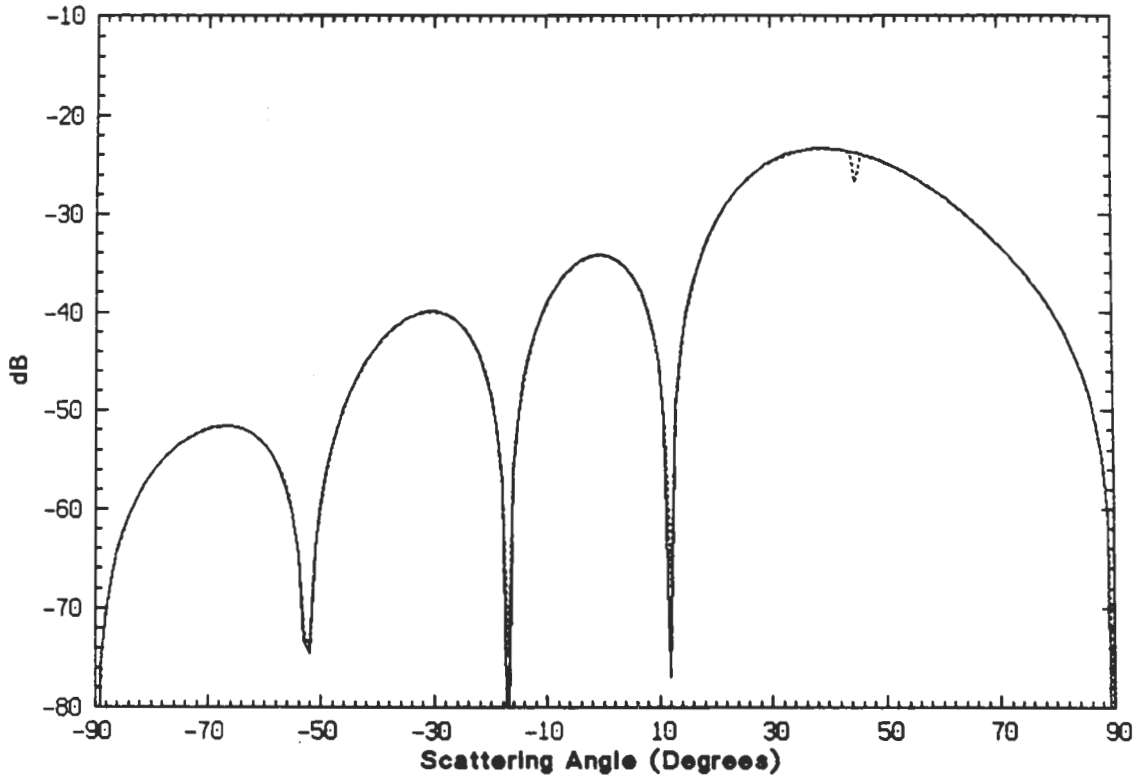

Figure 5.11: Normalized bistatic echo width (σ/λ_0) of an impedance insert with $w = 2\lambda_0$, $\eta_1 = 44 - i44$, $\eta_0 = 40 - i40$ ($\Delta = 0.1$) at $\phi_0 = 45$ degrees for E polarization: (——) perturbation technique, (- - - - -) GTD technique.

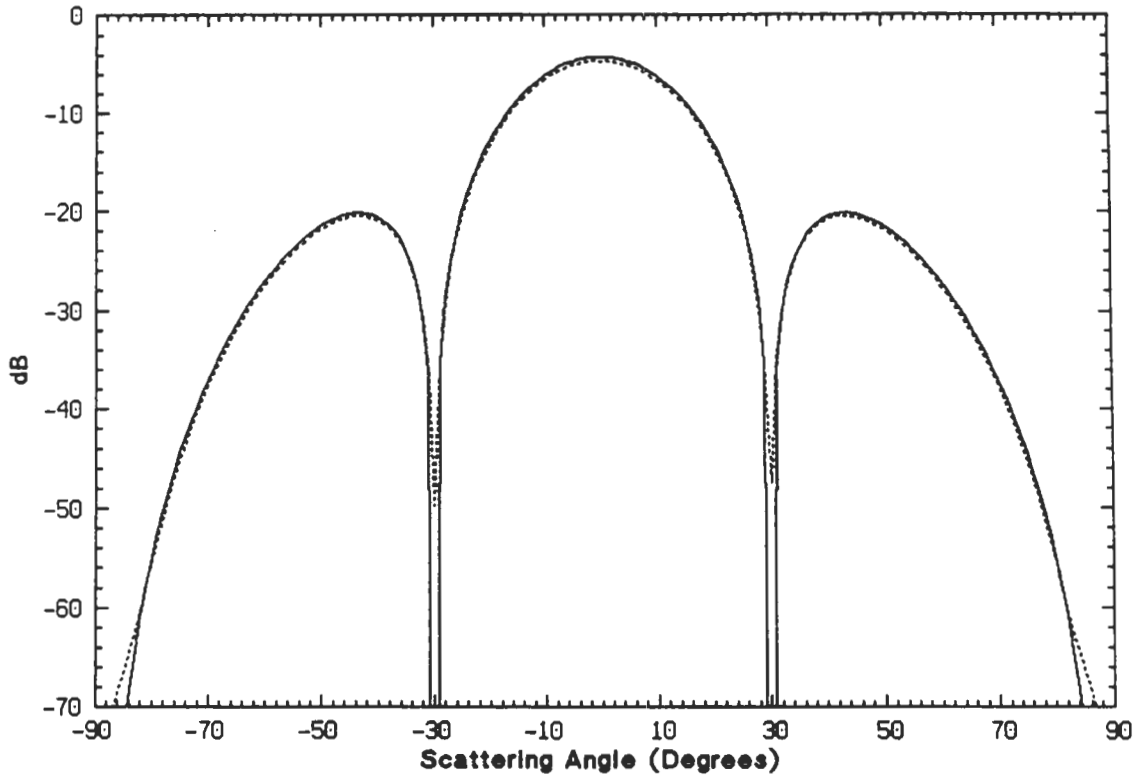

Figure 5.12: Normalized bistatic echo width (σ/λ_0) of an impedance insert with $w = 2\lambda_0$, $\eta_1 = 60 - i60$, $\eta_0 = 40 - i40$ ($\Delta = 0.5$) at $\phi_0 = 0$ degrees for E polarization: (——) perturbation technique, (- - - - -) GTD technique.

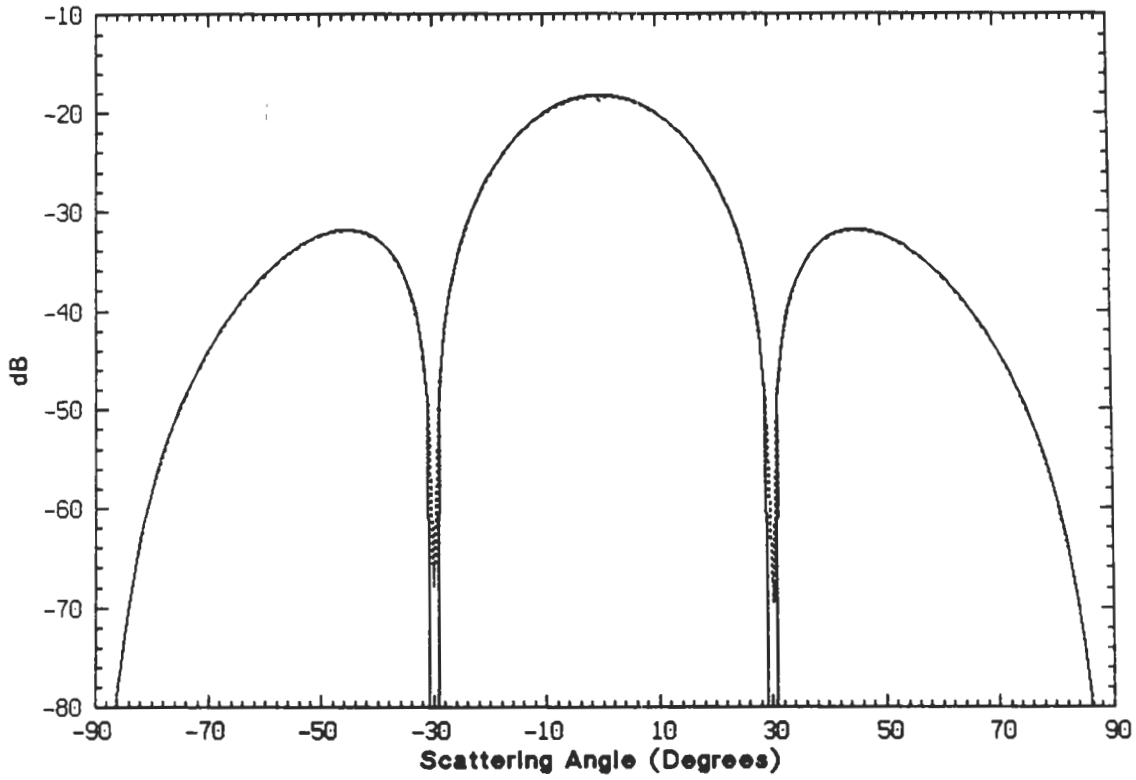

Figure 5.13: Normalized bistatic echo width (σ/λ_0) of an impedance insert with $w = 2\lambda_0$, $\eta_1 = 44 - i44$, $\eta_0 = 40 - i40$ ($\Delta = 0.1$) at $\phi_0 = 0$ degrees for H polarization: (——) perturbation technique, (- - - - -) GTD technique.

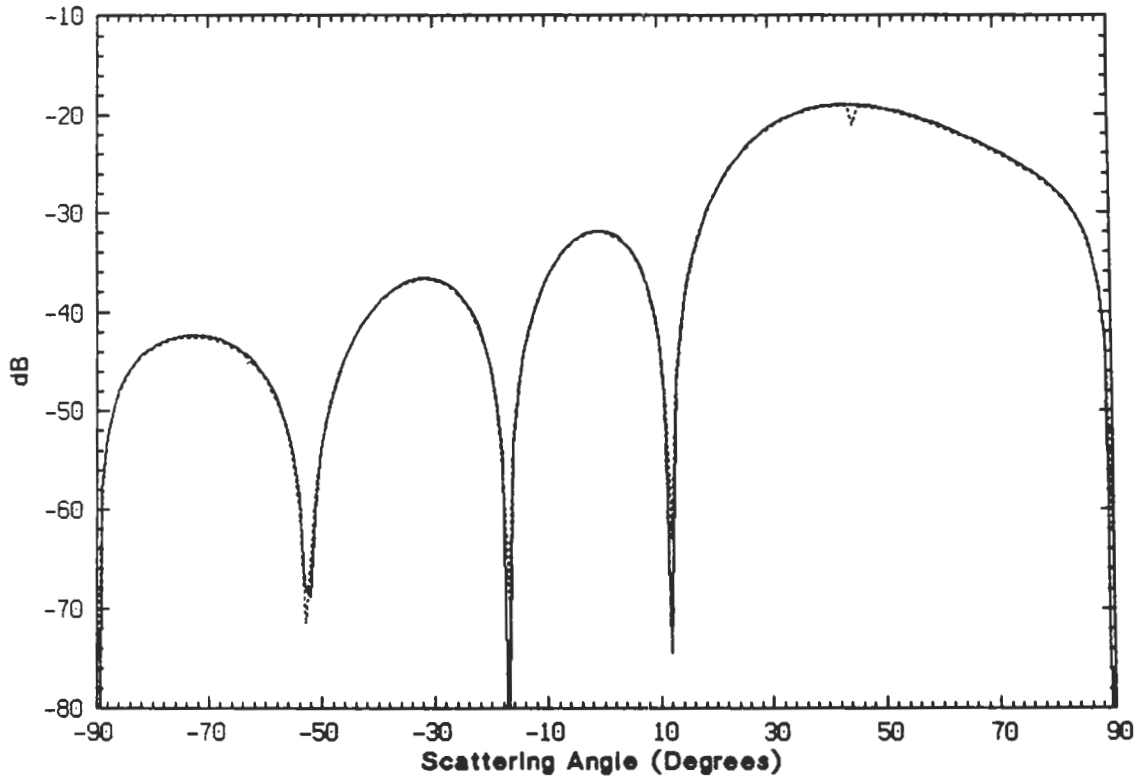

Figure 5.14: Normalized bistatic echo width (σ/λ_0) of an impedance insert with $w = 2\lambda_0$, $\eta_1 = 44 - i44$, $\eta_0 = 40 - i40$ ($\Delta = 0.1$) at $\phi_0 = 45$ degrees for H polarization: (——) perturbation technique, (- - - - -) GTD technique.

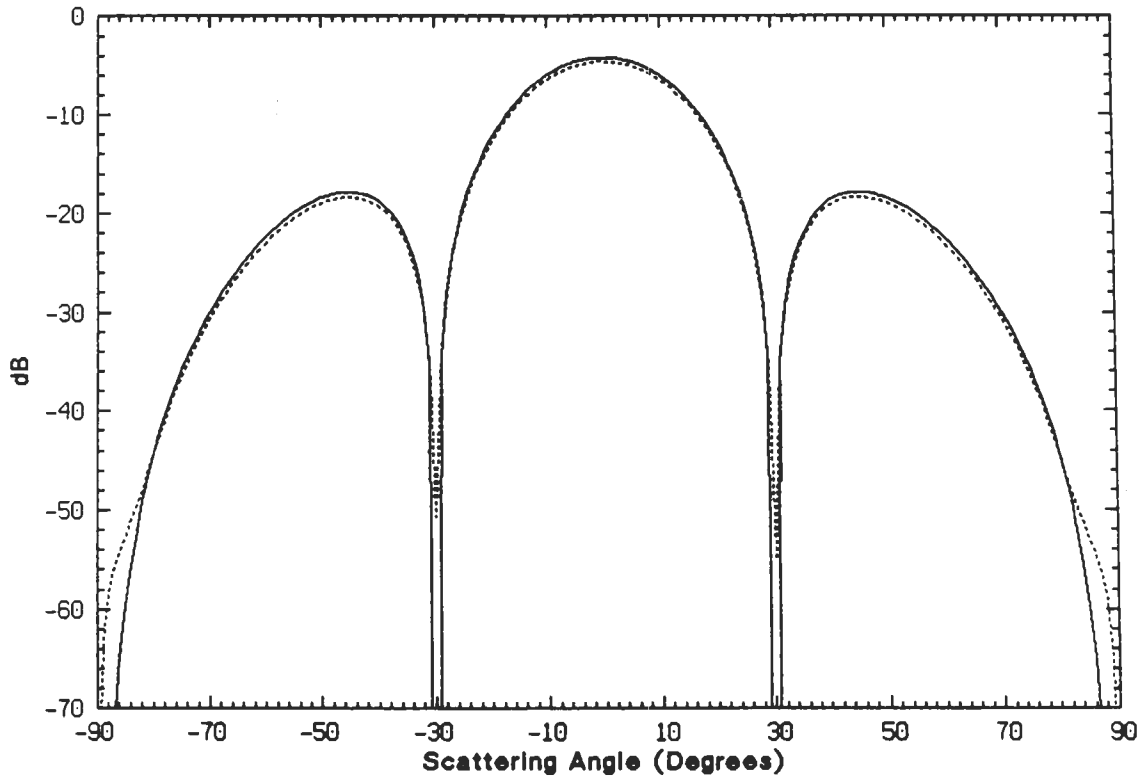

Figure 5.15: Normalized bistatic echo width (σ/λ_0) of an impedance insert with $w = 2\lambda_0$, $\eta_1 = 60 - i60$, $\eta_0 = 40 - i40$ ($\Delta = 0.5$) at $\phi_0 = 0$ degrees for H polarization: (——) perturbation technique, (- - - - -) GTD technique.

5.6 Scattering Model for a Variable Thickness Dielectric Slab

Consider a dielectric slab whose thickness is a function of x (see Fig. 5.16). Let the thickness be

$$T(x) = \tau_0(1 + \frac{w^2}{x^2 + w^2} \cdot \Delta)$$

where w is a measure of the width and Δ is the height of the dielectric hump. the hump may have a different dielectric constant from that of the underlying slab. This thickness function resembles the variation in thickness of a vegetation leaf and in this case w and Δ are random variables.

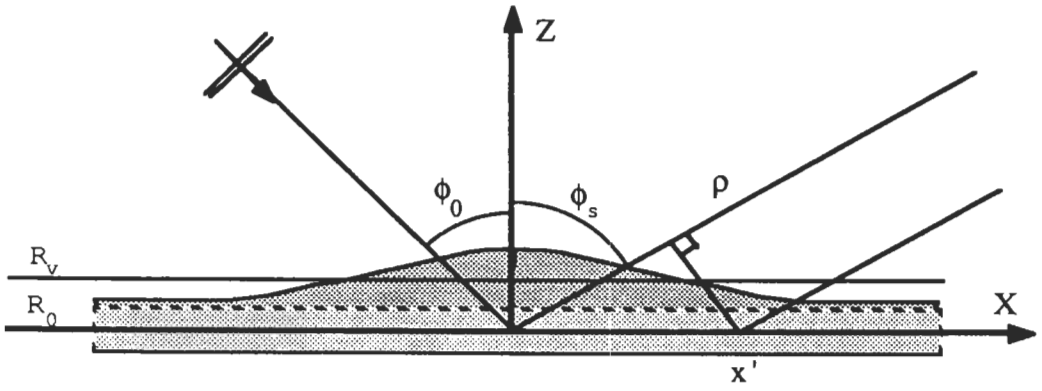

Figure 5.16: Geometry of a dielectric slab with a hump.

If the dielectric slab is electrically thin, it can be represented by two parallel resistive sheets one with a constant thickness τ_0 and the other one with a variable thickness

$$\tau(x) = \frac{w^2}{x^2 + w^2}\Delta\tau_0$$

where we assume here that $\Delta \ll 1$. Resistivity of the underlying and the top sheets are respectively denoted by R_0 and R_v which can be obtained from equation (2.3). These parallel sheets can be replaced by an equivalent sheet whose resistivity is equal

to that of the two parallel resistors R_0 and R_v, i.e.

$$R(x) = \frac{R_0 R_v}{R_0 + R_v}.$$

By substituting the expressions for R_0 and R_v in the above equation and then approximating the resultant expression to the first order of Δ it can be shown that

$$R(x) = R_0 \frac{\tau_0}{\tau_0 + \tau(x)} = R_0 \frac{1}{1 + \frac{w^2\Delta}{x^2+w^2}} \simeq R_0(1 - \frac{w^2}{x^2+w^2}\Delta)$$

The perturbation function then takes the form

$$r(x) = \frac{-w^2}{x^2 + w^2}.$$

and the transform of this is

$$\tilde{r}(\alpha) = -\pi w e^{-w|\alpha|}$$

The Fourier transforms of the first components of the induced current for E and H polarization can be obtained from (5.39) and (5.40) respectively, and are

$$\tilde{J}_1^e(\alpha) = \frac{4Y_0^2 R_0 \cos\phi_0}{1 + 2Y_0 R_0 \cos\phi_0} \cdot \frac{\sqrt{1 - \frac{\alpha^2}{k_0^2}}}{1 + 2Y_0 R_0 \sqrt{1 - \frac{\alpha^2}{k_0^2}}} \cdot (\pi w e^{-w|\alpha - k_0 \sin\phi_0|}) \tag{5.76}$$

$$\tilde{J}_1^h(\alpha) = \frac{-4Y_0^2 R_0 \cos\phi_0}{\cos\phi_0 + 2Y_0 R_0} \cdot \frac{1}{2Y_0 R_0 + \sqrt{1 - \frac{\alpha^2}{k_0^2}}} \cdot (\pi w e^{-w|\alpha - k_0 \sin\phi_0|}). \tag{5.77}$$

The far field amplitude associated with the first component of the induced current can be obtained from expressions similar to (5.74 and (5.75). Hence,

$$\mathbf{P}_e(\phi_0, \phi_s) = \hat{y} \frac{-k_0 Y_0 R_0 \cos\phi_0}{1 + 2Y_0 R_0 \cos\phi_0} \cdot \frac{\cos\phi_s}{1 + 2Y_0 R_0 \cos\phi_s} \cdot (\pi w \Delta e^{-k_0 w|\sin\phi_s - \sin\phi_0|}), \tag{5.78}$$

$$\mathbf{P}_h(\phi_0, \phi_s) = \hat{\phi} \frac{-k_0 Y_0 R_0 \cos\phi_0}{\cos\phi_0 + 2Y_0 R_0} \cdot \frac{\cos\phi_s}{2Y_0 R_0 + \cos\phi_s} \cdot (\pi w \Delta e^{-k_0 w|\sin\phi_s - \sin\phi_0|}). \tag{5.79}$$

If w and Δ are independent random variables such that w is Gaussian with mean and standard deviation w_0 and s respectively, its probability density function is

$$f_W(w) = \frac{1}{\sqrt{2\pi}s} e^{-(\frac{w - w_0}{s})^2}.$$

Assume also that the second moment of the random variable Δ is known. The mean value of the bistatic scattering width may now be calculated from (5.73), and by noting that

$$\langle w^2 e^{-2k_0 w|\sin\phi_s - \sin\phi_0|}\rangle = (s^2 + w_0^2) e^{(k_0^2 s^2|\sin\phi_s - \sin\phi_0|^2 - 2k_0 w_0|\sin\phi_s - \sin\phi_0|)},$$

we obtain the results

$$\langle \sigma_e(\phi_0, \phi_s)\rangle = 2\pi\lambda_0 \mid \frac{-k_0 Y_0 R_0 \cos\phi_0}{1 + 2Y_0 R_0 \cos\phi_0} \cdot \frac{\cos\phi_s}{1 + 2Y_0 R_0 \cos\phi_s} \mid^2 \langle\Delta^2\rangle \langle w^2 e^{-2k_0 w|\sin\phi_s - \sin\phi_0|}\rangle,$$

$$\langle \sigma_h(\phi_0, \phi_s)\rangle = 2\pi\lambda_0 \mid \frac{-k_0 Y_0 R_0 \cos\phi_0}{\cos\phi_0 + 2Y_0 R_0} \cdot \frac{\cos\phi_s}{2Y_0 R_0 + \cos\phi_s} \mid^2 \langle\Delta^2\rangle \langle w^2 e^{-2k_0 w|\sin\phi_s - \sin\phi_0|}\rangle.$$

The above is a first-order solution, and for a higher order solution, analytical results may not be achievable. When the height of the dielectric hump above the resistive sheet is not much smaller than the wavelength, the above solution fails to work for two reasons: 1) the solution is a first-order one in Δ, and 2) the dielectric hump cannot be modelled as a single resistive sheet. In such cases we have to resort to numerical techniques to get the solution. In the next section, the Green's function for a planar resistive sheet is obtained and used to derive an integral equation for the induced polarization current. A numerical technique is then employed to obtain the solution for a dielectric structure of arbitrary cross section above the resistive sheet. Results based on the perturbation technique and the moment method are then compared in Section 5.11.

5.7 Scattering from Dielectric Structures above Resistive and Impedance Sheets

In this section we seek the scattered field of a two dimensional dielectric object with arbitrary cross section above a uniform resistive or impedance sheet when the object is illuminated by a plane wave. The geometry of the problem is depicted in

Fig. 5.17. First, the Green's function is derived by obtaining the exact image of a line source and then the problem is expressed as an integral equation that can be solved numerically by the method of moments.

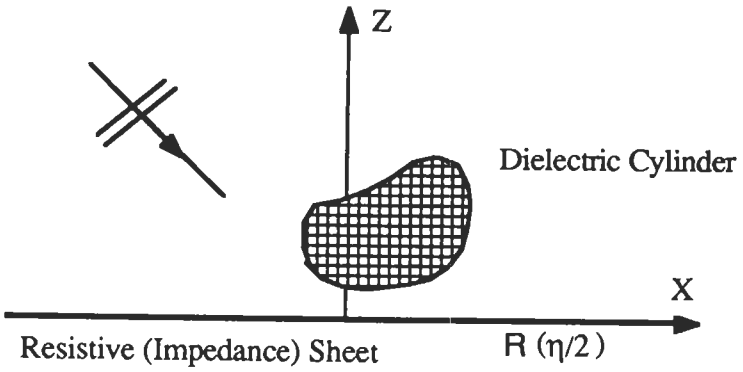

Figure 5.17: Geometry for the scattering problem of a dielectric cylinder above a uniform resistive or impedance sheet.

5.7.1 Exact Image of a Current Filament above Resistive Sheets

An integral representation for the image of a line source above a resistive sheet is derived. This representation has an excellent rate of convergence for most practical purposes and can be computed very easily. First, by using the electric Hertz potential, the exact image is derived for an electric current line source in the y direction. Following the same procedure, the image representation for a line source whose direction is parallel with the transverse plane ($x - z$ plane) is obtained next.

5.7.2 Line Current in Longitudinal Direction

Consider a uniform resistive sheet lying in the $x-y$ plane of a coordinate system (x, y, z). Assume a constant current is placed above the sheet at $p = (x', z')$ and the current density is given by

$$\mathbf{J} = \hat{y}\delta(x - x', z - z')$$

The electric Hertz potential in this case has only a longitudinal (y) component and must satisfy the wave equation, i.e.

$$(\nabla^2 + k_0^2)\Pi_y = -\frac{iZ_0}{k_0}\delta(x - x')\delta(z - z') \tag{5.80}$$

By taking the Fourier transform of both sides of the above equation with respect to x we obtain

$$[\frac{\partial^2}{\partial z^2} + (k_0^2 - k_x^2)]\tilde{\Pi}_y(k_x, z) = -\frac{iZ_0}{k_0}\delta(z - z')e^{ik_x x'} \tag{5.81}$$

where

$$\tilde{\Pi}_y(k_x, z) = \int_{-\infty}^{+\infty} \Pi_y(x, z)e^{ik_x x}\mathrm{d}x$$

is the Fourier transform of the electric Hertz potential. By dividing the space into three regions as shown in Fig. 5.18 and then imposing the radiation condition, the solution to the differential equation (5.81) in each region can be expressed by

$$\begin{aligned}
\tilde{\Pi}_y^1(k_x, z) &= c_1 e^{i(k_z z + k_x x')}\ , \\
\tilde{\Pi}_y^2(k_x, z) &= c_2 e^{i(k_z z + k_x x')} + c_3 e^{-i(k_z z - k_x x')}\ , \\
\tilde{\Pi}_y^3(k_x, z) &= c_4 e^{-i(k_z z - k_x x')}
\end{aligned} \tag{5.82}$$

where $k_z = \sqrt{k_0^2 - k_x^2}$ and branch of the square root is chosen such that $\sqrt{-1} = i$. The field quantities in terms of the Hertz potential are given by

$$E_y(x, z) = k_0^2 \Pi_y(x, z) \tag{5.83}$$

$$H_x(x,z) = ik_0 Y_0 \frac{\partial}{\partial z}\Pi_y(x,z) \tag{5.84}$$

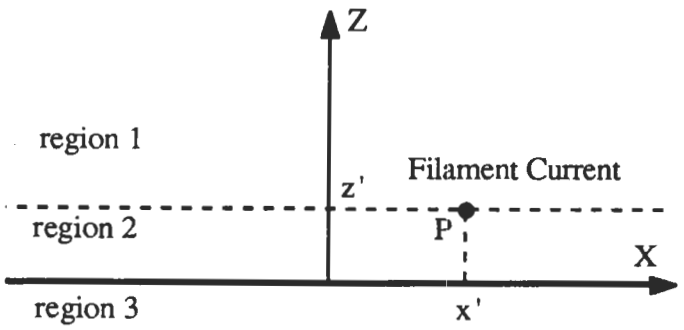

Figure 5.18: A constant line source above a uniform resistive sheet.

Continuity of the tangential electric field at $z = z'$ and the resistive sheet boundary conditions as given by (2.4)-(2.6) at $z = 0$ together with the equations (5.83) and (5.84) impose the following conditions on the Fourier transform of the Hertz potential

$$\begin{aligned} \tilde{\Pi}_y^1(k_x,z') - \tilde{\Pi}_y^2(k_x,z') &= 0 \ , \\ \tilde{\Pi}_y^2(k_x,0) - \tilde{\Pi}_y^3(k_x,0) &= 0 \ , \\ iRk_0Y_0[\tfrac{\partial}{\partial z}\tilde{\Pi}_y^2(k_x,0) - \tfrac{\partial}{\partial z}\tilde{\Pi}_y^3(k_x,0)] &= k_0^2\tilde{\Pi}_y^2(k_x,0) \end{aligned} \tag{5.85}$$

and from the jump condition we have

$$\frac{\partial}{\partial z}\tilde{\Pi}_y^1(k_x,z') - \frac{\partial}{\partial z}\tilde{\Pi}_y^2(k_x,z') = -\frac{iZ_0}{k_0} \ . \tag{5.86}$$

Upon substitution of (5.82) into (5.85) and (5.86), and then solving the resultant set of equations simultaneously, the unknown coefficients $c_1, \cdots, c_4$ can be obtained and

are given by

$$\begin{aligned} c_1 &= \frac{-1}{2k_0Y_0k_z}\left[\frac{-1}{1+\frac{2RY_0k_z}{k_0}}e^{ik_zz'} + e^{-ik_zz'}\right] \\ c_2 &= \frac{1}{2k_0Y_0k_z}\frac{1}{1+\frac{2RY_0k_z}{k_0}}e^{ik_zz'} \\ c_3 &= \frac{-1}{2k_0Y_0ik_z}e^{ik_zz'} \\ c_4 &= \frac{-1}{2k_0Y_0k_z}\frac{\frac{2RY_0k_z}{k_0}}{1+\frac{2RY_0k_z}{k_0}}e^{ik_zz'} \end{aligned} \tag{5.87}$$

The electric Hertz potential in each region can be obtained by taking the inverse Fourier transform. Let us represent the electric Hertz potential in the upper and lower half-spaces by $\Pi_y^+(x,z)$ and $\Pi_y^-(x,z)$ respectively, and then using the following identity

$$\int_{-\infty}^{+\infty}\frac{e^{i[k_x|z-z'|-k_x(x-x')]}}{k_z}\mathrm{d}k_x = \pi H_0^{(1)}(k_0\sqrt{(x-x')^2+(z-z')^2}) \tag{5.88}$$

we obtain

$$\begin{aligned} \Pi_y^+(x,z) = &\ \frac{-1}{4k_0Y_0}H_0^{(1)}(k_0\sqrt{(x-x')^2+(z-z')^2}) \\ &-\frac{1}{4k_0Y_0\pi}\int_{-\infty}^{+\infty}\frac{-1}{(1+\frac{2RY_0k_z}{k_0})k_z}e^{ik_x(z+z')-ik_x(x-x')}\mathrm{d}k_x \end{aligned} \tag{5.89}$$

$$\begin{aligned} \Pi_y^-(x,z) = -&\ \frac{1}{4k_0Y_0}H_0^{(1)}(k_0\sqrt{(x-x')^2+(-z+z')^2}) \\ &-\frac{1}{4k_0Y_0\pi}\int_{-\infty}^{+\infty}\frac{-1}{(1+\frac{2RY_0k_z}{k_0})k_z}e^{ik_x(-z+z')-ik_x(x-x')}\mathrm{d}k_x \end{aligned} \tag{5.90}$$

The first term in the (5.89) and (5.90) represents the effect of the current filament in absence of the resistive sheet while the second term is due to the image of the current filament. Unfortunately the integral representing the contribution of the image does not have a closed form and its convergence rate is very poor. To achieve the image contribution in an efficient way consider the following transformation

$$\int_0^{+\infty}e^{-\alpha\nu}e^{-k_z\nu}\mathrm{d}\nu = \frac{1}{\alpha+k_z} \qquad \text{provided } Re[\alpha] > -Re[k_z]\ . \tag{5.91}$$

The choice of the branch cut for k_z guarantees that $Re[k_z]$ is nonnegative as k_x takes any real number, therefore the sufficient condition for (5.91) is

$$Re[\alpha] > 0.$$

By defining $\alpha = \frac{k_0}{2RY_0}$ we note that the above condition is satisfied ($Re[\alpha] = \frac{k_0^2 \tau_c''}{2} > 0$) and the integral representing the image contribution in the upper half-space can be written as

$$\int_{-\infty}^{+\infty} \frac{-1}{(1+\frac{k_x}{\alpha})k_z} e^{ik_x(z+z')-ik_x(x-x')} \mathrm{d}k_x = \int_0^{+\infty} -\alpha e^{-\alpha\nu} [\int_{-\infty}^{+\infty} \frac{e^{ik_x(z+z'+i\nu)-ik_x(x-x')}}{k_z} \mathrm{d}k_x] \mathrm{d}\nu.$$

Employing the identity given by (5.88), the electric Hertz potential in the upper half-space is given by

$$\begin{aligned} \Pi_y^+(x,z) = \; & \tfrac{-1}{4k_0Y_0}[H_0^{(1)}(k_0\sqrt{(x-x')^2+(z-z')^2}) \\ & - \textstyle\int_0^{+\infty} \alpha e^{-\alpha\nu} H_0^{(1)}(k_0\sqrt{(x-x')^2+(z+z'+i\nu)^2}\mathrm{d}\nu]. \end{aligned} \tag{5.92}$$

In the same manner the electric Hertz potential for the lower half-space is found to be

$$\begin{aligned} \Pi_y^-(x,z) = \; & \tfrac{-1}{4k_0Y_0}[H_0^{(1)}(k_0\sqrt{(x-x')^2+(-z+z')^2}) \\ & - \textstyle\int_0^{+\infty} \alpha e^{-\alpha\nu} H_0^{(1)}(k_0\sqrt{(x-x')^2+(-z+z'+i\nu)^2}\mathrm{d}\nu]. \end{aligned} \tag{5.93}$$

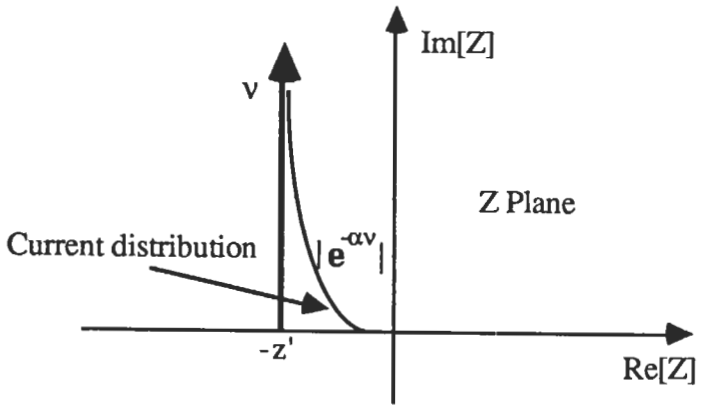

Figure 5.19: The location of the image of the line source in the complex z plane.

This integral representation converges very fast because both functions in the integrand are exponentially decaying. Also from this representation it can be deduced

that the image of a line current above a resistive sheet is a half plane current with exponential distribution and is located in the complex z plane occupying the region $-z'-i\infty < z < -z'$ (see Fig. 5.19). The validity of the image representation can be checked by considering some special limiting cases. Suppose the resistivity is very small (approaching the perfect conductor) which implies that $\mid \alpha \mid \gg 1$. In this case the integral in (5.92) can be approximated by

$$\int_0^{+\infty} \alpha e^{-\alpha\nu} H_0^{(1)}(k_0\sqrt{(x-x')^2+(z+z'+i\nu)^2})\mathrm{d}\nu \approx$$
$$H_0^{(1)}(k_0\sqrt{(x-x')^2+(z+z')^2}) \int_0^{+\infty} \alpha e^{-\alpha\nu}\mathrm{d}\nu = H_0^{(1)}(k_0\sqrt{(x-x')^2+(z+z')^2})$$

(contribution to the integral comes mostly from point $\nu = 0$) which is the image for the perfectly conducting case. An asymptotic behavior of the integral in terms of a convergent series of inverse power of α can be obtained by performing integration by parts repeatedly, thus

$$\int_0^{+\infty} \alpha e^{-\alpha\nu} H_0^{(1)}(k_0\sqrt{(x-x')^2+(z+z'+i\nu)^2})\mathrm{d}\nu = \sum_{n=0}^{\infty}(\frac{-1}{\alpha})^n h^{(n)}(0) \qquad (5.94)$$

where $h^{(n)}(0)$ is the n^{th} derivative of $H_0^{(1)}(k_0\sqrt{(x-x')^2+(z+z'+i\nu)^2})$ with respect to ν evaluated at zero. The first order of approximation is

$$\sum_{n=0}^{\infty}(\frac{-1}{\alpha})^n h^{(n)}(0) \approx h(0) - h'(0)\frac{1}{\alpha} \approx h(\frac{-1}{\alpha}) = H_0^{(1)}(k_0\sqrt{(x-x')^2+(z+z'-\frac{i}{\alpha})^2})$$

which is a line image located in the complex plane at $z = -z' + \frac{i}{\alpha}$. The other asymptotic behavior of interest is the far field approximation where the point of observation is far from the image point, i.e. $\rho_2 = \sqrt{(x-x')^2+(z+z')^2} \gg \lambda_0$ (see Fig. 5.20). In this condition

$$\sqrt{(x-x')^2+(z+z'+i\nu)^2} \approx \rho_2(1+\frac{i\nu\cos\phi_2}{\rho_2}), \qquad (5.95)$$

where we have assumed that $\rho_2 \gg \nu$. The validity of this assumption comes from the fact that the integrand of (5.92) is approximately zero if $\nu > \nu_{max}$ for some finite

ν_{max}. Now by using the large argument expansion of the Hankel function and then substituting for α we get

$$\lim_{\rho_2 \to \infty} \int_0^{+\infty} -\alpha e^{-\alpha\nu} H_0^{(1)}(k_0\sqrt{(x-x')^2+(z+z'+i\nu)^2})\mathrm{d}\nu \approx$$
$$\sqrt{\frac{2}{\pi\rho_2}} e^{i(k_0\rho_2-\frac{\pi}{4})} \frac{-1}{1+2Y_0 R\cos\phi} \ .$$

Note that the last term in the above equation is the plane wave reflection coefficient for the E polarization case. This result is identical to the asymptotic value of the integral given in (5.89) evaluated by the saddle point technique.

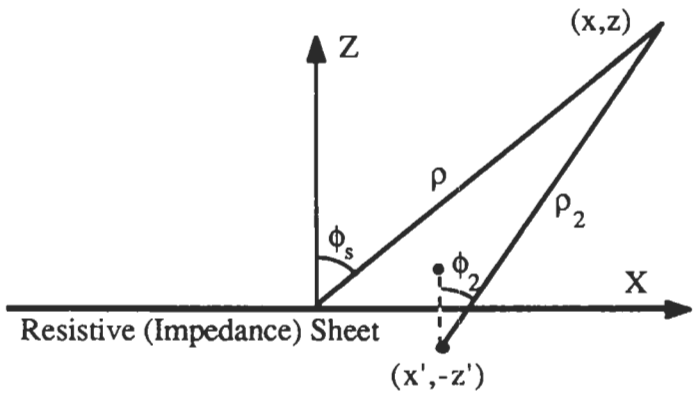

Figure 5.20: Geometry of image point for far field approximation.

5.7.3 Line Current in the Transverse Plane

Here we separate the problem into two problems: 1) when the current is in x direction and 2) when the current is in the z direction. First consider the situation where the current filament above the resistive sheet is in the x direction and its current density is given by

$$\mathbf{J} = \hat{x}\delta(x-x', z-z').$$

The electric Hertz potential has only an x component and must satisfy the wave equation as given in (5.80). The analysis of obtaining the electric Hertz potential ($\Pi_x(x,z)$) is similar to the previous case. The Fourier transform of the Hertz potential must satisfy an equation similar to (5.81), and the solution is identical to those given in (5.82). The field quantities in terms of the electric Hertz potential are given by

$$\mathbf{E} = k_0^2\left[\Pi_x(x,z) + \frac{1}{k_0^2}\frac{\partial^2}{\partial x^2}\Pi_x(x,z)\right]\hat{x} + \frac{\partial^2}{\partial x \partial z}\Pi_x(x,z)\hat{z} \tag{5.96}$$

$$\mathbf{H} = -ik_0 Y_0 \frac{\partial}{\partial z}\Pi_x(x,z)\hat{y} \tag{5.97}$$

The following relations for the Fourier transform of the Hertz potential can be obtained by using equations (5.96) and (5.97) and applying the continuity of the tangential electric field at $z = z'$ and the resistive sheet boundary conditions at $z = 0$

$$\begin{aligned}
[\frac{\partial^2}{\partial z^2}\tilde{\Pi}_x^1(k_x,z') - \frac{\partial^2}{\partial z^2}\tilde{\Pi}_x^2(k_x,z')] &= 0\ , \\
[\frac{\partial^2}{\partial z^2}\tilde{\Pi}_x^2(k_x,0) - \frac{\partial^2}{\partial z^2}\tilde{\Pi}_x^3(k_x,0)] &= 0\ , \\
iRk_0Y_0[\frac{\partial}{\partial z}\tilde{\Pi}_x^2(k_x,0) - \frac{\partial}{\partial z}\tilde{\Pi}_x^3(k_x,0)] &= -\frac{\partial^2}{\partial z^2}\tilde{\Pi}_x^2(k_x,0)\ , \\
\frac{\partial}{\partial z}\tilde{\Pi}_x^1(k_x,z') - \frac{\partial}{\partial z}\tilde{\Pi}_x^2(k_x,z') &= \frac{i}{k_0Y_0}\ ,
\end{aligned}$$

where the last equation comes from the jump condition. The unknown coefficients $c1,\cdots,c4$ in this case are given by

$$\begin{aligned}
c_1 &= \frac{-1}{2k_0Y_0k_z}[\frac{-1}{1+\frac{2RY_0k_0}{k_z}}e^{ik_zz'} + e^{-ik_z'}] \\
c_2 &= \frac{1}{2k_0Y_0k_z}\frac{-1}{1+\frac{2RY_0k_0}{k_z}}e^{ik_zz'} \\
c_3 &= \frac{-1}{2k_0Y_0k_z}e^{ik_zz'} \\
c_4 &= \frac{-1}{2k_0Y_0k_z}(1+\frac{-1}{1+\frac{2RY_0k_0}{k_z}})e^{ik_zz'}
\end{aligned}$$

The electric Hertz potential in the upper and lower half-spaces can be obtained by taking the inverse Fourier transform and then using the identity (5.88). Thus in the

upper and lower half-spaces we have

$$\Pi_x^+(x,z) = \frac{-1}{4k_0Y_0}[H_0^{(1)}(k_0\sqrt{(x-x')^2+(z-z')^2}) - H_0^{(1)}(k_0\sqrt{(x-x')^2+(z+z')^2})] - \frac{1}{4k_0Y_0\pi}\int_{-\infty}^{+\infty}\frac{1}{(1+\frac{k_z}{2RY_0k_0})k_z}e^{ik_z(z+z')-ik_x(x-x')}\mathrm{d}k_x \quad (5.98)$$

$$\Pi_x^-(x,z) = -\frac{1}{4k_0Y_0\pi}\int_{-\infty}^{+\infty}\frac{1}{(1+\frac{k_z}{2RY_0k_0})k_z}e^{ik_z(-z+z')-ik_x(x-x')}\mathrm{d}k_x. \quad (5.99)$$

The integral in (5.98) represents the contribution of the difference between resistive sheet and perfect conductor images.

Now suppose the current filament is in the z direction and as a result the electric Hertz potential has only a z component. The analysis in this case is very similar to the previous cases. The only difference is that we should use the continuity of the normal component of the electric field at $z = z'$ rather than the tangential component. Also note that the field components in terms of the electric Hertz potential are given by

$$\mathbf{E} = k_0^2\frac{\partial^2}{\partial x\partial z}\Pi_z(x,z)\hat{x} + k_0^2\left[\Pi_z(x,z) + \frac{1}{k_0^2}\frac{\partial^2}{\partial x^2}\Pi_z(x,z)\right]\hat{z} \quad (5.100)$$

$$\mathbf{H} = ik_0Y_0\frac{\partial}{\partial z}\Pi_z(x,z)\hat{y}$$

Following an identical procedure as in the previous case the Hertz potential can be obtained as

$$\Pi_z^+(x,z) = \frac{-1}{4k_0Y_0}[H_0^{(1)}(k_0\sqrt{(x-x')^2+(z-z')^2}) + H_0^{(1)}(k_0\sqrt{(x-x')^2+(z+z')^2})] + \frac{1}{4\pi k_0Y_0}\int_{-\infty}^{+\infty}\frac{1}{(1+\frac{k_z}{2RY_0k_0})k_z}e^{ik_z(z+z')-ik_x(x-x')}\mathrm{d}k_x \quad (5.101)$$

$$\Pi_z^-(x,z) = -\frac{1}{4\pi k_0Y_0}\int_{-\infty}^{+\infty}\frac{1}{(1+\frac{k_z}{2RY_0k_0})k_z}e^{ik_z(-z+z')-ik_x(x-x')}\mathrm{d}k_x. \quad (5.102)$$

The integral in expressions (5.98) and (5.101) does not have a closed form and is not appropriate for numerical calculation. A better representation for this integral can be obtained by employing a transformation similar to (5.91). By defining $\beta =$

$(2RY_0k_0)$ and noting that $Re[\beta] = \frac{2\epsilon''}{\tau|\epsilon-1|^2} > 0$, we have

$$\int_{-\infty}^{+\infty} \frac{1}{(1+\frac{k_x}{2RY_0k_0})k_x} e^{ik_x(z+z')-ik_x(x-x')} \mathrm{d}k_x =$$
$$\pi \int_0^{+\infty} \beta e^{-\beta\nu} H_0^{(1)}(k_0\sqrt{(x-x')^2+(z+z'+i\nu)^2}) \mathrm{d}\nu.$$

This representation has a much better rate of convergence when compared to the original form. The rate of convergence depends upon the real part of β and the wavenumber. The asymptotic value of this representation for large values of β can be obtained by the same technique as in (5.94) and we have

$$\int_0^{+\infty} \beta e^{-\beta\nu} H_0^{(1)}(k_0\sqrt{(x-x')^2+(z+z'+i\nu)^2}) \mathrm{d}\nu =$$
$$\sum_{n=0}^{\infty} (\tfrac{-1}{\beta})^n h^{(n)}(0) \approx H_0^{(1)}(k_0\sqrt{(x-x')^2+(z+z'-i/\beta)^2})$$

Another asymptotic value of interest is the far field which can be obtained by using the large argument approximation of the Hankel functions and the expression given in (5.95). Therefore the contribution of the image in the far zone can be approximated by

$$\lim_{\rho\to\infty}[H_0^{(1)}(k_0\sqrt{(x-x')^2+(z+z')^2})$$
$$- \int_0^{+\infty} \beta e^{-\beta\nu} H_0^{(1)}(k_0\sqrt{(x-x')^2+(z+z'+i\nu)^2}) \mathrm{d}\nu] \approx \sqrt{\tfrac{2}{\pi\rho}} e^{i(k_0\rho-\frac{\pi}{4})} \tfrac{1}{1+2RY_0\sec\phi}$$

Employing the new representation in equations (5.98)-(5.99) and (5.101)-(5.102) the electric Hertz potential for x- and z-directed currents are given by

$$\Pi_x^+(x,z) = \frac{-1}{4k_0Y_0}[H_0^{(1)}(k_0\sqrt{(x-x')^2+(z-z')^2}) - H_0^{(1)}(k_0\sqrt{(x-x')^2+(z+z')^2})$$
$$+ \int_0^{+\infty} \beta e^{-\beta\nu} H_0^{(1)}(k_0\sqrt{(x-x')^2+(z+z'+i\nu)^2}) \mathrm{d}\nu], \qquad (5.103)$$
$$\Pi_x^-(x,z) = -\frac{1}{4k_0Y_0} \int_0^{+\infty} \beta e^{-\beta\nu} H_0^{(1)}(k_0\sqrt{(x-x')^2+(-z+z'+i\nu)^2} \mathrm{d}\nu, \qquad (5.104)$$

$$\Pi_z^+(x,z) = \frac{-1}{4k_0Y_0}[H_0^{(1)}(k_0\sqrt{(x-x')^2+(z-z')^2}) + H_0^{(1)}(k_0\sqrt{(x-x')^2+(z+z')^2})$$
$$- \int_0^{+\infty} \beta e^{-\beta\nu} H_0^{(1)}(k_0\sqrt{(x-x')^2+(z+z'+i\nu)^2}) \mathrm{d}\nu], \qquad (5.105)$$
$$\Pi_z^-(x,z) = -\frac{1}{4k_0Y_0} \int_0^{+\infty} \beta e^{-\beta\nu} H_0^{(1)}(k_0\sqrt{(x-x')^2+(-z+z'+i\nu)^2}) \mathrm{d}\nu. \qquad (5.106)$$

5.8 Exact Image of a Current Filament above Impedance Sheets

In Section 5.2 it was demonstrated that an impedance surface characterized by surface impedance η can be replaced by a perfect magnetic conductor plus an electric current sheet. This fictitious current is identical to the current on the equivalent resistive sheet ($R = \eta/2$). Further it was shown that the scattered field for impedance sheet is twice of the scattered field for the equivalent resistive sheet. Therefore the image of a current filament over an impedance sheet can be obtained from the expressions derived for resistive sheet by replacing R with $\eta/2$, doubling the expressions, and adding the contribution of the image of the current filament above the magnetic wall. By following the above procedure and employing equation (5.92), the electric Hertz potential for a y-directed current filament above the impedance sheet can be obtained from

$$\begin{aligned}\Pi_y(x,z) = \; & \tfrac{-1}{4k_0Y_0}[H_0^{(1)}(k_0\sqrt{(x-x')^2+(z-z')^2}) + H_0^{(1)}(k_0\sqrt{(x-x')^2+(z+z')^2}) \\ & -2\int_0^{+\infty}\alpha' e^{-\alpha'\nu}H_0^{(1)}(k_0\sqrt{(x-x')^2+(-z+z'+i\nu)^2}\mathrm{d}\nu].\end{aligned} \tag{5.107}$$

where $\alpha' = \frac{k_0}{\eta Y_0}$. By defining $\beta' = \eta Y_0 k_0$ and from equations (5.101) and (5.102) the electric Hertz potential for x- and z-directed current are respectively given by

$$\begin{aligned}\Pi_x^+(x,z) = \; & \tfrac{-1}{4k_0Y_0}[H_0^{(1)}(k_0\sqrt{(x-x')^2+(z-z')^2}) - H_0^{(1)}(k_0\sqrt{(x-x')^2+(z+z')^2}) \\ & +2\int_0^{+\infty}\beta' e^{-\beta'\nu}H_0^{(1)}(k_0\sqrt{(x-x')^2+(z+z'+i\nu)^2})\mathrm{d}\nu],\end{aligned} \tag{5.108}$$

$$\begin{aligned}\Pi_z^+(x,z) = \; & \tfrac{-1}{4k_0Y_0}[H_0^{(1)}(k_0\sqrt{(x-x')^2+(z-z')^2}) + H_0^{(1)}(k_0\sqrt{(x-x')^2+(z+z')^2}) \\ & -2\int_0^{+\infty}\beta' e^{-\beta'\nu}H_0^{(1)}(k_0\sqrt{(x-x')^2+(z+z'+i\nu)^2})\mathrm{d}\nu],\end{aligned} \tag{5.109}$$

5.9 Derivation of Integral Equations

Suppose the dielectric object above the resistive sheet is illuminated by a plane wave whose direction of propagation is denoted by angle ϕ_0 measured from normal to the resistive sheet. The incident field induces conduction and displacement currents in the dielectric object which together are known as a polarization current given by

$$\mathbf{J}_e = -ik_0 Y_0(\epsilon(x,z)-1)\mathbf{E}^t \tag{5.110}$$

where $\epsilon(x,z)$ is the relative dielectric constant of the object and $\mathbf{E}^t$ is the total electric field inside the dielectric body. If the incident, reflected, and scattered field respectively are denoted by $\mathbf{E}^i$, $\mathbf{E}^r$, and $\mathbf{E}^s$, then

$$\mathbf{E}^t = \mathbf{E}^i + \mathbf{E}^r + \mathbf{E}^s$$

Let us first consider the E polarization case where the electric field is perpendicular to the plane of incidence. The incident field is given by (5.1) and the reflected field in this polarization is found to be

$$\mathbf{E}^r = \hat{y}\frac{-1}{1+2RY_0\cos\phi_0}e^{ik_0(\sin\phi_0 x-\cos\phi_0 z)}. \tag{5.111}$$

In this case the incident field excites y-directed polarization current, which leads to a scattered field in the y direction that can be obtained using equations (5.83) and (5.92) as follows

$$E_y^s = \frac{-k_0 Z_0}{4}\iint_s J_y(x',z')G_y(x,z;x',z')\mathrm{d}x'\mathrm{d}z' \tag{5.112}$$

where

$$\begin{aligned} G_y(x,z;x',z') = \; & H_0^{(1)}(k_0\sqrt{(x-x')^2+(z-z')^2}) \\ & -\textstyle\int_0^{+\infty}\alpha e^{-\alpha\nu}H_0^{(1)}(k_0\sqrt{(x-x')^2+(z+z'+i\nu)^2})\mathrm{d}\nu. \end{aligned}$$

Now an integral equation for the polarization current can be obtained by substituting (5.1),(5.111), and (5.112) into (5.110) which yeilds

$$\begin{aligned} J_y(x,z) = \; & -ik_0 Y_0(\epsilon(x,z)-1)e^{ik_0 \sin\phi_0 x}(e^{-ik_0\cos\phi_0 z} - \tfrac{1}{1+2RY_0\cos\phi_0}e^{ik_0\cos\phi_0 z}) \\ & + \tfrac{ik_0^2}{4}(\epsilon(x,z)-1)\iint_s J_y(x',z')G_y(x,z;x',z')\mathrm{d}x'\mathrm{d}z'. \end{aligned} \tag{5.113}$$

In the H polarization case the incidence field is given by (5.8) and the reflected field in the absence of the dielectric structure above the sheet is of the form

$$\mathbf{E}^r = \frac{1}{1+2RY_0\sec\phi_0}(\cos\phi_0\hat{x} - \sin\phi_0\hat{z})e^{ik_0(\sin\phi_0 x+\cos\phi_0 z)}. \tag{5.114}$$

The induced polarization current has both x and z components which are denoted by $J_x(x,z)$ and $J_z(x,z)$ respectively. The scattered field can be evaluated using the expressions for the electric Hertz potential as given in (5.96) and (5.100) and are of the following form

$$\begin{aligned} E_x^s = \; & \tfrac{-k_0 Z_0}{4}(1+\tfrac{1}{k_0^2}\tfrac{\partial^2}{\partial x^2})\iint_s J_x(x',z')G_x(x,z;x',z')\mathrm{d}x'\mathrm{d}z' \\ & -\tfrac{Z_0}{4k_0}\tfrac{\partial^2}{\partial x\partial z}\iint_s J_z(x',z')G_z(x,z;x',z')\mathrm{d}x'\mathrm{d}z', \end{aligned} \tag{5.115}$$

$$\begin{aligned} E_z^s = \; & \tfrac{-Z_0}{4k_0}\tfrac{\partial^2}{\partial x\partial z}\iint_s J_x(x',z')G_x(x,z;x',z')\mathrm{d}x'\mathrm{d}z' \\ & -\tfrac{k_0 Z_0}{4}(1+\tfrac{1}{k_0^2}\tfrac{\partial^2}{\partial z^2})\iint_s J_z(x',z')G_z(x,z;x',z')\mathrm{d}x'\mathrm{d}z', \end{aligned} \tag{5.116}$$

where

$$\begin{aligned} G_x(x,z;x',z') = \; & H_0^{(1)}(k_0\sqrt{(x-x')^2+(z-z')^2}) - H_0^{(1)}(k_0\sqrt{(x-x')^2+(z+z')^2}) \\ & + \textstyle\int_0^{+\infty}\beta e^{-\beta\nu}H_0^{(1)}(k_0\sqrt{(x-x')^2+(z+z'+i\nu)^2})\mathrm{d}\nu, \\ G_z(x,z;x',z') = \; & H_0^{(1)}(k_0\sqrt{(x-x')^2+(z-z')^2}) + H_0^{(1)}(k_0\sqrt{(x-x')^2+(z+z')^2}) \\ & - \textstyle\int_0^{+\infty}\beta e^{-\beta\nu}H_0^{(1)}(k_0\sqrt{(x-x')^2+(z+z'+i\nu)^2})\mathrm{d}\nu. \end{aligned}$$

Upon substitution of the incident, reflected, and scattered field as given in equations (5.8), (5.114), and (5.115), (5.116) respectively into (5.110) the following coupled

integral equations for the induced current can be derived

$$\begin{aligned} J_x(x,z) = \; & -ik_0 Y_0(\epsilon(x,z)-1)\cos\phi_0 e^{ik_0\sin\phi_0 x}(-e^{-ik_0\cos\phi_0 z} + \tfrac{1}{1+2RY_0\sec\phi_0} e^{ik_0\cos\phi_0 z}) \\ & + \tfrac{i}{4}(\epsilon(x,z)-1)(k_0^2 + \tfrac{\partial^2}{\partial x^2}) \iint_s J_x(x',z') G_x(x,z;x',z')\mathrm{d}x'\mathrm{d}z' \\ & + \tfrac{i}{4}(\epsilon(x,z)-1)\tfrac{\partial^2}{\partial x \partial z} \iint_s J_z(x',z') G_z(x,z;x',z')\mathrm{d}x'\mathrm{d}z', \end{aligned} \tag{5.117}$$

$$\begin{aligned} J_z(x,z) = \; & ik_0 Y_0(\epsilon(x,z)-1)\sin\phi_0 e^{ik_0\sin\phi_0 x}(e^{-ik_0\cos\phi_0 z} + \tfrac{1}{1+2RY_0\sec\phi_0} e^{ik_0\cos\phi_0 z}) \\ & + \tfrac{i}{4}(\epsilon(x,z)-1)\tfrac{\partial^2}{\partial x \partial z} \iint_s J_x(x',z') G_x(x,z;x',z')\mathrm{d}x'\mathrm{d}z' \\ & + \tfrac{i}{4}(\epsilon(x,z)-1)(k_0^2 + \tfrac{\partial^2}{\partial z^2}) \iint_s J_z(x',z') G_z(x,z;x',z')\mathrm{d}x'\mathrm{d}z'. \end{aligned} \tag{5.118}$$

5.10 The Method of Moment Solution

There is no known exact solution for the integral equations that were developed in the previous section. In this section an approximate numerical solution of these equations is obtained by employing the moment method.

Let us divide the cross section of the dielectric structure into N sufficiently small rectangular cells such that the dielectric constant and the polarization current can be approximated by constant values over each cell.

5.10.1 E Polarization

First consider the integral equation (5.113) which correspond to the E polarization case. Using the point matching technique the integral equation can be cast into a matrix equation of the following form

$$[\mathcal{Z}][\mathcal{J}] = [\mathcal{V}] \tag{5.119}$$

where $[\mathcal{Z}]$ is the impedance matrix, $[\mathcal{J}]$ is the unknown vector whose entries are the value of polarization current at the center of each cell, i.e. (x_n, z_n), and finally $[\mathcal{V}]$ is

the excitation vector whose entries are given by

$$v_n = ik_0 Y_0(\epsilon(x_n, z_n) - 1)e^{ik_0 \sin\phi_0 x_n}(e^{-ik_0 \cos\phi_0 z_n} - \frac{1}{1 + 2RY_0 \cos\phi_0} e^{ik_0 \cos\phi_0 z_n})$$

The off-diagonal elements of the impedance matrix can be obtained by approximating the Green's function *via* its Taylor series expansion around the midpoint of each cell and then performing the integration analytically (see Appendix B). This technique allows us to choose very small cell sizes without incurring too much error because of the adjacent cells . For diagonal elements the free space Green's function is approximated by its small argument expansion and then integration is performed analytically over the cell area. This allows us to choose rectangular shape cells instead of squares that are approximated by circles of equal areas in the traditional method [Richmond 1965]. In order to give the expressions for elements of the impedance matrix, let us define the following functions

$$U(r^q_{mn}, \theta^q_{mn}) = -H_0^{(1)}(k_0 r^q_{mn}) \cos^2\theta^q_{mn} + \frac{H_1^{(1)}(k_0 r^q_{mn})}{k_0 r^q_{mn}}(\cos^2\theta^q_{mn} - \sin^2\theta^q_{mn}) \quad (5.120)$$

$$V(r^q_{mn}, \theta^q_{mn}) = -H_0^{(1)}(k_0 r^q_{mn}) \sin^2\theta^q_{mn} + \frac{H_1^{(1)}(k_0 r^q_{mn})}{k_0 r^q_{mn}}(\sin^2\theta^q_{mn} - \cos^2\theta^q_{mn}) \quad (5.121)$$

where r^q_{mn} and θ^q_{mn} are defined as

$$r^q_{mn} = \begin{cases} \sqrt{(x_m - x_n)^2 + (z_m - z_n)^2} & \text{if } q = s \\ \sqrt{(x_m - x_n)^2 + (z_m + z_n)^2} & \text{if } q = i \\ \sqrt{(x_m - x_n)^2 + (z_m + z_n + i\nu)^2} & \text{if } q = c \end{cases} \quad (5.122)$$

$$\theta^q_{mn} = \begin{cases} \arctan(\frac{z_m - z_n}{x_m - x_n}) & \text{if } q = s \\ \arctan(\frac{z_m + z_n}{x_m - x_n}) & \text{if } q = i \\ \arctan(\frac{z_m + z_n + i\nu}{x_m - x_n}) & \text{if } q = c \end{cases} \quad (5.123)$$

The diagonal entries are given by

$$\begin{aligned} z_{nn} = \; & -1 - \tfrac{1}{\pi}(\epsilon(x_n, z_n) - 1)\{\tfrac{k_0^2 \Delta x_n \Delta z_n}{2}[\ln(\tfrac{k_0}{2}\sqrt{\Delta x_n^2 + \Delta z_n^2}) + \gamma - \tfrac{i\pi}{2} - \tfrac{3}{2}] \\ & + (\tfrac{k_0 \Delta x_n}{2})^2 \arctan(\tfrac{\Delta z_n}{\Delta x_n}) + (\tfrac{k_0 \Delta z_n}{2})^2 (\tfrac{\pi}{2} - \arctan(\tfrac{\Delta z_n}{\Delta x_n}))\} \\ & - \tfrac{i k_0^2 \Delta x_n \Delta z_n}{4}(\epsilon(x_n, z_n) - 1)\alpha \int_0^\infty e^{-\alpha\nu} H_0^{(1)}(k_0 r_{mn}^c) \mathrm{d}\nu, \end{aligned} \tag{5.124}$$

and the non-diagonal entries are expressed by

$$\begin{aligned} z_{mn} = \; & \tfrac{i k_0^2 \Delta x_n \Delta z_n}{4}(\epsilon(x_m, z_m) - 1)\{H_0^{(1)}(k_0 r_{mn}^s) + \tfrac{(k_0 \Delta x_n)^2}{24} U(r_{mn}^s, \theta_{mn}^s) \\ & + \tfrac{(k_0 \Delta z_n)^2}{24} V(r_{mn}^s, \theta_{mn}^s) - \alpha \int_0^\infty e^{-\alpha\nu} H_0^{(1)}(k_0 r_{mn}^c) \mathrm{d}\nu\}, \end{aligned} \tag{5.125}$$

Here, Δx_n and Δz_n are the dimension of the n^{th} rectangular cell and $\gamma = 0.57721$ is Euler's constant.

The integrals in the (5.124) and (5.125) are evaluated numerically using the Gauss-legendre quadrature technique. It should be mentioned here that when the observation and source points are both close to the surface ($k_0(z_m + z_n) \ll 1$) for some value of $\nu = \nu_0$, the distance function $r_0 = \sqrt{(x_m - x_n)^2 + (z_m + z_n + i\nu_0)^2}$ becomes very small. Consequently the integrand of the integral representing the image contribution varies very sharply around this point. In order to evaluate the integral accurately, the contribution of the integrand around ν_0 should be evaluated analytically. The integrand achieves its maximum when the absolute value of the distance function is minimum. This minimum occurs at

$$\nu_0 = \sqrt{(x_m - x_n)^2 - (z_m + z_n)^2} \tag{5.126}$$

If the argument of the square root in (5.126) is negative, then the distance function takes its minimum at $\nu_0 = 0$. Figure 5.21 shows the integrand function in (5.125) when both observation and source points are very close to the surface. The analytical evaluation of the integral around the point ν_0 can be performed by using the small

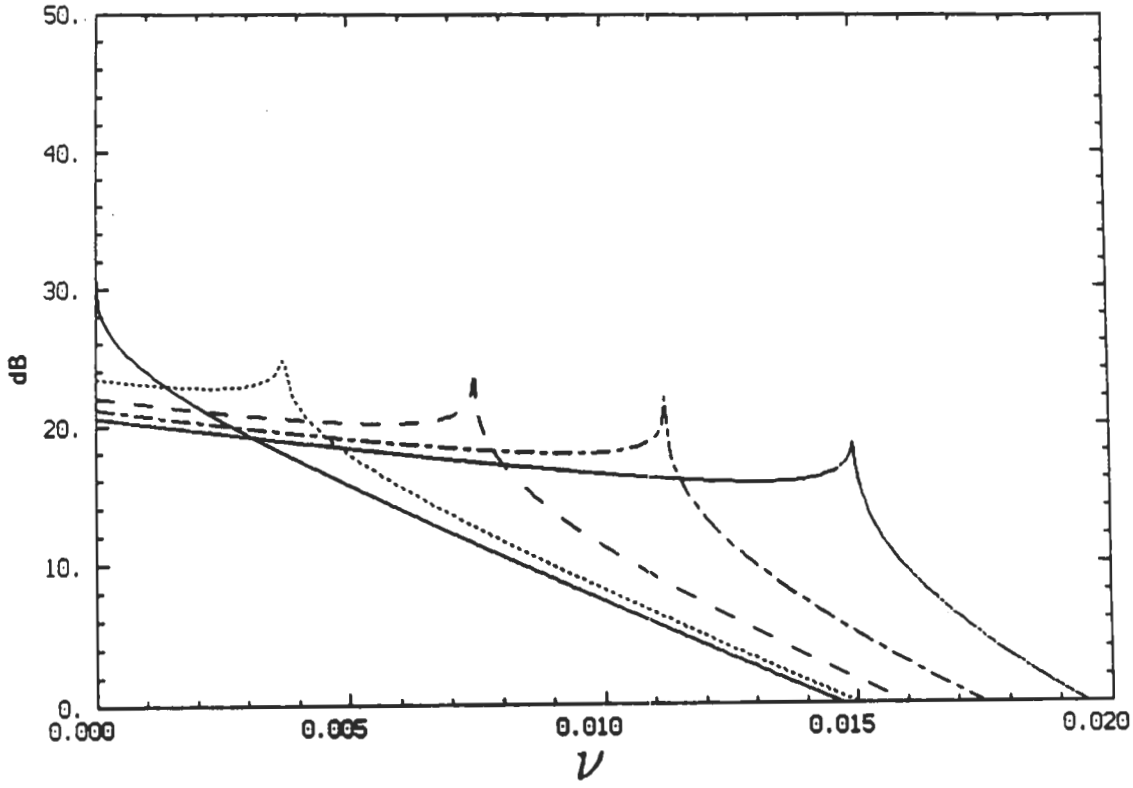

Figure 5.21: The absolute value of the integrand function in (5.125) for $\alpha = 112 - i230$ at 10 GHz, $z_m + z_n = 6 \times 10^{-5}\lambda_0$, and five values of $x_m - x_n$: (——) 0, (- - - - -) $\lambda_0/8$, (— —) $\lambda_0/4$, (— - —) $3\lambda_0/8$, (— - - - —) $\lambda_0/2$.

argument expansion of the Hankel function, i.e.

$$e^{-\alpha\nu}H_0^{(1)}(k_0r_{mn}^c) \approx e^{-\alpha\nu_0}[1+\frac{2i\gamma}{\pi}+\frac{2i}{\pi}\ln(\frac{k_0r_{mn}^c}{2})] \qquad \nu_0-\Delta\nu \le \nu \le \nu_0+\Delta\nu$$

and

$$\int_{\nu_0-\Delta\nu}^{\nu_0+\Delta\nu} e^{-\alpha\nu}H_0^{(1)}(k_0r_{mn}^c)\mathrm{d}\nu = e^{-\alpha\nu_0}[2\Delta\nu(1+\frac{i2\gamma}{\pi})+\frac{i2}{\pi}I_1]$$

where

$$\begin{aligned} I_1 = \; & \tfrac{i}{2}(z_m+z_n+i\nu_0)\ln\tfrac{r_0^2-\Delta\nu^2-i2\Delta\nu(z_m+z_n+i\nu_0)}{r_0^2-\Delta\nu^2+i2\Delta\nu(z_m+z_n+i\nu_0)}+\tfrac{x_m-x_n}{2}\ln\tfrac{r_0^2+\Delta\nu^2+2\Delta\nu(x_m-x_n)}{r_0^2+\Delta\nu^2-2\Delta\nu(x_m-x_n)} \\ & -\Delta\nu[2-\ln\tfrac{k_0^2}{4}\sqrt{(r_0^2-\Delta\nu^2)^2+4\Delta\nu^2(z_m+z_n+i\nu_0)^2}]. \end{aligned}$$

For self-image calculation we note that $x_m = x_n$ which renders $\nu_0 = 0$ and

$$\int_0^{\Delta\nu} e^{-\alpha\nu}H_0^{(1)}(k_0r_{mn}^c)\mathrm{d}\nu = [\Delta\nu(1+\frac{i2\gamma}{\pi})+\frac{2}{\pi}I_1']$$

where

$$I_1' = (z_m+z_n)\ln\frac{z_m+z_n+i\Delta\nu}{z_m+z_n}+i\Delta\nu[\ln\frac{k_0(z_m+z_n+i\Delta\nu)}{2}-1]$$

5.10.2 H Polarization

In the H polarization case, using the same partitioning of the cross section of the dielectric body the coupled integral equations (5.117) and (5.118) can be cast into the following coupled matrix equation

$$\begin{aligned} \mathcal{Z}_1\mathcal{J}_x+\mathcal{Z}_2\mathcal{J}_z &= \mathcal{V}_x \\ \mathcal{Z}_3\mathcal{J}_x+\mathcal{Z}_4\mathcal{J}_z &= \mathcal{V}_z \end{aligned} \tag{5.127}$$

where as before $\mathcal{Z}_1, \cdots, \mathcal{Z}_4$ are $N \times N$ impedance matrices and $\mathcal{V}_x$ and $\mathcal{V}_z$ are the excitation vectors. The above coupled matrix equations can be represented by a $2N \times 2N$ matrix equation similar to (5.119) with

$$[\mathcal{J}] = \begin{bmatrix} \mathcal{J}_x \\ \mathcal{J}_z \end{bmatrix}, \quad [\mathcal{Z}] = \begin{bmatrix} \mathcal{Z}_1 & \mathcal{Z}_2 \\ \mathcal{Z}_3 & \mathcal{Z}_4 \end{bmatrix}, \text{and} \quad [\mathcal{V}] = \begin{bmatrix} \mathcal{V}_x \\ \mathcal{V}_z \end{bmatrix}.$$

The elements of the excitation vector are given by $(m = 1, \cdots, N)$

$$v_m = ik_0 Y_0(\epsilon(x_m, z_m) - 1)\cos\phi_0 e^{ik_0 \sin\phi_0 x_m}(-e^{-ik_0\cos\phi_0 z_m} + \frac{1}{1+2RY_0\sec\phi_0} e^{ik_0\cos\phi_0 z_m})$$

$$v_{m+N} = -ik_0 Y_0(\epsilon(x_m, z_m) - 1)\sin\phi_0 e^{ik_0\sin\phi_0 x_m}$$
$$\cdot(e^{-ik_0\cos\phi_0 z_m} + \frac{1}{1+2RY_0\sec\phi_0} e^{ik_0\cos\phi_0 z_m})$$

Here again the entries of the impedance matrix are obtained by expansion of the Green's function over each cell as explained in the E polarization case. Because of the higher degree of singularity of the Green's function in this case using these expansions is even more important to avoid anomalous errors. The following derivative of the functions defined by (5.120) and (5.121) are needed to obtain the entries of the impedance matrix

$$\begin{aligned}\frac{\partial^2}{\partial x^2}U(r^q_{mn}, \theta^q_{mn}) = \; & k_0^2\{H_0^{(1)}(k_0 r^q_{mn})[\cos^2\theta^q_{mn}(\tfrac{3}{8}\cos^2\theta^q_{mn} + \tfrac{1}{8}\sin^2\theta^q_{mn}) \\ & + \tfrac{2\sin^2\theta^q_{mn}}{(k_0 r^q_{mn})^2}(3\cos^2\theta^q_{mn} - \sin^2\theta^q_{mn})] \\ & + H_1^{(1)}(k_0 r^q_{mn})[\tfrac{5}{k_0 r^q_{mn}}\cos^2\theta^q_{mn}\sin^2\theta^q_{mn} - \tfrac{4\sin^2\theta^q_{mn}}{(k_0 r^q_{mn})^3} \\ & \cdot(3\cos^2\theta^q_{mn} - \sin^2\theta^q_{mn})] \\ & + H_2^{(1)}(k_0 r^q_{mn})[-\tfrac{1}{2}\cos^4\theta^q_{mn} + \tfrac{\sin^2\theta^q_{mn}}{(k_0 r^q_{mn})^2}(-9\cos^2\theta^q_{mn} + \sin^2\theta^q_{mn})] \\ & + H_4^{(1)}(k_0 r^q_{mn})[\tfrac{1}{8}\cos^2\theta^q_{mn}(\cos^2\theta^q_{mn} - \sin^2\theta^q_{mn})]\}\end{aligned} \tag{5.128}$$

$$\begin{aligned}\frac{\partial^2}{\partial z^2}U(r^q_{mn}, \theta^q_{mn}) = \; & k_0^2\{H_0^{(1)}(k_0 r^q_{mn})[\sin^2\theta^q_{mn}(\tfrac{3}{8}\cos^2\theta^q_{mn} + \tfrac{1}{8}\sin^2\theta^q_{mn}) \\ & + \tfrac{2\cos^2\theta^q_{mn}}{(k_0 r^q_{mn})^2}(\cos^2\theta^q_{mn} - 3\sin^2\theta^q_{mn})] \\ & + H_1^{(1)}(k_0 r^q_{mn})[-\tfrac{4}{k_0 r^q_{mn}}\cos^2\theta^q_{mn}\sin^2\theta^q_{mn} + \tfrac{4\cos^2\theta^q_{mn}}{(k_0 r^q_{mn})^3} \\ & \cdot(3\sin^2\theta^q_{mn} - \cos^2\theta^q_{mn})] \\ & + H_2^{(1)}(k_0 r^q_{mn})[-\tfrac{1}{2}\sin^2\theta^q_{mn}\cos^2\theta^q_{mn} + \tfrac{\cos^2\theta^q_{mn}}{(k_0 r^q_{mn})^2}(9\sin^2\theta^q_{mn} - \cos^2\theta^q_{mn})] \\ & + H_4^{(1)}(k_0 r^q_{mn})[\tfrac{1}{8}\sin^2\theta^q_{mn}(\cos^2\theta^q_{mn} - \sin^2\theta^q_{mn})]\}\end{aligned} \tag{5.129}$$

$$\begin{aligned}\frac{\partial^2}{\partial x\partial z}U(r^q_{mn},\theta^q_{mn}) = \; & k_0^2\sin\theta^q_{mn}\cos\theta^q_{mn}\{H_0^{(1)}(k_0r^q_{mn})[\tfrac{3}{8}\cos^2\theta^q_{mn}+\tfrac{1}{8}\sin^2\theta^q_{mn}\\ & +\tfrac{4}{(k_0r^q_{mn})^2}(\sin^2\theta^q_{mn}-\cos^2\theta^q_{mn})]\\ & +H_1^{(1)}(k_0r^q_{mn})[\tfrac{1}{k_0r^q_{mn}}(2\sin^2\theta^q_{mn}-3\cos^2\theta^q_{mn})+\tfrac{8}{(k_0r^q_{mn})^3}\\ & \cdot(\cos^2\theta^q_{mn}-\sin^2\theta^q_{mn})]\\ & +H_2^{(1)}(k_0r^q_{mn})[-\tfrac{1}{2}\cos^2\theta^q_{mn}+\tfrac{5}{(k_0r^q_{mn})^2}(\cos^2\theta^q_{mn}-\sin^2\theta^q_{mn})]\\ & +H_4^{(1)}(k_0r^q_{mn})[\tfrac{1}{8}(\cos^2\theta^q_{mn}-\sin^2\theta^q_{mn})]\}\end{aligned} \tag{5.130}$$

$$\begin{aligned}\frac{\partial^2}{\partial x^2}V(r^q_{mn},\theta^q_{mn}) = \; & k_0^2\{H_0^{(1)}(k_0r^q_{mn})[\cos^2\theta^q_{mn}(\tfrac{3}{8}\sin^2\theta^q_{mn}+\tfrac{1}{8}\cos^2\theta^q_{mn})\\ & +\tfrac{2\sin^2\theta^q_{mn}}{(k_0r^q_{mn})^2}(\sin^2\theta^q_{mn}-3\cos^2\theta^q_{mn})]\\ & +H_1^{(1)}(k_0r^q_{mn})[\tfrac{\sin^2\theta^q_{mn}}{k_0r^q_{mn}}(-4\cos^2\theta^q_{mn}+\sin^2\theta^q_{mn})+\tfrac{4\sin^2\theta^q_{mn}}{(k_0r^q_{mn})^3}\\ & \cdot(3\cos^2\theta^q_{mn}-\sin^2\theta^q_{mn})]\\ & +H_2^{(1)}(k_0r^q_{mn})[-\tfrac{1}{2}\sin^2\theta^q_{mn}\cos^2\theta^q_{mn}+\tfrac{\sin^2\theta^q_{mn}}{(k_0r^q_{mn})^2}(9\cos^2\theta^q_{mn}-\sin^2\theta^q_{mn})]\\ & +H_4^{(1)}(k_0r^q_{mn})[\tfrac{1}{8}\cos^2\theta^q_{mn}(\sin^2\theta^q_{mn}-\cos^2\theta^q_{mn})]\}\end{aligned} \tag{5.131}$$

$$\begin{aligned}\frac{\partial^2}{\partial z^2}V(r^q_{mn},\theta^q_{mn}) = \; & k_0^2\{H_0^{(1)}(k_0r^q_{mn})[\sin^2\theta^q_{mn}(\tfrac{3}{8}\sin^2\theta^q_{mn}+\tfrac{1}{8}\cos^2\theta^q_{mn})\\ & +\tfrac{2\cos^2\theta^q_{mn}}{(k_0r^q_{mn})^2}(3\sin^2\theta^q_{mn}-\cos^2\theta^q_{mn})]\\ & +H_1^{(1)}(k_0r^q_{mn})[\tfrac{5}{k_0r^q_{mn}}\sin^2\theta^q_{mn}\cos^2\theta^q_{mn}-\tfrac{4\cos^2\theta^q_{mn}}{(k_0r^q_{mn})^3}\\ & \cdot(3\sin^2\theta^q_{mn}-\cos^2\theta^q_{mn})]\\ & +H_2^{(1)}(k_0r^q_{mn})[-\tfrac{1}{2}\sin^4\theta^q_{mn}-\tfrac{\cos^2\theta^q_{mn}}{(k_0r^q_{mn})^2}(9\sin^2\theta^q_{mn}-\cos^2\theta^q_{mn})]\\ & +H_4^{(1)}(k_0r^q_{mn})[\tfrac{1}{8}\sin^2\theta^q_{mn}(\sin^2\theta^q_{mn}-\cos^2\theta^q_{mn})]\}\end{aligned} \tag{5.132}$$

$$\begin{aligned}\frac{\partial^2}{\partial x\partial z}V(r^q_{mn},\theta^q_{mn}) = \; & k_0^2\sin\theta^q_{mn}\cos\theta^q_{mn}\{H_0^{(1)}(k_0r^q_{mn})[\tfrac{3}{8}\sin^2\theta^q_{mn}+\tfrac{1}{8}\cos^2\theta^q_{mn}\\ & +\tfrac{4}{(k_0r^q_{mn})^2}(\cos^2\theta^q_{mn}-\sin^2\theta^q_{mn})]\\ & +H_1^{(1)}(k_0r^q_{mn})[\tfrac{1}{k_0r^q_{mn}}(2\cos^2\theta^q_{mn}-3\sin^2\theta^q_{mn})+\tfrac{8}{(k_0r^q_{mn})^3}\\ & \cdot(\sin^2\theta^q_{mn}-\cos^2\theta^q_{mn})]\\ & +H_2^{(1)}(k_0r^q_{mn})[-\tfrac{1}{2}\sin^2\theta^q_{mn}+\tfrac{5}{(k_0r^q_{mn})^2}(\sin^2\theta^q_{mn}-\cos^2\theta^q_{mn})]\\ & +H_4^{(1)}(k_0r^q_{mn})[\tfrac{1}{8}(\sin^2\theta^q_{mn}-\cos^2\theta^q_{mn})]\}\end{aligned} \tag{5.133}$$

The non-diagonal elements of the impedance matrix are given by

$$\begin{aligned}z_{1mn} = \; & \tfrac{ik_0^2\Delta x_n\Delta z_n}{4}(\epsilon(x_m,z_m)-1)\{H_0^{(1)}(k_0r^s_{mn})\sin^2\theta^s_{mn}+\tfrac{H_1^{(1)}(k_0r^s_{mn})}{(k_0r^s_{mn})}(\cos^2\theta^s_{mn}\\ & -\sin^2\theta^s_{mn})+\tfrac{(\Delta x_n)^2}{24}(\tfrac{\partial^2}{\partial x^2}+k_0^2)U(r^s_{mn},\theta^s_{mn})+\tfrac{(\Delta z_n)^2}{24}(\tfrac{\partial^2}{\partial x^2}+k_0^2)V(r^s_{mn},\theta^s_{mn})\\ & -H_0^{(1)}(k_0r^i_{mn})\sin^2\theta^i_{mn}-\tfrac{H_1^{(1)}(k_0r^i_{mn})}{(k_0r^i_{mn})}(\cos^2\theta^i_{mn}-\sin^2\theta^i_{mn})\\ & -\tfrac{(\Delta x_n)^2}{24}(\tfrac{\partial^2}{\partial x^2}+k_0^2)U(r^i_{mn},\theta^i_{mn})-\tfrac{(\Delta z_n)^2}{24}(\tfrac{\partial^2}{\partial x^2}+k_0^2)V(r^i_{mn},\theta^i_{mn})\\ & +\beta\int_0^\infty e^{-\beta\nu}[H_0^{(1)}(k_0r^c_{mn})\sin^2\theta^c_{mn}+\tfrac{H_1^{(1)}(k_0r^c_{mn})}{(k_0r^c_{mn})}(\cos^2\theta^c_{mn}-\sin^2\theta^c_{mn})]\mathrm{d}\nu\},\end{aligned} \tag{5.134}$$

$$\begin{aligned}z_{2mn} = \; & \tfrac{ik_0^2\Delta x_n\Delta z_n}{4}(\epsilon(x_m,z_m)-1)\{[-H_0^{(1)}(k_0r^s_{mn})+\tfrac{2H_1^{(1)}(k_0r^s_{mn})}{(k_0r^s_{mn})}]\cos\theta^s_{mn}\sin\theta^s_{mn}\\ & +\tfrac{(\Delta x_n)^2}{24}\tfrac{\partial^2}{\partial x\partial z}U(r^s_{mn},\theta^s_{mn})+\tfrac{(\Delta z_n)^2}{24}\tfrac{\partial^2}{\partial x\partial z}V(r^s_{mn},\theta^s_{mn})\\ & +[-H_0^{(1)}(k_0r^i_{mn})+\tfrac{2H_1^{(1)}(k_0r^i_{mn})}{(k_0r^i_{mn})}]\cos\theta^i_{mn}\sin\theta^i_{mn}\\ & +\tfrac{(\Delta x_n)^2}{24}\tfrac{\partial^2}{\partial x\partial z}U(r^i_{mn},\theta^i_{mn})+\tfrac{(\Delta z_n)^2}{24}\tfrac{\partial^2}{\partial x\partial z}V(r^i_{mn},\theta^i_{mn})\\ & -\beta\int_0^\infty e^{-\beta\nu}[(-H_0^{(1)}(k_0r^c_{mn})+\tfrac{2H_1^{(1)}(k_0r^c_{mn})}{(k_0r^c_{mn})})\cos\theta^c_{mn}\sin\theta^c_{mn}]\mathrm{d}\nu\},\end{aligned} \tag{5.135}$$

$$\begin{aligned}z_{3mn} = \; & \tfrac{ik_0^2\Delta x_n\Delta z_n}{4}(\epsilon(x_m,z_m)-1)\{[-H_0^{(1)}(k_0r^s_{mn})+\tfrac{2H_1^{(1)}(k_0r^s_{mn})}{(k_0r^s_{mn})}]\cos\theta^s_{mn}\sin\theta^s_{mn}\\ & +\tfrac{(\Delta x_n)^2}{24}\tfrac{\partial^2}{\partial x\partial z}U(r^s_{mn},\theta^s_{mn})+\tfrac{(\Delta z_n)^2}{24}\tfrac{\partial^2}{\partial x\partial z}V(r^s_{mn},\theta^s_{mn})\\ & -[-H_0^{(1)}(k_0r^i_{mn})+\tfrac{2H_1^{(1)}(k_0r^i_{mn})}{(k_0r^i_{mn})}]\cos\theta^i_{mn}\sin\theta^i_{mn}\\ & -\tfrac{(\Delta x_n)^2}{24}\tfrac{\partial^2}{\partial x\partial z}U(r^i_{mn},\theta^i_{mn})-\tfrac{(\Delta z_n)^2}{24}\tfrac{\partial^2}{\partial x\partial z}V(r^i_{mn},\theta^i_{mn})\\ & +\beta\int_0^\infty e^{-\beta\nu}[(-H_0^{(1)}(k_0r^c_{mn})+\tfrac{2H_1^{(1)}(k_0r^c_{mn})}{(k_0r^c_{mn})})\cos\theta^c_{mn}\sin\theta^c_{mn}]\mathrm{d}\nu\},\end{aligned} \tag{5.136}$$

$$
\begin{aligned}
z_{4mn} = \; & \tfrac{ik_0^2\Delta x_n\Delta z_n}{4}(\epsilon(x_m,z_m)-1)\{H_0^{(1)}(k_0r_{mn}^s)\cos^2\theta_{mn}^s+\tfrac{H_1^{(1)}(k_0r_{mn}^s)}{(k_0r_{mn}^s)}(\sin^2\theta_{mn}^s \\
& -\cos^2\theta_{mn}^s)+\tfrac{(\Delta x_n)^2}{24}(\tfrac{\partial^2}{\partial z^2}+k_0^2)U(r_{mn}^s,\theta_{mn}^s)+\tfrac{(\Delta z_n)^2}{24}(\tfrac{\partial^2}{\partial z^2}+k_0^2)V(r_{mn}^s,\theta_{mn}^s) \\
& +H_0^{(1)}(k_0r_{mn}^i)\cos^2\theta_{mn}^i+\tfrac{H_1^{(1)}(k_0r_{mn}^i)}{(k_0r_{mn}^i)}(\sin^2\theta_{mn}^i-\cos^2\theta_{mn}^i) \\
& +\tfrac{(\Delta x_n)^2}{24}(\tfrac{\partial^2}{\partial z^2}+k_0^2)U(r_{mn}^i,\theta_{mn}^i)+\tfrac{(\Delta z_n)^2}{24}(\tfrac{\partial^2}{\partial z^2}+k_0^2)V(r_{mn}^i,\theta_{mn}^i) \\
& -\beta\int_0^\infty e^{-\beta\nu}[H_0^{(1)}(k_0r_{mn}^c)\cos^2\theta_{mn}^c+\tfrac{H_1^{(1)}(k_0r_{mn}^c)}{(k_0r_{mn}^c)}(\sin^2\theta_{mn}^c-\cos^2\theta_{mn}^c)]\mathrm{d}\nu\}.
\end{aligned}
\tag{5.137}
$$

Noting that $\cos\theta_{nn}^i=\cos\theta_{nn}^c=0$ and $\sin\theta_{nn}^i=\sin\theta_{nn}^c=1$, the diagonal elements are of the following form

$$
\begin{aligned}
z_{1nn} = \; & -1-\tfrac{1}{\pi}(\epsilon(x_n,z_n)-1)\{\tfrac{k_0^2\Delta x_n\Delta z_n}{4}[\ln(\tfrac{k_0}{4}\sqrt{\Delta x_n^2+\Delta z_n^2})+\gamma-\tfrac{i\pi}{2}-\tfrac{3}{2}] \\
& +2\arctan(\tfrac{\Delta z_n}{\Delta x_n})+(\tfrac{k_0\Delta z_n}{2})^2(\tfrac{\pi}{2}-\arctan(\tfrac{\Delta z_n}{\Delta x_n}))\} \\
& \tfrac{ik_0^2\Delta x_n\Delta z_n}{4}(\epsilon(x_m,z_m)-1)\{-H_0^{(1)}(k_0r_{nn}^i)+\tfrac{H_1^{(1)}(k_0r_{nn}^i)}{(k_0r_{nn}^i)} \\
& -\tfrac{(\Delta x_n)^2}{24}(\tfrac{\partial^2}{\partial x^2}+k_0^2)U(r_{nn}^i,\theta_{nn}^i)-\tfrac{(\Delta z_n)^2}{24}(\tfrac{\partial^2}{\partial x^2}+k_0^2)V(r_{nn}^i,\theta_{nn}^i) \\
& +\beta\int_0^\infty e^{-\beta\nu}[H_0^{(1)}(k_0r_{nn}^c)-\tfrac{H_1^{(1)}(k_0r_{nn}^c)}{(k_0r_{nn}^c)}]\mathrm{d}\nu\},
\end{aligned}
\tag{5.138}
$$

$$
z_{2nn} = \; z_{3nn}=0 \tag{5.139}
$$

$$
\begin{aligned}
z_{4nn} = \; & -1-\tfrac{1}{\pi}(\epsilon(x_n,z_n)-1)\{\tfrac{k_0^2\Delta x_n\Delta z_n}{4}[\ln(\tfrac{k_0}{4}\sqrt{\Delta x_n^2+\Delta z_n^2})+\gamma-\tfrac{i\pi}{2}-\tfrac{3}{2}] \\
& +2(\tfrac{\pi}{2}-\arctan(\tfrac{\Delta z_n}{\Delta x_n}))+(\tfrac{k_0\Delta x_n}{2})^2\arctan(\tfrac{\Delta z_n}{\Delta x_n}))\} \\
& \tfrac{ik_0^2\Delta x_n\Delta z_n}{4}(\epsilon(x_m,z_m)-1)\{\tfrac{H_1^{(1)}(k_0r_{nn}^i)}{(k_0r_{nn}^i)} \\
& +\tfrac{(\Delta x_n)^2}{24}(\tfrac{\partial^2}{\partial z^2}+k_0^2)U(r_{nn}^i,\theta_{nn}^i)+\tfrac{(\Delta z_n)^2}{24}(\tfrac{\partial^2}{\partial z^2}+k_0^2)V(r_{nn}^i,\theta_{nn}^i) \\
& -\beta\int_0^\infty e^{-\beta\nu}\tfrac{H_1^{(1)}(k_0r_{nn}^c)}{(k_0r_{nn}^c)}\mathrm{d}\nu\}.
\end{aligned}
\tag{5.140}
$$

The distance function in the integrand of all the integrals in (5.134)-(5.137) assumes a very small number when the observation and source points are both close to the surface of the resistive sheet. Since the singularity of the integrands in this case are much higher than the E polarization case, analytical evaluation of the integrals

around the point ν_0 is even more important. For example the integrand in equation (5.134) can be approximated by

$$e^{-\beta\nu}[H_0^{(1)}(k_0r_{mn}^c)\sin^2\theta_{mn}^c + \frac{H_1^{(1)}(k_0r_{mn}^c)}{(k_0r_{mn}^c)}(\cos^2\theta_{mn}^c - \sin^2\theta_{mn}^c)] \approx e^{-\beta\nu_0}\{H_0^{(1)}(k_0r_0)$$
$$\cdot\frac{(z_m+z_n+i\nu_0)^2}{(r_{mn}^c)^2} - [\frac{i2}{\pi}\frac{1}{(k_0r_{mn}^c)^2} + (\frac{i}{2\pi} - \frac{i\gamma}{\pi} - \frac{1}{2}) - \frac{i}{\pi}\ln\frac{k_0r_0}{2}]\frac{(x_m-x_n)^2-(z_m+z_n+i\nu_0)^2}{(r_{mn}^c)^2}\}$$

where the small argument expansion of $H_1^{(1)}(k_0r_{mn}^c)$ is used and ν is set to ν_0 everywhere except in the denominators. Figure 5.22 shows the variation of the integrand as a function of ν for some typical values of source and observation points, and Fig. 5.23 compares the integrand with its approximation. It should be noted here that the phase of integrand varies very rapidly around ν_0 resulting in a faster variation of the integrand than what is shown in Fig. 5.22. If the integrand in (5.134) around the $\Delta\nu$ neighborhood of ν_0 is denoted by S_1 then

$$\begin{aligned} S_1 = \; & e^{-\beta\nu_0}\{H_0^{(1)}(k_0r_0)(z_m+z_n+i\nu_0)^2 - [(\frac{i}{2\pi} - \frac{i\gamma}{\pi} - \frac{1}{2}) - \frac{i}{\pi}\ln\frac{k_0r_0}{2}] \\ & \cdot[(x_m-x_n)^2 - (z_m+z_n+i\nu_0)^2]\}I_2 \\ & -e^{-\beta\nu_0}\frac{2i}{\pi k_0^2}[(x_m-x_n)^2 - (z_m+z_n+i\nu_0)^2]I_3 \end{aligned}$$

where

$$I_2 = \frac{1}{2(x_m-x_n)}\ln\frac{r_0^2+\Delta\nu^2+2(x_m-x_n)\Delta\nu}{r_0^2+\Delta\nu^2-2(x_m-x_n)\Delta\nu},$$
$$I_3 = \frac{\Delta\nu}{(x_m-x_n)^2}\frac{r_0^2-\Delta\nu^2-2(z_m+z_n+i\nu_0)^2}{(r_0^2-\Delta\nu^2)^2+4\Delta\nu^2(z_m+z_n+i\Delta\nu_0)^2} + \frac{1}{4(x_m-x_n)^3}\ln\frac{r_0^2+\Delta\nu^2+2(x_m-x_n)\Delta\nu}{r_0^2+\Delta\nu^2-2(x_m-x_n)\Delta\nu}.$$

In evaluation of the diagonal elements, we set $x_m = x_n$, which leads to $\nu_0 = 0$ and the integral in (5.138) is approximated by

$$\text{Integrand} \approx (\frac{i}{2\pi} - \frac{i\gamma}{\pi} - \frac{1}{2}) + \frac{i}{\pi}\ln\frac{k_0(z_m+z_n+i\nu)}{2} + \frac{i2}{\pi}\frac{1}{k_0^2(z_m+z_n+i\nu)^2}$$

If S_1' is the integral between 0 and $\Delta\nu$, then

$$S_1' = \frac{i2}{\pi k_0^2}I_3' + \frac{i}{\pi}I_2' + (\frac{i}{2\pi} - \frac{i\gamma}{\pi} - \frac{1}{2})\Delta\nu,$$

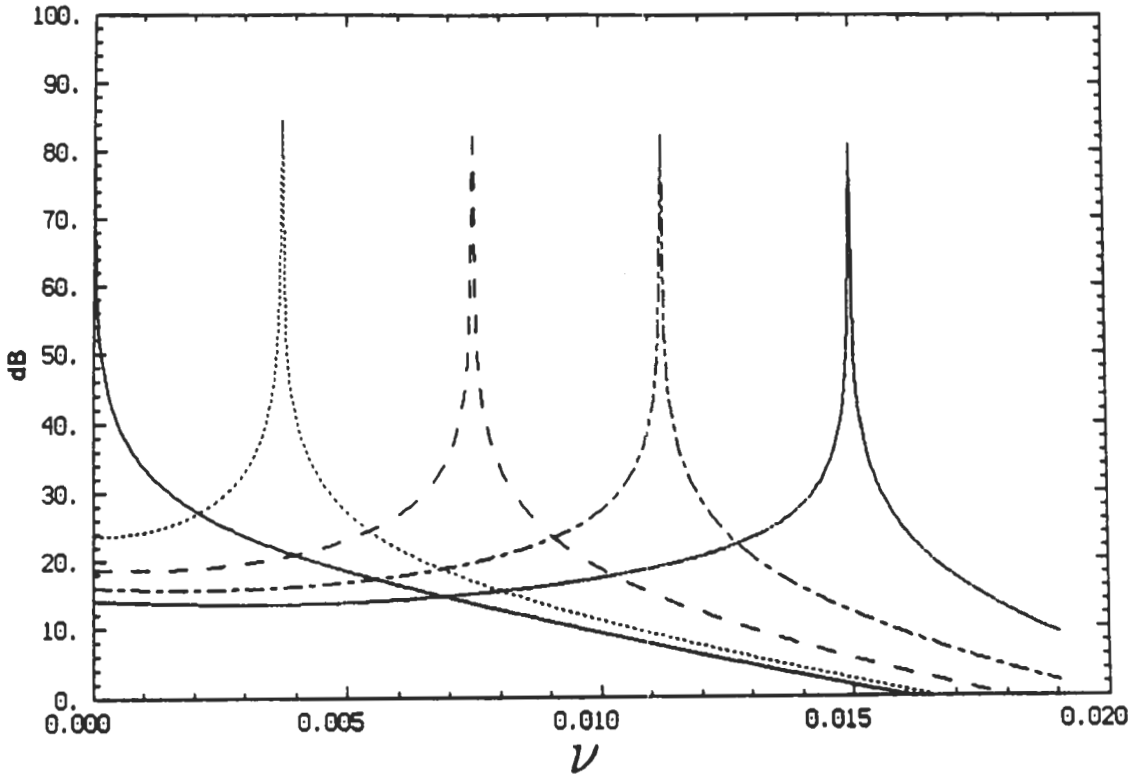

Figure 5.22: The absolute value of the integrand function in (5.134) for $\beta = 75+i154$ at 10 GHz, $z_m + z_n = 6 \times 10^{-5}\lambda_0$, and five values of $x_m - x_n$: (——) 0, (- - - - -) $\lambda_0/8$, (— —) $\lambda_0/4$, (— —) $3\lambda_0/8$, (— - - - —) $\lambda_0/2$.

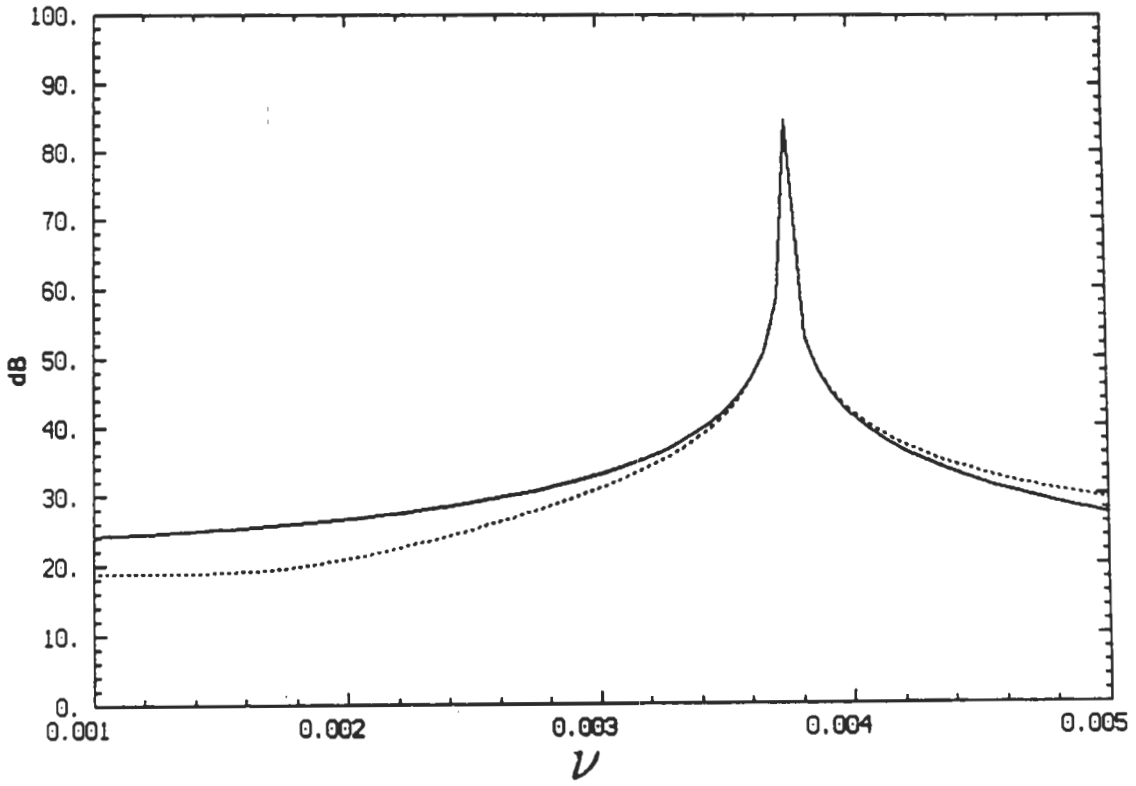

Figure 5.23: The absolute value of the integrand function in (5.134) and its approximation for $\beta = 75 + i154$ at 10 GHz, $z_m + z_n = 6 \times 10^{-5}\lambda_0$, and $x_m - x_n = \lambda_0/8$: (——) integrand, (- - - - -) approximation of integrand.

where

$$I_2' = -i[(z_m + z_n)\ln\tfrac{z_m+z_n+i\Delta\nu}{z_m+z_n} + i\Delta\nu\ln\tfrac{k_0(z_m+z_n+i\Delta\nu)}{2} - i\Delta\nu]$$

$$I_3' = \tfrac{\Delta\nu}{(z_m+z_n)(z_m+z_n+i\Delta\nu)}$$

To extract the contribution of the integrand in (5.135) around ν_0 we use similar approximations as in (5.134). If this integral is denoted by S_2, then

$$S_2 = e^{-\beta\nu_0}(x_m - x_n)(z_m + z_n + i\nu_0)\{[H_0^{(1)}(k_0r_0) + (\tfrac{i}{\pi} - \tfrac{i2\gamma}{\pi} - 1) - \tfrac{i2}{\pi}\ln\tfrac{k_0r_0}{2}]I_2\tfrac{4i}{\pi k_0^2}I_3\}.$$

The integral in (5.136) around the point ν_0 is approximated by S_3 where

$$S_3 = S_2$$

and similarly for the integral in (5.137) if S_4 represents the integral around ν_0 then

$$S_4 = e^{-\beta\nu_0}\{H_0^{(1)}(k_0r_0)(x_m - x_n)^2 + [(\tfrac{i}{2\pi} - \tfrac{i\gamma}{\pi} - \tfrac{1}{2}) - \tfrac{i}{\pi}\ln\tfrac{k_0r_0}{2}] \cdot[(x_m - x_n)^2 - (z_m + z_n + i\nu_0)^2]\}I_2 - e^{-\beta\nu_0}\tfrac{2i}{\pi k_0^2}[(x_m - x_n)^2 - (z_m + z_n + i\nu_0)^2]I_3$$

When $x_m = x_n$ then $\nu_0 = 0$ and this integral is represented by

$$S_4' = \frac{i2}{\pi k_0^2}I_3' - \frac{i}{\pi}I_2' + (\frac{i}{2\pi} - \frac{i\gamma}{\pi} - \frac{1}{2})\Delta\nu,$$

5.10.3 Far Field Evaluation

Once the system of linear equation (5.119) for the polarization current has been solved the scattered field due to the dielectric structure at any point in the upper half-space can be obtained by means of (5.112) and (5.115) and (5.116) for E and H polarization respectively. Here again it is convenient to approximate the integral representing the scattered field by a summation of integrals over each cell. For E

polarization we get

$$E_y^s(x,z) = \frac{-k_0 Z_0}{4} \sum_{n=1}^{N} J_y(x_n, z_n)\Delta x_n \Delta z_n \{H_0^{(1)}(k_0 r_n^s) + \frac{(k_0\Delta x_n)^2}{24} U(r_n^s, \theta_n^s) + \frac{(k_0\Delta z_n)^2}{24} V(r_n^s, \theta_n^s) - \alpha \int_0^\infty e^{-\alpha\nu} H_0^{(1)}(k_0 r_n^c)\mathrm{d}\nu\}, \tag{5.141}$$

where r_n^q and θ_n^q ($q = s$ or c) are similar to those defined in equations (5.122) and (5.123) with x_m and z_m replaced with x and z respectively. The far zone radiation pattern may be obtained by employing expression (5.141) and the large argument expansion of the Hankel function (keeping the terms up to the order $\rho^{\frac{1}{2}}$). If the angle between the direction of observation and normal to the sheet is denoted by ϕ_s as shown in Fig. 5.20, then

$$r_n^s \approx \rho - x_n \sin\phi_s - z_n \cos\phi_s$$

Finally employing the definition of far field amplitude as given by (5.72) in the upper half-space ($|\ \phi_s\ | < \frac{\pi}{2}$) we have

$$\mathbf{P}_e^+(\phi_0, \phi_s) = \hat{y}\frac{-k_0 Z_0}{4} \sum_{n=1}^{N} J_y(x_n, z_n)\Delta x_n \Delta z_n \{[1 - \frac{(k_0\Delta x_n)^2}{24}\sin^2\phi_s - \frac{(k_0\Delta z_n)^2}{24}\cos^2\phi_s] \cdot e^{-ik_0 \sin\phi_s x_n}(e^{-ik_0\cos\phi_s z_n} - \frac{1}{1+2RY_0\cos\phi_s} e^{ik_0\cos\phi_s z_n})\}. \tag{5.142}$$

The far field amplitude in the lower half-space also can be found if we use the Green's function for the lower half-space as given by equation (5.93). Again employing the distant approximations, the far field amplitude in the lower half-space ($|\ \phi_s\ | > \frac{\pi}{2}$) can be obtained from

$$\mathbf{P}_e^-(\phi_0, \phi_s) = \hat{y}\frac{-k_0 Z_0}{4} \sum_{n=1}^{N} J_y(x_n, z_n)\Delta x_n \Delta z_n [1 - \frac{(k_0\Delta x_n)^2}{24}\sin^2\phi_s - \frac{(k_0\Delta z_n)^2}{24}\cos^2\phi_s] \cdot e^{-ik_0(\sin\phi_s x_n + \cos\phi_s z_n)} \cdot \frac{-2RY_0\cos\phi_s}{1-2RY_0\cos\phi_s}. \tag{5.143}$$

The scattered field in the H polarization case can be obtained from equations (5.115) and (5.116) which can basically be expressed in a form similar to (5.141). In

far zone such expression can be simplified by noting that

$$\begin{aligned}
\frac{1}{k_0^2}\frac{\partial^2}{\partial x^2}H_0^{(1)}(r_n^q,\theta_n^q) &\approx -H_0^{(1)}(r_n^q,\theta_n^q)\cos^2\theta_n^q \\
\frac{1}{k_0^2}\frac{\partial^2}{\partial z^2}H_0^{(1)}(r_n^q,\theta_n^q) &\approx -H_0^{(1)}(r_n^q,\theta_n^q)\sin^2\theta_n^q \\
\frac{1}{k_0^2}\frac{\partial^2}{\partial x\partial z}H_0^{(1)}(r_n^q,\theta_n^q) &\approx -H_0^{(1)}(r_n^q,\theta_n^q)\cos\theta_n^q\sin\theta_n^q
\end{aligned}$$

and further as distance from origin to the observation point (ρ) approaches to infinity then $\theta_n^q \rightarrow \pi/2-\phi_s$. Under the mentioned conditions we notice that the scattered field in the polar coordinate system has only a $\hat{\phi}$ component. Using the large argument expansion of the Hankel functions and contribution of the image in the far zone, the far field amplitude in the upper half-space is of the following form

$$\begin{aligned}
\mathbf{P}_h^+(\phi_0,\phi_s) = \; & \hat{\phi}\tfrac{k_0 Z_0}{4}\textstyle\sum_{n=1}^{N}\Delta x_n\Delta z_n[1-\frac{(k_0\Delta x_n)^2}{24}\sin^2\phi_s-\frac{(k_0\Delta z_n)^2}{24}\cos^2\phi_s] \\
& \cdot e^{-ik_0\sin\phi_s x_n}\{J_z(x_n,z_n)\sin\phi_s(e^{-ik_0\cos\phi_s z_n}+\tfrac{e^{ik_0\cos\phi_s z_n}}{1+2RY_0\sec\phi_s}) \\
& -J_x(x_n,z_n)\cos\phi_s(e^{-ik_0\cos\phi_s z_n}-\tfrac{e^{ik_0\cos\phi_s z_n}}{1+2RY_0\sec\phi_s})\},
\end{aligned} \tag{5.144}$$

and in the lower half-space ($|\,\phi_s\,| > \frac{\pi}{2}$) we get

$$\begin{aligned}
\mathbf{P}_h^-(\phi_0,\phi_s) = \; & \hat{\phi}\tfrac{k_0 Z_0}{4}\textstyle\sum_{n=1}^{N}\Delta x_n\Delta z_n[1-\frac{(k_0\Delta x_n)^2}{24}\sin^2\phi_s-\frac{(k_0\Delta z_n)^2}{24}\cos^2\phi_s] \\
& \cdot e^{-ik_0(\sin\phi_s x_n+\cos\phi_s z_n)}\cdot[J_z(x_n,z_n)\sin\phi_s-J_x(x_n,z_n)\cos\phi_s] \\
& \cdot(\tfrac{-2RY_0\sec\phi_s}{1-2RY_0\sec\phi_s}).
\end{aligned} \tag{5.145}$$

5.11 Numerical Results

In this section the results of the perturbation solution for variable thickness dielectric slabs are compared with the numerical solution based on the exact image theory for a resistive sheet in conjunction with the moment method. In the numerical solution the hump of the slab is considered as the dielectric object and the constant-thickness portion of the slab is modelled by a resistive sheet (see Fig. 5.16). In all of the test cases the dielectric slab is assumed to be homogeneous with

$\epsilon = 36 + i17$, $\tau_0 = \lambda_0/100$, $\Delta = 0.3$, and $\lambda_0 = 3$ cm. These parameters correspond to $R_0 = 180 + i270$, $\alpha = 112 - i230$ and $\beta = 75 + i154$. Figures 5.24-5.31 show the bistatic echo width and the phase of the far field amplitude of a dielectric hump over the resistive sheet for $w = \lambda_0/15$ and $w = \lambda_0/25$ at incidence angle $\phi_0 = 0$ and $\phi_0 = 45$ for both polarizations. In each figure the results based on the perturbation technique are compared with the numerical results. The agreement is very good in spite of the fact that the perturbation solution is only a first order one. For larger dielectric structures the perturbation technique cannot be used and the moment method is the only available method of solution. For example, the central vein of a vegetation leaf can be modelled as a square dielectric cylinder above a resistive sheet. Figure 5.32 shows the bistatic echo width of a square cylinder with dimensions $\lambda_0/10 \times \lambda_0/10$ in free space, above a perfect conductor and above a resistive sheet, at normal incidence with $f = 10$ GHz, $\epsilon = 36 + i17$, and $R_0 = 180 + i270$ for E polarization. Similar plots for H polarization are presented in Fig. 5.33. Figure 5.34 show the backscattered echo width of the same structure with the same parameters for E and H polarizations. It can be deduced that the dielectric hump has a broad radiation pattern and if the resistive sheet were finite this would be the main contributor to the scattered field away from the specular direction.

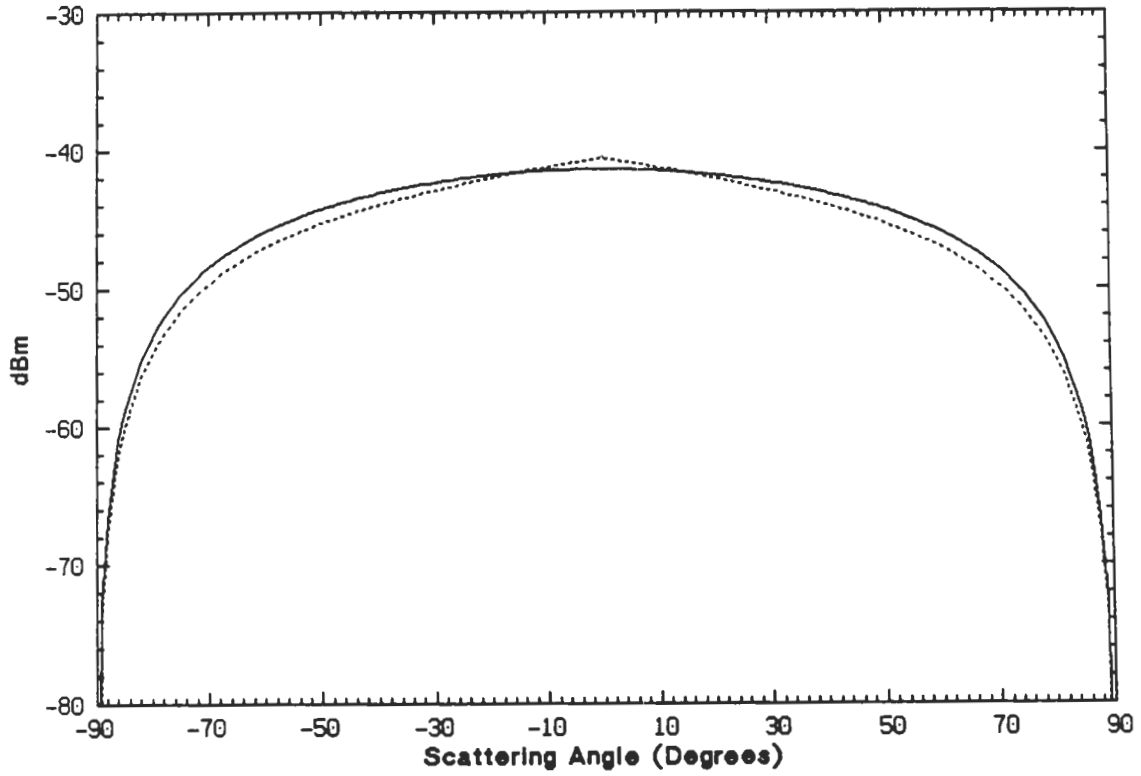

Figure 5.24: Bistatic echo width of a dielectric hump with $\epsilon = 36 + i17$, $\Delta = 0.3$, and $w = \lambda_0/15$ over a resistive sheet with $R_0 = 180 + i270$ ($\alpha = 112 - i230$) at $f = 10$ GHz and $\phi_0 = 0$ degrees for E polarization: (——) numerical technique, (- - - - -) perturbation technique.

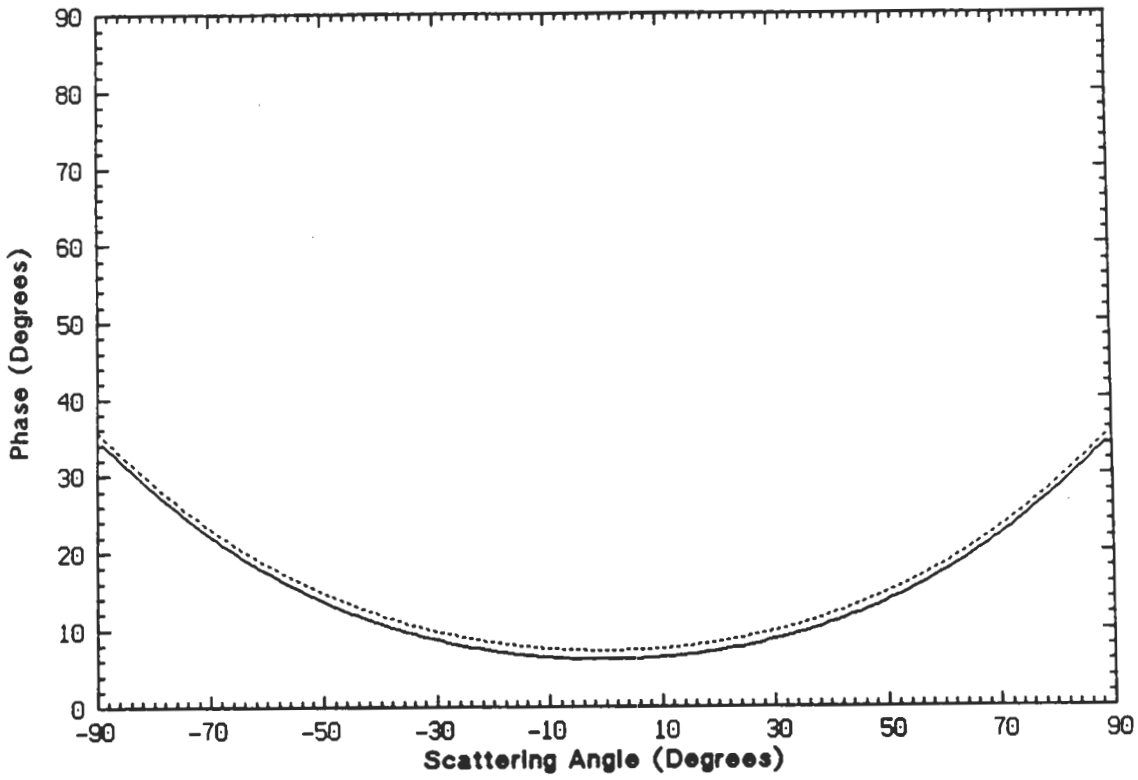

Figure 5.25: Phase of the far field amplitude of a dielectric hump with $\epsilon = 36 + i17$, $\Delta = 0.3$, and $w = \lambda_0/15$ over a resistive sheet with $R_0 = 180 + i270$ ($\alpha = 112 - i230$) at $f = 10$ GHz and $\phi_0 = 0$ degrees for E polarization: (——) numerical technique, (- - - - -) perturbation technique.

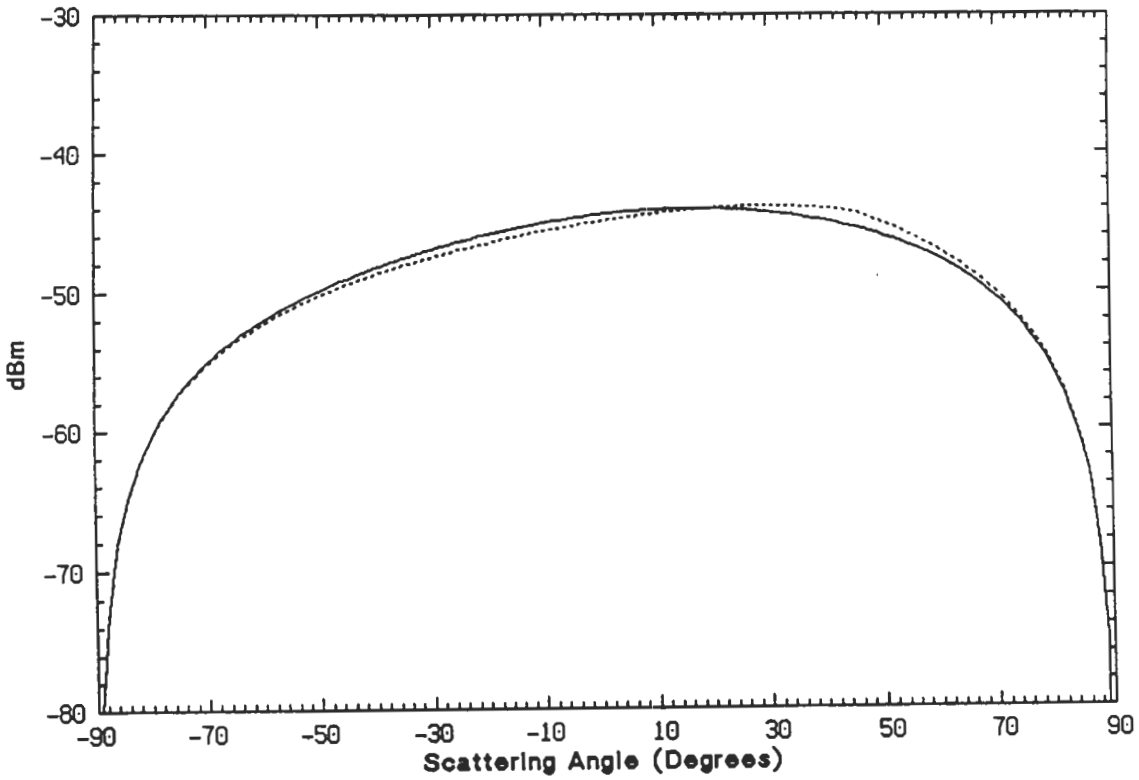

Figure 5.26: Bistatic echo width of a dielectric hump with $\epsilon = 36 + i17$, $\Delta = 0.3$, and $w = \lambda_0/15$ over a resistive sheet with $R_0 = 180 + i270$ ($\alpha = 112 - i230$) at $f = 10$ GHz and $\phi_0 = 45$ degrees for E polarization: (——) numerical technique, (- - - - -) perturbation technique.

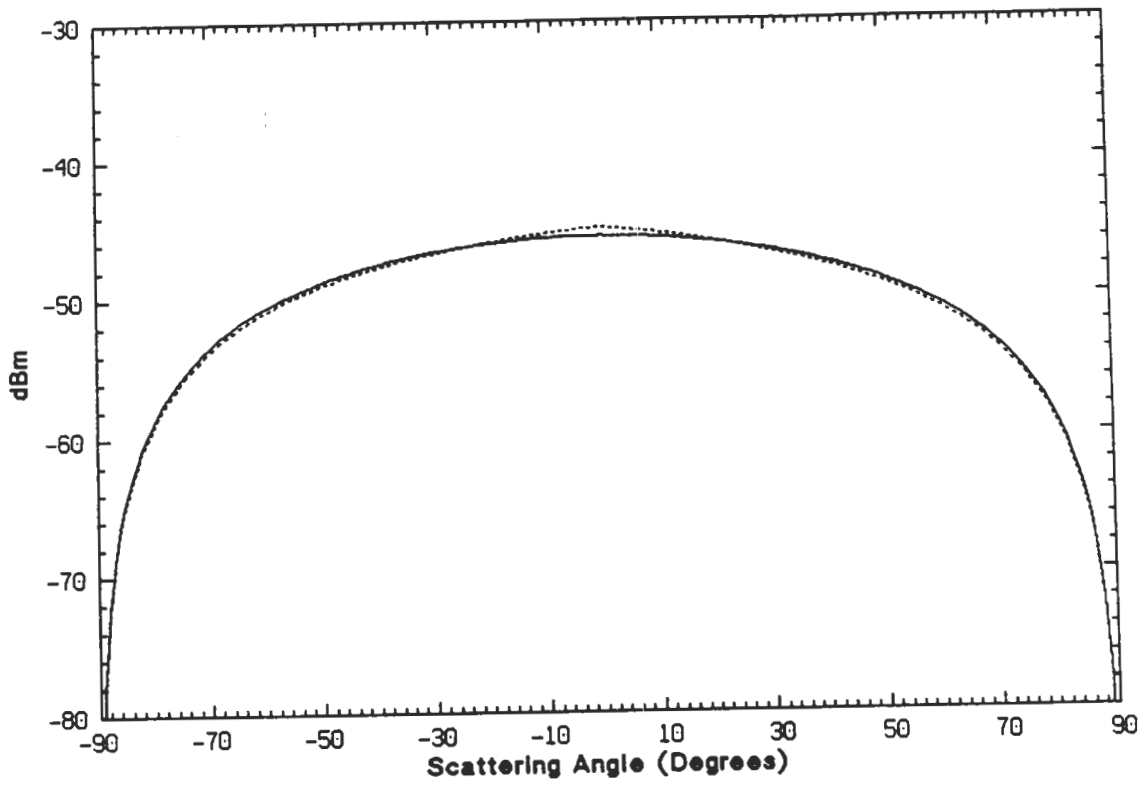

Figure 5.27: Bistatic echo width of a dielectric hump with $\epsilon = 36 + i17$, $\Delta = 0.3$, and $w = \lambda_0/25$ over a resistive sheet with $R_0 = 180 + i270$ ($\alpha = 112 - i230$) at $f = 10$ GHz and $\phi_0 = 0$ degrees for E polarization: (——) numerical technique, (- - - - -) perturbation technique.

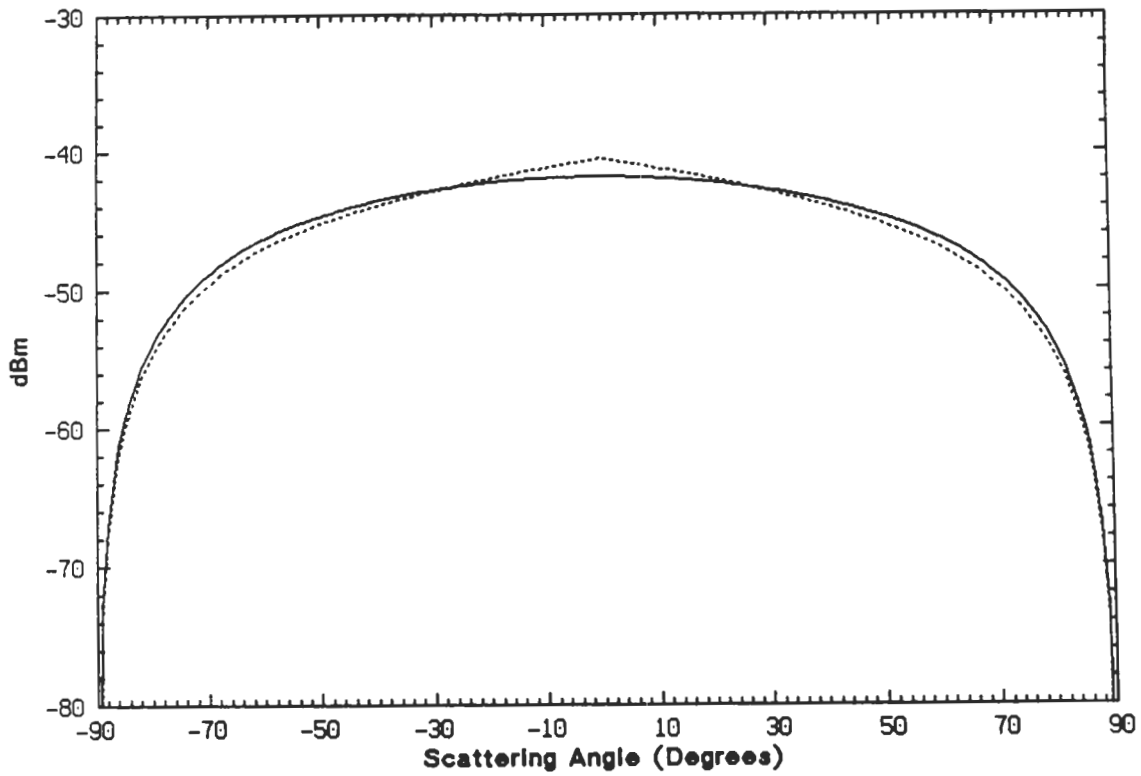

Figure 5.28: Bistatic echo width of a dielectric hump with $\epsilon = 36 + i17$, $\Delta = 0.3$, and $w = \lambda_0/15$ over a resistive sheet with $R_0 = 180 + i270$ ($\beta = 75 + i154$) at $f = 10$ GHz and $\phi_0 = 0$ degrees for H polarization: (——) numerical technique, (- - - - -) perturbation technique.

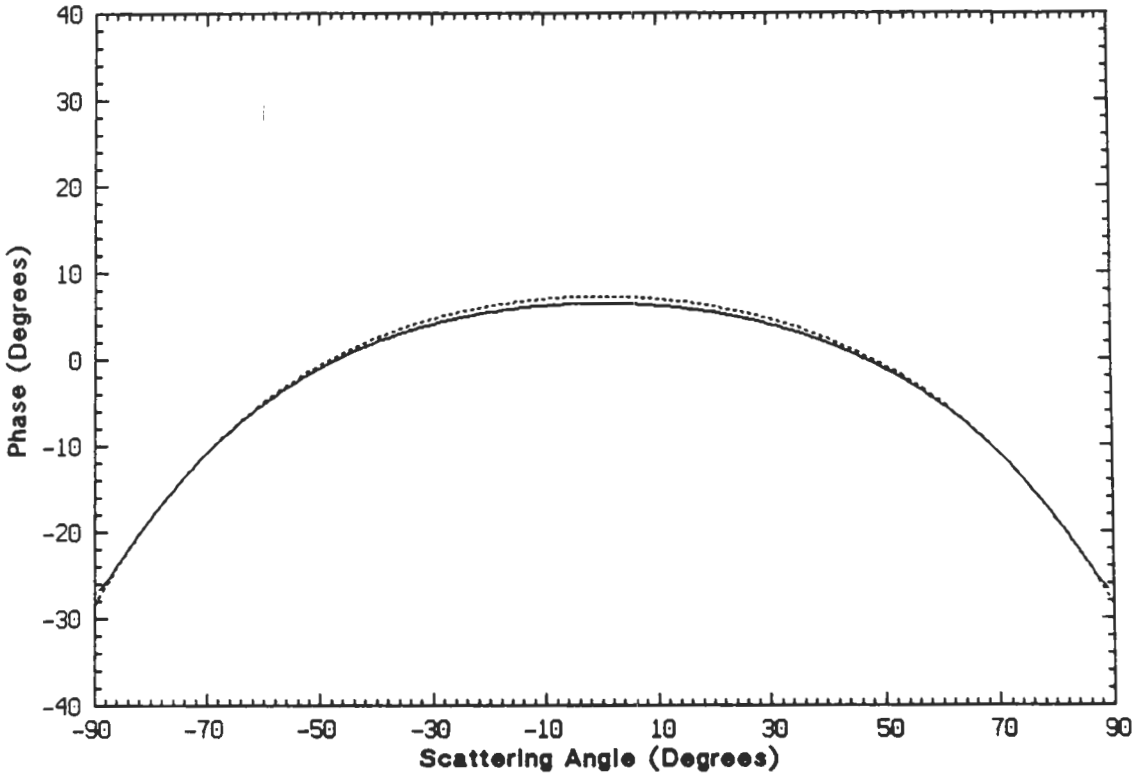

Figure 5.29: Phase of the far field amplitude of a dielectric hump with $\epsilon = 36 + i17$, $\Delta = 0.3$, and $w = \lambda_0/15$ over a resistive sheet with $R_0 = 180 + i270$ ($\beta = 75 + i154$) at $f = 10$ GHz and $\phi_0 = 0$ degrees for H polarization: (——) numerical technique, (- - - - -) perturbation technique.

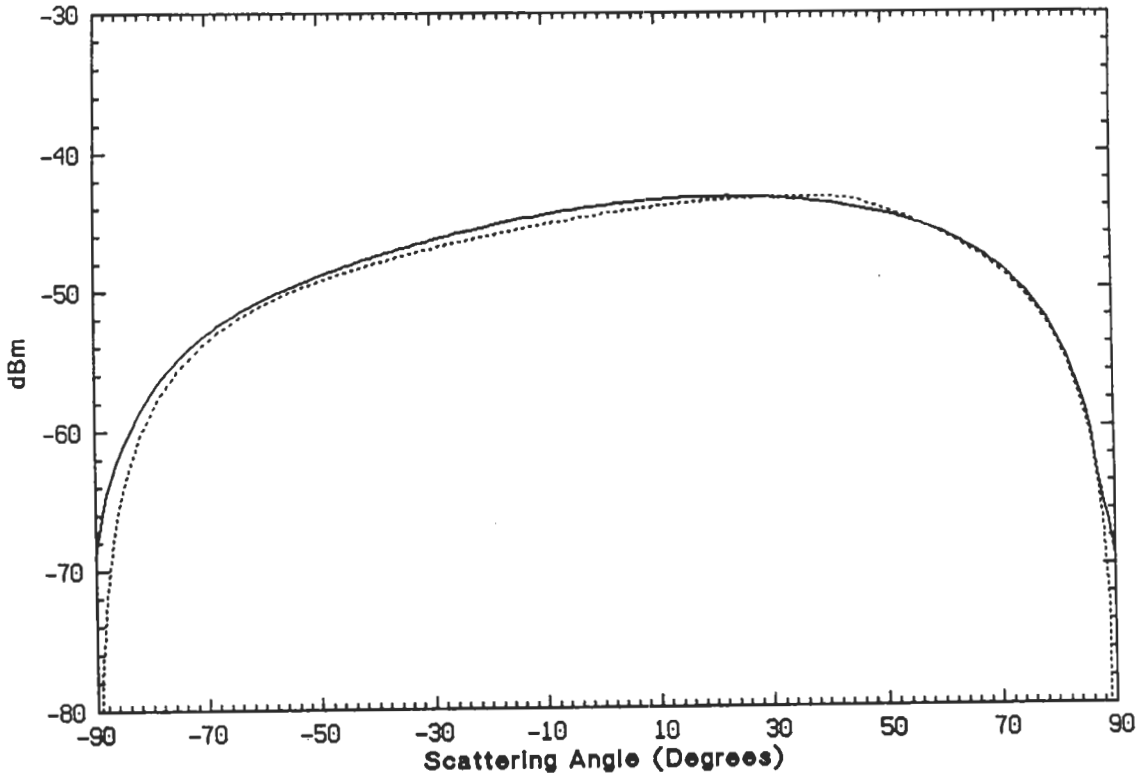

Figure 5.30: Bistatic echo width of a dielectric hump with $\epsilon = 36+i17$, $\Delta = 0.3$, and $w = \lambda_0/15$ over a resistive sheet with $R_0 = 180+i270$ ($\beta = 75+i154$) at $f = 10$ GHz and $\phi_0 = 45$ degrees for H polarization: (——) numerical technique, (- - - - -) perturbation technique.

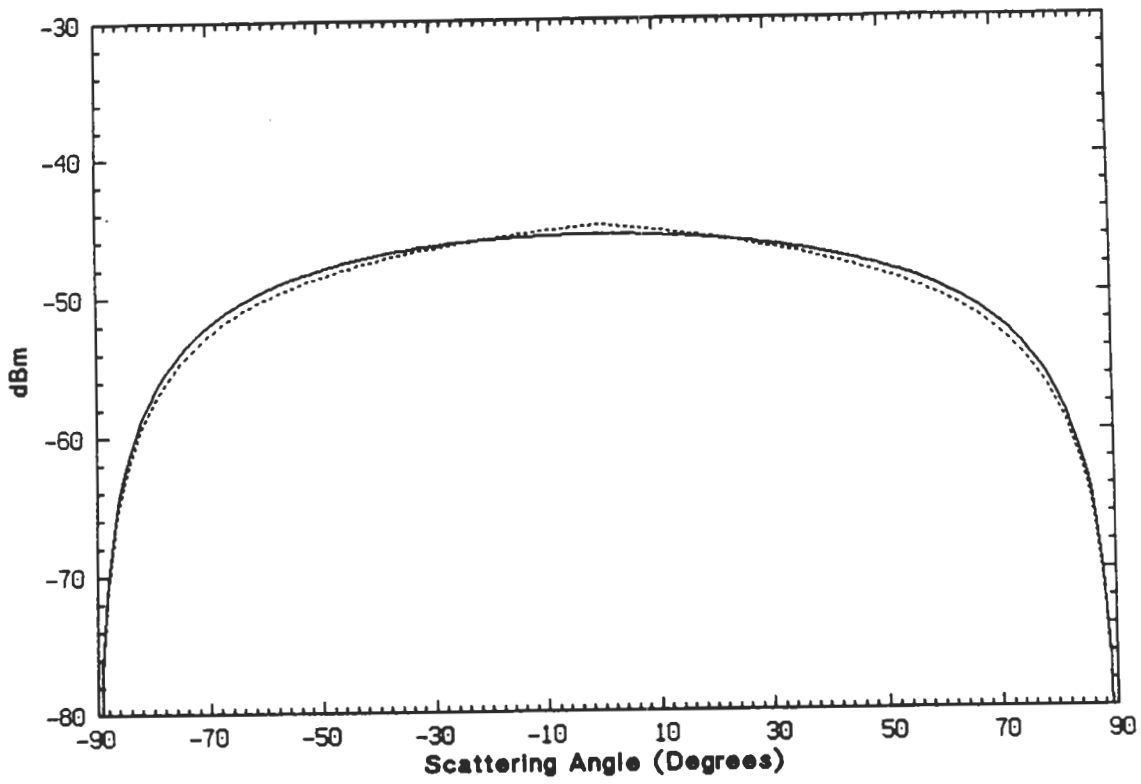

Figure 5.31: Bistatic echo width of a dielectric hump with $\epsilon = 36 + i17$, $\Delta = 0.3$, and $w = \lambda_0/25$ over a resistive sheet with $R_0 = 180 + i270$ ($\beta = 75 + i154$) at $f = 10$ GHz and $\phi_0 = 0$ degrees for H polarization: (——) numerical technique, (- - - - -) perturbation technique.

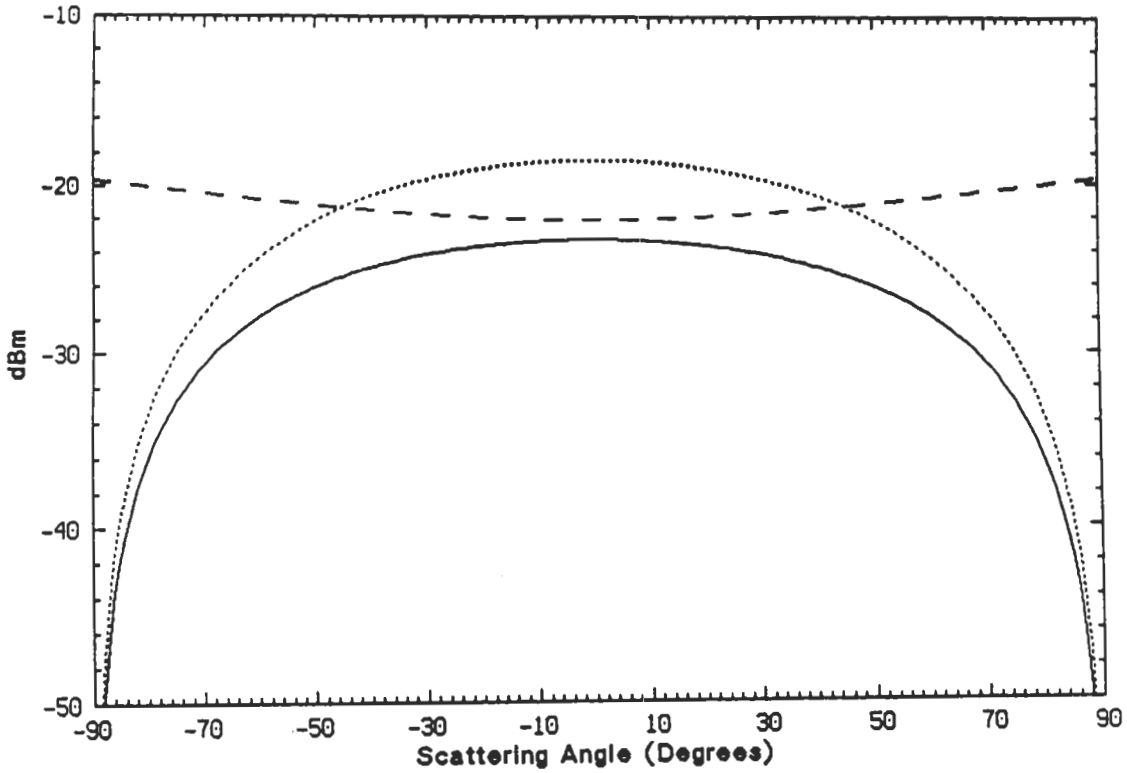

Figure 5.32: Bistatic echo width of a $\lambda_0/10 \times \lambda_0/10$ square dielectric cylinder with $\epsilon = 36 + i17$, at $f = 10$ GHz and $\phi_0 = 0$ degrees for E polarization: (——) cylinder over resistive sheet $R_0 = 180 + i270$, (- - - - -) cylinder over perfect conductor, (— —) cylinder in free space.

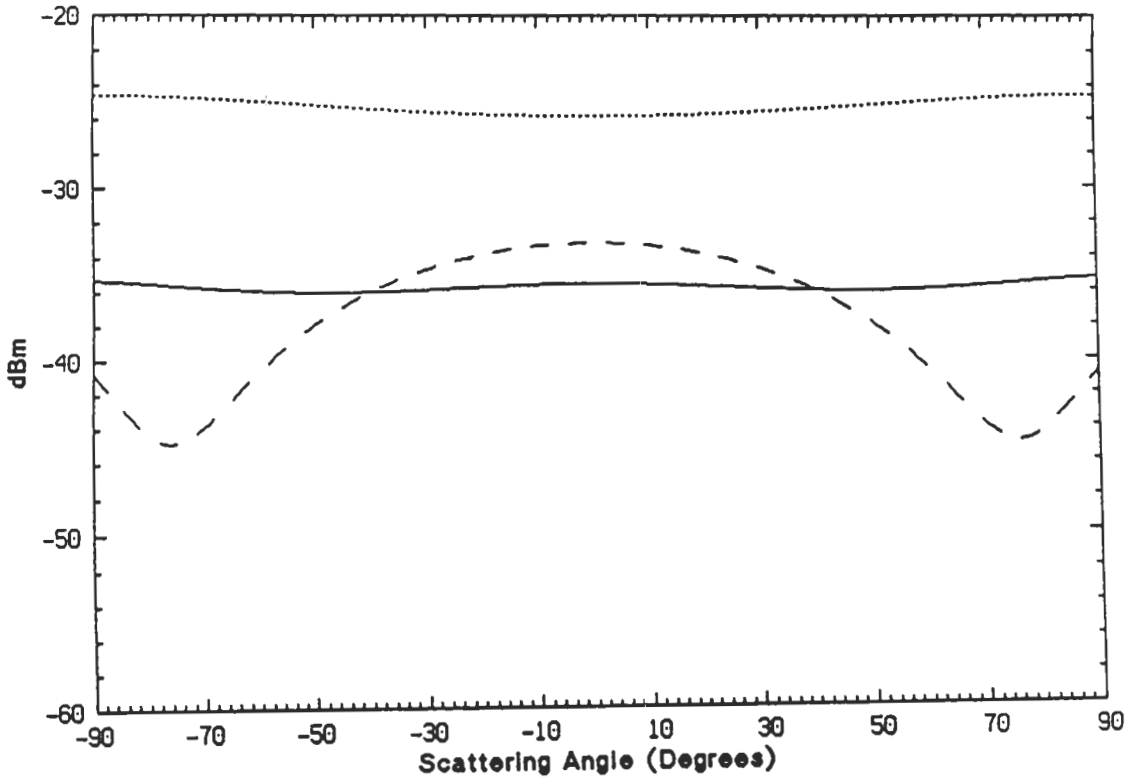

Figure 5.33: Bistatic echo width of a $\lambda_0/10 \times \lambda_0/10$ square dielectric cylinder with $\epsilon = 36 + i17$, at $f = 10$ GHz and $\phi_0 = 0$ degrees for H polarization: (——) cylinder over resistive sheet $R_0 = 180 + i270$, (- - - - -) cylinder over perfect conductor, (— —) cylinder in free space.

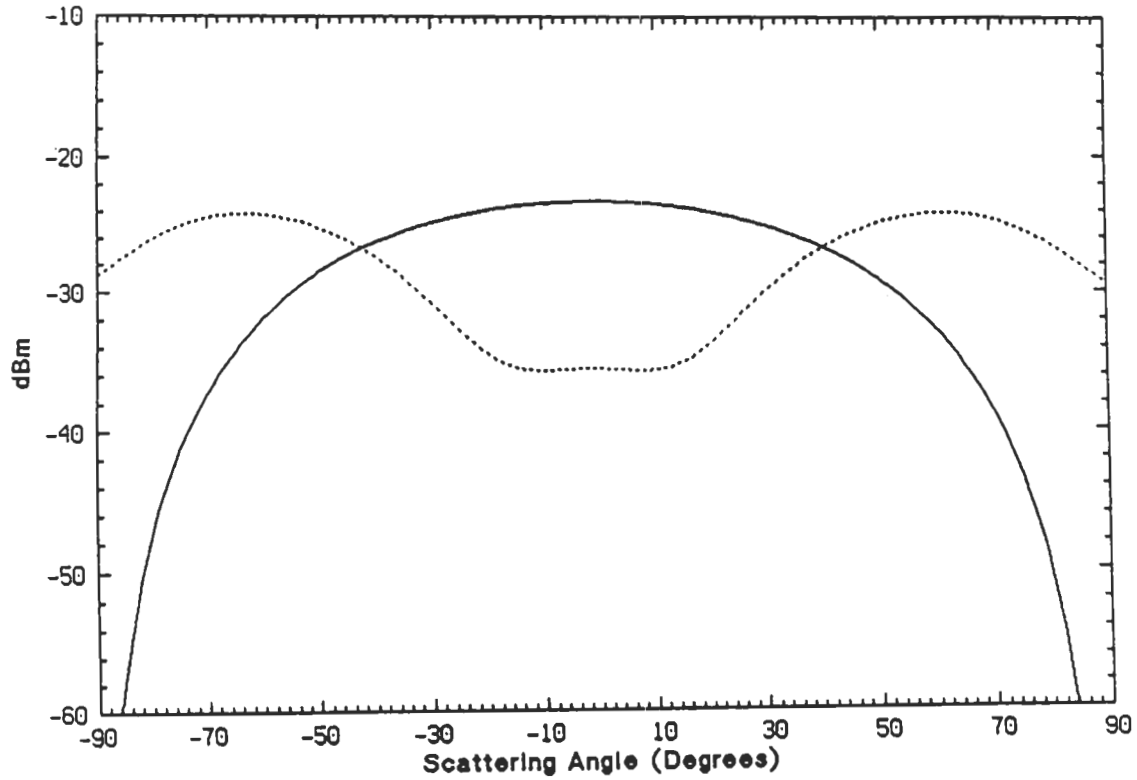

Figure 5.34: Backscattering echo width of a $\lambda_0/10 \times \lambda_0/10$ square dielectric cylinder over resistive sheet $R_0 = 180 + i270$ with $\epsilon = 36 + i17$ at $f = 10$ GHz: (——) E polarization, (- - - - -) H polarization.

5.12 Conclusions

Problems of scattering from variable resistive and impedance sheets have been studied using a perturbation technique in the Fourier domain. A recursive form for the n^{th} component of the induced current on the resistive sheet was derived which, in principle, allows evaluation of the current to the desired order of perturbation. Having analytical expression for the induced current in the Fourier domain culminates in having an analytical form for the far field amplitude. The solution for the induced current on an impedance sheet is identical to that of a resistive sheet whose resistivity is twice the impedance of the surface impedance.

The validity of the technique was checked in two limiting cases where the variation in the perturbation function is sharp in either the spatial or the Fourier domain. It was shown that the perturbation method is capable of handling both. The first order expression for the induced current was obtained analytically for an arbitrary perturbation, but the ability to obtain analytical expressions for the higher orders depends on the perturbation function. For a periodic resistivity, a closed form solution for any arbitrary order of perturbation was obtained. The results based on the perturbation method were compared with an exact solution based on the moment method. The analytical results were also checked against a GTD solution for the impedance insert problem and excellent agreement was observed. The moment method results for the problem of a dielectric hump over a resistive sheet using an exact image representation were also compared with the perturbation solution . Agreement between the analytical and numerical solutions is excellent. It was found that the required order of perturbation is proportional to the perturbation constant Δ and the width of the perturbation in the spatial domain, i.e. L for a periodic perturbation and w for the

impedance insert and dielectric hump problems. It was concluded that a vein and a variation in the thickness of a leaf do not have a significant effect near the specular direction, but in other directions they are substantial contributors to the scattered field.

CHAPTER VI

LOW FREQUENCY SCATTERING FROM CYLINDRICAL STRUCTURES AT OBLIQUE INCIDENCE

6.1 Introduction

Electromagnetic scattering properties of vegetation needles and very thin twigs are studied in this chapter. In previous chapters high frequency techniques were employed for planar leaves whose lateral dimensions are large compared with the incident wave length λ_0. At much lower frequencies and/or for smaller leaves whose dimensions are all small compared with λ_0, Rayleigh scattering theory is applicable. The far zone scattered field is then attributable to induced electric and magnetic dipoles, and for plane wave incidence, the dependence on the direction and polarization of the incident field can be made explicit by introducing the electric and magnetic polarizability tensors [Kleinman and Senior, 1986]. The tensor elements are functions only of the geometry and material of the scatterer and are expressible as weighted surface integrals of certain potentials which can be obtained from the solutions of elementary integral equations.

Classical Rayleigh scattering theory is extended to the case of a homogeneous dielectric cylinder of arbitrary cross section whose transverse dimensions are much

smaller than λ_0. This intermediate situation is provided by a pine needle whose transverse dimensions are small compared with the wavelength but whose length is much greater than λ_0. Vegetation needles usually come with circular, semi-circular, triangular, or circular sector cross section.

For a plane wave incident obliquely on a homogeneous dielectric cylinder of infinite length, the field at any point outside the cylinder can be written as the sum of contributions from line dipoles whose moments per unit length are expressible in terms of polarizability tensors. Integral equations are derived from which to determine the tensor elements and results are presented for a variety of cylinders and material constants. The generalization to a cylinder of finite length is now trivial. In accordance with the physical optics approximation, it is assumed that the surface field is the same as that on the infinite cylinder, leading immediately to an expression for the far field in terms of the same polarizability tensors.

6.2 Infinite Cylinders

A homogeneous dielectric cylinder of arbitrary cross section is oriented with its generators parallel to the z axis of a Cartesian coordinate system (x, y, z) (see Fig. 6.1). The relative permittivity and permeability of the dielectric are ϵ and μ respectively, and the cylinder is illuminated by the linearly polarized plane wave

$$\mathbf{E}^i = \hat{a} e^{ik_0 \hat{k}^i \cdot \bar{r}}, \qquad \mathbf{H}^i = Y_0 \hat{b} e^{ik_0 \hat{k}^i \cdot \bar{r}} \tag{6.1}$$

propagating in the direction

$$\hat{k}_i = \hat{x} \sin\beta \cos\phi_0 + \hat{y} \sin\beta \sin\phi_0 + \hat{z} \cos\beta \ . \tag{6.2}$$

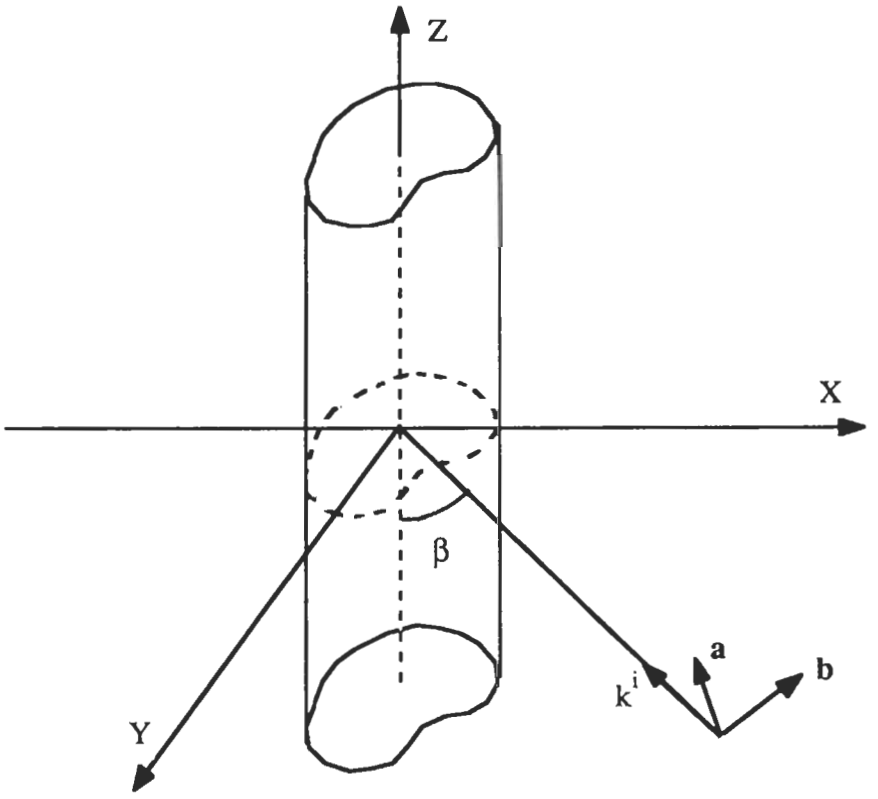

Figure 6.1: Infinite cylinder geometry.

The unit vectors $\hat{a}$ and $\hat{b}$ specifying the directions of the incident electric and magnetic fields are such that

$$\hat{a} \times \hat{b} = \hat{k}^i, \qquad \hat{k}^i \cdot \hat{a} = \hat{k}^i \cdot \hat{b} = 0 \ .$$

Since the cylinder is uniform in the z direction, the scattered field must have the same z dependence as the incident field, namely $e^{ik_0 z \cos\beta}$. If, for brevity, this factor is omitted, the electric and magnetic Hertz vectors defining the scattered field can be written as

$$\mathbf{\Pi}_e(x,y) = \frac{-Z_0}{4k_0} \int_S \mathbf{J}_e(x',y') H_0^{(1)}(k_0 \sin\beta \sqrt{(x-x')^2 + (y-y')^2}) \mathrm{d}x' \mathrm{d}y' \ , \quad (6.3)$$

$$\mathbf{\Pi}_m(x,y) = \frac{-Y_0}{4k_0} \int_S \mathbf{J}_m(x',y') H_0^{(1)}(k_0 \sin\beta \sqrt{(x-x')^2 + (y-y')^2}) \mathrm{d}x' \mathrm{d}y' \quad (6.4)$$

where $\mathbf{J}_e$ and $\mathbf{J}_m$ are the induced electric and magnetic currents, $H_0^{(1)}$ is the Hankel function of the first kind of zeroth order, and the integration is over the cross section S of the cylinder. In terms of the Hertz vectors the scattered fields are

$$\begin{aligned} \mathbf{E}^s &= \nabla\nabla \cdot \mathbf{\Pi}_e + k_0^2 \mathbf{\Pi}_e + ik_0 Z_0 \nabla \times \mathbf{\Pi}_m, \\ \mathbf{H}^s &= \nabla\nabla \cdot \mathbf{\Pi}_m + k_0^2 \mathbf{\Pi}_m - ik_0 Y_0 \nabla \times \mathbf{\Pi}_e \end{aligned} \quad (6.5)$$

and we note that

$$\nabla = \nabla_t + ik_0 \cos\beta \hat{z} \quad (6.6)$$

where ∇_t is the transverse operator which, in Cartesian coordinates, is

$$\nabla_t = \hat{x}\frac{\partial}{\partial x} + \hat{y}\frac{\partial}{\partial y}.$$

From (6.5) and (6.6) the field components become

$$\begin{aligned} E_x^s &= k_0^2 \Pi_{ex} + \tfrac{\partial^2}{\partial x^2}\Pi_{ex} + \tfrac{\partial^2}{\partial x \partial y}\Pi_{ey} + ik_0 \cos\beta \tfrac{\partial}{\partial x}\Pi_{ez} + ik_0 Z_0 (\tfrac{\partial}{\partial y}\Pi_{mz} - ik_0 \cos\beta \Pi_{my}) \\ E_y^s &= \tfrac{\partial^2}{\partial x \partial y}\Pi_{ex} + k_0^2 \Pi_{ey} + \tfrac{\partial^2}{\partial y^2}\Pi_{ey} - ik_0 \cos\beta \tfrac{\partial}{\partial y}\Pi_{ez} + ik_0 Z_0 (\tfrac{\partial}{\partial y}\Pi_{mz} - ik_0 \cos\beta \Pi_{mx}) \\ E_z^s &= ik_0 \cos\beta \tfrac{\partial}{\partial x}\Pi_{ex} + ik_0 \cos\beta \tfrac{\partial}{\partial y}\Pi_{ey} + k_0^2 \sin^2\beta \Pi_{ez} + ik_0 Z_0 (\tfrac{\partial}{\partial x}\Pi_{my} - \tfrac{\partial}{\partial y}\Pi_{mx}) \end{aligned}$$

$$H_x^s = -ik_0Y_0(\frac{\partial}{\partial y}\Pi_{ez} - ik_0\cos\beta\Pi_{ey}) + k_0^2\Pi_{mx} + \frac{\partial^2}{\partial x^2}\Pi_{mx} + \frac{\partial^2}{\partial x\partial y}\Pi_{my} + ik_0\cos\beta\frac{\partial}{\partial x}\Pi_{mz}$$

$$H_y^s = -ik_0Y_0(\frac{\partial}{\partial y}\Pi_{ez} - ik_0\cos\beta\Pi_{ex}) + \frac{\partial^2}{\partial x\partial y}\Pi_{mx} + k_0^2\Pi_{my} + \frac{\partial^2}{\partial y^2}\Pi_{my} + ik_0\cos\beta\frac{\partial}{\partial y}\Pi_{mz}$$

$$H_z^s = -ik_0Y_0(\frac{\partial}{\partial x}\Pi_{ey} - \frac{\partial}{\partial y}\Pi_{ex}) + ik_0\cos\beta\frac{\partial}{\partial x}\Pi_{mx} + ik_0\cos\beta\frac{\partial}{\partial y}\Pi_{my} + k_0^2\sin^2\beta\Pi_{mz}$$

If d is a typical transverse dimension of the cylinder and k_0d, $k_0 \mid N \mid d \ll 1$ where $N = (\epsilon\mu)^{\frac{1}{2}}$ is the refractive index, the currents and the Hertz vectors can be expanded in power of k_0 with only the lowest order terms retained. This is also true in the expressions (6.5) for the scattered field, and shows that in the near field of the cylinder

$$\mathbf{E}^s = \nabla_t\nabla_t\cdot\mathbf{\Pi}_e, \qquad \mathbf{H}^s = \nabla_t\nabla_t\cdot\mathbf{\Pi}_m \tag{6.7}$$

implying

$$E_z^s = H_z^s = 0.$$

Thus, at low frequencies the electric and magnetic fields decouple, with the scattered electric field determined by the electric current (and, hence, permittivity) alone, and the magnetic field by the magnetic current (and permeability). Since the solution for the magnetic field can be deduced from that for the electric field by replacing ϵ and $\hat{a}$ by μ and $Y_0\hat{b}$, it is now sufficient to take $\mu = 1$ corresponding to a non-magnetic dielectric.

To determine the static field, the Hankel function in (6.3) is replaced by its small argument expansion:

$$H_0^{(1)}(k_0\sin\beta \mid \bar{\rho} - \bar{\rho}' \mid) \approx 1 + \frac{i2}{\pi}\gamma + \frac{i2}{\pi}\ln(k_0\sin\beta \mid \bar{\rho} - \bar{\rho}' \mid).$$

where $\bar{\rho}$ is the two-dimensional position vector and $\gamma = 0.5772157\cdots$ is Euler's constant. On inserting this into (6.7) and noting that

$$\nabla_t\ln(k_0\sin\beta \mid \bar{\rho} - \bar{\rho}' \mid) = \nabla_t\ln \mid \bar{\rho} - \bar{\rho}' \mid,$$

the lowest order scattered field becomes

$$\mathbf{E}^s(\bar{\rho}) = \quad -\nabla_t\{\tfrac{iZ_0}{2\pi k_0}\int_S \mathbf{J}_{et}(\bar{\rho}')\cdot\nabla_t \ln \mid \bar{\rho}-\bar{\rho}' \mid \mathrm{d}s'\},$$

with

$$\mathbf{J}_{et}(\bar{\rho}) = J_{ex}(\bar{\rho})\hat{x} + J_{ey}(\bar{\rho})\hat{y}$$

Since $\frac{i}{\omega}\mathbf{J}_{et} = \mathbf{P}$ is simply the dipole moment per unit area, it follows that

$$\mathbf{E}^s = -\nabla_t\Phi^s(\bar{\rho}) \tag{6.8}$$

where

$$\Phi^s(\bar{\rho}) = \frac{iZ_0}{2\pi k_0}\int_S \mathbf{J}_{et}(\bar{\rho}')\cdot\nabla_t \ln \mid \bar{\rho}-\bar{\rho}' \mid \mathrm{d}s', \tag{6.9}$$

is the two-dimensional electrostatic potential.

To the zeroth order in k_0 the incident electric field is

$$\mathbf{E}^i = \hat{a} = a_x\hat{x} + a_y\hat{y} + a_z\hat{z}$$

which can be written as

$$\mathbf{E}^i = -\nabla_t\Phi^i + a_z\hat{z} \tag{6.10}$$

with

$$\Phi^i = -a_x(x+c_1) - a_y(y+c_2) \tag{6.11}$$

where c_1, c_2 are arbitrary constants. The total potential is then

$$\Phi = \Phi^i + \Phi^s$$

and the dependence on $\hat{a}$ can be made explicit by writing

$$\Phi = a_x \Phi_1 + a_y \Phi_2 \tag{6.12}$$

with a similar decomposition for Φ^i and Φ^s.

In terms of the total field the polarization current is

$$\mathbf{J}_e(\bar{\rho}) = -ik_0 Y_0(\epsilon - 1)(\mathbf{E}^i + \mathbf{E}^s) \tag{6.13}$$

and since $E_z^s = 0$,

$$J_{ez}(\bar{\rho}) = -ik_0 Y_0(\epsilon - 1)a_z \tag{6.14}$$

in agreement with the result of Van Bladel [1963]. Also

$$\mathbf{J}_{et}(\bar{\rho}) = -ik_0 Y_0(\epsilon - 1)(a_x \hat{x} + a_y \hat{y} - \nabla_t \Phi^s),$$

that is

$$\mathbf{J}_{et}(\bar{\rho}) = ik_0 Y_0(\epsilon - 1)\nabla_t(a_x \Phi_1 + a_y \Phi_2), \tag{6.15}$$

and the derivation and solution of integral equations for Φ_1 and Φ_2 are discussed in Section 6.4.

6.3 Polarizability Tensors

At large distances $\rho \gg k_0 d^2$ from the cylinder, the Hankel function in the expressions (6.3), (6.4) for $\mathbf{\Pi}_e$, $\mathbf{\Pi}_m$ can be replaced by its large argument expansion. Thus

$$\begin{aligned} \mathbf{\Pi}_e &\approx -\frac{Z_0}{4k_0}\sqrt{\frac{2}{\pi k_0 \rho \sin\beta}}\, e^{ik_0(\rho\sin\beta + z\cos\beta) - i\frac{\pi}{4}} \int_S \mathbf{J}_e(\bar{\rho}')\mathrm{d}s' \\ &= \frac{i}{4}\sqrt{\frac{2}{\pi k_0 \rho \sin\beta}}\, e^{ik_0(\rho\sin\beta + z\cos\beta) - i\frac{\pi}{4}}(\epsilon - 1) \int_S \left\{-\nabla_t(a_x \Phi_1 + a_y \Phi_2) + a_z \hat{z}\right\} \mathrm{d}s' \end{aligned} \tag{6.16}$$

in which the z dependence has been restored, and since

$$\int_S \nabla_t' \Phi(\bar{\rho}') \mathrm{d}s' = \int_C \Phi(\bar{\rho}') \hat{n}' \mathrm{d}c'$$

where $\hat{n}$ is the outward unit vector normal to the boundary C of S,

$$\begin{aligned} \mathbf{\Pi}_e = \; & \tfrac{i}{4}\sqrt{\tfrac{2}{\pi k_0 \rho \sin\beta}} e^{ik_0(\rho\sin\beta + z\cos\beta) - i\frac{\pi}{4}} (\epsilon - 1) \\ & \cdot \{ - \textstyle\int_C (a_x \Phi_1 + a_y \Phi_2) \hat{n}' \mathrm{d}c' + A a_z \hat{z} \} \end{aligned} \tag{6.17}$$

where A is the cross-sectional area of the cylinder.

Similarly, if Ψ is the total magnetostatic potential such that

$$\mathbf{H} = -Y_0 \nabla_t \Psi + Y_0 b_z \hat{z}$$

with

$$\Psi = b_x \Psi_1 + b_y \Psi_2,$$

we have

$$\begin{aligned} \mathbf{\Pi}_m = \; & \tfrac{i}{4}\sqrt{\tfrac{2}{\pi k_0 \rho \sin\beta}} e^{ik_0(\rho\sin\beta + z\cos\beta) - i\frac{\pi}{4}} (\mu - 1) \\ & \cdot \{ - \textstyle\int_C (b_x \Psi_1 + b_y \Psi_2) \hat{n}' \mathrm{d}c' + A b_z \hat{z} \} \end{aligned} \tag{6.18}$$

and from the z dependence in (6.16) and (6.17) it is evident that the scattering is confined to the forward cone $\hat{k}^s \cdot \hat{z} = \cos\beta$. In the far zone, $\nabla \approx ik_0 \hat{k}^s$, and hence

$$\mathbf{E}^s = \sqrt{\frac{2}{\pi k_0 \rho \sin\beta}} e^{ik_0(\rho\sin\beta + z\cos\beta) - i\frac{\pi}{4}} \mathbf{S}$$

with

$$\begin{aligned} \mathbf{S} = \; & -\tfrac{ik_0^2}{4} \{ \hat{k}^s \times \hat{k}^s \times (\epsilon - 1) [- \textstyle\int_C (a_x \Phi_1 + a_y \Phi_2) \hat{n}' \mathrm{d}c' + A b_z \hat{z}] \\ & + \hat{k}^s \times (\mu - 1) [- \textstyle\int_C (b_x \Psi_1 + b_y \Psi_2) \hat{n}' \mathrm{d}c' + A b_z \hat{z}] \}. \end{aligned} \tag{6.19}$$

The scattering is attributable to electric and magnetic line dipoles along the z axis. The electric dipole moment per unit length is

$$\mathrm{p} = \epsilon_0 (\epsilon - 1) \left\{ - \int_C (a_x \Phi_1 + a_y \Phi_2) \hat{n}' \mathrm{d}c' + A b_z \hat{z} \right\} \tag{6.20}$$

and if

$$\mathbf{p} = \epsilon_0 \mathbf{P} \cdot \hat{a} \ , \tag{6.21}$$

the elements of the polarizability tensor $\mathbf{P}$ are

$$\begin{aligned}
&P_{xx} = -(\epsilon - 1) \int_C \Phi_1 \hat{n}' \cdot \hat{x} \mathrm{d}c', && P_{xy} = -(\epsilon - 1) \int_C \Phi_2 \hat{n}' \cdot \hat{x} \mathrm{d}c' \\
&P_{yx} = -(\epsilon - 1) \int_C \Phi_1 \hat{n}' \cdot \hat{y} \mathrm{d}c', && P_{yy} = -(\epsilon - 1) \int_C \Phi_2 \hat{n}' \cdot \hat{y} \mathrm{d}c' \\
&P_{zz} = (\epsilon - 1) A, \\
&P_{xz} = P_{zx} = P_{yz} = P_{zy} = 0.
\end{aligned} \tag{6.22}$$

The elements are functions only of the geometry and permittivity of the cylinder and are real if ϵ is. Using reciprocity it can be shown that the tensor is symmetric, i.e. $P_{yx} = P_{xy}$, and if the cylinder is symmetric about either the x or y axis, the tensor is diagonal ($P_{yx} = P_{xy} = 0$) in the given coordinate system.

Similarly, the magnetic dipole moment per unit length is

$$\mathbf{m} = Y_0(\mu - 1) \left\{ - \int_C (b_x \Psi_1 + b_y \Psi_2) \hat{n}' \mathrm{d}c' + A b_z \hat{z} \right\}$$

and if[1]

$$\mathbf{m} = Y_0 \mathbf{M} \cdot \hat{b},$$

the magnetic polarizability tensor $\mathbf{M}$ differs from $\mathbf{P}$ only in having μ and Ψ in place of ϵ and Φ. Clearly, for a non-magnetic dielectric, $\mathbf{m} = 0$. In terms of the tensors

$$\mathbf{S} = -\frac{ik_0^2}{4} \left\{ \hat{k}^s \times \hat{k}^s \times [\mathbf{P} \cdot \mathbf{a}] + \hat{k}^s \times [\mathbf{M} \cdot \mathbf{b}] \right\}. \tag{6.23}$$

and the dependence on the incident and scattered field directions is now explicit.

[1] $\mathbf{M}$ differs in sign from the magnetic polarizability tensor usually defined (see, for example, Keller et at, 1972).

6.4 Tensor Elements

To compute the tensor elements it is necessary to determine the potential on the boundary C, and one way to do this is using integral equations. For brevity, we shall confine attention to the electrostatic potential Φ_1.

From (6.9) and (6.15) the scattered field potential is

$$\Phi_1^s(\bar{\rho}) = \frac{\epsilon - 1}{2\pi} \int_S \nabla_t' \Phi_1(\bar{\rho}') \cdot \nabla_t' \ln \mid \bar{\rho} - \bar{\rho}' \mid \mathrm{d}s'.$$

and since

$$\nabla_t' \Phi_1(\bar{\rho}') \cdot \nabla_t' \ln \mid \bar{\rho} - \bar{\rho}' \mid = \nabla_t' \cdot (\Phi_1(\bar{\rho}') \nabla_t' \ln \mid \bar{\rho} - \bar{\rho}' \mid) - \Phi_1(\bar{\rho}') \nabla_t'^2 \ln \mid \bar{\rho} - \bar{\rho}' \mid,$$

we have

$$\Phi^s(\bar{\rho}) = \frac{\epsilon - 1}{2\pi} \int_C \nabla_t' \Phi_1(\bar{\rho}') \cdot \frac{\partial}{\partial n'} \ln \mid \bar{\rho} - \bar{\rho}' \mid \mathrm{d}c' - \frac{\epsilon - 1}{2\pi} \Delta,$$

where

$$\Delta = \int_S \Phi_1(\bar{\rho}') \nabla_t'^2 \ln \mid \bar{\rho} - \bar{\rho}' \mid \mathrm{d}s'$$

When the observation point is on the boundary, the boundary condition gives

$$\Phi_1^s = \Phi_1 + x + c_1$$

and for a piecewise smooth surface, $\Delta = \alpha \Phi_1(\bar{\rho})$ where α is equal to the angle subtended by the surface at the point $\bar{\rho}$. Thus, for a smooth surface, $\alpha = \pi$, and an integral equation for Φ_1 on C is then

$$\left(\frac{\epsilon + 1}{2}\right) \Phi_1(\bar{\rho}) - \left(\frac{\epsilon - 1}{2\pi}\right) \int_C \Phi_1(\bar{\rho}') \frac{\cos \theta'}{\mid \bar{\rho} - \bar{\rho}' \mid} \mathrm{d}c' = -x - c_1 \tag{6.24}$$

where θ' is shown in Fig. 6.2.

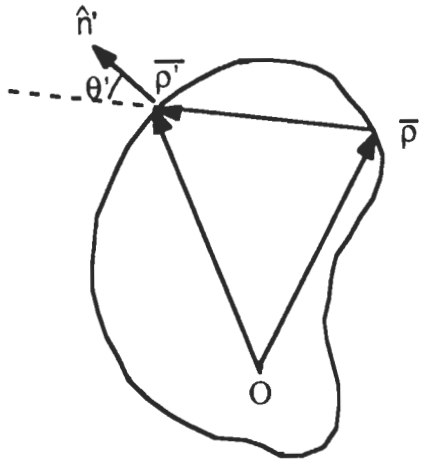

Figure 6.2: Transverse plane geometry.

One of the few geometries for which an analytical solution of (6.24) is possible is a circular cylinder. If the radius is r,

$$\frac{\cos\theta'}{|\,\bar{\rho}-\bar{\rho}'\,|}=\frac{1}{2r}$$

independent of position on C. The integral on the left hand side of (6.24) is therefore independent of $\bar{\rho}$, which forces $\Phi_1(\bar{\rho})$ to be a linear function of x independent of y. By simple substitution it is found that

$$\Phi_1(\bar{\rho})=-\frac{2x}{\epsilon+1}-c_1$$

and hence

$$\frac{P_{xx}}{A}=\frac{P_{yy}}{A}=2\frac{\epsilon-1}{\epsilon+1} \tag{6.25}$$

with

$$\frac{P_{zz}}{A}=\epsilon-1. \tag{6.26}$$

These are consistent with the eigenfunction expansion for a homogeneous cylinder at oblique incidence [Ruck et al, 1970] when only two terms in the series are retained,

and are identical to the tensor elements for a long thin spheroid when normalized to the volume. For $\epsilon = \epsilon' + i\epsilon''$ the real and imaginary parts of P_{xx}/A (see (6.25)) are plotted as functions of ϵ' for a variety of ϵ'' in Figs. 6.3 and 6.4 respectively.

With other geometries it is a trivial matter to solve the integral equation numerically, and a moment method code has been developed for this purpose. The contour is divided into N segments small enough to treat the potential as constant over each, and point matching is then employed to convert the equation into a set of N linear equations of the form

$$\mathcal{Z}\mathcal{X} = \mathcal{Y} \tag{6.27}$$

where $\mathcal{Z}$ is the impedance matrix, $\mathcal{X}$ is the potential (unknown) vector and $\mathcal{Y}$ is the excitation (known) vector. The elements of the impedance matrix are

$$Z_{mn} = \begin{cases} -\frac{\epsilon-1}{2\pi} \frac{\Delta_n \cos\theta_{mn}}{\sqrt{(x_m-x_n)^2+(y_m-y_n)^2}} & m \neq n \\ \frac{\epsilon+1}{2} & m = n \end{cases} \tag{6.28}$$

where Δ_n is the length of the n^{th} segment.

The tensor elements have been computed for cylinders whose cross section are the semicircle, equilateral triangle and square shown in Fig. 6.5, and in each case symmetry about the y axis diagonalizes the tensor. In Figs. 6.6 through 6.9 the real and imaginary parts of P_{xx}/A and P_{yy}/A for the semicircular cylinder are plotted as functions of ϵ'. Qualitatively, the curves are similar to those for the circular cylinder, and this prompted a search for simple analytical formulas. Since the scattering vanishes if $\epsilon = 1$ and the integral equation (6.24) shows that the potential is infinite if $\epsilon = -1$, it was assumed that (for example)

$$\frac{P_{xx}}{A} = c_0 \frac{\epsilon - 1}{\epsilon + 1} \cdot \frac{\epsilon + c_1}{\epsilon + c_2}$$

where c_0, c_1, and c_2 are constants, and after a few trials an excellent fit to the data was obtained with the empirical formulas

$$\frac{P_{xx}}{A} = 3.00\frac{\epsilon - 1}{\epsilon + 1} \cdot \frac{\epsilon + 1.05}{\epsilon + 2.20} \tag{6.29}$$

$$\frac{P_{yy}}{A} = 1.56\frac{\epsilon - 1}{\epsilon + 1} \cdot \frac{\epsilon + 2.60}{\epsilon + 2.00} \tag{6.30}$$

The error is less than two percent. The analogous results for the triangular and square cylinders are

$$\frac{P_{xx}}{A} = \frac{P_{yy}}{A} = 2.64\frac{\epsilon - 1}{\epsilon + 1} \cdot \frac{\epsilon + 4.17}{\epsilon + 5.95} \tag{6.31}$$

and

$$\frac{P_{xx}}{A} = \frac{P_{yy}}{A} = 2.16\frac{\epsilon - 1}{\epsilon + 1} \cdot \frac{\epsilon + 3.38}{\epsilon + 3.76} \tag{6.32}$$

respectively, and the latter agree with the values reported by Mei and Van Bladel [1963].

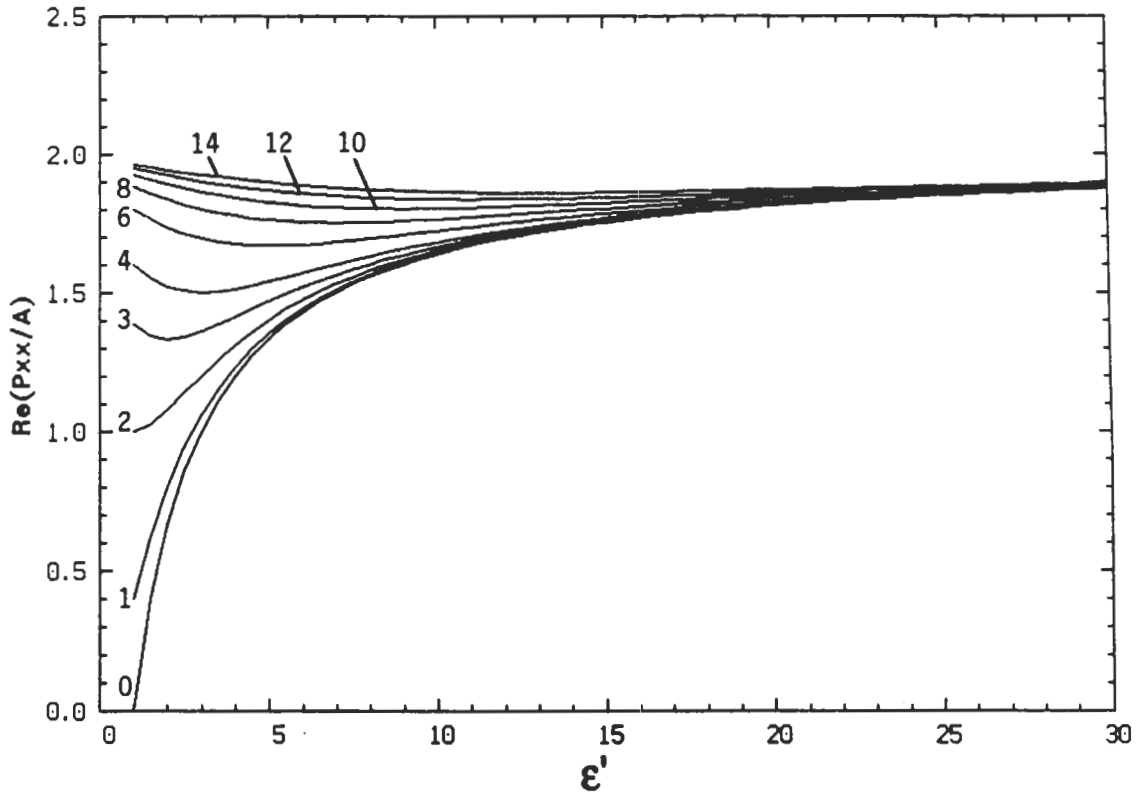

Figure 6.3: Real part of the normalized polarizability tensor element P_{xx}/A for a circular cylinder with the ϵ'' indicated.

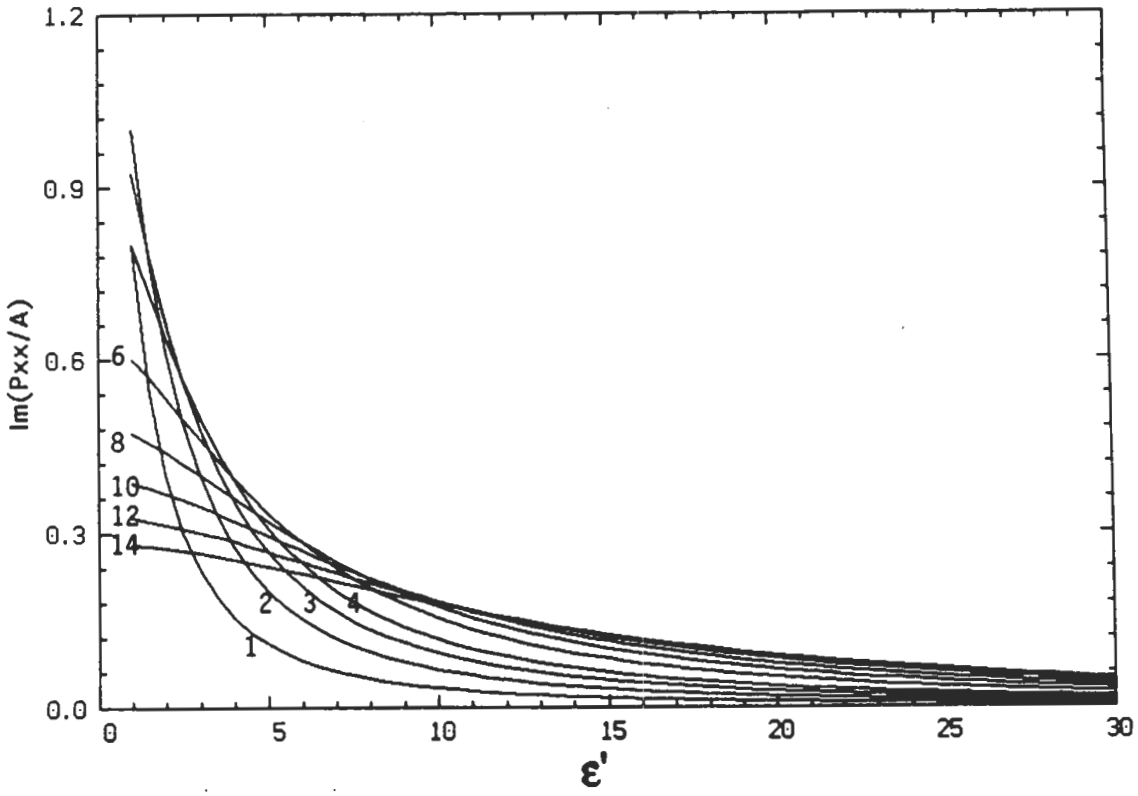

Figure 6.4: Imaginary part of the normalized polarizability tensor element P_{xx}/A for a circular cylinder with the ϵ'' indicated.

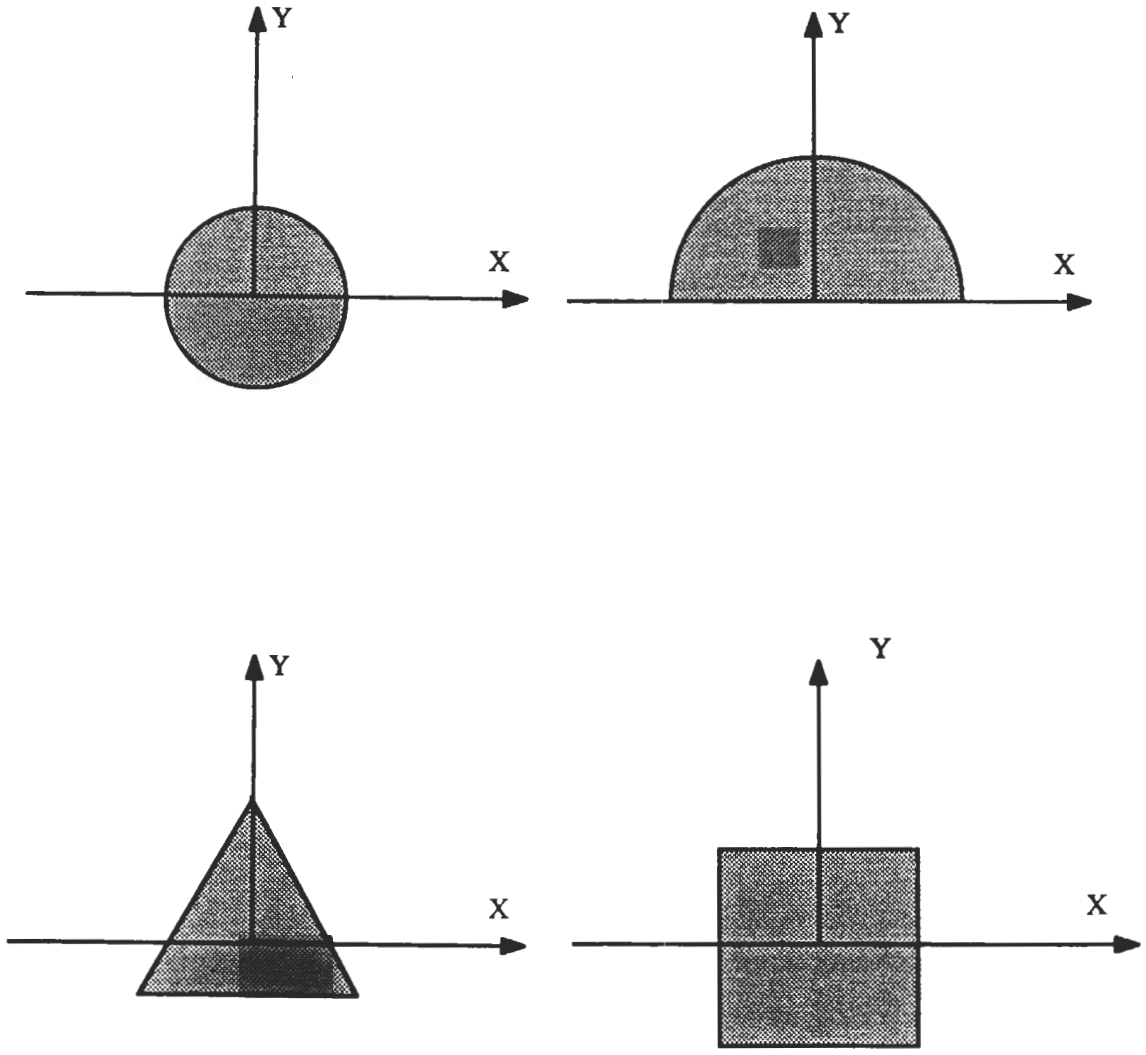

Figure 6.5: Circular, semicircular, triangular and square cylinders .

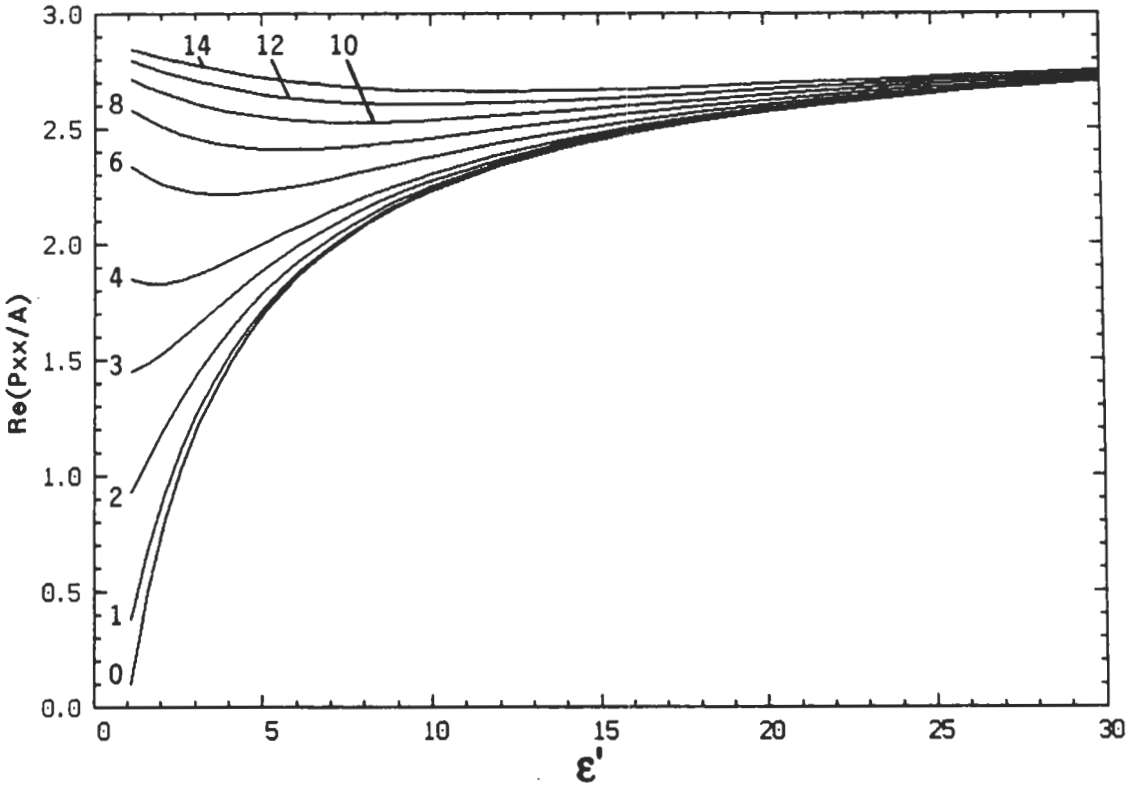

Figure 6.6: Real part of the normalized polarizability tensor element P_{xx}/A for a semicircular cylinder with the ϵ'' indicated.

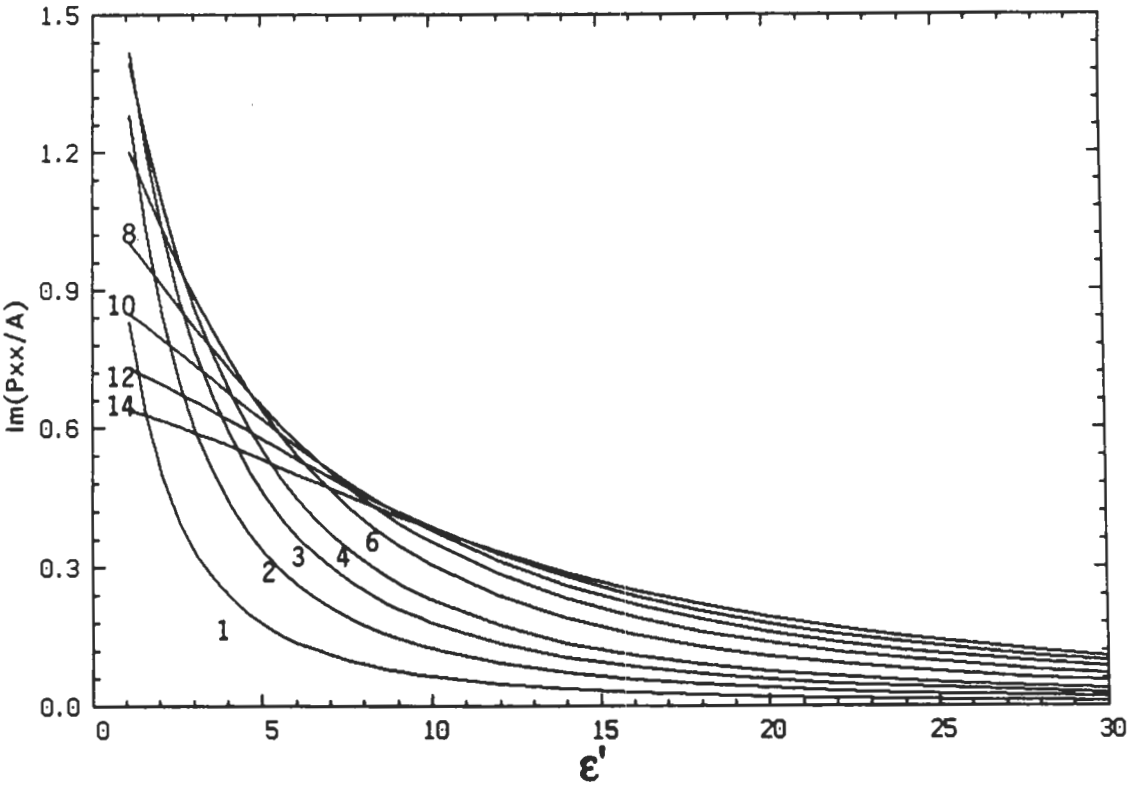

Figure 6.7: Imaginary part of the normalized polarizability tensor element P_{xx}/A for a semicircular cylinder with the ϵ'' indicated.

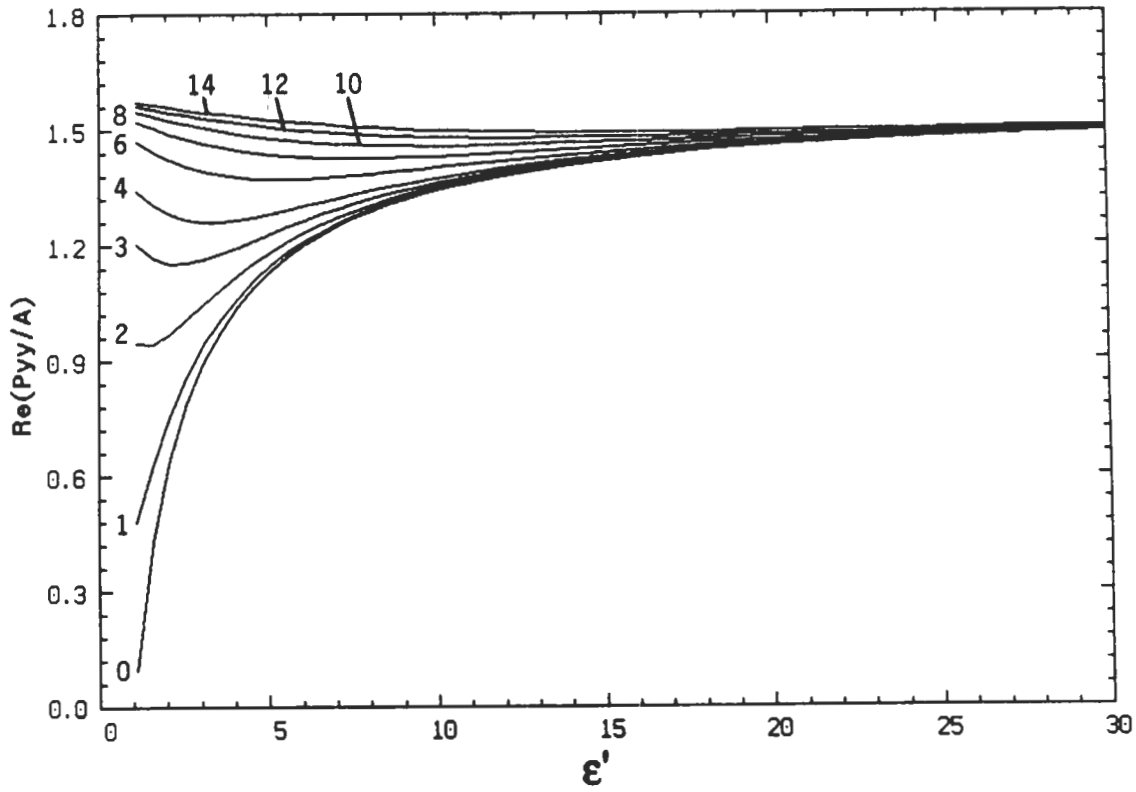

Figure 6.8: Real part of the normalized polarizability tensor element P_{yy}/A for a semicircular cylinder with the ϵ'' indicated.

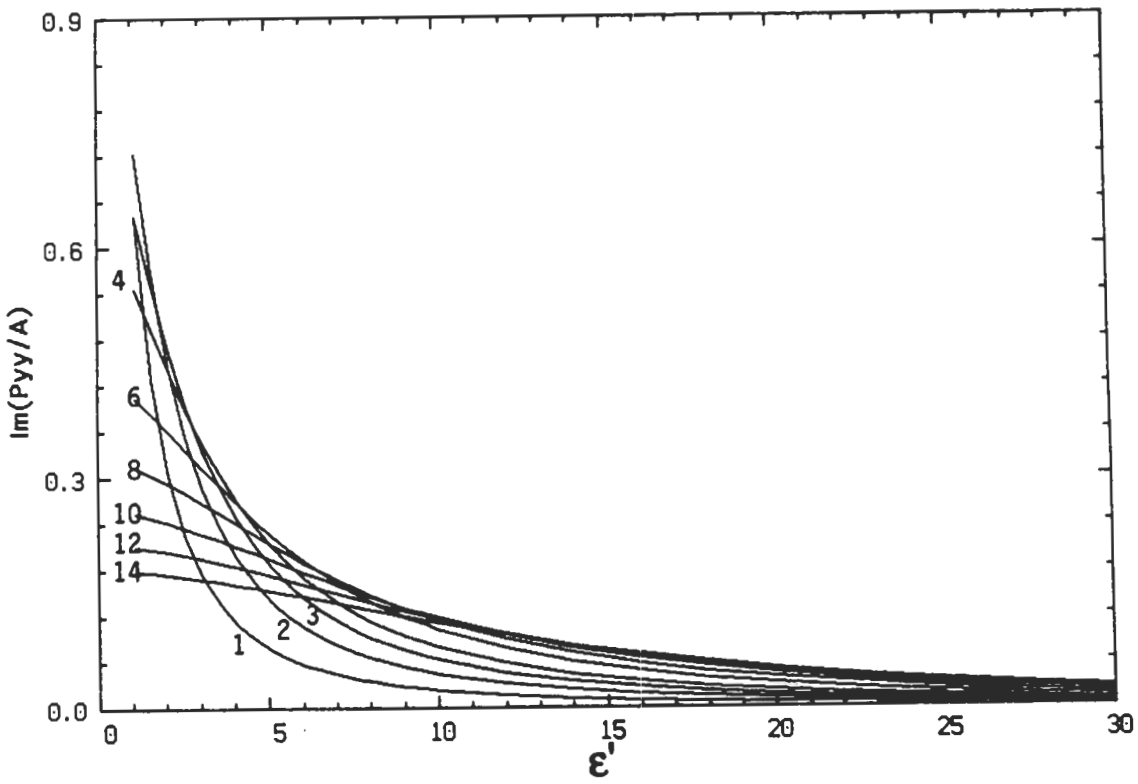

Figure 6.9: Imaginary part of the normalized polarizability tensor element P_{yy}/A for a semicircular cylinder with the ϵ'' indicated.

6.5 Finite Cylinder

In accordance with the physical optics approximation, it is assumed that for a cylinder of finite length $l \gg \lambda_0$ the surface fields are the same as those for the infinite cylinder. To determine the far field the three dimensional Green's function is employed in place of the Hankel function. The scattering is no longer confined to the forward cone and if, as before, the scattering direction is $\hat{k}_s$, the integration with respect to z can be carried out immediately and gives $(\ell \sin U)/U$ where

$$U = \frac{k_0 \ell}{2} \left(\hat{k}_s \cdot \hat{z} - \cos \beta \right). \tag{6.33}$$

The far field amplitude, defined as the coefficient of $re^{-ik_0 r}\mathbf{E}^s$ in the far zone, is then

$$\mathbf{S} = -\frac{k_0^2}{4\pi} \left\{ \hat{k}_s \times \hat{k}_s \times [\ell \mathbf{P} \cdot \hat{a}] + \hat{k}_s \times [\ell \mathbf{M} \cdot \hat{b}] \right\} \frac{\sin U}{U}.$$

where $\mathbf{P}$ and $\mathbf{M}$ are the tensors previously defined. As expected, for large $k_0 \ell$ the scattering decreases rapidly away from the forward cone $\hat{k}_s \cdot \hat{z} = \cos \beta$.

6.6 Conclusions

The preceding analysis provides an extension of Rayleigh scattering theory to cylindrical dielectric bodies whose transverse dimensions are small compared with the wavelength but whose length is much greater than λ_0. The results are strikingly similar to those for bodies all of whose dimensions are much less than λ_0 [Kleinman and Senior, 1986], and for a circular cylinder of infinite length the polarization tensor elements normalized to the cross section area A are identical to the elements for a thin prolate spheroid (or "rod") when normalized to the volume V. Of course, for a cylinder of finite length, $V = \ell A$, and apart from the factor $\sin U/U$, the same formulas are applicable for $\ell \gg \lambda_0$ and $\ell \ll \lambda_0$.

Qualitatively, the variation of P_{xx}/A and P_{yy}/A as functions of ϵ' for fixed ϵ'' is similar for all four cylinder cross sections considered, but there are significant quantitative differences. For a semicircle, for example, the normalized elements differ by almost a factor 2 from those for a circle, and such shape dependence is greater than that typical of a small body in the Rayleigh region. It would appear that accurate modelling of the cross section is more important when $\ell \gg \lambda_0$, and for remote sensing applications we note that many pine needles are almost semicircular.

CHAPTER VII

SCATTERING FROM CYLINDRICAL BODIES

7.1 Introduction

Trunk and branches are the significant parts of a tree canopy. For remote sensing study of a forested area, electromagnetic scattering of tree trunk and branches are of concern. At microwave frequencies and higher the trunk and branches of almost any tree is much larger than the wavelength λ_0 and depending on frequency their diameter varies from fraction of a wavelength to many wavelengths. A simple geometry that best describes branches is a cylinder. As explained in Section 1.3 the dielectric constant of a branch is high and lossy. Thus a branch may be modelled by a non-magnetic lossy dielectric cylinder with arbitrary cross section.

Study of circular cylinder is of great importance for two reasons: 1) an exact analytical solution exists which can be used for comparison purposes 2) branches and trunk of many tree spicies are almost circular. The analytical solution for infinite circular cylinder has been known for a long time [van de Hults, 1957]. Approximate solution for a cylinder of finite length are also given by Ruck et al [1970]. In this chapter we derive an approximate solution (semi-exact) for a finite cylinder with arbitrary orientation which is superior to that given in Ruck et al. This solution is

exact as regards to the transverse resonances and assumes the currents on the surface are the same as if the cylinder were infinite in length.

Approximate physical optics expressions for scattered field are also derived for a finite cylinder with arbitrary cross section and orientation. These results can easily be extended to include stratified dielectric cylinders. It is shown that for lossy dielectric cylinders the physical optics results are in a very good agreement with the exact solution at high frequencies.

7.2 Exact Solution for a Circular Cylinder

Suppose a homogeneous non-magnetic infinite circular cylinder of radius ρ_1 is illuminated by a plane wave of arbitrary polarization. The cylinder is oriented so that its axis is coincident with the z' axis of a local Cartesian coordinate system (x', y', z'). Further assume that the incident propagation vector $\hat{k}_i$ lies in the $x' - z'$ plane with

$$\hat{k}_i \cdot \hat{x}' = -\sin\beta\ , \qquad \hat{k}_i \cdot \hat{z}' = \cos\beta \tag{7.1}$$

and

$$\begin{aligned} \mathbf{E}_i \cdot \hat{z}' &= e_z e^{ik_0(-x'\sin\beta + z'\cos\beta)} \\ \mathbf{H}_i \cdot \hat{z}' &= Y_0 h_z e^{ik_0(-x'\sin\beta + z'\cos\beta)} \end{aligned} \tag{7.2}$$

from which the other field components can be found. Since the cylinder is infinite in the z direction, it follows that all the field components must have the same z-dependency as the incident field namely $e^{ik_{0z}\cos\beta}$, implying $\frac{\partial}{\partial z} = ik_0\cos\beta$. Circular cylinder is one of the few geometries for which an exact scattering solution exist. From Maxwell's equation it can be shown that the z components of electric and magnetic fields must satisfy the wave equation in terms of which other field components

can be obtained. For a medium with relative dielectric constant ϵ we have

$$\begin{aligned}
E_\rho &= \tfrac{1}{ik_0(\epsilon-\cos^2\beta)}\left\{-\tfrac{1}{\rho}\tfrac{\partial}{\partial\phi}Z_0H_z - \cos\beta\tfrac{\partial}{\partial\rho}E_z\right\} ,\\
E_\phi &= \tfrac{1}{ik_0(\epsilon-\cos^2\beta)}\left\{-\tfrac{\partial}{\partial\rho}Z_0H_z - \tfrac{\cos\beta}{\rho}\tfrac{\partial}{\partial\phi}E_z\right\} ,\\
Z_0H_\rho &= \tfrac{1}{ik_0(\epsilon-\cos^2\beta)}\left\{\tfrac{\epsilon}{\rho}\tfrac{\partial}{\partial\phi}E_z - \cos\beta\tfrac{\partial}{\partial\rho}Z_0H_z\right\}\\
Z_0H_\phi &= \tfrac{1}{ik_0(\epsilon-\cos^2\beta)}\left\{-\epsilon\tfrac{\partial}{\partial\rho}E_z - \tfrac{\cos\beta}{\rho}\tfrac{\partial}{\partial\phi}Z_0H_z\right\} .
\end{aligned}$$

In this case the wave equation is separable and the incident and scattered fields can be expanded in terms of cylindrical eigen functions. By noting that

$$e^{-ik_0x\sin\beta} = \sum_{-\infty}^{+\infty}(-i)^m J_m(k_0\rho\sin\beta)e^{im\phi} ,$$

it can be shown that at the surface $\rho = \rho_1$ the tangential components of the total field are

$$\begin{aligned}
E_z &= \textstyle\sum_{m=-\infty}^{+\infty}(-i)^m\left\{e_zJ_m(x_0) + A_mH_m^{(1)}(x_0)\right\}e^{im\phi'+ik_0z'\cos\beta}\\
H_z &= Y_0\textstyle\sum_{m=-\infty}^{+\infty}(-i)^m\left\{h_zJ_m(x_0) + B_mH_m^{(1)}(x_0)\right\}e^{im\phi'+ik_0z'\cos\beta}
\end{aligned} \tag{7.3}$$

$$\begin{aligned}
E_\phi = \tfrac{1}{ik_0\sin^2\beta}Y_0\textstyle\sum_{m=-\infty}^{\infty}(-i)^m&\left\{k_0\sin\beta\left[h_zJ_m'(x_0) + B_mH_m^{(1)\,\prime}(x_0)\right]\right.\\
&\left.-\tfrac{im\cos\beta}{\rho_1}\left[e_zJ_m(x_0) + A_mH_m^{(1)}(x_0)\right]\right\}e^{im\phi'+ik_0z'\cos\beta}\\
H_\phi = \tfrac{Y_0}{ik_0\sin^2\beta}\textstyle\sum_{m=-\infty}^{\infty}(-i)^m&\left\{-k_0\sin\beta\left[e_zJ_m'(x_0) + A_mH_m^{(1)\,\prime}(x_0)\right]\right.\\
&\left.-\tfrac{im\cos\beta}{\rho_1}\left[h_zJ_m(x_0) + B_mH_m^{(1)}(x_0)\right]\right\}e^{im\phi'+ik_0z'\cos\beta}
\end{aligned} \tag{7.4}$$

where J_m and $H_m^{(1)}$ are the Bessel and Hankel functions respectively of order m, a prime attached to a function denotes the derivative, and $x_0 = k_0\rho_1\sin\beta$. When the boundary conditions at $\rho = \rho_1$ are imposed, we obtain [Ruck et al, 1970, pp. 273-274]:

$$\begin{aligned}
A_m &= C_m^{TM}e_z + i\bar{C}_mh_z\\
B_m &= C_m^{TE}h_z - i\bar{C}_me_z
\end{aligned} \tag{7.5}$$

where

$$C_m^{TM} = -\frac{V_m P_m - q_m^2 J_m(x_0) H_m^{(1)}(x_0) J_m^2(x_1)}{P_m N_m - \left[q_m H_m^{(1)}(x_0) J_m(x_1)\right]^2}$$

$$C_m^{TE} = -\frac{M_m N_m - q_m^2 J_m(x_0) H_m^{(1)}(x_0) J_m^2(x_1)}{P_m N_m - \left[q_m H_m^{(1)}(x_0) J_m(x_1)\right]^2} \tag{7.6}$$

$$\bar{C}_m = i\frac{2}{\pi x_0 \sin\beta} \frac{q_m J_m^2(x_1)}{P_m N_m - \left[q_m H_m^{(1)}(x_0) J_m(x_1)\right]^2}$$

with

$$\begin{aligned} x_1 &= k_0\rho_1\sqrt{\epsilon - \cos^2\beta} \\ q_m &= mk_0\rho_1\cos\beta\left(\tfrac{1}{x_1^2} - \tfrac{1}{x_0^2}\right) \\ V_m &= k_0\rho_1\left\{\tfrac{\epsilon}{x_1}J_m(x_0)J_m'(x_1) - \tfrac{1}{x_0}J_m'(x_0)J_m(x_1)\right\} \\ P_m &= k_0\rho_1\left\{\tfrac{1}{x_1}H_m^{(1)}(x_0)J_m'(x_1) - \tfrac{1}{x_0}H_m^{(1)\,\prime}(x_0)J_m(x_1)\right\} \\ N_m &= k_0\rho_1\left\{\tfrac{\epsilon}{x_1}H_m^{(1)}(x_0)J_m'(x_1) - \tfrac{1}{x_0}H_m^{(1)\,\prime}(x_0)J_m(x_1)\right\} \\ M_m &= k_0\rho_1\left\{\tfrac{1}{x_1}J_m(x_0)J_m'(x_1) - \tfrac{1}{x_0}J_m'(x_0)J_m(x_1)\right\} . \end{aligned} \tag{7.7}$$

By invoking the field equivalence principle, the scattered field outside the cylinder region can be attributed to fictitious electric $\mathbf{J}_e$ and magnetic $\mathbf{J}_m$ surface currents given by

$$\mathbf{J}_e = \hat{n}' \times \mathbf{H} , \qquad \mathbf{J}_m = -\hat{n}' \times \mathbf{E} \tag{7.8}$$

where $\mathbf{E}$ and $\mathbf{H}$ are the total electric and magnetic field over the surface of the cylinder and $\hat{n}'$ is the unit vector outward normal to the surface. The surface currents are therefore

$$\begin{aligned} \mathbf{J}_e = {} & Y_0(\sin\phi'\hat{x}' - \cos\phi'\hat{y}')\textstyle\sum_{m=-\infty}^{+\infty}(-i)^m\{h_z J_m(x_0) + B_m H_m^{(1)}(x_0)\}e^{im\phi'+ik_0z'\cos\beta} \\ & -\tfrac{Y_0}{ik_0\sin^2\beta}\hat{z}'\textstyle\sum_{m=-\infty}^{+\infty}(-i)^m\left\{k_0\sin\beta\left[e_z J_m'(x_0) + A_m H_m^{(1)\,\prime}(x_0)\right]\right. \\ & \left. +\tfrac{im\cos\beta}{\rho_1}\left[h_z J_m(x_0) + B_m H_m^{(1)}(x_0)\right]\right\}e^{im\phi'+ik_0z'\cos\beta} , \end{aligned} \tag{7.9}$$

$$\begin{aligned} \mathbf{J}_m = {} & -(\sin\phi'\hat{x}' - \cos\phi'\hat{y}')\textstyle\sum_{m=-\infty}^{+\infty}(-i)^m\{e_z J_m(x_0) + A_m H_m^{(1)}(x_0)\}e^{im\phi'+ik_0z'\cos\beta} \\ & -\tfrac{Y_0}{ik_0\sin^2\beta}\hat{z}'\textstyle\sum_{m=-\infty}^{+\infty}(-i)^m\left\{k_0\sin\beta\left[h_z J_m'(x_0) + B_m H_m^{(1)\,\prime}(x_0)\right]\right. \\ & \left. -\tfrac{im\cos\beta}{\rho_1}\left[e_z J_m(x_0) + A_m H_m^{(1)\,\prime}(x_0)\right]\right\}e^{im\phi'+ik_0z'\cos\beta} . \end{aligned} \tag{7.10}$$

In order to find the scattered fields for a cylinder of finite length $b(\gg \lambda_0)$, $-\frac{b}{2} < z' < \frac{b}{2}$, we may assumed that the currents on the curved sides are the same as those on the infinite cylinder. If the effect of the end caps is ignored, the Hertz vectors describing the scattered field are

$$\begin{aligned}\mathbf{\Pi}_e(\mathbf{r}) &= \frac{e^{ik_0 r}}{r}\left(\frac{iZ_0}{4\pi k_0}\right)\int_{-\frac{b}{2}}^{\frac{b}{2}}\int_0^{2\pi}\mathbf{J}_e e^{-ik_0\rho_1 B\cos(\phi'-\tilde{\phi})}e^{ik_0(\hat{k}_i-\hat{k}_s)\cdot\hat{z}'z'}\rho_1 \mathrm{d}\phi'\mathrm{d}z' \\ \mathbf{\Pi}_m(\mathbf{r}) &= \frac{e^{ik_0 r}}{r}\left(\frac{iY_0}{4\pi k_0}\right)\int_{-\frac{b}{2}}^{\frac{b}{2}}\int_0^{2\pi}\mathbf{J}_m e^{-ik_0\rho_1 B\cos(\phi'-\tilde{\phi})}e^{ik_0(\hat{k}_i-\hat{k}_s)\cdot\hat{z}'z'}\rho_1 \mathrm{d}\phi'\mathrm{d}z'\end{aligned} \tag{7.11}$$

where $\tilde{\phi}$ and B are given by

$$B = \left\{[\hat{k}_s\cdot\hat{x}']^2 + [\hat{k}_s\cdot\hat{y}']^2\right\}^{\frac{1}{2}}$$

and

$$\cos\tilde{\phi} = \frac{1}{B}\hat{k}_s\cdot\hat{x}'\,, \qquad \sin\tilde{\phi} = \frac{1}{B}\hat{k}_s\cdot\hat{y}'\,.$$

The integrations in (7.11) can be carried out exactly. The z' integration produces $b\frac{\sin V}{V}$ with $V = \frac{1}{2}k_0 b(\hat{k}_i - \hat{k}_s)\cdot\hat{z}'$ and

$$\begin{aligned}\int_0^{2\pi} e^{-ik_0\rho_1 B\cos(\phi'-\tilde{\phi})}e^{im\phi'}\mathrm{d}\phi' &= 2\pi(-i)^m J_m(y_0)e^{im\tilde{\phi}} \\ \int_0^{2\pi}\cos\phi' e^{-ik_0\rho_1 B\cos(\phi'-\tilde{\phi})}e^{im\phi'}\mathrm{d}\phi' &= 2\pi(-i)^m\left\{i\cos\tilde{\phi}J_m'(y_0) + \sin\tilde{\phi}\frac{m}{y_0}J_m(y_0)\right\}e^{im\tilde{\phi}} \\ \int_0^{2\pi}\sin\phi' e^{-ik_0\rho_1 B\cos(\phi'-\tilde{\phi})}e^{im\phi'}\mathrm{d}\phi' &= 2\pi(-i)^m\left\{i\sin\tilde{\phi}J_m'(y_0) - \cos\tilde{\phi}\frac{m}{y_0}J_m(y_0)\right\}e^{im\tilde{\phi}}\end{aligned} \tag{7.12}$$

where $y_0 = k_0\rho_1 B$. Hence, the scattering amplitude is

$$\mathbf{S} = \frac{k_0\rho_1 b}{2\sin\beta}\left\{(D^e e_z + i\bar{D}^e h_z)\hat{k}_s\times(\hat{k}_s\times\hat{z}') + (D^h h_z - i\bar{D}^h e_z)\hat{k}_s\times\hat{z}'\right\}\frac{\sin V}{V} \tag{7.13}$$

with

$$
\begin{aligned}
D^e = \; & \sum_{m=-\infty}^{+\infty}(-1)^m \Big\{ J_m'(x_0)J_m(y_0) - \tfrac{\sin\beta}{B} J_m(x_0)J_m'(y_0) + C_m^{TM}\Big[H_m^{(1)\,\prime}(x_0)J_m(y_0) \\
& - \tfrac{\sin\beta}{B} H_m^{(1)}(x_0)J_m'(y_0)\Big] + \tfrac{m\cos\beta}{x_0}\Big(1 - \tfrac{\hat{k}_s\cdot\hat{z}'}{\cos\beta}\tfrac{x_0\sin\beta}{y_0 B}\Big)\bar{C}_m H_m^{(1)}(x_0)J_m(y_0)\Big\} e^{im\tilde{\phi}} \\
D^h = \; & \sum_{m=-\infty}^{+\infty}(-1)^m \Big\{ J_m'(x_0)J_m(y_0) - \tfrac{\sin\beta}{B} J_m(x_0)J_m'(y_0) + C_m^{TE}\Big[H_m^{(1)\,\prime}(x_0)J_m(y_0) \\
& - \tfrac{\sin\beta}{B} H_m^{(1)}(x_0)J_m'(y_0)\Big] + \tfrac{m\cos\beta}{x_0}\Big(1 - \tfrac{\hat{k}_s\cdot\hat{z}'}{\cos\beta}\tfrac{x_0\sin\beta}{y_0 B}\Big)\bar{C}_m H_m^{(1)}(x_0)J_m(y_0)\Big\} e^{im\tilde{\phi}} \\
\bar{D}^e = \; & \sum_{m=-\infty}^{+\infty}(-1)^m \Big\{ \bar{C}_m\Big[H_m^{(1)\,\prime}(x_0)J_m(y_0) - \tfrac{\sin\beta}{B} H_m^{(1)}(x_0)J_m'(y_0)\Big] \\
& + \tfrac{m\cos\beta}{x_0}\Big(1 - \tfrac{\hat{k}_s\cdot\hat{z}'}{\cos\beta}\tfrac{x_0\sin\beta}{y_0 B}\Big)\Big[J_m(x_0) + C_m^{TE}H_m^{(1)}(x_0)\Big]J_m(y_0)\Big\} e^{im\tilde{\phi}} \\
\bar{D}^h = \; & \sum_{m=-\infty}^{+\infty}(-1)^m \Big\{ \bar{C}_m\Big[H_m^{(1)\,\prime}(x_0)J_m(y_0) - \tfrac{\sin\beta}{B} H_m^{(1)}(x_0)J_m'(y_0)\Big] \\
& + \tfrac{m\cos\beta}{x_0}\Big(1 - \tfrac{\hat{k}_s\cdot\hat{z}'}{\cos\beta}\tfrac{x_0\sin\beta}{y_0 B}\Big)\Big[J_m(x_0) + C_m^{TM}H_m^{(1)}(x_0)\Big]J_m(y_0)\Big\} e^{im\tilde{\phi}} \; .
\end{aligned}
\tag{7.14}
$$

The elements of the scattering matrix in the global coordinate system as defined in Section 1.4 are

$$
\begin{aligned}
S_{VV} = -\Big\{ & \Big[D^e(\hat{v}_i\cdot\hat{z}') + i\bar{D}^e(\hat{h}_i\cdot\hat{z}')\Big](\hat{v}_s\cdot\hat{z}') + \Big[D_h(\hat{h}_i\cdot\hat{z}') \\
& - i\bar{D}^h(\hat{v}_i\cdot\hat{z}')\Big](\hat{h}_s\cdot\hat{z}')\Big\}\tfrac{k_0\rho_1 b}{2\sin\beta}\tfrac{\sin V}{V}
\end{aligned}
\tag{7.15}
$$

$$
\begin{aligned}
S_{VH} = -\Big\{ & \Big[D^e(\hat{h}_i\cdot\hat{z}') - i\bar{D}^e(\hat{v}_i\cdot\hat{z}')\Big](\hat{v}_s\cdot\hat{z}') - [D_h(\hat{v}_i\cdot\hat{z}') \\
& + i\bar{D}^h(\hat{h}_i\cdot\hat{z}')\Big](\hat{h}_s\cdot\hat{z}')\Big\}\tfrac{k_0\rho_1 b}{2\sin\beta}\tfrac{\sin V}{V}
\end{aligned}
\tag{7.16}
$$

$$
\begin{aligned}
S_{HV} = -\Big\{ & \Big[D^e(\hat{v}_i\cdot\hat{z}') + i\bar{D}^e(\hat{h}_i\cdot\hat{z}')\Big](\hat{h}_s\cdot\hat{z}') - \Big[D^h(\hat{h}_i\cdot\hat{z}') \\
& - i\bar{D}^h(\hat{v}_i\cdot\hat{z}')\Big](\hat{v}_s\cdot\hat{z}')\Big\}\tfrac{k_0\rho_1 b}{2\sin\beta}\tfrac{\sin V}{V}
\end{aligned}
\tag{7.17}
$$

$$
\begin{aligned}
S_{HH} = -\Big\{ & \Big[D^e(\hat{h}_i\cdot\hat{z}') - i\bar{D}^e(\hat{v}_i\cdot\hat{z}')\Big](\hat{h}_s\cdot\hat{z}') + \Big[D^h(\hat{v}_i\cdot\hat{z}') \\
& + i\bar{D}^h(\hat{h}_i\cdot\hat{z}')\Big](\hat{v}_s\cdot\hat{z}')\Big\}\tfrac{k_0\rho_1 b}{2\sin\beta}\tfrac{\sin V}{V}
\end{aligned}
\tag{7.18}
$$

where $\hat{v}_i$, $\hat{h}_i$, $\hat{v}_s$, and $\hat{h}_s$ are given by (1.9) and (1.10). The orientation of the cylinder in the global coordinate system can be specified completely by specifying the axis of the cylinder. If the z' axis is defined by polar angles θ_c and ϕ_c, then

$$
\hat{z}' = \sin\theta_c\cos\phi_c\hat{x} + \sin\theta_c\sin\phi_c\hat{y} + \cos\theta_c\hat{z} \; . \tag{7.19}
$$

In terms of polar coordinates of incidence, scattered, and the cylinder axis vectors we have

$$\begin{aligned} \hat{k}_i \cdot \hat{x}' &= -\sin\beta = -C \\ \hat{k}_i \cdot \hat{z}' &= \cos\theta_c \cos\theta_i + \sin\theta_c \sin\theta_i \cos(\phi_i - \phi_c) \end{aligned} \tag{7.20}$$

where

$$C = \left\{1 - [\cos\theta_c \cos\theta_i + sin\theta_c \sin\theta_i \cos(\phi_i - \phi_c)]^2\right\}^{\frac{1}{2}} \tag{7.21}$$

Also

$$\begin{aligned} \hat{v}_i \cdot \hat{z}' &= -\cos\theta_c \sin\theta_i + \sin\theta_c \cos\theta_i \cos(\phi_i - \phi_c) \\ \hat{h}_i \cdot \hat{z}' &= -\sin\theta_c \sin(\phi_i - \phi_c) \ . \end{aligned} \tag{7.22}$$

and for the scattered field

$$\begin{aligned} \hat{k}_s \cdot \hat{x}' = \ & \tfrac{1}{C}\left\{\sin^2\theta_c \sin\theta_i \sin\theta_s \cos(\phi_i - \phi_c)\cos(\phi_s - \phi_c) + \sin\theta_c \cos\theta_c \right. \\ & [\sin\theta_i \cos\theta_s \cos(\phi_i - \phi_c) + \cos\theta_i \sin\theta_s \cos(\phi_s - \phi_c)] \\ & \left. - \sin^2\theta_c \cos\theta_i \cos\theta_s - \sin\theta_i \sin\theta_s \cos(\phi_i - \phi_s)\right\} \\ \hat{k}_s \cdot \hat{y}' = \ & \tfrac{1}{C}\left\{\cos\theta_c \sin\theta_i \sin\theta_s \sin(\phi_i - \phi_s) + \sin\theta_c \cos\theta_i \sin\theta_s \sin(\phi_s - \phi_c)\right. \\ & \left. - \sin\theta_c \sin\theta_i \cos\theta_s \sin(\phi_i - \phi_c)\right\} \\ \hat{k}_s \cdot \hat{z}' = \ & \cos\theta_c \cos\theta_s + \sin\theta_c \sin\theta_s \cos(\phi_s - \phi_c) \end{aligned} \tag{7.23}$$

with

$$\begin{aligned} \hat{v}_s \cdot \hat{z}' &= -\cos\theta_c \sin\theta_s + \sin\theta_c \cos\theta_s \cos(\phi_s - \phi_c) \\ \hat{h}_s \cdot \hat{z}' &= -\sin\theta_c \sin(\phi_s - \phi_c) \ . \end{aligned} \tag{7.24}$$

The expressions given by (7.15)-(7.18) differ from, and are potentially more accurate than, those given by Ruck et al (1970). In effect, the far field amplitude for the cylinder of finite length b is given in terms of the far field of the infinite cylinder by simply multiplying a factor proportional to $b\frac{\sin V}{V}$. Since the field of the infinite cylinder exists only on the forward scattering cone having $\hat{k}_s \cdot \hat{z}' = \hat{k}_i \cdot \hat{z}' = \cos\beta$, the polarization characteristics are those appropriate to these aspects alone. On the

cone $B = \sin\beta$, so that $y_0 = x_0$. Equation (7.13) then reduces to

$$\mathbf{S} = -\frac{ib}{\pi \sin^2\beta}\frac{\sin V}{V}\sum_{m=-\infty}^{+\infty}(-1)^m\left\{A_m\hat{k}_s \times (\hat{k}_s \times \hat{z}') + B_m\hat{k}_s \times \hat{z}'\right\}e^{im\phi}\ ,$$

that is

$$\mathbf{S} = -\frac{ib}{\pi \sin^2\beta}\frac{\sin V}{V}\sum_{m=-\infty}^{+\infty}(-1)^m\left\{-\cos\beta A_m\hat{\rho} + B_m\hat{\phi} + \sin\beta A_m\hat{z}\right\}e^{im\phi}\ , \qquad (7.25)$$

and the sum is proportional to the far zone scattered electric field in the two-dimensional case.

The improved accuracy which (7.13) provides is, however, limited. Because the effect of the cylinder caps is ignored and the termination of the curved sides is not correctly modelled by simply truncating the current, the accuracy of (7.13) and, hence, the scattering matrix elements, deteriorates with increasing $\hat{k}_i \cdot \hat{z}'$ and/or $\hat{k}_s \cdot \hat{z}'$, but for aspects which are not too oblique, the transverse resonances of the cylinder should be accurately simulated.

7.3 Physical Optics Approximation

The semi-exact solution for circular cylinder given in the previous section is rather complicated and becomes very inefficient when radius of the cylinder is large compared with the wavelength. In fact the convergence rate of the series given by (7.14) is very poor when x_0 and/or y_0 are large. To treat stratified cylinders we have to deal with even a more complicated form and when the cylinder cross section is not circular there is no exact solution available. Under such conditions approximate solutions must be considered. An approximate solution at low frequencies was discussed in Chapter 6 and a high frequency approximation (physical optics) will be given here for lossy dielectric cylinders with large radius of curvature.

7.3.1 Cylinder of Arbitrary Cross Section

Suppose the surface of the cylinder is such that the radius of curvature is much larger than the wave length and there is a unique normal $\hat{n}'$ at each point on the cylinder. Thus, at high frequencies, each portion of the surface appears locally flat, and if it is regarded as part of an infinite plane, the local boundary value problem is that of a plane wave incident on a dielectric half space.

For the incident plane wave

$$\mathbf{E}^i = \mathbf{E}_0 e^{ik_0 \hat{k}_i \cdot \mathbf{r}} , \qquad \mathbf{H}^i = \mathbf{H}_0 e^{ik_0 \hat{k}_i \cdot \mathbf{r}} \tag{7.26}$$

let $\hat{t}$ be a unit vector perpendicular to the plane of incidence. Then by decomposing the incident field into vectors parallel and perpendicular to the plane of incidence we get

$$\mathbf{E}^i = \{A(\hat{k}_i \times \hat{t}) + B\hat{t}\} e^{ik_0 \hat{k}_i \cdot \mathbf{r}}$$

implying

$$\mathbf{H}^i = Y_0 \{B(\hat{k}_i \times \hat{t}) - A\hat{t}\} e^{ik_0 \hat{k}_i \cdot \mathbf{r}} .$$

The reflected plane wave is

$$\mathbf{E}^r = \{AR_H(\hat{k}_r \times \hat{t}) + BR_E\hat{t}\} e^{ik_0 \hat{k}_r \cdot \mathbf{r}} ,$$

$$\mathbf{H}^r = \{BR_E(\hat{k}_r \times \hat{t}) - AR_H\hat{t}\} e^{ik_0 \hat{k}_r \cdot \mathbf{r}} ,$$

where

$$\hat{k}_r = \hat{k}_i - 2(\hat{k}_i \cdot \hat{n}')\hat{n}' \tag{7.27}$$

and R_E, R_H are the Fresnel reflection coefficients. Clearly

$$A = -Z_0 \mathbf{H}_0 \cdot \hat{t} , \qquad B = \mathbf{E}_0 \cdot \hat{t} ,$$

and in the lit region the standard physical optics approximations to the equivalent surface currents are

$$\mathbf{J}_e = \hat{n}' \times (\mathbf{H}^i + \mathbf{H}^r) \,, \qquad \mathbf{J}_m = -\hat{n}' \times (\mathbf{E}^i + \mathbf{E}^r)$$

and therefore

$$\mathbf{J}_e = -\left\{Y_0(1 - R_E)(\mathbf{E}_0 \cdot \hat{t})(\hat{n}' \cdot \hat{k}_i)\hat{t} - (1 + R_H)(\mathbf{H}_0 \cdot \hat{t})\hat{n}' \times \hat{t}\right\} e^{ik_0 \hat{k}^i \cdot \mathbf{r}} \tag{7.28}$$

$$\mathbf{J}_m = -\left\{Z_0(1 - R_H)(\mathbf{H}_0 \cdot \hat{t})(\hat{n}' \cdot \hat{k}_i)\hat{t} + (1 + R_E)(\mathbf{E}_0 \cdot \hat{t})\hat{n}' \times \hat{t}\right\} e^{ik_0 \hat{k}^i \cdot \mathbf{r}} \,. \tag{7.29}$$

On the assumption that the loss is sufficient to prevent any penetration through, the electric and magnetic surface currents are zero on the shadowed region of the surface. Expressions (7.28) and (7.29) are equivalent to, but simpler than, those given by Beckmann [1965, p.85], and their symmetry is noteworthy.

Now the physical optics approximations to the electric and magnetic Hertz vectors in the far zone can be obtained and are of the following form

$$\mathbf{\Pi}_e(\mathbf{r}) = \tfrac{e^{ik_0 r}}{r}\left(-\tfrac{i}{4\pi k_0}\right) \int_{lit} \left\{(1 - R_E)(\mathbf{E}_0 \cdot \hat{t})(\hat{n}' \cdot \hat{k}_i)\hat{t} - Z_0(1 + R_H)(\mathbf{H}_0 \cdot \hat{t})\hat{n}' \times \hat{t}\right\} e^{ik_0(\hat{k}_i - \hat{k}_s)\cdot \mathbf{r}'} \mathrm{d}s'$$

$$\mathbf{\Pi}_m(\mathbf{r}) = \tfrac{e^{ik_0 r}}{r}\left(-\tfrac{i}{4\pi k_0}\right) \int_{lit} \left\{(1 - R_H)(\mathbf{H}_0 \cdot \hat{t})(\hat{n}' \cdot \hat{k}_i)\hat{t} + Y_0(1 + R_E)(\mathbf{E}_0 \cdot \hat{t})\hat{n}' \times \hat{t}\right\} e^{ik_0(\hat{k}_i - \hat{k}_s)\cdot \mathbf{r}'} \mathrm{d}s'$$

and the scattering amplitude is

$$\begin{aligned} \mathbf{S} = \tfrac{ik_0}{4\pi} \int_{lit} \Big\{ & (1 - R_E)(\mathbf{E}_0 \cdot \hat{t})(\hat{n}' \cdot \hat{k}_i)\hat{k}_s \times (\hat{k}_s \times \hat{t}) + (1 + R_E)(\mathbf{E}_0 \cdot \hat{t})\hat{k}_s \times (\hat{n}' \times \hat{t}) \\ & + Z_0(1 - R_H)(\mathbf{H}_0 \cdot \hat{t})(\hat{n}' \cdot \hat{k}_i)\hat{k}_s \times \hat{t} - Z_0(1 + R_H)(\mathbf{H}_0 \cdot \hat{t})\hat{k}_s \times \hat{k}_s \\ & \times (\hat{n}' \times \hat{t})\Big\} e^{ik_0(\hat{k}_i - \hat{k}_s)\cdot \mathbf{r}'} \mathrm{d}s' \end{aligned} \tag{7.30}$$

where the integration is confined to the illuminated portion of the surface.

With any cylinder whose local reflection coefficients R_E and R_H can be determined, the integral can be evaluated, and a convenient method to employ is the

stationary phase approximation which leads to an analytical expression for **S**. If, for simplicity, it is assumed that the cylinder is convex, there is a single SP point which is also the specular reflection point of geometrical optics. When the non-exponential portion of the integrand is evaluated at the SP point, the elements of the scattering matrix are found to be

$$S_{VV} = -\left\{R_H(\hat{n}' \cdot \hat{v}_i)(\hat{n}' \cdot \hat{v}_s) + R_E(\hat{n}' \cdot \hat{h}_i)(\hat{n}' \cdot \hat{h}_s)\right\} \frac{\hat{n}' \cdot \hat{k}_i}{|\hat{n}' \times \hat{k}_i|^2} Q \tag{7.31}$$

$$S_{VH} = -\left\{R_H(\hat{n}' \cdot \hat{h}_i)(\hat{n}' \cdot \hat{v}_s) - R_E(\hat{n}' \cdot \hat{v}_i)(\hat{n}' \cdot \hat{h}_s)\right\} \frac{\hat{n}' \cdot \hat{k}_i}{|\hat{n}' \times \hat{k}_i|^2} Q \tag{7.32}$$

$$S_{HV} = -\left\{R_H(\hat{n}' \cdot \hat{v}_i)(\hat{n}' \cdot \hat{h}_s) - R_E(\hat{n}' \cdot \hat{h}_i)(\hat{n}' \cdot \hat{v}_s)\right\} \frac{\hat{n}' \cdot \hat{k}_i}{|\hat{n}' \times \hat{k}_i|^2} Q \tag{7.33}$$

$$S_{HH} = -\left\{R_H(\hat{n}' \cdot \hat{h}_i)(\hat{n}' \cdot \hat{h}_s) + R_E(\hat{n}' \cdot \hat{v}_i)(\hat{n}' \cdot \hat{v}_s)\right\} \frac{\hat{n}' \cdot \hat{k}_i}{|\hat{n}' \times \hat{k}_i|^2} Q \tag{7.34}$$

where we have used (7.27) with $\hat{k}_r$ replaced by $\hat{k}_s$ to simplify the expressions, and

$$Q = -\frac{ik_0}{2\pi} \int_{lit} e^{ik_0(\hat{k}_i - \hat{k}_s)\cdot \mathbf{r}'} \mathrm{d}s' \,. \tag{7.35}$$

The boundary of the lit region is the curve $\hat{n}' \cdot \hat{k}_i = 0$ on the surface, and as $\hat{k}_s$ approaches $\hat{k}_i$, the specular point approaches the boundary. More importantly, the parameter which is assumed large in the SP approximation tends to zero as $\hat{k}_s \to \hat{k}_i$ and the method fails, but an alternative evaluation is now possible. For $\hat{k}_s = \hat{k}_i$, $R_E = R_H = -1$ and the terms in braces in the integrand of (7.30) reduce to $-2(\hat{n}' \cdot \hat{k}_i)\mathbf{E}_0$, giving

$$\mathbf{S} = -\frac{i}{\lambda_0}\mathbf{E}_0 \int_{lit} \hat{n}' \cdot \hat{k}_i \mathrm{d}s' = \frac{iA_p}{\lambda_0}\mathbf{E}_0 \tag{7.36}$$

where A_p is the planar area enclosed by the boundary of the illuminated and shadowed regions on the surface. There is no depolarization and we observe that (7.36) is identical to the result for a flat plate whose projected area perpendicular to $\hat{k}_i$ is A_p.

The above results are valid for any impenetrable convex body of large dimensions whose local reflection coefficients R_E and R_H are known, and can be generalized to a non-convex body which may possess more than one SP point. We shall now examine the special cases of a circular cylinder for which the integral expression for Q can be evaluated analytically.

7.3.2 Circular Cylinder

Consider the right circular cylinder as specified in Section 7.2. The unit normal vector to the surface and position vector on the surface are respectively given by

$$\begin{aligned} \hat{n}' &= \cos\phi'\hat{x}' + \sin\phi'\hat{y}' \\ \mathbf{r}' &= \rho_1(\cos\phi'\hat{x}' + \sin\phi'\hat{y}') + z'\hat{z}' \end{aligned}$$

and if ϕ' is measured from the plane defined by $\hat{k}_i$ and $\hat{z}'$, the illuminated region is $|\phi'| < \frac{\pi}{2}$ with $-\frac{b}{2} < z' < \frac{b}{2}$. Then

$$Q = -\frac{ik_0\rho_1}{2\pi}\int_{-\frac{b}{2}}^{\frac{b}{2}}\int_{-\frac{\pi}{2}}^{\frac{\pi}{2}} e^{-ik_0B\rho_1\cos(\phi'-\tilde{\phi})}e^{-ik_0(\hat{k}_s-\hat{k}_i)\cdot\hat{z}'z'}\,\mathrm{d}\phi'\mathrm{d}z' \tag{7.37}$$

where $\tilde{\phi}$ and B are defined as before. The z' integration can be carried out immediately, giving $b\frac{\sin V}{V}$ and provided $k_0B\rho_1 >> 1$, the ϕ' integral can be evaluated using the SP method. The SP point is $\phi' = \tilde{\phi}$ giving

$$Q = -\frac{ib}{\pi}\sqrt{\frac{k_0\rho_1}{2B}}e^{-ik_0B\rho_1}\left\{\mathcal{F}\left[\sqrt{\frac{k_0B\rho_1}{2}}\left(\frac{\pi}{2}+\tilde{\phi}\right)\right]+\mathcal{F}\left[\sqrt{\frac{k_0B\rho_1}{2}}\left(\frac{\pi}{2}-\tilde{\phi}\right)\right]\right\}\frac{\sin V}{V}, \tag{7.38}$$

and at aspects for which $\sqrt{\frac{k_0B\rho_1}{2}}(\frac{\pi}{2}\pm\tilde{\phi}) \gg 1$, the expression can be simplified using (3.16)

$$Q = b\sqrt{\frac{k_0B\rho_1}{2B\pi}}e^{-i\frac{\pi}{4}-ik_0B\rho_1}\frac{\sin V}{V}. \tag{7.39}$$

The above results fail in the forward scattering direction for which $B = 0$, but in directions close to forward, an alternative approximation is possible. In near forward directions $(\hat{k}_s - \hat{k}_i) \cdot \hat{x}' \approx 0$ and $\hat{k}_s \cdot \hat{y}' \ll 1$, thus

$$\begin{aligned} \mathbf{S} &\approx -\frac{ib\rho_1}{\lambda_0}\mathbf{E}_0 \frac{\sin V}{V} \int_{-\frac{\pi}{2}}^{\frac{\pi}{2}} \hat{n}' \cdot \hat{k}_i e^{-ik_0\rho_1\left\{(\hat{k}_s - \hat{k}_i)\cdot\hat{x}'\cos\phi' + \hat{k}_s\cdot\hat{y}'\sin\phi'\right\}} \mathrm{d}\phi' \\ &\approx -\frac{ib\rho_1}{\lambda_0}(\hat{k}_i \cdot \hat{x}')\frac{\sin V}{V}\mathbf{E}_0 \int_{-\frac{\pi}{2}}^{\frac{\pi}{2}} \cos\phi' e^{ik_0\rho_1(\hat{k}_s\cdot\hat{y}')\sin\phi'} \mathrm{d}\phi' \\ &= -\frac{2ib\rho_1}{\lambda_0}(\hat{k}_i \cdot \hat{x}')\frac{\sin V}{V}\frac{\sin W}{W}\mathbf{E}_0 \end{aligned} \tag{7.40}$$

with

$$W = k_0\rho_1(\hat{k}_s \cdot \hat{y}') \ .$$

When $\hat{k}_s = \hat{k}_i$ implying $\hat{k}_s \cdot \hat{y}' = 0$ and, hence, $W = V = 0$, (7.40) reduces to (7.36).

Because of the importance of the solution for a circular cylinder, it is desirable to express the results in a global coordinate system (X, Y, Z). In (7.31) - (7.34) all quantities with the possible exception of Q are evaluated at the stationary phase point such that

$$\hat{k}_s = \hat{k}_i - 2(\hat{k}_i \cdot \hat{n}')\hat{n}' \ . \tag{7.41}$$

At the SP point

$$\hat{n}' = \cos\tilde{\phi}\hat{x}' + \sin\tilde{\phi}\hat{y}'$$

using (7.41) we have

$$\hat{n}' = \frac{1}{B}\left\{(\hat{k}_s - \hat{k}_i)\cdot\hat{x}'\hat{x}' + (\hat{k}_s\cdot\hat{y}')\hat{y}'\right\}$$

and it can be shown that in scattering directions other than forward

$$B = -2\hat{n}' \cdot \hat{k}_i \ .$$

Then

$$\begin{aligned} \hat{n}' \cdot \hat{v}_i &= \frac{1}{BC}\left\{\left[(\hat{k}_s - \hat{k}_i)\cdot\hat{x}'\right](\hat{k}_i\cdot\hat{z}')(\hat{v}_i\cdot\hat{z}') - (\hat{k}_s\cdot\hat{y}')(\hat{h}_i\cdot\hat{z}')\right\} \\ \hat{n}' \cdot \hat{h}_i &= \frac{1}{BC}\left\{\left[(\hat{k}_s - \hat{k}_i)\cdot\hat{x}'\right](\hat{k}_i\cdot\hat{z}')(\hat{h}_i\cdot\hat{z}') + (\hat{k}_s\cdot\hat{y}')(\hat{v}_i\cdot\hat{z}')\right\} \end{aligned} \tag{7.42}$$

which can be evaluated using (7.20) - (7.23), and

$$\begin{aligned} \hat{n}' \cdot \hat{v}_s &= \tfrac{1}{B}\{\cos\theta_i \sin\theta_s - \sin\theta_i \cos\theta_s \cos(\phi_i - \phi_s)\} \\ \hat{n}' \cdot \hat{h}_s &= -\tfrac{1}{B}\sin\theta_i \sin(\phi_i - \phi_s) \end{aligned} \tag{7.43}$$

7.4 Numerical Results

From a physical point of view, the scattering from a dielectric cylinder of radius comparable to or greater than the wavelength can be attributed to two types of mechanism: ray reflections from the surface and from multiple internal bounces, for example, the glory ray; and surface waves which propagate around the cylinder, shedding energy as they go. The latter are the main source of the field in the geometric shadow of perfectly conducting and very lossy cylinders. For a lossless cylinder, the internally-reflected rays produce a backscattered field which is an extremely complicated function of frequency and is almost noise-like even for the largest values of $k_0\rho_1$. If the cylinder is lossy, however, these resonances diminish as $k_0\rho_1$ and/or the loss tangent increases. This is illustrated in Figs. 7.1 and 7.2 where the normalized backscattering cross section $\frac{\sigma}{(k_0\rho_1 b^2)}$ is plotted as a function of $k_0\rho_1$ for E (or TM) or H (or TE) polarizations respectively for $\epsilon = 10 + i\epsilon''$ with $\epsilon'' = 1, 2$ and 5.

Principal plane bistatic scattering patterns for a homogeneous cylinder having $\rho_1 = 2\lambda_0$ and $\epsilon = 10 + i5$ computed using the physical optics approximations are shown in Figs. 7.3 and 7.4 for TM and TE polarizations respectively. The quantity plotted is the normalized scattering cross section $\frac{\sigma}{\sigma_0}$ where $\sigma_0 = k_0\rho_1 b^2$ is the physical optics value for the backscattering cross section of a perfectly conducting cylinder, and the ratio is therefore independent of the length b of the cylinder. The solid curves were computed using (7.31) and (7.34) with Q given by (7.39), and we note that the angular dependence (including the Brewster angle effect for H-polarization)

is attributable to the reflection coefficients R_E and R_H. The (common) dashed curves are based on (7.40).

In Figs. 7.5 and 7.6 the exact solution for a cylinder with $\epsilon = 10+i5$ are compared with the physical optics prediction, and the agreement is excellent for $k_0\rho_1 \geq 3$. For this same material, the bistatic scattering patterns for a cylinder of radius $\rho_1 = 2\lambda_0$ are compared in Figs. 7.7 and 7.8. The physical optics results provide a good approximation to the exact data at most angles of scatter. Comparison with the exact solution (see Figs. 7.7 and 7.8) shows that the best approximation is obtained by using the near-forward scattering expression (7.40) for the main and (perhaps) the first one or two side lobes, and (7.31), (7.34) and (7.39) at other angles.

7.5 Conclusions

Expressions for the scattering matrix elements of cylindrical structures of finite length in the global coordinate system are given. For cylinder with circular cross section the expressions are semi-exact in the sense that the equivalent surface currents on the surface of the cylinder is approximated by the surface currents that would exist if the cylinder were infinite in length. These expressions are potentially more accurate than those given by Ruck et al [1970]. At high frequencies physical optics approximation is used. The standard physical optics currents in conjunction with the stationary phase approximation provide a simple expression for the far field amplitude of finite length cylinders with arbitrary cross section. For lossy cylinders with $\rho_1 > \lambda_0$ the physical optics results are in a very good agreement with the semi-exact solution.

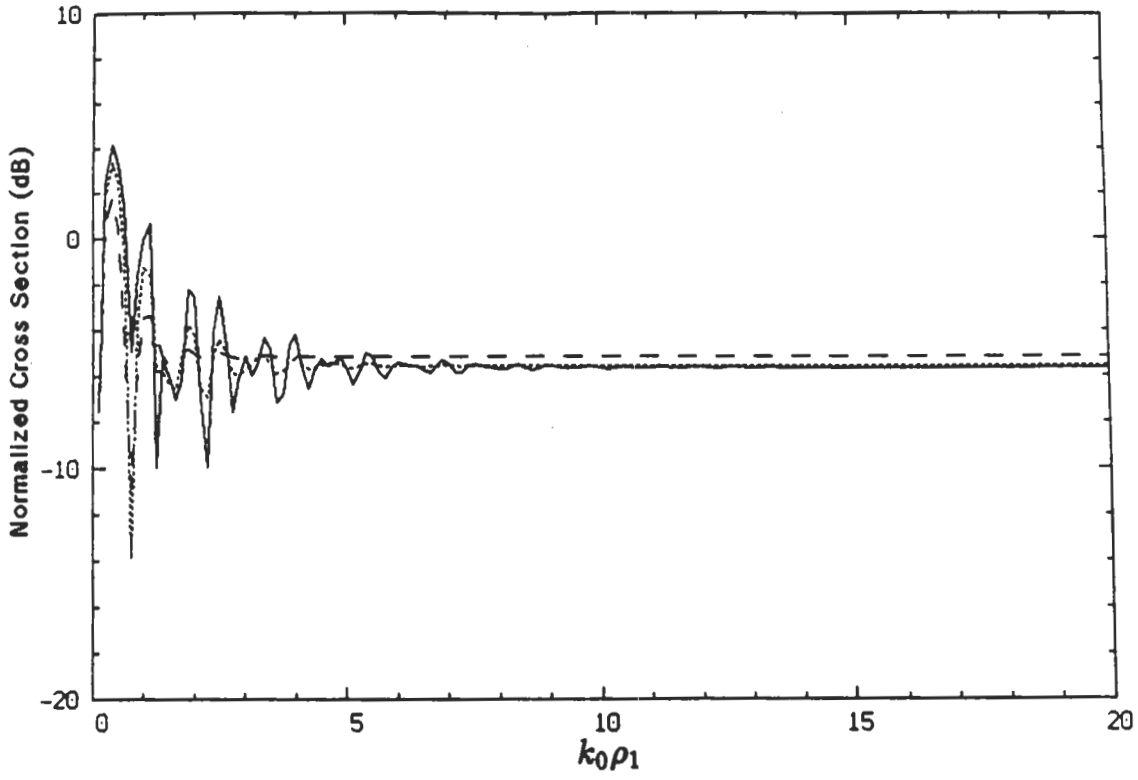

Figure 7.1: Normalized backscattering cross section $\sigma/(k_0\rho_1 b^2)$ of a circular cylinder versus $k_0\rho_1$ for E polarization and different loss tangents: (——) $\epsilon = 10 + i1$, (- - -) $\epsilon = 10 + i2$, (– –) $\epsilon = 10 + i5$.

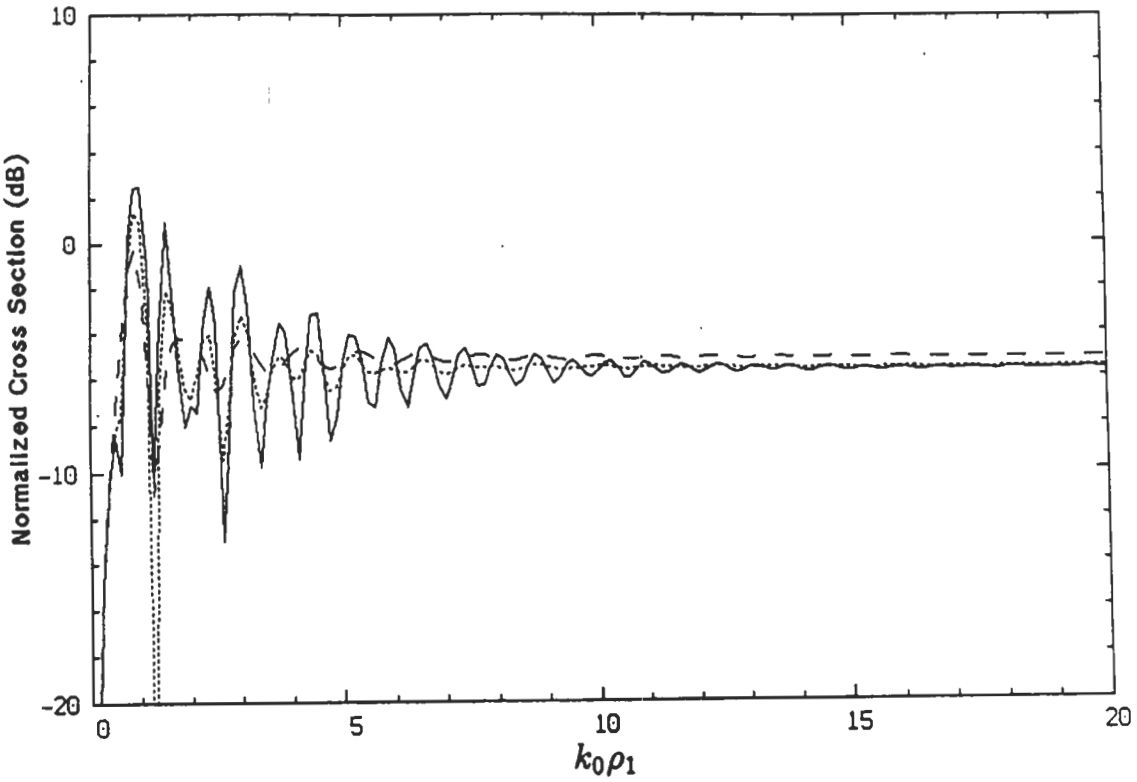

Figure 7.2: Normalized backscattering cross section $\sigma/(k_0\rho_1 b^2)$ of a circular cylinder versus $k_0\rho_1$ for H polarization and different loss tangents: (——) $\epsilon = 10 + i1$, (- - -) $\epsilon = 10 + i2$, (– –) $\epsilon = 10 + i5$.

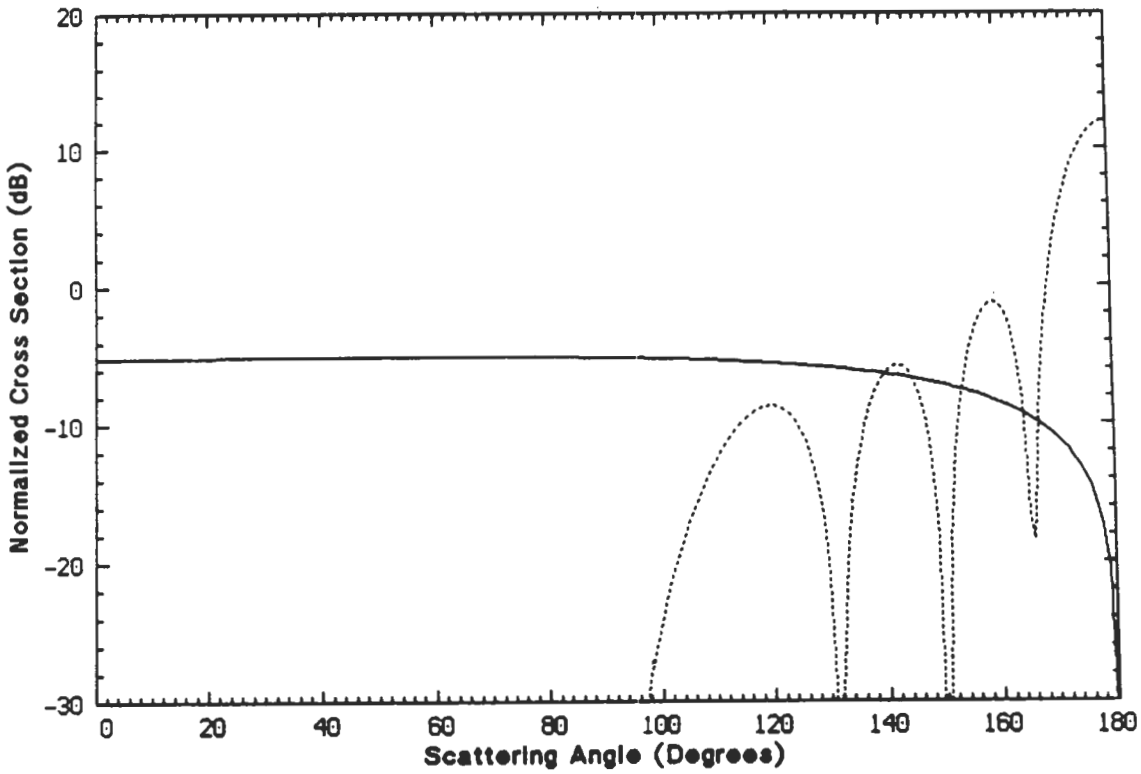

Figure 7.3: Normalized bistatic scattering cross section $\frac{\sigma}{k_0 ab^2}$ of a finite cylinder with radius $\rho_1 = 2\lambda_0$ and $\epsilon = 10 + i5$ for E polarization using physical optics: (——) stationary phase expression, (- - -) forward scattering expression.

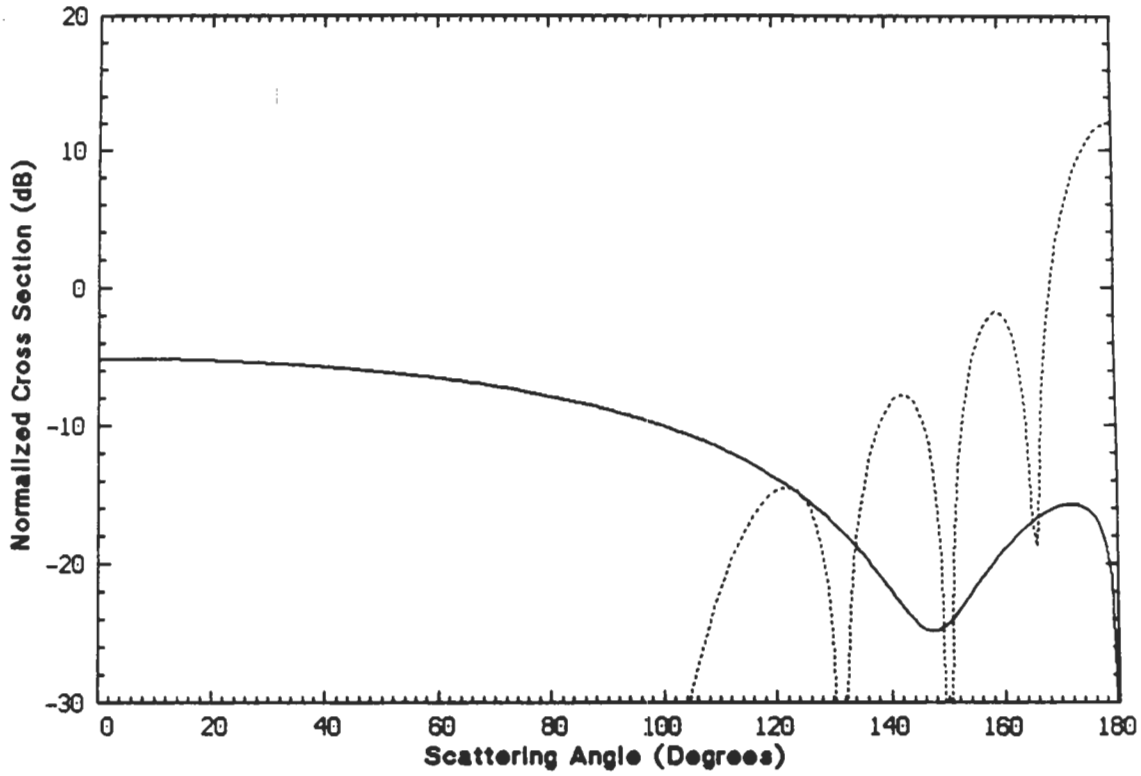

Figure 7.4: Normalized bistatic scattering cross section $\frac{\sigma}{k_0 ab^2}$ of a finite cylinder with radius $\rho_1 = 2\lambda_0$ and $\epsilon = 10 + i5$ for H polarization using physical optics: (——) stationary phase expression, (- - -) forward scattering expression.

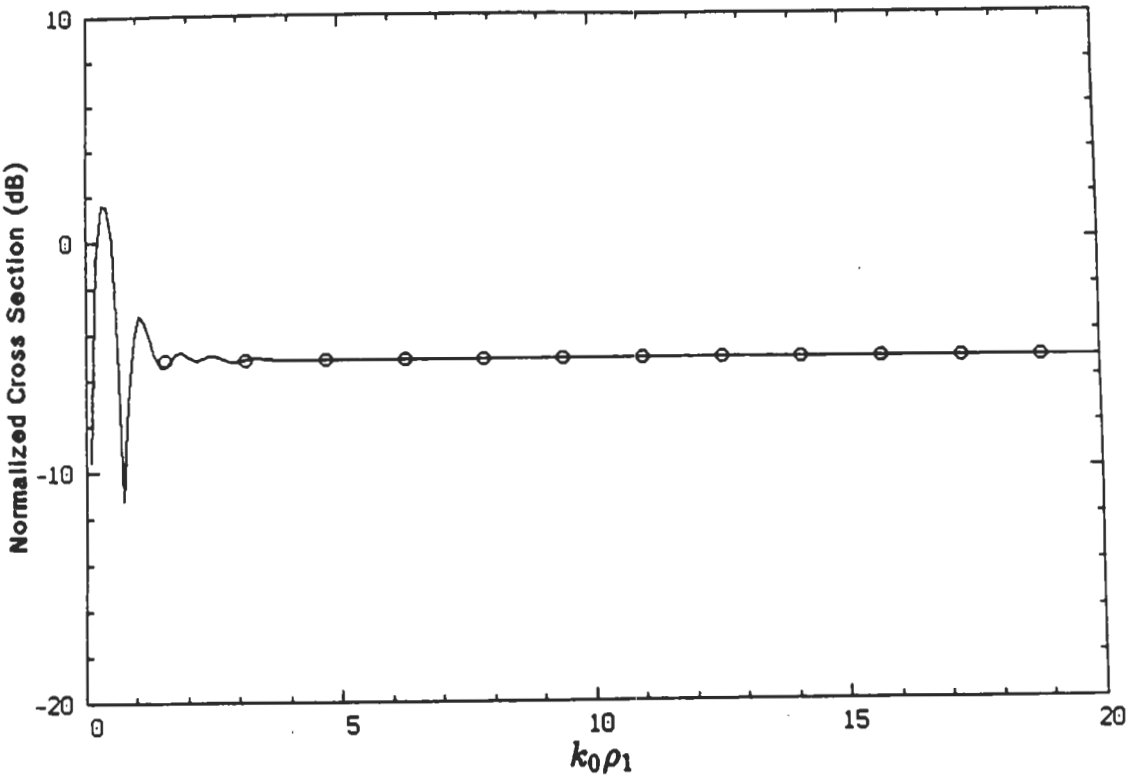

Figure 7.5: Normalized backscattering cross section $\sigma/(k_0\rho_1 b^2)$ of a circular cylinder with $\epsilon = 10 + i5$ versus $k_0\rho_1$ for E polarization: (——) exact solution, (o o o) physical optics.

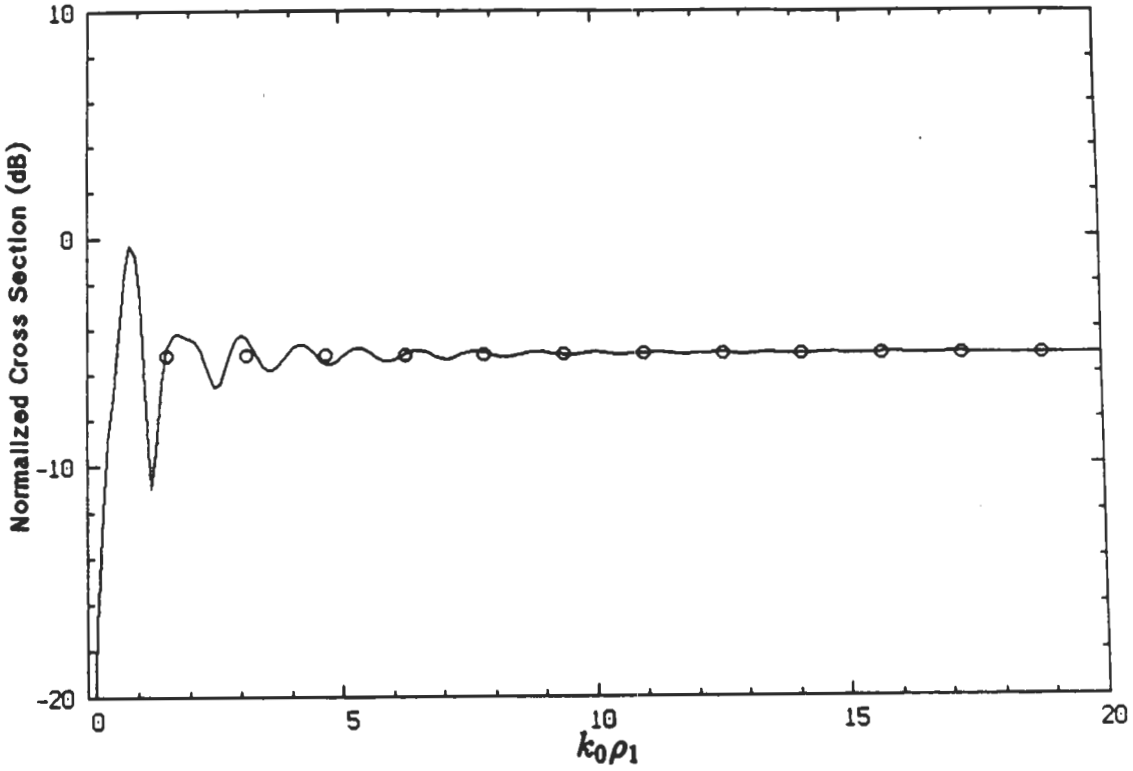

Figure 7.6: Normalized backscattering cross section $\sigma/(k_0\rho_1 b^2)$ of a circular cylinder with $\epsilon = 10 + i5$ versus $k_0\rho_1$ for H polarization: (——) exact solution, (o o o) physical optics.

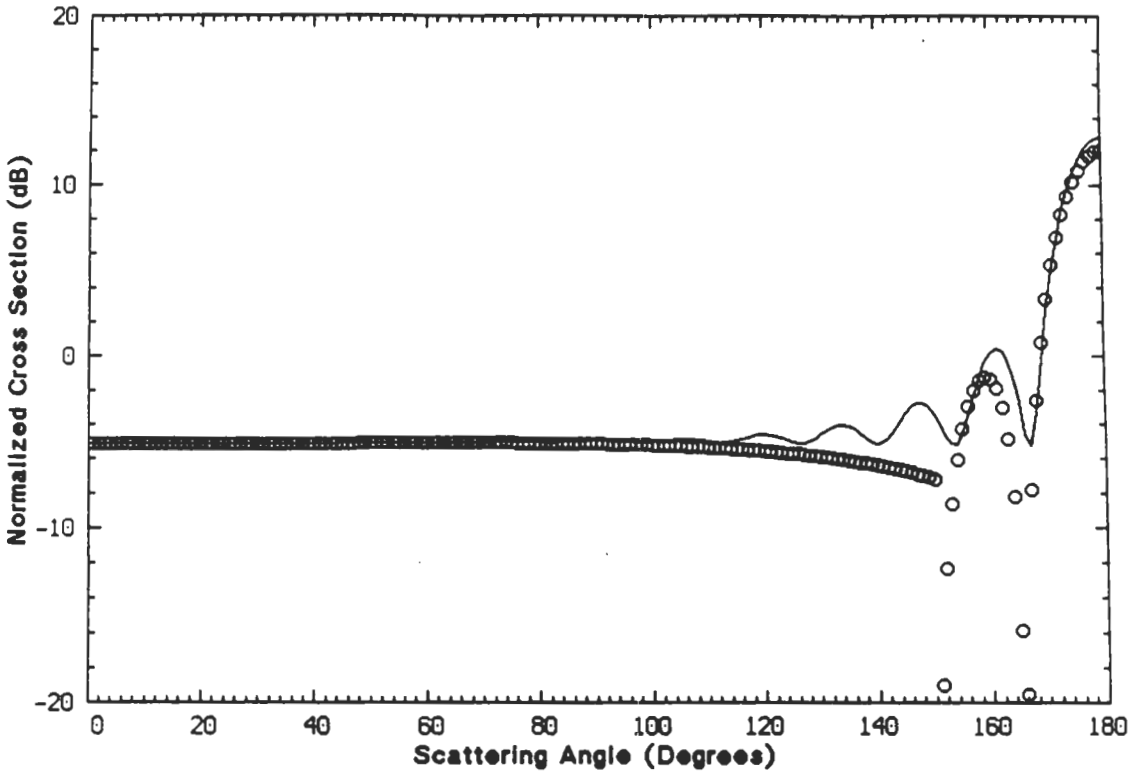

Figure 7.7: Normalized bistatic scattering cross section $\sigma/(k_0\rho_1 b^2)$ of a circular cylinder with $\rho_1 = 2\lambda_0$ and $\epsilon = 10 + i5$ for E polarization: (——) exact solution, (o o o) physical optics.

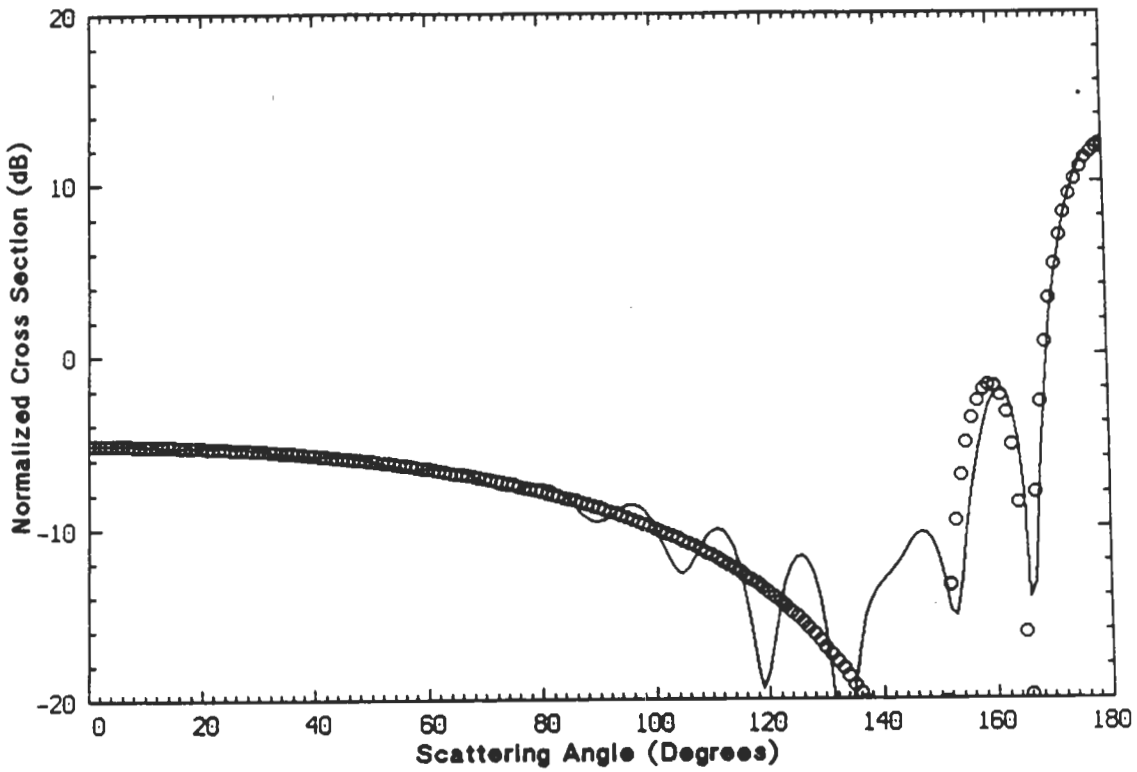

Figure 7.8: Normalized bistatic scattering cross section $\sigma/(k_0\rho_1 b^2)$ of a circular cylinder with $\rho_1 = 2\lambda_0$ and $\epsilon = 10 + i5$ for H polarization: (——) exact solution, (o o o) physical optics.

CHAPTER VIII

HIGH FREQUENCY SCATTERING FROM CORRUGATED STRATIFIED CYLINDERS

8.1 Introduction

From a scattering point of view, a tree trunk can be viewed as a multi-layer dielectric cylinder. The outer layer is rough with almost a periodic pattern and the roughness height is proportional to the diameter of the cylinder. This layer consists of dead cells with almost no water content; hence, its dielectric constant is low and slightly lossy. The inner layers that carry high dielectric fluids have very high and lossy dielectric constants. In modeling a tree, the branches and trunk usually are considered to be homogeneous smooth cylinders [Durden et al, 1988; Karam and Fung,1988]. In this chapter the effect of bark and its roughness on scattering is studied.

The literature concerning the problem of scattering from cylinders with rough surfaces is relatively scarce. To our knowledge the first treatment of a problem of this sort was given by Clemmow [1959] where a perturbation solution to an eigen function-expansion was obtained for a perfectly conducting cylinder with almost circular cross section, and only the E polarization case was considered. This technique is restricted to very smooth and small roughness functions. Other perturbation techniques for

perfectly conducting cylinders with very small roughness have also been developed [Cabayan and Murphy, 1973; Tong 1974]. None of the existing techniques can handle dielectric rough cylinders, particularly when the roughness height is on the order of the wavelength.

Under the assumption that the bark roughness is a regular corrugation in only the angular direction (i.e., ignoring variations in the axial direction) and the radius of curvature of the cylinder is much larger than the wavelength and the period of corrugation, an approximate solution to the scattering problem is obtained. In this solution, each point on the surface of the cylinder is approximated by its tangential plane. Then the polarization current in the periodic tangential surface is obtained numerically. Once the polarization current in the corrugations is found, the scattered field due to the corrugations together with the scattered field from the smooth cylinder (when the corrugation is removed) give rise to the total scattered field. The scattered field for a smooth cylinder is obtained using new physical optics surface currents that are more convenient than the traditional ones.

8.2 Scattering from Periodic Corrugated Planar Dielectric Surface

In this section we seek a numerical solution for the total field (or polarization current) inside a periodic inhomogeneous layer lying over a stratified dielectric half-space illuminated by a plane wave. The geometry of the scattering problem is shown in Fig. 8.1. First the two-dimensional Green's function for a stratified dielectric medium is found. Using Floquet's theorem these results are extended to the periodic case. Then the problem will be formulated as an integral equation that can be solved numerically by the method of moments.

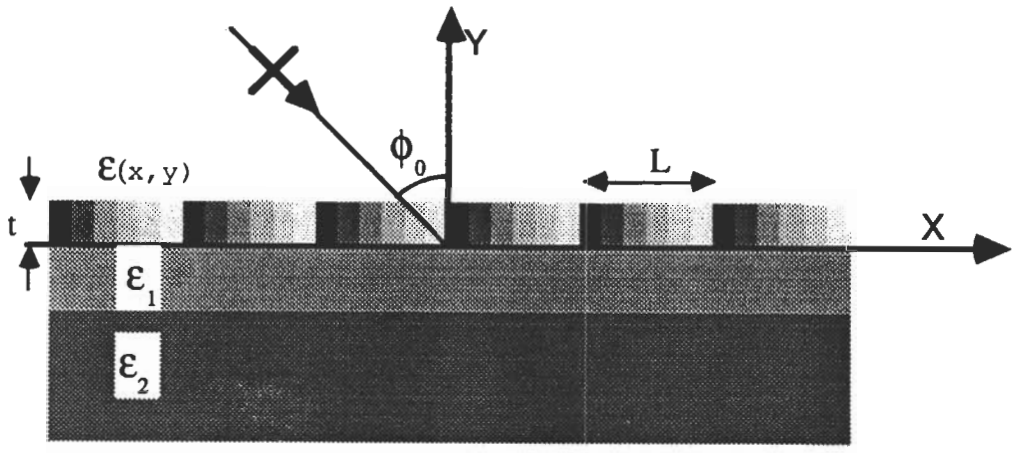

Figure 8.1: Geometry of a periodic inhomogeneous dielectric layer over a stratified dielectric half-space.

8.2.1 Two-dimensional Green's Function for a Stratified Dielectric Half Space

For a volume distribution of electric current ($\mathbf{J}_e$) occupying region V in free space, the corresponding Hertz vector is given by (1.2) and the resulting fields are given by (1.3) with $\mathbf{\Pi}_m = 0$. Since in the two-dimensional problems $\frac{\partial}{\partial z} = 0$, from equation (1.3) the field components in terms of the Hertz vector potential can be expanded as:

$$\begin{aligned} E_x &= k_0^2 \left(1 + \tfrac{1}{k_0^2}\tfrac{\partial^2}{\partial x^2}\right)\Pi_x + \tfrac{\partial^2}{\partial x \partial y}\Pi_y \\ E_y &= \tfrac{\partial^2}{\partial y \partial x}\Pi_x + k_0^2 \left(1 + \tfrac{1}{k_0^2}\tfrac{\partial^2}{\partial y^2}\right)\Pi_y \\ E_z &= k_0^2 \Pi_z \end{aligned} \tag{8.1}$$

The Hertz vector potential associated with an infinite current filament located at point (x', y') in free space with amplitude I_p and orientation $\hat{p}$ is of the form

$$\Pi_p(x,y) = \frac{-Z_0}{4k_0} H_0^{(1)}(k_0\sqrt{(x-x')^2 + (y-y')^2}) I_p \qquad p = x, y \text{ or } z. \tag{8.2}$$

The corresponding field components can be obtained by inserting (8.2) into (8.1) and

then by employing the identity

$$H_0^{(1)}(k_0\sqrt{(x-x')^2+(y-y')^2}) = \frac{1}{\pi}\int_{-\infty}^{+\infty}\frac{e^{ik_y|y-y'|-ik_x(x-x')}}{k_y}\mathrm{d}k_x \tag{8.3}$$

the resulting fields can be expressed in terms of continuous spectrum of plane waves. In (8.4) $k_y = \sqrt{k_0^2 - k_x^2}$ and the branch of the square root is chosen such that $\sqrt{-1} = i$.

In the presence of the dielectric half-space, when the current filament is in the upper half-space, each plane wave, is reflected at the air-dielectric interface according to Fresnel's law. It should be noted that the incidence angle of each plane wave, in general, is complex and is given by

$$\gamma = \arctan(\frac{k_x}{k_y}).$$

The net effect of the dielectric half-space on the radiated field can be obtained by superimposing all of the reflected plane waves that are of the following form

$$R_q(\gamma)e^{ik_y(y+y')-ik_x(x-x')}, \qquad q = E \text{ or } H.$$

where $R_q(\gamma)$ is the Fresnel reflection coefficient. The total reflected field can now be obtained by noting that

$$E_x^r = -R_H(\gamma)E_x^i$$

$$E_y^r = R_H(\gamma)E_y^i$$

$$E_z^r = R_E(\gamma)E_z^i$$

and since the direction of propagation along the y axis is reversed for the reflected waves, the operator $\frac{\partial}{\partial y}$ for the x and y components of the reflected field must be replaced by $-\frac{\partial}{\partial y}$. Thus,

$$\begin{aligned}
E_x^r &= -\tfrac{k_0 Z_0}{4\pi}[-I_x(1+\tfrac{1}{k_0^2}\tfrac{\partial^2}{\partial x^2}) + I_y\tfrac{1}{k_0^2}\tfrac{\partial^2}{\partial x\partial y}]\textstyle\int_{-\infty}^{+\infty} R_H(\gamma)\tfrac{e^{ik_y(y+y')-ik_x(x-x')}}{k_y}\mathrm{d}k_x,\\
E_y^r &= -\tfrac{k_0 Z_0}{4\pi}[-I_x\tfrac{1}{k_0^2}\tfrac{\partial^2}{\partial y\partial x} + I_y(1+\tfrac{1}{k_0^2}\tfrac{\partial^2}{\partial y^2})]\textstyle\int_{-\infty}^{+\infty} R_H(\gamma)\tfrac{e^{ik_y(y+y')-ik_x(x-x')}}{k_y}\mathrm{d}k_x,\\
E_z^r &= -\tfrac{k_0 Z_0}{4\pi}I_z\textstyle\int_{-\infty}^{+\infty} R_E(\gamma)\tfrac{e^{ik_y(y+y')-ik_x(x-x')}}{k_y}\mathrm{d}k_x.
\end{aligned} \tag{8.4}$$

In matrix notation the total field in the upper half-space can be represented by

$$\mathbf{E} = \begin{bmatrix} G_{xx} & G_{xy} & 0 \\ G_{yx} & G_{yy} & 0 \\ 0 & 0 & G_{zz} \end{bmatrix} \begin{bmatrix} I_x \\ I_y \\ I_z \end{bmatrix}, \tag{8.5}$$

where

$$\begin{aligned}
G_{xx} = & -\tfrac{k_0 Z_0}{4}(1+\tfrac{1}{k_0^2}\tfrac{\partial^2}{\partial x^2})[H_0^{(1)}(k_0\sqrt{(x-x')^2+(y-y')^2}) \\
& -\tfrac{1}{\pi}\int_{-\infty}^{+\infty} R_H(\gamma)\tfrac{e^{ik_y(y+y')-ik_x(x-x')}}{k_y}\mathrm{d}k_x], \\
G_{xy} = & -\tfrac{Z_0}{4k_0}\tfrac{\partial^2}{\partial x\partial y}[H_0^{(1)}(k_0\sqrt{(x-x')^2+(y-y')^2}) \\
& +\tfrac{1}{\pi}\int_{-\infty}^{+\infty} R_H(\gamma)\tfrac{e^{ik_y(y+y')-ik_x(x-x')}}{k_y}\mathrm{d}k_x], \\
G_{yx} = & -\tfrac{Z_0}{4k_0}\tfrac{\partial^2}{\partial y\partial x}[H_0^{(1)}(k_0\sqrt{(x-x')^2+(y-y')^2}) \\
& -\tfrac{1}{\pi}\int_{-\infty}^{+\infty} R_H(\gamma)\tfrac{e^{ik_y(y+y')-ik_x(x-x')}}{k_y}\mathrm{d}k_x], \\
G_{yy} = & -\tfrac{k_0 Z_0}{4}(1+\tfrac{1}{k_0^2}\tfrac{\partial^2}{\partial y^2})[H_0^{(1)}(k_0\sqrt{(x-x')^2+(y-y')^2}) \\
& +\tfrac{1}{\pi}\int_{-\infty}^{+\infty} R_H(\gamma)\tfrac{e^{ik_y(y+y')-ik_x(x-x')}}{k_y}\mathrm{d}k_x], \\
G_{zz} = & -\tfrac{k_0 Z_0}{4}[H_0^{(1)}(k_0\sqrt{(x-x')^2+(y-y')^2}) \\
& +\tfrac{1}{\pi}\int_{-\infty}^{+\infty} R_E(\gamma)\tfrac{e^{ik_y(y+y')-ik_x(x-x')}}{k_y}\mathrm{d}k_x]
\end{aligned} \tag{8.6}$$

are the elements of the dyadic Green's function for two-dimensional layered dielectric half-space problems. If an electric current distribution $\mathbf{J}_e$ occupies region S in the upper half-space, the radiated electric field at any point in the upper half-space can be obtained from:

$$\begin{aligned}
E_x^s(x,y) = & \int_S [G_{xx}(x,y;x',y')J_x(x',y') + G_{xy}(x,y;x',y')J_y(x',y')]\mathrm{d}x'\mathrm{d}y' \\
E_y^s(x,y) = & \int_S [G_{yx}(x,y;x',y')J_x(x',y') + G_{yy}(x,y;x',y')J_y(x',y')]\mathrm{d}x'\mathrm{d}y' \\
E_z^s(x,y) = & \int_S G_{zz}(x,y;x',y')J_z(x',y')\mathrm{d}x'\mathrm{d}y'
\end{aligned} \tag{8.7}$$

8.2.2 Far Field Evaluation

In scattering problems the quantity of interest usually is the far field expression. Here we derive the approximate form of the Green's function in the far zone using

the saddle-point technique. All the elements of the dyadic Green's function have an integral of the form

$$I = \frac{1}{\pi}\int_{-\infty}^{+\infty} R_q(\gamma)\frac{e^{ik_y(y+y')-ik_x(x-x')}}{k_y}\mathrm{d}k_x \tag{8.8}$$

Using the standard change of variable

$$k_x = k_0 \sin\gamma$$

the integration contour is changed from the real axis in the complex k_x-plane to contour Γ in γ-plane as shown in Fig. 8.2. Also by defining

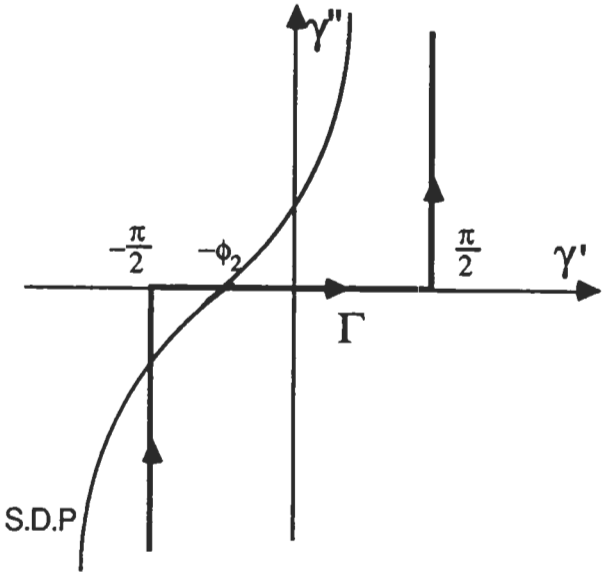

Figure 8.2: Contour of integration and steepest descent path in γ-plane.

$$x - x' = \rho_2 \sin\phi_2, \qquad y + y' = \rho_2 \cos\phi_2$$

integral (8.8) in γ-plane becomes:

$$I = \frac{1}{\pi}\int_{\Gamma} R_q(\gamma) e^{ik_0\rho_2\cos(\gamma+\phi_2)}\mathrm{d}\gamma$$

The saddle point is the solution of

$$\frac{\mathrm{d}}{\mathrm{d}\gamma}\cos(\gamma+\phi_2) = 0$$

implies $\gamma = -\phi_2$. When $k_0\rho_2 \gg 1$ the approximate value of I can be obtained by deforming the contour of integration from Γ to the steepest descent path (S.D.P.) given by

$$\mathrm{Im}[i\cos(\gamma + \phi_2)] = 1.$$

There are some poles associated with the reflection coefficient function ($R_q(\gamma)$) of a layered dielectric medium that are captured when the contour is deformed. The contribution of these poles gives rise to surface waves, but their effect can be ignored if the dielectric materials are lossy and observation point is away from the interface. Under these conditions we get

$$\begin{aligned} I &= \tfrac{1}{\pi} R_q(-\phi_2) \int_{S.D.P.} e^{ik_0\rho_2\cos(\gamma+\phi_2)} \mathrm{d}\gamma \\ &\approx \sqrt{\tfrac{2}{\pi k_0\rho_2}} e^{i(k_0\rho_2 - \pi/4)} R_q(\phi_2), \end{aligned}$$

where we have used the fact that R_q is an even function. Also the large argument expansion of the Hankel function can be used for distant approximations, i.e.

$$H_0^{(1)}(k_0\sqrt{(x-x')^2 + (y-y')^2}) \approx \sqrt{\frac{2}{\pi k_0\rho_1}} e^{i(k_0\rho_1 - \pi/4)},$$

where $\rho_1 = \sqrt{(x-x')^2 + (y-y')^2}$. From Fig. 8.3 it is seen that in the far zone the following approximations can be used also

$$\begin{aligned} \phi_1 &= \phi_2 = \phi, \\ \rho_1 &= \rho - x'\sin\phi - y'\cos\phi, \\ \rho_2 &= \rho - x'\sin\phi + y'\cos\phi. \end{aligned}$$

These approximations can be inserted into expressions for the dyadic Green's function given by (8.6). The far field approximation of derivatives of the Hankel function and integral I can be obtained by retaining the terms up to the order $\rho^{-1/2}$ and discarding the rest. Thus the expressions for the Green's function elements in the

far zone become:

$$
\begin{aligned}
G_{xx} &= -\frac{k_0 Z_0}{4}\sqrt{\frac{2}{\pi k_0 \rho}}e^{i(k_0\rho-\pi/4)}\cos^2\phi e^{-ik_0\sin\phi x'}[e^{-ik_0\cos\phi y'} - R_H(\phi)e^{ik_0\cos\phi y'}] \\
G_{xy} &= \frac{k_0 Z_0}{4}\sqrt{\frac{2}{\pi k_0 \rho}}e^{i(k_0\rho-\pi/4)}\sin\phi\cos\phi e^{-ik_0\sin\phi x'}[e^{-ik_0\cos\phi y'} + R_H(\phi)e^{ik_0\cos\phi y'}] \\
G_{yx} &= \frac{k_0 Z_0}{4}\sqrt{\frac{2}{\pi k_0 \rho}}e^{i(k_0\rho-\pi/4)}\sin\phi\cos\phi e^{-ik_0\sin\phi x'}[e^{-ik_0\cos\phi y'} - R_H(\phi)e^{ik_0\cos\phi y'}] \\
G_{yy} &= -\frac{k_0 Z_0}{4}\sqrt{\frac{2}{\pi k_0 \rho}}e^{i(k_0\rho-\pi/4)}\sin^2\phi e^{-ik_0\sin\phi x'}[e^{-ik_0\cos\phi y'} + R_H(\phi)e^{ik_0\cos\phi y'}] \\
G_{zz} &= -\frac{k_0 Z_0}{4}\sqrt{\frac{2}{\pi k_0 \rho}}e^{i(k_0\rho-\pi/4)}e^{-ik_0\sin\phi x'}[e^{-ik_0\cos\phi y'} + R_E(\phi)e^{ik_0\cos\phi y'}].
\end{aligned}
\tag{8.9}
$$

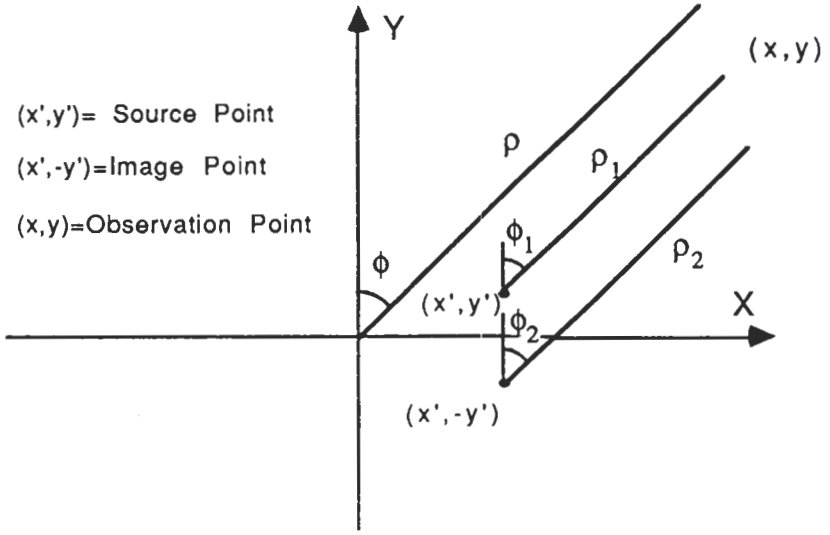

Figure 8.3: Geometry of the line source and its image.

It can easily be shown that for an electric current distribution $\mathbf{J}_e$ the radiated far field does not have a $\hat{\rho}$ component and the far field amplitude defined by

$$\mathbf{E} = \sqrt{\frac{2}{\pi k_0 \rho}}e^{i(k_0\rho-\pi/4)}\mathbf{S}$$

has components

$$
\begin{aligned}
S_\phi &= \frac{k_0 Z_0}{4}\{\int_S \cos\phi J_x(x',y')e^{-ik_0\sin\phi x'}[e^{-ik_0\cos\phi y'} - R_H(\phi)e^{ik_0\cos\phi y'}]\mathrm{d}x'\mathrm{d}y' \\
&\quad - \int_S \sin\phi J_y(x',y')e^{-ik_0\sin\phi x'}[e^{-ik_0\cos\phi y'} + R_H(\phi)e^{ik_0\cos\phi y'}]\mathrm{d}x'\mathrm{d}y'\}, \\
S_z &= -\frac{k_0 Z_0}{4}\int_S J_z(x',y')e^{-ik_0\sin\phi x'}[e^{-ik_0\cos\phi y'} + R_E(\phi)e^{ik_0\cos\phi y'}]\mathrm{d}x'\mathrm{d}y',
\end{aligned}
\tag{8.10}
$$

8.2.3 Reflection Coefficient of a Layered Dielectric Half-Space

Consider a multilayer dielectric half-space as shown in Fig. 8.4. Interface of the m^{th} and $(m+1)^{th}$ layers is located at $y = -d_m$ with $d_0 = 0$. The relative permittivity and permeability of each region is represented by ϵ_m and μ_m respectively. Suppose a plane wave whose plane of incidence is parallel with $x - y$ plane is illuminating the stratified medium from above. From symmetry considerations, $\frac{\partial}{\partial z} = 0$, which implies that the field components in each region can be separated into E- and H-polarized waves. It can be shown from Maxwell's equation that the E- and H-polarized waves are dual of each other, i.e. one can be obtained from the other upon replacing E_m with H_m, H_m with $-E_m$, and $\epsilon_m(\mu_m)$ with $\mu_m(\epsilon_m)$. For E polarization the field

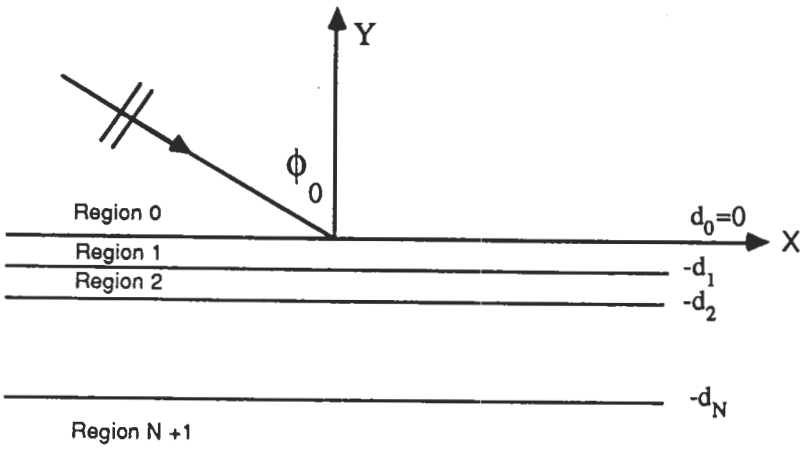

Figure 8.4: Plane wave reflection from a multi-layer dielectric half-space.

components in region m can be represented by

$$E_{my} = [c_m^i e^{-ik_{my}y} + c_m^r e^{ik_{my}y}]e^{ik_0 \sin\phi_0 x}$$

$$H_{mx} = \frac{Y_0 k_{my}}{k_0 \mu_m}[c_m^i e^{-ik_{my}y} - c_m^r e^{ik_{my}y}]e^{ik_0 \sin\phi_0 x}$$

where ϕ_0 is the incidence angle and $k_{my} = k_0\sqrt{\epsilon_m\mu_m - \sin^2\phi_0}$. The coefficient c_m^i and c_m^r are the amplitude of the wave travelling in the $-z$ and $+z$ direction, respectively, in region m. In region 0, $c_0^i = 1$, and $c_0^r = R_E$ is the total reflection coefficient and in

region $N+1$, which is semi-infinite, $c^r_{N+1} = 0$. Imposing the boundary conditions, which requires continuity tangential electric and magnetic fields at each dielectric interface, we can relate the field amplitudes in the m^{th} to those of $(m+1)^{th}$ region.

After some simple algebraic manipulation, the following recursive relationship can be obtained

$$\frac{c^r_m}{c^i_m} = \frac{(c^r_{m+1}/c^i_{m+1}) + \Gamma^E_m e^{i2k_{(m+1)x}d_m}}{(c^r_{m+1}/c^i_{m+1})\Gamma^E_m + e^{i2k_{(m+1)x}d_m}} e^{i2k_{my}d_m} \tag{8.11}$$

where

$$\Gamma^E_m = \frac{\mu_{m+1}k_{my} - \mu_m k_{(m+1)y}}{\mu_{m+1}k_{my} + \mu_m k_{(m+1)y}}.$$

Starting from $c^r_{N+1}/c^i_{N+1} = 0$ and using (8.11) repeatedly $R_E = c^r_0/c^i_0$ can be found. To find R_H the reflection coefficient for H polarization, the duality relationship can be applied and an identical recursive formulation as given in (8.11) can be obtained. The only difference is that Γ^E_m becomes Γ^H_m which is given by

$$\Gamma^H_m = \frac{\epsilon_{m+1}k_{my} - \epsilon_m k_{(m+1)y}}{\epsilon_{m+1}k_{my} + \epsilon_m k_{(m+1)y}}.$$

8.2.4 Scattering from Inhomogeneous Periodic Dielectric Layer above a Half-Space Layered Medium

Consider an inhomogeneous dielectric layer of thickness t ontop of a stratified half-space dielectric medium as shown in Fig. 8.1. The permittivity of the inhomogeneous layer is represented by $\epsilon(x,y)$ which is a periodic function of x with period L. Suppose this structure is illuminated by a plane wave whose angle of incidence and polarization respectively are ϕ_0 and $\hat{p}$. For an E-polarized wave $\hat{p} = \hat{z}$ and for an H-polarized wave $\hat{p} = -\cos\phi_0\hat{x} - \sin\phi_0\hat{y}$, thus the incident wave may be represented by

$$\mathbf{E}^i = \hat{p}e^{ik_0(\sin\phi_0 x - \cos\phi_0 y)}. \tag{8.12}$$

A polarization current distribution is induced in the inhomogeneous layer. This current gives rise to a scattered field that can be obtained from (8.7). The polarization current is proportional to the total field within the inhomogeneous layer. The total field is comprised of the incident field, the reflected field which would have existed in the absence of the inhomogeneous layer, and the scattered field, i.e.

$$\mathbf{E}^t = \mathbf{E}^i + \mathbf{E}^r + \mathbf{E}^s.$$

The polarization current in terms of the total field is given by

$$\mathbf{J}_e(x,y) = -ik_0 Y_0(\epsilon(x,y) - 1)\mathbf{E}^t. \tag{8.13}$$

Upon substitution of expression (8.7) for $\mathbf{E}^s$ into (8.13) a set of integral equations for polarization current can be obtained; for E polarization we have

$$\begin{aligned} J_z(x,y) = \; & -ik_0 Y_0(\epsilon(x,y) - 1)\{e^{ik_0 \sin\phi_0 x}[e^{-ik_0 \cos\phi_0 y} + R_E(\phi_0)e^{ik_0 \cos\phi_0 y}] \\ & + \int_0^t \int_{-\infty}^{+\infty} J_z(x',y')G_{zz}(x,y;x',y')\mathrm{d}x'\mathrm{d}y'\}, \end{aligned} \tag{8.14}$$

and for H polarization

$$\begin{aligned} J_x(x,y) = \; & -ik_0 Y_0(\epsilon(x,y) - 1)\{\cos\phi_0 e^{ik_0 \sin\phi_0 x}[-e^{-ik_0 \cos\phi_0 y} + R_H(\phi_0)e^{ik_0 \cos\phi_0 y}] \\ & + \int_0^t \int_{-\infty}^{+\infty}[J_x(x',y')G_{xx}(x,y;x',y') + J_y(x',y')G_{xy}(x,y;x',y')]\mathrm{d}x'\mathrm{d}y'\}, \\ J_y(x,y) = \; & -ik_0 Y_0(\epsilon(x,y) - 1)\{-\sin\phi_0 e^{ik_0 \sin\phi_0 x}[e^{-ik_0 \cos\phi_0 y} + R_H(\phi_0)e^{ik_0 \cos\phi_0 y}] \\ & + \int_0^t \int_{-\infty}^{+\infty}[J_x(x',y')G_{yx}(x,y;x',y') + J_y(x',y')G_{yy}(x,y;x',y')]\mathrm{d}x'\mathrm{d}y'\}. \end{aligned} \tag{8.15}$$

Since there is no closed-form representation for the kernel of these integral equations, finding the solution, even numerically, seems impossible. But by employing Floquet's theorem the integral equations can be reduced to a form which is amenable to numerical solution. The fact that the permittivity of the inhomogeneous layer is periodic in x,excluding a phase factor, all the field quantities are required to be periodic in x

. Therefore the polarization current must satisfy

$$\mathbf{J}_e(x+nL,y) = \mathbf{J}_e(x,y)e^{ik_0 \sin\phi_0 nL} \tag{8.16}$$

Now by using (8.16) the integration with respect to x can be simplified significantly by breaking the integral into multiples of a period, that is

$$\begin{aligned} I_{zz} &= \int_{-\infty}^{+\infty} G_{zz}(x,y;x',y')J_z(x',y')\mathrm{d}x'\mathrm{d}y' \\ &= \sum_{n=-\infty}^{+\infty} \int_{x_0+nL}^{x_0+(n+1)L} G_{zz}(x,y;x',y')J_z(x',y')\mathrm{d}x'\mathrm{d}y' \end{aligned} \tag{8.17}$$

At this stage, if the variable x' is changed to $x'+nL$ and property (8.16) is used, I_{zz} becomes

$$I_{zz} = \int_{x_0}^{x_0+L} G^p_{zz}(x,y;x',y')J_z(x',y')\mathrm{d}x'\mathrm{d}y'$$

where

$$G^p_{zz}(x,y;x',y') = \sum_{n=-\infty}^{+\infty} G_{zz}(x,y;x'-nL,y')e^{ik_0 \sin\phi_0 nL}$$

If the expression for G_{zz} as given by (8.6) is inserted in the above equation and the order of summation and integration is interchanged, and then the identity

$$\sum_{n=-\infty}^{+\infty} e^{inL(k_0 \sin\phi_0 + k_x)} = 2\pi \sum_{n=-\infty}^{+\infty} \delta[(k_x + k_0 \sin\phi_0)L - 2\pi n]$$

is employed, the periodic Green's function simplifies to

$$G^p_{zz}(x,y;x',y') = -\frac{k_0 Z_0}{2L} \sum_{n=-\infty}^{+\infty} [e^{ik_{ny}|y-y'|} + R_E(\gamma_n)e^{ik_{ny}(y+y')}]\frac{e^{-ik_{nx}(x-x')}}{k_{ny}} \tag{8.18}$$

where

$$k_{nx} = \frac{2\pi n}{L} - k_0 \sin\phi_0, \qquad k_{ny} = \sqrt{k_0^2 - k_{nx}^2},$$

and

$$\gamma_n = \arctan(\frac{k_{nx}}{k_{ny}}).$$

Other elements of the periodic Green's function can also be obtained in the same manner

$$
\begin{aligned}
G^p_{xx}(x,y;x',y') &= -\tfrac{k_0 Z_0}{2L}(1+\tfrac{1}{k_0^2}\tfrac{\partial^2}{\partial x^2})\textstyle\sum_{n=-\infty}^{+\infty}[e^{ik_{ny}|y-y'|} - R_H(\gamma_n)e^{ik_{ny}(y+y')}]\tfrac{e^{-ik_{nx}(x-x')}}{k_{ny}} \\
G^p_{xy}(x,y;x',y') &= -\tfrac{Z_0}{2Lk_0}\tfrac{\partial^2}{\partial x\partial y}\textstyle\sum_{n=-\infty}^{+\infty}[e^{ik_{ny}|y-y'|} + R_H(\gamma_n)e^{ik_{ny}(y+y')}]\tfrac{e^{-ik_{nx}(x-x')}}{k_{ny}} \\
G^p_{yx}(x,y;x',y') &= -\tfrac{Z_0}{2Lk_0}\tfrac{\partial^2}{\partial y\partial x}\textstyle\sum_{n=-\infty}^{+\infty}[e^{ik_{ny}|y-y'|} - R_H(\gamma_n)e^{ik_{ny}(y+y')}]\tfrac{e^{-ik_{nx}(x-x')}}{k_{ny}} \\
G^p_{yy}(x,y;x',y') &= -\tfrac{k_0 Z_0}{2L}(1+\tfrac{1}{k_0^2}\tfrac{\partial^2}{\partial y^2})\textstyle\sum_{n=-\infty}^{+\infty}[e^{ik_{ny}|y-y'|} + R_H(\gamma_n)e^{ik_{ny}(y+y')}]\tfrac{e^{-ik_{nx}(x-x')}}{k_{ny}}.
\end{aligned}
\tag{8.19}
$$

The integral equations (8.14) and (8.15) now take the following form

$$
\begin{aligned}
J_z(x,y) = \; & -ik_0Y_0(\epsilon(x,y)-1)\{e^{ik_0\sin\phi_0 x}[e^{-ik_0\cos\phi_0 y} + R_E(\phi_0)e^{ik_0\cos\phi_0 y}] \\
& + \textstyle\int_0^t\int_{-L/2}^{+L/2} J_z(x',y')G^p_{zz}(x,y;x',y')\mathrm{d}x'\mathrm{d}y'\}, \\
J_x(x,y) = \; & -ik_0Y_0(\epsilon(x,y)-1)\{\cos\phi_0 e^{ik_0\sin\phi_0 x}[-e^{-ik_0\cos\phi_0 y} + R_H(\phi_0)e^{ik_0\cos\phi_0 y}] \\
& + \textstyle\int_0^t\int_{-L/2}^{+L/2}[J_x(x',y')G^p_{xx}(x,y;x',y') + J_y(x',y')G^p_{xy}(x,y;x',y')]\mathrm{d}x'\mathrm{d}y'\}, \\
J_y(x,y) = \; & -ik_0Y_0(\epsilon(x,y)-1)\{-\sin\phi_0 e^{ik_0\sin\phi_0 x}[e^{-ik_0\cos\phi_0 y} + R_H(\phi_0)e^{ik_0\cos\phi_0 y}] \\
& + \textstyle\int_0^t\int_{-L/2}^{+L/2}[J_x(x',y')G^p_{yx}(x,y;x',y') + J_y(x',y')G^p_{yy}(x,y;x',y')]\mathrm{d}x'\mathrm{d}y'\}.
\end{aligned}
\tag{8.20}
$$

Far away from the surface ($y \gg \lambda_0$), contribution of only a few terms of the summations in (8.19) are observable. These terms correspond to values of n such that k_{ny} is real and they are known as the Bragg modes (see (5.61)). Among all the Bragg modes the mode corresponding to $n = 0$ carries most of the scattered energy and this is specifically true when $L < \lambda$. The scattered field due to this mode is a plane wave and for E and H Polarization, respectively, we have

$$
\begin{aligned}
\mathbf{E}_E = \; & \tfrac{-Z_0}{2L\cos\phi_0}\{\textstyle\int_0^t\int_{-L/2}^{+L/2} J_z(x',y')[e^{-ik_0\cos\phi_0 y'} + R_E e^{ik_0\cos\phi_0 y'}]e^{-ik_0\sin\phi_0 x'}\mathrm{d}x'\mathrm{d}y'\} \\
& \cdot e^{ik_0(\cos\phi_0 y + \sin\phi_0 x)}\hat{z}
\end{aligned}
\tag{8.21}
$$

$$\begin{aligned}\mathbf{E}_H = & -\frac{Z_0}{2L\cos\phi_0}\{\cos\phi_0 \int_0^t \int_{-L/2}^{+L/2} J_x(x',y')[e^{-ik_0\cos\phi_0 y'} - R_H e^{ik_0\cos\phi_0 y'}]e^{-ik_0\sin\phi_0 x'}\mathrm{d}x'\mathrm{d}y' \\ & - \sin\phi_0 \int_0^t \int_{-L/2}^{+L/2} J_y(x',y')[e^{-ik_0\cos\phi_0 y'} + R_H e^{ik_0\cos\phi_0 y'}]e^{-ik_0\sin\phi_0 x'}\mathrm{d}x'\mathrm{d}y'\} \\ & \cdot(\cos\phi_0\hat{x} - \sin\phi_0\hat{y})e^{ik_0(\cos\phi_0 y + \sin\phi_0 x)}\end{aligned} \tag{8.22}$$

8.2.5 Numerical Implementation

It is very unlikely to find an analytical solution to the equations as given by (8.20) even for the simplest form of $\epsilon(x,y)$. However an approximate numerical solution can be obtained using the standard moment method with point matching technique. In this method the cross section of the inhomogeneous layer over one period is discretized into small rectangular segments over which the dielectric constant and polarization current can be assumed to be constant. Now in equation (8.20) the integrals over one period of the inhomogeneous layer can be broken up into summation of integrals over each segment where the polarization current is constant.

Let pq designate a cell whose center coordinate is $(x_p, y_q) = (p\Delta x, q\Delta y)$, where p and q are some integers and Δx and Δy are dimensions of the rectangular segments. If the polarization currents as given by (8.20) are evaluated at the center of uv-cell (point matching) the integral equations can be cast into matrix equations. The matrices formed by this technique are known as the impedance matrices. The solution to this matrix equation gives the polarization current at the center of each segment.

After a simple integration of the periodic Green's functions over the area of pq-cell, it can be shown that the entries of the impedance matrix for E polarization (TM

case) are of the form

$$Z(u,v;p,q) = \begin{cases} \frac{2ik_0^2}{L}(\epsilon(u,v)-1)\sum_{n=-\infty}^{+\infty}[e^{ik_{ny}|y_v-y_q|} + R_E(\gamma_n)e^{ik_{ny}(y_v+y_q)}]\frac{\sin(k_{ny}\Delta y/2)}{k_{nx}k_{ny}^2} \\ \quad \cdot \sin(k_{nx}\Delta x/2)e^{-ik_{nx}(x_u-x_p)} & v \neq q \\ \frac{2ik_0^2}{L}(\epsilon(u,v)-1)\sum_{n=-\infty}^{+\infty}[-ie^{ik_{ny}\Delta y/2} + i + R_E(\gamma_n)e^{i2k_{ny}y_v} \\ \quad \cdot \sin(k_{ny}\Delta y/2)]\frac{1}{k_{nx}k_{ny}^2}\sin(k_{nx}\Delta x/2)e^{-ik_{nx}(x_u-x_p)} & v = q \; u \neq p \\ -1 + \frac{2ik_0^2}{L}(\epsilon(u,v)-1)\sum_{n=-\infty}^{+\infty}[-ie^{ik_{ny}\Delta y/2} + i + R_E(\gamma_n)e^{i2k_{ny}y_v} \\ \quad \cdot \sin(k_{ny}\Delta y/2)]\frac{1}{k_{nx}k_{ny}^2} \cdot \sin(k_{nx}\Delta x/2) & v = q \; u = p. \end{cases} \tag{8.23}$$

For H polarization (TE case) the integral equations for J_x and J_y are coupled, which result in coupled matrix equations that can be combined into a single matrix equation. The resultant impedance matrix consists of four sub-matrices of the following form

$$\mathcal{Z} = \begin{bmatrix} \mathcal{Z}_1 & \mathcal{Z}_2 \\ \mathcal{Z}_3 & \mathcal{Z}_4 \end{bmatrix},$$

whose entries are given by

$$Z_1(u,v;p,q) = \begin{cases} \frac{2ik_0^2}{L}(\epsilon(u,v)-1)\sum_{n=-\infty}^{+\infty}[e^{ik_{ny}|y_v-y_q|} - R_H(\gamma_n)e^{ik_{ny}(y_v+y_q)}]\frac{(1-k_{nx}^2/k_0^2)}{k_{nx}k_{ny}^2} \\ \quad \cdot \sin(k_{ny}\Delta y/2)\sin(k_{nx}\Delta x/2)e^{-ik_{nx}(x_u-x_p)} & v \neq q \\ \frac{2ik_0^2}{L}(\epsilon(u,v)-1)\sum_{n=-\infty}^{+\infty}[-ie^{ik_{ny}\Delta y/2} + i - R_H(\gamma_n)e^{i2k_{ny}y_v} \\ \quad \cdot \sin(k_{ny}\Delta y/2)]\frac{(1-k_{nx}^2/k_0^2)}{k_{nx}k_{ny}^2}\sin(k_{nx}\Delta x/2)e^{-ik_{nx}(x_u-x_p)} \\ & v = q \; u \neq p \\ -1 + \frac{2ik_0^2}{L}(\epsilon(u,v)-1)\sum_{n=-\infty}^{+\infty}[-ie^{ik_{ny}\Delta y/2} + i - R_H(\gamma_n)e^{i2k_{ny}y_v} \\ \quad \cdot \sin(k_{ny}\Delta y/2)]\frac{(1-k_{nx}^2/k_0^2)}{k_{nx}k_{ny}^2} \cdot \sin(k_{nx}\Delta x/2) & v = q \; u = p, \end{cases} \tag{8.24}$$

$$Z_2(u,v;p,q) = \begin{cases} \frac{2i}{L}(\epsilon(u,v)-1)\sum_{n=-\infty}^{+\infty}[\mathrm{sgn}(y_v-y_q)e^{ik_{ny}|y_v-y_q|} + R_H(\gamma_n)e^{ik_{ny}(y_v+y_q)}] \\ \quad \cdot\frac{1}{k_{ny}}\sin(k_{ny}\Delta y/2)\sin(k_{nx}\Delta x/2)e^{-ik_{nx}(x_u-x_p)} & v \neq q \\ \frac{2i}{L}(\epsilon(u,v)-1)\sum_{n=-\infty}^{+\infty} R_H(\gamma_n)e^{i2k_{ny}y_v}\sin(k_{ny}\Delta y/2)\frac{1}{k_{ny}} \\ \quad \cdot\sin(k_{nx}\Delta x/2)e^{-ik_{nx}(x_u-x_p)} & v = q, \end{cases} \tag{8.25}$$

$$Z_3(u,v;p,q) = \begin{cases} \frac{2i}{L}(\epsilon(u,v)-1)\sum_{n=-\infty}^{+\infty}[\mathrm{sgn}(y_v-y_q)e^{ik_{ny}|y_v-y_q|} - R_H(\gamma_n)e^{ik_{ny}(y_v+y_q)}] \\ \quad \cdot\frac{1}{k_{ny}}\sin(k_{ny}\Delta y/2)\sin(k_{nx}\Delta x/2)e^{-ik_{nx}(x_u-x_p)} & v \neq q \\ \frac{2i}{L}(\epsilon(u,v)-1)\sum_{n=-\infty}^{+\infty} -R_H(\gamma_n)e^{i2k_{ny}y_v}\sin(k_{ny}\Delta y/2)\frac{1}{k_{ny}} \\ \quad \cdot\sin(k_{nx}\Delta x/2)e^{-ik_{nx}(x_u-x_p)} & v = q, \end{cases} \tag{8.26}$$

$$Z_4(u,v;p,q) = \begin{cases} \frac{2ik_0^2}{L}(\epsilon(u,v)-1)\sum_{n=-\infty}^{+\infty}\{(1-\frac{k_{ny}^2}{k_0^2})[e^{ik_{ny}|y_v-y_q|} + R_H(\gamma_n)e^{ik_{ny}(y_v+y_q)}] \\ \quad \frac{1}{k_{nx}k_{ny}^2}\cdot\sin(k_{ny}\Delta y/2)\sin(k_{nx}\Delta x/2)e^{-ik_{nx}(x_u-x_p)}\} & v \neq q \\ \frac{2ik_0^2}{L}(\epsilon(u,v)-1)\sum_{n=-\infty}^{+\infty}[-i(1-\frac{k_{ny}^2}{k_0^2})e^{ik_{ny}\Delta y/2} + i + R_H(\gamma_n)(1-\frac{k_{ny}^2}{k_0^2}) \\ \quad \cdot\sin(k_{ny}\Delta y/2)e^{i2k_{ny}y_v}]\frac{1}{k_{nx}k_{ny}^2}\sin(k_{nx}\Delta x/2)e^{-ik_{nx}(x_u-x_p)} \\ & v = q\ u \neq p \\ -1+\frac{2ik_0^2}{L}(\epsilon(u,v)-1)\sum_{n=-\infty}^{+\infty}[-i(1-\frac{k_{ny}^2}{k_0^2})e^{ik_{ny}\Delta y/2} + i + R_H(\gamma_n) \\ \quad \cdot(1-\frac{k_{ny}^2}{k_0^2})\sin(k_{ny}\Delta y/2)e^{i2k_{ny}y_v}]\frac{1}{k_{nx}k_{ny}^2}\sin(k_{nx}\Delta x/2) \\ & v = q\ u = p. \end{cases} \tag{8.27}$$

In (8.25) and (8.26) $\mathrm{sgn}(x)$ is the sign function defined by

$$\mathrm{sgn}(x) = \begin{cases} +1 & \text{if } x > 0 \\ -1 & \text{if } x < 0. \end{cases} \tag{8.28}$$

All series in (8.25), (8.26), and (8.27) are exponentially convergent and thus the series can be truncated for relatively small n. This is also the case for (8.24) except for one term in the summand of the expressions corresponding to $v = q$. The convergence

rate of

$$S = \sum_{n=-\infty}^{+\infty} i\frac{(1 - k_{nx}^2/k_0^2)}{k_{nx}k_{ny}^2} \cdot \sin(k_{nx}\Delta x/2)e^{-ik_{nx}(x_u - x_p)} \tag{8.29}$$

is very poor and in order to improve the convergence rate the standard trick is to add and subtract a series whose summand is asymptotic to the original series. For large n

$$k_{nx} \approx \frac{2\pi n}{L} \qquad k_{ny} \approx i\frac{2\pi n}{L}$$

and the summand is approximated by

$$\frac{i}{k_0^2}\frac{L}{2\pi n}\sin(k - nx\Delta x/2)e^{-ik_{nx}(x_u - x_p)}$$

where the asymptotic forms for k_{nx} and k_{ny} are only used in the amplitude factor. It can be shown that

$$\sum_{n=-\infty, n\neq 0}^{+\infty} \frac{e^{in\alpha}}{n} = i\mathrm{sgn}(\alpha)(\pi - \mid \alpha \mid) \tag{8.30}$$

where α is a real number. By employing (8.30), a closed form for the asymptotic series (S_{app}) can be obtained and is given by

$$S_{app} = \begin{cases} \frac{L}{2k_0^2}e^{-ik_{nx}(x_u - x_p)}[sgn(x_p - x_u)(1 - \frac{2|x_p - x_u|}{L})\sin(k_0 \sin\phi_0 \Delta x/2) & \\ \quad -\frac{i\Delta x}{L}\cos(k_0 \sin\phi_0 \Delta x/2)] & x_p \neq x_u \\ \frac{iL}{2k_0^2}(1 - \frac{\Delta x}{L})\cos(k_0 \sin\phi_0 \Delta x/2) & x_u = x_p \end{cases}$$

Now (8.29) can be written as

$$S = \frac{i}{k_0^2}\sum_{n=-\infty, n\neq 0}^{+\infty}[\frac{k_0^2 - k_{nx}^2}{k_{nx}k_{ny}^2} - \frac{L}{2\pi n}]\sin(k_{nx}\Delta x/2)e^{-ik_{nx}(x_u - x_p)} + \frac{i\sin(k_0 \sin\phi_0 \Delta x/2)}{k_0^3 \sin\phi_0} + S_{app}$$

in which case the series converges very fast.

The right-hand-side of the matrix equations may be represented by an excitation vector whose elements, for E polarization, are

$$b(u,v) = ik_0 Y_0(\epsilon(x_u, y_v) - 1)e^{ik_0 \sin\phi_0 x_u}[e^{-ik_0 \cos\phi_0 y_v} + R_E(\phi_0)e^{ik_0 \cos\phi_0 y_v}]$$

The excitation vector for H polarization is made up of two sub-vectors with entries

$$b_1(u,v) = ik_0 Y_0(\epsilon(x_u, y_v) - 1)\cos\phi_0 e^{ik_0 \sin\phi_0 x_u}[-e^{-ik_0 \cos\phi_0 y_v} + R_H(\phi_0)e^{ik_0 \cos\phi_0 y_v}],$$

$$b_2(u,v) = -ik_0 Y_0(\epsilon(x_u, y_v) - 1)\sin\phi_0 e^{ik_0 \sin\phi_0 x_u}[e^{-ik_0 \cos\phi_0 y_v} + R_H(\phi_0)e^{ik_0 \cos\phi_0 y_v}].$$

We point out that the inhomogeneous layer may have an arbitrary thickness profile with a maximum height t. In such cases we may assume that the layer has a constant thickness t and the permittivity corresponding to air-filled points is 1.

8.3 High Frequency Scattering from Stratified Cylinders

For dielectric cylinders with large radii of curvature, physical optics may be used to obtain the scattered field provided the dielectric has sufficient loss to prevent significant penetration through the cylinder (see Section 7.3). The dielectric loss also suppresses the effects of creeping waves which enhances the physical optics results. If the dielectric cylinder is stratified, the physical optics approximation could still be used if the radius of curvature of all the interface contours are much larger than the wavelength.

Two types of physical optics approximations can be applied: 1) surface integral and 2) volume integral approximation . In surface integral physical optics the equivalent surface currents are approximated by electric and magnetic surface currents of the infinite tangential plane. In the latter method the volumetric polarization current is estimated by finding the internal field using geometrical optics ray tracing. Of the two techniques, the surface integral physical optics is much easier to employ.

The standard physical optics surface currents are given by (7.28) and (7.29). New physical optics surface currents that are more convenient to work with are examined. These currents can be obtained by noting that the reflected plane wave from a dielectric interface can be generated by equivalent electric and magnetic current sheets. These currents are normal to the plane of incidence and their density is proportional to the incident field amplitude, polarization, and associated Fresnel reflection coefficient. Suppose the incident field is given by (7.26) and the normal to the cylinder surface is represented by the unit vector $\hat{n}$. The unit vector normal to the plane of incidence is

$$\hat{t} = \frac{\hat{n} \times \hat{k}_i}{| \hat{n} \times \hat{k}_i |},$$

in terms of which the new physical optics electric and magnetic currents are given by

$$\mathbf{J}_e = -2Y_0(\mathbf{E}_0 \cdot \hat{t}) \cos\phi_i R_E(\phi_i) e^{ik_0 \hat{k}_i \cdot \mathbf{r}} \hat{t} \tag{8.31}$$

$$\mathbf{J}_m = -2Z_0(\mathbf{H}_0 \cdot \hat{t}) \cos\phi_i R_H(\phi_i) e^{ik_0 \hat{k}_i \cdot \mathbf{r}} \hat{t} \tag{8.32}$$

Here, R_E and R_H are Fresnel reflection coefficients and ϕ_i is the local angle of incidence given by

$$\phi_i = \arccos(-\hat{n} \cdot \hat{k}_i).$$

In shadow regions on the surface ($\phi_i > \pi/2$) the currents are zero.

Suppose a stratified cylinder with arbitrary cross section is illuminated by a plane wave travelling in $-x$ direction ($\hat{k}_i = -\hat{x}$) as shown in Fig. 8.5. The outer surface of the cylinder is described by a smooth function $\rho(\phi)$. For E-polarized wave ($\mathbf{E}_0 = \hat{z}$) only electric current and for H-polarized wave ($\mathbf{H}_0 = Y_0\hat{z}$) only magnetic current

is induced on the cylinder surface as given by (8.31) and (8.32). It can easily be shown that in the far zone of the cylinder in a direction denoted by ϕ_s, the far field amplitudes for E and H polarization respectively are given by

$$\mathbf{S}_E = \hat{z}\frac{k_0}{2}\int_{\text{lit}} \cos\phi_i R_E(\phi_i) e^{-ik_0\rho(\phi')(\cos\phi' + \cos(\phi' - \phi_s))}\sqrt{\rho^2(\phi') + \rho'^2(\phi')}\,\mathrm{d}\phi' \qquad (8.33)$$

$$\mathbf{S}_H = \hat{\phi}\frac{k_0}{2}\int_{\text{lit}} \cos\phi_i R_H(\phi_i) e^{-ik_0\rho(\phi')(\cos\phi' + \cos(\phi' - \phi_s))}\sqrt{\rho^2(\phi') + \rho'^2(\phi')}\,\mathrm{d}\phi' \qquad (8.34)$$

where the integral is taken over the lit region and ρ' is the derivative of ρ with respect to ϕ. If the surface of the cylinder is convex the integral in (8.33) and (8.34) can be

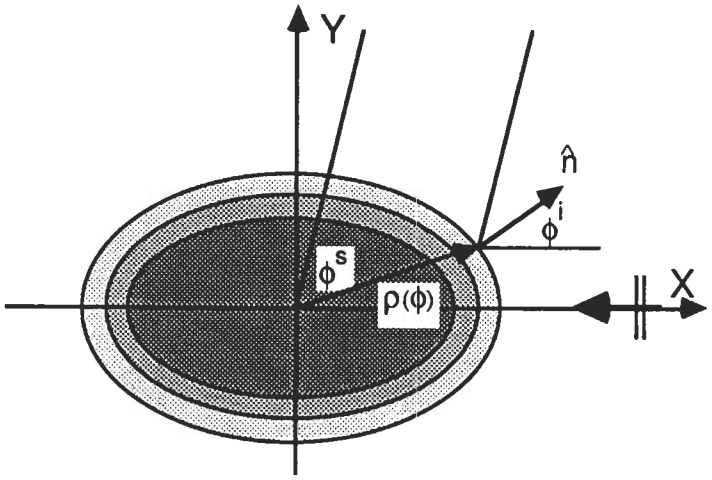

Figure 8.5: Geometry of scattering problem of a stratified cylinder.

evaluated using the stationary phase technique. The stationary point (ϕ_{SP}) is the root of the equation

$$\frac{\mathrm{d}}{\mathrm{d}\phi'}\rho(\phi')\left(\cos\phi' + \cos(\phi' - \phi_s)\right) = 0.$$

By noting that at the stationary point $\phi_i = \phi_s/2$ and

$$\sqrt{\rho^2(\phi') + \rho'^2(\phi')} = \frac{\rho(\phi_{SP})}{\cos(\phi_{SP} - \phi_s/2)},$$

and also by defining

$$g = \frac{\mathrm{d}^2}{\mathrm{d}\phi'^2}[\rho(\phi')\left(\cos\phi' + \cos(\phi' - \phi_s)\right)]_{\phi'=\phi_{SP}}$$

equations (8.33) and (8.34) become

$$\mathbf{S}_E = \hat{z}\cos(\frac{\phi_s}{2})R_E(\frac{\phi_s}{2})\frac{\rho(\phi_{SP})}{\cos(\phi_{SP}-\phi_s/2)}\sqrt{\frac{k_0\pi}{2\mid g\mid}}e^{-ik_0\rho(\phi_{SP})(\cos\phi_{SP}+\cos(\phi_{SP}-\phi_s))} \cdot e^{-i\mathrm{sgn}(g)\frac{\pi}{4}}, \quad (8.35)$$

$$\mathbf{S}_H = \hat{\phi}\cos(\frac{\phi_s}{2})R_H(\frac{\phi_s}{2})\frac{\rho(\phi_{SP})}{\cos(\phi_{SP}-\phi_s/2)}\sqrt{\frac{k_0\pi}{2\mid g\mid}}e^{-ik_0\rho(\phi_{SP})(\cos\phi_{SP}+\cos(\phi_{SP}-\phi_s))} \cdot e^{-i\mathrm{sgn}(g)\frac{\pi}{4}}. \quad (8.36)$$

For a circular cylinder of radius a these expressions simplify to

$$\mathbf{S}_E = \hat{z}\frac{1}{2}\sqrt{k_0\pi a\cos(\phi_s/2)}R_E(\frac{\phi_s}{2})e^{-i2k_0a\cos(\phi_s/2)}e^{i\pi/4} \quad (8.37)$$

$$\mathbf{S}_H = \hat{\phi}\frac{1}{2}\sqrt{k_0\pi a\cos(\phi_s/2)a}R_H(\frac{\phi_s}{2})e^{-i2k_0a\cos(\phi_s/2)}e^{i\pi/4} \quad (8.38)$$

To verify the validity of the physical optics expressions with new set of physical optics currents we compare expressions (8.37) and (8.38) for a layered circular cylinder with the exact series solution [Ruck et al, 1970, pp. 259]. Let us consider a two-layer cylinder with inner and outer radii of $a_1 = 10cm$ and $a = 10.5cm$ respectively. The dielectric constant of the inner and outer layers respectively are $15 + i7$ and $4 + i1$. These values are so chosen to simulate a tree with smooth bark. Figures 8.6 and 8.7 compare the normalized backscattering cross section ($\sigma/\pi a$) of the cylinder for E and H polarizations using physical optics expressions and exact series solution. In these figures the cross section of the cylinder in absence of the outer layer (bark) is also plotted to demonstrate the effect of the bark on reducing the cross section of the cylinder. For frequencies above 2 GHz ($k_0a = 4.2$) the agreement between the two solution is excellent. The bark layer plays the role of an impedance transformer which reduces the cross section of the cylinder by 14 dB around $k_0a = 16$.

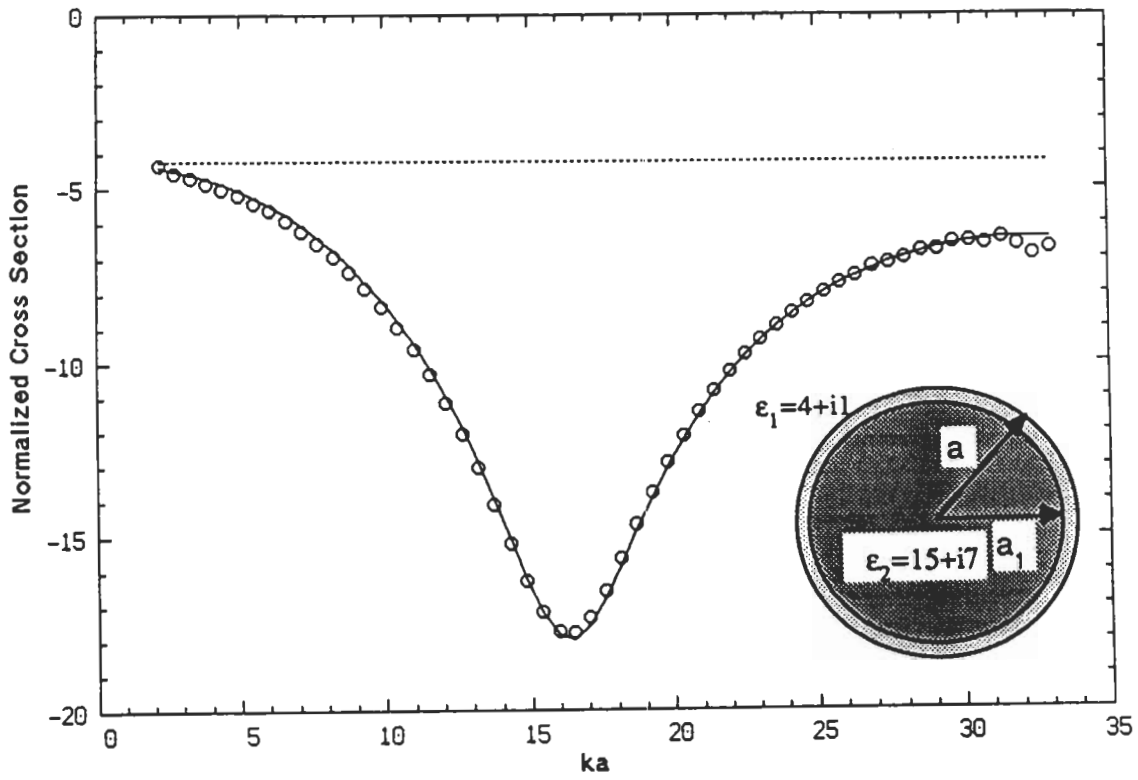

Figure 8.6: Normalized backscattering cross section ($\frac{\sigma}{\pi a}$) of a two-layer dielectric cylinder with $a = 10.5cm$, $a_1 = 10cm$, $\epsilon_1 = 15+i7$, $\epsilon_2 = 4+i1$ versus $k_0 a$ for TM case: (——) physical optics solution, (o o o) exact solution, (- - -) physical optics solution for homogeneous cylinder $a = 10.5cm$ $\epsilon = 15+i7$.

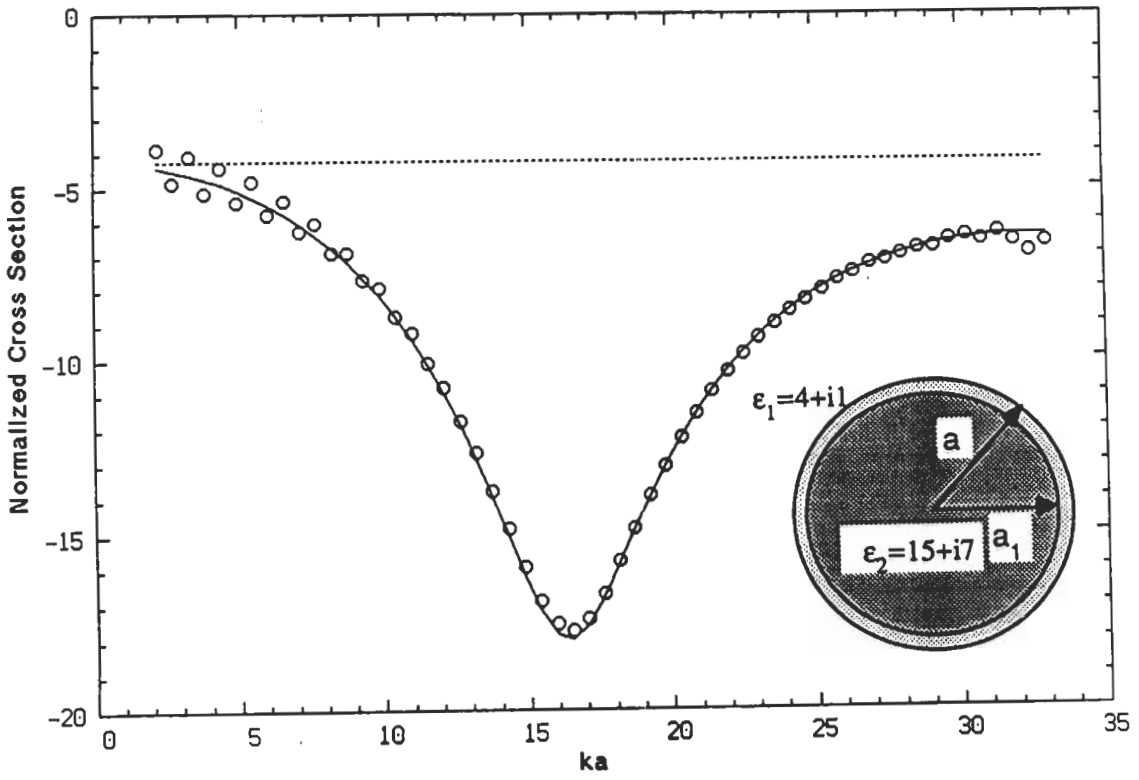

Figure 8.7: Normalized backscattering cross section ($\frac{\sigma}{\pi a}$) of a two-layer dielectric cylinder with $a = 10.5cm$, $a_1 = 10cm$, $\epsilon_1 = 15 + i7$, $\epsilon_2 = 4 + i1$ versus $k_0 a$ for TE case: (——) physical optics solution, (o o o) exact solution, (- - -) physical optics solution for homogeneous cylinder $a = 10.5cm$ $\epsilon = 15 + i7$.

8.4 Scattering from Corrugated Cylinder

Consider a corrugated dielectric cylinder with arbitrary cross section as shown in Fig. 8.8. Assume the corrugation geometry is such that the humps are identical and of equal distance L from each other. Further assume that if the corrugation is removed the surface of the cylinder would be denoted as before by $\rho(\phi)$ and the radius of curvature at each point is much larger than the wavelength and L. Under

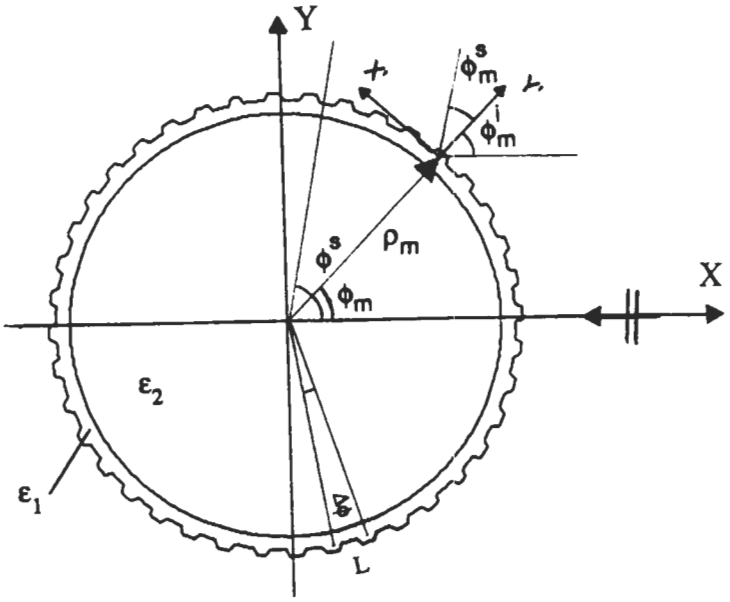

Figure 8.8: A corrugated cylinder geometry.

these conditions each point on the cylinder surface can be replaced, approximately, by a periodic corrugated surface. The accuracy of this approximation is in the order of physical optics approximation for smooth cylinders.

Suppose the cylinder is illuminated by a plane wave travelling in $-x$ direction and let us denote the tangential coordinate at the center of each hump by (x', y') where $\hat{y}'$ coincides with the outward normal unit vector $(\hat{n}(\phi))$. If the origin of the prime coordinate system corresponding to the m^{th} hump is located at (ρ_m, ϕ_m) we

have

$$\phi_m = \sum_{\ell=1}^{m} \Delta\phi_\ell - \frac{\pi}{2}, \tag{8.39}$$

$$\Delta\phi_{\ell+1} = \frac{L}{\sqrt{\rho^2(\phi_\ell) + \rho'^2(\phi_\ell)}}, \tag{8.40}$$

where $\Delta\phi_1$ is a known quantity. The local incidence angle at the m^{th} hump can be obtained from

$$\phi_m^i = \arccos(\hat{n}(\phi_m) \cdot \hat{x})$$

and the induced current in the m^{th} hump can be approximated by that of the periodic corrugated surface when the incidence angle is ϕ_m^i. The scattering direction is denoted by ϕ_s as before and the scattering direction for the m^{th} local coordinate is given by

$$\phi_m^s = \phi_s - \phi_m^i.$$

The far field due to the m^{th} hump ($\mathbf{S}_m$), depending on the polarization, can be obtained from (8.10) and we note that those humps with $|\phi_m^s| > \pi/2$ do not contribute to the far field. The total contribution of the cylinder corrugation to the far field is the vector sum of the fields due to each hump modified by a phase factor to correct for the relative positions of the humps. Therefore

$$\mathbf{S}_c = \sum_m \mathbf{S}_m e^{-ik_0 x_m} e^{-ik_0(x_m \cos\phi_s + y_m \sin\phi_s)}, \tag{8.41}$$

where

$$x_m = \rho_m \cos\phi_m,$$

$$y_m = \rho_m \sin\phi_m.$$

The total scattered field may now be obtained from

$$\mathbf{S} = \mathbf{S}_c + \mathbf{S}_s,$$

where $\mathbf{S}_s$ is the far field amplitude of the smooth cylinder.

8.5 Numerical Results

To examine the effect of surface corrugation on scattering from corrugated cylinders, we consider a two-layer circular cylinder with uniform corrugation. The pertinent parameters are chosen as follows: each hump is a $\lambda/8 \times \lambda/8$ square with dielectric constant $\epsilon_1 = 4 + i1$, the distance between humps is $L = \lambda/4$, the thickness and dielectric constant of outer layer are $\lambda/2$ and $4 + i1$ respectively, and the radius and the dielectric constant of inner layer are 10λ and $15 + i7$ respectively. For the corresponding periodic surface all the components of the induced current in each hump are obtained by the moment method and the amplitude and phase of the total current ($\int_s J(x', y')\mathrm{d}x'\mathrm{d}y'$) are plotted in Figs. 8.9 and 8.10. Figures 8.11-8.14 show the amplitude and the phase of the zeroth Bragg mode as given in (8.21) and (8.22), the reflected wave in the absence of the corrugations, and the sum of the two waves (total reflected wave) as a function of incidence angle. For E polarization (Fig. 8.11) the total reflected wave is less than the reflected wave in the absence of corrugation (reduction in the scattered field). In this case, as far as the total reflected field is concerned, the corrugation can be replaced by a homogeneous dielectric layer with thickness $\lambda/8$ and $\epsilon = 2.6 + i0.58$. For H polarization (Fig. 8.13) the total reflected wave is weaker than the reflected wave in the absence of the corrugation for angles less than the Brewster angle and vice versa for angles greater than the Brewster angle.

Once the induced current versus angle is obtained the bistatic scattered field can

be computed from (8.41). Figures 8.15 and 8.15 show the far field amplitude due to the corrugation (S_c) and smooth cylinder (S_s) and the total far field amplitude ($S_c + S_s$). To examine the role of the outer layer, the far field amplitude of the cylinder when the outer layer is removed is also plotted. It is seen that the smooth bark reduces the scattered field by 3 dB and the corrugation on the bark further reduces the scattered field by another 8 dB. In Fig. 8.16 the total far field amplitude , for TM case, of the corrugated cylinder is compared with a smooth cylinder when corrugation is replaced by an equivalent layer (thickness=$\lambda/8$, $\epsilon = 2.6 + i0.58$). Excellent agreement is obtained.

8.6 Conclusions

A hybrid solution based on the moment method and physical optics approximation is obtained for corrugated layered cylinders. The only restriction on the physical dimensions is the radius of curvature (r) of the cylinder where we require $r \gg \lambda$. Also new physical optics expressions for the equivalent surface current on the dielectric structure is introduced. This method is employed to investigate the effect of bark and its roughness on the scattering from tree trunks and branches. It is shown that the bark and its roughness both reduce the radar cross section. The low contrast dielectric bark layer manifest its effect more significantly at higher frequencies where the bark thickness and its roughness are a considerable fraction of the wavelength. It is also demonstrated that the roughness of the bark can be replaced with a homogeneous layer for the TM case. This suggests the possibility of replacing the roughness with an anisotropic layer for the case of an arbitrary polarization.

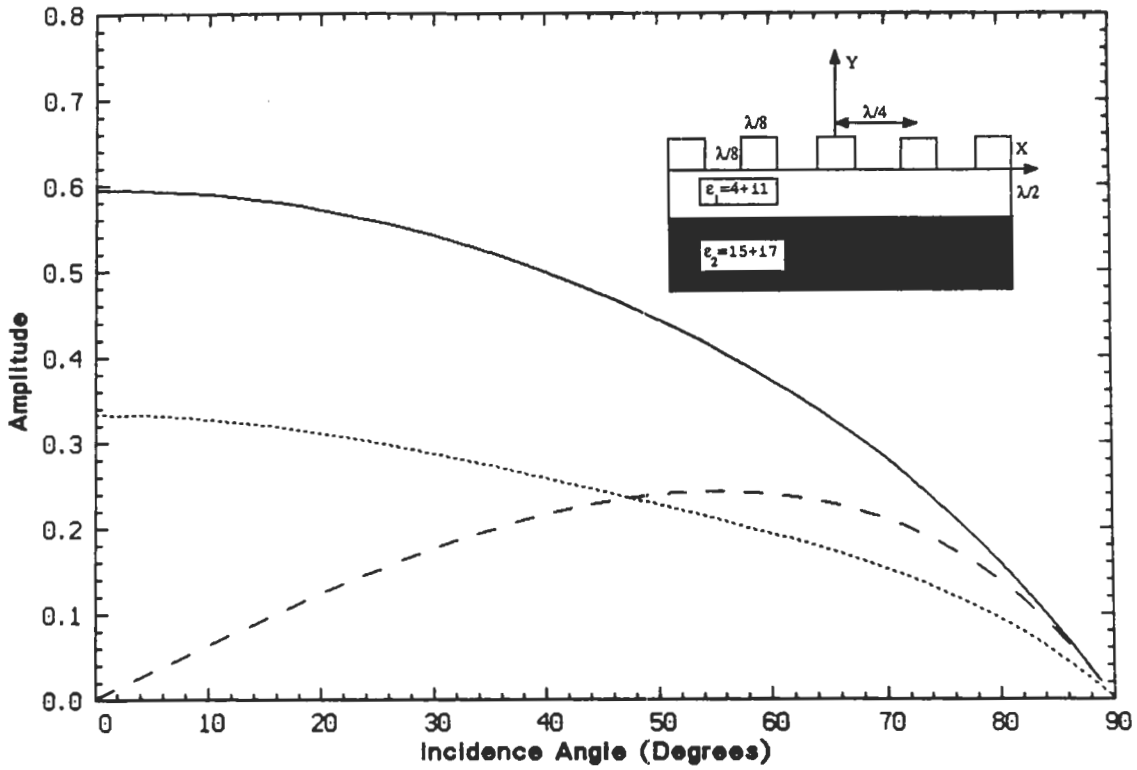

Figure 8.9: Amplitude of the total induced current in a two-layer periodic corrugated surface versus incidence angle: (——) z component of the current (E polarization), (- - -) x component of current and (– –) y component of the current (H polarization).

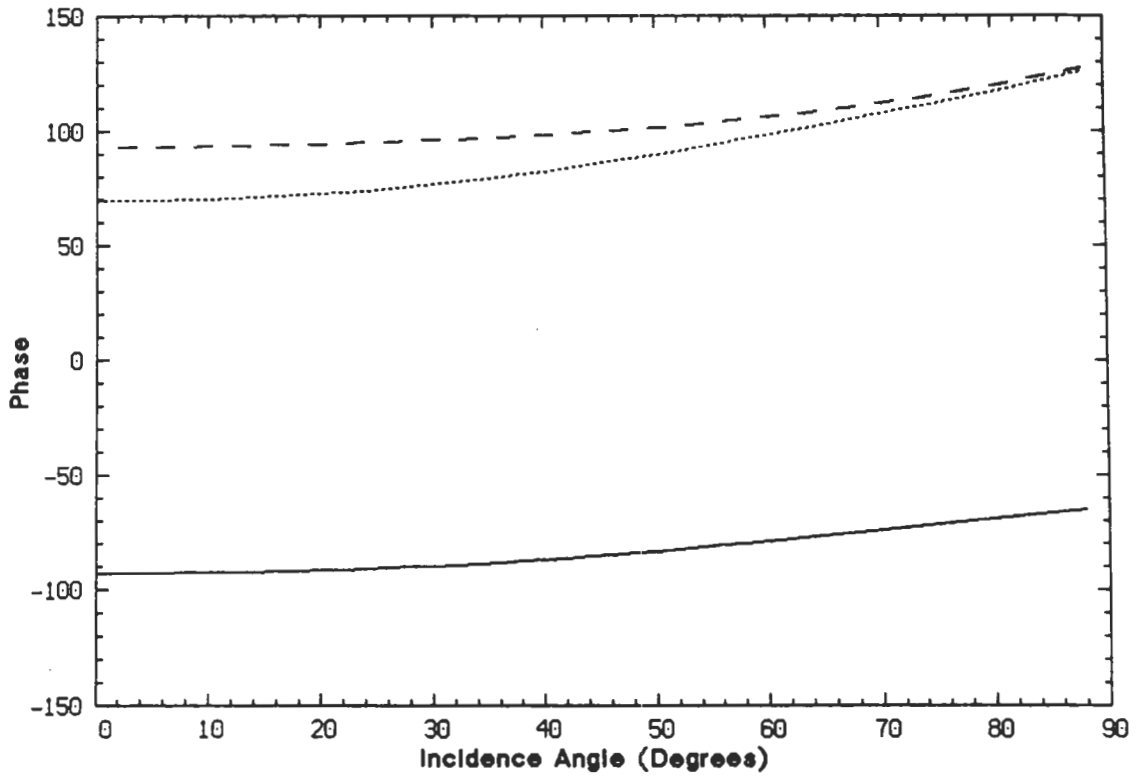

Figure 8.10: Phase of the total induced current in a two-layer periodic corrugated surface versus incidence angle: (——) z component of the current (E polarization), (- - -) x component of current and (– –) y component of the current (H polarization).

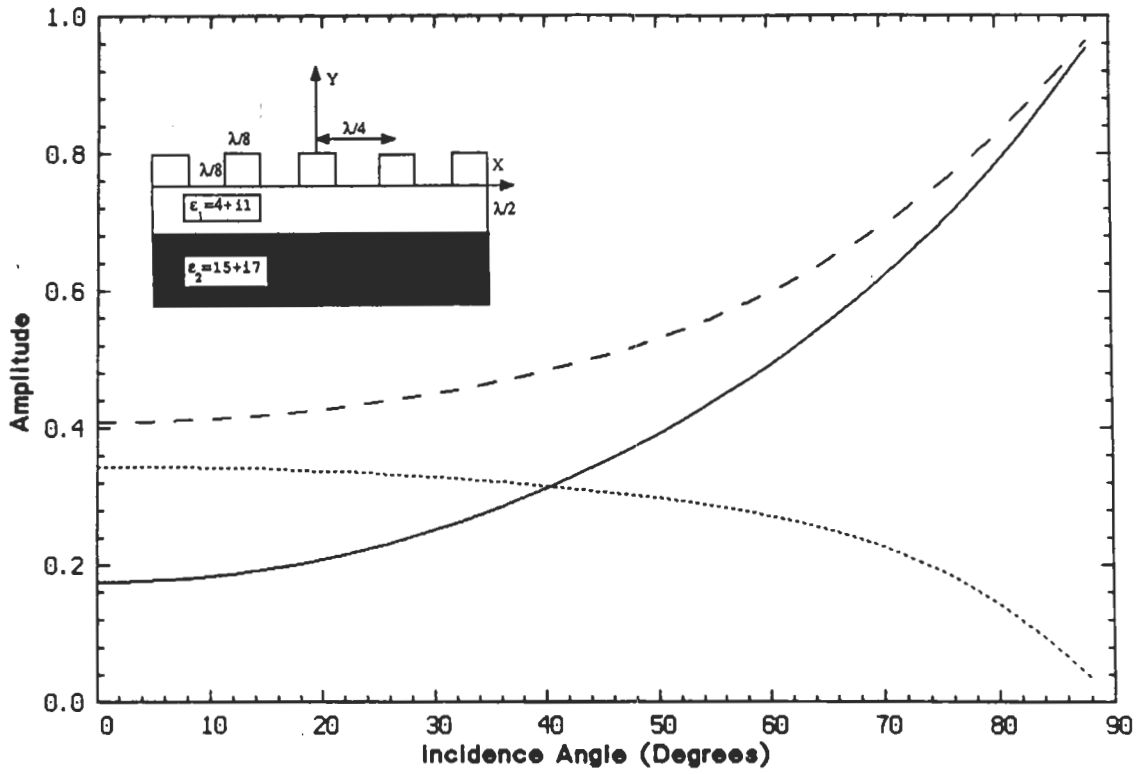

Figure 8.11: Amplitude of the reflected field from a two-layer periodic corrugated surface versus incidence angle for E polarization: (- - -) zeroth order Bragg mode, (– –) reflected field in absence of corrugation, (——) total reflected field.

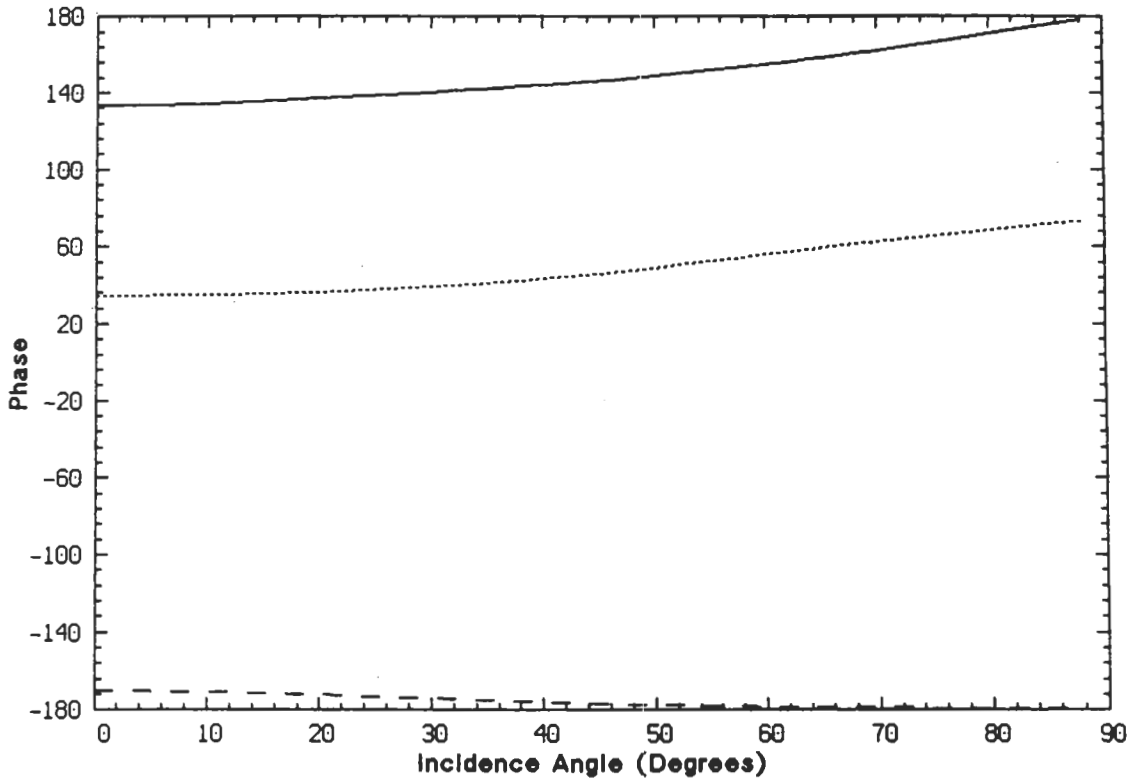

Figure 8.12: Phase of the reflected field from a two-layer periodic corrugated surface versus incidence angle for E polarization: (- - -) zeroth order Bragg mode, (– –) reflected field in absence of corrugation, (——) total reflected field.

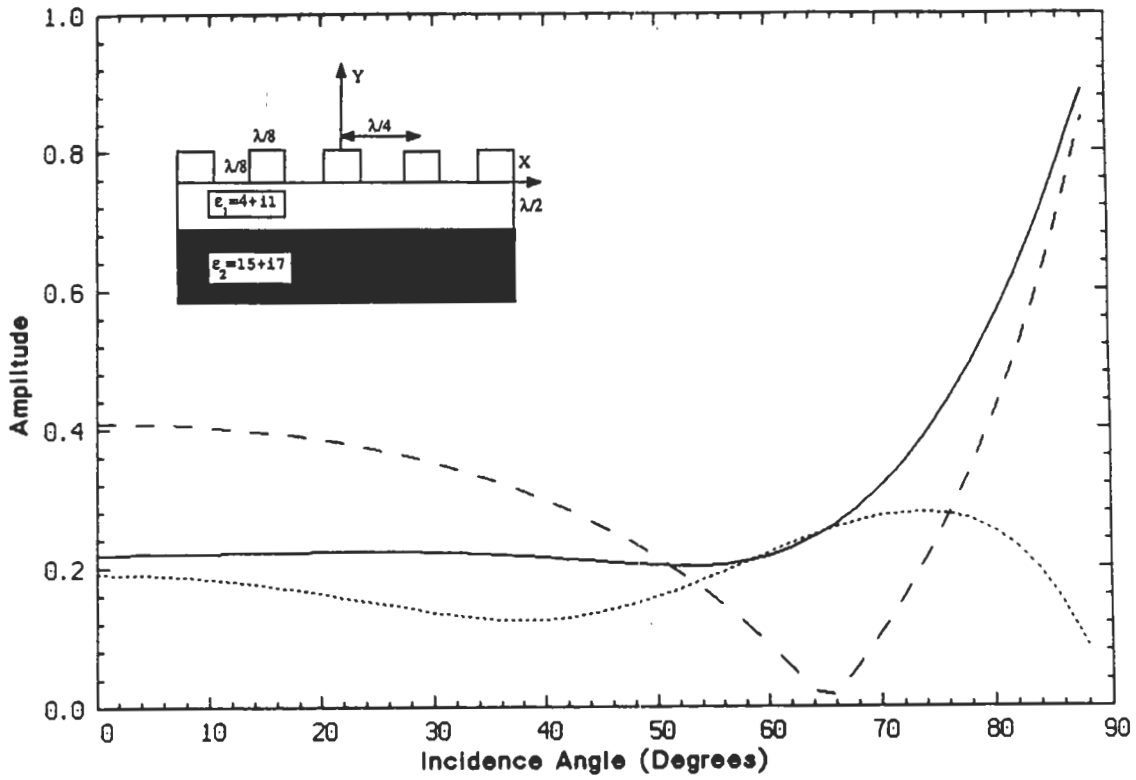

Figure 8.13: Amplitude of the reflected field from a two-layer periodic corrugated surface versus incidence angle for H polarization: (- - -) zeroth order Bragg mode, (– –) reflected field in absence of corrugation, (——) total reflected field.

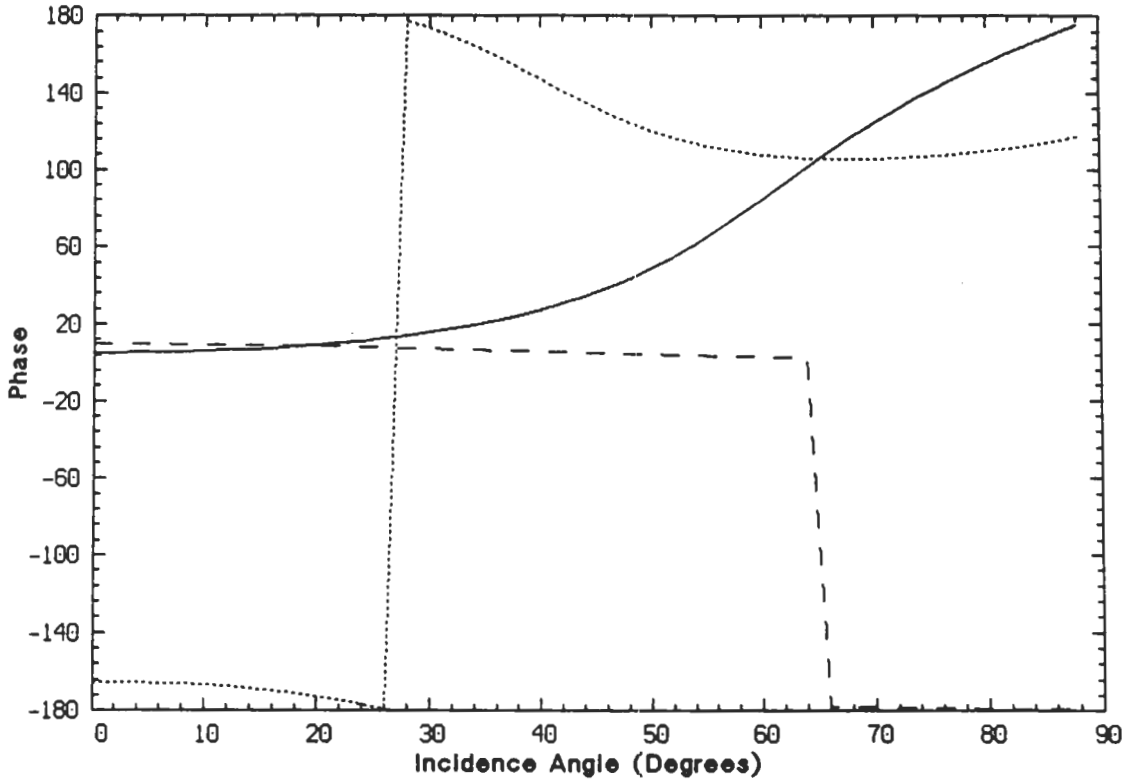

Figure 8.14: Phase of the reflected field from a two-layer periodic corrugated surface versus incidence angle for H polarization: (- - -) zeroth order Bragg mode, (– –) reflected field in absence of corrugation, (——) total reflected field.

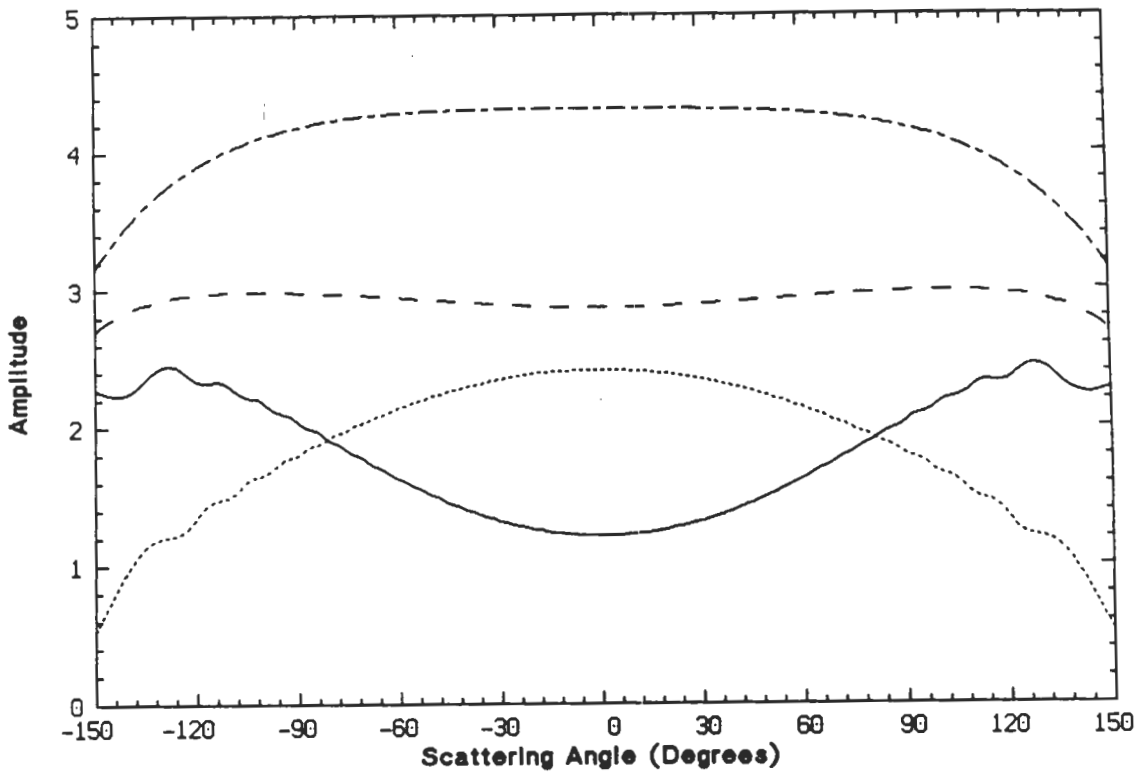

Figure 8.15: Far field amplitude of a corrugated cylinder for TM case with $a = 10.5\lambda_0$, $a_1 = 10\lambda_0$, $L = \lambda_0/4$, $\epsilon_1 = 4 + i1$, and $\epsilon_2 = 15 + i7$; (- - -) contribution of corrugation (S_c), (– –) contribution of smooth cylinder (S_s), (——) total far field amplitude ($S_s + S_c$), and (– - –) far field amplitude for smooth cylinder in absence of corrugation and outer layer.

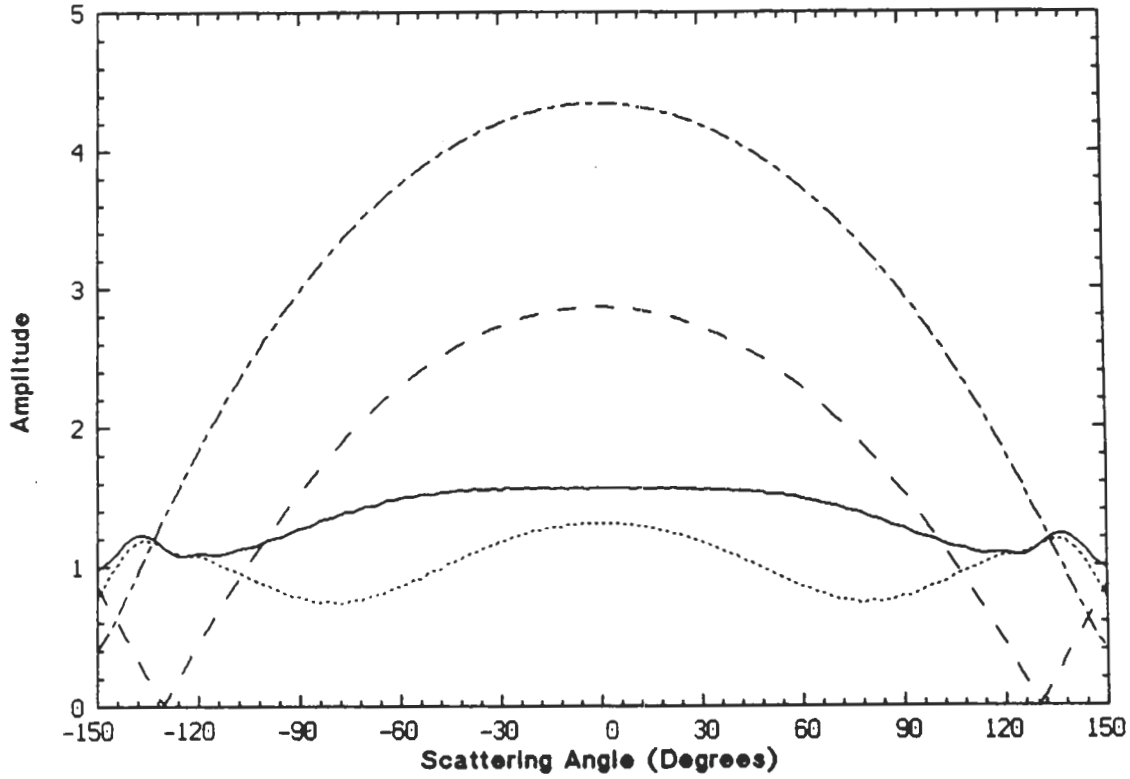

Figure 8.16: Far field amplitude of a corrugated cylinder for TE case with $a = 10.5\lambda_0$, $a_1 = 10\lambda_0$, $L = \lambda_0/4$, $\epsilon_1 = 4 + i1$, and $\epsilon_2 = 15 + i7$; (- - -) contribution of corrugation (S_c), (– –) contribution of smooth cylinder (S_s), (——) total far field amplitude ($S_s + S_c$), and (– - –) far field amplitude for smooth cylinder in absence of corrugation and outer layer.

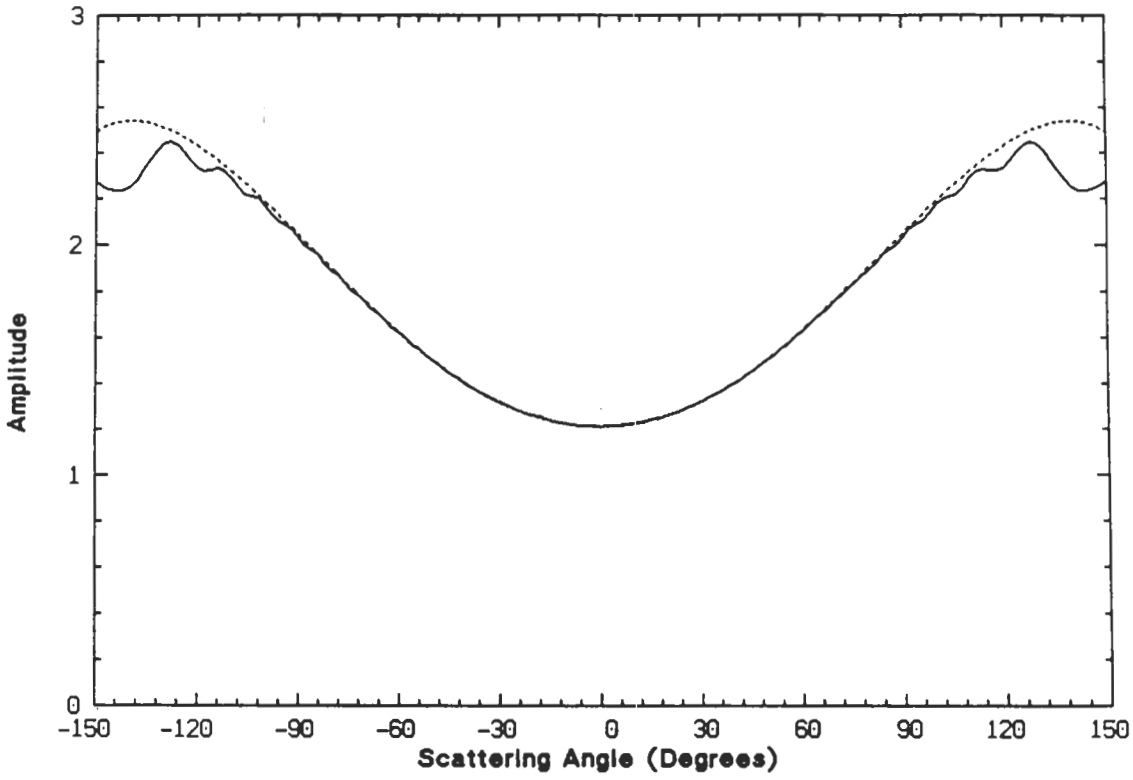

Figure 8.17: Far field amplitude of the corrugated cylinder (——) and equivalent three-layer cylinder (- - -) for TM case.

CHAPTER IX

SCATTERING FROM A FOREST CANOPY

9.1 Introduction

A forest canopy is considered to be an inhomogeneous medium which consists of randomly oriented discrete scatterers, namely leaves or needles and branches, above a ground layer. As discussed in Chapter 1, depending on the frequency range desired, there are two approaches to obtain a scattering model for a forest canopy, continuous and discrete random medium techniques. In the continuous case the random medium is modelled by assuming that its permittivity $\epsilon(x, y, z)$ is a random process whose statistical behavior is known [Tsang et al pp.319, 1985; Lang, 1981; Tsang and Kong 1978]. In the discrete case it is assumed that the particles are sparse in the medium and the single scattering theory is applied [Ulaby et al, Chapter 13, 1986; Tsang et al, Chapter 3, 1985; Karam et al, 1987].

At microwave frequencies and above, the vector radiative transfer approach is appropriate to model forested areas. The single scattering models that were developed in previous chapters can be used directly in this model and the effect of different physical parameters of the constituent particles on scattering can be investigated.

The forest canopy is modelled as two horizontal layers (Fig. 9.1), a crown layer of height d above a trunk layer of height H_t. The crown layer, comprised of leaves

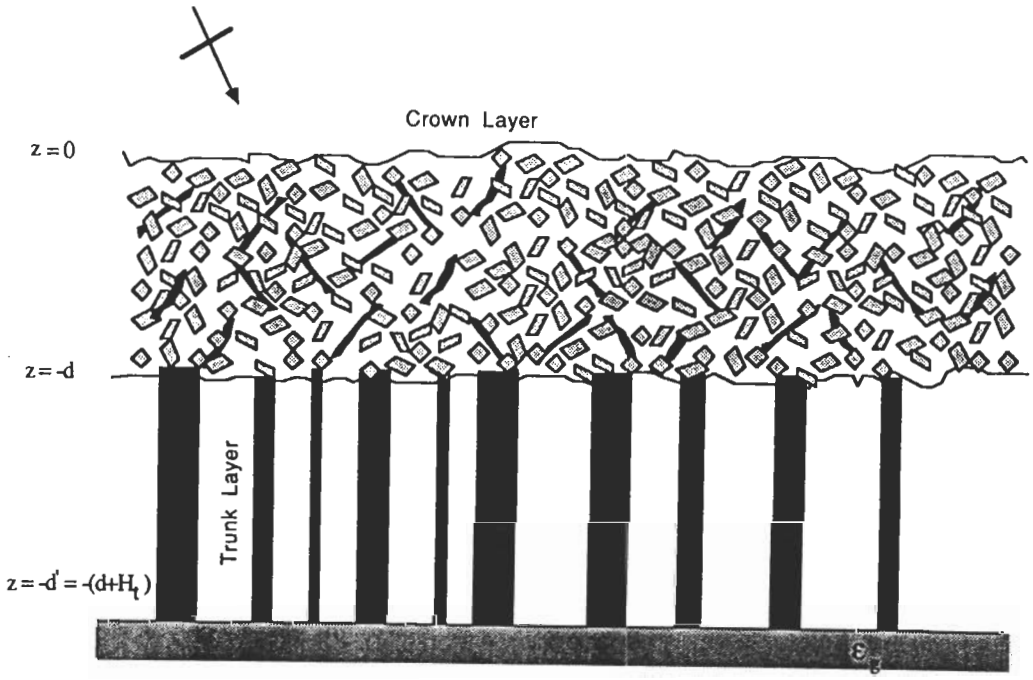

Figure 9.1: Forest canopy model.

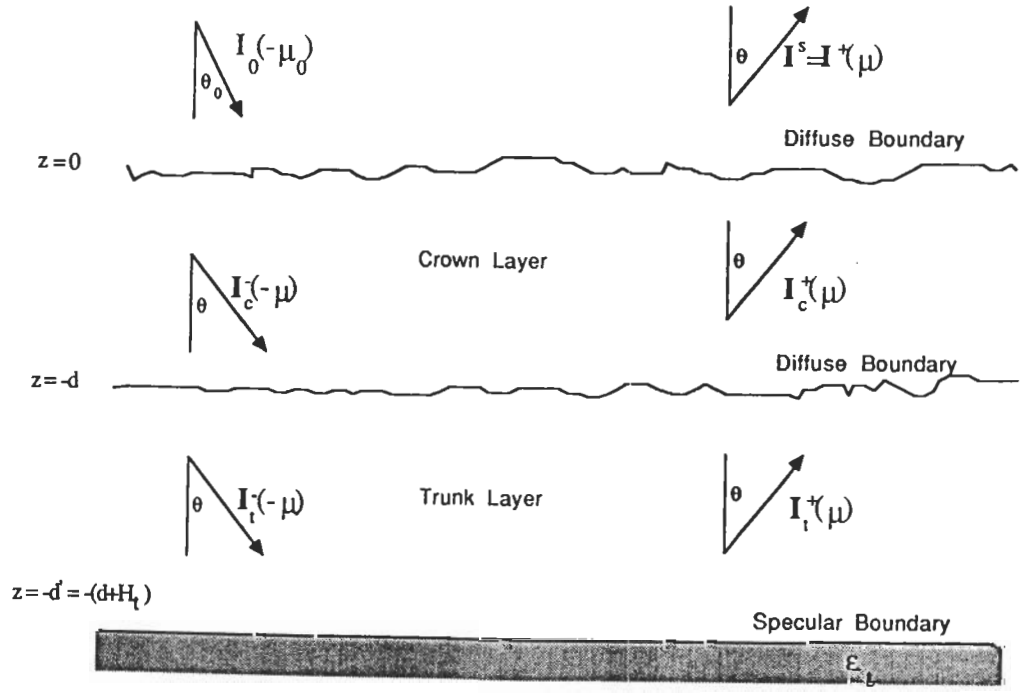

Figure 9.2: Problem Geometry.

and branches, is assumed to be continuous in the horizontal direction and statistically homogeneous over the crown volume. The trunk layer is assumed to consist of vertical, homogeneous, dielectric cylinders. The air-crown interface and the crown-trunk interface are treated as diffuse boundaries, and the interface between the trunk layer and the ground layer is considered a specular surface. The problem is formulated using the radiative transfer equation and the scattering intensity $\mathbf{I}^s$ (Stokes vector) in the form of a first-order solution is given.

9.2 Basic definitions

The simplified geometry of the problem is depicted in Fig. 9.2. The boundaries at $z = 0$ and $z = -d$ are assumed to be diffuse, and the bottom boundary at $z = -d' = -(d + H_t)$ is treated as a specular surface with a dielectric constant ϵ_g.

The vector radiative transfer problem is formulated in terms of the vector specific intensity $\mathbf{I}$ [Ulaby et al, 1986, pp. 1085-1092]. For an elliptically polarized monochromatic plane wave given by (1.8) $\mathbf{I}$ is defined through the modified Stokes parameters I_v, I_h, U, and V as follows:

$$\mathbf{I} = \begin{bmatrix} I_v \\ I_h \\ U \\ V \end{bmatrix} = \frac{1}{\eta} \begin{bmatrix} |E_v|^2 \\ |E_h|^2 \\ 2\mathrm{Re}(E_v E_h^*) \\ 2\mathrm{Im}(E_v E_h^*) \end{bmatrix} \tag{9.1}$$

The standard approach used for defining the bistatic scattering coefficient of a distributed target of area A is to compute the field scattered by the target in the direction of interest as a result of illumination by a plane wave. Thus, the incident illumination is a plane wave, whereas the scattered field is a spherical wave. For a spherical wave, the vector specific intensity also is defined in terms of Stokes parame-

ters, but the definition includes normalization by the solid angle $A\cos\theta_s/r^2$, where r is the distance between the distributed target and the observation point and θ_s is the angle between the outward normal to A and the vector defining the direction from the target to the observation point. Hence, the scattered intensity from a random medium is defined as:

$$\mathbf{I}^s = \begin{bmatrix} I_v^s \\ I_h^s \\ U^s \\ V^s \end{bmatrix} = \frac{r^2}{Z_0 A\cos\theta_s} \begin{bmatrix} \langle \mid E_v^s \mid^2 \rangle \\ \langle \mid E_h^s \mid^2 \rangle \\ 2\mathrm{Re}(\langle E_v^s E_h^{s*} \rangle) \\ 2\mathrm{Im}(\langle E_v^s E_h^{s*} \rangle) \end{bmatrix} \tag{9.2}$$

where $\langle \quad \rangle$ denotes ensemble average.

The bistatic scattering coefficient $\sigma^\circ_{\alpha\beta}$ corresponding to a β-polarized incident plane wave giving rise to α-polarized spherical wave is defined as:

$$\sigma^\circ_{\alpha\beta} = \frac{4\pi r^2}{A} \cdot \frac{\langle \mid E_\alpha^s \mid^2 \rangle}{\mid E_\beta^i \mid^2}, \tag{9.3}$$

where $\alpha, \beta = v$ or h polarization. Using (1.8) for $\mid E_\beta^i \mid^2$ and (9.2) for $\langle \mid E_\alpha^s \mid^2 \rangle$, (9.3) can be written as:

$$\sigma^\circ_{\alpha\beta}(\pi - \theta_0, \phi_0; \theta_s, \phi_s) = \frac{4\pi\cos\theta_s I_\alpha^s(\theta_s, \phi_s)}{I_\beta^i(\pi - \theta_0, \phi_0)} \tag{9.4}$$

where $(\pi - \theta_0, \phi_0)$ denotes the direction of the downward-going incident intensity and (θ_s, ϕ_s) denotes the direction of the upward-going scattered intensity. We note that $\theta_s = \theta_0$ and $\phi_s = \pi + \phi_0$ corresponds to scattering in the backward direction.

9.3 Phase and Extinction Matrices

9.3.1 Phase Matrix

For a single particle in the global coordinate system (X, Y, Z) with some orientation angles (θ_j, ϕ_j) the scattering matrix $\mathbf{S}(\theta_s, \phi_s; \theta_i, \phi_i; \theta_j, \phi_j)$ is defined in (1.11)

where (θ_i, ϕ_i) and (θ_s, ϕ_s) denote directions of incidence and scattering respectively. In fact the scattering matrix relates the incident field components to the components of the scattered field in the desired directions. Counterpart of the scattering matrix for modified Stokes vector is the Stokes matrix $\mathbf{L}(\theta_s, \phi_s; \theta_i, \phi_i; \theta_j, \phi_j)$ which relates the scattered modified Stokes vector $\mathbf{I}^s$ to the incident modified Stokes vector $\mathbf{I}^i$ by [Ulaby et al.,1986,p.1088]

$$\mathbf{I}^s = \frac{1}{r^2}\mathbf{L}(\theta_s, \phi_s; \theta_i, \phi_i; \theta_j, \phi_j) \cdot \mathbf{I}^i \tag{9.5}$$

where $\mathbf{L}(\theta_s, \phi_s; \theta_i, \phi_i; \theta_j, \phi_j)$ is the Stokes matrix and is given by

$$\mathbf{L} = \begin{bmatrix} |S_{vv}|^2 & |S_{vh}|^2 & \mathrm{Re}(S_{vh}^* S_{vv}) & -\mathrm{Im}(S_{vh}^* S_{vv}) \\ |S_{hv}|^2 & |S_{hh}^*|^2 & \mathrm{Re}(S_{hh}^* S_{hv}) & -\mathrm{Im}(S_{hh}^* S_{hv}) \\ 2\mathrm{Re}(S_{vv} S_{hv}^*) & 2\mathrm{Re}(S_{vh} S_{hh}^*) & \mathrm{Re}(S_{vv} S_{hh}^* + S_{vh} S_{hv}^*) & -\mathrm{Im}(S_{vv} S_{hh}^* - S_{vh} S_{hv}^*) \\ 2\mathrm{Im}(S_{vv} S_{hv}^*) & 2\mathrm{Im}(S_{vh} S_{hh}^*) & \mathrm{Im}(S_{vv} S_{hh}^* + S_{vh} S_{hv}^*) & Re(S_{vv} S_{hh}^* - S_{vh} S_{hv}^*) \end{bmatrix}. \tag{9.6}$$

If the particles in the medium are positioned and oriented randomly, we may add the scattered Stokes vectors of the particles incoherently. This can be justified by noting that the phase of the scattered wave from a particle depends on its position and if the distribution of the scatterers is sufficiently random, the phase distribution of the scattered field becomes uniform. Suppose the medium is comprised of particles with known size and orientation distribution functions and the number of particles per unit volume is denote by N, then the phase matrix of this medium is defined by

$$\mathbf{P}(\theta_s, \phi_s; \theta_i, \phi_i) = N\langle \mathbf{L} \rangle \tag{9.7}$$

where $\langle \quad \rangle$ is ensemble average over the size and orientation of the particles. The phase matrix $\mathbf{P}_c(\theta_s, \phi_s; \theta_i, \phi_i)$ relates the average intensity scattered by a unit volume

of the crown layer into the direction (θ_s, ϕ_s) to the intensity incident upon the unit volume from the direction (θ_i, ϕ_i). It should be pointed out that in the trunk layer the trunks are assumed to be vertical and usually the density is given by the number per unit area (N_t). Thus the phase matrix in trunk layer is defined by

$$\mathbf{P}_t(\theta_s, \phi_s; \theta_i, \phi_i) = \frac{N_t}{H_t}\langle \mathbf{L} \rangle \tag{9.8}$$

where $\langle \quad \rangle$ is the ensemble average over the size of the trunks.

9.3.2 Extinction Matrix

The extinction matrix characterizes the attenuation of the Stokes parameters due to absorption and scattering. For a medium with low concentration of particles, the attenuation rate can be obtained from the extinction cross section of the individual scatterers. By applying the optical theorem, the extinction cross section, σ_{ext}^p ($p = v$ or h), is given by

$$\sigma_{ext}^p = \frac{4\pi}{k_0}\mathrm{Im}[S_{pp}(\theta_s, \phi_s; \theta_i, \phi_i; \theta_j, \phi_j)],$$

from which the extinction coefficient can be obtained through

$$\kappa_p = N\langle \sigma_{ext}^p \rangle \tag{9.9}$$

To find a better estimate of the coherent field along the propagation direction (θ_i, ϕ_i), Foldy's approximation can be employed. The coupled equations for vertical and horizontal mean field in this approximation is of the following form [Tsang et al.,1985,p.139]

$$\frac{dE_v}{ds} = (ik_0 + M_{vv})E_v + M_{vh}E_h \tag{9.10}$$

$$\frac{dE_h}{ds} = M_{hv}E_v + (ik_0 + M_{hh})E_h \tag{9.11}$$

where s is the distance along the direction of propagation and

$$M_{mn} = \frac{i2\pi N}{k_0}\langle S_{mn}(\theta_s, \phi_s; \theta_i, \phi_i; \theta_j, \phi_j)\rangle \qquad m, n = v, h \tag{9.12}$$

Using the definition of the modified Stokes parameters and (9.10) and (9.11) the following coupled differential equation is found

$$\frac{d}{ds}\mathbf{I} = -\boldsymbol{\kappa}\mathbf{I} \tag{9.13}$$

where $\boldsymbol{\kappa}$ is the extinction matrix and is given by

$$\boldsymbol{\kappa} = \begin{bmatrix} -2\mathrm{Re}(M_{vv}) & 0 & -\mathrm{Re}(M_{vh}) & -\mathrm{Im}(M_{vh}) \\ 0 & -2\mathrm{Re}(M_{hh}) & -\mathrm{Re}(M_{hv}) & \mathrm{Im}(M_{hv}) \\ -2\mathrm{Re}(M_{hv}) & -2\mathrm{Re}(M_{vh}) & -[\mathrm{Re}(M_{vv}) + \mathrm{Re}(M_{hh})] & [\mathrm{Im}(M_{vv}) - \mathrm{Im}(M_{hh})] \\ 2\mathrm{Im}(M_{hv}) & -2\mathrm{Im}(M_{vh}) & -[\mathrm{Im}(M_{vv}) - \mathrm{Im}(M_{hh})] & -[\mathrm{Re}(M_{vv}) + \mathrm{Re}(M_{hh})] \end{bmatrix}. \tag{9.14}$$

The effective propagation constant of the mean field can be obtained from the eigenvalues of the matrix formed by the right hand side coefficients of equations (9.10) and (9.11). The two eigenvalues are given by

$$K_1 = k_0 - \frac{i}{2}[M_{vv} + M_{hh} + r] \tag{9.15}$$

$$K_2 = k_0 - \frac{i}{2}[M_{vv} + M_{hh} - r] \tag{9.16}$$

where

$$r = [(M_{vv} - M_{hh})^2 + 4M_{hv}M_{vh}]^{\frac{1}{2}} \tag{9.17}$$

The eigenvectors corresponding to K_1 and K_2 are denoted by $[1, b_1]$ and $[b_2, 1]$ respectively, and b_1 and b_2 are given by

$$b_1 = \frac{2M_{hv}}{M_{vv} - M_{hh} + r}$$

$$b_2 = \frac{2M_{vh}}{-M_{vv} + M_{hh} - r}$$

The corresponding effective propagation constant of the coherent Stokes parameters can be obtained from eigenvalue solution of equation (9.13). The eigenvalues of extinction matrix are given by [Tsang et al.,1985]

$$\boldsymbol{\Lambda}(\theta,\phi) = \begin{bmatrix} \lambda_1 \\ \lambda_2 \\ \lambda_3 \\ \lambda_4 \end{bmatrix} = \begin{bmatrix} 2\mathrm{Im}[K_1] \\ iK_2^* - iK_1 \\ iK_1^* - iK_2 \\ 2\mathrm{Im}[K_2] \end{bmatrix} \tag{9.18}$$

The eigenmatrix $\mathbf{Q}(\theta,\phi)$ is also defined in such a way that the columns of $\mathbf{Q}(\theta,\phi)$ are the eigenvectors of the extinction matrix and is given by

$$\mathbf{Q}(\theta,\phi) = \begin{bmatrix} 1 & b_2^* & b_2 & |\, b_2 \,|^2 \\ |\, b_1 \,|^2 & b_1 & b_1^* & 1 \\ 2\mathrm{Re}[b_1] & 1 + b_1 b_2^* & 1 + b_2 b_1^* & 2\mathrm{Re}[b_2] \\ -2\mathrm{Im}[b_1] & -i(1 - b_1 b_2^*) & i(1 - b_2 b_1^*) & 2\mathrm{Im}[b_2] \end{bmatrix} \tag{9.19}$$

It is worth noting that at high frequencies or generally for particles with no depolarization where $M_{vh} = M_{hv} = 0$ the eigenmatrix $\mathbf{Q}$ is independent of the particles shape and orientation. In this case the eigenmatrix and its inverse are given by

$$\mathbf{Q} = \begin{bmatrix} 1 & 0 & 0 & 0 \\ 0 & 0 & 0 & 1 \\ 0 & 1 & 1 & 0 \\ 0 & -i & i & 0 \end{bmatrix}, \qquad \mathbf{Q}^{-1} = \begin{bmatrix} 1 & 0 & 0 & 0 \\ 0 & 0 & \frac{1}{2} & \frac{i}{2} \\ 0 & 0 & \frac{1}{2} & -\frac{i}{2} \\ 0 & 1 & 0 & 0 \end{bmatrix}$$

9.4 Radiative Transfer Equations

When formulating the radiative transfer problem for bounded media, the standard practice is to split the intensity vector into upward-going ($\mathbf{I}^+(\theta,\phi,z)$) and downward-

going ($\mathbf{I}^-(\theta,\phi,z)$) components, noting that θ varies between 0 and $\pi/2$ [Ulaby et al., 1987, pp.1090-1092]. In the crown layer , the intensity ($\mathbf{I}_c^+(\theta,\phi,z)$) travelling in the upward direction (θ,ϕ) and the intensity ($\mathbf{I}_c^-(\pi-\theta,\phi,z)$) travelling in the downward direction $(\pi-\theta,\phi)$ must satisfy the coupled radiative transfer equations

$$\begin{aligned} \tfrac{d}{dz}\mathbf{I}_c^+(\mu,\phi,z) &= -\tfrac{\boldsymbol{\kappa}_c^+}{\mu}\mathbf{I}_c^+(\mu,\phi,z) + \mathbf{F}_c^+(\mu,\phi,z)\ , \qquad -d \le z \le 0 \\ -\tfrac{d}{dz}\mathbf{I}_c^-(-\mu,\phi,z) &= -\tfrac{\boldsymbol{\kappa}_c^-}{\mu}\mathbf{I}_c^-(-\mu,\phi,z) + \mathbf{F}_c^-(-\mu,\phi,z)\ , \qquad -d \le z \le 0 \end{aligned} \tag{9.20}$$

where $\boldsymbol{\kappa}_c^{\pm}$ is the extinction matrix of the crown layer, $\mu = \cos\theta$, and $-\mu = \cos(\pi-\theta)$. The source functions $\mathbf{F}_c^+(\mu,\phi,z)$ and $\mathbf{F}_c^-(-\mu,\phi,z)$ account for directing the energy incident upon an elemental volume from all directions into the direction (θ,ϕ) and $(\pi-\theta,\phi)$, respectively and are given by

$$\begin{aligned} \mathbf{F}_c^+(\mu,\phi,z) &= \tfrac{1}{\mu}[\textstyle\int_0^{2\pi}\int_0^1 \mathbf{P}_c(\mu,\phi;\mu',\phi')\mathbf{I}_c^+(\mu',\phi',z)\mathrm{d}\Omega' \\ &\quad + \textstyle\int_0^{2\pi}\int_0^1 \mathbf{P}_c(\mu,\phi;-\mu',\phi')\mathbf{I}_c^-(-\mu',\phi',z)\mathrm{d}\Omega'] \\ \mathbf{F}_c^-(-\mu,\phi,z) &= \tfrac{1}{\mu}[\textstyle\int_0^{2\pi}\int_0^1 \mathbf{P}_c(-\mu,\phi;\mu',\phi')\mathbf{I}_c^+(\mu',\phi',z)\mathrm{d}\Omega' \\ &\quad + \textstyle\int_0^{2\pi}\int_0^1 \mathbf{P}_c(-\mu,\phi;-\mu',\phi')\mathbf{I}_c^-(-\mu',\phi',z)\mathrm{d}\Omega'] \end{aligned} \tag{9.21}$$

where $d\Omega' = d\mu' d\phi' = \sin\theta' d\theta' d\phi'$, and $\mathbf{P}_c(\mu,\phi;\mu',\phi')$ is the phase matrix of the crown layer. Equations identical with (9.20) and (9.21) may be written for the trunk layer $(-d' \le z \le -d)$ upon replacing the subscript c with the subscript t. In equation (7.13) it was shown that the far field amplitude of a long cylinder is proportional to $\sin V/V$ and thus the phase matrix of the trunk layer has a similar dependency, i.e.

$$\mathbf{P}_t(\theta_s,\phi_s;\theta_i,\phi_i) \sim \left\{\frac{\sin[k_0 H_t(\cos\theta_i - \cos\theta_s)/2]}{k_0 H_t(\cos\theta_i - \cos\theta_s)/2}\right\}^2$$

For the forest canopy the height of the trunk layer is assumed to be much larger than the wavelength ($H_t \gg \lambda$). Thus the following approximation can be employed

$$\frac{\sin[k_0 H_t(\cos\theta_i - \cos\theta_s)/2]}{k_0 H_t(\cos\theta_i - \cos\theta_s)/2} \approx \delta_k(\mu_s - \mu_i)$$

where δ_k is the Kronecker delta function and is defined by

$$\delta_k(\mu_s - \mu_i) = \begin{cases} 1; & \mu_s = \mu_i \\ 0; & \text{otherwise} \end{cases}$$

As a result of this approximation the cylinders in the trunk layer can only generate upward-going (downward-going) intensity when they are illuminated by an upward-going (downward-going) intensity. Therefore the source functions in the trunk layer are given by

$$\begin{aligned} \mathbf{F}_t^+(\mu,\phi,z) &= \tfrac{1}{\mu}\int_0^{2\pi} \mathbf{P}_t(\mu,\phi;\mu,\phi')[\int_0^1 \mathbf{I}_t^+(\mu',\phi',z)\delta_k(\mu-\mu')\mathrm{d}\mu']\mathrm{d}\phi' \\ \mathbf{F}_t^-(-\mu,\phi,z) &= \tfrac{1}{\mu}\int_0^{2\pi} \mathbf{P}_t(-\mu,\phi;-\mu,\phi')[\int_0^1 \mathbf{I}_t^-(-\mu',\phi',z)\delta_k(\mu-\mu')\mathrm{d}\mu']\mathrm{d}\phi' \end{aligned} \tag{9.22}$$

where the quantity in the bracket is the representation of the specific intensity for a two dimensional problem.

The solution to differential equations (9.20) and (9.21) can formally be expressed as

$$\mathbf{I}_c^+(\mu,\phi,z) = e^{-\boldsymbol{\kappa}_c^+(z+d)/\mu}\mathbf{I}_c^+(\mu,\phi,-d) + \int_{-d}^{z} e^{-\boldsymbol{\kappa}_c^+(z-z')/\mu}\mathbf{F}_c^+(\mu,\phi,z')\mathrm{d}z' \tag{9.23}$$

$$\mathbf{I}_c^-(-\mu,\phi,z) = e^{\boldsymbol{\kappa}_c^- z/\mu}\mathbf{I}_c^-(-\mu,\phi,0) + \int_{z}^{0} e^{\boldsymbol{\kappa}_c^-(z-z')/\mu}\mathbf{F}_c^-(-\mu,\phi,z')\mathrm{d}z' \tag{9.24}$$

where

$$\begin{aligned} \boldsymbol{\kappa}_c^+ &= \boldsymbol{\kappa}_c(\theta,\phi)\ , \\ \boldsymbol{\kappa}_c^- &= \boldsymbol{\kappa}_c(\pi-\theta,\phi), \end{aligned} \tag{9.25}$$

and the following notation has been adopted

$$e^{-\boldsymbol{\kappa}_c z/\mu} = \mathbf{Q}_c(\mu,\phi)\mathbf{D}_c(\mu,\phi;-z/\mu)\mathbf{Q}_c^{-1}(\mu,\phi) \tag{9.26}$$

where $\mathbf{Q}_c(\mu,\phi)$ is a matrix whose columns are eigen vectors of the extinction matrix $\boldsymbol{\kappa}_c(\mu,\phi)$, and $\mathbf{D}_c(\mu,\phi;-z/\mu)$ is a diagonal matrix whose diagonal elements are of the following form

$$[\mathbf{D}_c(\mu,\phi;-z/\mu)]_{ii} = e^{-\lambda_i(\mu,\phi)z/\mu}$$

with $\lambda_i(\mu,\phi)$ being the i^{th} eigen value of $\boldsymbol{\kappa}_c(\mu,\phi)$.

Similarly the vector specific intensities $\mathbf{I}_t^+$ and $\mathbf{I}_t^-$ in the trunk layer are given by

$$\mathbf{I}_t^+(\mu,\phi,z) = e^{-\boldsymbol{\kappa}_t^+(z+d')/\mu}\mathbf{I}_t^+(\mu,\phi,-d') + \int_{-d'}^{z} e^{-\boldsymbol{\kappa}_t^+(z-z')/\mu}\mathbf{F}_t^+(\mu,\phi,z')\mathrm{d}z' \qquad (9.27)$$

$$\mathbf{I}_t^-(-\mu,\phi,z) = e^{\boldsymbol{\kappa}_t^-(z+d)/\mu}\mathbf{I}_t^-(-\mu,\phi,-d) + \int_{z}^{-d} e^{\boldsymbol{\kappa}_t^-(z-z')/\mu}\mathbf{F}_t^-(-\mu,\phi,z')\mathrm{d}z' \qquad (9.28)$$

where the subscript t denotes that the propagation and scattering processes are taking place in the trunk layer. If we limit our solution to first-order scattering, the first-order contribution of the trunk layer is observable only on the surface of a cone with generating angle θ_0 which includes the backscattering direction.

9.5 First-Order Solution for Bistatic Scattering

Because there is no reflection at the (diffuse) air-crown boundary ($z = 0$) and the crown-trunk boundary ($z = -d$), the following boundary conditions must be satisfied:

$$\mathbf{I}_c^-(-\mu,\phi,0) = \mathbf{I}_0\delta(\mu-\mu_0)\delta(\phi-\phi_0)\ , \qquad (9.29)$$

$$\mathbf{I}_c^+(\mu,\phi,-d) = \mathbf{I}_t^+(\mu,\phi,-d)\ , \qquad (9.30)$$

$$\mathbf{I}_t^-(-\mu,\phi,-d) = \mathbf{I}_c^-(-\mu,\phi,-d)\ . \qquad (9.31)$$

At the bottom boundary ($z = -d'$), the boundary condition is

$$\mathbf{I}_t^+(\mu,\phi,-d') = \mathbf{R}(\mu)\mathbf{I}_t^-(-\mu,\phi,-d')\ , \qquad (9.32)$$

where $\mathbf{R}(\mu)$ is the reflectivity matrix of the specular surface and is given by [Tsang and Kong, 1978; Ulaby et al.,1986, pp. 1183]

$$\mathbf{R}(\mu) = \begin{bmatrix} |R_v|^2 & 0 & 0 & 0 \\ 0 & |R_h|^2 & 0 & 0 \\ 0 & 0 & Re(R_vR_h^*) & -Im(R_vR_h^*) \\ 0 & 0 & Im(R_vR_h^*) & Re(R_vR_h^*) \end{bmatrix}$$

where R_v and R_h are the v-polarized and h-polarized Fresnel reflection coefficients of the specular surface at incidence angle θ.

In order to obtain scattering behavior of the layered media, we need to solve for $\mathbf{I}_c^+(\mu,\phi,z)$ and then evaluate it at $z=0$. Upon setting $z=-d$ in (9.24), inserting the result in (9.28), and then evaluating the resultant expression at $z=-d'$, the downward-going intensity at the bottom surface can be obtained. Now the upward-going intensity at the bottom surface ($\mathbf{I}_t^+(\mu,\phi,-d')$) can be found by using the boundary condition (9.32). The expression for $\mathbf{I}_t^+(\mu,\phi,-d')$ can be inserted into equation (9.27) and then the latter can be evaluated at $z=-d$ to obtain an expression for $\mathbf{I}_t^+(\mu,\phi,-d)$. Finally by inserting the resultant expression for $\mathbf{I}_t^+(\mu,\phi,-d)$ into equation (9.23), we end up with the expression

$$\begin{aligned}\mathbf{I}_c^+(\mu,\phi,z) &= e^{-\boldsymbol{\kappa}_c^+(z+d)/\mu}\mathbf{R}'(\mu,\phi)\cdot[e^{-\boldsymbol{\kappa}_c^- d/\mu}\mathbf{I}_c^-(-\mu,\phi,0)\\ &\quad+\int_{-d}^{0}e^{-\boldsymbol{\kappa}_c^-(d+z')/\mu}\mathbf{F}_c^-(-\mu,\phi,z')\mathrm{d}z']+\int_{-d}^{z}e^{-\boldsymbol{\kappa}_c^+(z-z')/\mu}\mathbf{F}_c^+(\mu,\phi,z')\mathrm{d}z'\\ &\quad e^{-\boldsymbol{\kappa}_c^+(z+d)/\mu}[e^{-\boldsymbol{\kappa}_t^+ H_t/\mu}\mathbf{R}\int_{-d'}^{-d}e^{-\boldsymbol{\kappa}_t^-(z'+d')/\mu}\mathbf{F}_t^-(-\mu,\phi,z')\mathrm{d}z'\\ &\quad\int_{-d'}^{-d}e^{-\boldsymbol{\kappa}_t^+(z'+d)/\mu}\mathbf{F}_t^+(\mu,\phi,z')\mathrm{d}z'] \qquad (9.33)\end{aligned}$$

where

$$\mathbf{R}'(\mu,\phi)=e^{-\boldsymbol{\kappa}_t^+ H_t/\mu}\cdot\mathbf{R}(\mu)\cdot e^{-\boldsymbol{\kappa}_t^- H_t/\mu}.$$

The matrix $\mathbf{R}'(\mu,\phi)$ accounts for extinction in the trunk layer and reflection at the specular surface. The above expression is given in terms of the source functions $\mathbf{F}_c^{\pm}$ and $\mathbf{F}_t^{\pm}$ which in turn are given by (9.21) and (9.22) in terms of $\mathbf{I}_c^{\pm}$ and $\mathbf{I}_t^{\pm}$. Thus we need to solve the coupled integral equations (9.22),(9.27),(9.28), and (9.33) to obtain $\mathbf{I}_c^+(\mu,\phi,0)$. If the scattering albedo of the medium is small, we can solve the integral equations using an iterative approach. We shall start with the zeroth-order solutions, which are obtained by setting $\mathbf{P}_c(\mu,\phi;\mu',\phi')=\mathbf{P}_t(\mu,\phi;\mu',\phi')=0$ in

(9.21) and (9.22) which renders $\mathbf{F}_c^{\pm}(\mu,\phi,z) = \mathbf{F}_t^{\pm}(-\mu,\phi,z) = 0$. Using the boundary conditions given by (9.29)-(9.33) the zeroth-order specific intensities are given by

$$\begin{aligned}
\mathbf{I}_{c0}^{-}(-\mu,\phi,z) &= e^{\boldsymbol{\kappa}_c^{-} z/\mu}\mathbf{I_0}\delta(\mu-\mu_0)\delta(\phi-\phi_0) \\
\mathbf{I}_{t0}^{-}(-\mu,\phi,z) &= e^{\boldsymbol{\kappa}_t^{-}(z+d)/\mu}e^{-\boldsymbol{\kappa}_c^{-} d/\mu}\mathbf{I_0}\delta(\mu-\mu_0)\delta(\phi-\phi_0) \\
\mathbf{I}_{t0}^{+}(\mu,\phi,z) &= e^{-\boldsymbol{\kappa}_t^{+}(z+d')/\mu}\mathbf{R}e^{-\boldsymbol{\kappa}_t^{-} H_t/\mu}e^{-\boldsymbol{\kappa}_c^{-} d/\mu}\mathbf{I_0}\delta(\mu-\mu_0)\delta(\phi-\phi_0) \\
\mathbf{I}_{c0}^{+}(\mu,\phi,z) &= e^{-\boldsymbol{\kappa}_c^{+}(z+d)/\mu}e^{-\boldsymbol{\kappa}_t^{+} H_t/\mu}\mathbf{R}e^{-\boldsymbol{\kappa}_t^{-} H_t/\mu}e^{-\boldsymbol{\kappa}_c^{-} d/\mu}\mathbf{I_0}\delta(\mu-\mu_0)\delta(\phi-\phi_0)
\end{aligned} \tag{9.34}$$

where the symbols $\mathbf{I}_{c0}^{\pm}$ and $\mathbf{I}_{t0}^{\pm}$ are used to denote the zeroth-order solutions of $\mathbf{I}_c^{\pm}$ and $\mathbf{I}_t^{\pm}$, respectively.

The zeroth-order solution corresponds to propagation of the coherent wave through the medium with the scattering ignored, except for its contribution to extinction. To obtain the first-order solution, we first need to use (9.34) in (9.21) and (9.22) to compute the first-order source functions $\mathbf{F}_{c1}^{\pm}$ and $\mathbf{F}_{t1}^{\pm}$, and then insert the result in (9.33). This process leads to:

$$\begin{aligned}
\mathbf{I}_1^{+}(\mu,\phi,z) \;=\; & e^{-\boldsymbol{\kappa}_c^{+}(z+d)/\mu}\mathbf{R}'(\mu,\phi)e^{-\boldsymbol{\kappa}_c^{-} d/\mu} \\
& \delta(\mu-\mu_0)\delta(\phi-\phi_0)\mathbf{I_0} + \frac{1}{\mu}e^{-\boldsymbol{\kappa}_c^{+}(z+d)/\mu}\mathbf{R}'(\mu,\phi) \\
& \cdot\{\int_{-d}^{0}[e^{-\boldsymbol{\kappa}_c^{-}(z'+d)/\mu}\mathbf{P}_c(-\mu,\phi;\mu_0,\phi_0)e^{-\boldsymbol{\kappa}_c^{+}(z'+d)/\mu_0}\mathbf{R}'(\mu_0,\phi_0) \\
& \cdot e^{-\boldsymbol{\kappa}_c^{-} d/\mu_0} + e^{-\boldsymbol{\kappa}_c^{-}(z'+d)/\mu}\mathbf{P}_c(-\mu,\phi;-\mu_0,\phi_0)e^{\boldsymbol{\kappa}_c^{-} z'/\mu_0}]\mathrm{d}z'\}\mathbf{I_0} \\
& +\frac{1}{\mu}\{\int_{-d}^{z}[e^{-\boldsymbol{\kappa}_c^{+}(z-z')/\mu}\mathbf{P}_c(\mu,\phi;\mu_0,\phi_0)e^{-\boldsymbol{\kappa}_c^{+}(z'+d)/\mu_0}\mathbf{R}'(\mu_0,\phi_0)e^{-\boldsymbol{\kappa}_c^{-} d/\mu_0} \\
& +e^{-\boldsymbol{\kappa}_c^{+}(z-z')/\mu}\mathbf{P}_c(\mu,\phi;-\mu_0,\phi_0)e^{\boldsymbol{\kappa}_c^{-} z'/\mu_0}]\mathrm{d}z'\}\mathbf{I_0} \\
& +\frac{1}{\mu}e^{-\boldsymbol{\kappa}_c^{+}(z+d)/\mu}e^{-\boldsymbol{\kappa}_t^{+} H_t/\mu}\mathbf{R}[\int_{-d'}^{-d}e^{-\boldsymbol{\kappa}_t^{-}(z'+d')/\mu}\mathbf{P}_t(-\mu,\phi;-\mu,\phi_0) \\
& e^{\boldsymbol{\kappa}_t^{-}(z'+d)/\mu_0}\mathrm{d}z'] \cdot e^{-\boldsymbol{\kappa}_c^{-} d/\mu_0}\delta_k(\mu-\mu_0)\mathbf{I_0} \\
& +\frac{1}{\mu}e^{-\boldsymbol{\kappa}_c^{+}(z+d)/\mu}\int_{-d'}^{-d}e^{\boldsymbol{\kappa}_t^{+}(z'+d')/\mu}\mathbf{P}_t(\mu,\phi;\mu,\phi_0)e^{-\boldsymbol{\kappa}_t^{+}(z'+d')/\mu_0}\mathrm{d}z' \\
& \cdot\mathbf{R}e^{-\boldsymbol{\kappa}_t^{-} H_t/\mu_0}e^{-\boldsymbol{\kappa}_c^{-} d/\mu_0}\delta_k(\mu-\mu_0)\mathbf{I_0}
\end{aligned} \tag{9.35}$$

where it is understood that $\boldsymbol{\kappa}^{\pm}_{c,t}/\mu = \boldsymbol{\kappa}^{\pm}_{c,t}(\mu,\phi)/\mu$ and $\boldsymbol{\kappa}^{\pm}_{c,t}/\mu_0 = \boldsymbol{\kappa}^{\pm}_{c,t}(\mu_0,\phi_0)/\mu_0$. To find an expression for the intensity emerging from the crown layer at $z = 0$, we shall first define the integrals in (9.35) in terms of equivalent matrices. Using the definition given by (9.25)

$$\begin{aligned}\mathbf{A}_1(\mu,\phi;\mu_0,\phi_0) &= \int_{-d}^{0} \mathbf{D}_c(-\mu,\phi;-(z'+d)/\mu)\mathbf{Q}_c^{-1}(-\mu,\phi)\mathbf{P}_c(-\mu,\phi;\mu_0,\phi_0) \\ &\quad \mathbf{Q}_c(\mu_0,\phi_0)\mathbf{D}_c(\mu_0,\phi_0;-(z'+d)/\mu_0)\mathrm{d}z', \qquad (9.36)\end{aligned}$$

whose $(ij)^{th}$ element is given by

$$\begin{aligned}[\mathbf{A}_1(\mu,\phi;\mu_0,\phi_0)]_{ij} &= \frac{1-exp[-(\lambda_i(-\mu,\phi)/\mu+\lambda_j(\mu_0,\phi_0)/\mu_0)d]}{\lambda_i(-\mu,\phi)/\mu+\lambda_j(\mu_0,\phi_0)/\mu_0} \\ &\quad \cdot[\mathbf{Q}_c^{-1}(-\mu,\phi)\mathbf{P}_c(-\mu,\phi;\mu_0,\phi_0)\mathbf{Q}_c(\mu_0,\phi_0)]_{ij}.\end{aligned}$$

In a similar manner,

$$\begin{aligned}\mathbf{A}_2(\mu,\phi;\mu_0,\phi_0) &= \int_{-d}^{0} \mathbf{D}_c(-\mu,\phi;-(z'+d)/\mu)\mathbf{Q}_c^{-1}(-\mu,\phi)\mathbf{P}_c(-\mu,\phi;-\mu_0,\phi_0) \\ &\quad \mathbf{Q}_c(-\mu_0,\phi_0)\mathbf{D}_c(-\mu_0,\phi_0;z'/\mu_0)\mathrm{d}z' \qquad (9.37)\end{aligned}$$

$$\begin{aligned}[\mathbf{A}_2(\mu,\phi;\mu_0,\phi_0)]_{ij} &= \frac{exp[-\lambda_i(-\mu,\phi)d/\mu]-exp[-\lambda_j(-\mu_0,\phi_0)d/\mu_0]}{-\lambda_i(-\mu,\phi)/\mu+\lambda_j(-\mu_0,\phi_0)/\mu_0} \\ &\quad \cdot[\mathbf{Q}_c^{-1}(-\mu,\phi)\mathbf{P}_c(-\mu,\phi;-\mu_0,\phi_0)\mathbf{Q}_c(-\mu_0,\phi_0)]_{ij},\end{aligned}$$

$$\begin{aligned}\mathbf{A}_3(\mu,\phi;\mu_0,\phi_0) &= \int_{-d}^{0} \mathbf{D}_c(\mu,\phi;z'/\mu)\mathbf{Q}_c^{-1}(\mu,\phi)\mathbf{P}_c(\mu,\phi;\mu_0,\phi_0) \\ &\quad \mathbf{Q}_c(\mu_0,\phi_0)\mathbf{D}_c(\mu_0,\phi_0;-(z'+d)/\mu_0)\mathrm{d}z' \qquad (9.38)\end{aligned}$$

$$\begin{aligned}[\mathbf{A}_3(\mu,\phi;\mu_0,\phi_0)]_{ij} &= \frac{exp[-\lambda_j(\mu_0,\phi_0)d/\mu_0]-exp[-\lambda_i(\mu,\phi)d/\mu]}{\lambda_i(\mu,\phi)/\mu-\lambda_j(\mu_0,\phi_0)/\mu_0} \\ &\quad \cdot[\mathbf{Q}_c^{-1}(\mu,\phi)\mathbf{P}_c(\mu,\phi;\mu_0,\phi_0)\mathbf{Q}_c(\mu_0,\phi_0)]_{ij},\end{aligned}$$

and

$$\begin{aligned}\mathbf{A}_4(\mu,\phi;\mu_0,\phi_0) &= \int_{-d}^{0} \mathbf{D}_c(\mu,\phi;z'/\mu)\mathbf{Q}_c^{-1}(\mu,\phi)\mathbf{P}_c(\mu,\phi;-\mu_0,\phi_0) \\ &\quad \mathbf{Q}_c(-\mu_0,\phi_0)\mathbf{D}_c(-\mu_0,\phi_0;z'/\mu_0)\mathrm{d}z' \qquad (9.39)\end{aligned}$$

$$[\mathbf{A}_4(\mu,\phi;\mu_0,\phi_0)]_{ij} = \frac{1-exp[-(\lambda_i(\mu,\phi)/\mu+\lambda_j(-\mu_0,\phi_0)/\mu_0)d]}{\lambda_i(\mu,\phi)/\mu+\lambda_j(-\mu_0,\phi_0)/\mu_0} \cdot[\mathbf{Q}_c^{-1}(\mu,\phi)\mathbf{P}_c(\mu,\phi;-\mu_0,\phi_0)\mathbf{Q}_c(-\mu_0,\phi_0)]_{ij}$$

$$\mathbf{A}_5(\mu,\phi;\mu_0,\phi_0) = \int_{-d'}^{-d}\mathbf{D}_t(-\mu,\phi;-(z'+d)/\mu)\mathbf{Q}_t^{-1}(-\mu,\phi)\mathbf{P}_t(-\mu,\phi;-\mu,\phi_0) \mathbf{Q}_t(-\mu_0,\phi_0)\mathbf{D}_t(-\mu_0,\phi_0;(z'+d)/\mu_0)\mathrm{d}z' \tag{9.40}$$

$$[\mathbf{A}_5(\mu,\phi;\mu_0,\phi_0)]_{ij} = \frac{exp[-\lambda_i(-\mu,\phi)H_t/\mu]-exp[-\lambda_j(-\mu_0,\phi_0)H_t/\mu_0]}{-\lambda_i(-\mu,\phi)/\mu+\lambda_j(-\mu_0,\phi_0)/\mu_0} \cdot[\mathbf{Q}_t^{-1}(-\mu,\phi)\mathbf{P}_t(-\mu,\phi;-\mu,\phi_0)\mathbf{Q}_t(-\mu_0,\phi_0)]_{ij},$$

$$\mathbf{A}_6(\mu,\phi;\mu_0,\phi_0) = \int_{-d'}^{-d}\mathbf{D}_t(\mu,\phi;(z'+d)/\mu)\mathbf{Q}_t^{-1}(\mu,\phi)\mathbf{P}_t(\mu,\phi;\mu,\phi_0) \mathbf{Q}_t(\mu_0,\phi_0)\mathbf{D}_t(\mu_0,\phi_0;-(z'+d')/\mu_0)\mathrm{d}z' \tag{9.41}$$

$$[\mathbf{A}_6(\mu,\phi;\mu_0,\phi_0)]_{ij} = \frac{exp[-\lambda_j(\mu_0,\phi_0)H_t/\mu_0]-exp[-\lambda_i(\mu,\phi)H_t/\mu]}{\lambda_i(\mu,\phi)/\mu-\lambda_j(\mu_0,\phi_0)/\mu_0} \cdot[\mathbf{Q}_t^{-1}(\mu,\phi)\mathbf{P}_t(\mu,\phi;\mu,\phi_0)\mathbf{Q}_t(\mu_0,\phi_0)]_{ij}.$$

In view of these matrices, (9.35) can be evaluated at $z=0$ and written in the form

$$\begin{aligned}
\mathbf{I}^s(\mu,\phi) &= \mathbf{I}_1^+(\mu,\phi,0) \\
&= e^{-\boldsymbol{\kappa}_c^+ d/\mu}\mathbf{R}'(\mu_0,\phi_0)e^{-\boldsymbol{\kappa}_c^- d/\mu_0}\delta(\mu-\mu_0)\delta(\phi-\phi_0)\mathbf{I}_0 \\
&\quad +\frac{1}{\mu}e^{-\boldsymbol{\kappa}_c^+ d/\mu}\mathbf{R}'(\mu,\phi)\mathbf{Q}_c(-\mu,\phi)\mathbf{A}_1\mathbf{Q}_c^{-1}(\mu_0,\phi_0)\mathbf{R}'(\mu_0,\phi_0)e^{-\boldsymbol{\kappa}_c^- d/\mu_0}\mathbf{I}_0 \\
&\quad +\frac{1}{\mu}e^{-\boldsymbol{\kappa}_c^+ d/\mu}\mathbf{R}'(\mu,\phi)\mathbf{Q}_c(-\mu,\phi)\mathbf{A}_2\mathbf{Q}_c^{-1}(-\mu_0,\phi_0)\mathbf{I}_0 \\
&\quad +\frac{1}{\mu}\mathbf{Q}_c(\mu,\phi)\mathbf{A}_3\mathbf{Q}_c^{-1}(\mu_0,\phi_0)\mathbf{R}'(\mu_0,\phi_0)e^{-\boldsymbol{\kappa}_c^- d/\mu_0}\mathbf{I}_0 \\
&\quad +\frac{1}{\mu}\mathbf{Q}_c(\mu,\phi)\mathbf{A}_4\mathbf{Q}_c^{-1}(-\mu_0,\phi_0)\mathbf{I}_0 \\
&\quad +\frac{1}{\mu}e^{-\boldsymbol{\kappa}_c^+ d/\mu}e^{-\boldsymbol{\kappa}_t^+ H_t/\mu}\mathbf{R}\mathbf{Q}_t(-\mu,\phi)\mathbf{A}_5\mathbf{Q}_t^{-1}(-\mu_0,\phi_0)e^{-\boldsymbol{\kappa}_c^- d/\mu_0}\delta_k(\mu-\mu_0)\mathbf{I}_0 \\
&\quad +\frac{1}{\mu}e^{-\boldsymbol{\kappa}_c^+ d/\mu}\mathbf{Q}_t(\mu,\phi)\mathbf{A}_6\mathbf{Q}_t^{-1}(\mu_0,\phi_0)\mathbf{R}e^{-\boldsymbol{\kappa}_t^- H_t/\mu_0}e^{-\boldsymbol{\kappa}_c^- d/\mu_0}\delta_k(\mu-\mu_0)\mathbf{I}_0
\end{aligned} \tag{9.42}$$

The seven terms contained in (9.42), which are diagrammed in Fig. 9.3, represent:

Term ds This is a coherent reflection term resulting from *direct* propagation of the incident intensity through the layers down to the bottom boundary, followed by *specular* reflection by the specular boundary, and then followed with direct propagation through the layers to the upper boundary. This term exist only in the specular direction $(\theta, \phi) = (\theta_0, \phi_0)$, and in that case, its magnitude is equal to $\mathbf{I}_0$, reduced by the product of the two-way attenuation and the reflection coefficient.

Term 1 This term represents propagation of the incident intensity through the two layers to the bottom boundary, followed with specular reflection at θ_0, then bistatic scattering by the vegetation material in the crown layer downward in a direction $(\pi - \theta, \phi)$ such that after specular reflection by the lower surface a second time at θ, the reflected intensity propagates upward through the two layers along the direction (θ, ϕ).

Term 2a This term represents propagation of the incident intensity $\mathbf{I}_0$ into the crown layer along the direction (θ_0, ϕ_0), followed with bistatic scattering by the vegetation material downward along the direction $(\pi - \theta, \phi)$, and then followed with specular reflection by the lower boundary upward through the layers along the direction (θ, ϕ).

Term 2b This is the complement of term 2. It represents propagation of the incident intensity $\mathbf{I}_0$ through the layers down to the bottom boundary, specular reflection at θ_0, upward propagation at θ_0, then bistatic scattering by the vegetation in the direction (θ, ϕ).

Term 3 This term does not involve reflection by the bottom boundary. It repre-

sents incidence at $(\pi - \theta_0, \phi_0)$ followed by bistatic scattering upward along the direction (θ, ϕ). For a semi-infinite layer, the other four term vanish and only this term remains.

Term 4a This term represents the propagation of the incident intensity in the crown layer (i.e. attenuation only but no change in direction), followed by bistatic scattering by the trunks down to the ground surface, followed by bistatic reflection by the surface boundary, and then direct propagation through the trunk and crown layers.

Term 4b This term is the complement of term 5 (same path, but in reverse direction). This term and term 5 will be referred to as *ground-trunk* term. Contribution of these terms is observable only on the surface of a cone with generating angle θ_0.

With $\mathbf{I}^s(\mu, \phi)$ given by (9.42), the expression for the bistatic scattering coefficient may now be readily found by inserting (9.42) into (9.4). For the backscattering case, we set $\theta = \theta_0$ and $\phi = \phi_0 + \pi$ in (9.36)-(9.42). For an azimuthally symmetric medium, this condition causes the diagonal components of $\mathbf{A}_2$,$\mathbf{A}_3$ $\mathbf{A}_5$, and $\mathbf{A}_6$ to become indeterminate. Application of L'Hopital's rule, however, leads to

$$\lim_{\mu \to \mu_0} [\mathbf{A}_2(\mu, \phi; \mu_0, \phi_0)]_{ii} = d e^{-\lambda_i(\mu_0) d/\mu_0} \cdot [\mathbf{Q}_c^{-1}(-\mu, \phi)\mathbf{P}_c(-\mu, \phi; -\mu_0, \phi_0)\mathbf{Q}_c(-\mu_0, \phi_0)]_{ii}.$$

The same result applies to $\mathbf{A}_3$,$\mathbf{A}_5$, and $\mathbf{A}_6$. The backscattered intensity can be related to the incident intensity through a matrix $\mathbf{T}(\theta_0, \phi_0)$,

$$\mathbf{I}^s = \mathbf{T}(\theta_0, \phi_0)\mathbf{I}_0$$

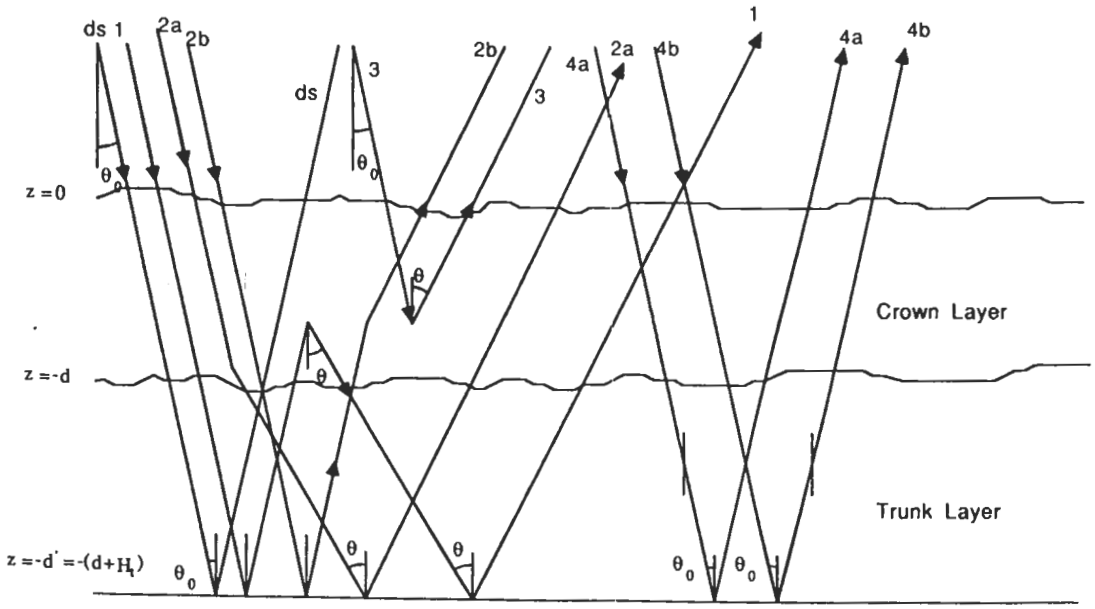

Figure 9.3: Scattering terms for the bistatic case.

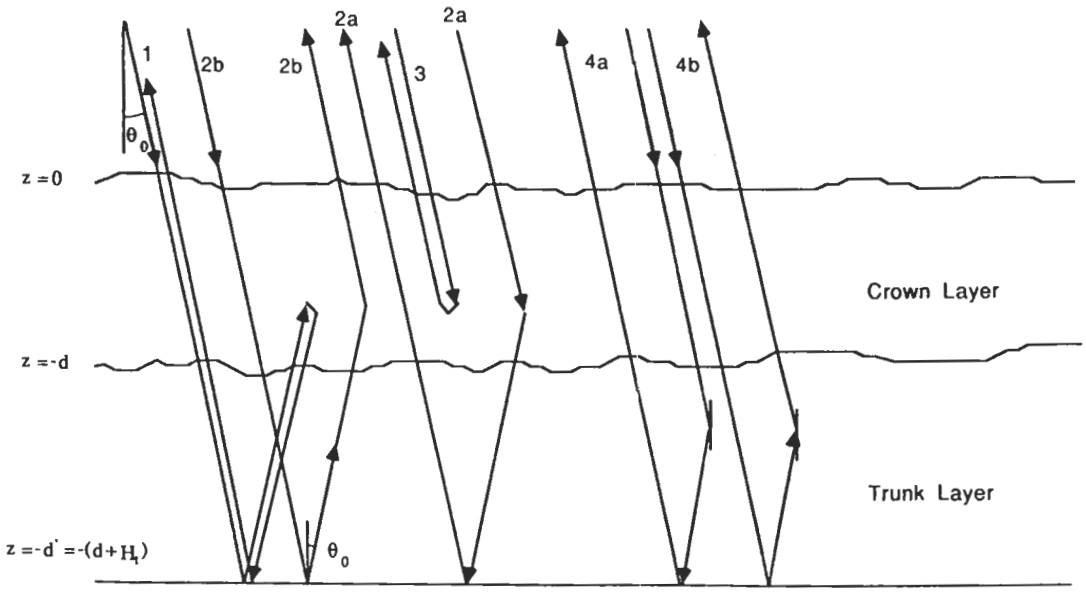

Figure 9.4: Scattering terms for the backscattering case.

where

$$
\begin{aligned}
\mathbf{T}(\theta_0,\phi_0) \;=\; & \frac{1}{\mu_0} e^{-\boldsymbol{\kappa}_c^{+} d/\mu_0} \\
& \cdot \mathbf{R}'(\mu_0,\phi_0+\pi)\mathbf{Q}_c(-\mu_0,\phi_0+\pi) \\
& \mathbf{A}_1 \mathbf{Q}_c^{-1}(\mu_0,\phi_0)\mathbf{R}'(\mu_0,\phi_0) e^{-\boldsymbol{\kappa}_c^{-} d/\mu_0} \\
& + \frac{1}{\mu_0} e^{-\boldsymbol{\kappa}_c^{+} d/\mu_0} \mathbf{R}'(\mu_0,\phi_0+\pi)\mathbf{Q}_c(-\mu_0,\phi_0+\pi)\mathbf{A}_2 \mathbf{Q}_c^{-1}(-\mu_0,\phi_0) \\
& + \frac{1}{\mu_0} \mathbf{Q}_c(\mu_0,\phi_0+\pi)\mathbf{A}_3 \mathbf{Q}_c^{-1}(\mu_0,\phi_0)\mathbf{R}'(\mu_0,\phi_0) e^{-\boldsymbol{\kappa}_c^{-} d/\mu_0} \\
& + \frac{1}{\mu_0} \mathbf{Q}_c(\mu_0,\phi_0+\pi)\mathbf{A}_4 \mathbf{Q}_c^{-1}(-\mu_0,\phi_0) \\
& + \frac{1}{\mu_0} e^{-\boldsymbol{\kappa}_c^{+} d/\mu_0} e^{-\boldsymbol{\kappa}_t^{+} H_t/\mu_0} \mathbf{R}(\mu_0)\mathbf{Q}_t(-\mu_0,\phi_0+\pi)\mathbf{A}_5 \mathbf{Q}_t^{-1}(-\mu_0,\phi_0) e^{-\boldsymbol{\kappa}_c^{-} d/\mu_0} \\
& + \frac{1}{\mu_0} e^{-\boldsymbol{\kappa}_c^{+} d/\mu_0} \mathbf{Q}_t(\mu_0,\phi_0+\pi)\mathbf{A}_6 \mathbf{Q}_t^{-1}(\mu_0,\phi_0)\mathbf{R}(\mu_0) e^{-\boldsymbol{\kappa}_t^{-} H_t/\mu_0} e^{-\boldsymbol{\kappa}_c^{-} d/\mu_0}
\end{aligned}
\tag{9.43}
$$

The backscattering coefficients thus become

$$\sigma^{\circ}_{vv} = 4\pi[\mathbf{T}(\theta_0,\phi_0)]_{11}\cos\theta_0 \tag{9.44}$$

$$\sigma^{\circ}_{hh} = 4\pi[\mathbf{T}(\theta_0,\phi_0)]_{22}\cos\theta_0 \tag{9.45}$$

$$\sigma^{\circ}_{hv} = 4\pi[\mathbf{T}(\theta_0,\phi_0)]_{21}\cos\theta_0 \tag{9.46}$$

$$\sigma^{\circ}_{vh} = 4\pi[\mathbf{T}(\theta_0,\phi_0)]_{12}\cos\theta_0. \tag{9.47}$$

Figure 9.4 depicts the scattering mechanisms for the backscattering case.

9.6 Numerical Results

We are now in a position to investigate the effect of different physical parameters of constituents of a forest canopy on its backscattering cross section coefficient (σ°) using single scattering models developed in the previous chapters. Considering different canopy cases and performing sensitivity analysis on each cases is beyond the

scope of this thesis, but examining a simple canopy stand demonstrates the ability and performance of the radiative transfer first-order solution.

We consider a canopy with a leaf-dominated crown layer [1] whose thickness is $2m$ and a trunk layer consisting of homogeneous vertical cylinder with $H_t = 8m$. The leaves in the crown layer are flat and square having thickness $\tau = 0.3mm$, lateral dimensions $5.5cm \times 5.5cm$, and gravimetric moisture content 0.8. To obtain the phase matrix of the crown layer expressions (2.38)-(2.41) were used in which the x' axis of the leaf coordinate is assumed to be parallel to the $X-Y$ plane. Further it is assumed that the normal to the leaf surface has a uniform distribution and number density of the leaves is $833/m^3$. The cylinder in the trunk layer are circular with diameter $24cm$ and height $8m$. The gravimetric moisture content of the trunks is 0.5 and their number density is $N_t = 0.11/m^2$. The ground surface is smooth and made up of 10% sand, 30% slit, and 60% clay with volumetric moisture content 0.15.

Table 9.1 gives dielectric constant of leaves and trunks [Ulaby and El-Rayes, 1987] and dielectric constant of ground surface [Hallikainen et al, 1985] for L-, C-, and X-band frequencies. Figures 9.5-9.8 show transmissivity (power transmission

Frequency	Leaf	Trunk	Soil
1.62 GHz	$34.6 + i17.0$	$15.9 + i10.7$	$16.1 + i1.5$
4.75 GHz	$30.3 + i13.8$	$13.0 + i8.0$	$6.9 + i0.7$
1.62 GHz	$25.7 + i14.0$	$11.0 + i7.4$	$5.8 + i1.4$

Table 9.1: Dielectric constant of leaves, trunks, and soil at L-, C-, and X-band frequencies.

coefficient) in the crown layer as a function of incidence angle and leaf density for L-

[1] Branches are neglected.

,C-, and X-band frequencies and for both v and h polarizations. The loss in the crown layer increases with increasing frequency, angle of incidence, and number density. In Figs. 9.9-9.12 the backscattering cross section coefficient of the canopy at C-band is plotted versus incidence angle for four transmit and receive antenna polarization configurations. In these figures contribution of different terms in (9.43) as depicted in Fig. 9.4 are shown. Similar plots are shown in Figs. 9.13-9.16 for X-band. Since reciprocity is not preserved in the physical optics approximation, σ^o_{hv} and σ^o_{vh} are not exactly identical as shown in Figs. 9.10-9.11 and 9.14-9.15.

9.7 Conclusions

A forest canopy is modelled as a statistically homogeneous three-layer medium. The crown layer may be comprised of distributions of leaves or vegetation needles and branches. The trunk layer consists of vertical dielectric cylinders which may be radially inhomogeneous. The third layer is a homogeneous dielectric half space with a smooth surface. The problem is formulated using the vector radiative transfer equations and a first-order solution is obtained. The analytical nature of this solution enables us to study the effect of different scattering mechanism in the medium. This solution, however, is not appropriate when the density of the constituent particles is high and a higher order solution is needed for such cases. The appropriate frequency range for this model is determined by the frequency range over which single scattering models are valid.

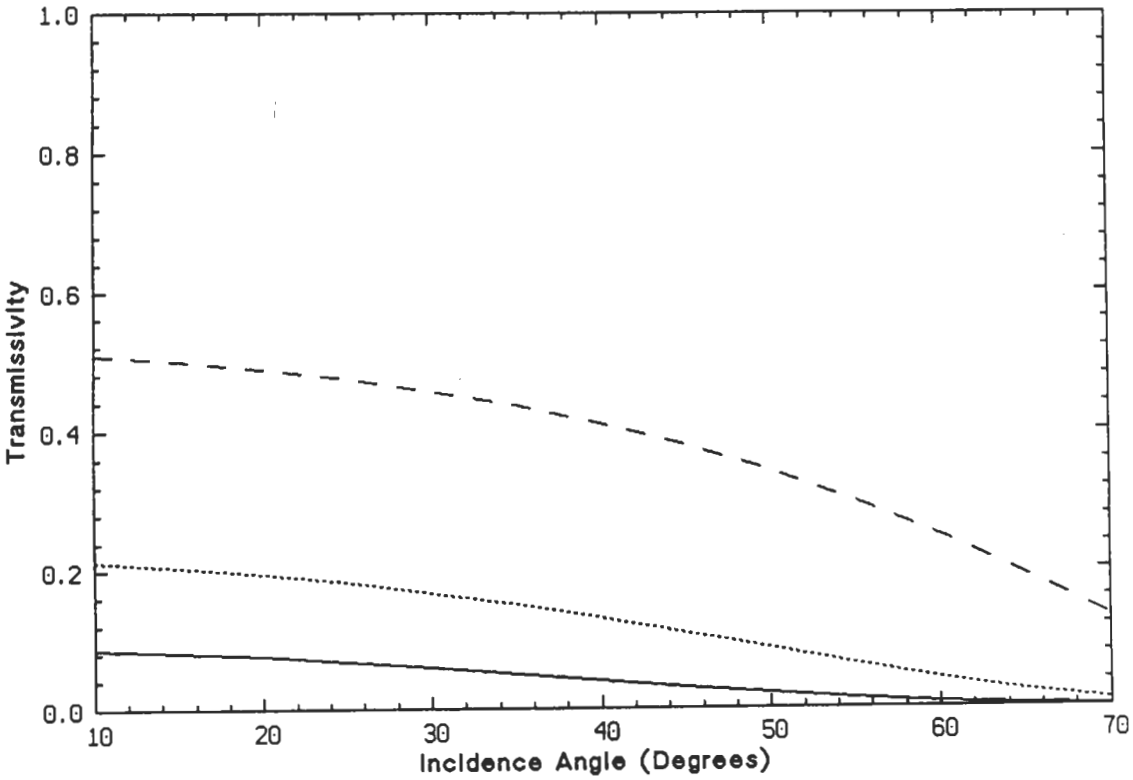

Figure 9.5: Transmissivity of the crown layer versus incidence angle for v polarization; (——) X-band, (- - -) C-band, and (– –) L-band.

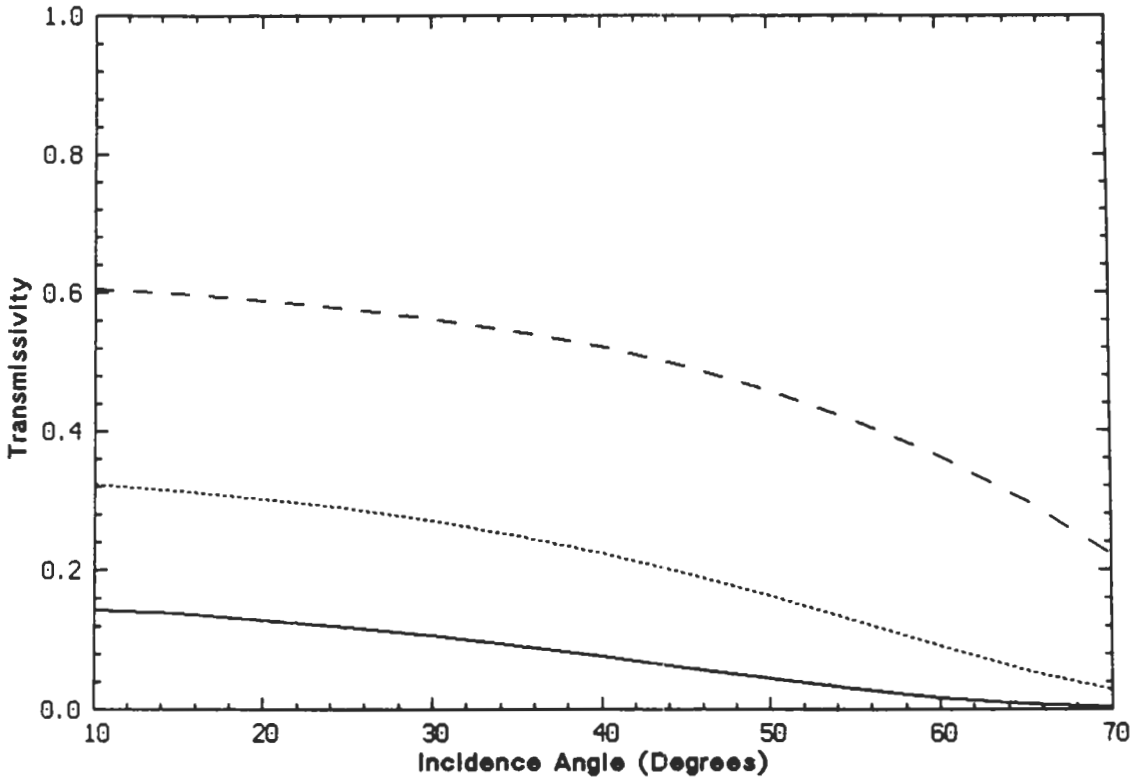

Figure 9.6: Transmissivity of the crown layer versus incidence angle for h polarization; (——) X-band, (- - -) C-band, and (– –) L-band.

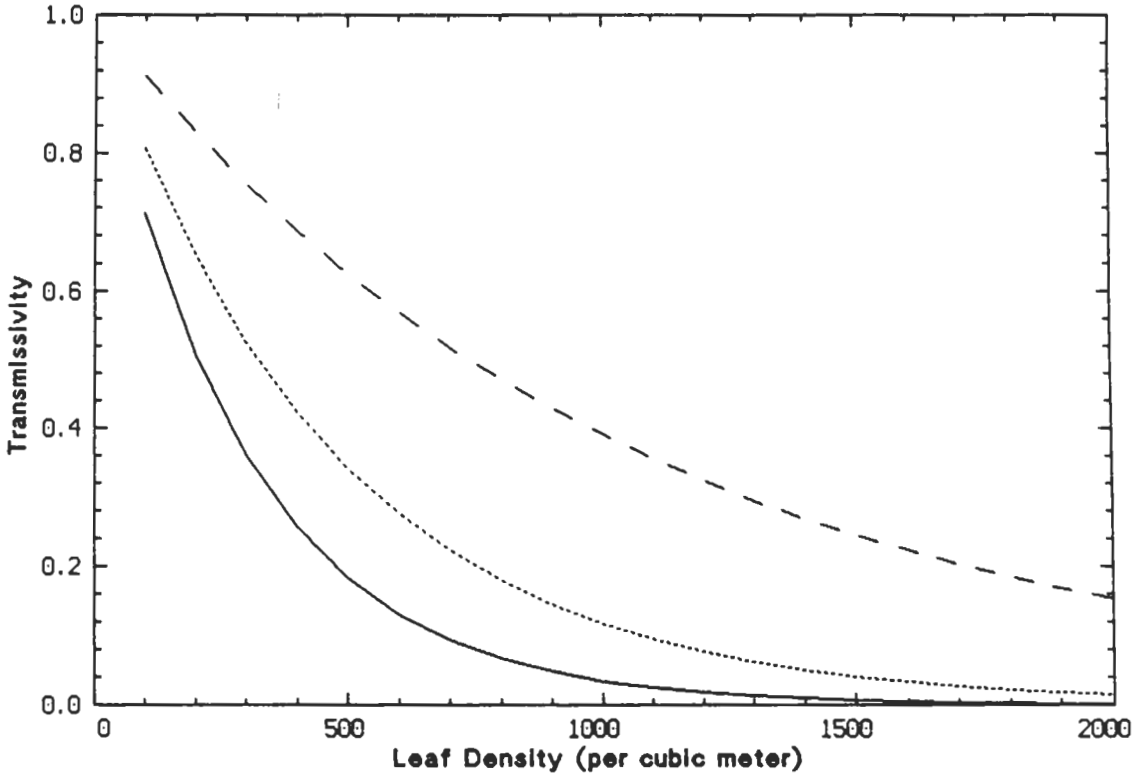

Figure 9.7: Transmissivity of the crown layer versus leaf density for v polarization; (——) X-band, (- - -) C-band, and (– –) L-band.

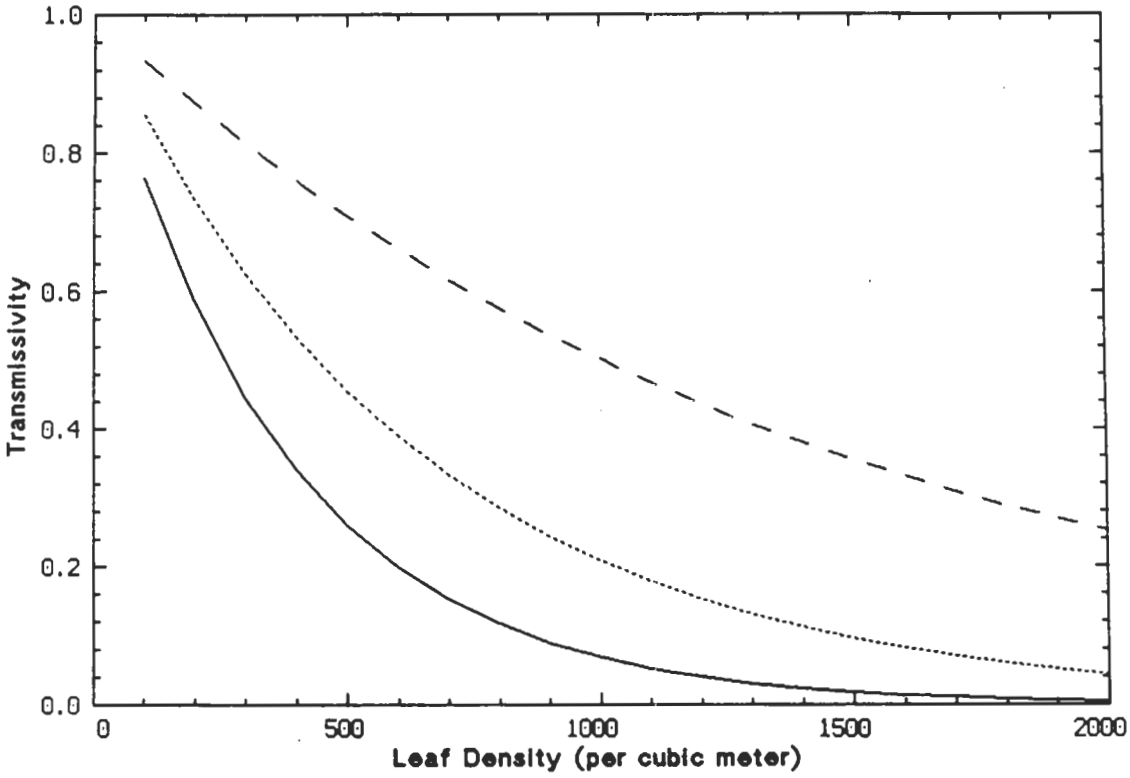

Figure 9.8: Transmissivity of the crown layer versus leaf density for h polarization; (——) X-band, (- - -) C-band, and (– –) L-band.

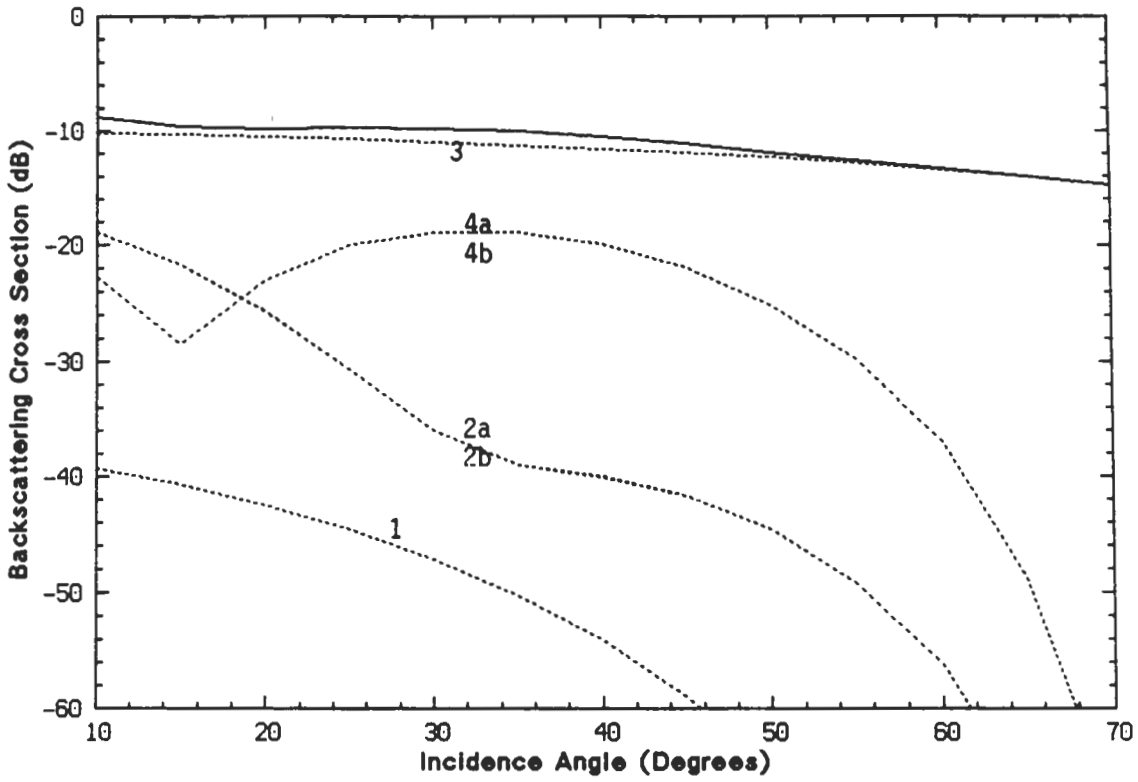

Figure 9.9: Backscattering cross section coefficient σ°_{vv} of the forest canopy at C-band versus incidence angle; (——) total value and (- - -) contribution of individual terms.

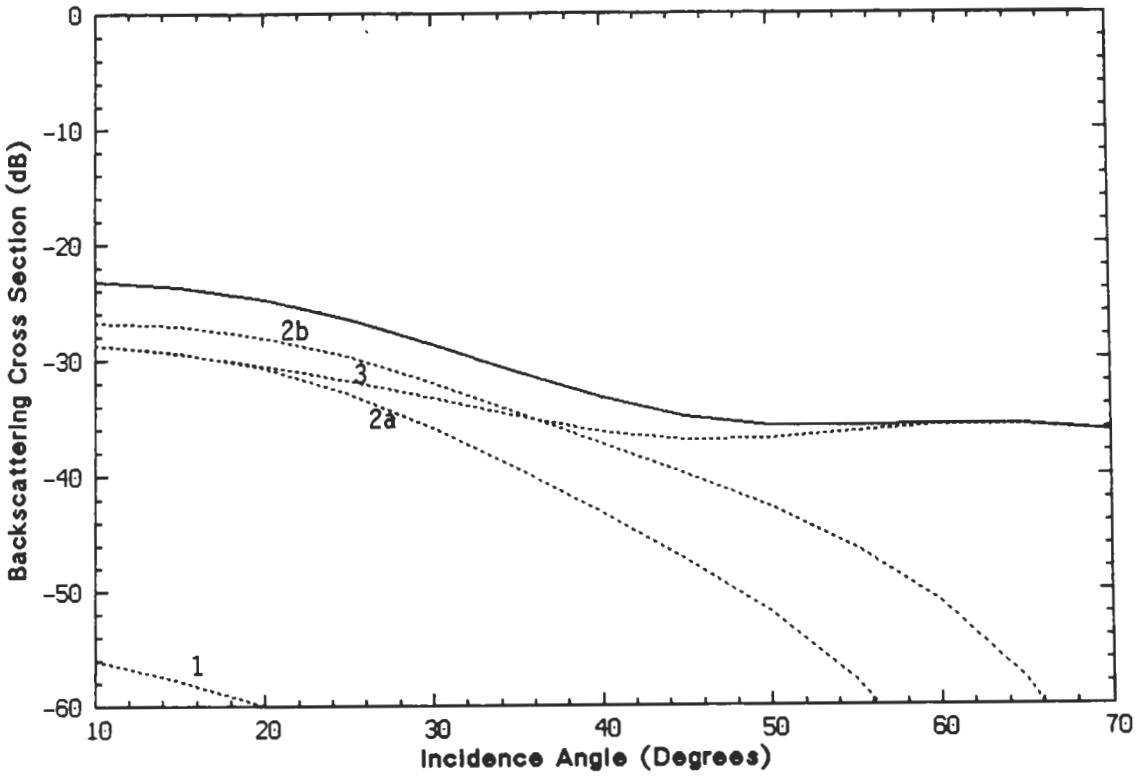

Figure 9.10: Backscattering cross section coefficient σ°_{vh} of the forest canopy at C-band versus incidence angle; (——) total value and (- - -) contribution of individual terms.

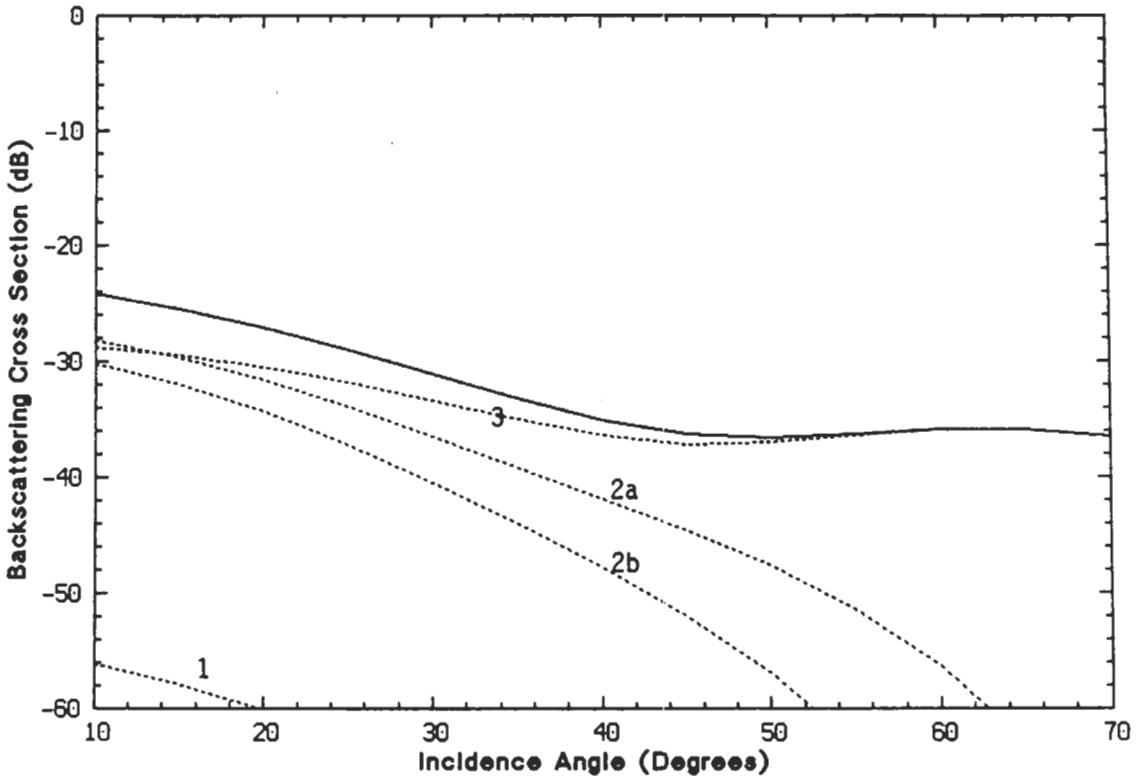

Figure 9.11: Backscattering cross section coefficient σ°_{hv} of the forest canopy at C-band versus incidence angle; (——) total value and (- - -) contribution of individual terms.

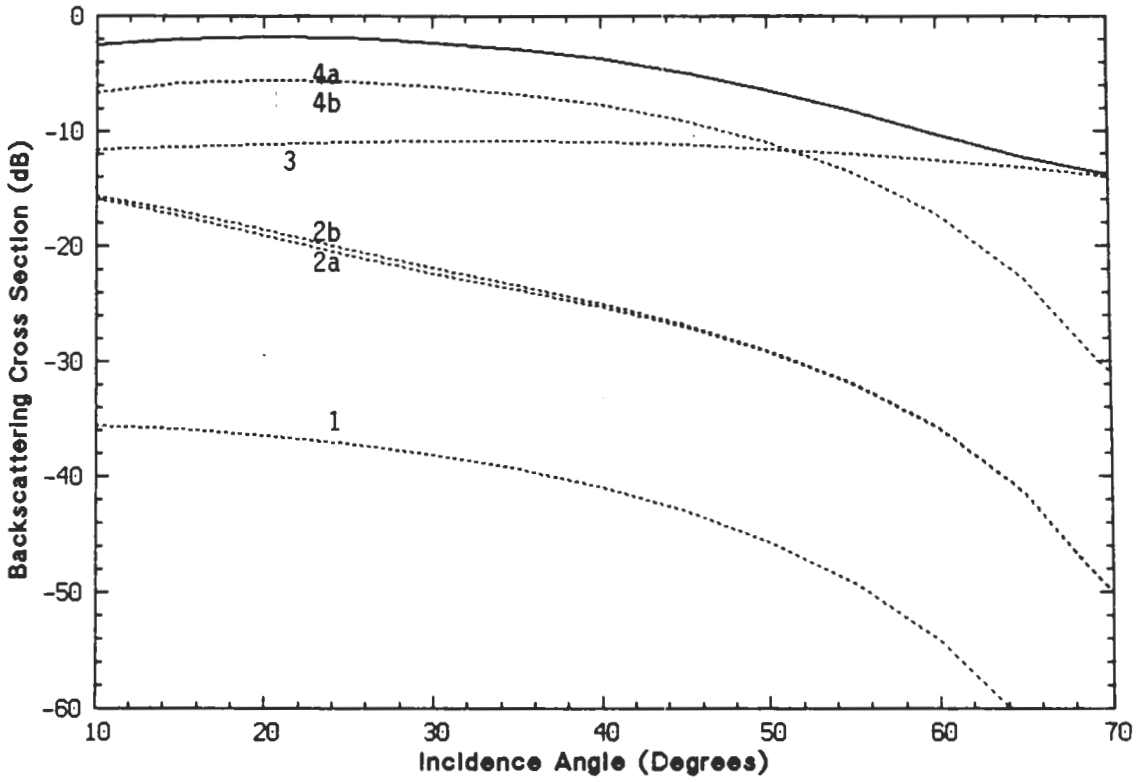

Figure 9.12: Backscattering cross section coefficient σ°_{hh} of the forest canopy at C-band versus incidence angle; (——) total value and (- - -) contribution of individual terms.

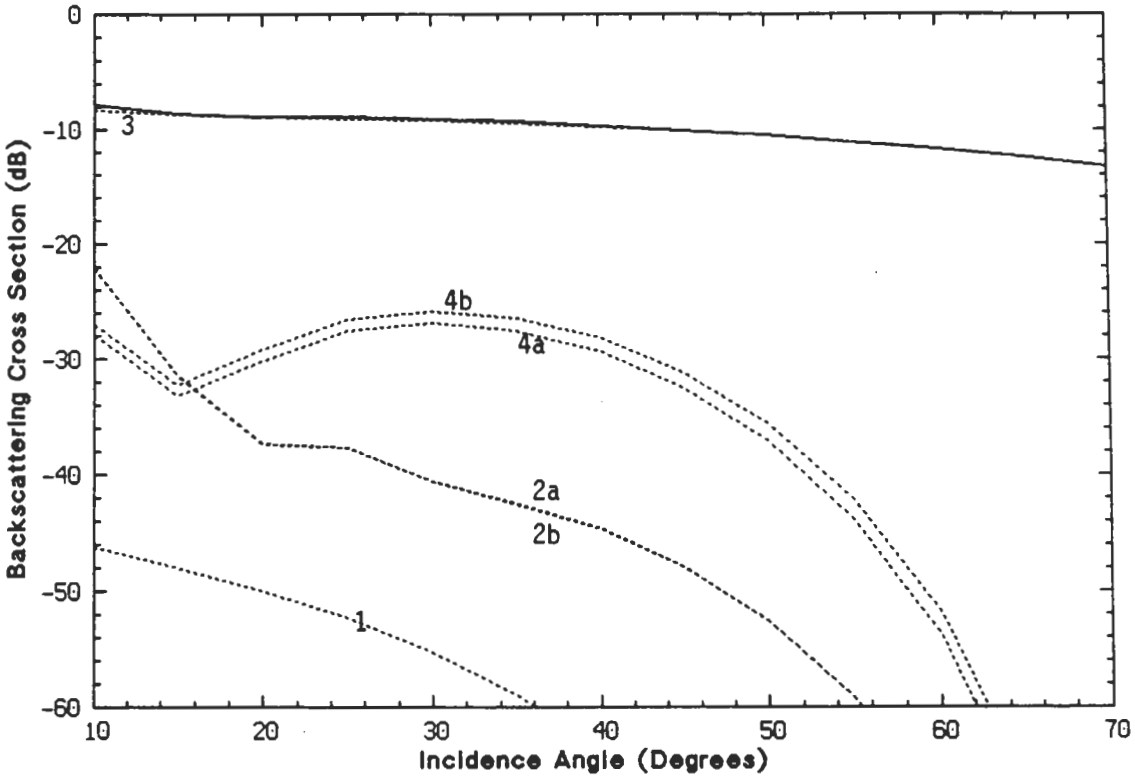

Figure 9.13: Backscattering cross section coefficient σ°_{vv} of the forest canopy at X-band versus incidence angle; (——) total value and (- - -) contribution of individual terms.

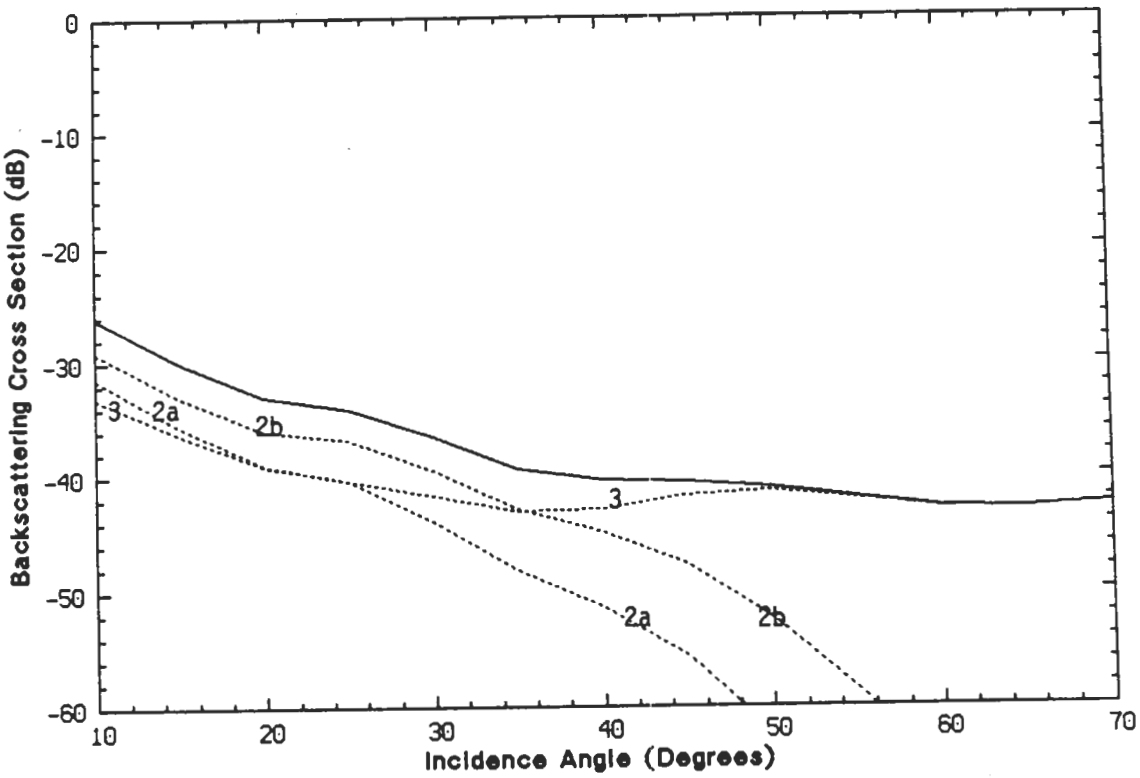

Figure 9.14: Backscattering cross section coefficient σ°_{vh} of the forest canopy at X-band versus incidence angle; (——) total value and (- - -) contribution of individual terms.

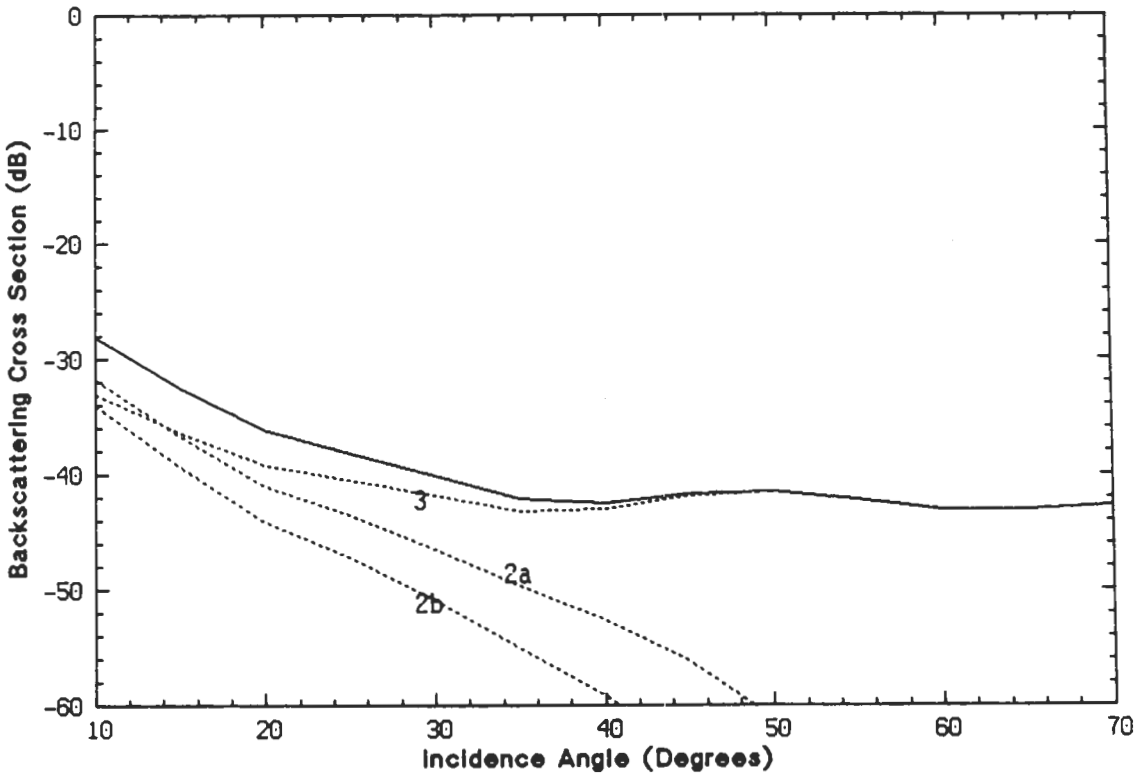

Figure 9.15: Backscattering cross section coefficient σ°_{hv} of the forest canopy at X-band versus incidence angle; (——) total value and (- - -) contribution of individual terms.

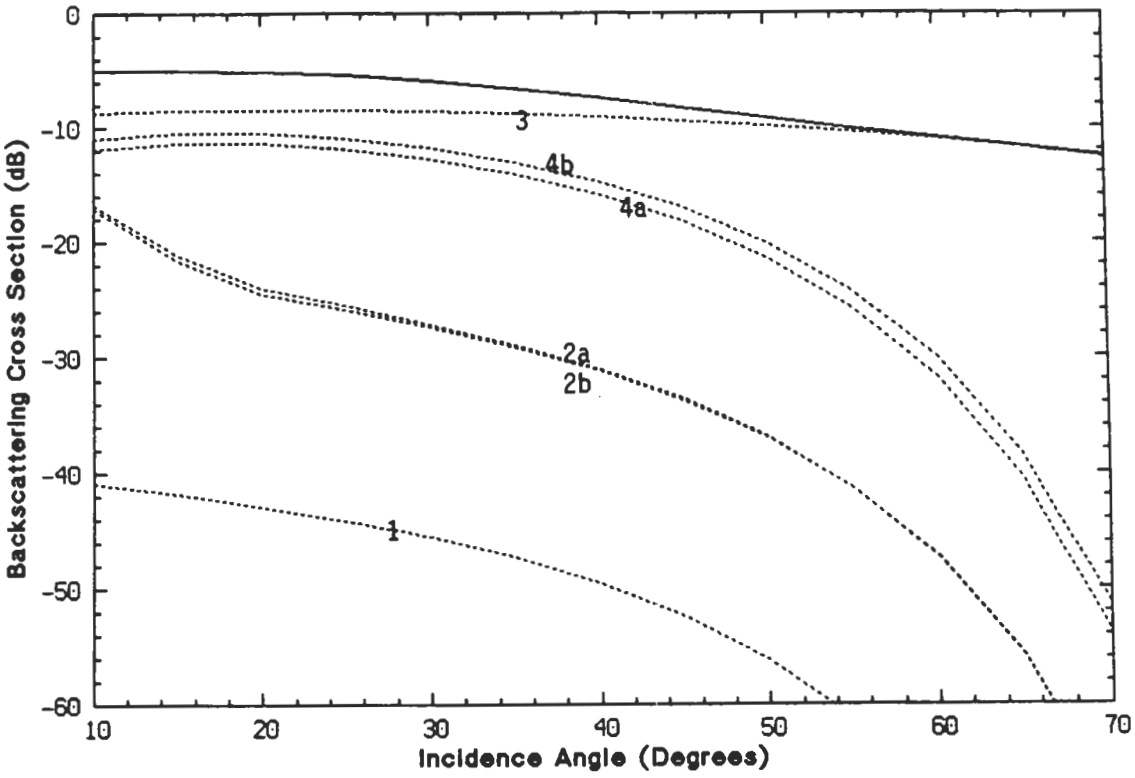

Figure 9.16: Backscattering cross section coefficient σ°_{hh} of the forest canopy at X-band versus incidence angle; (——) total value and (- - -) contribution of individual terms.

CHAPTER X

CONCLUSIONS AND RECOMMENDATIONS

10.1 Summary

This thesis provides models for several problems associated with scattering from vegetation-covered land. A major part of the thesis is devoted to developments of single scattering models for elements of the vegetation canopy and examination of their scattering behavior. These models serve as input functions in a first-order solution of the vector radiative transfer equations for scattering from a three-layer forest canopy. In this section we summarize the important results of each chapter.

In Chapter 2 it is shown that the resistive sheet model, in conjunction with the physical optics approximation, faithfully reproduces the dominant features of the scattering patterns of flat leaves. This high frequency model provides satisfactory results when the dimensions of the leaf are larger than a wavelength. The resistivity of the sheet is entirely specified by the moisture content and thickness of the leaf. By comparison of the numerical results with experimental measurements, it is concluded that the model retains its accuracy over a wide range of moisture contents and aspect angles.

Using resistive sheet and physical optics approximations, the model is extended to the case of a curved leaf in Chapter 3. A simple analytical expression for radar cross

section reduction produced by the curvature is obtained by applying a stationary phase approximation. It is concluded that the curvature has a significant effect in reducing the scattering cross section around the specular direction and broadens the scattering pattern.

In Chapter 4 the results obtained in Chapter 2 and 3 are extended to higher frequencies by modelling a leaf using a stack of combined sheets. This model accounts for the effect of inhomogeneity in the cross section of the leaves which has a significant effect on scattering at millimeter wavelengths. In this chapter two types of physical optics approximations are compared and superiority of the VIPO technique over the SCPO technique is shown by comparing their results with the moment method solution.

Chapter 5 is devoted to examination of the effect of nonuniform thickness profile and variation of the moisture content on the scattering behavior of a leaf. A new perturbation technique in the Fourier domain is introduced. Solution of the induced current on a variable resistive or impedance sheet can be obtained, in principle, to any desired order of perturbation. An analytical solution for the induced current when the perturbation function is periodic is given. The results based on the perturbation technique are compared with the moment method solution for periodic resistive sheets, a third order GTD solution for impedance insert, and a moment method solution for scattering by dielectric structures above resistive and impedance sheets. Excellent agreement is obtained in all cases. For the numerical solution of scattering from dielectric objects above resistive and impedance sheets a new representation for Green's function of the problem is obtained. In this representation exact expressions for the image of a line source above resistive and impedance sheets are given which are very efficient for numerical calculation.

By calculating the scattered field for different cases of a typical dielectric hump it is concluded that a vein and a variation in the thickness of a leaf do not have a significant effect near the specular direction, but in other directions they are substantial contributors to the scattered field.

Rayleigh scattering theory is extended to the two-dimensional problems in Chapter 6. For cylindrical structures of infinite length and arbitrary cross section whose transverse dimensions are much smaller than the wavelength, the field at any point outside the cylinder is written as the sum of contributions from line dipoles whose moments per unit length are expressible in terms of polarizability tensors. The tensor elements are derived from solution of an integral equation for the static potential. Empirical formulations for tensor elements of variety of cylinder cross sections are given and it is shown that there exists a significant shape dependence. Extension of the results to a cylinder of finite length is accomplished by using physical optics approximation. These results are applicable to vegetation needles whose cross sections have dimensions that are much smaller than a wavelength but whose length is larger than the wavelength.

Scattering models for branches and tree trunk are given in Chapter 7. A new expression for the far field amplitude of a circular cylinder of finite length b with $b \gg \lambda_0$ is obtained. These expressions are more accurate than existing results [Ruck et al, 1970] away from the specular cone. Simple expressions using physical optics approximation are also provided for a cylinder with arbitrary cross section.

The effect of the bark layer and its roughness on scattering are considered in Chapter 8. A hybrid solution based on the moment method and Physical optics approximation is obtained for corrugated layered cylinders. The only restriction on the physical dimensions is the radius of curvature (r) of the cylinder where we

require $r \gg \lambda_0$. Also a new physical optics expressions for equivalent surface current on dielectric structure is introduced. It is shown that the bark and its roughness both reduce the radar cross section. The low contrast dielectric bark layer has most effect at higher frequencies where the bark thickness and its roughness are a considerable fraction of wavelength. It is also demonstrated that the roughness of the bark can be replaced by a homogeneous layer for the TM case.

In Chapter 9 a first-order solution for the radiative transfer equations of a three-layer random medium is given. Inputs to this model are the scattering matrices of the canopy constituents and their orientation and size distribution functions. the analytical nature of this solution enables us to study the effect of different scattering mechanism in the medium. This solution is particularly suitable for media of sparsely distributed particles; a higher order solution is needed when the number density of particles is high. The appropriate frequency range for this model is determined by the frequency range over which single scattering models are valid.

10.2 Future Work and Recommendations

The single scattering models provided in this thesis or those avaliable in the literature are mostly valid in either high or low frequency regimes. Obtaining effective analytical or empirical models in the resonance regime is an obvious extension of this work.

In Chapter 8 it is shown that the regular roughness of dielectric cylinders could be modelled by an anisotropic layer which simplifies calculation of the scattered field. Establishing a connection between physical dimensions, geometry, and dielectric constant of the roughness to the thickness and equivalent dielectric constant of the equivalent layer is the next step to complete the problem.

Numerous modifications and improvements may be suggested for the radiative transfer model of the forest canopy. To make the model more realistic the ground layer may be considered rough, the cylinders in the trunk region may be considered to have an angular distribution, and the crown layer may be considered to be statistically inhomogeneous. In principle, obtaining solutions to all these modifications is possible, but the added complexity also increases computation time. It will be necessary to evaluate the significance of each modification before integrating it in the model.

APPENDICES

APPENDIX A

TECHNIQUE FOR MEASURING THE DIELECTRIC CONSTANT OF THIN MATERIALS

A.1 Introduction

Prompted by the need for a practical technique for measuring the microwave dielectric constant of vegetation leaves, solutions were sought for the voltage reflection coefficient measured at the input of a rectangular waveguide containing a thin slab placed in a plane orthogonal to the propagation direction (see Fig. A.1). The slab is modelled as a resistive sheet, which was shown (Chapter 2) to be an excellent approach for characterizing the radar cross section of a vegetation leaf over a wide range of moisture conditions (and a correspondingly wide range of the relative dielectric constant ϵ).

To evaluate the accuracy of the technique for measuring the real and imaginary parts of ϵ from measurements of the complex reflection coefficient Γ, an exact solution for Γ of the slab will be obtained in Section A.3 and then used to simulate the measurement process for given values of ϵ. The evaluation is performed in Section A.4 by comparing the true value of ϵ with that predicted by the resistive sheet expression. It turns out that the resistive sheet solution is identical with the zeroth-

order approximation of the exact solution for Γ . One of the attractive features of the zeroth-order solution is that it provides an explicit expression for ϵ in terms of Γ.

The evaluation shows that the zeroth-order solution provides an excellent estimate for the real part of the dielectric constant, ϵ' , if the slab thickness τ is sufficiently small to satisfy the condition $\tau \leq 0.05\lambda_0\sqrt{|\epsilon|}$, where λ_0 is the free space wavelength. For a typical leaf-thickness of 0.3 mm, this condition is satisfied for any moisture condition if the frequency $f \leq 15$ GHz. A much more stringent condition on τ is required in order for the zeroth-order solution to give accurate values for ϵ'' ; namely $\tau \leq 0.01\lambda_0\sqrt{|\epsilon|}$ and $\epsilon''/\epsilon' \geq 0.1$, or equivalently, $f \leq 1.5$ GHz for vegetation leaves. To relax this limitation, alternate solutions for Γ are obtained in Section A.3 by invoking approximations that lead to first-order and second-order solutions whose forms are invertible to give explicit expressions for ϵ . Use of the second-order solution is found to extend the frequency range from 1.5-12 GHz for a leaf with a high moisture content and to higher frequencies for drier leaves.

Section A.5 presents 8-12 GHz spectra of the dielectric constant ϵ for vegetation leaves, teflon and rock slices, all measured using the technique developed in this appendix. Where possible, the results are compared with measurements made by other techniques.

A.2 Model for a Thin Resistive Sheet

Consider the rectangular waveguide diagrammed in Fig. A.1. The guide is terminated with a matched load, has dimensions $a \times b$, and contains a thin resistive sheet of thickness τ at $z = 0$. The waveguide dimensions are such that only the TE_{10} mode can propagate in the guide.

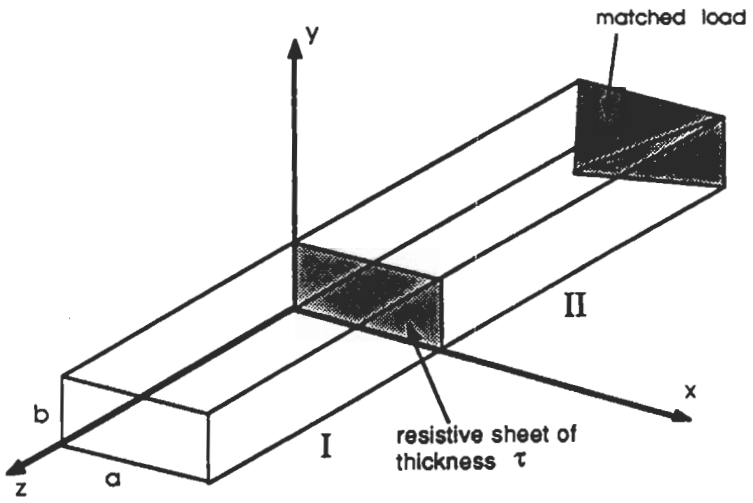

Figure A.1: Rectangular waveguide with thin resistive sheet of thickness t at z = 0.

We seek a relationship between the input voltage reflection coefficient Γ and the relative complex dielectric constant of the sheet material ϵ . To this end, we shall develop expressions for the electric and magnetic fields in Regions I and II and then apply the appropriate boundary conditions. If ψ_I and ψ_{II} are the electric potentials in regions I and II, respectively, solutions of the scalar Helmholtz equation

$$(\nabla^2 + k_0^2)\Psi_{I,II} = 0 \tag{A.1}$$

for the TE_{10} mode leads to [Harrington, pp. 148-149, 1961]:

$$\Psi_I = \cos(\tfrac{\pi x}{a})[C_1 e^{-ik_z z} + C_2 e^{ik_z z}] \ , \qquad z \geq 0 \tag{A.2}$$

$$\Psi_{II} = \cos(\tfrac{\pi x}{a}) C_3 e^{-ik_z z} \ , \qquad z \leq 0 \tag{A.3}$$

The constants C_1 and C_2 represent the magnitudes of the incident and reflected waves in Region I, C_3 represents the magnitude of the wave traveling towards the matched load in Region II, and

$$k_z = \sqrt{k_0^2 - (\frac{\pi}{a})^2} = \frac{\pi}{\lambda_0 a}\sqrt{4a^2 - \lambda_0^2}. \tag{A.4}$$

The components of E and H may be obtained from (A.2) and (A.3) by applying the relations [Harrington, pp. 130, 1961].

$$\mathbf{E} = -\nabla \times (\psi \hat{z}) \ , \qquad \mathbf{H} = i\omega\epsilon(\psi \hat{z}) + \frac{-1}{i\omega\mu}\nabla\nabla \cdot (\psi \hat{z}) \ . \tag{A.5}$$

The field quantities, in the plane $z = 0$, must satisfy the resistive sheet boundary conditions as given by (2.4)-(2.6). The resistivity of the sheet in terms of it dielectric constant and thickness is also given by (2.3). The condition for continuity of the tangential electric field from Region I to Region II and the boundary condition for the magnetic field requires that

$$\hat{z} \times (\mathbf{E}_I - \mathbf{E}_{II}) = 0 \qquad \hat{z} \times (\mathbf{H}_I - \mathbf{H}_{II}) = \mathbf{J}. \tag{A.6}$$

The unknown coefficients $C1$, $C2$, $C3$ can be obtained by applying the boundary conditions. The complex voltage reflection coefficient is then found to be

$$\Gamma = \frac{C_2}{C_1} = -\frac{k_0^2\tau(\epsilon - 1)}{k_0^2\tau(\epsilon - 1) + 2ik_z} \tag{A.7}$$

from which an explicit expression for ϵ is obtained,

$$\epsilon = 1 - \frac{2ik_z\Gamma}{k_0^2\tau(1+\Gamma)} = 1 - \frac{i\left(\frac{\lambda_0}{2\pi a}\right)\sqrt{4a^2 - \lambda_0^2}}{\tau(1 + 1/\Gamma)}. \tag{A.8}$$

Thus, by measuring the complex reflection coefficient Γ and the sheet thickness τ we can compute ϵ directly. This technique can be very useful for measuring the dielectric constant of vegetation leaves and other similarly thin slabs. Its success, however, depends on two factors: 1) the ability to measure both the magnitude and phase of Γ accurately, which now is possible with the HP-8510 vector network analyzer, and 2) the validity of the thin-sheet assumption underlying the derivation that led to (A.8). To examine the range of validity of this assumption and to quantify it in the form of specific limits, we shall first derive the expression for the reflection

coefficient when a dielectric slab of arbitrary thickness is placed in the waveguide, and then compare the exact solution with the solution given by (A.7) and (A.8).

A.3 Model for a Slab of Arbitrary Thickness

The waveguide section shown in Fig. A.2 is terminated in a matched load and contains a dielectric slab extending from $z = 0$ to $z = -\tau$. The electric potentials in

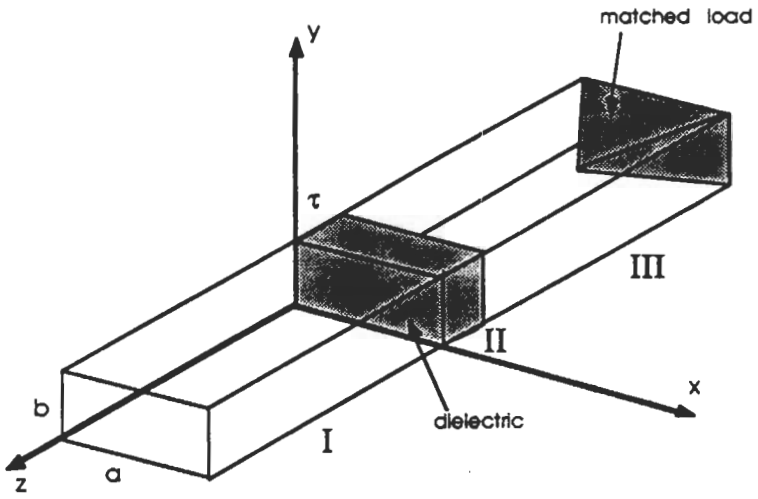

Figure A.2: Rectangular waveguide with a dielectric slab occupying region II (between $z = 0$ and $z = -\tau$).

regions I, II, and III are

$$\Psi_I = \cos(\tfrac{\pi x}{a})[C_1 e^{-ik_z z} + C_2 e^{ik_z z}] \ , \quad z \geq 0$$

$$\Psi_{II} = \cos(\tfrac{\pi x}{a})[C_3 e^{-ik_{z2} z} + C_4 e^{ik_{z2} z}] \ , \quad 0 \geq z \geq -\tau$$

$$\Psi_{III} = \cos(\tfrac{\pi x}{a}) C_5 e^{-ik_z z} \ , \quad -\tau \geq z$$

where k_z is given by (A.4) and k_{z2} is given by

$$k_{z2} = \frac{\pi}{\lambda a}\sqrt{4\epsilon a^2 - \lambda_0^2}. \tag{A.9}$$

Upon using the relationship given by (A.5) to obtain $\mathbf{E}$ and $\mathbf{H}$ in each of the three regions, and then applying the continuity conditions of tangential $\mathbf{E}$ and $\mathbf{H}$ fields

at the boundaries $z = 0$ and $z = -\tau$, we obtain the following expression for the reflection coefficient

$$\Gamma = \frac{C_2}{C_1} = \frac{i[(k_{z2}/k_z)^2 - 1]\sin(k_{z2}\tau)}{2(\frac{k_{z2}}{k_z})\cos(k_{z2}\tau) - i[(k_{z2}/k_z)^2 + 1]\sin(k_{z2}\tau)}. \tag{A.10}$$

We shall refer to (A.10) as the exact solution for Γ .

A.3.1 Second-Order Solution

If $k_{z2}\tau$ is small and we use the approximations

$$\sin k_{z2}\tau \approx k_{z2}\tau \tag{A.11}$$

$$\cos k_{z2}\tau \approx 1 - \frac{1}{2}(k_{z2}\tau)^2. \tag{A.12}$$

The expressions given by (A.10) can be simplified to give the second-order solution

$$\Gamma \approx \frac{-(\epsilon - 1)}{\left(1 - \frac{1}{2}(\frac{\lambda_0}{a})^2 + i\tau k_z(\frac{\lambda_0}{2a})^2 + 2i\frac{k_z}{\tau k_0^2}\right) + (1 - i\tau k_z)\,\epsilon} \tag{A.13}$$

from which we obtain the following explicit expression for the second-order solution of the relative dielectric constant:

$$\epsilon = \epsilon_2 \approx \frac{1 - \left[1 - \frac{1}{2}(\frac{\lambda_0}{a})^2 + i\tau k_z(\frac{\lambda_0}{2a})^2 + 2i\frac{k_z}{\tau k_0^2}\right]\Gamma}{1 + (1 - i\tau k_z)\Gamma} \tag{A.14}$$

A.3.2 First-Order Solution

If, instead of the approximation given by (A.12), we were to set $\cos(k_{2z}\tau) \approx 1$ in (A.10) (i.e., ignoring second and higher order powers of $(k_{z2}\tau)$), we would obtain the result

$$\Gamma \approx \frac{-(\epsilon - 1)}{\epsilon + \left(1 - \frac{1}{2}(\frac{\lambda_0}{a})^2\right) + 2i\frac{k_z}{\tau k_0^2}} \tag{A.15}$$

which can then be solved to obtain the expression

$$\epsilon = \epsilon_1 \approx \frac{1 - \left[1 - \frac{1}{2}(\frac{\lambda_0}{a})^2 + 2i\frac{k_z}{\tau k_0^2}\right]\Gamma}{1 + \Gamma} \tag{A.16}$$

for the first-order estimate of ϵ .

A.3.3 Zeroth-Order Solution

If $\epsilon \gg 1$, we may use the approximation

$$\frac{\epsilon + \left(1 - \frac{1}{2}(\frac{\lambda_0}{a})^2\right)}{\epsilon - 1} \approx 1 \tag{A.17}$$

since $-1 \leq 1 - \frac{1}{2}(\frac{\lambda_0}{a})^2 < 1$. Equation (A.15) then leads to

$$\begin{aligned} \epsilon = \epsilon_0 &\approx 1 - \frac{2ik_x\Gamma}{\tau k_0^2(\Gamma+1)} \\ &= 1 - \frac{i(\lambda_0/2\pi a)\sqrt{4a^2-\lambda_0^2}}{\tau(1+1/\Gamma)} \end{aligned} \tag{A.18}$$

which is identical with the resistive-sheet approximation given by (A.8).

A.4 Sensitivity Analysis

The second order solution for Γ , given by (A.13), was based on assuming that $k_{z2}\tau \ll 1$ and on retaining terms up to and including the second power in the series expressions for $\sin k_{z2}\tau$ and $\cos k_{z2}\tau$. In the first-order solution, only the zeroth- and first-order terms were retained. The purpose of these derivations is to use them for computing ϵ from measured values of the complex reflection coefficient Γ . The accuracies of the approximate expressions given by (A.14) and (A.16), corresponding to the second-order and first-order solutions for ϵ , respectively, depends on the magnitude of $k_{z2}\tau$. For a standard waveguide operated in the TE_{10} mode, the dimension a is on the order of $3\lambda_0/4$. Hence,

$$k_{z2} = k_0\tau\sqrt{\epsilon - (\lambda_0/2a)^2} \approx k_0\tau\sqrt{\epsilon - 4/9}\ .$$

If we require that $k_0\tau\sqrt{\epsilon}$ be small, then k_{z2} will be smaller still.

The zeroth-order solution (A.18) is only applicable if ϵ is sufficiently large to allow the approximation given by (A.17) to be used in (A.15). Hence for ϵ large, the first-order and zeroth-order solutions should yield comparable results.

To evaluate these approximate expressions for ϵ , we conducted the following sensitivity analysis. We selected specific values of the waveguide width a, the wavelength λ_0 , and the relative complex dielectric constant of the slab, ϵ . We then computed Γ using the exact solution (A.10). The computed value of Γ was then used in (A.18), (A.16), and (A.14) to compute the zeroth-order, first-order, and second-order estimates of ϵ . We denote these ϵ_0, ϵ_1, and ϵ_2.

Our first example of this procedure is Figs. A.3 and A.4 where we show plots of ϵ_0, ϵ_1, and ϵ_2 at 10 GHz as a function of τ for a slab with true dielectric constant $\epsilon = 2 + i0.01$. We observe that ϵ_0', ϵ_1', and ϵ_2' in Fig. A.3 each provide values that are within 1 percent of ϵ' for $\tau \leq 1mm$. Among the three approximations, ϵ_0' is the most accurate, in spite of the fact that the left-hand side of (A.17) is equal to 2, rather than approximately equal to 1 as required by (A.17). This insensitivity of Γ to the first term in the denominator of (A.15) is because this term is much smaller than the second term in the denominator of (A.15), thereby exercising a minor influence on the final expression for ϵ' .

Measuring ϵ' of a material usually is not a difficult problem, but measuring ϵ'' of a low-loss material can be. The errors associated with using the approximations leading to ϵ_0'', ϵ_1'', and ϵ_2'' are shown in Fig. A.4 in the form of deviations from the true value $\epsilon'' = 0.01$. For $\tau \leq 1mm$, the relative error is 20 percent for ϵ_2'', 50 percent for ϵ_1'', and the estimate provided by ϵ_0'' is grossly inaccurate. Hence, in spite of the fact that ϵ_0' provides a good estimate of ϵ', the zeroth order solution is inadequate for estimating ϵ''.

Figs. A.5 and A.6 shows results for a material with $\epsilon = 20 + i10$. again ϵ_0' provides an adequate estimate of ϵ' over a wide range of thickness τ. For the imaginary part, however, ϵ_2'' consistently provides more accurate estimates of ϵ'' than those provided

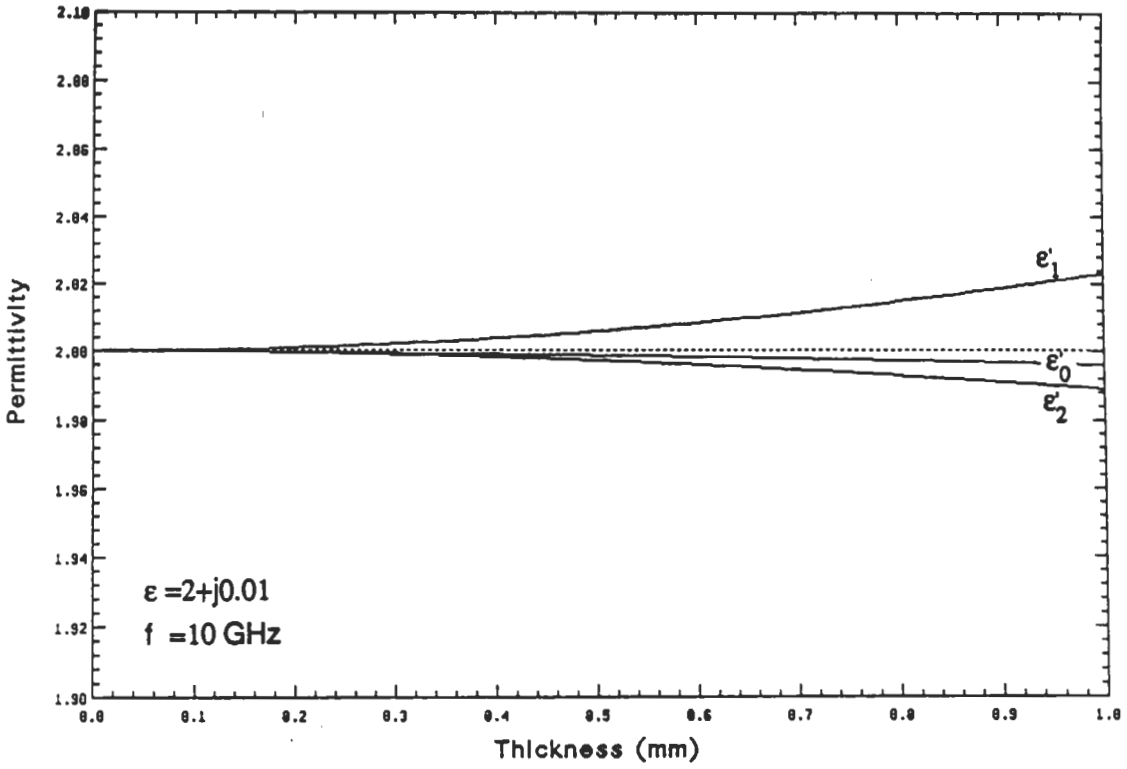

Figure A.3: Relative permittivities (real part of ϵ) obtained from A.14, A.16, and A.18 versus thickness for a slab with $\epsilon = 2 + i0.01$.

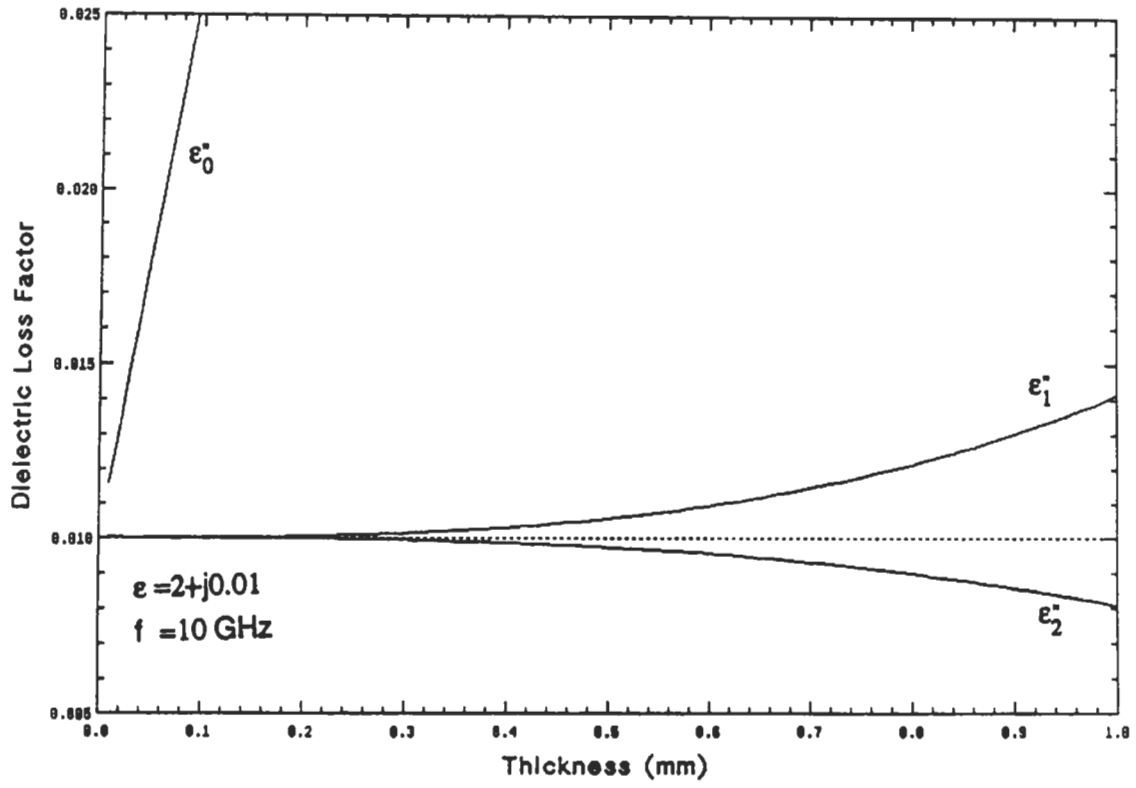

Figure A.4: Dielectric loss factors (imaginary part of ϵ) obtained from A.14, A.16, and A.18 versus thickness for a slab with $\epsilon = 2 + i0.01$.

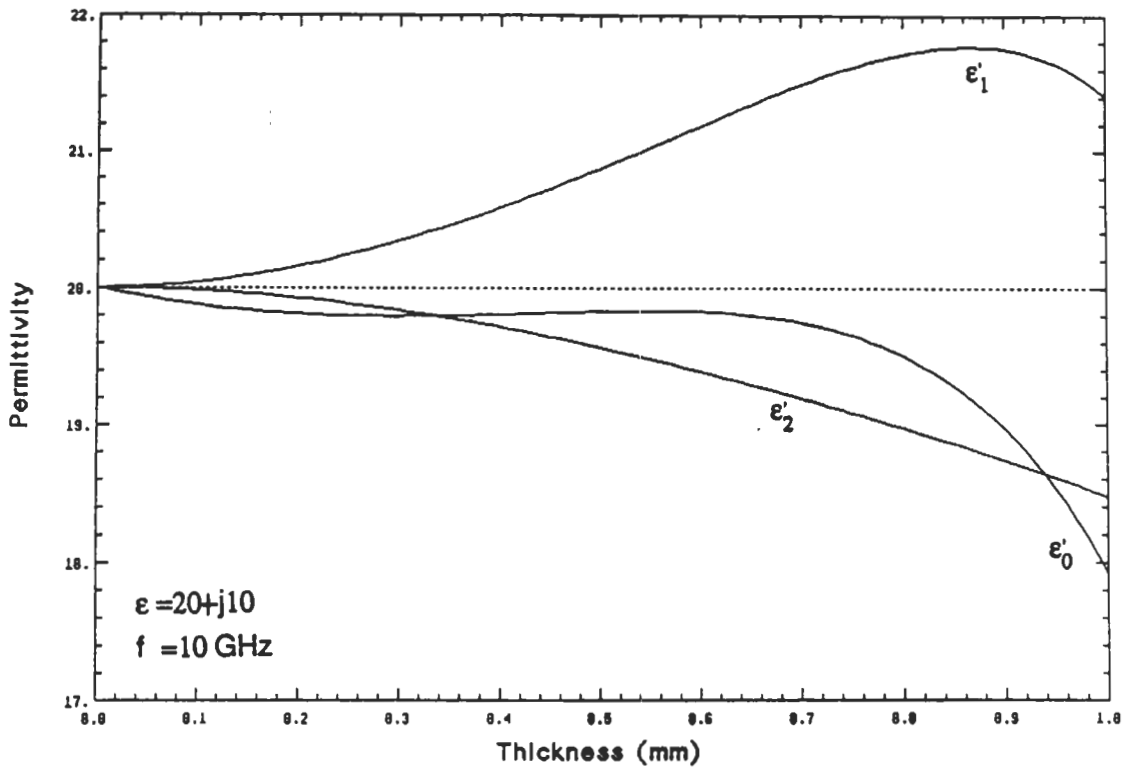

Figure A.5: Relative permittivities (real part of ϵ) obtained from A.14, A.16, and A.18 versus thickness for a slab with $\epsilon = 20 + i10$.

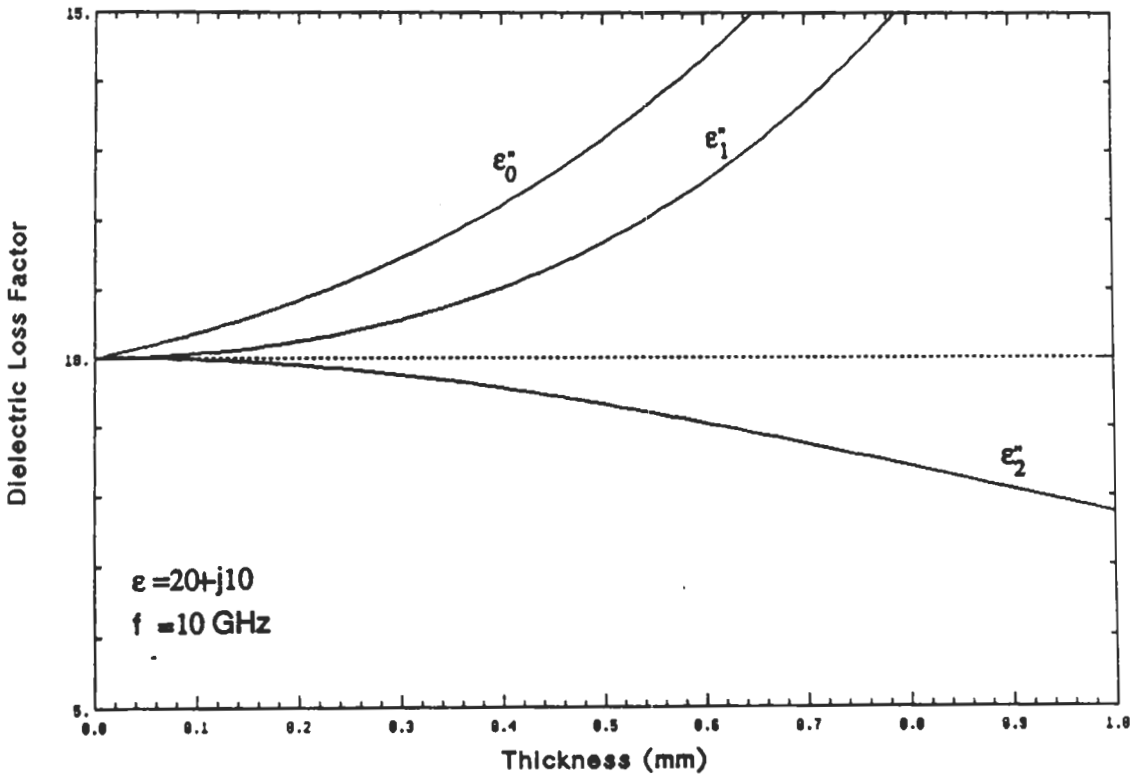

Figure A.6: Dielectric loss factors (imaginary part of ϵ) obtained from A.14, A.16, and A.18 versus thickness for a slab with $\epsilon = 20 + i10$.

by either ϵ_0'' or ϵ_1''.

A summary of the relative accuracies of the three approximations ϵ_0, ϵ_1, and ϵ_2, is presented in Table A.1 for slab thicknesses τ equal to 1 percent and 5 percent of $\lambda_0/\sqrt{|\epsilon|}$. The entries in the table are the maximum relative errors in percent. For ϵ', for example, the maximum relative error is defined as

$$e_0' = \max|\frac{\epsilon_0' - \epsilon'}{\epsilon'}| \times 100$$

where ϵ_0' is provided by (A.18) and ϵ' is the true value of the slab permittivity.

Maximum	$\tau\sqrt{\|\epsilon\|}/\lambda_0 = 0.01$			$\tau\sqrt{\|\epsilon\|}/\lambda_0 = 0.05$		
Error %	ϵ''/ϵ'			ϵ''/ϵ'		
	10^{-2}	10^{-1}	1	10^{-2}	10^{-1}	1
e_0'	0.114	0.341	2.920	3.107	2.672	17.05
e_0''	182.8	18.35	1.445	934.0	96.70	10.11
e_1'	0.127	0.124	0.060	3.293	3.216	1.916
e_1''	0.434	0.267	0.018	33.06	8.629	2.727
e_2'	0.063	0.062	0.029	1.538	1.506	0.866
e_2''	0.215	0.132	0.091	15.11	3.926	2.238

Table A.1: Maximum relative errors associated with the expressions for ϵ_0, ϵ_1 and ϵ_2.

A.5 DIELECTRIC MEASUREMENTS

A.5.1 Measurement System

A HP-8510A vector network analyzer was used in conjunction with a HP-8511 parameter test set and a HP-9000 computer (Fig. A.7) to measure the amplitude and

phase of the reflection coefficient Γ of dielectric slabs placed in a waveguide sample-holder. The arrangement shown in Fig. A.7 consists of a waveguide section connected to the HP-8511 through a coax-to-waveguide adapter on one end and to a waveguide section terminated in a matched load on the other end. A thin piece of styrofoam is placed in the sample-holder section at a distance τ from the waveguide opening (junction between the two waveguide sections) where τ is equal to the thickness of the dielectric sample. Another thin piece of styrofoam is placed on the other side of the sample (in the empty waveguide section) to keep the sample in place.

After placing the sample in the waveguide, the network analyzer is used to measure the complex reflection coefficient over the frequency range of interest. In the present setup, the frequency coverage is from 8 GHz to 12 GHz.

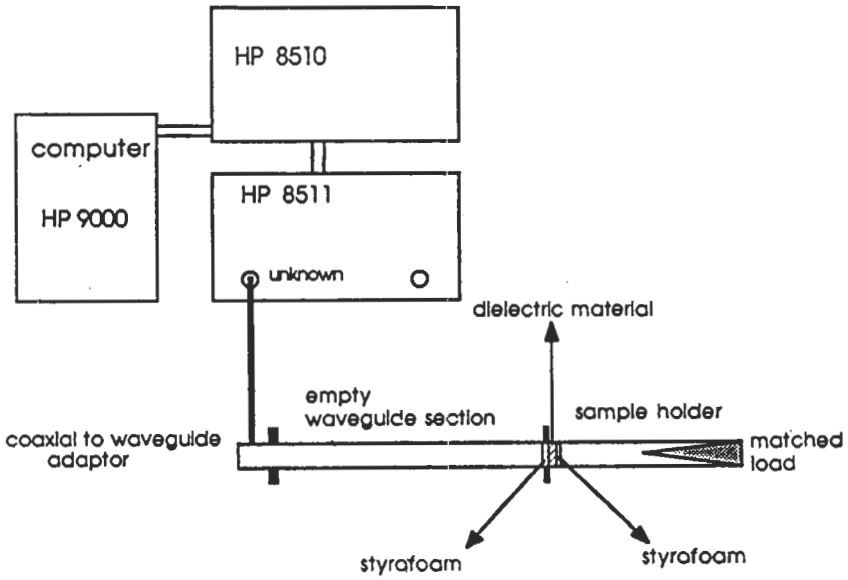

Figure A.7: Measurement system.

A.5.2 Measurement Accuracy

The accuracy of the dielectric constant measurement is critically based upon the accuracy with which the reflection coefficient Γ can be measured. The measurement

of Γ may contain some random, nonrepeatable errors caused by system noise and environmental variations as well as certain systematic errors that are repeatable and, therefore, correctable. To correct the systematic errors, the measurement system is calibrated using three independent standards whose reflection coefficients are known over the frequency range under consideration. These include a short-circuited load, a matched load, and an offset short.

A.5.3 Sample Measurements

The technique described in the previous sections was used to measure the 8-12 GHz dielectric spectra of three types of rock materials (each cut in the shape of a thin slab with a cross-section equal to that of the waveguide's) and a thin leaf of vegetation material with a gravimetric moisture content of 90 percent. In addition, a thin slab of teflon with $\epsilon = 2.0 + i0.005$ was measured also. The results are given in Figs. A.8-A.10. The results for teflon were found to be in excellent agreement with those measured for a thick sample for both ϵ' and ϵ'' . The measured permittivities of the rock samples are essentially constant over the 8-12 GHz band (Fig. A.8), and for two of the samples (rhyolite and rhyodlacite) the measured permittivity compares very well with values measured by a coaxial probe using an approximate reflection technique [El-Rayes and Ulaby].

The plots in Fig. A.9 display ϵ'', the relative dielectric loss factor, for teflon and the three rock samples. We have no reason to expect ϵ of rocks to exhibit a dispersive behavior in the 8-12 GHz frequency region, and therefore, we suspect that the observed variability, particularly in the 8-9 GHz range, is an artifact of the measurement system.

The example shown in Fig. A.10 is for a leaf of vegetation. Its gravimetric mois-

ture was 0.9 and its thickness $0.23mm$. The continuous curves represent the values of ϵ' and ϵ'' measured with the waveguide technique and the circles represent values calculated using a model [Ulaby and El-Rayes] with an accuracy of ± 20 percent. Within this range of accuracy, the data and the model are in good agreement.

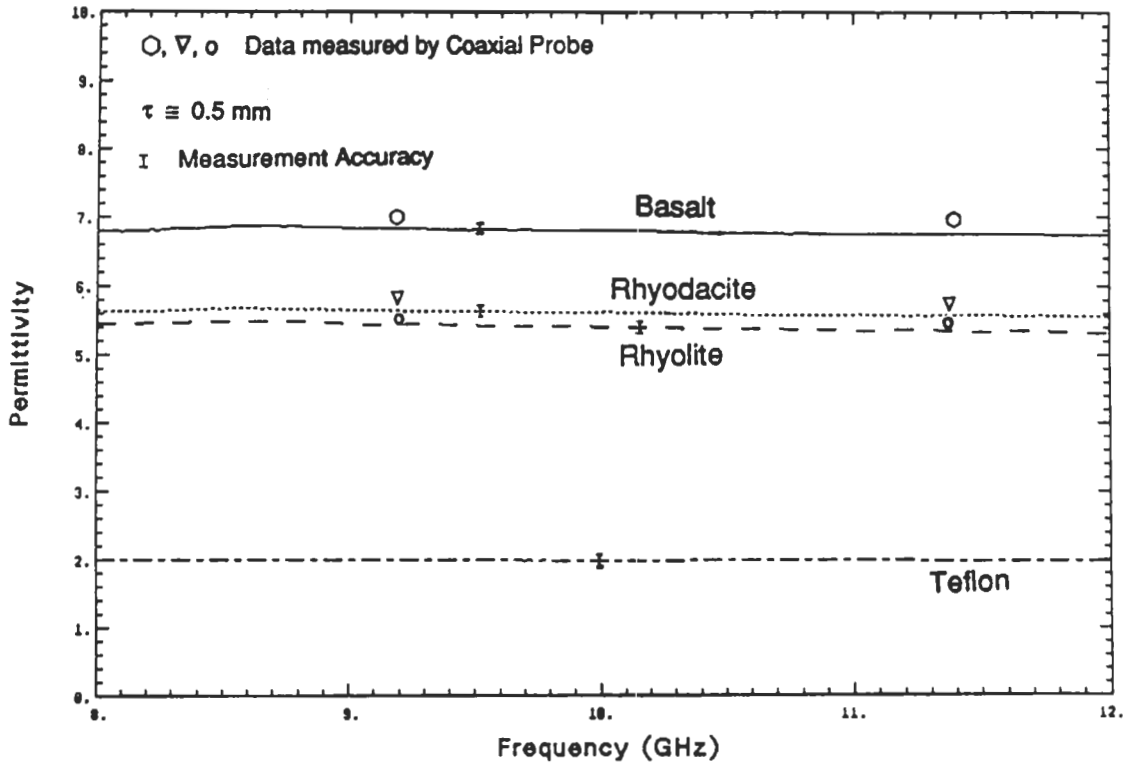

Figure A.8: Measured relative permittivity of teflon and three rock samples.

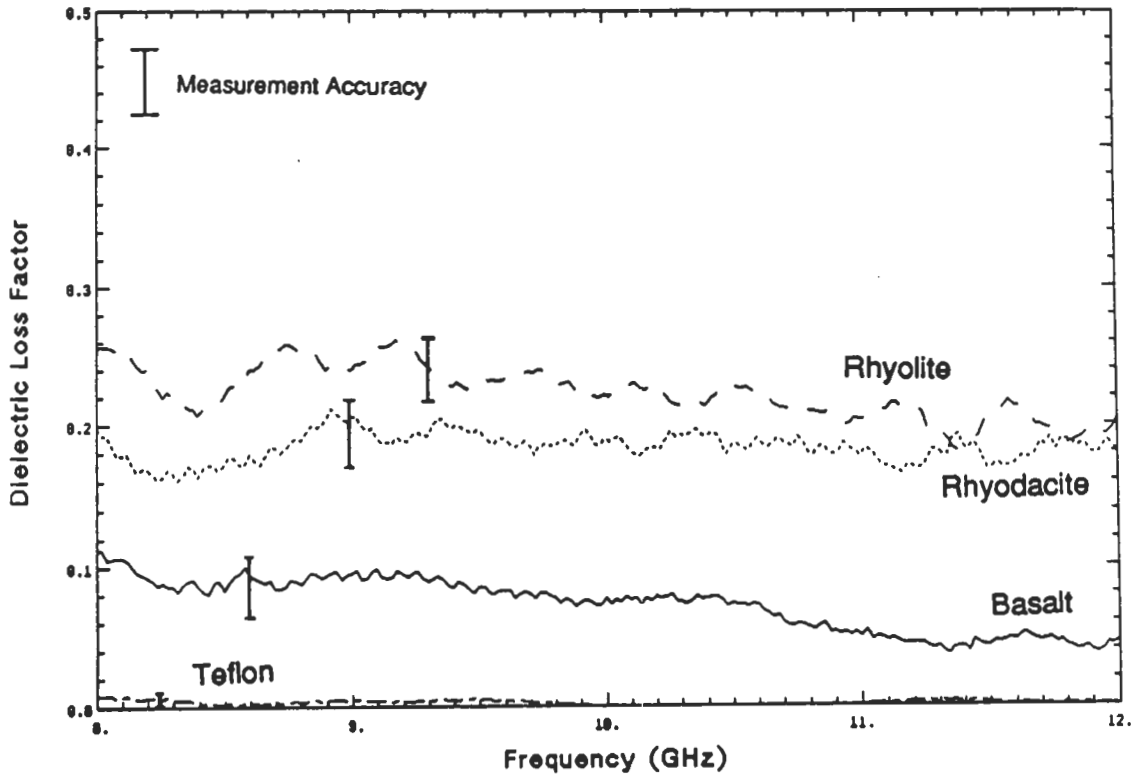

Figure A.9: Measured dielectric loss factor of teflon and three rock samples.

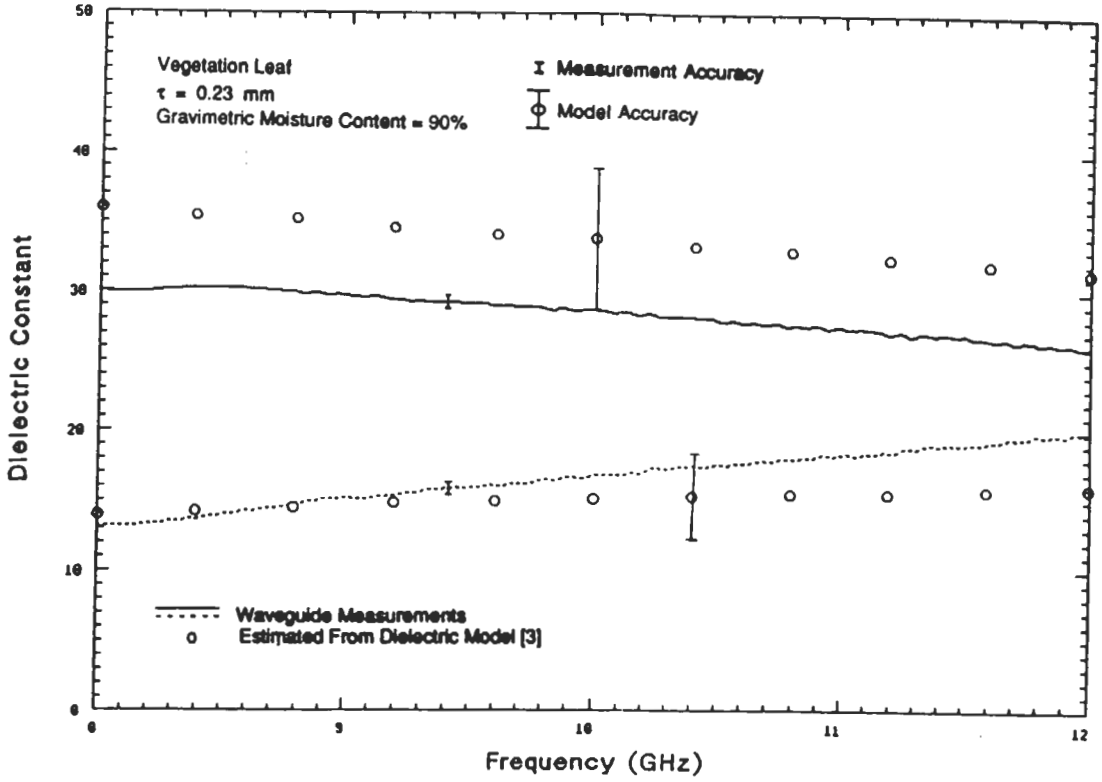

Figure A.10: Measured relative dielectric constant of a vegetation leaf.

APPENDIX B

TWO DIMENSIONAL SCATTERING BY CYLINDRICAL STRUCTURES WITH HIGH REFRACTIVE INDEX

B.1 Introduction

A numerical solution for the problem of electromagnetic scattering by a lossy inhomogeneous cylinder of arbitrary cross section is discussed. An integro-differential equation is employed to obtain the moment method solution using a pulse expansion function and the point matching technique. In this method the cross section of the scatterer is partitioned into small cells over which the dielectric constant and the unknown field quantities can be assumed constant. Then the integral equation is cast into a linear system of equations that can be solved by various numerical methods. This technique was developed many years ago [Richmond 1965 & 1966; Harrington 1968] and has been applied successfully for cylinders with relatively small refractive indices. The integral equation operator given by Harrington is such that in the TE case (the electric field vector perpendicular to the axis of the cylinder), when using pulse expansion functions, numerical computation does not converge to the exact solution. To obtain accurate results in this case more complicated expansion functions such as the linear expansion function [Hill et al. 1983] or the rooftop expansion func-

tion [Langan & Willton 1986], must be used. To avoid using complicated expansion functions and to reduce computation time, we use an integral equation where the pulse functions are in the domain of the integro-differential operator for both TE and TM (the magnetic field vector perpendicular to the axis of the cylinder) cases.

It is known, in principle, that the accuracy of the solution is proportional to the dimension of the cells relative to the wavelength, which in turn is governed by the dielectric constant of the cylinder material. The accepted criterion for the cell dimension is $d < 0.1\lambda_0/\sqrt{|\epsilon_r|}$ where λ_0 is the wavelength in free space and ϵ_r is the relative permittivity of the dielectric material.

Biological tissues usually have high water content, as a result of which their dielectric constant is very high and lossy. In application of the moment method to biological scatterers, the cell size must be chosen very small compared to the free-space wavelength. Since the argument of the Green's function becomes very small, contribution of self-cell and adjacent cells must be evaluated very carefully to avoid anomalous errors.

Unlike the TE case in which approximations on deforming the cell shape can culminate in substantial error, the solution for the TM case is not very sensitive the the shape of the cells. When using the moment method with traditional impedance matrix elements [Richmond 1965 & 1966], as the dimension of the cells gets very small, the technique becomes vulnerable to two sources of error: 1) error due to deformation of cell shapes to circles of equivalent area, and 2) errors associated with the evaluation of the mutual impedance of adjacent cells. The effect of the latter again is much more significant in the TE case than the TM case because of higher degree of singularity in the kernel of the integral equation.

For a scatterer with fixed dimensions, as the dielectric constant increases the

impedance matrix becomes larger and so does the error due to matrix inversion. This problem is unavoidable in general but the error can be reduced by using double-precision variables in the numerical code.

B.2 Formulation

Let us consider an inhomogeneous infinite cylinder with arbitrary cross section S as illustrated in Fig. 1. The axis of the cylinder is parallel to the z axis and the surrounding medium is assumed to be free space. Let the relative permittivity of the cylinder be $\epsilon_r(x,y)$ and its relative permeability be unity ($\mu_r = 1$). Suppose the electric field in the absence of the cylinder (the incident field) is not dependent upon z and is represented by $\mathbf{E}^i(x,y)$. The cylinder perturbs the incident field and the difference between the perturbed (total) and incident field is known as the scattered field; thus,

$$\mathbf{E}^t(\bar{\rho}) = \mathbf{E}^i(\bar{\rho}) + \mathbf{E}^s(\bar{\rho}), \tag{B.1}$$

where $\bar{\rho}$ is the position vector in cylindrical coordinates. From Maxwell's equations it can be shown that a volumetric current density of the form

$$\mathbf{J}_e(\bar{\rho}) = -ik_0 Y_0[\epsilon_r(\bar{\rho}) - 1]\mathbf{E}^t(\bar{\rho}), \qquad \bar{\rho} \in S, \tag{B.2}$$

known as the polarization current, in free space, can replace the cylinder to reproduce the scattered field. Therefore the scattered field, can be obtained from:

$$\mathbf{E}^s(\bar{\rho}) = -ik_0 Z_0 \int_s \mathbf{J}_e(\bar{\rho'}) \cdot \overline{\overline{\Gamma}}(\bar{\rho}, \bar{\rho'}) \mathrm{d}s', \tag{B.3}$$

where $\overline{\overline{\Gamma}}(\bar{\rho}, \bar{\rho'})$ is the two-dimensional dyadic Green's function given by (5.4). Using (B.1), (B.2),and (B.3) an integral equation for the unknown polarization current can be obtained,

$$\mathbf{J}_e(\bar{\rho}) = -ik_0 Y_0[\epsilon_r(\bar{\rho}) - 1]\{\mathbf{E}^i(\bar{\rho}) - ik_0 Z_0 \int_s \mathbf{J}_e(\bar{\rho'}) \cdot \overline{\overline{\Gamma}}(\bar{\rho}, \bar{\rho'}) \mathrm{d}s'\}.$$

If the incident field has a uniform polarization, then the problem may be decoupled into TM and TE problems. For the TM case the incident, scattered, and hence, the polarization current have only z components and the integral equation is

$$\begin{aligned} J_z(x,y) = \; & -ik_0 Y_0[\epsilon_r(x,y)-1]E_z^i(x,y) + i\tfrac{k_0^2}{4}[\epsilon_r(x,y)-1] \\ & \int_s J_z(x',y')H_0^{(1)}(k_0 \mid \vec{\rho}-\vec{\rho'} \mid)\mathrm{d}x'\mathrm{d}y'\}. \end{aligned} \tag{B.4}$$

In the TE case both x and y components of the polarization current are induced and they satisfy the following coupled integro-differential equations

$$\begin{aligned} J_x(x,y) = \; & -ik_0 Y_0[\epsilon_r(x,y)-1]E_x^i(x,y) + \tfrac{i}{4}[\epsilon_r(x,y)-1] \\ & \cdot\{(\tfrac{\partial^2}{\partial x^2}+k_0^2)\int_s J_x(x',y')H_0^{(1)}(k_0 \mid \vec{\rho}-\vec{\rho'} \mid)\mathrm{d}x'\mathrm{d}y' \\ & +\tfrac{\partial^2}{\partial x\partial y}\int_s J_y(x',y')H_0^{(1)}(k_0 \mid \vec{\rho}-\vec{\rho'} \mid)\mathrm{d}x'\mathrm{d}y'\} \\ J_y(x,y) = \; & -ik_0 Y_0[\epsilon_r(x,y)-1]E_y^i(x,y) + \tfrac{i}{4}[\epsilon_r(x,y)-1] \\ & \cdot\{\tfrac{\partial^2}{\partial x\partial y}\int_s J_x(x',y')H_0^{(1)}(k_0 \mid \vec{\rho}-\vec{\rho'} \mid)\mathrm{d}x'\mathrm{d}y' \\ & +(\tfrac{\partial^2}{\partial y^2}+k_0^2)\int_s J_y(x',y')H_0^{(1)}(k_0 \mid \vec{\rho}-\vec{\rho'} \mid)\mathrm{d}x'\mathrm{d}y'\} \end{aligned} \tag{B.5}$$

The resultant integro-differential operators obtained for the polarization current do not impose any restriction on the functional form of the current, in particular, the pulse function is in the domain of the operators. It should be noted here that the kernel of the integral equation (Green's function) for the TE case is more singular ($\frac{1}{\rho^2}$) than for the TM case ($\ln\rho$).

There is no known solution for these integral equations in general, but their forms are amenable to numerical solution.

B.3 Numerical Analysis

An approximate numerical solution for the integral equations that were developed in the previous section is given using the method of moment in conjunction with the pulse expansion function and the point-matching technique. The cross section of

the scatterer is divided into N rectangular cells that are small enough so that the polarization current and relative permittivity can be assumed to be constant. The unknown current can be approximated by

$$J_p(x,y) = \sum_{m=1}^{N} J_m P(x - x_m, y - y_m), \quad p = x, y, \text{ or } z \tag{B.6}$$

where J_m are the unknown coefficients to be determined and $P(x - x_m, y - y_m)$ is the pulse function defined by

$$P(x - x_m, y - y_m) = \begin{cases} 1 & | x - x_m | < \frac{\Delta X_m}{2}, \quad | y - y_m | < \frac{\Delta Y_m}{2} \\ 0 & \text{otherwise} \end{cases} \tag{B.7}$$

By inserting the current as expanded in (B.6) into integral equations (B.4) and (B.5) and then setting the observation point at the center of the m$^{\text{th}}$ cell, a linear set of equations is formed. In matrix notation, these linear equations can be represented by

$$[\mathcal{Z}^{TM}][\mathcal{J}_z] = [\mathcal{E}_z] \tag{B.8}$$

for the TM case, where $[\mathcal{Z}^{TM}]$ is the impedance matrix, $[\mathcal{J}_z]$ is the unknown vector, and $[\mathcal{E}_z]$ is the excitation vector. Similarly for the TE case the coupled integral equation (B.5) in matrix form becomes

$$\begin{aligned} \mathcal{Z}_1^{TE}\mathcal{J}_x + \mathcal{Z}_2^{TE}\mathcal{J}_y &= \mathcal{E}_x \\ \mathcal{Z}_3^{TE}\mathcal{J}_x + \mathcal{Z}_4^{TE}\mathcal{J}_y &= \mathcal{E}_y \end{aligned} \tag{B.9}$$

where as before $\mathcal{Z}_1^{TE}, \cdots, \mathcal{Z}_4^{TE}$ are $N \times N$ impedance matrices and $\mathcal{E}_x$ and $\mathcal{E}_y$ are the excitation vectors. The above coupled matrix equation can be represented by a $2N \times 2N$ matrix equation similar to (B.8).

Although the variation of the polarization current and dielectric constant over each cell is ignored, this cannot be done for the Green's function. Actually for cells

close to the observation point, the Green's function varies considerably and its contribution must be evaluated more precisely. Let us denote the function representing the Green's function contribution by

$$I_n(x,y) = \int_{x_n-\frac{\Delta X_n}{2}}^{x_n+\frac{\Delta X_n}{2}} \int_{y_n-\frac{\Delta Y_n}{2}}^{y_n+\frac{\Delta Y_n}{2}} H_0^{(1)}(k_0\sqrt{(x-x')^2+(y-y')^2})\mathrm{d}x'\mathrm{d}y' \qquad \text{(B.10)}$$

where $1 \leq n \leq N$. If the observation point (x,y) is different from (x_n,y_n) , then the integrand in (B.10) is not singular and since $\mid x'-x_n \mid \leq \frac{\Delta X_n}{2}$ and $\mid y'-y_n \mid \leq \frac{\Delta Y_n}{2}$, its Taylor series expansion may be substituted. By retaining the terms up to the cubic order in the expansion of the Hankel function, the function (B.10) is found to be:

$$\begin{aligned} I_n(x,y) = \; & \Delta X_n \Delta Y_n \{H_0^{(1)}(k_0\sqrt{(x-x_n)^2+(y-y_n)^2}) + \tfrac{(k_0\Delta X_n)^2}{24} A(x-x_n,y-y_n) + \\ & \tfrac{(k_0\Delta Y_n)^2}{24} B(x-x_n,y-y_n)\}, \end{aligned} \qquad \text{(B.11)}$$

where

$$A(x-x_n,y-y_n) = A(r_n,\theta_n) = -H_0^{(1)}(k_0r_n)\cos^2\theta_n + \frac{H_1^{(1)}(k_0r_n)}{k_0r_n}(\cos^2\theta_n - \sin^2\theta_n), \qquad \text{(B.12)}$$

$$B(x-x_n,y-y_n) = B(r_n,\theta_n) = -H_0^{(1)}(k_0r_n)\sin^2\theta_n + \frac{H_1^{(1)}(k_0r_n)}{k_0r_n}(\sin^2\theta_n - \cos^2\theta_n) \qquad \text{(B.13)}$$

with the following definition for a pair of local polar coordinates:

$$\begin{aligned} r_n &= \sqrt{(x-x_n)^2+(y-y_n)^2} \\ \theta_n &= \arctan(\tfrac{x_n-x}{y_n-y}). \end{aligned} \qquad \text{(B.14)}$$

The second order derivatives of $I_n(x,y)$ are also needed for calculation of the impedance

matrix elements for the TE case, and are given by

$$
\begin{aligned}
(\tfrac{\partial^2}{\partial x^2}+k_0^2)I_n(x,y) = \;& \Delta X_n \Delta Y_n k_0^2 \{H_0^{(1)}(k_0 r_n)\sin^2\theta_n + \tfrac{H_1^{(1)}(k_0 r_n)}{k_0 r_n}(\cos^2\theta_n - \sin^2\theta_n) \\
& + \tfrac{\Delta X^2}{24}(\tfrac{\partial^2}{\partial x^2}+k_0^2)A(r_n,\theta_n)\tfrac{\Delta Y^2}{24}(\tfrac{\partial^2}{\partial x^2}+k_0^2)B(r_n,\theta_n)\} \\
(\tfrac{\partial^2}{\partial y^2}+k_0^2)I_n(x,y) = \;& \Delta X_n \Delta Y_n k_0^2 \{H_0^{(1)}(k_0 r_n)\cos^2\theta_n + \tfrac{H_1^{(1)}(k_0 r_n)}{k_0 r_n}(\sin^2\theta_n - \cos^2\theta_n) \\
& \tfrac{\Delta X^2}{24}(\tfrac{\partial^2}{\partial y^2}+k_0^2)A(r_n,\theta_n)\tfrac{\Delta Y^2}{24}(\tfrac{\partial^2}{\partial y^2}+k_0^2)B(r_n,\theta_n)\}
\end{aligned}
\tag{B.15}
$$

where

$$
\begin{aligned}
\tfrac{\partial^2}{\partial x^2}A(r_n,\theta_n) = \;& k_0^2\{H_0^{(1)}(k_0 r_n)[\cos^2\theta_n(\tfrac{3}{8}\cos^2\theta_n + \tfrac{1}{8}\sin^2\theta_n) \\
& + \tfrac{2\sin^2\theta_n}{(k_0 r_n)^2}(3\cos^2\theta_n - \sin^2\theta_n)] \\
& + H_1^{(1)}(k_0 r_n^q)[\tfrac{5}{k_0 r_n^q}\cos^2\theta_n^q \sin^2\theta_n^q - \tfrac{4\sin^2\theta_n}{(k_0 r_n)^3}(3\cos^2\theta_n - \sin^2\theta_n)] \\
& + H_2^{(1)}(k_0 r_n)[-\tfrac{1}{2}\cos^4\theta_n + \tfrac{\sin^2\theta_n}{(k_0 r_n)^2}(-9\cos^2\theta_n + \sin^2\theta_n)] \\
& + H_4^{(1)}(k_0 r_n)[\tfrac{1}{8}\cos^2\theta_n(\cos^2\theta_n - \sin^2\theta_n)]\},
\end{aligned}
\tag{B.16}
$$

$$
\begin{aligned}
\tfrac{\partial^2}{\partial x^2}A(r_n,\theta_n) = \;& k_0^2\{H_0^{(1)}(k_0 r_n)[\sin^2\theta_n(\tfrac{3}{8}\cos^2\theta_n + \tfrac{1}{8}\sin^2\theta_n) \\
& + \tfrac{2\cos^2\theta_n}{(k_0 r_n)^2}(\cos^2\theta_n - 3\sin^2\theta_n)] \\
& + H_1^{(1)}(k_0 r_n)[-\tfrac{4}{k_0 r_n}\cos^2\theta_n \sin^2\theta_n + \tfrac{4\cos^2\theta_n}{(k_0 r_n)^3}(3\sin^2\theta_n - \cos^2\theta_n)] \\
& + H_2^{(1)}(k_0 r_n)[-\tfrac{1}{2}\sin^2\theta_n \cos^2\theta_n + \tfrac{\cos^2\theta_n}{(k_0 r_n)^2}(9\sin^2\theta_n - \cos^2\theta_n)] \\
& + H_4^{(1)}(k_0 r_n)[\tfrac{1}{8}\sin^2\theta_n(\cos^2\theta_n - \sin^2\theta_n)]\},
\end{aligned}
\tag{B.17}
$$

$$
\begin{aligned}
\tfrac{\partial^2}{\partial x^2}B(r_n,\theta_n) = \;& k_0^2\{H_0^{(1)}(k_0 r_n)[\cos^2\theta_n(\tfrac{3}{8}\sin^2\theta_n + \tfrac{1}{8}\cos^2\theta_n) \\
& + \tfrac{2\sin^2\theta_n}{(k_0 r_n)^2}(\sin^2\theta_n - 3\cos^2\theta_n)] \\
& + H_1^{(1)}(k_0 r_n)[\tfrac{\sin^2\theta_n}{k_0 r_n}(-4\cos^2\theta_n + \sin^2\theta_n) + \tfrac{4\sin^2\theta_n}{(k_0 r_n)^3}(3\cos^2\theta_n - \sin^2\theta_n)] \\
& + H_2^{(1)}(k_0 r_n)[-\tfrac{1}{2}\sin^2\theta_n \cos^2\theta_n + \tfrac{\sin^2\theta_n}{(k_0 r_n)^2}(9\cos^2\theta_n - \sin^2\theta_n)] \\
& + H_4^{(1)}(k_0 r_n)[\tfrac{1}{8}\cos^2\theta_n(\sin^2\theta_n - \cos^2\theta_n)]\},
\end{aligned}
\tag{B.18}
$$

$$\begin{aligned}\frac{\partial^2}{\partial z^2}B(r_n,\theta_n) = \; & k_0^2\{H_0^{(1)}(k_0r_n)[\sin^2\theta_n(\tfrac{3}{8}\sin^2\theta_n+\tfrac{1}{8}\cos^2\theta_n)\\ & +\tfrac{2\cos^2\theta_n}{(k_0r_n)^2}(3\sin^2\theta_n-\cos^2\theta_n)]\\ & +H_1^{(1)}(k_0r_n)[\tfrac{5}{k_0r_n}\sin^2\theta_n\cos^2\theta_n-\tfrac{4\cos^2\theta_n}{(k_0r_n)^3}(3\sin^2\theta_n-\cos^2\theta_n)]\\ & +H_2^{(1)}(k_0r_n)[-\tfrac{1}{2}\sin^4\theta_n-\tfrac{\cos^2\theta_n}{(k_0r_n)^2}(9\sin^2\theta_n-\cos^2\theta_n)]\\ & +H_4^{(1)}(k_0r_n)[\tfrac{1}{8}\sin^2\theta_n(\sin^2\theta_n-\cos^2\theta_n)]\}.\end{aligned} \tag{B.19}$$

We also note that an exact analytical expression for $\frac{\partial^2}{\partial x\partial y}I_n(x,y)$ can be obtained without using the Taylor expansion and is given by

$$\begin{aligned}\frac{\partial^2}{\partial x\partial y}I_n(x,y) = \; & H_0^{(1)}(k_0\sqrt{(x-x_n-\tfrac{\Delta X_n}{2})^2+(y-y_n-\tfrac{\Delta Y_n}{2})^2})\\ & -H_0^{(1)}(k_0\sqrt{(x-x_n-\tfrac{\Delta X_n}{2})^2+(y-y_n+\tfrac{\Delta Y_n}{2})^2})\\ & -H_0^{(1)}(k_0\sqrt{(x-x_n+\tfrac{\Delta X_n}{2})^2+(y-y_n-\tfrac{\Delta Y_n}{2})^2})+\\ & H_0^{(1)}(k_0\sqrt{(x-x_n+\tfrac{\Delta X_n}{2})^2+(y-y_n+\tfrac{\Delta Y_n}{2})^2})\end{aligned} \tag{B.20}$$

When the observation point is in the center of the cell itself, the Taylor series expansion cannot be used. In this case we can employ the small argument expansion of the Hankel function, i.e.

$$H_0^{(1)}(x)\approx(1-\frac{x^2}{4})+\frac{2i}{\pi}[(\ln\frac{x}{2}+\gamma)(1-\frac{x^2}{4})+\frac{x^2}{4}]. \tag{B.21}$$

Then at the center of the cell (self-cell contribution), we have

$$\begin{aligned}I_n(x_n,y_n) = \; & \tfrac{i4}{\pi}\{\tfrac{k_0^2\Delta X_n\Delta Y_n}{2}[\gamma-\tfrac{i\pi+3}{2}+\ln(\tfrac{k_0\sqrt{(\Delta X_n)^2+(\Delta Y_n)^2}}{2})]\\ & +(\tfrac{k_0\Delta X_n}{2})^2\arctan(\tfrac{\Delta Y_n}{\Delta X_n})+(\tfrac{k_0\Delta Y_n}{2})^2(\tfrac{\pi}{2}-\arctan(\tfrac{\Delta Y_n}{\Delta X_n}))\}.\end{aligned} \tag{B.22}$$

Using the same expansion we can also get

$$\begin{aligned}(\tfrac{\partial^2}{\partial x^2}+k_0^2)I_n(x_n,y_n) = \; & \tfrac{i4}{\pi}\{\tfrac{k_0^2\Delta X_n\Delta Y_n}{4}[\gamma-\tfrac{i\pi+3}{2}+\ln(\tfrac{k_0\sqrt{(\Delta X_n)^2+(\Delta Y_n)^2}}{2})]\\ & +2\arctan(\tfrac{\Delta Y_n}{\Delta X_n})+(\tfrac{k_0\Delta Y_n}{2})^2(\tfrac{\pi}{2}-\arctan(\tfrac{\Delta Y_n}{\Delta X_n}))\},\end{aligned} \tag{B.23}$$

$$\begin{aligned}(\tfrac{\partial^2}{\partial y^2}+k_0^2)I_n(x_n,y_n) = \; & \tfrac{i4}{\pi}\{\tfrac{k_0^2\Delta X_n\Delta Y_n}{4}[\gamma-\tfrac{i\pi+3}{2}+\ln(\tfrac{k_0\sqrt{(\Delta X_n)^2+(\Delta Y_n)^2}}{2})]\\ & +2(\tfrac{\pi}{2}-\arctan(\tfrac{\Delta Y_n}{\Delta X_n}))+(\tfrac{k_0\Delta X_n}{2})^2\arctan(\tfrac{\Delta Y_n}{\Delta X_n})\}.\end{aligned} \tag{B.24}$$

The evaluation of the second order derivatives of $I_n(x,y)$ (expressions in (B.15)) gives accurate results when $r_n \geq \lambda/60$. For smaller values of r_n the small argument expression for the Hankel function can be used. In such cases we have

$$\begin{aligned} (\tfrac{\partial^2}{\partial x^2} + k_0^2) I_n(x,y) = &\quad F_1(x,y) - F_2(x,y) \\ (\tfrac{\partial^2}{\partial y^2} + k_0^2) I_n(x,y) = &\quad G_1(x,y) - G_2(x,y) \end{aligned} \tag{B.25}$$

where

$$\begin{aligned} F_i(x,y) = &\quad k_0^2 \tfrac{\Delta X_n}{2} b_{ni} (\tfrac{3i}{\pi} - \tfrac{2i\gamma}{\pi} - 1) + (\tan \tfrac{a_{n2}}{b_{ni}} - \tan \tfrac{a_{n1}}{b_{ni}})(\tfrac{2i}{\pi} - \tfrac{ik_0^2 b_{ni}}{\pi}) \\ &- \tfrac{ib_{ni}k_0^2}{\pi} [a_{n2} \ln \tfrac{\sqrt{a_{n2}^2 + b_{ni}^2}}{2} - a_{n1} \ln \tfrac{\sqrt{a_{n1}^2 + b_{ni}^2}}{2}] \\ G_i(x,y) = &\quad k_0^2 \tfrac{\Delta Y_n}{2} a_{ni} (\tfrac{3i}{\pi} - \tfrac{2i\gamma}{\pi} - 1) + (\tan \tfrac{b_{n2}}{a_{ni}} - \tan \tfrac{b_{n1}}{a_{ni}})(\tfrac{2i}{\pi} - \tfrac{ik_0^2 a_{ni}}{\pi}) \\ &- \tfrac{ia_{ni}k_0^2}{\pi} [b_{n2} \ln \tfrac{\sqrt{b_{n2}^2 + a_{ni}^2}}{2} - b_{n1} \ln \tfrac{\sqrt{b_{n1}^2 + a_{ni}^2}}{2}] \end{aligned} \tag{B.26}$$

with

$$a_{ni} = \begin{cases} x - x_n - \frac{\Delta X_n}{2} & i = 1 \\ x - x_n + \frac{\Delta X_n}{2} & i = 2 \end{cases} \tag{B.27}$$

$$b_{ni} = \begin{cases} y - y_n - \frac{\Delta Y_n}{2} & i = 1 \\ y - y_n + \frac{\Delta Y_n}{2} & i = 2 \end{cases} \tag{B.28}$$

Now we are in a position to express the impedance matrix elements in terms of $I_n(x,y)$. The off-diagonal entries of the impedance matrix for the TM case are given by

$$Z_{mn}^{TM} = \frac{ik_0^2}{4} [\epsilon_r(x_m, y_m) - 1] I_n(x_m, y_m) \tag{B.29}$$

and the diagonal entries are

$$Z_{nn}^{TM} = \frac{ik_0^2}{4} [\epsilon_r(x_n, y_n) - 1] I_n(x_n, y_n) - 1 \tag{B.30}$$

For TE polarization, where the impedance matrix is composed of four sub-impedance

matrices, the off-diagonal elements of each matrix are

$$\begin{aligned} Z_{1mn}^{TE} &= \tfrac{i}{4}[\epsilon_r(x_m,y_m)-1][(\tfrac{\partial^2}{\partial x^2}+k_0^2)I_n(x_m,y_m)] \\ Z_{2mn}^{TE} &= \tfrac{i}{4}[\epsilon_r(x_m,y_m)-1][\tfrac{\partial^2}{\partial x\partial y}I_n(x_m,y_m)] \\ Z_{3mn}^{TE} &= Z_{2mn}^{TE} \\ Z_{4mn}^{TE} &= \tfrac{i}{4}[\epsilon_r(x_m,y_m)-1][(\tfrac{\partial^2}{\partial y^2}+k_0^2)I_n(x_m,y_m)] \end{aligned} \tag{B.31}$$

and the diagonal elements are given by

$$\begin{aligned} Z_{1nn}^{TE} &= \tfrac{i}{4}[\epsilon_r(x_n,y_n)-1][(\tfrac{\partial^2}{\partial x^2}+k_0^2)I_n(x_n,y_n)]-1 \\ Z_{2nn}^{TE} &= 0 \\ Z_{3nn}^{TE} &= 0 \\ Z_{4nn}^{TE} &= \tfrac{i}{4}[\epsilon_r(x_n,y_n)-1][(\tfrac{\partial^2}{\partial y^2}+k_0^2)I_n(x_n,y_n)]-1 \end{aligned} \tag{B.32}$$

The excitation vector elements for the TM and TE cases, respectively, are given by

$$e_m^{TM} = ik_0Y_0[\epsilon_r(x_m,y_m)-1]E_z^i(x_m,y_m), \tag{B.33}$$

and

$$e_m^{TE} = ik_0Y_0[\epsilon_r(x_m,y_m)-1]E_x^i(x_m,y_m), \tag{B.34}$$

$$e_{m+N}^{TE} = ik_0Y_0[\epsilon_r(x_m,y_m)-1]E_y^i(x_m,y_m). \tag{B.35}$$

Once the matrix equation is solved for the polarization current, the scattered field can be computed at any point. The primary interest is the far field expressions which can be obtained by employing the large argument expansion of the Hankel functions. The scattered field, in the far zone, is in the $\hat{z}$ and $\hat{\phi}$ directions for TM and TE polarization, respectively. If the polar coordinate of the scattering direction is denoted by (ρ,ϕ_s), in the far zone we have

$$r_n \approx \rho - x_n\cos\phi_s - y_n\sin\phi_s \tag{B.36}$$

and the far field amplitudes as defined by (5.72) for TM and TE cases are

$$\mathbf{P}^{TM} = \hat{z}\frac{-k_0 Z_0}{4}\sum_{n=1}^{N} J_z(x_n, z_n)\Delta X_n \Delta Y_n [1 - \frac{(k_0\Delta X_n)^2}{24}\cos^2\phi_s - \frac{(k_0\Delta Y_n)^2}{24}\sin^2\phi_s] \cdot e^{-ik_0(\cos\phi_s x_n + \sin\phi_s y_n)}, \tag{B.37}$$

$$\mathbf{P}^{TE} = \hat{\phi}\frac{k_0 Z_0}{4}\sum_{n=1}^{N} \Delta X_n \Delta Y_n [1 - \frac{(k_0\Delta X_n)^2}{24}\cos^2\phi_s - \frac{(k_0\Delta Y_n)^2}{24}\sin^2\phi_s] \cdot e^{-ik_0(\cos\phi_s x_n + \sin\phi_s y_n)}[J_y(x_n, z_n)\cos\phi_s - J_x(x_n, z_n)\sin\phi_s]. \tag{B.38}$$

B.4 Extension to Three-Dimensional Scattering

In this section we obtain a connection between the two- and three-dimensional radar cross sections of cylinders of infinite and finite length respectively. The finite cylinder is just a section of the infinite cylinder and if the length is large compared with the wavelength we can assume the polarization current to be identical with that of the infinite cylinder.

If the observation point is in $x - y$ plane and its direction is denoted by $\hat{k}_s$, the scattered field in the far zone of the cylinder is

$$\mathbf{E}^s \approx \frac{e^{ik_0 r}}{k_0 r}\frac{-ik_0^2 Z_0}{4\pi}\int_{-l/2}^{l/2}\int_s \hat{k}_s \times \hat{k}_s \times \mathbf{J}_e(r')e^{-ik_0\hat{k}_s\cdot r'}\mathrm{d}s'\mathrm{d}z' . \tag{B.39}$$

Since $\mathbf{J}$ is independent of the axial variable z, the z integration can be carried out, in which case the expression for the far field amplitude reduces to

$$\mathbf{S} = \frac{-ik_0^2 Z_0}{4\pi} l \int_s \hat{k}_s \times \hat{k}_s \times \mathbf{J}_e(\rho')e^{-ik_0\hat{k}_s\cdot\rho'}\mathrm{d}s' . \tag{B.40}$$

For an infinitely long cylinder the electric field in the far zone is approximated by

$$\mathbf{E}^s \approx \sqrt{\frac{2}{\pi k_0 \rho}}e^{i(k_0\rho - \pi/4)}\frac{k_0 Z_0}{4}\int_s \hat{k}_s \times \hat{k}_s \times \mathbf{J}_e(\rho')e^{-ik_0\hat{k}_s\cdot\rho'}\mathrm{d}s' . \tag{B.41}$$

which results in the two-dimensional far field amplitude

$$\mathbf{P} = \frac{k_0 Z_0}{4}\int_s \hat{k}_s \times \hat{k}_s \times \mathbf{J}_e(\rho')e^{-ik_0\hat{k}_s\cdot\rho'}\mathrm{d}s' . \tag{B.42}$$

A comparison of equations (B.40) and (B.42) shows that

$$\mathbf{S} = \frac{-2iL}{\lambda}\mathbf{P}, \tag{B.43}$$

and the relationship between the two- and three-dimensional radar cross sections is:

$$\sigma_3 = \frac{2L^2}{\lambda}\sigma_2. \tag{B.44}$$

BIBLIOGRAPHY

BIBLIOGRAPHY

[1] Attema, E. P. W., and F. T. Ulaby, "Vegetation model as a water cloud," *Radio Sci.*, 13, pp. 357-364, 1978.

[2] Bates, R.H.T., and D.J.N. Wall, "Chandrasekhar transformation improve convergence of computation of scattering from linearly stratified media," *IEEE Trans. Antennas Propag.*, 24, pp. 251-251, 1976.

[3] Beckmann, P., The Depolarization of Electromagnetic Waves, Boulder, Co: The Golem Press, 1968.

[4] Borel, C. C., and R. E. McIntosh. "A backscattering model for various foliated deciduous tree types at millimeter wavelengths," *Proceedings of IEEE Geoscience and Remote Sensing Symposium*, Zurich, 8-11 Sept. 1986.

[5] Bush, T. F., and F. T. Ulaby, "Radar return from a continuous vegetation canopy," *IEEE Trans. Antenna Propag.*, 24, pp. 269-276, May 1976.

[6] Cabayan, H.S., and R.C. Murphy, "Scattering of electromagnetic waves by rough perfectly conducting circular cylinders," *IEEE Trans. Antennas Propag.*, 21, pp. 893-895, 1973.

[7] Clemmow, P.C., and V.H. Weston, "Studies in radar cross section XXXVI-Diffraction of a plane wave by an almost circular cylinder," *Radiation Laboratory Report No. 2871-3-T*, The University of Michigan, Sept. 1959.

[8] Debye, P. (1929), Polar Molecules, Dover, New York.

[9] Dobson, M. C., 1987, personal communication.

[10] Durden, S.J., J.J. van Zyle, and H.A. Zebker, "Modeling and observation of the radar polarization signature of forested areas," *IEEE Trans. Geoscience and Remote Sensing*, 1988 (in press).

[11] Eftimiu, C., and P.L. Huddleston, "Natural frequencies and modes of finite open circular cylinders," *IEEE Trans. Antennas Propag.*, 31, pp. 910-917, 1983.

[12] El-Rayes, M. A., and F. T. Ulaby, "Microwave Dielectric Spectrum of Vegetation - Part I: Experimental Observations," *IEEE Trans. Geoscience and Remote Sensing*, 25, pp. 541-549, 1987.

[13] El-Rayes, M. A., and F. T. Ulaby, "Microwave dielectric behavior of vegetation material," *Radiation Laboratory Report No. 022132-4-T*, The University of Michigan, January 1987.

[14] Engheta, N., and C. Elachi, "Radar scattering from a diffuse vegetation layer over a smooth surface," *IEEE Geoscience and Remote Sensing*, 20, pp. 212-216, 1982.

[15] Fialkovskiy, A.T., "Diffraction of planar electromagnetic waves by a slot and a strip," *Radio Eng. Electron.*, 11, pp. 150-157, 1966.

[16] Hallikainen, M.T., F.T. Ulaby, M.C. Dobson, M.A. El-Rayes, and L.K. Wu, "Microwave dielectric behavior of wet soil–part I: Empirical models and experimental observations", *IEEE Trans. on Geoscience and Remote Sensing*, 23, pp. 25-34, 1985.

[17] Harrington, R.F., *Field Computation by Moment Methods.* New York: Macmillan, 1968.

[18] Harrington, R.F., Time-Harmonic Electromagnetic Fields, New York: McGraw-Hill, 1961.

[19] Harrington, R. F. and J. R. Mautz, "An Impedance Sheet Approximation for Thin Dielectric Shells," *IEEE Trans. Antennas Propag.*, 23, pp. 531-534, 1975.

[20] Herman, M.I., and J.L. Volakis, "High frequency scattering from polygonal impedance cylinders and strips," *IEEE Trans. Antennas Propag.*, 36, pp. 679-688, 1988.

[21] Herman, M.I., and J.L. Volakis, "High-frequency scattering by a resistive strip and extensions to conductive and impedance strips," *Radio Sci.*, 22, pp. 335-349, 1987.

[22] Hill, S.C., D.C. Chritensen, and C.H. Durney, "Power disposition patterns in magnetically-induced hyperthermia: A two-dimensional low-frequency numerical analysis," *Int. J. Radiat. Oncol. Biol. Phys.*, 1983.

[23] Hofer, R., and E. Shanda, "Signature of snow in the 5 to 94 GHz range," *Radio Sci.*, 13, pp. 365-369, 1978.

[24] Ishimaru, A., Wave Propagation and Scattering in Random Media, vols. 1,2 , New York: Academic, 1978.

[25] Karam, M.A., and A.K. Fung, "Electromagnetic scattering from a layer of finite length, randomly oriented, dielectric, circular cylinders over a rough interface with application to vegetation," *International Journal of Remote Sensing*, 9, pp. 1109-1134, 1988.

[26] Karam, M. A., A. K. Fung, and Y. M. M. Antar, "Scattering models for vegetation samples," *Proceeding of IEEE Geoscience and Remote Sensing Symposium*, vol. 2, pp. 1013-1018, 1987.

[27] Keller, J.B., R.E. Kleinman, and T.B.A. Senior, "Dipole moments in Rayleigh scattering," *J. Inst. Maths Applics*, 9, pp. 14-22, 1972.

[28] Khaskind, M.D., and L.A. Vainshteyn, "Diffraction of plane waves by a slit and a tape," *Radio Eng. Electron.* 9, pp.1492-1502, 1964.

[29] Kleinman, R.E., and T.B.A. Senior, Rayleigh scattering in Low and High Frequency Asymptotics (ed. V.K. and V.V. Vardan), North-Holland, Amsterdam, pp. 1-70, 1986.

[30] Lang, R. H., "Electromagnetic backscattering from a sparse distribution of lossy dielectric scatterers," *Radio Sci.*, 16, pp. 15-30, 1981.

[31] Langan, D.K., and D.R. Wilton, "Numerical solution of TE scattering by inhomogeneous two-dimensional composite dielectric/metallic bodies of arbitrary cross section," *Abstracts of 1986 Nat. Radio Sci. Meet.*, Philadelphia, PA, June 1986.

[32] LeVine, D. M., R. Meneghini, R. H. Lang, and S. S. Seker, "Scattering from arbitrarily oriented dielectric disks in the optics region," *J. Opt. Soc. Am.*, 73, pp. 1255-1262, 1983.

[33] LeVine, D. M., A. Schneider, R. H. Lang, and H. G. Carter, "Scattering from thin dielectric disks," *IEEE Trans. Antennas Propag.*, 33, pp. 1410-1413, 1985.

[34] Liepa, V.V., E. F. Knott, and T. B. A. Senior, "Scattering from two-dimensional bodies with absorber sheets," *Radiation Laboratory Report No. 011769-2-T*, The University of Michigan, May 1974.

[35] Mei, K., and J. Van Bladel, "Low-frequency scattering by rectangular cylinders," *IEEE Trans. Antennas Propag.*, 11, pp. 52-56, 1963.

[36] Rice, S.O., "Reflection of electromagnetic waves from slightly rough surfaces," *Commun. Pure Appl. Math.*, 4, pp. 361-378, 1951.

[37] Richmond, J.H., "Scattering by a dielectric cylinder of arbitrary cross section shape," *IEEE Trans. Antennas Propag.*, 13, pp. 334-341, 1965.

[38] —, "TE-wave scattering by dielectric a cylinder of arbitrary cross-section shape," *IEEE Trans. Antennas Propag.*, 14, pp. 460-464, July 1966.

[39] Rosenbaum, S.,and W. Bowles, "Clutter return from vegetated area," *IEEE Trans. Antenna Propag.*, 22, pp. 227-236, 1974.

[40] Ruck, G.T., D.E. Barrick, W.D. Stuart, and C.K. Krichbaum, Radar Cross Section Handbook, Volume 1, New York: Plenum Press, 1970.

[41] Senior, T.B.A., "Scattering by resistive strips," *Radio Sci.* 14, pp. 911-924, 1979.

[42] Senior, T.B.A., "Scattering by resistive strips and plates," *Radiation Laboratory Report No. 3889191-1-F*, The University of Michigan, 1985.

[43] Senior, T.B.A., and J.L. Volakis, "Sheet simulation of a thin dielectric layer," *Radio Sci.*, 22, pp. 1261-1272, 1987.

[44] Stephen, L.R., P. Diament, and S.P. Schlesinger, "Perturbation analysis of axially nonuniform electromagnetic structures using nonlinear phase progression," *IEEE Trans. Antennas Propag.*, 15, pp. 422-430, 1967.

[45] Stogryn, A., "Equation for calculating the dielectric constant of water," *IEEE Trans. Microwave Theory Techn.*, 19, pp. 733-736, 1971.

[46] Tong, T.C., "Scattering by a slightly rough cylinder and a cylinder with impedance boundary condition," *Int. J. Electron.*, 36, pp. 767-772, 1974.

[47] Tsang, L., and J.A. Kong, "Radiative transfer theory for active remote sensing of half-space random media, " *Radio Sci.*, 13, pp. 763-773, 1978.

[48] Tsang, L., J.A. Kong, and R.T. Shin, Theory of Microwave Remote Sensing, New York, NY: John Wiley and Sons, Wiley-Interscience, 1985.

[49] Tsang, L., J.A. Kong, and R.T. Shin, "Radiative transfer theory for active remote sensing of a layer of nonspherical particles," *Radio Sci.*, 19, pp. 629-642, 1984.

[50] Ulaby, F.T., R.K. Moore, and A.K. Fung, Microwave Remote Sensing: Active and Passive, Vol. III– Volume Scattering and Emission Theory, Advanced Systems and Applications, Dedham, MA: Artech House, Inc., 1986.

[51] Ulaby, F. T., and M. A. El-Rayes, "Microwave Dielectric Spectrum of Vegetation - Part II: Dual-Dispersion Model," *IEEE Trans. of Geoscience and Remote Sensing*, 25, pp. 550-557, 1987.

[52] Van Bladel, J., "Low-frequency scattering by cylindrical bodies," *Appl. Sci. Res.*, 10B, pp. 195-202, 1963.

[53] van de Hulst, H.C., Light Scattering by Small Particles, New York: Wiley, 1957.

[54] Waite, W. P., and H. C. McDonald, "Snow field mapping with k-band radar," *Remote Sensing of Environment*, I, pp. 143-150, 1969.

[55] Willis, T.M., H. Weil, and D.M. Le Vine, "Applicability of physical optics thin plate scattering formulas for remote sensing," *IEEE Trans. Geosci. Remote Sensing*, 26, pp. 153-160, 1988.

[56] Zebker, H.A., J.J. van Zyl, and D.N. Held, "Imaging Radar Polarimetry from Wave Synthesis," *J. Geophys. Res.*, 92, pp. 683-701, 1987.